

The Tenth Thermal and Fluids Analysis Workshop

Alok Majumdar, Compiler

Marshall Space Flight Center, Marshall Space Flight Center, Alabama

Proceeding of a workshop hosted and organized by the
NASA Marshall Space Flight Center Thermal and Fluids
Group and held at the Bevill Center, University of Alabama
in Huntsville, Alabama, September 13–17, 1999.

July 2001

The NASA STI Program Office...in Profile

Since its founding, NASA has been dedicated to the advancement of aeronautics and space science. The NASA Scientific and Technical Information (STI) Program Office plays a key part in helping NASA maintain this important role.

The NASA STI Program Office is operated by Langley Research Center, the lead center for NASA's scientific and technical information. The NASA STI Program Office provides access to the NASA STI Database, the largest collection of aeronautical and space science STI in the world. The Program Office is also NASA's institutional mechanism for disseminating the results of its research and development activities. These results are published by NASA in the NASA STI Report Series, which includes the following report types:

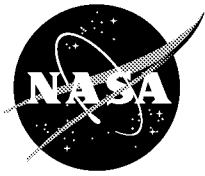
- **TECHNICAL PUBLICATION.** Reports of completed research or a major significant phase of research that present the results of NASA programs and include extensive data or theoretical analysis. Includes compilations of significant scientific and technical data and information deemed to be of continuing reference value. NASA's counterpart of peer-reviewed formal professional papers but has less stringent limitations on manuscript length and extent of graphic presentations.
- **TECHNICAL MEMORANDUM.** Scientific and technical findings that are preliminary or of specialized interest, e.g., quick release reports, working papers, and bibliographies that contain minimal annotation. Does not contain extensive analysis.
- **CONTRACTOR REPORT.** Scientific and technical findings by NASA-sponsored contractors and grantees.
- **CONFERENCE PUBLICATION.** Collected papers from scientific and technical conferences, symposia, seminars, or other meetings sponsored or cosponsored by NASA.
- **SPECIAL PUBLICATION.** Scientific, technical, or historical information from NASA programs, projects, and mission, often concerned with subjects having substantial public interest.
- **TECHNICAL TRANSLATION.** English-language translations of foreign scientific and technical material pertinent to NASA's mission.

Specialized services that complement the STI Program Office's diverse offerings include creating custom thesauri, building customized databases, organizing and publishing research results...even providing videos.

For more information about the NASA STI Program Office, see the following:

- Access the NASA STI Program Home Page at <http://www.sti.nasa.gov>
- E-mail your question via the Internet to help@sti.nasa.gov
- Fax your question to the NASA Access Help Desk at (301) 621-0134
- Telephone the NASA Access Help Desk at (301) 621-0390
- Write to:
NASA Access Help Desk
NASA Center for AeroSpace Information
7121 Standard Drive
Hanover, MD 21076-1320
(301)621-0390

NASA/CP—2001-211141



The Tenth Thermal and Fluids Analysis Workshop

Alok Majumdar, Compiler

Marshall Space Flight Center, Marshall Space Flight Center, Alabama

National Aeronautics and
Space Administration

Marshall Space Flight Center • MSFC, Alabama 35812

July 2001

Available from:

NASA Center for Aerospace Information
7121 Standard Drive
Hanover, MD 21076-1320
(301) 621-0390

National Technical Information Service
5285 Port Royal Road
Springfield, VA 22161
(703) 487-4650

FOREWORD

This yearly workshop focuses on applications of thermal and fluids analysis in the aerospace field. Its purpose is to bring industry, academia, and government together to share information and exchange ideas about analysis tools and methods. Originating from the Glenn Research Center, this was the first year the Thermal Fluids and Analysis workshop was held at the Marshall Space Flight Center.

While each workshop contains short courses, hands-on classes, and product overview lectures, only the technical papers and presentations are included in this document.

The organizers of this year's workshop consider it a privilege to participate in such an event. We would like to thank all the authors, presenters, and industry representatives who contributed to this year's success.

James W. Owen

Sheryl L. Kittredge

TABLE OF CONTENTS

THERMAL SPACECRAFT/PAYLOADS PAPER SESSION

Space Science Payloads Optical Properties Monitor (OPM) Mission Flight Anomalies Thermal Analyses

Craig P. Schmitz, AZ Technology, Inc.

Shuttle and Transfer Orbit Thermal Analysis and Testing of the Chandra X-Ray Observatory Charged-Coupled Device Imaging Spectrometer Radiator Shades

John R. Sharp, NASA MSFC

Thermal Analysis of a Finite Element Model in a Radiation Dominated Environment

Arthur T. Page, NASA MSFC

An Overview of the Thermal Challenges of Designing Microgravity Furnaces

Douglas G. Westra, NASA MSFC

Evaluation of the Use of Optical Fiber Thermometers for Thermal Control of the Quench Module Insert

Matthew R. Jones, University of Arizona, Jeffrey T. Farmer, NASA MSFC, and Shawn P. Breeding, TecMasters, Inc.

Characterization of the Heat Extraction Capability of a Compliant, Sliding, Thermal Interface for Use in a High Temperature, Vacuum Microgravity Furnace

Jenny Bellomy-Ezell, Sverdrup Tech., Inc., Jeff Farmer, NASA MSFC, Shawn Breeding and Reggie Spivey, TecMasters, Inc.

On the Application of ADI Methods to Predict Conjugate Phase Change and Diffusion Heat Transfer

Dean S. Schrage, Dynacs Engineering Company, Inc.

THERMAL PROPULSION/VEHICLES PAPER SESSION

Reusable Solid Rocket Motor Nozzle Joint-4 Thermal Analysis

J. Louie Clayton, NASA MSFC

Thermal/Pyrolysis Gas Flow Analysis of Carbon Phenolic Material

J. Louie Clayton

LOX System Prestart Conditioning on X-34

Brian K. Goode, NASA MSFC

STS-93 SSME Nozzle Tube Rupture Investigation

W. Dennis Romine, Rocketdyne Propulsion and Power, Boeing Corporation

Zero Gravity Cryogenic Vent System Concepts for Upper Stages

Robin H. Flachbart, James B. Holt, and Leon J. Hastings, NASA MSFC

Thermal Analysis of the Fastrac Chamber/Nozzle

Darrell Davis, NASA MSFC

INTERDISCIPLINARY PAPER SESSION

Method Improvements in Thermal Analysis of Mach 10 Leading Edges

Ruth M. Amundsen, NASA LaRC

A Steady State and Quasi-Steady Interface Between the Generalized Fluid System Simulation Program and the SINDA/G Thermal Analysis Program

Paul Schallhorn, Alok Majumdar, Sverdrup Tech., Inc., and Bruce Tiller, NASA MSFC

A Collaborative Analysis Tool for Thermal Protection Systems for Single Stage to Orbit Launch Vehicles

Reginald Alexander, NASA MSFC, Thomas Troy Stanley, International Space Systems, Inc.

Computation of Coupled Thermal-Fluid Problems in Distributed Memory Environment

H. Wei, H. M. Shang, and Y. S. Chen, Engineering Sciences, Inc.

Multi-Disciplinary Computing at CFDRC

W. J. Coirier, A. J. Przekwas, and V. J. Harrand, CFD Research Corporation

FLUIDS PAPER SESSION

Fluids 1a (Group Overviews)

Overview of Fluid Dynamic Activities at MSFC

Roberto Garcia, Lisa Griffin, and Ten-See Wang, NASA MSFC

Aerothermodynamics at NASA – Langley Research Center

K. James Weilmuenster, NASA LaRC

Fluids 1b (Vehicles and RBCC)

Computational Aerodynamic Design and Analysis of a Commercial Reusable Launch Vehicle

M. R. Mendenhall, H. S. Y. Chou, and J. F. Love, Nielsen Engineering Research

A Parallel Cartesian Approach for External Aerodynamics of Vehicles With Complex Geometries

M. J. Aftosmis, NASA Ames Research Center, M. J. Berger, and G. Adomavicius, Courant Institute

Parallelization of the Flow Field Dependent Variation Scheme for Solving the Triple Shock/Boundary Layer Interaction Problem

Richard Gregory Schunk, NASA MSFC, T. J. Chung, University of Alabama in Huntsville

Integration of RBCC Flowpath Analysis Tools

D. G. Messitt, Gencorp Aerojet

Ongoing Analyses of Rocket Based Combined Cycle Engines by the Applied Fluid Dynamics Analysis Group at Marshall Space Flight Center

Joseph H. Ruf, James B. Holt, and Francisco Canabal, NASA MSFC

Fluids 2a (Combustion)

Overview of the NCC

Nan-Suey Liu, NASA Glenn Research Center

An Unstructured CFD Model for Base Heating Analysis

Y. S. Chen, H. M. Shang, and Jiwen Liu, Engineering Sciences, Inc.

Optimization of a GO₂/GH₂ Impinging Injector Element

P. Kevin Tucker, NASA MSFC, and Wei Shyy and Rajkumar Vaidyanathan, University of Florida, Gainesville

Raman Spectroscopy for Instantaneous Multipoint, Multispecies Gas Concentration and Temperature Measurements in Rocket Engine Propellant Injector Flows

Joseph A. Wehrmeyer, Vanderbilt University, and Huu Phuoc Trinh, NASA MSFC

Fluids 2b (Acoustics)

Fastrac Gas Generator Testing

Tomas E. Nesman and Jay Dennis, NASA MSFC

Computational Aeroacoustic Analysis System Development

A. Hadid, W. Lin, E. Ascoli, S. Barson, and M. Sindir, Boeing/Rocketdyne

An Overview of Computational Aeroacoustic Modeling at NASA Langley

David P. Lockard, NASA Langley Research Center

Fluids 2c (Fluid Network and Thermal Environments Modeling)

Numerical Modeling of a Helium Pressurization System of Propulsion Test Article (PTA1)

Todd Steadman, Alok Majumdar, Sverdrup Technologies, Inc.,
Kimberly Holt, NASA MSFC

Analytical Assessment of a Gross Leakage Event Within the *International Space Station (ISS)* Node 2 Internal Active Thermal Control System (IATCS)

James M. Holt, NASA MSFC and Stephen E. Clanton, Sverdup
Technology, Inc.

Fluids 3 (Turbomachinery)

Time-Accurate Solutions of Incompressible Navier-Stokes Equations for Potential Turbopump Applications

Cetin Kiris, MCAT Institute and Dochan Kwak, NASA Ames
Research Center

Unshrouded Centrifugal Turbopump Impeller Design Methodology

George H. Prueger, Morgan Williams, Wei-chung Chen, John Paris,
Boeing/Rocketdyne, and Robert Williams and, Eric Stewart, NASA MSFC

Water Flow Performance of a Superscale Model of the Fastrac Liquid Oxygen Pump

Stephen Skelly, Thomas Zoladz, NASA MSFC

The Performance of Annular Diffusers Subject to Inlet Flow Field Variations and Exit Distortion

David Japikse, Concepts ETI

Rotor Design for the SSME Fuel Flowmeter

Bogdan Marcu, Boeing/Rocketdyne

Maximizing Multistage Axial Gas Turbine Efficiency Over a Range of Operating Conditions^{*}**

George S. Dulikravick, University of Texas at Arlington, Milan V. Petrovic, University of Belgrade, and Brian H. Dennis, Pennsylvania State University

The Off-Design Performance of a Carefully Instrumented Radial Inflow Turbine

David Japikse, Concepts ETI

Overview of Turbine Aerodynamic Analysis and Testing at MSFC^{*}**

Lisa W. Griffin, Susan T. Hudson, and Thomas F. Zoladz, NASA MSFC

3D Unsteady CFD Analysis of a Supersonic Turbine^{*}**

Daniel Dorney, Virginia Commonwealth University

INVITED FLUID LECTURE SESSION

Turbine Aerodynamic Design: An Overview of the Evolution of the Process and the Impact Computational Capability has Made on the End Item^{*}**

Frank W. Huber, Independent Consultant

Modeling Approximations for Multistage Flows in Turbomachinery^{*}**

Daniel J. Dorney, Virginia Commonwealth University and Douglas Sondak, Boston University

Liquid Rocket Injector Effects on Combustion Chamber Heat Flux^{*}**

Steven C. Fisher, Boeing/Rocketdyne Propulsion and Power

To Make It Fast – Make It Local^{*}**

Lynn Lewis, Silicon Graphics Incorporated, Global Professional Services

^{***} Marked papers were not available in electronic form. Please contact authors for a copy.



SPACE SCIENCE PAYLOADS OPTICAL PROPERTIES MONITOR (OPM) MISSION FLIGHT ANOMALIES THERMAL ANALYSES

Craig P. Schmitz
AZ Technology, Inc.
Huntsville, Alabama

ABSTRACT

The OPM was the first space payload that measured in-situ the optical properties of materials and had data telemetered to ground. The OPM was EVA mounted to the Mir Docking Module for an eight-month stay where flight samples were exposed to the Mir induced and natural environments. The OPM was comprised of three optical instruments; a total hemispherical spectral reflectometer, a vacuum ultraviolet spectrometer, and a total integrated scatterometer. There were also three environmental monitors; an atomic oxygen monitor, solar and infrared radiometers, and two temperature-controlled quartz crystal microbalances (to monitor contamination). Measurements were performed weekly and data telemetered to ground through the Mir data system. This paper will describe the OPM thermal control design and how the thermal math models were used to analyze anomalies which occurred during the space flight mission.

BACKGROUND

In 1986, the National Aeronautics and Space Administration (NASA) Office of Aeronautics and Space Technology (OAST) released an Announcement of Opportunity (AO) under the In-Space Technologies Experiment Program (IN-STEP). This AO was issued to seek new experiments for space flight that were under development by contractors or new experiments that were unable to be developed because of cost constraints. In response to this AO, the OPM experiment was proposed as an in-space materials laboratory to measure in-situ the effects of the space environment on thermal control materials, optical materials, and other materials of interest to the aerospace community. The OPM was selected and funded. The Marshall Space Flight Center (MSFC) in Huntsville, Alabama managed the project.

The OPM was launched on STS-81 on January 12, 1997. Mounted in a SpaceHab Double Rack, the OPM was Intravehicular Activity (IVA) transferred into the Mir Space Station on January 16, 1997. It was stowed for two and one-half months before deployment and powered up on the Mir Docking Module by the first joint Russian-American Extravehicular Activity (EVA) on April 29, 1997. On June 25, 1997, the OPM lost power because of the Progress collision into Mir's Spektr module and did not regain operational status until September 12, 1997. The OPM continued operation until January 2, 1998 when the OPM was powered down in preparation of the January 8, 1998 EVA to retrieve the OPM. After a successful Russian EVA retrieval, the OPM was later transferred IVA into the Shuttle (STS-89) and returned to Kennedy Space Center (KSC) on January 31, 1998.

A detailed description of the OPM Experiment including an overview of the system design and mission performance is provided in the "Optical Properties Monitor (OPM) System Report" ^[1]. Figure 1 is a photograph of the deployed OPM. The OPM is seen near the 2 o'clock position on the Docking Module. Figure 2 illustrates the OPM mounting orientation on the Mir Space Station. The baseline layout of the internal hardware is illustrated in Figure 3. This layout shows the locations of the electronics boxes, experiment subsystems, and sample carousel.

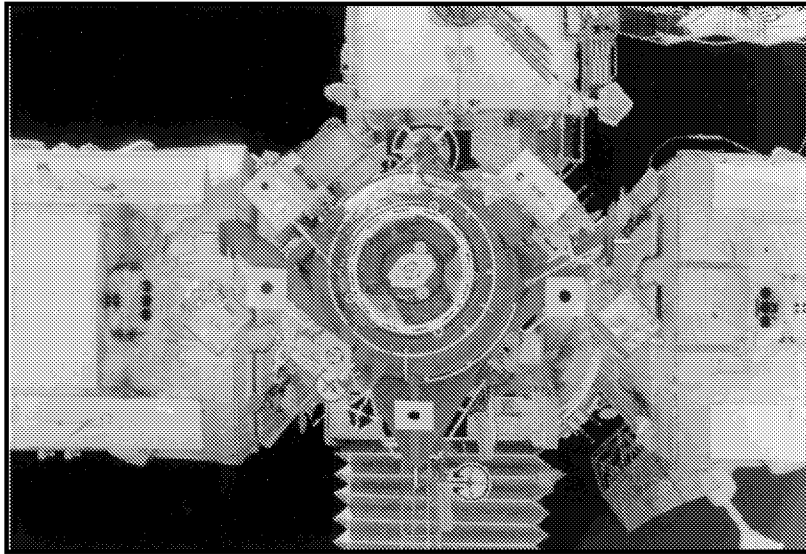


Figure 1: OPM on MIR (Docking Module End View).

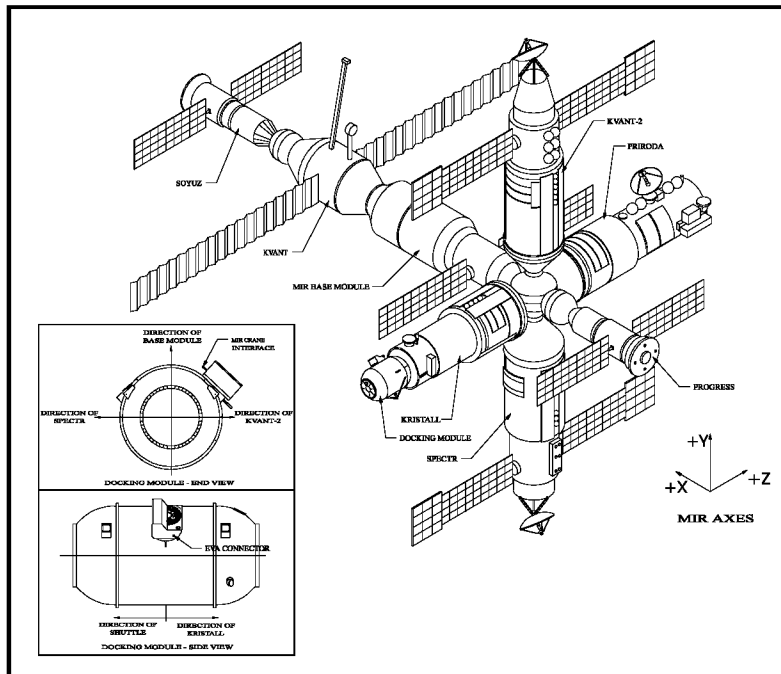


Figure 2: OPM Mounting Orientation on the Mir.

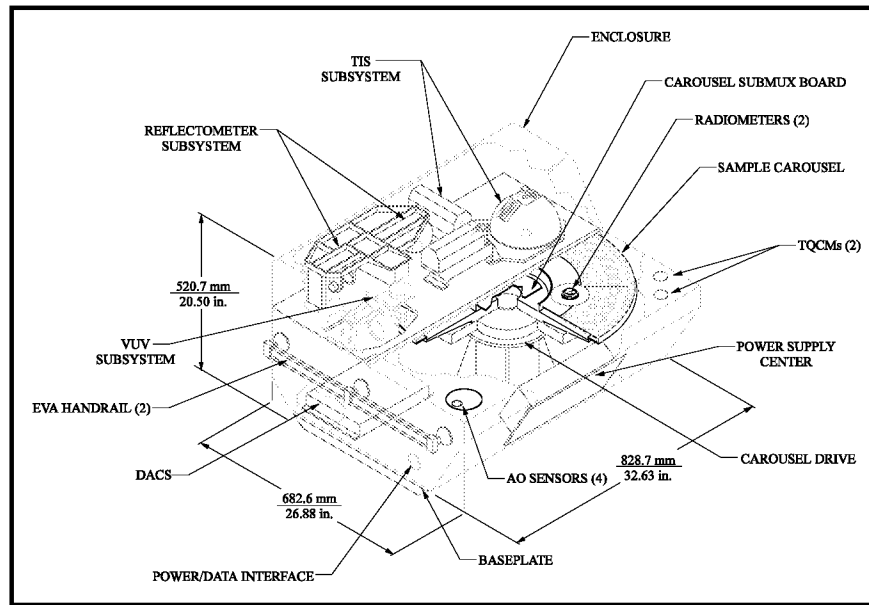


Figure 3: Layout of the Internal Hardware of the OPM.

OPM THERMAL CONTROL

The OPM experiment was modeled using SINDA'85/FLUINT^[2] and TRASYS^[3] to calculate the conduction and radiation heat transfer between the internal OPM components as well as its external environment. To assist in the accuracy of the model predictions, the OPM was added to the integrated Mir/Docking Module thermal models obtained from NASA/JSC^[4,5]. The results of the predicted thermal values dictated how the OPM thermal design was achieved for hot, cold, and nominal operating conditions. Further, the OPM timeline was analyzed to minimize peak input power requirements (kilowatts [kW], not kilowatt-hour [kWh]) and assess the internal temperature fluctuations to the OPM. These predicted thermal extremes were not to exceed the component minimum and maximum operating temperatures. Indeed, the OPM timeline was changed to modify the proposed measurement sequence which decreased the component temperature extremes and peak power (kW). However, the measurements sequence duration increased, increasing the total kWh.

Based on model predictions and the modified weekly timeline, the OPM was designed for passive thermal control with active heaters to maintain a minimum temperature of 0°C. The heaters maintained thermal control during the quiescent periods of operation when the OPM was operating in monitor mode (i.e. not performing measurements). During the measurement sequence, the heaters were switched off and the external thermal control coatings coupled with the thermal capacitance of the OPM provided sufficient thermal control. The OPM heater system design, located on the emissivity plate, consisted of two heater circuits with two 15-watt heater elements mounted in parallel in each circuit. Heater control was effected by using thermistors on this plate to thermostatically control their operation. Heater setpoints were selected approximately at 4°C (on) and 7°C (off). Thermal control was evaluated for materials exposed directly to the space environment as well as those not exposed. For exposed surfaces, the temperature control was achieved by the combination of various types of thermal control coatings, some having low solar absorptance or high solar reflectance coupled with either low thermal emittance (AZT custom coating) or high thermal emittance (white coating) in order to control absorption of direct solar irradiance and reflected solar irradiance from Mir and/or the earth (albedo). Low thermal emittance coatings were used to minimize radiation from selected OPM panels while high thermal emittance coatings were used on other panels to maximize the thermal radiation. The unexposed surfaces were covered with MLI to minimize heat transfer. The combination of materials provided the necessary thermal control to match the measurement sequence and overall timeline with the expected Mir environment.

The “Thermal Data Book for the OPM Experiment” [6] documents the details of the OPM thermal control system design including the TRASYS geometric math models, the SINDA thermal math models, the design analyses, and the thermal vacuum test program which was used to verify the math models. The “Mission Thermal Data Book for the OPM” [7] documents the OPM thermal flight data including the use of the thermal math models to evaluate the flight anomalies. A typical thermal profile, predicted by the models for the measurement sequence and compared to flight data, is shown in Figure 4.

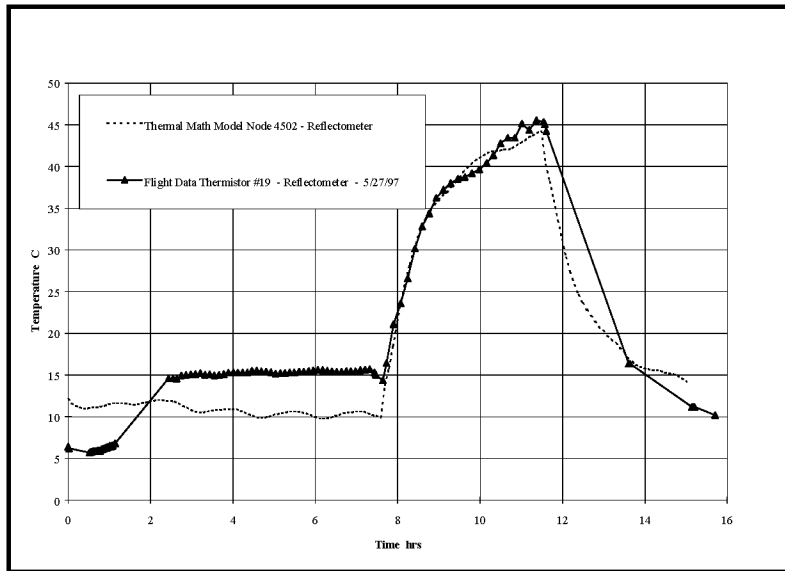


Figure 4: OPM Reflectometer Thermal Profile for the Measurement Sequence

INSTRUMENTATION

The OPM thermal instrumentation consisted of 31 thermistors. Each of the 31 thermistors is either epoxied directly to the OPM structure or epoxied into an aluminum-mounting block mechanically attached to the OPM structure. Table 1 provides a description of the 31-thermistor mounting locations.

Temperature data was recorded for each of the 31 thermistors throughout each of the 27 OPM measurement sequences/timelines. The nominal OPM measurement cycle timeline is shown in Figure 5. Figure 6 shows the combined set of 27 measurement cycle temperature profiles for Thermistor T28 located on the OPM Base Plate.

Temperature data was recorded for each of the 31 Thermistors throughout the mission while in the monitoring mode. Temperature monitor data was recorded using two different time intervals. For one two-hour period each day the monitor data was recorded using two-minute intervals. Figure 7 is an example of the two-minute monitor data for May 6-7 1997. This data provides information on the temperature variations that occur during a single 90-minute orbit. For the remainder of the day the monitor data was recorded using a two-hour time interval. This data provides information on the temperature variations that occur over a twenty-four hour period (sixteen orbits). The two-minute and two-hour monitor data have been combined into a single overall monitor data set.

All of the critical electronic components are mounted on either the Base Plate or the Emissivity Plate. During the monitoring mode (non-measurement cycle) all of the component temperatures are driven by one of these two locations. Figure 8 presents the temperature monitor data for the OPM Base Plate Thermistor (T28) and Emissivity Plate Thermistor (T09) for the month of June 1997.

Table 1: OPM Thermistor Mounting Locations.

| Thermistor # | Description | Location | Thermistor # | Description | Location |
|--------------|---------------------|---------------------|--------------|-----------------------|---------------------------|
| T00 | Thermistor VR1 | Carousel Tray 6 | T16 | Encl. Top Panel #1 | Top Panel- TQCM Side |
| T01 | Thermistor VR2 | Carousel Wheel 6 | T17 | Encl. Top Panel #2 | Top Panel - AO Side |
| T02 | Thermistor VR3 | Carousel Wheel 7 | T18 | Reflectometer #1 | Flex Mirror Mount |
| T03 | Thermistor VR4 | Carousel Tray 7 | T19 | Reflectometer #2 | Monochromator Motor Mount |
| T04 | Thermistor VR5 | Carousel Tray 8 | T20 | VUV | Main Support Bracket |
| T05 | Thermistor VR6 | Carousel Wheel 8 | T21 | TIS #1 | Green LASER (532 nm) |
| T06 | Thermistor VR7 | Carousel Tray 1 | T22 | TIS #2 | IR LASER (1064 nm) |
| T07 | Thermistor VR8 | Carousel Wheel 1 | T23 | AO | AO Motor Mount |
| T08 | Emissivity Plate #1 | E-Plate | T24 | DACS | DACS Mounting Flange |
| T09 | Emissivity Plate #2 | E-Plate | T25 | PSC | PSC Top Cover |
| T10 | Emissivity Plate #3 | E-Plate | T26 | PAC | PAC Top Cover |
| T11 | Emissivity Plate #4 | E-Plate | T27 | TQCM | TQCM Mounting Plate |
| T12 | Carousel Motor #1 | Carousel Motor | T28 | Enc. Base Plate | Base Plate |
| T13 | Carousel Motor #2 | Carousel Motor | T29 | Enc. Side Panel Left | Left Side Panel |
| T14 | Encl. Top Cover #1 | Top Cover Top Rib | T30 | Enc. Side Panel Right | Right Side Panel |
| T15 | Encl. Top Cover #2 | Top Cover Front Rib | | | |

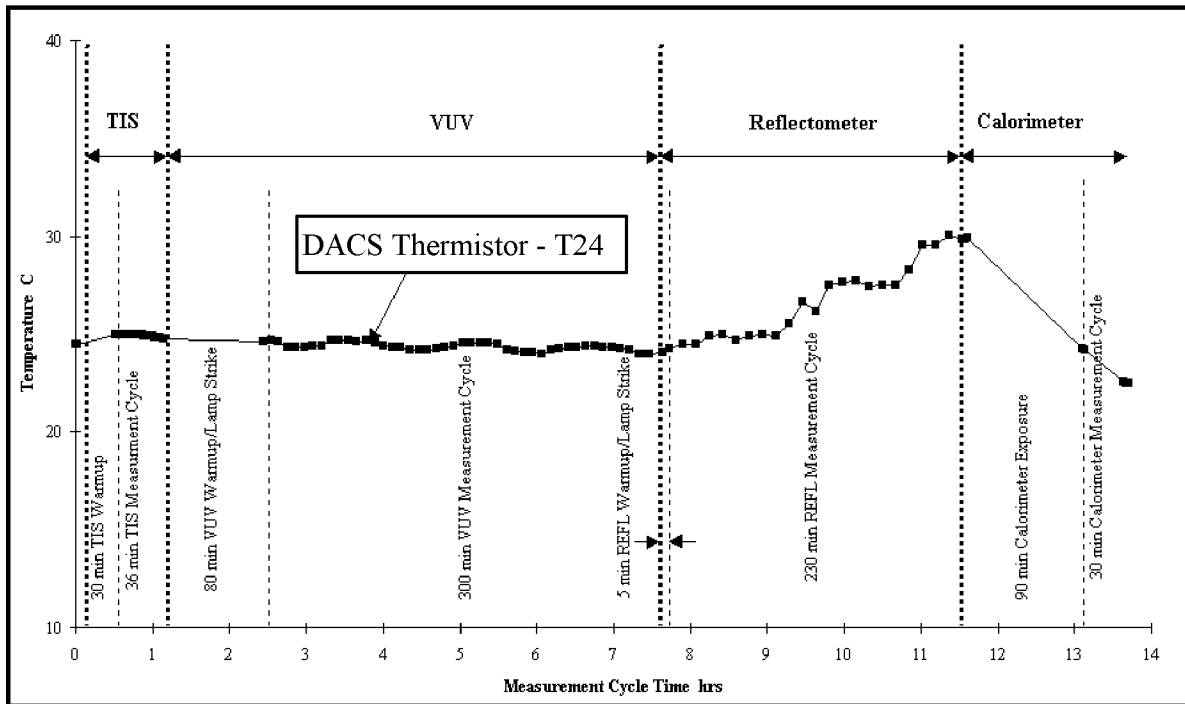


Figure 5: Nominal OPM Measurement Cycle Timeline.

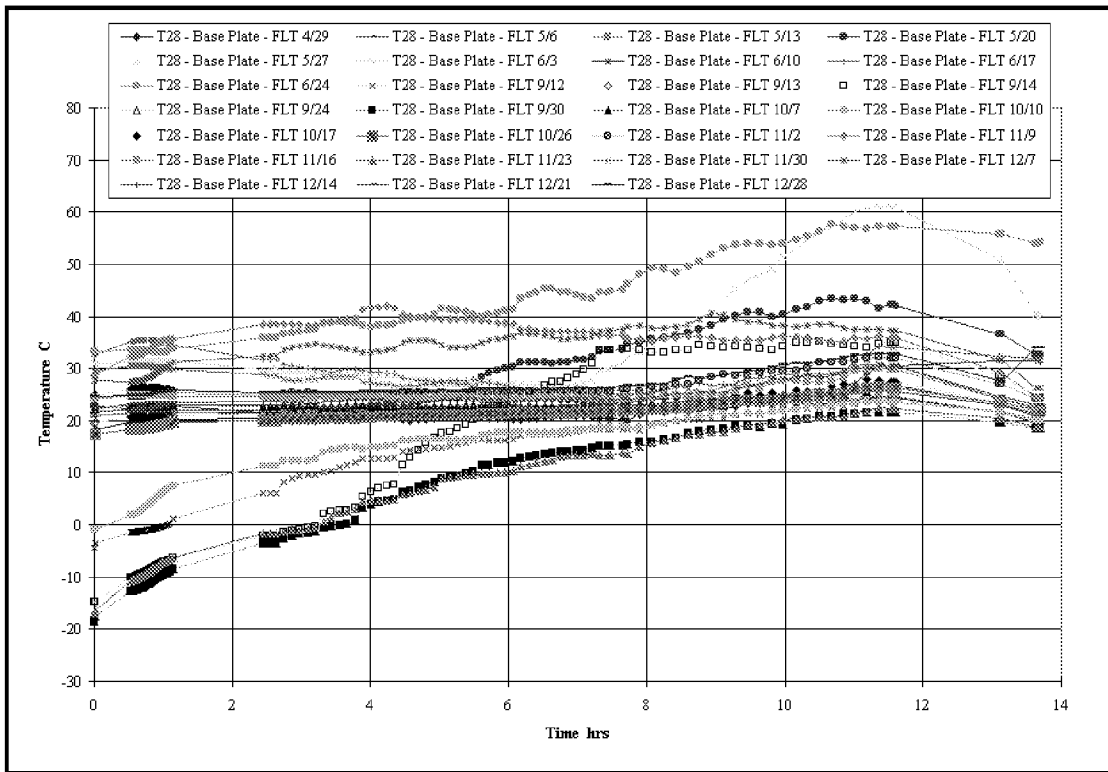


Figure 6: OPM Measurement Cycle Flight Data for Base Plate Thermistor (T28)

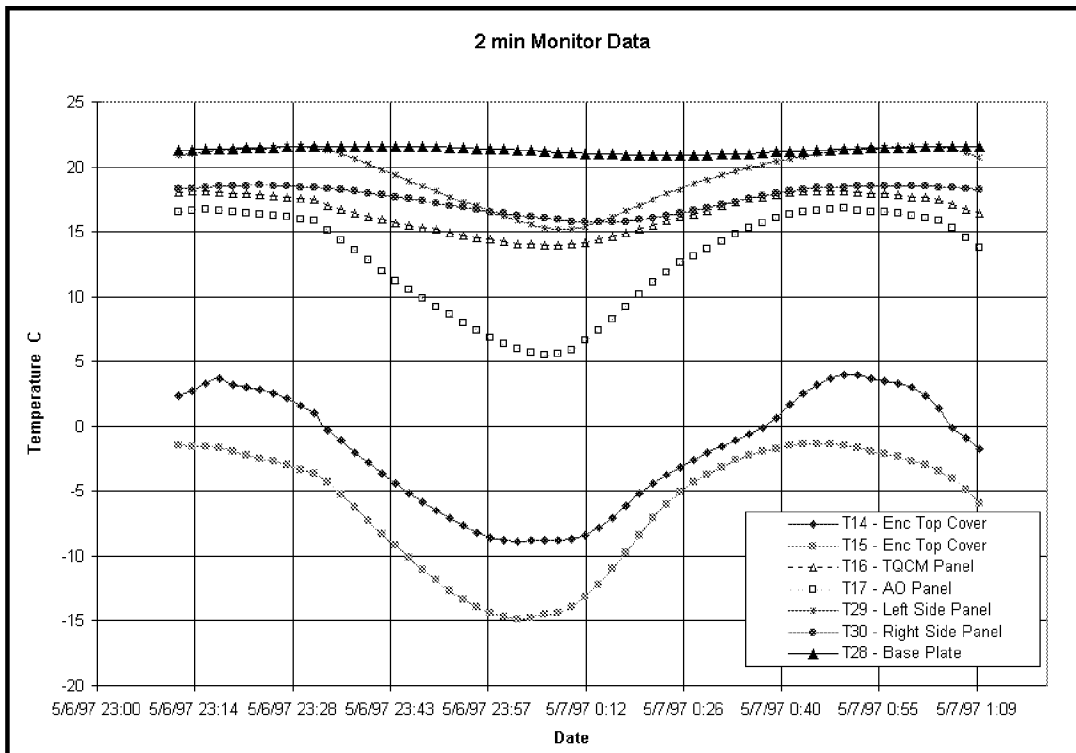


Figure 7: Example of OPM Two-Minute Monitor Data.

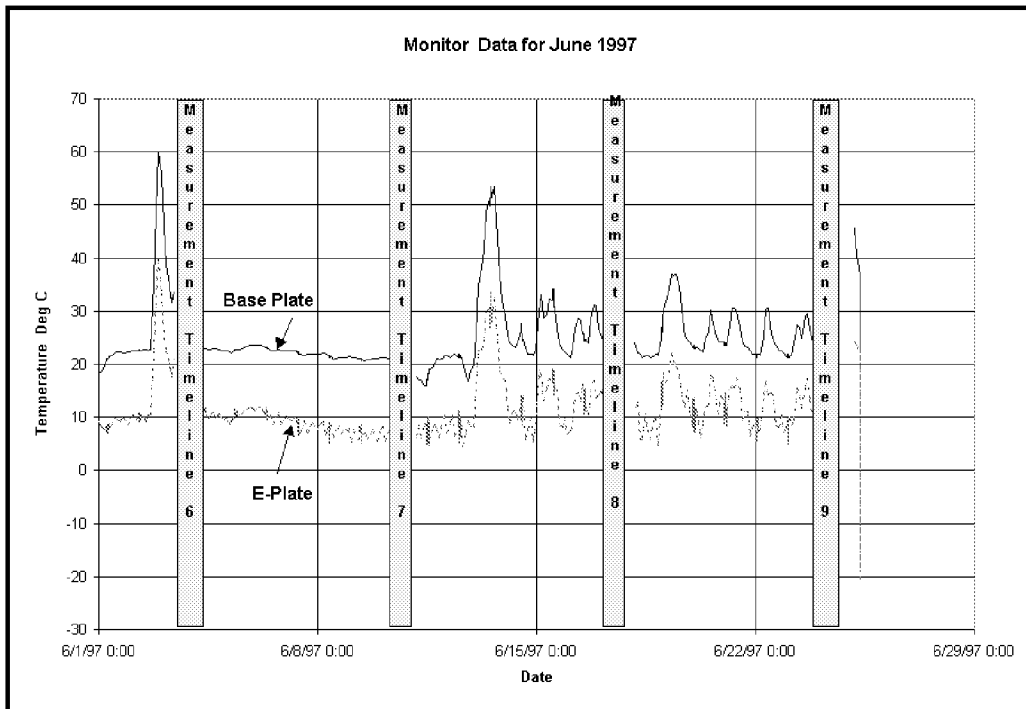


Figure 8: OPM Temperature Monitor Data for June 1997

OPM THERMAL VACUUM TEST

The OPM was designed for passive thermal control with supplemental active resistance heating to maintain an internal thermal environment between 0 and 40°C. The anticipated and documented Mir attitude orientation was gravity gradient for seventy to eighty percent of the time. To simulate this environment, the OPM was placed in a thermal vacuum chamber. Heat lamps were used to simulate the incident solar energy on the OPM. Based on thermal analyses for the OPM mounted on the Mir Docking Module, minimum and maximum operating temperatures were predicted for the “mission.” These thermal set points corresponded to OPM Base Plate temperatures of -5 and +5°C at the beginning of a measurement cycle. Multiple thermal cycles were conducted while at vacuum with functional tests performed at the minimum and maximum set points. Figure 9 illustrates the OPM Thermal Vacuum Test Cycles. Figure 10 is the OPM in the thermal vacuum chamber.

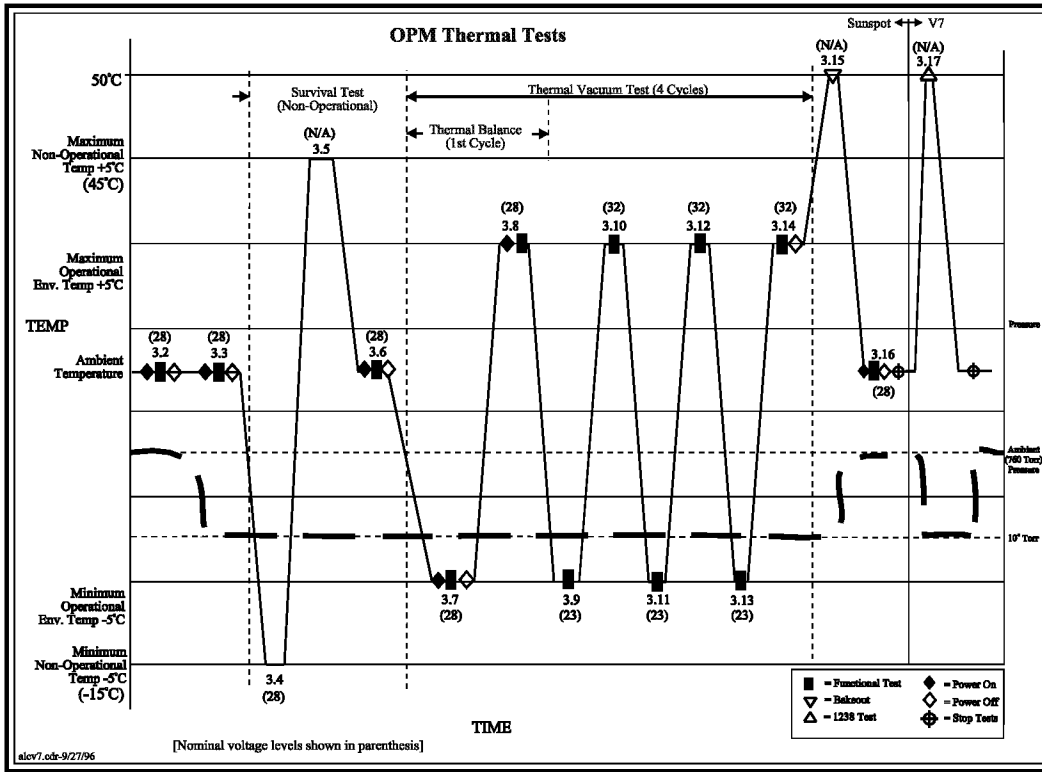


Figure 9: OPM Thermal Vacuum Test Cycles.

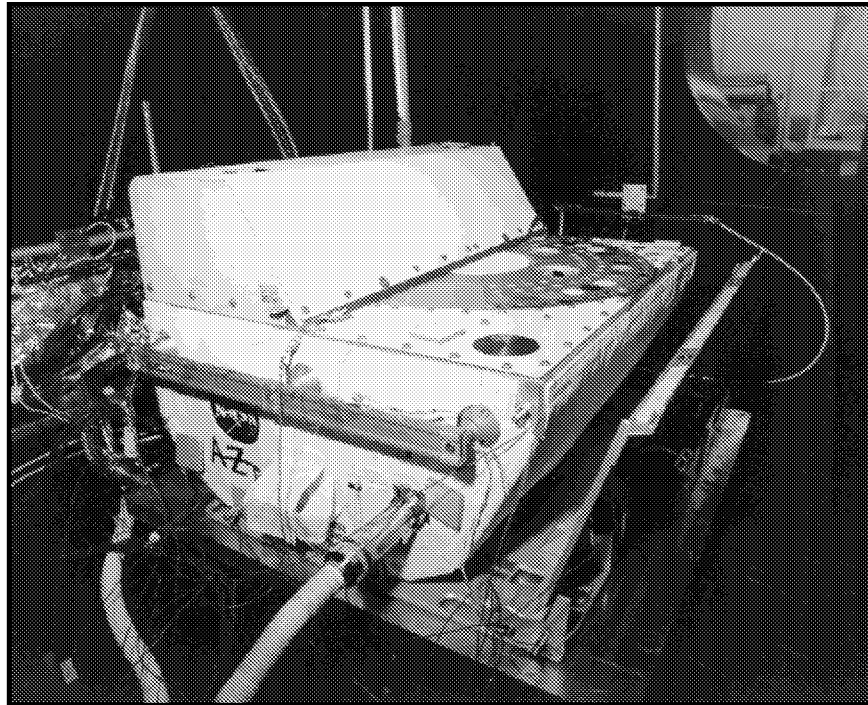


Figure 10: OPM in the Thermal Vacuum Chamber.

The thermal vacuum test began with a functional test at ambient pressure and temperature to ensure the OPM systems were setup and working properly. The chamber was evacuated to test pressure of at least 1×10^{-5} Torr (typically 3×10^{-6} Torr) and a second functional test conducted to check experiment operation at vacuum prior to beginning testing. The OPM was subjected to hot and cold survival temperatures, while non-operational, followed by a functional test at ambient temperature. Four thermal cycles were conducted, with the first concurrent with a thermal balance check to calibrate the thermal analyses to the actual hardware performance. Figure 11 is an example of the thermal balance temperature comparison between the thermistors located on the Reflectometer instrument and the OPM thermal models. The criterion for acceptable thermal balance was agreement within 5°C . The OPM proto-flight hardware successfully passed the thermal vacuum tests.

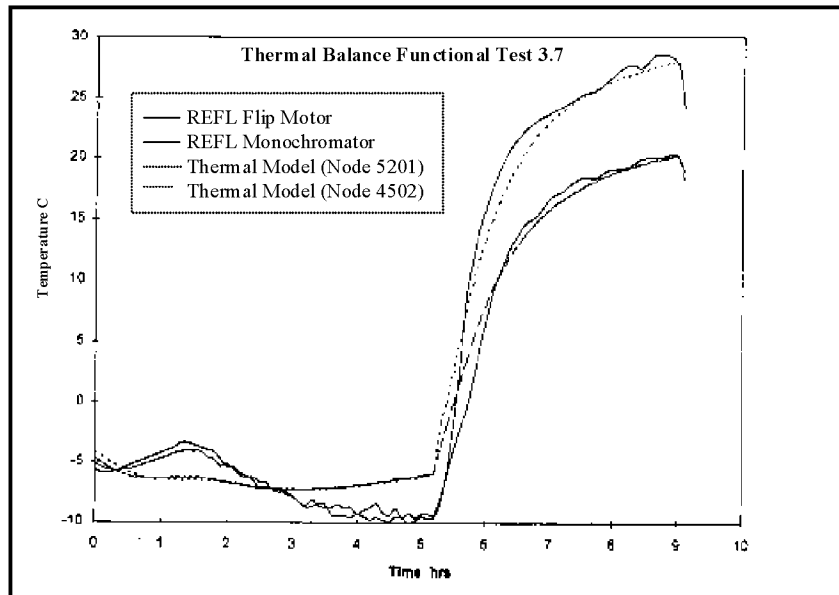


Figure 11: Thermal Balance Temperature Comparison for OPM Reflectometer Instrument.

OPM MISSION THERMAL DATA

For most space systems the primary purpose for development of thermal models is as a design tool. However, as the OPM program demonstrates, the thermal models in conjunction with flight temperature data can be extremely useful tools for evaluating the system performance and health.

One of the primary features of the OPM thermal control system is the use of Kapton-backed etched-foil electric heaters to maintain temperatures above the minimum limit temperature of 0°C . Figure 12 shows a typical temperature profile for the emissivity plate during two cycles of heaters "On" and "Off." The OPM heater "On" set point is 6500Ω that converts to 4.2°C . The OPM heater "Off" set point is 6000Ω which converts to 6.7°C . Note that the average of the emissivity plate thermistors T08 and T09 are used for controlling the heaters. The Figure 12 data is used as evidence that the heater system functioned within the design criteria.

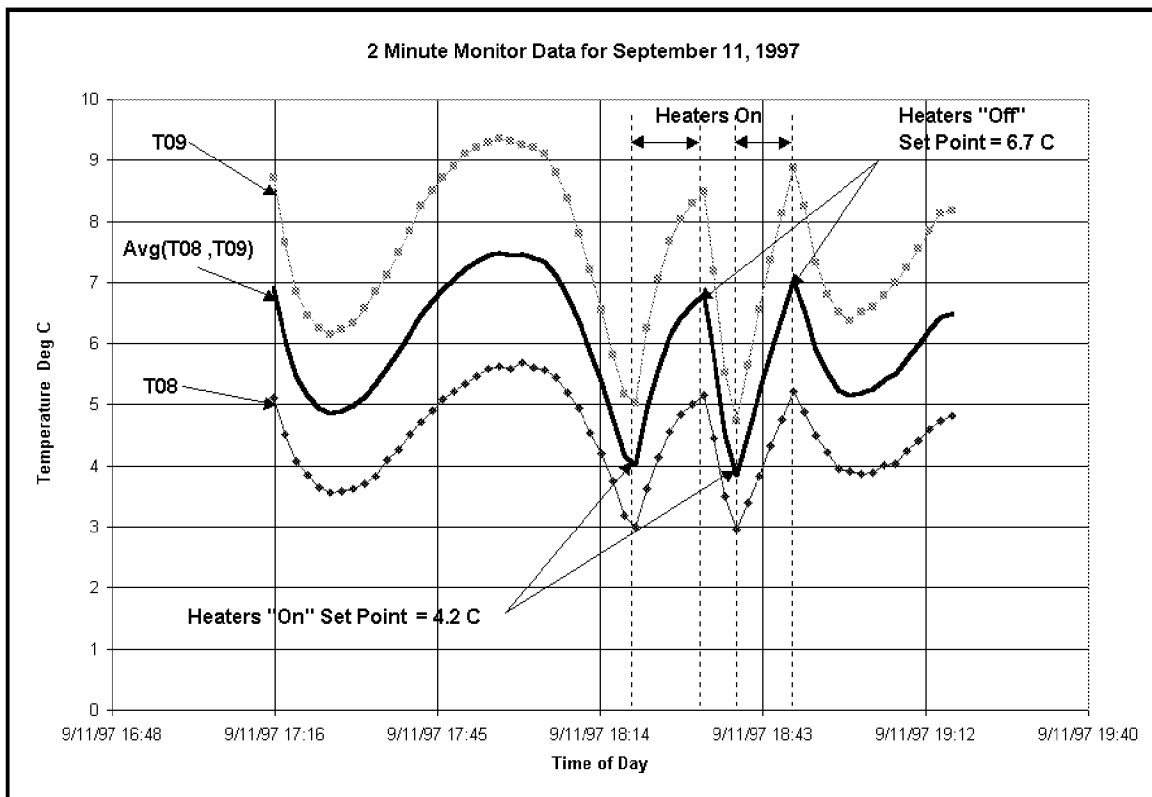


Figure 12: Typical OPM Heater Thermal Performance

In addition to evaluating specific components of the thermal control system, like the heater elements, the thermal data obtained from the OPM flight has been used to characterize the overall thermal performance of the OPM Thermal Control System. Figure 13 is an example of the temperature monitor data for the month of May, 1997. During this first month of deployment the system temperatures, represented by the base plate and emissivity plate thermistor data, was maintained between design limits (0-40°C). Figure 8, which summarizes the monitor data for June, shows the base plate temperature exceeds 40°C on June 3rd.

The thermal event on June 3 resulted in an anomaly investigation of the orbital attitude of the Mir space station. Figure 14 is an example of how the OPM thermal data was used to characterize the orbital attitude effects on OPM System temperatures. The 38 °C rise in base plate temperature on June 3rd is directly related to the attitude change of Mir. In this example the solar vector changed from 120 degrees from vertical, which is 30 degrees below the plane of the OPM sample carousel, to 25 degrees from vertical. In addition, this thermal event occurs during the four day period from June 3rd to June 7th during which the Mir orbit is 100 percent in the Sun (no Earth shadow). This set of orbital conditions describes the worst case hot orbital environment experienced by OPM. The preflight Mir attitudes used for design of OPM were Mir X-axis gravity gradient (70%), Mir X-axis solar inertial (20%) and undefined (10%). Since this attitude falls within the 10% undefined, the OPM design criteria was to maintain system temperatures below the maximum limit temperature (40°C) for a duration of 2.4 hours (10% of 1 day). The OPM base plate temperature after 2.4 hours is approximately 35°C which is below the design limit (40°C). The actual Mir attitude change lasted for 7.6 hours which exceeds the preflight design criteria and results in base plate temperatures of 60°C. Although the OPM base plate temperatures exceeded the design criteria on eight occasions (6/2, 6/13, 6/24, 11/3, 11/4, 11/27, 12/25, and 12/26) during monitoring mode and on three occasions (5/20, 6/3, and 6/24) during measurement cycles the only known temperature/external environment related failures of OPM hardware during the Mir mission is the radiometer sensor which failed on June 3rd.

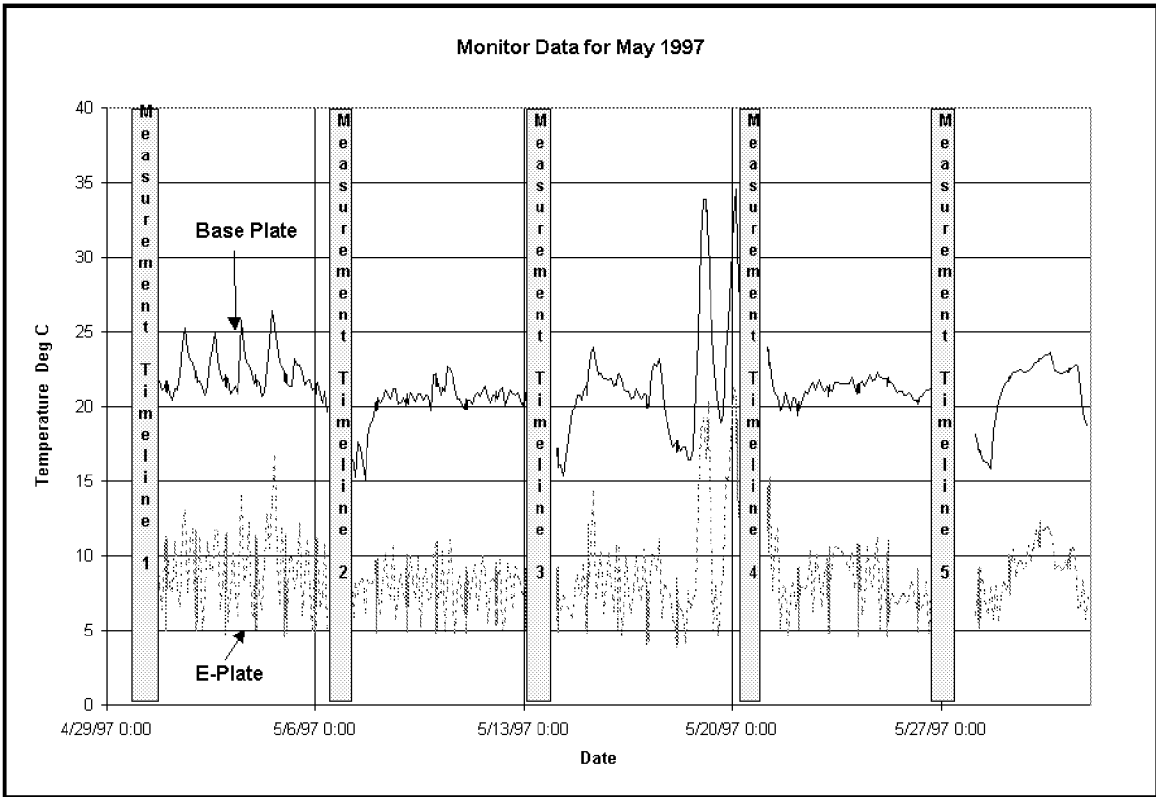


Figure 13: OPM Temperature Monitor Data for May 1997

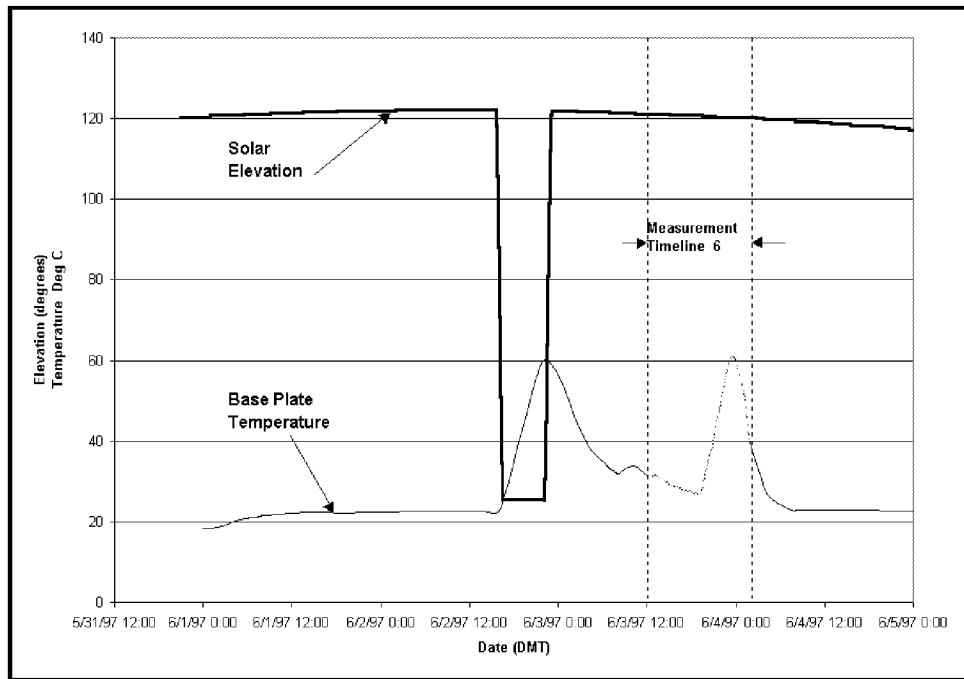


Figure 14: OPM Thermal Response to Mir Attitude Change on June 2, 1997

The first significant mission anomaly was the failure of the VUV instrument. The first indication of an anomaly with the VUV instrument occurred upon review of the first data transfer from Mir on April 30, 1997. This first data set included raw data from the measurement timeline which occurred on April 29. Included in this data were the raw data from the VUV instrument. This data was not within the expected measurement range. Immediately a fault analysis, and fault analysis tree were performed to determine possible causes for failure and possible courses of action for correcting the problem. The resulting fault tree resulted in a large number of possible causes for failure including bad detectors, VUV lamp sources, carousel position, data management software, etc. No direct evidence of the cause of the VUV failure was available real time during the mission. Visual inspection was the only methodology for evaluating many of the possible failure modes. However, the thermal data proved to be a very convincing indirect source of evidence pointing at the Deuterium Lamp as the most probably cause for failure.

Figure 15 is a comparison of the OPM April 29th Flight Data Thermistor T20 with parametric temperature profiles generated using the OPM SINDA thermal math model. Three parametric models were generated using SINDA. The first model assumes that the VUV was fully functional (20W lamp, 10W lamp heater and 4.5W stepper motors), the second model assumes that the lamp was not functional (10W lamp heater and 4.5W stepper motors), the third option assumes that both the lamp and the lamp heater are not functional (4.5W stepper motors). The model with both the lamp and lamp heater not functional shows excellent agreement with the flight data. This data was included in the VUV anomaly fault analysis which was performed during the OPM mission prior to retrieval. This thermal evidence was one of the key factors that identified the lamp as the most probable cause of the VUV anomaly. Post flight inspection of the OPM VUV confirmed that the lamp did not function due to a broken lamp heater element.

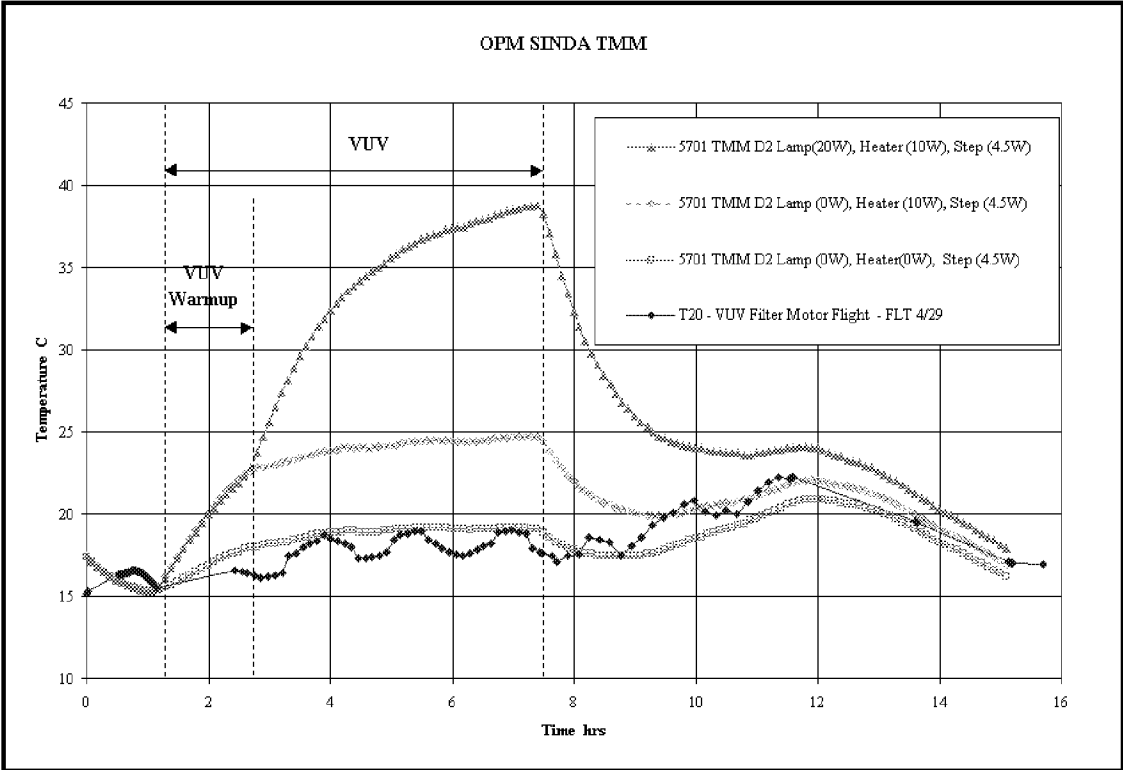


Figure 15: Typical VUV Thermal Profile.

The other major OPM mission anomaly was the loss of Mir power. This anomaly affected OPM in two significant ways. The first is the loss of power to OPM itself. The second is the resulting reduction in attitude control of Mir which continued to occur throughout the remainder of the OPM Mir mission.

The OPM experiment was flown on Mir without a real time clock. Mission elapsed time was recorded using an elapsed time clock. The result is that significant errors between the mission elapsed time and real time were produced during each of the OPM power losses. The most significant of these power losses resulted from the Progress collision with Spektr on June 25th. The collision occurred on June 25, 1997 on the Mir Station while practicing manual rendezvous procedures. Upon collision, the crew reacted quickly to seal off the leaking Spektr module and to conserve power. The OPM power was then severed in order to conserve battery power. The power remained off until September 12, 1997, when the OPM was officially repowered. Later, the OPM Team discovered the OPM power was not shut down by turning the power breaker to the "Off" position in the Docking Module and/or in the Krystal module. Instead, once the Krystal module was repowered, the power to OPM began cycling. In fact, the OPM experiment was powered up when the Mir Station entered the sunlight, and went off (unpowered) when it went beyond the terminator. When this was realized, the OPM was powered down at the power breaker until ready for official power up. Figure 16 shows the estimated power on/off status chart for the period between September 12 and October 12, 1997. The OPM did not have a real-time clock, only an elapsed timer so the exact times cannot be determined. The time is given in Decead Moscow Time (DMT) - the time used by the Mir crew.

The OPM temperature data combined with the Mir attitude data (Figure 17) and the OPM "ON" timeline (Figure 16) obtained from the Mir daily activity reports has been used to adjust the OPM mission elapsed time to a best estimate of real time. Table 2 summarizes the correction factors which have been applied to the mission elapsed time beginning with the powering "ON" of OPM on September 9, 1997. No correction has been applied to the period between September 9 and 15 due to a lack of significant Mir attitude events or accurate OPM Power status information. Figure 18 is an example of how the OPM base plate responded to Mir attitude changes on November 6 - 11, 1997. This data incorporates the seven-hour correction to the timeline as shown in Table 2. Note that "loss of power" is an anomaly that was beyond the scope of the OPM mission. The OPM design was shown to be capable of fully recovering from this condition. Sufficient thermal data was recorded to allow a reconstruction of the mission timeline within the accuracy of the 2-hour monitoring data. No science data was lost or rendered unusable due to the inaccuracy of the reconstructed mission timeline.

The OPM experiment lost Mir power on several occasions after the June 25th collision. On at least six occasions the OPM was restarted from a "Cold Soak" condition (Base Plate below -10°C). Four of the restarts were immediately followed by an OPM measurement cycle (9/12, 9/14, 9/24, and 11/23). Two of the restarts occurred during monitoring mode (~9/9 and 10/21). Figure 19 shows the rate at which the OPM recovers to nominal temperatures after a cold restart on October 21, 1997. Both the base plate and the emissivity plate are above 0°C within five hours of restart. Note that "loss of power" is an anomaly which was beyond the scope of the OPM mission. However, the OPM design was shown to be fully capable of recovering from this condition.

OPM "ON" TIME

DMT

| NASA 5 (Mike Foale), NASA 6 (Dave Wolf) | | Hour | | | | | | | | | | | | | | | | | | | | | | | | DAY | CUM |
|---|-------------|------|---|---|---|---|---|---|---|---|----|----|----|----|----|----|----|----|----|----|----|----|----|----|----|-------|-------|
| DAY | | 1 | 2 | 3 | 4 | 5 | 6 | 7 | 8 | 9 | 10 | 11 | 12 | 13 | 14 | 15 | 16 | 17 | 18 | 19 | 20 | 21 | 22 | 23 | 24 | | |
| MD 120, Fri Sep 12, 1997 | | | | | | | | | | | | | | | | | | | | | | | | | | 9.5* | 9.5 |
| MD 121 | | | | | | | | | | | | | | | | | | | | | | | | | | 24 | 33.5 |
| MD 123 Sun Sep 14, 1997 | | | | | | | | | | | | | | | | | | | | | | | | | | 21 | 54.5 |
| MD 122 Mon Sep 15, 1997 | | | | | | | | | | | | | | | | | | | | | | | | | | 16 | 70.5 |
| MD 124 Tue Sep 16, 1997 | | | | | | | | | | | | | | | | | | | | | | | | | | 5.5 | 76 |
| MD 125 | | | | | | | | | | | | | | | | | | | | | | | | | | 0 | 76 |
| MD 126 | | | | | | | | | | | | | | | | | | | | | | | | | | 0 | 76 |
| MD 127 Fri, Sep 19, 1997 | | | | | | | | | | | | | | | | | | | | | | | | | | 12? | 88 |
| MD 128 | | | | | | | | | | | | | | | | | | | | | | | | | | 24 | 112 |
| MD 129 | | | | | | | | | | | | | | | | | | | | | | | | | | 24 | 136 |
| MD 130 Mon, Sep 22, 1997 | | | | | | | | | | | | | | | | | | | | | | | | | | 4.4 | 140.4 |
| MD 131 Tue, Sep 23, 1997 | | | | | | | | | | | | | | | | | | | | | | | | | | 9 | 149.4 |
| MD 132 Wed, Sep 24, 1997 | PLND (MSMT) | | | | | | | | | | | | | | | | | | | | | | | | | 24 | 173.4 |
| MD 133 | | | | | | | | | | | | | | | | | | | | | | | | | | 24 | 197.4 |
| MD 134 | | | | | | | | | | | | | | | | | | | | | | | | | | 24 | 221.4 |
| MD 135 | | | | | | | | | | | | | | | | | | | | | | | | | | 24 | 245.4 |
| MD 136 | | | | | | | | | | | | | | | | | | | | | | | | | | 24 | 269.4 |
| MD 137 | | | | | | | | | | | | | | | | | | | | | | | | | | 24 | 293.4 |
| MD 138 | | | | | | | | | | | | | | | | | | | | | | | | | | 24 | 317.4 |
| MD 139 Wed, Oct 1, 1997 | PLND (MSMT) | | | | | | | | | | | | | | | | | | | | | | | | | 24 | 341.4 |
| MD 140 | | | | | | | | | | | | | | | | | | | | | | | | | | 24 | 365.4 |
| MD 008 | | | | | | | | | | | | | | | | | | | | | | | | | | 24 | 389.4 |
| MD 009 | | | | | | | | | | | | | | | | | | | | | | | | | | 24 | 413.4 |
| MD 010 | | | | | | | | | | | | | | | | | | | | | | | | | | 24 | 437.4 |
| MD 011 | | | | | | | | | | | | | | | | | | | | | | | | | | 24 | 461.4 |
| MD 012 | | | | | | | | | | | | | | | | | | | | | | | | | | 24 | 485.4 |
| MD 013 Wed, Oct 8, 1997 | PLND (MSMT) | | | | | | | | | | | | | | | | | | | | | | | | | 24 | 509.4 |
| MD 014 | | | | | | | | | | | | | | | | | | | | | | | | | | 14.7 | 524.1 |
| MD 015 (MSMT- Actual) | | | | | | | | | | | | | | | | | | | | | | | | | | 11.7* | 535.8 |
| MD 016 | | | | | | | | | | | | | | | | | | | | | | | | | | 24 | 559.8 |
| MD 017 Sun, Oct 12, 1997 | | | | | | | | | | | | | | | | | | | | | | | | | | 24 | 583.8 |

*Measurement Timeline

Figure 16: OPM "ON" TIME - Measurement Timeline

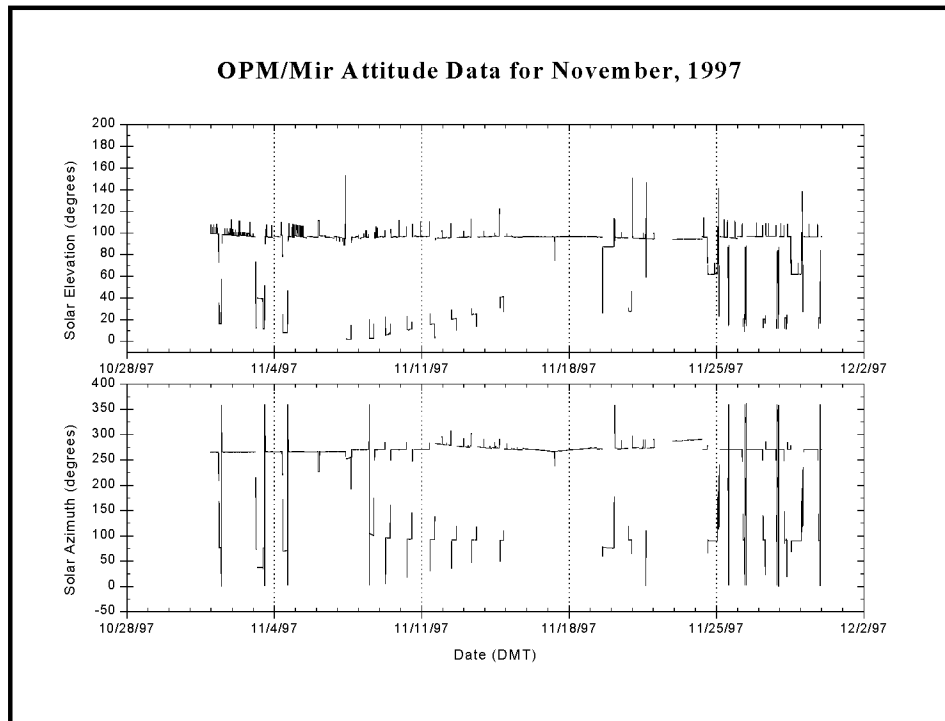


Figure 17: OPM/Mir Attitude Data for November, 1997.

Table 2: OPM Mission Elapsed Time Correction.

| MET | | Correction hrs:min:sec | Corrected Timeline | |
|----------------|----------------|---------------------------|--------------------|---------------|
| Start | End | | Start | End |
| 9/9/97 17:15 | 9/15/97 17:18 | 0:00:00 | 9/9/97 17:15 | 9/15/97 17:18 |
| 9/22/97 1:41 | 9/22/97 3:41 | 56:00:00 | 9/24/97 9:41 | 9/24/97 11:41 |
| 9/23/97 1:10 | 9/28/97 23:18 | 36:00:00 | 9/24/97 13:10 | 9/30/97 11:18 |
| 10/1/97 0:18 | 10/10/97 1:37 | -10:53:00 | 9/30/97 13:25 | 10/9/97 14:44 |
| 10/10/97 21:05 | 10/19/97 15:13 | 14:00:00 | 10/11/97 11:05 | 10/20/97 5:13 |
| 10/19/97 15:13 | 10/20/97 23:15 | 56:22:00 | 10/21/97 23:35 | 10/23/97 7:37 |
| 10/23/97 1:16 | 10/24/97 21:33 | 8:22:00 | 10/23/97 9:38 | 10/25/97 5:55 |
| 10/25/97 11:33 | 11/21/97 18:03 | 7:00:00 | 10/25/97 18:33 | 11/22/97 1:03 |
| 11/22/97 11:55 | 12/31/97 15:22 | 42:23:00 | 11/24/97 6:18 | 1/2/98 9:45 |

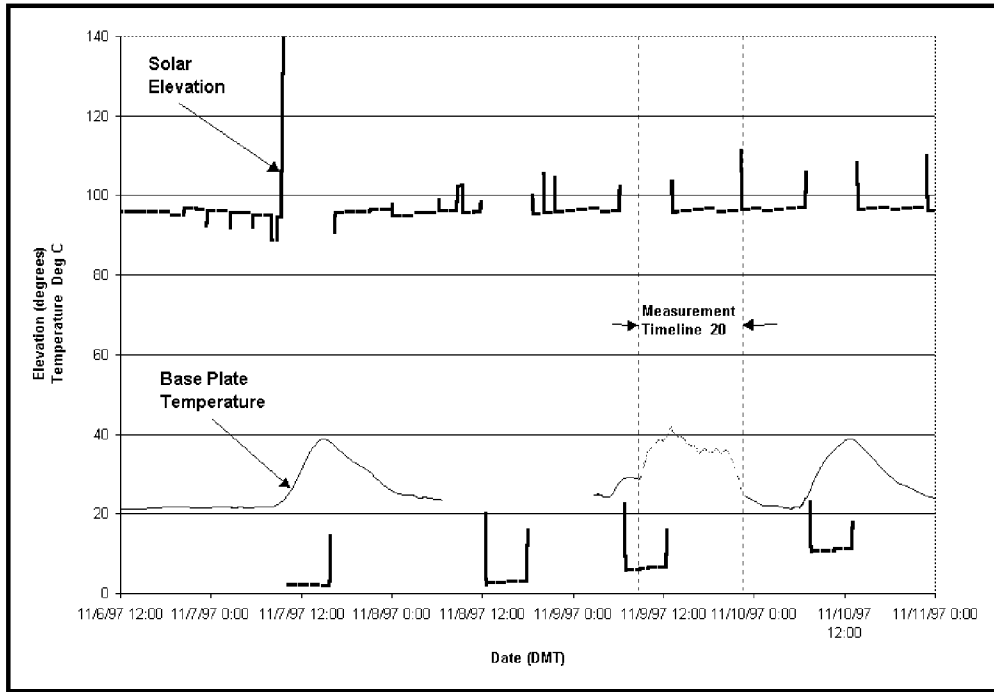


Figure 18: OPM Thermal Response to Mir Attitude change on November 6-11, 1997.

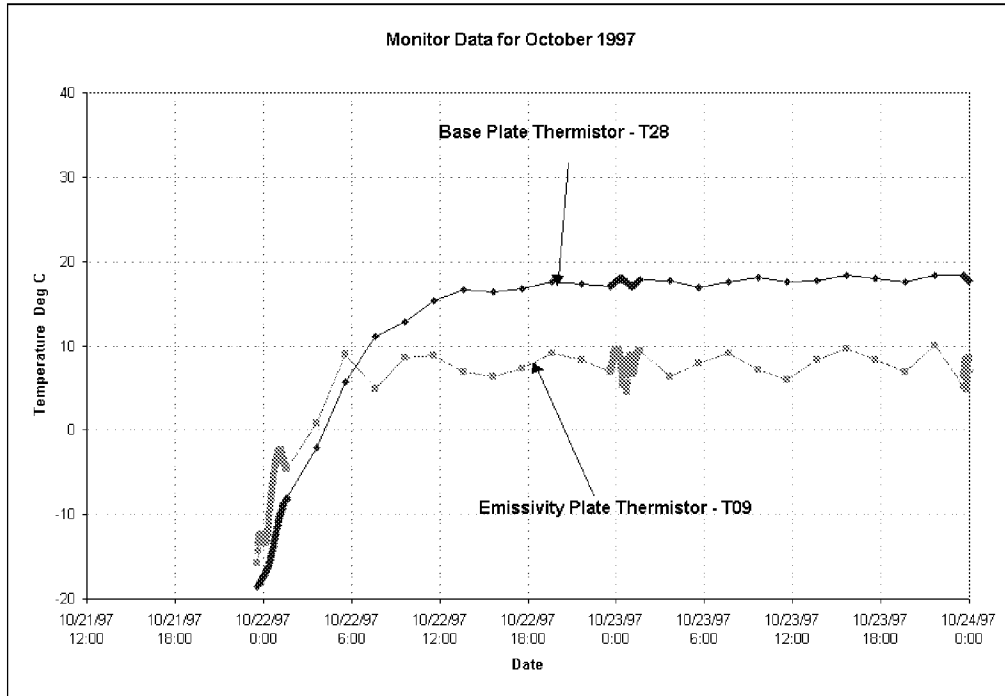


Figure 19: OPM Restart Temperature Response on October 21, 1997.

SUMMARY AND CONCLUSIONS

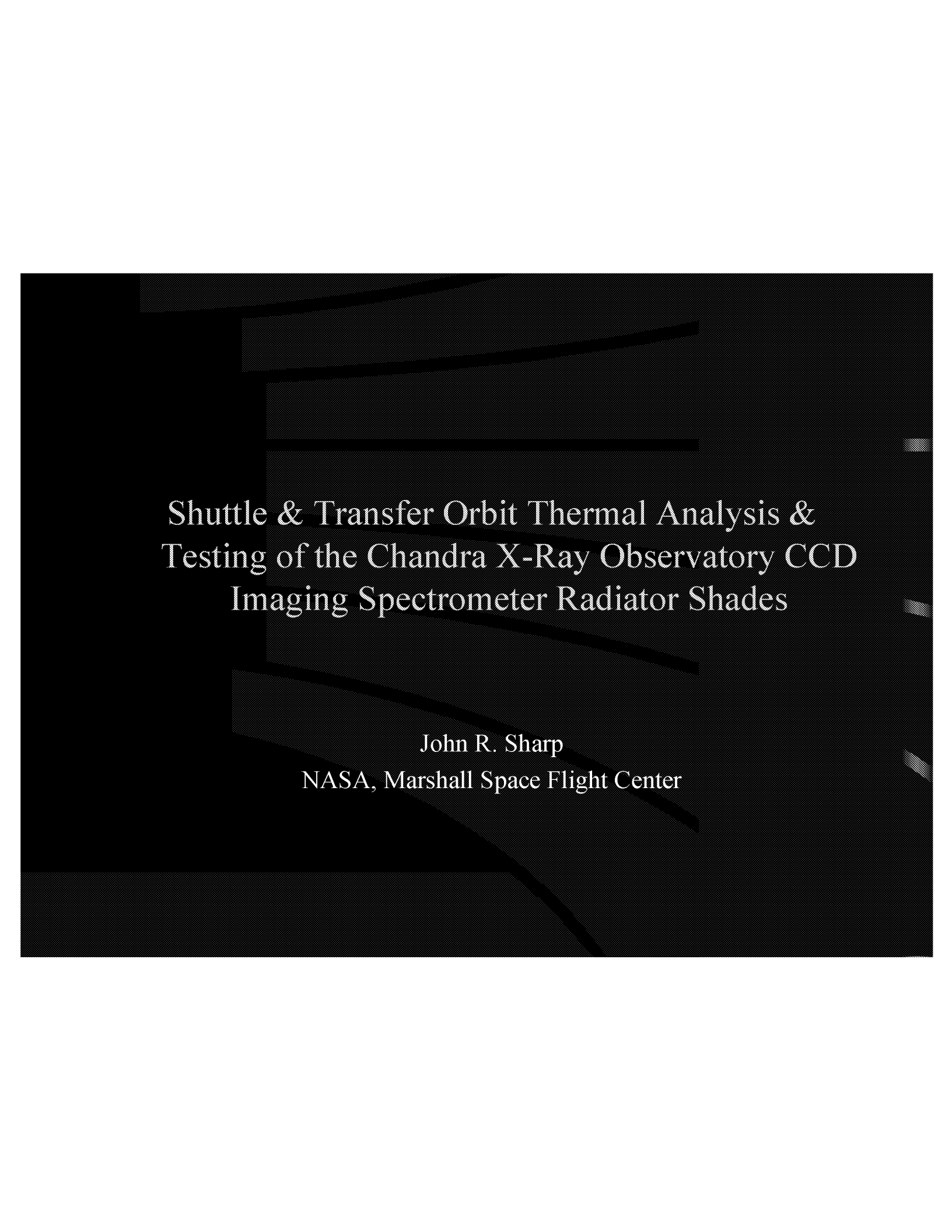
A thermal control system was designed for the OPM Experiment. Detailed SINDA and TRASYS models were developed for the OPM which were used to evaluate system health and performance. Thermal flight data and thermal analysis techniques were demonstrated to be critical sources of information in the evaluation of flight anomalies.

ACKNOWLEDGEMENTS

The author wishes to acknowledge the contributions of Donald Wilkes/OPM Principal Investigator and Leigh Hummer/OPM Chief Engineer of AZ Technology, Inc., NASA/MSFC for overall management and test support, NASA/HQ for primary funding support, and NASA/JSC for funding, Mir, and EVA support.

REFERENCES

1. "Optical Properties Monitor (OPM) System Report," AZ Technology, Report Number 91-1-118-164, February 3, 1999 (Draft).
2. "SINDA/FLUINT, Systems Improved Numerical Differencing Analyzer and Fluid Integrator, Version 2.2," MCR-86-594, Martin Marietta Corporation, Denver Aerospace, September 1988.
3. "Thermal Radiation Analysis System (TRASYS II)," COSMIC Program #MSC20448 and #MSC21030, June 1983.
4. "Mir Geothermal and Thermal Math Models," SSD93D0366A, Rockwell International, Rev. A, April 1994.
5. "Mir-2 Docking Module Geometries and Thermal Math Model Descriptions," SSD94D0365, Rockwell International, Dec. 1994.
6. Schmitz, Craig P., "Thermal Data Book for the Optical Properties Monitor (OPM) Experiment," AZ Technology, Report Number 91-1-118-145, April 22, 1997.
7. Schmitz, Craig P., "Mission Thermal Data Book for the Optical properties Monitor (OPM) Experiment," AZ Technology, Report Number 91-1-118-166, February 18, 1999 (Draft).

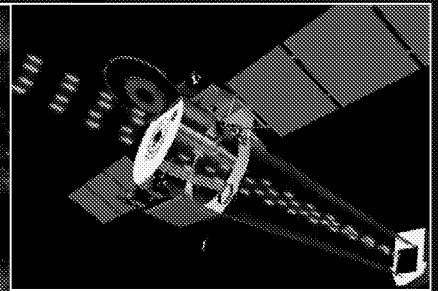
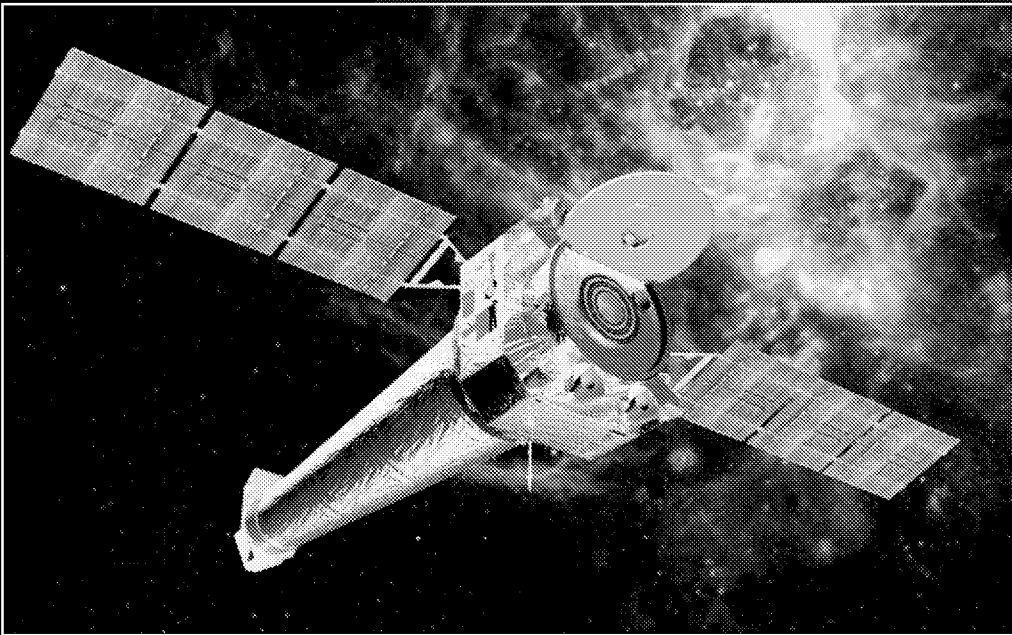


Shuttle & Transfer Orbit Thermal Analysis &
Testing of the Chandra X-Ray Observatory CCD
Imaging Spectrometer Radiator Shades

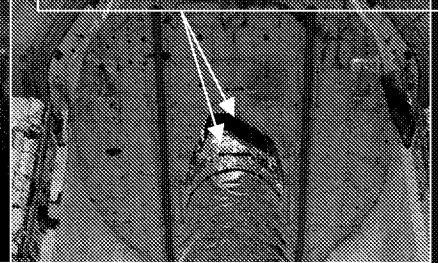
John R. Sharp
NASA, Marshall Space Flight Center

Introduction

- Chandra X-Ray Observatory
- Advanced CCD Imaging Spectrometer (ACIS)
 - CCD cooled to $-120\text{ }^{\circ}\text{C} \pm 1\text{ }^{\circ}\text{C}$. Utilizes “Shades” to optimize Radiator environment

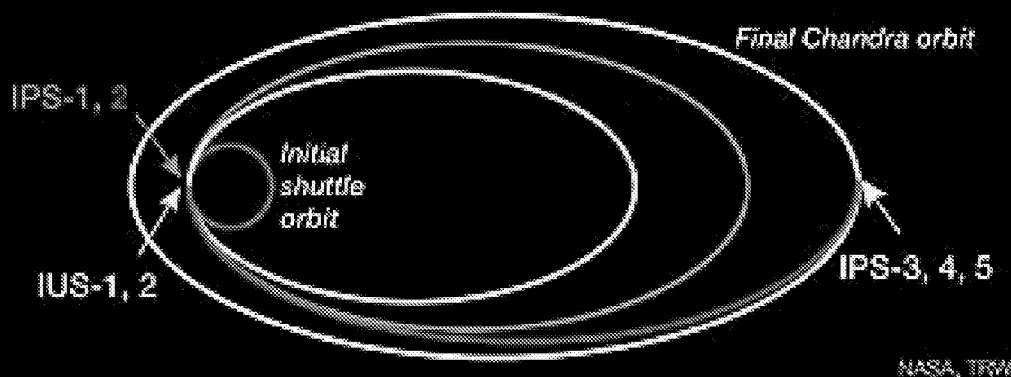


ACIS Radiator Shades



Introduction (Cont.)

- Chandra launched aboard STS-93 into ~130nm LEO
- Transfer to final orbit consisted of 2 Inertial Upper Stage burns and 5 Integral Propulsion System Burns
- Final target orbit: 10,000 km x 140,000 km

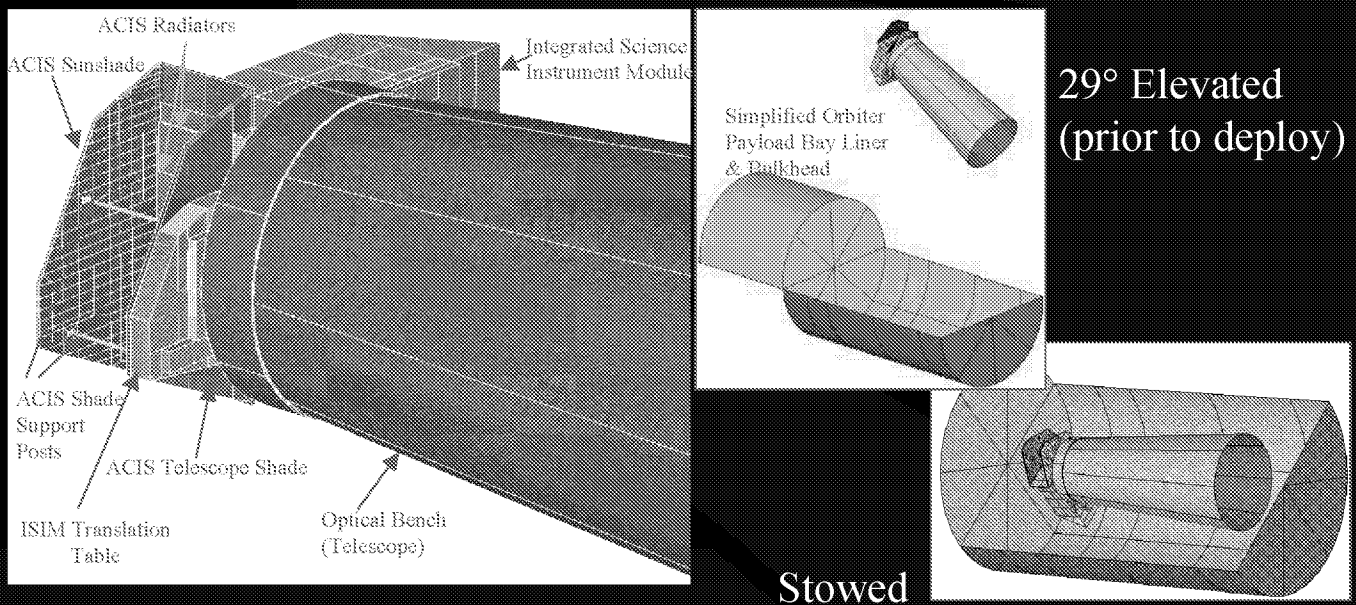


Introduction (Cont.)

- Transfer Orbit thermal analyses of Chandra w/low fidelity radiator shades did not show temperature exceedances.
- MSFC highly detailed models developed of shades revealed that LEO heating and subsequent transfer orbit solar impingement on high α/ε goldized Kapton resulted in very high localized temperatures.
- This overview discusses the analytical results and solutions/testing of over-temperature problem

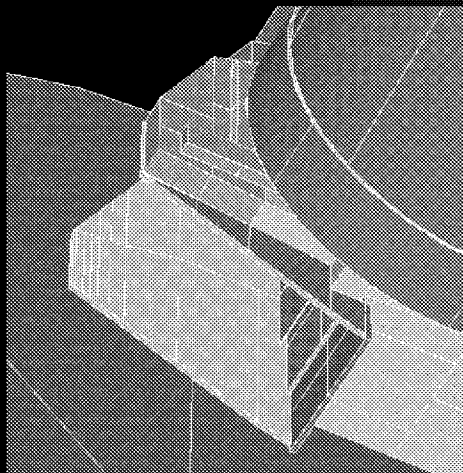
LEO & Transfer Orbit Analyses

- Geometric Modeling in TSS w/specularity
 - 800 surfaces to represent radiator facesheets, support posts and edgefill
 - 3 Orbital Heating configurations (In-bay, elevated stack & free flying)

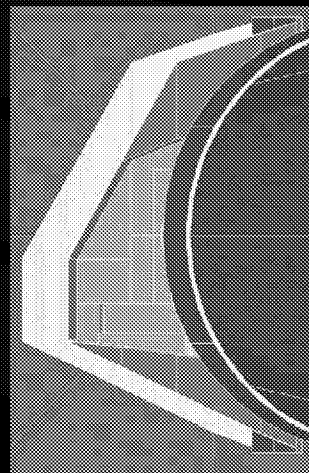


LEO & Transfer Orbit Analyses

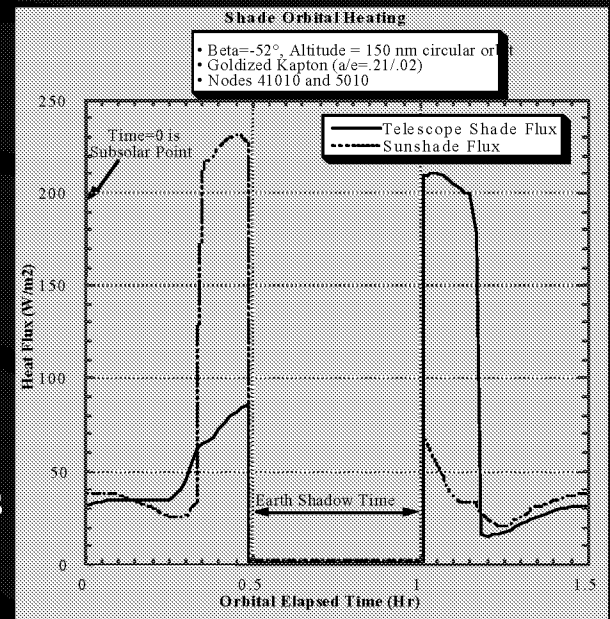
- Low Earth Orbital Heating Calculations
 - TSS used to calculate LEO heating to determine worst Beta Angle
 - $\beta = -52^\circ$ exposes larger area to solar impingement for longer time



Sun View of Shades at Terminator Entry
($\beta = -52^\circ$)



Sun View of Shades at Terminator Entry
($\beta = 0^\circ$)

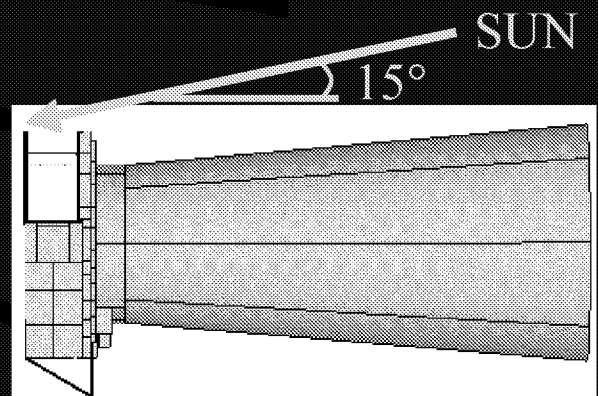


$\beta = -52^\circ$ LEO Heat Flux

LEO & Transfer Orbit Analyses

- Transfer Orbit Heating Calculations
 - TSS used to calculate heating post-IUS 320 km x 64,000 km orbit
 - Free Drift & burn attitudes assumed to result in worst-case solar view

| Event Time (HR:MIN) | Start (HR:MIN) | Event Duration (HR:MIN) | Event Description |
|---------------------|----------------|-------------------------|---|
| 000 | | 3:50 | +ZLV, $\beta = -52^\circ$ Stowed Shuttle Orbit |
| 3:50 | | 0:35 | Deep Space Viewing IMU Alignment |
| 4:25 | | 11:25 | +ZLV, $\beta = -52^\circ$ Stowed Shuttle Orbit |
| 15:30 | | 0:35 | Deep Space Viewing IMU Alignment |
| 16:25 | | 5:15 | +ZLV, $\beta = -52^\circ$ Stowed Shuttle Orbit |
| 21:40 | | 1:54 | -ZSI Elevated Stack |
| 23:34 | | 0:10 | Sun on ACIS sunshade during post-deploy free drift |
| 23:44 | | 0:31 | -ZSI Free Flight, low earth orbit |
| 24:15 | | 0:20 | IUS SRM burns, full sun on ACIS sunshade |
| 24:35 | | 16:54 | Post SRM burns -ZSI thermal attitude, 320km X 64000km orbit |
| 42:29 | | 0:30 | IPS-1 burn, full sun on ACIS sunshade |
| 41:59 | | | Analysis Complete |

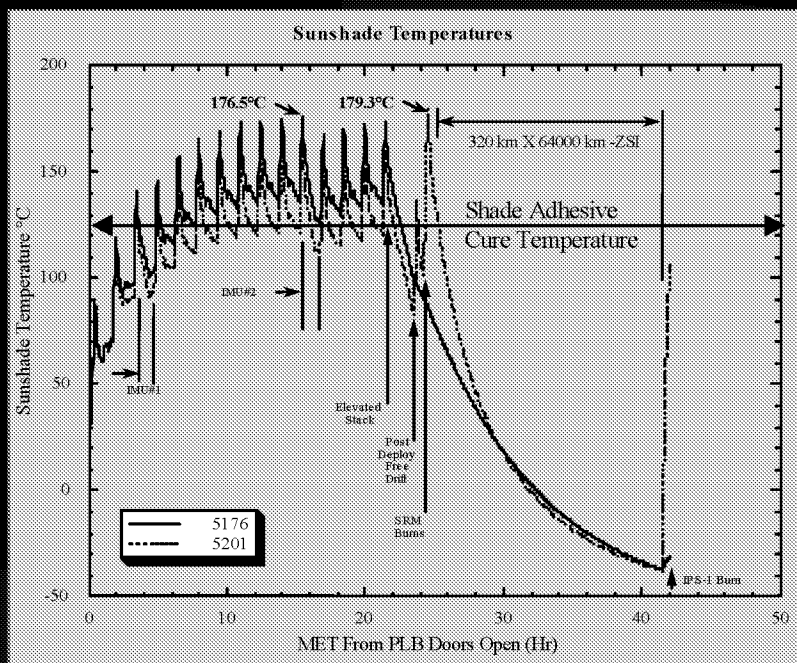


Free Drift & Burn Attitude Solar Heating

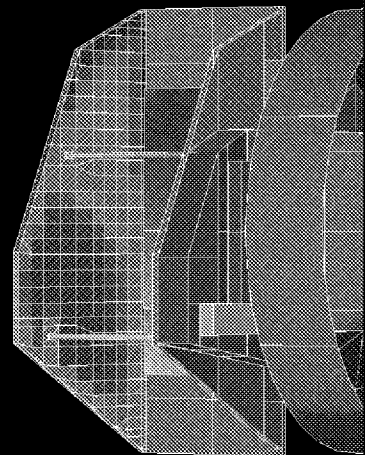
Worst-Case Hot Transfer Orbit Timeline

LEO & Transfer Orbit Analyses

- Results:
 - Temperatures reach ~180°C during LEO, which is 55 °C above adhesive cure temperature used to bond Kapton to facesheet & facesheet to core.

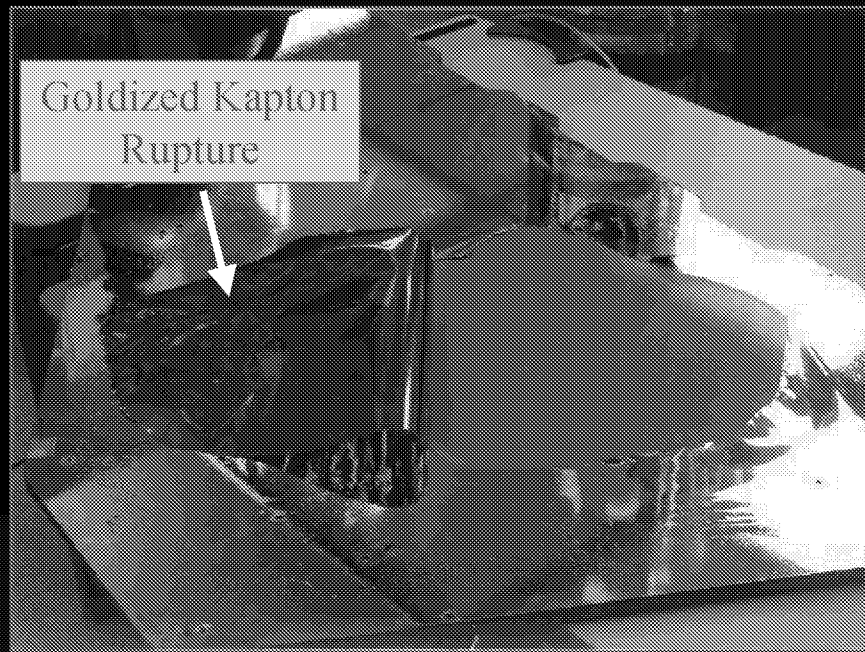


360.00
 344.21
 328.42
 312.63
 296.84
 281.05
 265.26
 249.47
 233.68
 217.89
 202.11
 186.32
 170.53
 154.74
 138.95
 123.16
 107.37
 91.58
 75.79
 60.00



Thermal Testing @ LMAC

- Due to high MSFC temperature predictions, an EU shade was tested to 180 °C @ LMAC.
 - Bubbling of goldized Kapton noticed at ~120 °C. Rupture at 180 °C dwell due to moisture desorption and outgassing

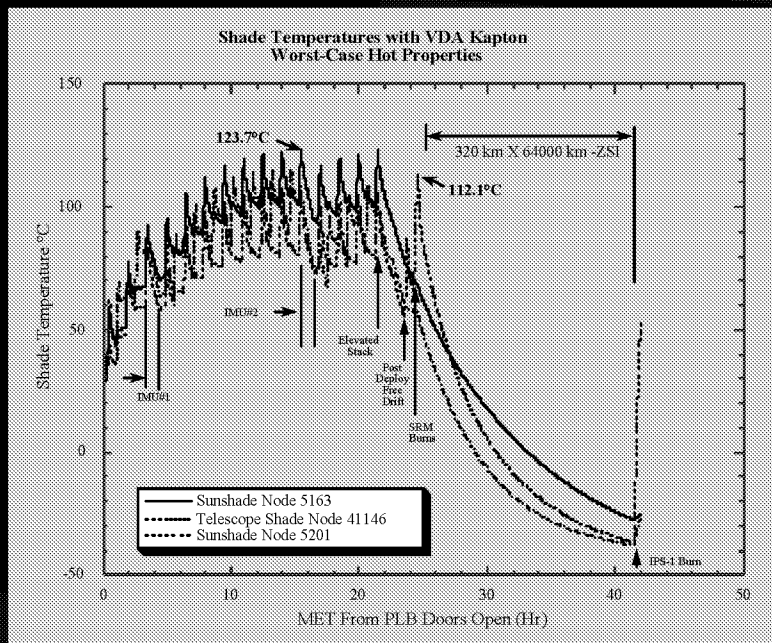


Problem Resolution

- Several options were generated for solving the debonding/overheating issue:
 - Options to lower temperature could not affect subsequent on-orbit performance (e.g., reaching $-120\text{ }^{\circ}\text{C}$ focal plane)
 - LMAC proposed crosscuts in Kapton to allow outgassing
 - Rebuilding shade w/higher temp adhesive ruled out by cost/schedule
 - Operational workarounds not feasible due to effects on rest of Observatory, JSC/IUS interface impacts, schedule.
 - MSFC proposed overcoating existing shade with vapor-deposited aluminum (VDA) to lower solar absorptance to 0.10-0.12 with increase in emittance from 0.02 to 0.03. ($\alpha/\epsilon \sim 4.0$ instead of ~ 10.0)
 - Overcoating required intermediate Chrome for robustness and overcoat of silicon dioxide

VDA Overcoat Analyses

- Worst-Case Analysis w/VDA is 123.7 °C.
- RSS of assumption uncertainty reduces to 102 °C



| Case Description | Shuttle (ZLV) Operations | |
|------------------|------------------------------|-------------------------------|
| | Sunshade Hottest Temperature | Telescope Hottest Temperature |
| Nominal | 82.0°C | 83.0°C |
| ΔT_a | 12.5°C | 13.7°C |
| ΔT_e | 12.2°C | 11.1°C |
| ΔT_c | 9.0°C | 7.0°C |
| RSS Hot | 101.6°C | 102.0°C |
| Worst Hot | 123.7°C | 121.4°C |

Note: Nominal $\alpha / \epsilon = 0.10 / 0.03$ and $\epsilon^* = 0.015$. Hot $\alpha = 0.12$.

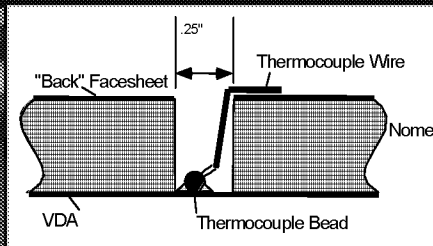
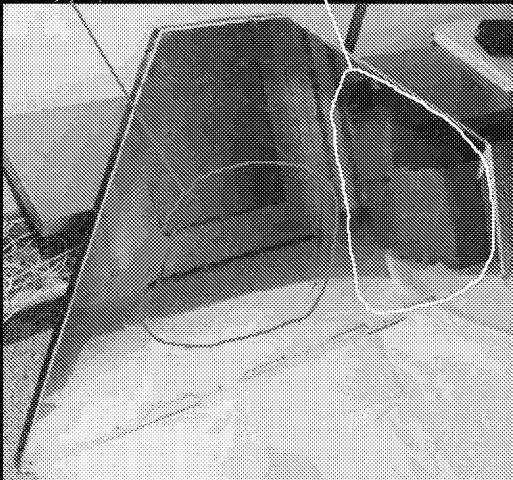
$$T_{RSS-HOT} = T_{NOMINAL} + \left[\Delta T_{c^*}^2 + \Delta T_e^2 + \Delta T_a^2 \right]^{0.5}$$

| | Nominal | Worst-Case Hot |
|-------------------------|---------|----------------|
| Solar Absorptance | 0.10 | 0.12 |
| Hemispherical Emittance | 0.03 | 0.02 |
| MLI effective emittance | 0.015 | 0.005 |

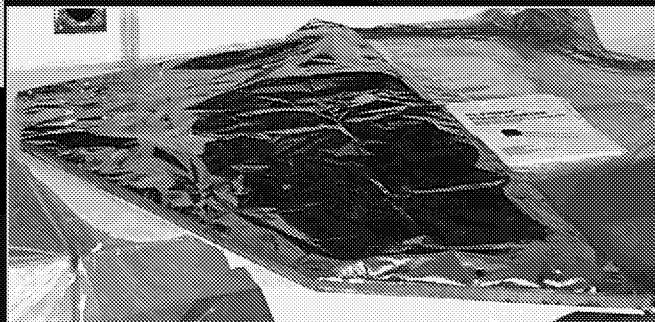
VDA Overcoat Testing @ MSFC

- Thermocouples bonded w/high temp., thermally conductive adhesive to backside of VDA facesheet via holes drilled through back facesheet/core

Pristine Shade Area for Cycle Testing
Previously Ruptured Shade Area

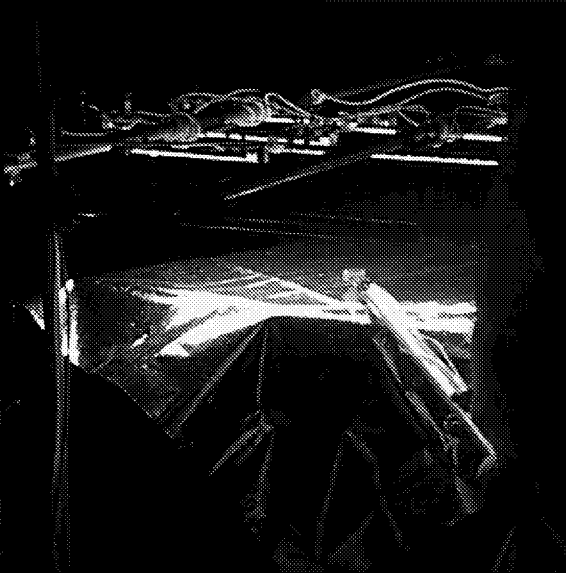


**Thermocouple
Mounting**

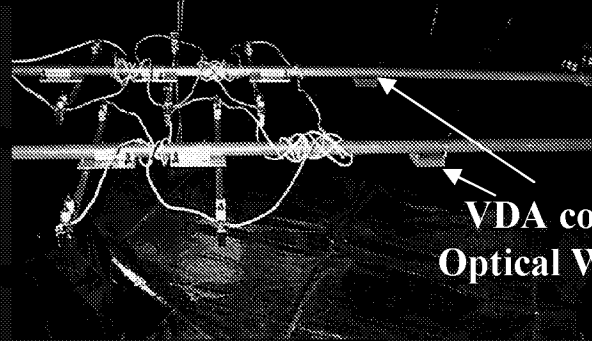


VDA Overcoat Testing @ MSFC

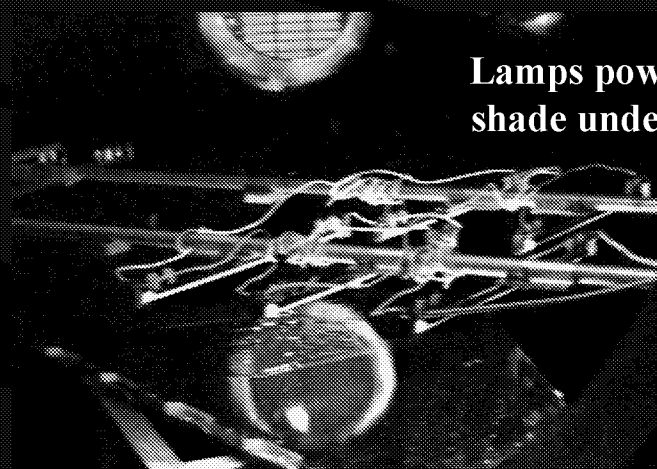
- Infra-red lamp arrays positioned to radiatively heat the VDA surface.



**IR Lamp Flux Mapping
with Water-Cooled
Pyrheliometer**



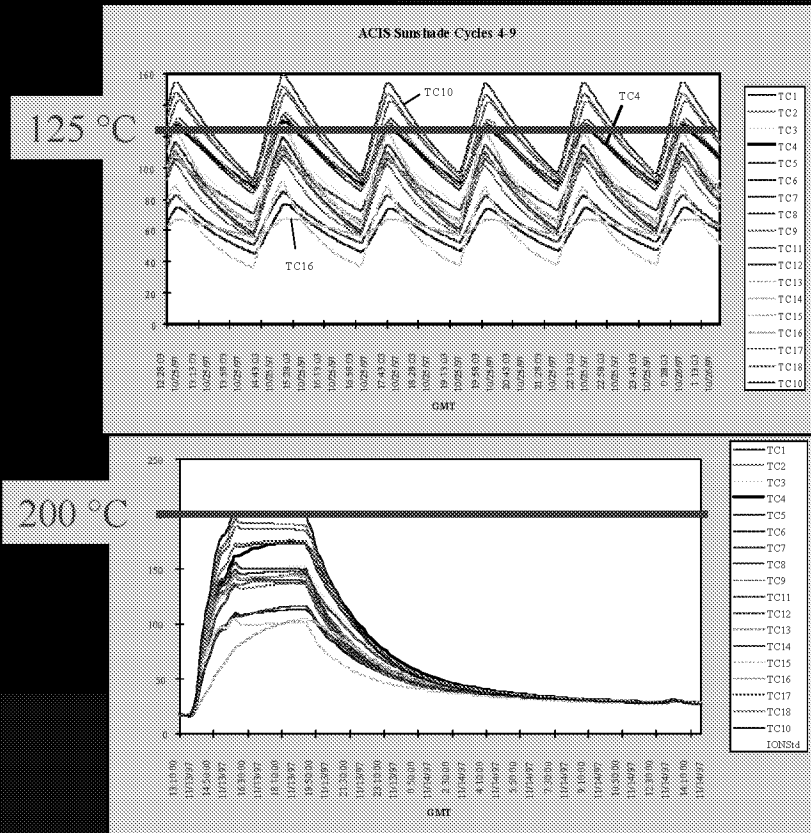
**VDA coupons used as
Optical Witness Samples**



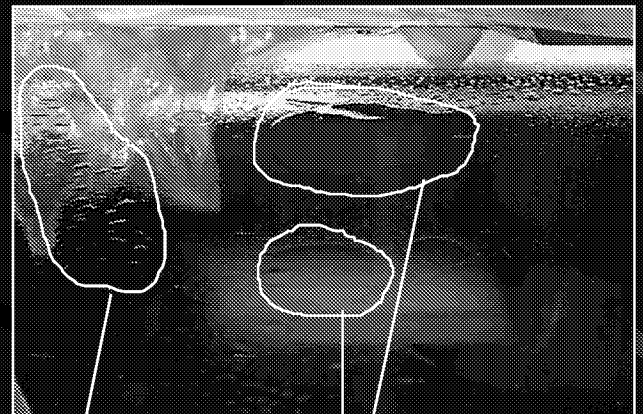
**Lamps powered with
shade under vacuum**

VDA Overcoat Testing @ MSFC

- 24 Cycles to above 125 °C performed. Unit removed for Inspection, then replaced into chamber for crosscut venting hot soak test (>180 °C)



Post-Cycle Test:

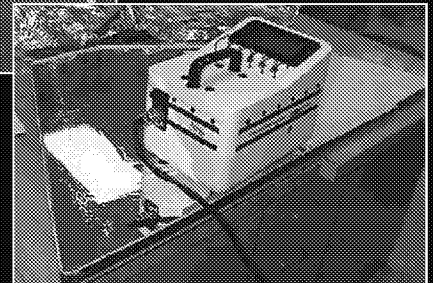
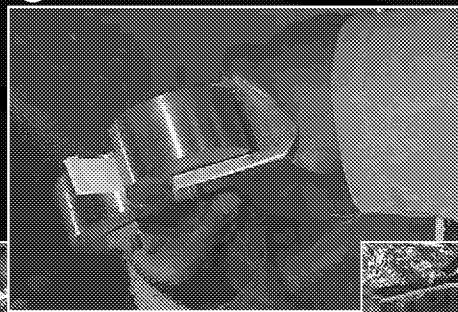
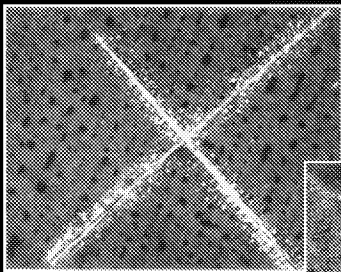


Cluster of Small bubbles

Larger Delaminated Areas

Post-MSFC Test Evaluation

- Following the T/V testing, the shades were visually inspected and evaluated:
 - Crosscuts in “bubble” areas were found to not fully penetrate Kapton
 - A “Tape test” performed to test adhesion
 - Solar absorptance & emittance compared to pre-test on shade and Optical Witness Samples (No Change)
- Based on MSFC analysis/testing, the Chrome/VDA/SiO₂ overcoat approved for flight.





THERMAL ANALYSIS OF A FINITE ELEMENT MODEL IN A RADIATION DOMINATED ENVIRONMENT

Arthur T. Page

*National Aeronautics And Space Administration
George C. Marshall Space Flight Center
MSFC, AL 35812*

ABSTRACT

This paper presents a brief overview of thermal analysis, evaluating the University of Arizona mirror design, for the Next Generation Space Telescope (NGST) Pre-Phase A vehicle concept. Model building begins using Thermal Desktop™, by Cullimore and Ring Technologies, to import a NASTRAN bulk data file from the structural model of the mirror assembly. Using AutoCAD® capabilities, additional surfaces are added to simulate the thermal aspects of the problem which, for due reason, are not part of the structural model. Surfaces are then available to accept thermophysical and thermo-optical properties. Thermal Desktop™ calculates radiation conductors using Monte Carlo simulations. Then Thermal Desktop™ generates the SINDA input file having a one-to-one correspondence with the NASTRAN node and element definitions. A model is now available to evaluate the mirror design in the radiation dominated environment, conduct parametric trade studies of the thermal design, and provide temperatures to the finite element structural model.

INTRODUCTION

The NGST, Figure 1, is NASA's planned successor to the Hubble Space Telescope. NGST is being designed as a large imaging and spectroscopic instrument capable of observing sources in the near infrared (IR) wavelengths. Marshall Space Flight Center's (MSFC) role in this evolving program includes feasibility studies and technology development demonstrations for the optical telescope assembly (OTA). MSFC's Thermal Control Systems Group also supports the program office at Goddard Space Flight Center (GSFC) as a member of the integrated analysis team. The University of Arizona (UofA) is one of several participants in the NGST Mirror System Demonstrator contracts developing technology for large, lightweight optics. Each of the participant's mirror designs will eventually be evaluated for relative performance by the integrated analysis team using a baseline Telescope design commonly referred to as the "yardstick" design.

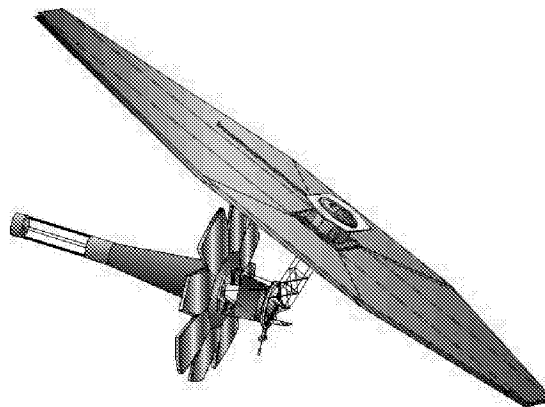


Figure 1: GSFC Pre-Phase A NGST conceptual design ¹

TELESCOPE DESCRIPTION

The NGST Telescope is composed of four major subsystems, Figure 2, which include the Sunshade, Primary Mirror (PM) Assembly, Secondary Mirror (SM) with mast, and the Integrated Scientific Instrument Module (ISIM). The Sunshade is a deployable structure basically acting as multi-layer insulation (MLI) to block direct solar energy from the OTA. The PM assembly is also a deployable structure too large to launch in a fixed position. The central petal is fixed and surrounded by deployable petals. Once deployed, the PM assembly has a diameter of approximately 8.5 meters. The SM is mounted at the end of a composite mast attached to the central petal of the PM.

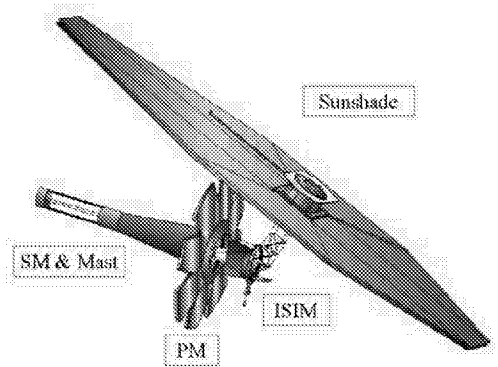


Figure 2: NGST Major Subsystems

Since the Telescope investigates near IR sources, the primary mirror must be maintained at stable temperatures near 35 Kelvin. The NGST baseline orbit is at the 'L2' Lagrangian point, Figure 3. The L2 point is located at an altitude of approximately 3 times the distance from the earth to the moon. It remains on the anti-sun side of the earth. This orbit, along with the Sunshade, provides a cold environment at very stable conditions

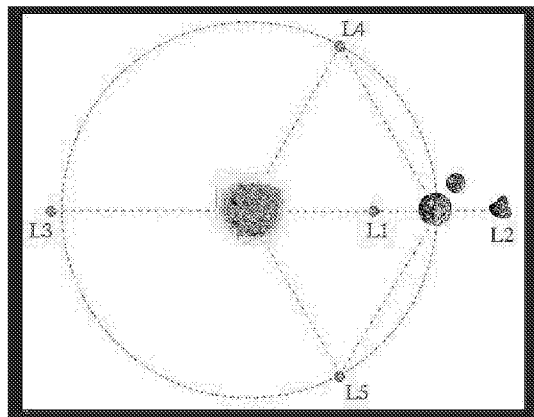


Figure 3: Lagrangian Points relative to the sun and earth orbit ¹

The NGST attitude is defined relative to the solar vector. Figure 4 shows how the attitude changes from having the Sunshade normal to the solar vector, which is the hottest attitude, by slewing to as much as $\pm 27^\circ$ off axis, which is the coldest attitude.

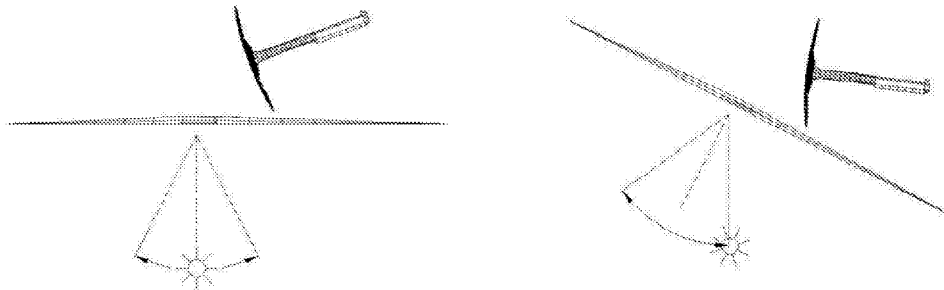


Figure 4: NGST slew maneuver

Figure 5 shows the UofA demonstrator mirror design for a single petal. The mirror is hexagonal shaped. Structural models of this mirror are scaled up to about 3 m flat-to-flat to fit the “yardstick” Telescope design. The front mirror surface is glass approximately 2 mm thick. The glass is held in place by a complex assembly of linkages attached to the backside of the mirror on one end and the actuators on the other end. Behind the glass mirror is the Reaction Structure. The Reaction Structure is an open-cell honeycomb composite. It includes a front and back face but remains open-cell as an assembly. Actuators are mounted inside the cells of the reaction plate.

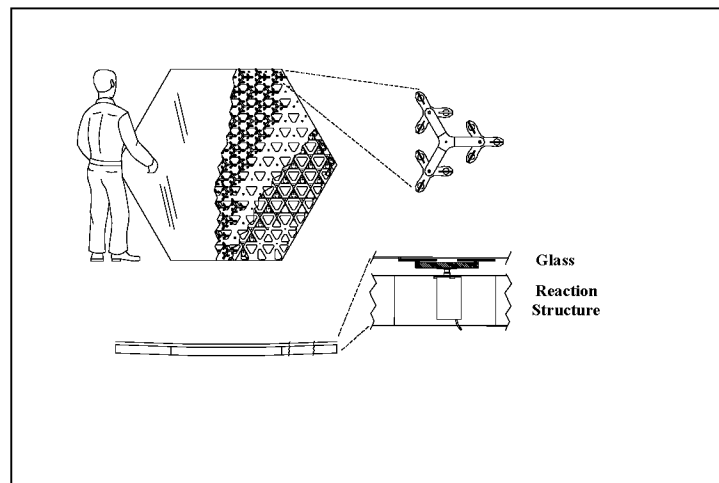


Figure 5: University Of Arizona NGST Demonstrator Mirror²

ANALYTICAL OBJECTIVES

Mirror temperature effects are integrated into stress analysis, along with dynamic loading. The combined effects are inputs to the optical analysis which evaluates performance of the individual petals and overall assembly. This integrated analysis effort is used to compare relative performance of the various mirror designs, requirements for individual components such as the actuators, and effects of other subsystem conceptual designs such as the SM mast and ISIM. This effort also evaluates the necessity for cryo-figuring, effects of material selection, and effects of mounting techniques.

More specifically, the first objective for the thermal analysis is to determine the maximum mirror temperatures during the hot case attitude. This data is used to determine mirror deformations from ambient conditions and evaluate the requirement for cryo-figuring. The second major objective is to determine the mirror temperature response to a slew maneuver from the hot case attitude to the cold case attitude. This data is used to evaluate mirror performance following the slew to determine when perturbations to the optical performance stabilize. The data is also used to determine the required travel for actuators to correct for thermal deformations. Another major objective is to compare temperatures and eventually stress magnitudes, dynamic response, and optical performance between the detailed petal and the corresponding simplified petal. This data is used to determine the amount of surface detail necessary in the integrated model to accurately evaluate overall performance criteria among the various disciplines.

In order to meet these objectives, the thermal analysis process follows a simple path. Sunshade temperatures are provided as boundary conditions from GSFC for the hot and cold attitudes. The NASTRAN FEM model is imported into Thermal Desktop™ and converted to thermal entities. Thermophysical properties, thermo-optical properties, and surface thicknesses are defined. Surfaces/solids are added as necessary. The SINDA thermal network is constructed and radiation conductors calculated. Temperatures are calculated using SINDA. Steady-state temperatures are calculated at the hot attitude and then the boundary conditions are changed to reflect the slew maneuver and a transient solution is completed. Temperatures are exported back to the NASTRAN FEM with a one-to-one correspondence between calculated temperatures and grid points. Although this is a simple path, the analytical process is not without significant challenges. These are discussed in the next section.

ANALYTICAL CHALLENGES

NGST performance and environmental requirements pose challenges to the integrated analysis effort that only a few years ago would have been insurmountable. Previous telescopes, with strict optical performance requirements, often chose to maintain mirror elements near ambient conditions with strict requirements on the thermal control system (TCS) design. Optical performance can then rely on stable temperatures that remain near manufacturing conditions of the mirror elements. Likewise, mirror elements are usually mounted inside a spacecraft structure allowing TCS designs to dampen temperature excursions due to environmental changes. Such luxuries are not afforded NGST. Due to NGST IR imaging requirements, optical elements must be near 35 K during operation, thereby making thermal effects over a large temperature span play a major role in optical performance. NGST also requires a large mirror assembly which necessitates lightweight, deployable elements. Mirror elements are too large to be enclosed in a spacecraft structure. The thin surfaces, naturally, have large temperature gradients. In summary, integration analysis and most notably thermal analysis becomes much more important for the NGST design and performance evaluation.

Integration analysis passes thermal and dynamic responses to stress models which combine the various loads into final mirror deformations. The deformations are then passed on to optical models to evaluate final performance. Therefore, the stress model serves as the primary gateway of data sharing among disciplines. Several challenges exist for this integration. First, there must be a routine interface between the stress FEM and the thermal model to evaluate changing designs. There are many mirror designs, optical assembly designs, TCS designs, etc. Likewise, the use of structural FEM in thermal analysis almost always dictates a large number of surfaces and grid points/nodes. Second, the thermal model must evaluate temperatures of surfaces with specular optical properties, driven by a radiation dominated environment.

Historically, thermal software packages that interface with FEM's cannot perform full radiation analysis to calculate radiation conductors, orbital heating, and add surfaces as part of the TCS design. Some do not provide a means to calculate non-linear temperature responses. In addition, most of these packages do not provide an interface to SINDA which remains the tried and true workhorse of thermal analysts throughout NASA. The packages that do provide an interface are sometimes not viable for continuously changing designs or designs driven by radiation. Therefore, a gap results which greatly hinders integrated thermal analysis.

Within recent years a very few software packages have evolved that do provide, to one degree or another, interfaces to FEM's used by other analytical disciplines, interfaces to CAD packages used by designers, and finally, they are capable of full thermal analysis with radiation. Thermal Desktop™, which runs within AutoCAD®, is one of the most notable developments that does provide these capabilities. Thermal Desktop™ is used for NGST because of its capability to import NASTRAN FEM's, calculate radiation conductors for a very large number of surfaces, add thermal design features, quickly change material properties and geometry, evaluate surfaces with specular properties, and post-process temperatures for direct export back to NASTRAN. There are many other features within the package that are not used for NGST analysis. Some of the more notable features are the capability to evaluate articulating surfaces and the capability to reduce the number of surfaces in the model while maintaining the original interface to FEM's grid points.

THERMAL/STRUCTURAL MODEL

With the Sunshade added, the NASTRAN FEM has 2,015 elements (surfaces) and 1,466 grid points (nodes) once imported into Thermal Desktop™, Figure 6. The detailed mirror has 785 elements (surfaces) while the simplified mirrors have only 26 elements (surfaces) per petal. The FEM includes the Sunshade, PM Petals, SM Mast, and SM. The FEM also includes the Reaction Structure for the detailed petal. This NASTRAN FEM serves as the basic model used to share data among the various disciplines conducting integrated analysis. Post-processed results from the thermal analysis provide temperatures for each of these grid points in the NASTRAN FEM. The ISIM is not included in this model because the baseline model used for comparison had no ISIM. This model does not include elements for the Reaction Structure behind the simplified petals.

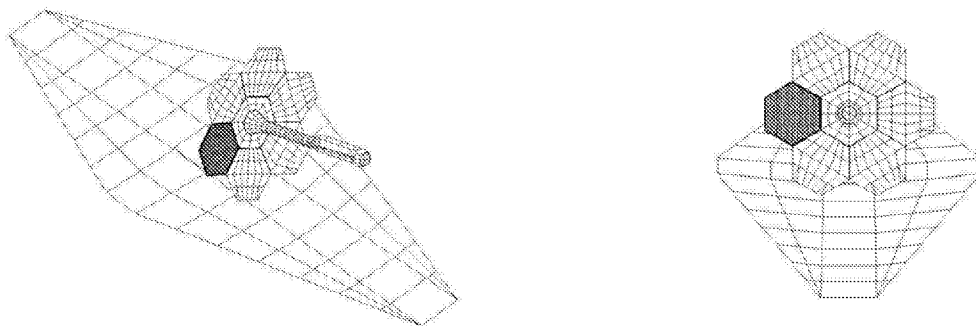


Figure 6: NASTRAN FEM of NGST with the UofA mirror design

Thermal analysis must consider radiation between the mirror petals and Reaction Structure and between the Reaction Structure and Sunshade, Figure 7. Modeling the open-cell structure is discussed below. Using AutoCAD® features, the simplified petal surfaces are copied and translated behind the mirror providing new surfaces for a simplified Reaction Structure with identical detail, Figure 8. Using Thermal Desktop™ the new surfaces are put in a separate submodel. Once the simplified Reaction Structure is added, the thermal model has 2,219 surfaces and 1,689 nodes.

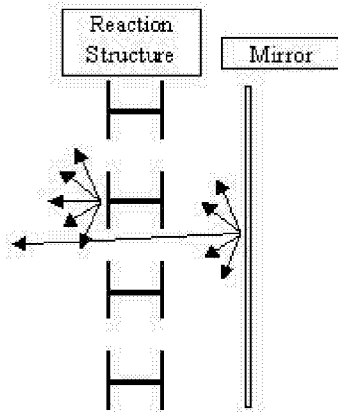


Figure 7: Radiation interchange toward the backside of the Mirror

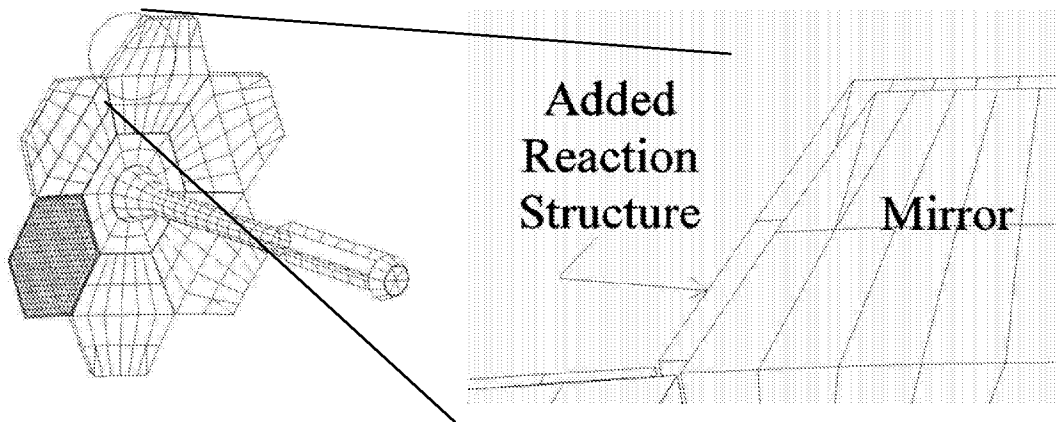


Figure 8: Reaction Structure surfaces added to the thermal model

The next step in developing the thermal model is defining thicknesses and material properties of the various planer surfaces. Thicknesses and material properties are used to calculate nodal thermal capacitance and linear conductors to adjacent nodes. Surfaces are selected using a multitude of options within either AutoCAD[®] or Thermal Desktop[™]. The PM is borasilicate glass while the Reaction Structure and SM Mast are laminated composites. Properties are given in Tables 1 & 2. If material properties near 30 K are available they are used. Otherwise, properties are set to those used in the “yardstick” analysis. The PM surfaces are set to the actual glass thickness of 2 mm. The SM Mast surfaces are set to the actual thickness of 3 mm. The Reaction Structure surfaces are set to the actual thickness of the single facesheet toward the PM which is 0.76 mm. This simplifies the honeycomb assembly and provides conservative predictions on lateral temperature gradients. However, the material density of the Reaction Structure is increased to include the total thermal capacity of the two facesheets and honeycomb webs. This maintains accuracy for the transient analysis.

| Material | Thermal Conductivity (W/m/K) | Density (kg/m ³) | Specific Heat (J/kg/K) |
|--------------------|------------------------------|------------------------------|------------------------|
| Borosilicate | 0.15 | 2352.8 | 37.6 |
| Composite | 8.72 | 2155.4 | 10.04 |
| Reaction Structure | 8.72 | 11324.3 | 10.04 |

Table 1: Thermophysical Properties

| Surface | Material | Emissivity |
|--------------------|-----------------|------------|
| Sunshade | VDA | 0.03 |
| Primary Mirror | Coating? | 0.03 |
| Secondary Mirror | Glass | 0.03 |
| Reaction Structure | Composite @40 K | 0.4 |
| Composite | Composite @40 K | 0.4 |

Table 2: Surface Emissivity

The next step before beginning calculations is selecting the necessary surfaces to be included in the radiation analysis and defining optical properties for those surfaces. This is a simple task for all structures except one. A difficult situation exists with the honeycomb Reaction Structure. The structure is open-cell. Therefore, the backside of the PM glass “sees” through the Reaction Structure to the Sunshade, Figure 7. A detailed model of each individual cell would require too many surfaces to handle in the radiation analysis. As a common alternative, simplifying assumptions are used. Optical properties for this structure include 11% transmissivity in the IR wavelength. The transmissivity value is determined by importing design drawings of the facesheet. Again, using AutoCAD® techniques, the relative surface area of the open-cells to facesheet is calculated.

Radiation conductors are now calculated and a SINDA network file is generated. The final analysis uses a total of 414,945 radiation conductors and 5,179 linear conductors.

RESULTS

As a checkout procedure, the temperatures are first calculated using only the radiation network. In this case only the front mirror surface is active. This helps evaluate the radiation network and gives a quick comparison of the detailed petal, to the left, and simplified petal, to the right. Mirror temperatures, Figure 9, show symmetry across the PM assembly along a vertical axis as expected. It also shows good agreement between the detailed and simplified petal. There is a shadow of the SM Mast toward the top of the PM assembly as it blocks radiation from the warmer Sunshade below.

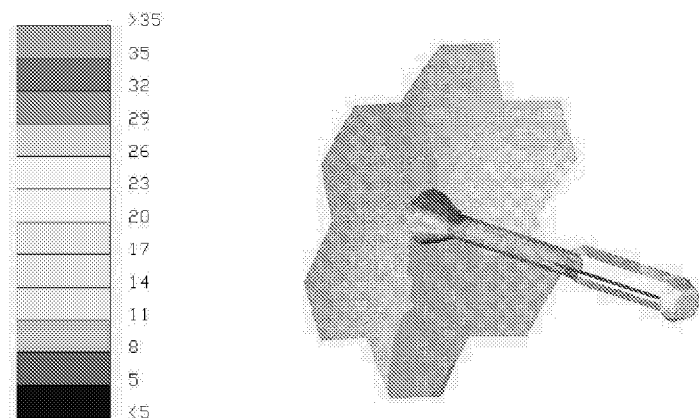


Figure 9: Results from a checkout run with radiation only

With the checkout complete the conduction network is added to the SINDA model. Calculations for the hot case attitude show a maximum mirror temperature around 32 K, Figures 10 & 11. The temperature gradient across the PM assembly is about 10 K. The central petal has the largest gradient of any single petal.

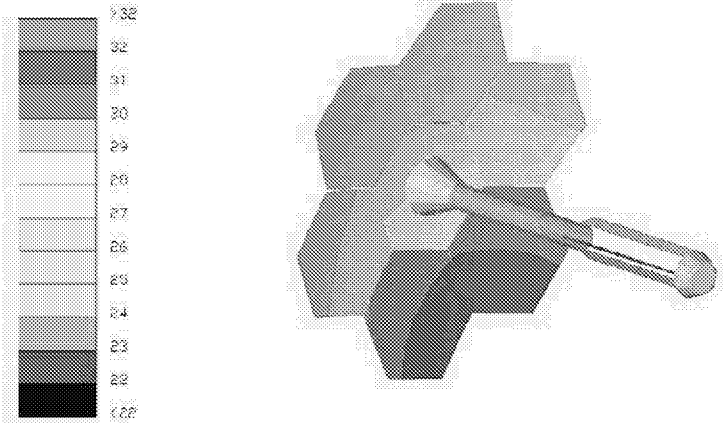


Figure 10: Final hot case results- isometric view

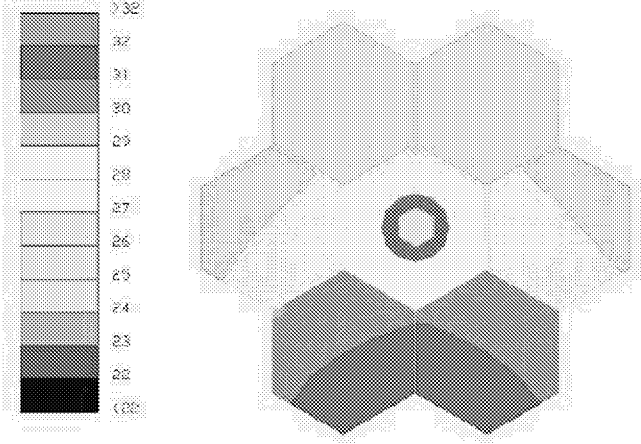


Figure 11: Final hot case results- front view

There is a large gradient at the interface between petals. Eventually, latches and/or hinges will be included that may have significant effects on these gradients. It should be noted that these temperatures are not considered the best possible with the UofA mirror design. Future analysis, to improve performance, should consider options to eliminate direct radiation from the backside of the Mirror to the Sunshade. Gradients can be easily reduced with the addition of insulation, for example. Temperatures for the entire vehicle are given in Figure 12.

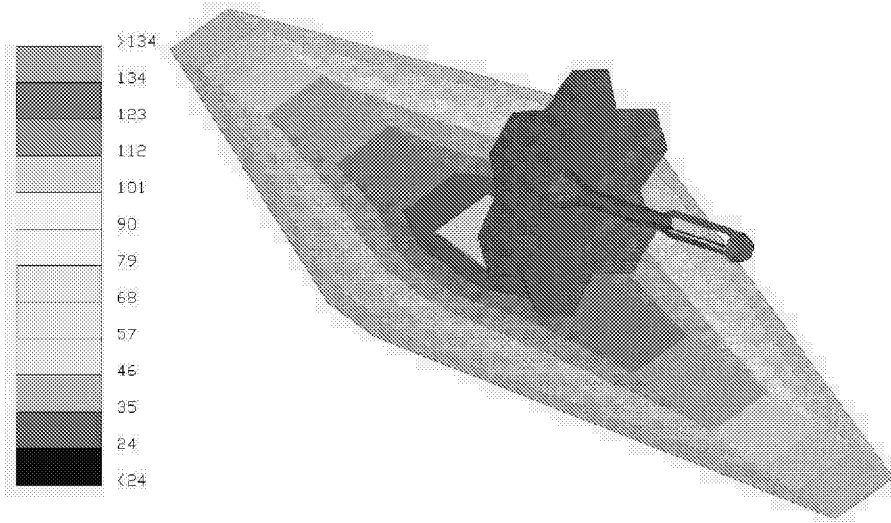


Figure 12: Final hot case results- entire vehicle

During the maximum slew maneuver Sunshade temperatures decrease about 2 K on average. Figure 13 shows how the Mirror and OTA structure respond to the different environment. Although the Mirror is lightweight, the radiation coupling to the Sunshade is small. Therefore, Mirror temperatures continue to decrease for a long time following the slew. Transient temperatures are used in the stress analysis to provide thermal deformations over a period of time following the slew. This information is used to determine when optical stability is achieved. Although Mirror temperatures continue to change many days following the slew, the rate of temperature change decreases a great deal after about 36 hours, Figure 14.

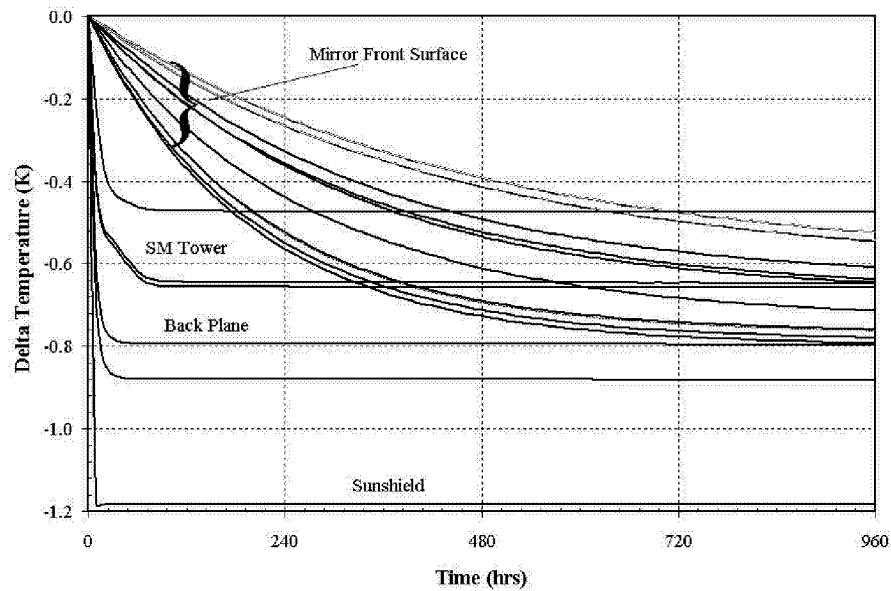


Figure 13: Slew Maneuver- Temperature Change From Initial Conditions

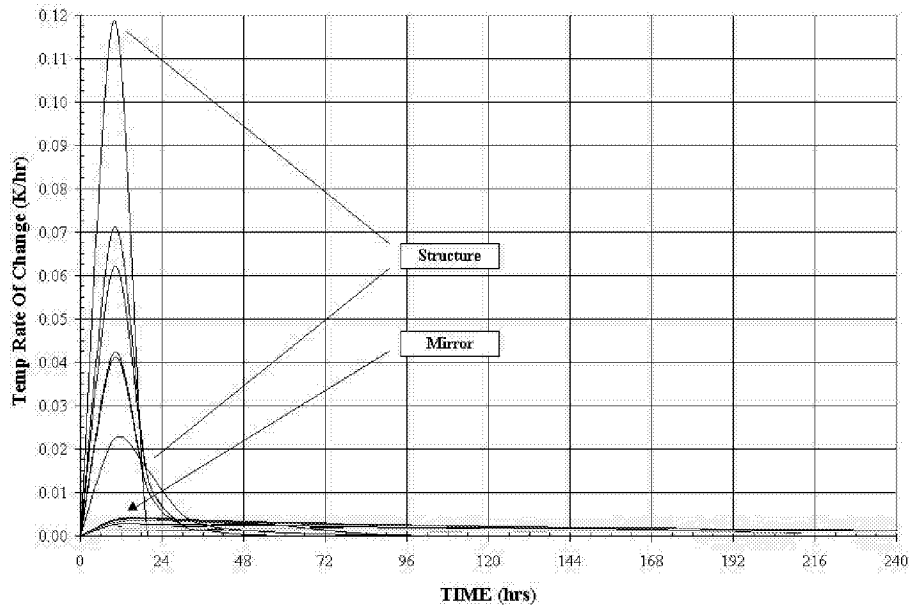


Figure 14: Slew Maneuver- Rate of Temperature Change

CONCLUSIONS

Initial calculations show that the L2 orbit combined with the Sunshade design result in Mirror temperatures at or below 32 K. Temperatures of the simplified petal show the same degree of fidelity in gradients as the detailed petal. Therefore, the simplified petals do reflect the required amount of detail to accurately evaluate temperatures. Mirror temperatures continue to decrease many days following a 27° slew maneuver. As a result of this effort, a thermal model now exists to conduct parametric trade studies that evaluate various design changes to reduce gradients and improve the optical performance. The thermal model can be quickly modified to reflect design changes as the project matures.

This effort also demonstrates that Thermal Desktop™ is a useful tool to perform thermal analysis on FEM models in an environment dominated by radiation interchange. The release of Thermal Desktop™ is a major advancement in tools available to the thermal analysis. Thermal analysis can now play a more active role in the integrated analysis and concurrent engineering design effort.

REFERENCES

- [1] National Aeronautics and Space Administration, Goddard Space Flight Center, Next Generation Space Telescope Internet Home Page.
- [2] University Of Arizona, Next Generation Space Telescope Mirror System Demonstrator Critical Design Review.



AN OVERVIEW OF THE THERMAL CHALLENGES OF DESIGNING MICROGRAVITY FURNACES

Douglas G. Westra
NASA Marshall Space Flight Center

ABSTRACT

Marshall Space Flight Center is involved in a wide variety of microgravity projects that require furnaces, with hot zone temperatures ranging from 300 °C to 2300 °C, requirements for gradient processing and rapid quench, and both semi-conductor and metal materials. On these types of projects, the thermal engineer is a key player in the design process.

Microgravity furnaces present unique challenges to the thermal designer. One challenge is designing a sample containment assembly that achieves dual containment, yet allows a high radial heat flux. Another challenge is providing a high axial gradient but a very low radial gradient.

These furnaces also present unique challenges to the thermal analyst. First, there are several orders of magnitude difference in the size of the thermal “conductors” between various parts of the model. A second challenge is providing high fidelity in the sample model, and connecting the sample with the rest of the furnace model, yet maintaining some sanity in the number of total nodes in the model.

The purpose of this paper is to present an overview of the challenges involved in designing and analyzing microgravity furnaces and how some of these challenges have been overcome. The thermal analysis tools presently used to analyze microgravity furnaces and will be listed. Challenges for the future and a description of future analysis tools will be given.

INTRODUCTION

Marshall Space Flight Center (MSFC) is the Lead Center for NASA’s Microgravity Research Program and manages microgravity research projects at Marshall and other NASA Centers. One of the disciplines that Marshall is responsible for managing is materials science. A fundamental goal of microgravity materials science research is to better understand how buoyancy driven convection and sedimentation affect the processing of the materials. By suppressing these gravity driven phenomena in the microgravity environment of low earth orbit (LEO), other phenomena normally obscured by gravity may be investigated. Studying the phenomena normally obscured by gravity allows the gravity driven phenomena to be better understood as well.

Scientists from the academic and research communities apply to NASA to become Principal Investigators in various materials science disciplines. The materials science discipline that is discussed here is directional solidification processing of metals and semi-conductors. This specific discipline requires high temperature furnaces that must meet challenging thermal requirements. These thermal requirements include providing a large thermal gradient in the sample, a rapid quench at the end of processing, and very stringent isothermal specifications within certain sections of the sample, to name a few. While meeting these thermal requirements, containment of (sometimes-hazardous) materials and all other safety requirements must be met. Many times, meeting the safety requirements makes meeting the thermal requirements extremely difficult. Temperature measurement and other types of instrumentation issues are also significant furnace design challenges.

Thermal mathematical modeling is very important in the design of these high temperature furnaces. Thermal mathematical modeling is used in the preliminary design of the furnace, aids in the design process, and is used to diagnose test data from the furnace. The thermal mathematical models must include the numerical representation of the PI's sample as well as the furnace in order to assess the sample's impact on the thermal performance of the furnace. This presents many challenges as well: adequately characterizing the sample without generating a huge amount of nodes, several orders of magnitude difference between thermal conductors in the model, and dealing with furnace control issues.

The main focus of this paper is to discuss the above referenced challenges. As an introduction to microgravity materials science processing of metals and semiconductors, two types of furnaces will be described. Following, some examples of sample systems and their containment will be described. Next, furnace processing and control will be outlined. Then, the challenges associated with furnace design and analysis will be discussed. Solutions that have been implemented and that are being considered will be included. Finally, conclusions will be discussed.

DESCRIPTION OF TWO TYPES OF MICROGRAVITY FURNACES

There are a wide variety of furnaces that are used for materials processing. However, there are two types that have been used for most of the furnaces designed and built by Marshall for metal and semi-conductor processing. These two furnaces are related: 1) Bridgman-Stockbarger and 2) Bridgman furnaces.

Figure 1 shows a cutaway view of a Bridgman-Stockbarger furnace. This particular furnace operates in an inert gas environment; however, Bridgman-Stockbarger furnaces may also be designed to operate in a vacuum environment.

There are three main zones in this furnace: a hot zone, an adiabatic zone, and a cold zone. The hot zone is designed to add heat to the sample radially such that the sample melts. Heat is radially extracted from the sample in the cold zone such that the sample re-solidifies. Ideally, there is no radial heat transfer in the adiabatic zone. The temperature difference between the hot zone and cold zone produces the required axial gradient in the sample. The optimally designed furnace will operate such that the location of the solid-liquid interface is located in the gradient zone. This is normally the gradient specified by the PI. It is desirable that this gradient is in the adiabatic zone for the following reason: since there is (ideally) no radial heat transfer in the adiabatic zone, the shape of the solid-liquid interface is flattest in the adiabatic zone. Since the furnace is designed so that the design gradient is located in the adiabatic zone, this zone is also commonly called the gradient zone.

A Bridgman-Stockbarger furnace has a "heated" cold zone as a distinguishing characteristic. The cold zone is only "cold" relative to the hot zone. That is, the required axial thermal gradient is achieved by operating the hot zone at temperatures on the order of 1200 – 2200 °C, while the cold zone operates on the order of 400 – 1000 °C. Bridgman-Stockbarger furnaces are typically used for semi-conductor directional solidification processing.

Figure 2 shows a Bridgman furnace design. This furnace operates in an inert gas environment. As with a Bridgman-Stockbarger, a Bridgman furnace may also be designed to operate in a vacuum environment. The Bridgman furnace has the same main components as the Bridgman-Stockbarger furnace: a hot zone, a gradient or adiabatic zone, and a cold zone. However, a Bridgman furnace has an actively cooled cold zone. The cold zone extracts heat from the sample at temperatures slightly warmer than ambient or cooler if necessary. There are other features on the particular furnaces shown: a quench block is on both and a vacuum block is shown on the furnace in Figure 2. On this Bridgman furnace, a water spray is used to quench or rapidly cool the sample. The vacuum block is used to remove the water and steam mixture that results when water is sprayed at a hot surface.

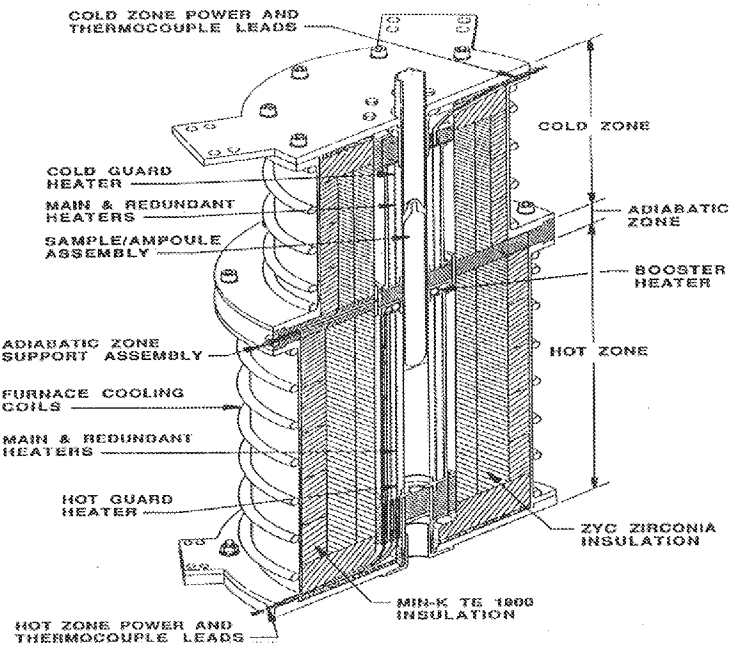


Figure 1: Bridgman-Stockbarger Furnace that operates in an inert gas environment.

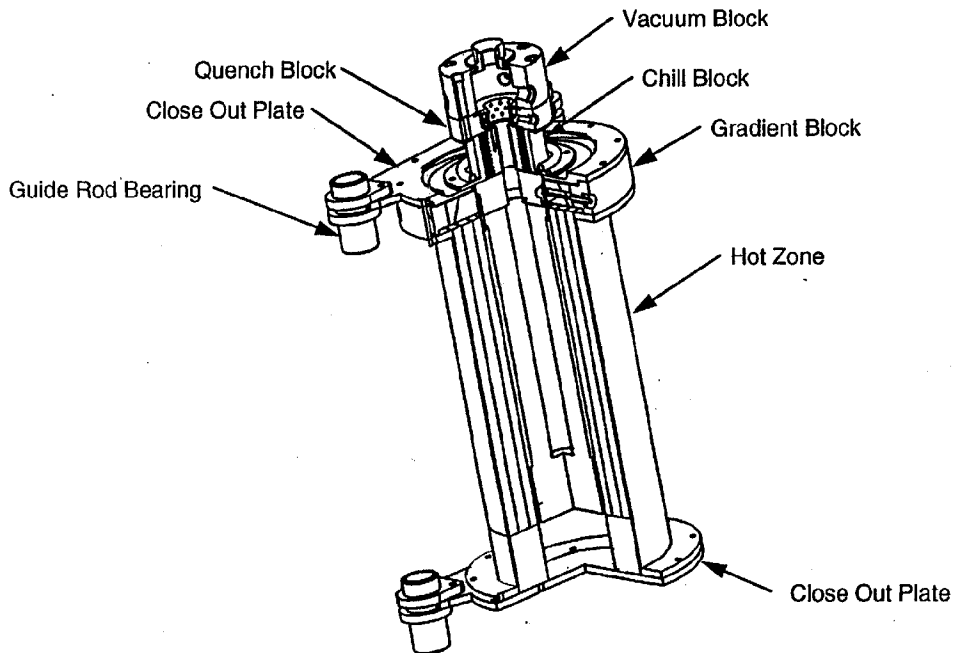


Figure 2: Bridgman Furnace that operates in an inert gas environment.

EXAMPLES OF SAMPLE CONTAINMENT ASSEMBLIES (SCA)

Figure 3 shows two sample containment assemblies (SCAs). The one on the left is that of a double-contained system. The sample is contained directly within an ampoule. Common ampoule materials are ceramics such as aluminum oxide (alumina), aluminum nitride, and graphite. The outer container is called the cartridge, normally constructed of metals. There is a gap between the ampoule and the cartridge. The materials or design of this gap will be explained in detail later on in this paper. The cartridge is affixed to the support structure of the SCA.

The right side of Figure 3 shows a single-contained SCA, or simply, a crucible. The crucible is made of the same materials as ampoules: ceramics such as aluminum nitride, etc. The SCA support structure is attached to the crucible material in this case.

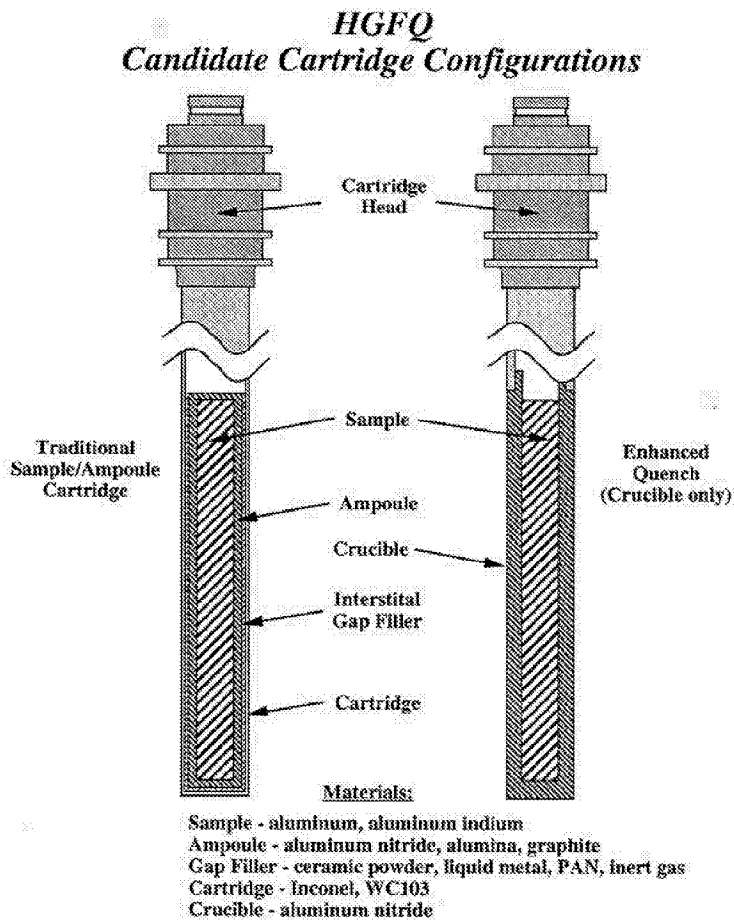


Figure 3: Two different Sample Container Assembly (SCA) Designs.

FURNACE PROCESSING AND CONTROL

Furnace processing normally begins by inserting the sample into the hot zone such that the entire sample is melted. The sample is left to “soak” in the hot zone for several hours so that it is of uniform temperature and composition. This is especially important with alloy materials.

After the soak period, the furnace is translated with respect to the sample so that in effect, the sample is “removed” from the furnace. Note, translating the furnace rather than the SCA is preferred so that the furnace, not the sample, absorbs any disturbances associated with this translation. The translation rate is on the order of millimeters per minute. As the sample is translated into the gradient (adiabatic) zone and then into the cold zone, the molten sample material solidifies. There are transients due to end effects, but the translation rate is often slow enough such that heat transfer can be characterized as a quasi-steady-state process. Some scientists will vary the translation rate during one sample run, which then produces a break in the quasi-steady-state process.

The structure and morphology of the solid-liquid front is very dependent on the material, the magnitude of the gradient, and the translation speed. An entire paper could be written on this subject, but this is beyond the scope of this paper. The phenomenon occurring at the solid-liquid interface and the resulting microstructure are what the PI controls via his science requirements. A point should be made that in alloys, the phase change is not isothermal. That is, the phase change takes place over a finite temperature range. Therefore, there is not a distinct spatial solid-liquid interface. Rather, there is a finite length of sample over which the phase change takes place. The length of the sample that contains both liquid and solid components is known as the mushy zone.

The characteristics of the solid-liquid interface or mushy zone cannot be seen while it is being processed. The nature of the solid-liquid interface or mushy zone may be predicted from the solidified microstructure after processing, but it cannot be known exactly. Therefore, it is desirable to take a snapshot of what is going on at the solid-liquid interface or mushy zone. This can be accomplished via rapid cooling or quench. When a quench occurs, the materials at the solid-liquid interface do not have time to change into their equilibrium morphology. The rapidness of the quench determines the quality of this snapshot. Therefore, it is desirable to make this quench as rapid as physically possible.

Refer back to the Bridgman-Stockbarger furnace, Figure 1. Notice that within the hot zone, there are four heaters shown: the hot guard heater, the main and redundant heaters, and the booster heater. The main and redundant heaters occupy most of the axial length of the hot zone, with the main heater radially inside the redundant heater. The redundant heater, as its name implies, is available in case the main heater fails. However, to lengthen the life of the main heater, both main and redundant are often operated simultaneously. With the redundant heater on, the main heater can operate at a lower power level, thus increasing its expected operating life.

The guard heater, located on the bottom or cold end of the hot zone, is designed to operate at a higher power density than the main/redundant heater. This helps to “guard” the sample from cooling due to heat losses out the end of the furnace. The higher power density that the guard heater provides helps keep the temperature profile at the end of the sample equal with the rest of the sample.

The booster heater, located adjacent to the gradient (adiabatic) zone, is also designed for a high power density. By “boosting” the heat going into the sample, the axial gradient in the sample may be increased exactly where it’s needed.

The cold zone in the Bridgman-Stockbarger furnace shown has main and redundant heaters and a guard heater, for the same reason as in the hot zone. A booster heater is not necessary in the cold zone. The main/redundant heater setpoint can be adjusted for optimum thermal gradient.

Although this level of detail is not shown in Figure 2, the hot zone of most Bridgman furnaces is designed with a guard heater, a main and redundant heater set, and a booster heater. The actively cooled cold zone on Bridgman heaters obviously contains no heaters. There is presently a Bridgman furnace being designed with two separately controlled booster heaters to allow for even better control and optimization of the thermal gradient in the sample.

FURNACE AND SCA DESIGN CHALLENGES

The design and operation of the furnace and SCA are very interdependent. Therefore, this section includes challenges associated with SCA design as well as furnace design.

FURNACE DESIGN CHALLENGES

There are several furnace design challenges that are critical to meeting the science requirements outlined by the PI. The challenges listed here are hot zone design, gradient (adiabatic) zone design, cold zone design, quench system design, control of multiple heaters in the hot zone, and temperature measurement.

Hot Zone Design

The purpose of the hot zone is to add heat to the sample radially to effect melting of the sample. There are two major challenges to this. The first is to control the hot zone inner diameter temperature so that the sample is driven to the temperature profile required by the PI. This issue is addressed below. The second challenge is to achieve the required temperature profile with as little power as possible. Therefore, sophisticated insulation design is required. Gas furnaces are insulated with high performance ceramic insulation such as Zirconium Oxide. The best performing insulation will often not withstand the extreme temperatures at the center of the hot zone. Therefore, a lower performing high temperature insulation is used in the center, with the higher performing (lower maximum temperature) towards the outside of the furnace. Refer back to Figure 1 to see the different insulation layers in the hot zone of an inert gas furnace.

Vacuum furnaces require high performance radiation shields, and many layers of them. Multiple shields with a low emissivity are used to restrict radiation heat transfer. Structural mechanisms for the heater substrate and for the radiation shields must be designed to minimize the thermal conduction path as well as to minimize radiation heat transfer.

Gradient (Adiabatic Zone) Design

The gradient zone should be designed to optimize the location and shape of the solid-liquid interface. Obviously, the gradient zone also serves as an insulation barrier between the hot zone and cold zone. Design features beside thermal insulation have been added to some furnaces at Marshall. For instance, in the Crystal Growth Furnace (CGF), a thermal shunt was used. The gradient zone had load-bearing structure within it; therefore, it could not be made entirely of low conductivity insulation. The thermal shunt conducted heat out radially, decreasing the cooling load of the cold zone. This shunt gave the furnace flexibility to accommodate multiple PIs with varying thermal requirements.

Cold Zone Design

The cold zone has the role of removing heat from the sample so that solidification occurs and so that the gradient requirement may be met.

The cold zone setpoint temperature in a Bridgman-Stockbarger furnace is usually high enough that radiation heat transfer is effective. The required gradient may be achieved by lowering or raising the cold zone setpoint temperature.

A Bridgman furnace cold zone usually operates at much cooler temperatures than a Bridgman-Stockbarger furnace. Water is an effective and common coolant for the cold zone. Radiation heat transfer at these lower temperatures is ineffective; therefore, it cannot be relied upon for meeting gradient requirements. Conduction heat transfer is the most effective means of transferring heat from the SCA to the cold zone at these relatively low temperatures.

One means of effecting conduction heat transfer from the SCA to the cold zone is to design the furnace such that a very small gap exists between the outside diameter of the SCA and the inside diameter of the cold zone. The entire furnace is then operated in an inert gas such as helium. The helium serves as the conduction path in the small annular gap between the SCA and cold zone. Helium gas is an attractive choice because among inert gases, it has one of the highest thermal conductivities (other than hydrogen, which is not used for obvious reasons). However, a helium gas environment has the disadvantage of severely degrading the thermal properties of hot zone insulation. Therefore, another solution has been implemented in a number of Bridgman furnaces at Marshall. This solution is to use either an argon gas environment or a vacuum environment with vel-therm in the cold zone. Vel-therm provides a sliding thermal contact interface. It is compliant and reliable. Argon gas with the vel-therm thermal interface provides a slightly better thermal conductance than helium gas by itself. Using argon rather than helium resulted in 50% savings in power applied to the hot zone of a particular Bridgman furnace at Marshall.

Quench System Design

This is one of the most challenging design issues. The goal of a quench system is to radially remove as much heat as possible from the outside surface of the SCA. There are a number of quench systems that have been used. Others are being considered. Table 1 lists these systems, along with their advantages/disadvantages and their nominal heat transfer rate.

Water spray has a high surface heat transfer rate, however, this high heat transfer rate occurs when the surface temperature is between the boiling point and the leidenfrost temperature of the coolant. The leidenfrost temperature is the temperature at which the cooling mechanism transforms to nucleate boiling: a very effective means of phase change cooling. The initial surface temperature of the quenched section will be centered at the phase change temperature of the sample material, well above the leidenfrost temperature for most PI materials (approximately 200 °C for water). At temperatures well above leidenfrost, a vapor barrier will form around the SCA surface, which is the reason for the severe degradation in heat transfer rate. Marshall has funded a Small Business Innovation Research (SBIR) Contract to optimize water spray characteristics and overcome some of the degradation that occurs at high temperatures. The SBIR contractor has made significant progress by optimizing water spray pattern, water droplet size, and water droplet velocity, such that the water droplets penetrate the steam barrier. Through these efforts, the heat transfer coefficient can be increased at temperatures well above 200 °C by raising the leidenfrost temperature. Despite these efforts, water spray still has some inherent problems: the water/steam must be recovered, there are concerns about water coming in contact with the furnace heater core, and issues with material contamination.

With a high-pressure gas quench, gas is stored at high pressure in a container outside the furnace enclosure. The gas is released into the annulus between the SCA and its enclosure. The high pressure and small cross-sectional area cause the gas to achieve sonic velocity in the annulus. This heat transfer rate achieved is up to 10,000 W/m²-K. Gas quench is very attractive, not only because it has less operating problems than water, but also because it has the potential of operating in-situ. That is, rather than translating the SCA

| | <i>Advantages</i> | <i>Disadvantages</i> | <i>Surface Heat Transfer Rate</i> |
|--|---|---|---|
| <i>Water Spray</i> | <ol style="list-style-type: none"> 1. High Quench Rate. 2. Well-Developed Technology. | <ol style="list-style-type: none"> 1. Vibration on sample. 2. Water / Steam must be Exhausted. 3. Low Quench Rate at High Temperature. 4. Contamination Hazard. | 2000 – 25000 W/m ² -K (very temperature dependent) |
| <i>High Pressure Gas</i> | <ol style="list-style-type: none"> 1. Steady and Moderate Quench Rate 2. Gas can be easily exhausted. 3. Well-suited to in-situ quench | <ol style="list-style-type: none"> 1. High Vibration on Sample 2. High Pressure Gas has Safety Issues | 2000 – 10000 W/m ² -K |
| <i>Clamp-on Device (No phase Change)</i> | <ol style="list-style-type: none"> 1. No gas/liquid to recover. 2. Easy operation | <ol style="list-style-type: none"> 1. High Vibration on Sample 2. Low Cooling Rate | 200 – 500 W/m ² -K |
| <i>Clamp-on Device (With phase Change)</i> | <ol style="list-style-type: none"> 1. No gas/liquid to recover. 2. High Quench Rate. | <ol style="list-style-type: none"> 1. Vibration on Sample 2. Containment of Liquid Metals 3. Seals at high temperatures. | 2000 – 10000 W/m ² -K |

(or furnace relative to the SCA) so that the solid-liquid front/mushy zone is in the cold zone or a separate quench zone, the sample is quenched in place. The solid-liquid/mushy zone is located in the gradient zone and the quenching mechanism is brought to it, in the gradient zone. Doing away with the pre-quench translation avoids a time delay and the vibration that may compromise the integrity of the morphology to be preserved with the quench.

Clamp-on devices have also been investigated. The basic concept is to press down on the quenched surface with a device that has a high heat capacity. One example is a collet mechanism made of copper. Thus far, clamp-on devices without a phase change material have not resulted in high enough surface heat transfer rates. The challenge is to effect an adequate heat transfer path between the clamp-on device and the quenched surface (the SCA outer diameter) without damaging the quenched surface or introducing excessive vibration. Plans are under way to improve the design of these devices using compliant materials that also allow adequate heat transfer from the clamp-on device to the quenched surface.

MSFC is also testing clamp-on devices that use a phase change material to serve as the thermal interface mechanism between the clamp-on device and the quenched surface. The phase change material becomes compliant to offer low thermal resistance as it changes phase from solid to liquid. In addition, the phase change material absorbs much of the heat, right at the quenched surface. At high initial quench surface temperatures such as in metal solidification processing, liquid metals are the only materials that can withstand the temperatures. On-going tests show that these devices hold a lot of promise.

Multi-Heater Control

As mentioned earlier, a hot zone has up to five separately controlled heaters: one or two boosters, a set of main and redundant heaters, and a guard heater. A cold zone may have up to three heaters. These heaters are coupled to each other. For example, if more heat is applied to the booster heater, the control measurement of the main heater will be affected as well as the booster heater. Therefore, very sophisticated heater control is necessary. In addition, tight isothermal requirements in the hot zone ($\pm 1^\circ\text{C}$) can make heater control even more difficult.

Temperature Measurement

Temperature measurement is very critical in microgravity furnaces. Two examples are heater control temperature measurement and furnace / sample performance characterization to assure that science requirements are met. Problems and solutions are discussed here.

Thermocouples are the most common measurement device for heater control. Control thermocouples can be stressed due to thermal expansion and exposure to high temperature over long periods of time. Thermocouples can lose calibration over time, especially at high temperatures. Therefore, heater control temperature measurement should have at least one level of redundancy; this allows continued operation if one of the control thermocouples fails. An alternative to using thermocouples is optical fiber thermometers, which transport and analyze the blackbody radiation being absorbed by a probe placed at the desired temperature measurement location. This method of temperature measurement also has its challenges, including having to be very careful about placement of the optical fiber.

Sample measurement can be extremely difficult. Depending on the sample, a thermocouple can be destroyed when it reacts with the sample. Liquid aluminum, for example, is extremely corrosive and can destroy a thermocouple after a relatively short exposure time. On double-contained SCA configurations, thermocouples can be placed in the annular gap between the ampoule and the cartridge, with the thermocouple bead bonded to the ampoule. This type of measurement provides good steady state or quasi-steady-state temperature measurement but is very limited for transient temperature measurement of the sample. Thermal analysis is often used to correlate the temperatures measured on the outside of the ampoule to the desired temperature measurement within the sample.

SCA DESIGN CHALLENGES

The design of the SCA is probably one of the most important and challenging design considerations for furnace design. Its design will affect the quality and magnitude of the gradient and even more so, the success of the quench.

Effect of SCA Gap on Gradient

Figure 4 shows a detailed cross-section of a two containment level SCA design. The thermal heat path down the SCA in the axial direction affects the thermal gradient in the sample. If the axial conductance of the SCA is on the order of or higher than that of the sample, more heat will flow from the hot zone to the cold zone through this path, and the magnitude of the axial thermal gradient will be reduced significantly.

The quality of the thermal axial gradient can also be affected by the thermal properties of the SCA. If the thermal conductance through the SCA is much greater than that of the sample, the solidification front will be closer to the cold zone near the wall than in the sample center. The opposite effect will occur if the

thermal conductance of the SCA is much less than that of the sample. The thermal conductance of the SCA cannot be matched exactly to that of the sample, but measures should be taken to minimize this effect.

Effect of SCA Gap on Quench Rate

The SCA thermal conductance affects quench rate significantly. Here, the conduction path in the radial direction is very important. Referring back to Figure 4, there are three major resistances between the quench medium on the outside of the cartridge to the sample: the cartridge wall, the filler gap, and the ampoule wall. The major challenge is the gap between the inside of the cartridge and the outside of the ampoule. Figure 5 shows the overall thermal conductance versus the gap heat transfer coefficient for three different ampoule materials. The figure shows that up to a gap heat transfer coefficient of $1000 \text{ W/m}^2\text{-K}$, the ampoule material is irrelevant. That is, for a gap thermal conductance of $1000 \text{ W/m}^2\text{-K}$ or below, the thermal resistance of the cartridge wall and of the ampoule wall are insignificant compared to that of the gap between them.

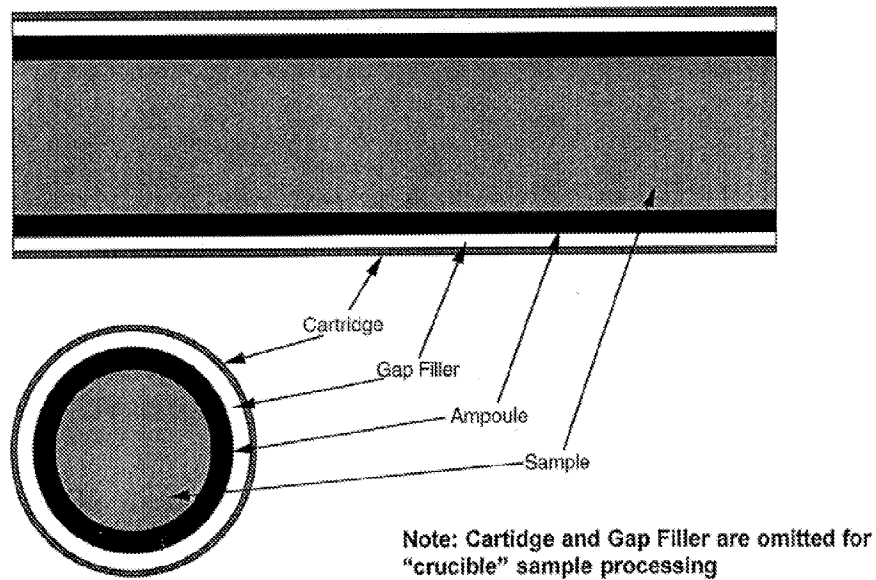


Figure 4: Sample Container Assembly (SCA) Cross-section.

Marshall has investigated the use of liquid metals such as certain indium alloys or crushed powders like alumina or boron nitride as heat transfer "filler" in the SCA gap. However, implementation of these design solutions has been impractical. Problems with thermal expansion of the liquid metals and too low of an effective thermal conductivity with the ceramic powders have been problems thus far.

Applying a metal coating to a ceramic ampoule material via Vacuum Plasma Spray (VPS) is an option being investigated. The metal coating has the purpose of holding the SCA together in case of ceramic failure during quench or other stress causing events. Whether this type of system meets safety requirements for hazardous materials is still being assessed.

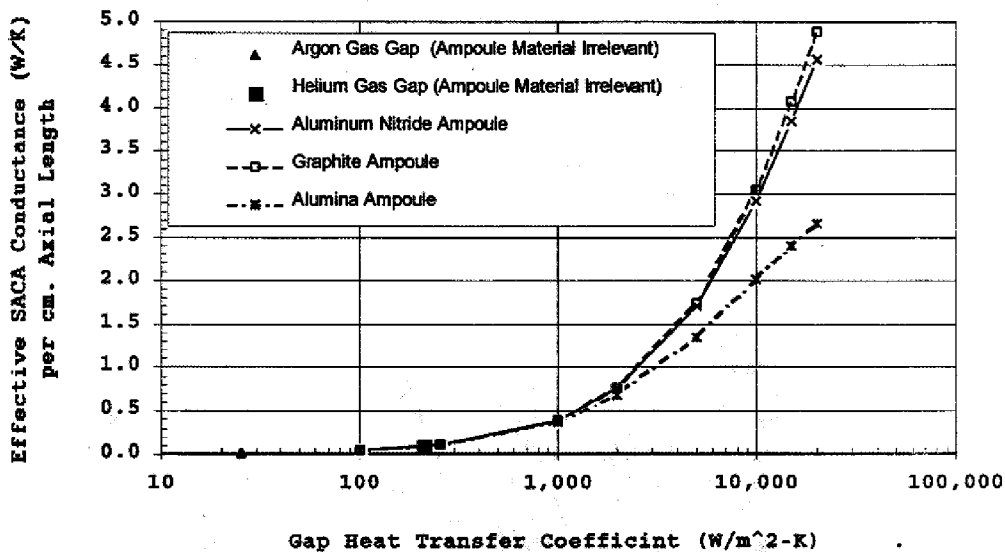


Figure 5: SCA Conductance vs. Gap Heat Transfer Coefficient for a 1.0 mm Gap.

FURNACE THERMAL ANALYSIS DESIGN CHALLENGES

Bridgman and Bridgman-Stockbarger furnaces have a cylindrical geometry, which lends itself to two-dimensional (2-D) axisymmetric thermal models. Figure 6 shows an example of a 2-D axisymmetric model of a Bridgman furnace.

A 2-D axisymmetric model has the advantage of requiring much fewer nodes than a 3-D model. Obviously, this type of model assumes isothermality in the theta (θ) direction. Even though most furnace and sample components are cylindrical and therefore axisymmetric, even the best-designed furnace will have some non-axisymmetric features (i.e., heater wire connections, thermocouples, water lines, structural components, insulation split down the middle for ease of construction, etc.). Assumptions and simplifications must be made to account for these deviations from axisymmetry. A 3-D model of some or the entire furnace may be necessary to assess the effect of these deviations on isothermality in the theta direction.

MULTI-HEATER CONTROL

Thermal analysis plays a key role in heater control. The cross coupling of heaters with each other can be modeled. The design setpoints can be programmed into the thermal model and the power required by each heater may be predicted. Accurate representations of the heater winding locations and heater winding density are critical for accurately predicting the power drawn by each heater. Thermal contact resistance between heater winding substrates and thermal properties are very important for accurate thermal modeling.

FINE MESH IN SAMPLE

Oftentimes, Principal Investigators depend on accurate and detailed predictions of their samples' operating temperatures. Therefore, a high level of fidelity is required in the sample. The modeled representation of the furnace may not require as much fidelity. Therefore, to avoid an enormous model, methods must be

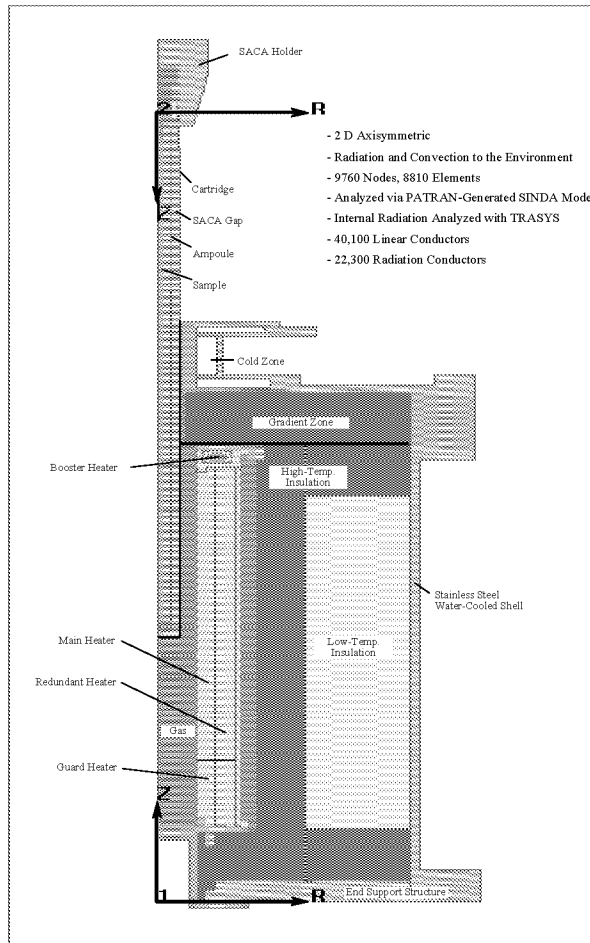


Figure 6: A Thermal 2-D Axisymmetric Model of a Bridgman Furnace.

employed to reduce the node spacing from sample to furnace level in the thermal model. Most modern mathematical modeling tools have mesh generators that allow either a gradual change in model fidelity or discontinuities in the mesh, with internal interpolation schemes communicating across the discontinuous interface.

An alternative to modeling the sample in detail in the furnace model is to model the sample at the lower fidelity of the furnace, and also in a separate more detailed model. Boundary conditions from the furnace/sample model are used as input for the more detailed sample model. This modeling scenario does allow one to run smaller furnace/sample models but has the disadvantage of requiring a lot of data manipulation. Iterations may be required so that the two models converge to one solution.

LARGE ORDER OF MAGNITUDE DIFFERENCE IN THERMAL “CONDUCTORS”

The nature of an axisymmetric thermal model contributes to large geometric variations between thermal conductors in the center of the model versus those near the outer diameter. The variation of thermal properties between the sample and the furnace insulation and the general practice of high fidelity modeling

of the sample (in the center of the model) and lower fidelity modeling of the furnace insulation (near the outer diameter of the model), adds to the problem.

THERMAL PROPERTIES

Thermal properties for samples, particularly alloys, are notoriously hard to come by. In fact, the purpose of some investigations is to determine thermal properties. In addition, there is often a large change in properties between liquid and solid with the mushy zone properties very hard to come by.

The thermal properties of ceramic insulation are often hard to find, or are defined only at one or two temperatures. In vacuum furnaces, the surface thermal properties are often very temperature dependent but known only at one or two temperatures. Manufacturing processes of ceramics (pyrolytic graphite vs. "normal" graphite) can also make for huge differences in thermal properties.

THERMAL TOOLS FOR MICROGRAVITY FURNACE: PAST, PRESENT, AND FUTURE

The most common thermal modeling tool used for microgravity furnaces is the Systems Improved Numerical Differencing Analyzer (SINDA), both SINDA '85 and GASKI SINDA. Graphical interfaces to SINDA, such as Thermal Desktop have improved its use and flexibility. Thermal Radiation Analysis System (TRASYS) is still used, but is giving way to better, more modern tools. RADCAD is an example.

PATRAN has become popular as a furnace design tool in the last few years. It has the advantage of being very quick for modeling simple furnaces or individual furnace components, yet allows a high degree of sophistication and detail when necessary. PATRAN has its own thermal (including radiation) modeler, but also has SINDA and TRASYS interfaces.

FIDAP has some of the advantages of PATRAN, but also has fluid analysis capabilities, allowing the user to model sample liquid convective flows. FIDAP also has excellent pre-processing and post-processing capabilities.

A tool that is going to be implemented for furnace design soon is ProCAST. ProCAST has been developed by the metal casting industry, and will allow transient modeling of a sample/furnace system as the sample is translated out of the furnace. ProCAST was developed for the metal casting industry and includes much of the detailed calculations that metallurgists are interested in.

CONCLUSIONS

Microgravity furnace design and analysis present unique challenges to the thermal designers. Particularly, the high temperatures, steep science requirements, and stringent safety requirements make the job of the thermal designer very difficult. This paper explains some of these challenges and presents some solutions. However, there is much to be done and much to be learned.

ACKNOWLEDGEMENTS

The author wishes to acknowledge the assistance of many fellow furnace designers. These include Jeff Farmer, Myscha Crouch, Monica Hammond, Ed Carrasquillo, and Chris Coppens at Marshall Space Flight Center; Scott Gilley, Barry Battista, Reggie Spivey, Shawn Breeding, and Mark Griffen at Tec-Masters, Inc; Bill Patterson at Pace and Waite; and Jenny Bellomy-Ezell and Stu Nelson at Sverdrup Technology, Inc. Without the camaraderie, advice, and shared experiences from these engineers over the last six years, this paper would not have been possible. Many others, from safety engineers to test engineers to project management to design are too numerous to mention.

REFERENCES

1. "High Gradient Furnace With Quench (HGFQ) Phase A/B Final Report." Prepared by HGFQ Product Development Team. July 1996.
2. National Aeronautics and Space Administration. "Marshall Space Flight Center Fiscal Year 1998 Annual Report."
3. Flemings, M.C. "Solidification Processing." 1973.
4. Totten, G.E.; Bates, C.E.; and Clinton, N.A. "Handbook of Quenchants and Quenching Technology." 1993.



EVALUATION OF THE USE OF OPTICAL FIBER THERMOMETERS FOR THERMAL CONTROL OF THE QUENCH MODULE INSERT

Matthew R. Jones

Department of Aerospace and Mechanical Engineering
The University of Arizona

Jeffrey T. Farmer

Marshall Space Flight Center
NASA

Shawn P. Breeding

Tec-Masters, Inc.

ABSTRACT

Issues regarding the use of optical fiber thermometers to control heater settings in a microgravity vacuum furnace are addressed. It is desirable to use these probes in environments such as the International Space Station, because they can be operated without re-calibration for extended periods. However, the analysis presented in this paper shows that temperature readings obtained using optical fiber thermometers can be corrupted by emissions from the fiber when extended portions of the probe are exposed to elevated temperatures.

INTRODUCTION

The Quench Module Insert (QMI) is a platform for conducting solidification experiments in a microgravity environment. Current plans call for the installation of the QMI in the Microgravity Science Research Rack #1 on the International Space Station. The design of the QMI is similar to that of a Bridgman furnace and consists of a heater core, insulation jacket, instrumentation, coolant loop components, and a quench system. The QMI hot zone assembly is shown in Figure 1. The heater core contains four heated zones: Booster 1, Booster 2, Main and Guard. The sensor plate is cooled in order to maintain the optical fiber thermometers (OFT) and other instrumentation at acceptable operating temperatures. The quenching occurs in a water-cooled chill block (not shown) which is located adjacent to Booster 1. This design produces the high thermal gradients required for directional solidification processing experiments.

Precise thermal control is necessary to perform the candidate experiments for the QMI, and there is concern that thermocouples will drift due to exposure to cyclical thermal environments during the extended period of time it is planned to have the QMI in orbit. This concern led to the inclusion of OFT in the design of the QMI. Preliminary designs call for the installation of Accufibers with sapphire blackbody sensors. Accufibers are a brand of OFT manufactured by LUXTRON Corporation. Product literature available from LUXTRON indicates that Accufibers have an accuracy of 0.2% at 1000 C and a resolution of 0.01 C. In

addition, Accufibers demonstrate excellent long-term stability and are immune to electromagnetic interference. In the proposed QMI design, the sapphire fiber is aligned with the axis of the QMI and an extended portion of the fiber is exposed to elevated temperatures. The analysis presented in this paper indicates that OFT readings will be corrupted under these conditions. Results obtained from a thermal model of the QMI are used to predict the temperature readings of an OFT probe. These predictions are consistent with readings obtained during the testing of a QMI prototype.

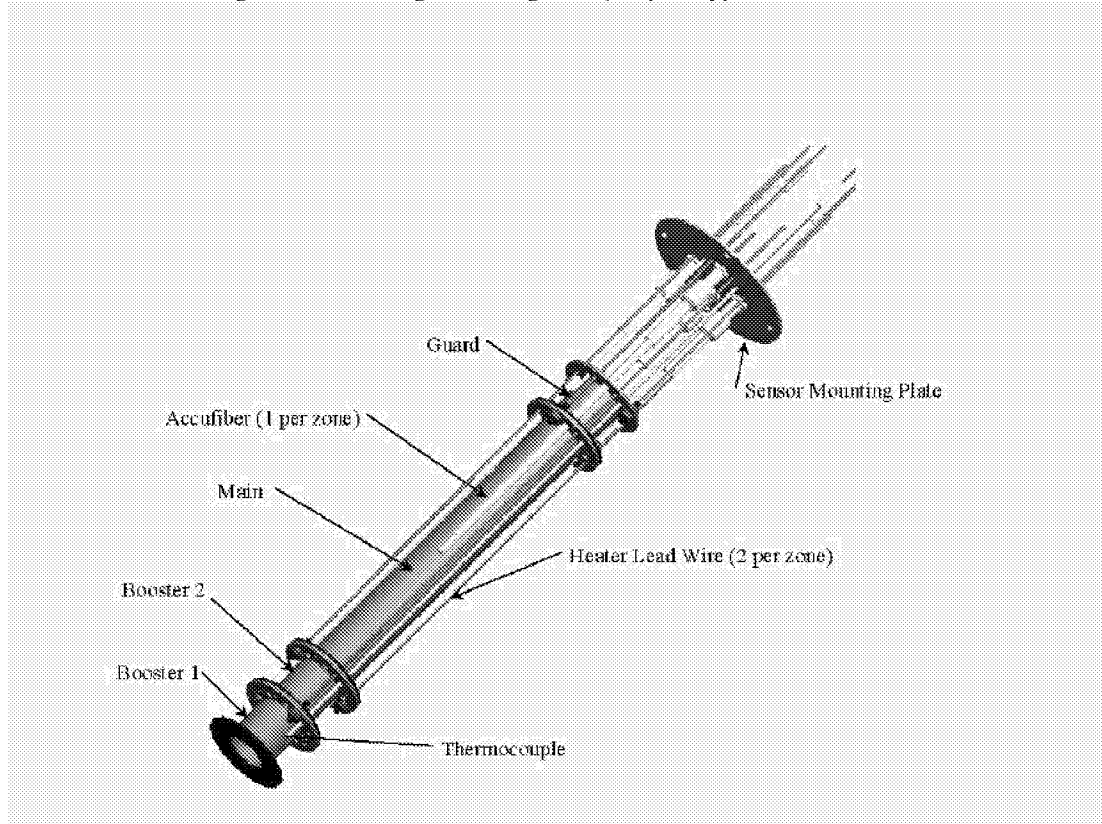


Figure 1: QMI Hot Zone (Heater Elements) Assembly¹.

OVERVIEW OF OPTICAL FIBER THERMOMETRY

This section summarizes the basic principles of OFT². An Accufiber sapphire blackbody sensor is illustrated in Figure 2. The probe consists of a sapphire (Al_2O_3) fiber whose sensing tip is given a metallic coating. The sensing tip of the fiber is essentially an isothermal cavity, so the emission from this cavity will be approximately equal to the emission from a blackbody. The other end of the fiber is attached to the OFT detection system.

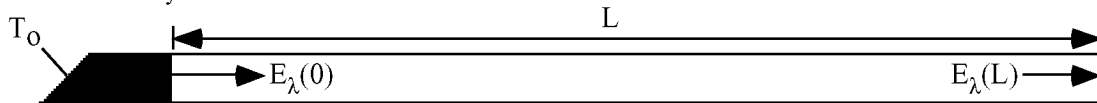


Figure 2: Schematic diagram for an Accufiber sapphire blackbody sensor. The sensing tip ($z=0$) is coated with a thin metallic film to create a small isothermal cavity at a temperature of T_0 . The radiative flux emitted by the cavity, $E_\lambda(0)$, is approximately equal to the spectral emissive power of a blackbody, $E_{b\lambda}(T_0)$.

Modeling the sapphire fiber as a non-scattering medium, the radiative flux propagating along the fiber is governed by³

$$\frac{dE_\lambda}{dz} = -K_{a\lambda}E_\lambda + K_{a\lambda}E_{b\lambda}(T(z)) \quad (1)$$

where E_λ is the spectral radiative flux ($\text{W}/\text{m}^2 \mu\text{m}$), $K_{a\lambda}$ is the spectral absorption coefficient (mm^{-1}) and $E_{b\lambda}(T(z))$ is the spectral emissive power of a blackbody at a temperature of $T(z)$. If the spectral absorption coefficient is independent of temperature, it is convenient to use the optical depth as the independent variable

$$t_\lambda = K_{a\lambda}z \quad (2)$$

Eq. (1) then becomes

$$\frac{dE_\lambda}{dt_\lambda} + E_\lambda = E_{b\lambda}(T(t_\lambda)) \quad (3)$$

Assuming that the sensing tip of the probe emits like a blackbody, the appropriate boundary condition for Eq. 3 is

$$E_\lambda(0) = E_{b\lambda}(T_0) \quad (4)$$

The solution to Eq. 3, subject to the boundary condition given by Eq. 4 is

$$E_{b\lambda}(T_0) = E_\lambda(t_{\lambda L}) \exp\{t_{\lambda L}\} - \int_0^{t_{\lambda L}} E_{b\lambda}(T(t_\lambda)) \exp\{t_\lambda\} dt_\lambda \quad (5)$$

where $t_{\lambda L} = K_{a\lambda}L$. The spectral radiative flux measured by the Accufiber detection system, M_λ , is related to the spectral radiative flux at the end of the sapphire fiber.

$$M_\lambda = E_\lambda(t_{\lambda L}) \Delta\lambda C \quad (6)$$

where $\Delta\lambda$ is the width of the band pass filter used by the Accufiber probe and C is a correction factor to account for various losses in the detection system. Substitution of Eq. 6 into Eq. 5 gives

$$E_{b\lambda}(T_0) = \frac{M_\lambda e^{t_{\lambda L}}}{\Delta\lambda C} - \int_0^{t_{\lambda L}} E_{b\lambda}(T(t_\lambda)) \exp\{t_\lambda\} dt_\lambda \quad (7)$$

The integral on the right hand side of Eq. 7 represents the portion of the measured spectral radiative flux that is due to emission by the fiber. This integral can be neglected if sapphire is a poor emitter at the wavelengths of interest ($K_{a\lambda} \ll 1$) or if the fiber is at a low enough temperature to ensure that the emission by the fiber is negligible at the wavelengths of interest ($T(t_\lambda) \ll T_0$).

The spectral emissive power of a blackbody at a temperature of T is given by Planck's equation.

$$E_{b\lambda}(T) = \frac{c_1}{\lambda^5 \left[\exp\left\{\frac{c_2}{\lambda T}\right\} - 1 \right]} \quad (8)$$

where the radiation constants are $c_1 = 3.7413 \times 10^8 \text{ W}\mu\text{m}^4/\text{m}^2$ and $c_2 = 14388 \mu\text{mK}^3$. For the wavelengths used by the Accufiber probe ($\lambda_1 = 0.80 \mu\text{m}$, $\lambda_2 = 0.95 \mu\text{m}$) and the temperature range of interest (400 - 1700 K), the exponential term is much larger than one. Therefore, Eq. 8 is well approximated using Wein's limit.

$$E_{b\lambda}(T) \approx \frac{c_1}{\lambda^5 \exp\left\{\frac{c_2}{\lambda T}\right\}} \quad (9)$$

The temperature reading obtained by the Accufiber probe, T_m , is calculated by neglecting the integral in Eq. 7. Substitution of Eq. 9 into Eq. 7 then gives

$$\exp\left\{-\frac{c_2}{\lambda T_m}\right\} = \frac{\lambda^5 M_\lambda e^{t_{\lambda L}}}{c_1 \Delta \lambda C} \quad (10)$$

Using the measurements at two wavelengths and Eq. 10, the following ratio can be formed.

$$\frac{\exp\left\{-\frac{c_2}{\lambda_1 T_m}\right\}}{\exp\left\{-\frac{c_2}{\lambda_2 T_m}\right\}} = \left(\frac{\lambda_1}{\lambda_2}\right)^5 \left(\frac{C \Delta \lambda_2}{C \Delta \lambda_1}\right) \left(\frac{M_{\lambda_1} e^{t_{\lambda_1 L}}}{M_{\lambda_2} e^{t_{\lambda_2 L}}}\right) \quad (11)$$

Assuming that $\Delta \lambda_1 \approx \Delta \lambda_2$ and that the losses in the Accufiber detection system do not depend on wavelength, T_m is given by

$$T_m = \frac{c_2}{(\lambda_2 - \lambda_1) \ln \left[\left(\frac{\lambda_1}{\lambda_2}\right)^5 \left(\frac{M_{\lambda_1} e^{t_{\lambda_1 L}}}{M_{\lambda_2} e^{t_{\lambda_2 L}}}\right) \right]} \quad (12)$$

ANALYSIS OF ERRORS DUE TO EMISSION BY THE FIBER

Clearly, temperatures obtained using Eq. 12 will only be accurate when the approximations employed in the derivation are satisfied. In particular, emission by the fiber will change the value of the radiative flux measured by the OFT detection system and result in inaccurate measurements when large portions of the sapphire fiber are at elevated temperatures.

RELATIONSHIP BETWEEN T_o AND T_m

Recall that the measured temperature is the temperature obtained when the integral in Eq. 7 is neglected. The relationship between the measured spectral radiative flux and the measured temperature is

$$\frac{M_\lambda e^{t_{\lambda L}}}{\Delta \lambda C} = \frac{c_1}{\lambda^5} \exp\left\{-\frac{c_2}{\lambda T_m}\right\} \quad (13)$$

Substituting Eq. 13 into Eq. 7 and solving for T_m gives

$$T_m = \frac{c_2 \left(\frac{1}{\lambda_2} - \frac{1}{\lambda_1}\right)}{\ln \left[\exp\left\{-\frac{c_2}{\lambda_1 T_o}\right\} + f(\lambda_1, T(t_{\lambda_1})) \right] - \ln \left[\exp\left\{-\frac{c_2}{\lambda_2 T_o}\right\} + f(\lambda_2, T(t_{\lambda_2})) \right]} \quad (14)$$

where

$$f(\lambda, T(t_\lambda)) = \frac{\lambda^5}{c_1} \int_0^{t_{\lambda L}} E_{b\lambda}(T(t_\lambda)) \exp\{t_\lambda\} dt_\lambda \quad (15)$$

and $T(t_\lambda)$ is the temperature profile along the sapphire fiber.

In order to evaluate Eq. 14 and assess the errors due to emission by the fiber, it is necessary to know the temperature profile along the fiber and the absorption coefficient of Al_2O_3 at the wavelengths of interest. The following sections address these matters.

TEMPERATURE PROFILE ALONG THE OPTICAL FIBER THERMOMETER

The OFT probes are inserted in a boron nitride sleeve that surrounds the heated core of the QMI. The probes are coupled radiatively to the sleeve in which they are housed. There is also a conduction path along the fibers to the sensor mounting plate. A SINDA model of the thermal environment of each fiber was developed to estimate the temperature profile along the fiber. A description of the geometry of the QMI and the SINDA thermal model is given elsewhere¹.

The SINDA model was used to calculate simulated OFT readings for the probes that are aligned with the Booster 1, Booster 2 and Main heating elements for the six cases listed in Table 1. The set points refer to the temperatures settings of the heating elements. Since the sensing tips of the OFT are positioned in the boron nitride sleeve and away from the heating elements, the set points are 10 to 40 C higher than the temperatures of the sensing tips. Figures 3 - 5 show the estimated temperature profiles for each of the three OFT probes.

Table 1. QMI Heater Set Points

| Case | Booster 1 Set Point (C) | Booster 2 Set Point (C) | Main Set Point (C) | Guard Set Point (C) |
|------|-------------------------|-------------------------|--------------------|---------------------|
| 1 | 600 | 600 | 600 | 600 |
| 2 | 600 | 600 | 650 | 650 |
| 3 | 900 | 900 | 900 | 900 |
| 4 | 900 | 900 | 950 | 950 |
| 5 | 1100 | 1100 | 1100 | 1100 |
| 6 | 1200 | 1150 | 1100 | 1100 |

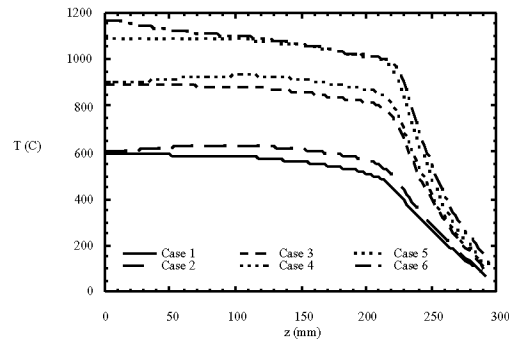


Figure 3: Estimated temperature profiles for Probe 1.

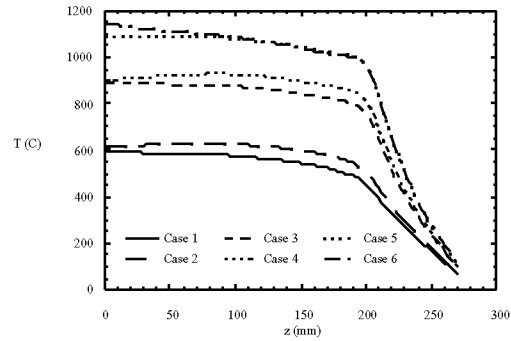


Figure 4: Estimated temperature profiles for Probe 2.

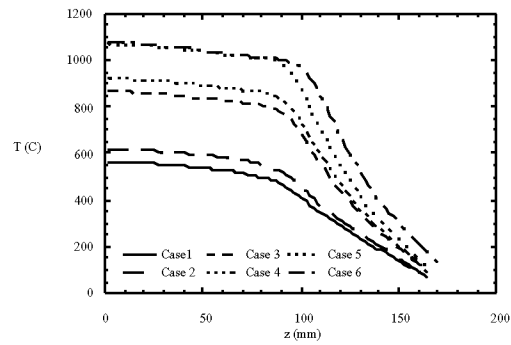


Figure 5: Estimated temperature profiles for Probe 3.

OPTICAL PROPERTIES OF SAPPHIRE

Brewster³ lists values for the real and imaginary parts of the refractive index a function of wavelength. At 1 μm , the imaginary part of the refractive index is $k = 6 \times 10^{-8}$. Assuming that the refractive index does not vary significantly with wavelength, the absorption coefficients at 0.80 and 0.95 μm can be calculated.

$$K_{a\lambda_1} = \frac{4\pi k}{\lambda_1} = 9.42 \times 10^{-4} \text{ mm}^{-1} \quad (16)$$

$$K_{a\lambda_2} = \frac{4\pi k}{\lambda_2} = 7.94 \times 10^{-4} \text{ mm}^{-1} \quad (17)$$

These values are consistent with the data published by Gryvnak and Burch⁴ as shown in Figure 6.

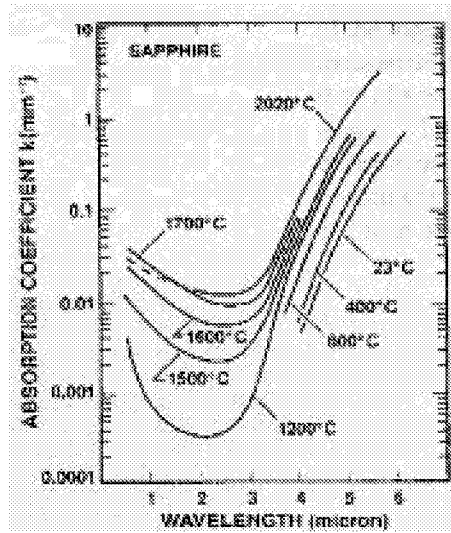


Figure 6: Spectral absorption coefficient of single crystal sapphire (Al_2O_3) at elevated temperatures⁴.

COMPARISON OF T_o AND T_m

Using the estimated temperature profiles shown in Figures 3 - 5 and the spectral absorption coefficients given by Eq. 16 and Eq. 17, the integral in Eq. 15 was evaluated numerically. Estimates for T_m were then calculated for each of the OFT temperature profiles. These values are compared with the temperature at the sensing tip of the OFT in Table 2.

Table 2. Comparison of OFT Readings and Sensing Tip Temperatures

| Probe | Case | OFT Readings (C) | OFT Sensing Tip Temperature (C) |
|-------|------|------------------|---------------------------------|
| 1 | 1 | 598 | 594 |
| 1 | 2 | 616 | 604 |
| 1 | 3 | 900 | 890 |
| 1 | 4 | 916 | 896 |
| 1 | 5 | 1102 | 1087 |
| 1 | 6 | 1171 | 1167 |
| 2 | 1 | 595 | 592 |
| 2 | 2 | 621 | 612 |
| 2 | 3 | 898 | 891 |
| 2 | 4 | 920 | 903 |
| 2 | 5 | 1100 | 1087 |
| 2 | 6 | 1145 | 1142 |
| 3 | 1 | 563 | 561 |
| 3 | 2 | 618 | 616 |
| 3 | 3 | 869 | 866 |
| 3 | 4 | 924 | 920 |
| 3 | 5 | 1075 | 1071 |
| 3 | 6 | 1085 | 1080 |

Comparison of the predicted OFT readings with the estimated sensing tip temperatures indicates that errors due to fiber emission increase as the length of fiber exposed to elevated temperatures increases. These results also show that the errors increase as temperatures increase.

COMPARISON OF PREDICTED AND MEASURED OFT TEMPERATURES

A prototype version of the QMI was tested at various heater settings, and the OFT readings were obtained for the six cases listed in Table 1. These measured values are compared with the predicted values in Table 3.

Table 3. Predicted and Measured OFT Temperature Readings

| Probe | Case | Predicted OFT Temperature Reading (C) | Measured OFT Temperature Reading (C) |
|-------|------|---------------------------------------|--------------------------------------|
| 1 | 1 | 598 | 586 |
| 1 | 2 | 616 | 591 |
| 1 | 3 | 900 | 873 |
| 1 | 4 | 916 | 879 |
| 1 | 5 | 1102 | 1064 |
| 1 | 6 | 1171 | 1132 |
| 2 | 1 | 595 | 612 |
| 2 | 2 | 621 | 639 |
| 2 | 3 | 898 | 910 |
| 2 | 4 | 920 | 938 |
| 2 | 5 | 1100 | 1115 |
| 2 | 6 | 1145 | 1146 |
| 3 | 1 | 563 | 576 |
| 3 | 2 | 618 | 620 |
| 3 | 3 | 869 | 857 |
| 3 | 4 | 924 | 904 |
| 3 | 5 | 1075 | 1052 |
| 3 | 6 | 1085 | 1059 |

The agreement between the measured and predicted OFT readings is somewhat imprecise. The measurements obtained from probe 1 are consistently lower than the predicted values. Measurements obtained using probe 2 are consistently higher than the predicted values. Since the temperatures in the boron nitride sleeve vary considerably, these results indicate that the location of the probe's sensing tips in the QMI prototype may differ from their location in the SINDA model. In addition, uncertainties regarding the thermal coupling between the OFT probes and their environment in the SINDA model make a precise interpretation of these results difficult.

SUMMARY AND CONCLUSIONS

The analysis presented in this paper demonstrates that an elevated temperature profile along the fiber will increase the temperature read by an OFT system due to radiative emission by the fiber. An expression that quantifies the errors due to fiber emission has been derived. The results presented in this paper show that the difference between the measured and tip temperatures decreases as the length of fiber exposed to elevated temperatures decreases. Also, the errors generally increase as temperatures increase.

Predictions of the OFT readings based on a SINDA model of the probes thermal environment were compared with OFT readings obtained during the testing of a prototype of the QMI. The agreement between the predicted and measured values is not exact, but is consistent with uncertainties regarding the exact position of the sensing tips of the probes and the thermal coupling between the probes and their surroundings. Efforts to more accurately characterize the thermal environment of the OFT are currently being made.

ACKNOWLEDGMENTS

MRJ wishes to acknowledge the support of NASA - Marshall Space Flight Center through an Intergovernmental Personnel Act Assignment Agreement.

REFERENCES

1. NASA-MSFC, Tec-Masters, Inc., Sverdrup Technologies 1999 *Thermal Design Data Book*, Quench Module Insert, Preliminary Design Review.
2. Dils, R. R. 1983 "High-temperature optical fiber thermometry," *Journal of Applied Physics*, Vol. 54 (3), pp. 1198-1201.
3. Brewster, M. Q. 1992 *Thermal Radiative Transfer & Properties*, John Wiley & Sons, New York.
4. Gryvnak, D. A. and Burch, D. E. 1965 "Optical and Infrared Properties of Al_2O_3 at Elevated Temperatures," *Journal of the Optical Society of America*, Vol. 55 (6) pp. 625-629.



Characterization of the Heat Extraction Capability of a Compliant, Sliding, Thermal Interface for Use in a High Temperature, Vacuum, Microgravity Furnace

Jenny Bellomy-Ezell

Sverdrup Technologies Inc., Huntsville, AL

Jeff Farmer

NASA Marshall Space Flight Center

Shawn Breeding, Reggie Spivey

TecMasters Inc., Huntsville, AL

ABSTRACT

A compliant, thermal interface material is tested to evaluate its thermal behavior at elevated temperatures, in vacuum conditions, and under varying levels of compression. Preliminary results indicate that the thermal performance of this polymer fiber-based, felt-like material is sufficient to meet thermal extraction requirements for the Quench Module Insert, a Bridgman furnace for microgravity material science investigation. This paper discusses testing and modeling approaches employed, gives of a status of characterization activities and provides preliminary test results.

Introduction

A common type of furnace used in Microgravity material science investigations is a Bridgman furnace consisting of hot zone for melting a long, thin, cylindrical sample (typically a metal alloy), and a cold zone for extracting heat from the sample to resolidify it. The primary function of this configuration is to induce a large temperature gradient along the length of the sample at approximately the location of the interface of the solid and liquid regions of the sample. Additionally, this furnace translates relative to the sample such that the translation rate of the furnace is equal to the rate at which the solid liquid interface moves (this corresponds to the solidification rate). An example of this type of furnace, currently being developed, is the Quench Module Insert (QMI), [Ref]. The QMI furnace will be installed as part of the Microgravity Science Research Facility (MSRF); one of the first science facilities planned to fly aboard the International Space Station (ISS).

In the current QMI design, the cold zone consists of the water-cooled outer section surrounding a conical shaped insert. On the inner diameter of this insert is a felt or velvet-like material that serves as the primary thermal interface with the sample assembly.

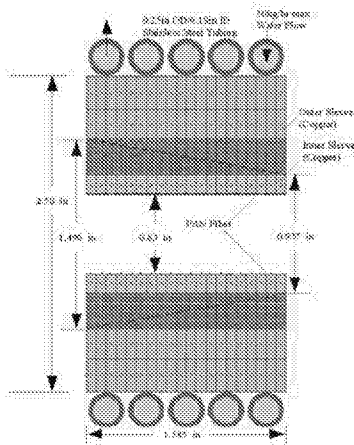


Figure 1. Schematic of Replaceable Cold Zone.

This felt is composed of carbon polymer fibers, which are perpendicularly attached to a substrate, which is then affixed to the replaceable cold zone insert. This material is a product called Vel-Therm and is produced by a

company in California called Energy Sciences Lab, Inc. This velvet-like material is both compliant, allowing the material to brush against the sample assembly surface during translation, and highly thermally conductive, providing for high heat extraction rates by the cold zone. These high heat extraction rates, in turn produce high sample thermal gradients required by the scientific investigations (>100 °C/cm for some QMI investigations) that will use this furnace.

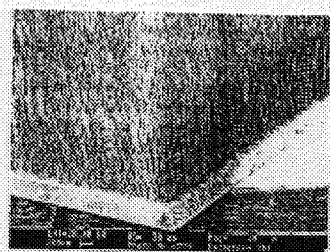


Figure 2. Isometric View of Oriented Fibers and Substrate Comprising the Vel-Therm felt.

This conductive couple is particularly important for QMI due to the vacuum environment in which it operates. Without this conductive couple, heat would have to be extracted from the sample via only radiation across the vacuum gap between the cold zone and sample assembly. At the temperatures required for the investigations using QMI, this would severely limit the heat extraction and consequently the attainable sample thermal gradients.

The Vel-Therm material was developed via a Small Business Innovative Research Contract, [ref]. In this early development work the thermal performance of the material was characterized in an air environment at low temperatures. In addition, since that early investigation the vendor, ESLI, has made substantial improvements in the material. Consequently, additional testing was required to characterize the thermal behavior of the new material and to do so in conditions resembling those of QMI, namely higher temperature and vacuum. The data derived from this activity is to be used to evaluate the material's performance sensitivity to various QMI design parameters and to provide quantitative data for use in the QMI thermal models. In addition, the data will be used to help select the appropriate Vel-Therm and set proper operating limits. This paper outlines the approach and results of this characterization.

Test Matrix

The test results of two different Vel-Therm types are presented in this paper. In designing the test setup, parameters were selected to simulate the actual furnace specifications as closely as possible. For example, the temperature the felt would be exposed to ranged from 100 to 600 °C in the furnace. Therefore, the setpoint temperatures bound this range. Also, for each felt tested, we wanted to examine different initial gap size settings. These gap settings were typically based on a percentage of felt height, which is the sum of fiber length, thickness of substrate and thickness of the adhesive.

Table 1. Vel-Therm Characterization Test Matrix

| Felt Type | Set Point Temp (°C) | Gap Size (mils) | Gap Size as % of felt height |
|------------------|--------------------------------|----------------------------|---|
| J80G | 100 - 600 | 95, 55 | 99, 40 |
| J120G | 100 - 600 | 120, 114 | 99, 95 |

Test Objectives and Approach

The main focus of this test is to measure the heat extraction rate of the Vel-Therm felt as specified by the effective heat transfer coefficient. This effective heat transfer coefficient, h_{eff} , is defined by the following equation:

$$h_{eff} = \frac{Q}{A(T_{Hot} - T_{Cold})}$$

Where Q is the heat extracted by cold zone through the felt interface; A is the area of the felt interface; T_{Hot} and T_{Cold} are the temperatures of the hot and cold surfaces, respectively, being coupled via the felt. More importantly, T_{hot} simulates the temperatures seen by the sample assembly and T_{cold} simulates the chill block temperatures.

The primary means of establishing the power being conducted through the felt was to measure the energy transferred to the water passing through the cold side assembly. Consequently, the effective heat transfer in terms of the measured parameters is given in the following equation.

$$h_{eff} = \frac{\dot{m}Cp(T_{out} - T_{in})}{A(T_{Hot} - T_{Cold})}$$

Where \dot{m} and Cp are the mass flow rate and the specific heat, respectively, of the cooling water. T_{out} and T_{in} are the outlet and inlet temperatures of the cooling water. A is the surface area over which the Vel-Therm felt is applied. T_{Hot} is the average temperature of the hot (or heated) surface and T_{Cold} is the average temperature of the cold (or cooled) surface. This assumes that the heat lost to the surroundings, either through conduction or radiation, from the cold surface is negligible. It was assumed, and confirmed via analysis, that each surface was approximately isothermal under the specific test conditions.

Test Fixture

Again, we wanted to measure the temperature delta across the water as our means of characterizing the heat transfer performance of the Vel-Therm. Therefore, the test fixture was designed to measure the heat transferred from the top surface of the hot side assembly, to the bottom surface of the chill block, which is actively cooled by a helical fluid loop just under the surface. Both the hot side assembly and the chill block are made of copper. The hot side assembly temperature was targeted to represent those typical of QMI sample assembly and the chill block was controlled to temperatures typical of the QMI cold zone. The two surfaces are coupled with the Vel-Therm, which is bonded to the chill block surface. The gap between the Hot Side Assembly and the Cold Side Assembly was positioned by a scissor-supported plate, which supports the Cold Side Assembly from above.

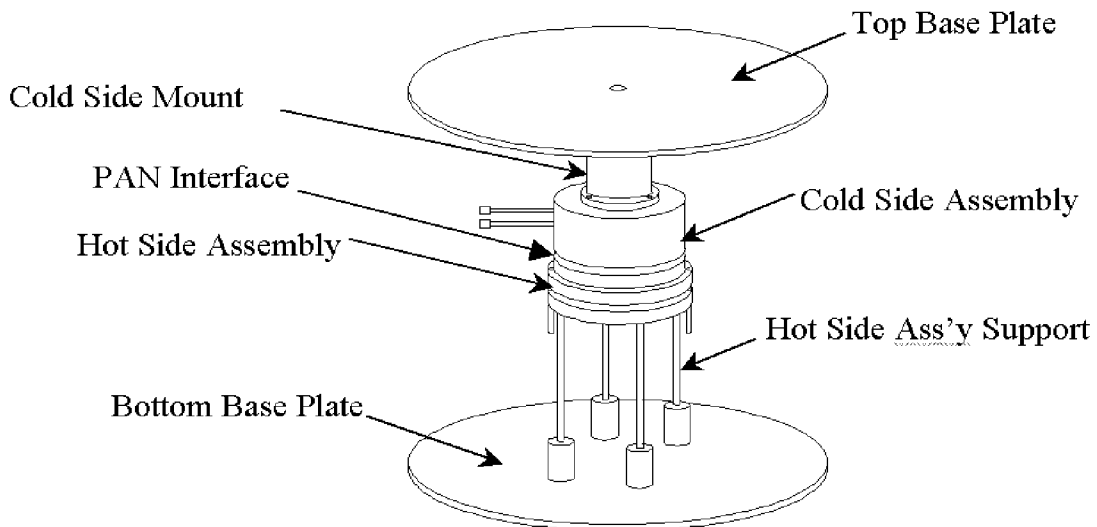


Figure 3. Isometric View of VEL-THERM Test Setup (not to scale)

We also wanted to minimize heat transfer to the chill block in areas other than the Vel-Therm interface. Therefore, to reduce heat loss from the bottom and sides of the Hot Side Assembly, a 6-layer molybdenum radiation shield was constructed around the circumference of the Hot Side Assembly. Additionally, the mating

surfaces of the chill block and hot copper were highly polished in order to minimize radiative coupling between the two surfaces. Furthermore, aluminized tape was adhered to the chill block's circumference to help prevent radiative gains in the chill block thereby further reducing inaccuracies in measured heat load.

Lastly, appropriate instrumentation was applied and the whole assembly was housed in a bell jar and vacuum conditions ($P < 10^{-4}$ mbar) imposed. Temperatures of the test assembly were monitored by twelve Type K thermocouples. RTD's were used to measure the water inlets and outlet temperatures.

Thermal Model

While some initial thermal analysis was performed via spreadsheet based hand calculations, the bulk detailed analysis is being performed using PATRAN and P3Thermal. P3Thermal is a geometry-based thermal analysis tool that uses PATRAN as the geometry modeler and mesh generator. P3Thermal accommodates conductive, radiative, and convective transfer in solids and also provides capabilities to assess advective heating of the coolant flow. Details of the PATRAN and P3Thermal are provided in reference 7. The geometric model of the test apparatus is depicted in Figure 4. The molybdenum shields are not shown so that the hot and cold copper assemblies may be viewed.

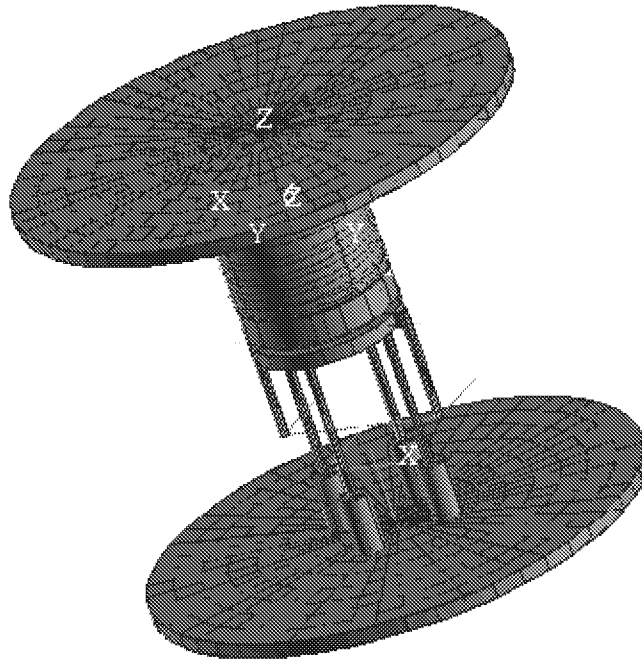


Figure 4. Isometric View of 3D Test Apparatus Test PATRAN/P3THERMAL Model without Radiation Shields. A number of boundary conditions were applied to the model to simulate the important heat flow paths and thermal sinks. Using P3Thermal, we were able to use multiple enclosures to capture the radiative exchange and heat loss. The area where the VEL-THERM felt is adhered to the chill block and in contact with the heated copper has a convection between regions boundary condition imposed. To accurately simulate the heat transfer to the chill block's helical fluid loop an advective boundary condition was imposed. The main focus of this on-going analysis is to predict the heater power levels and losses, water cooling rates and temperatures at key locations throughout the test apparatus. This model was also used to validate the isothermality of the chill block area where the Vel-Therm is applied.

Results and Error Assessment

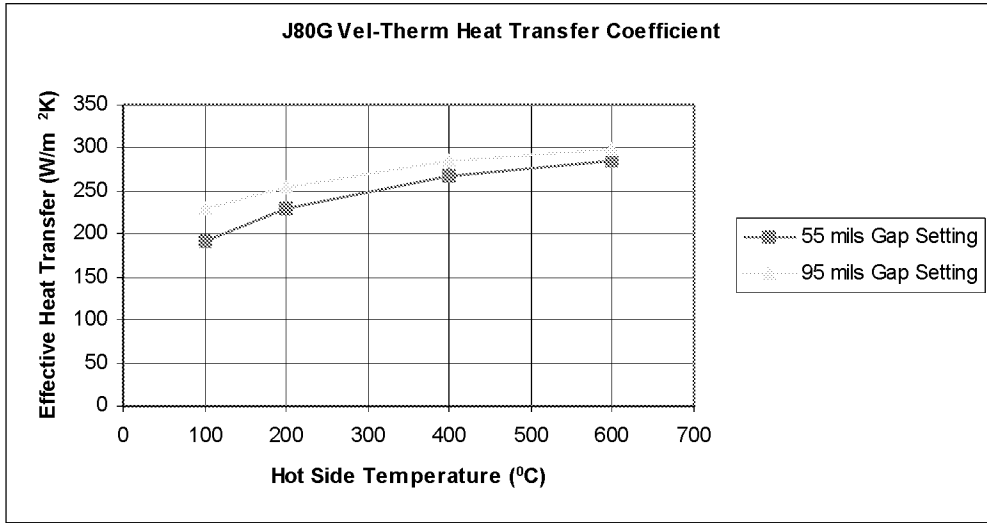
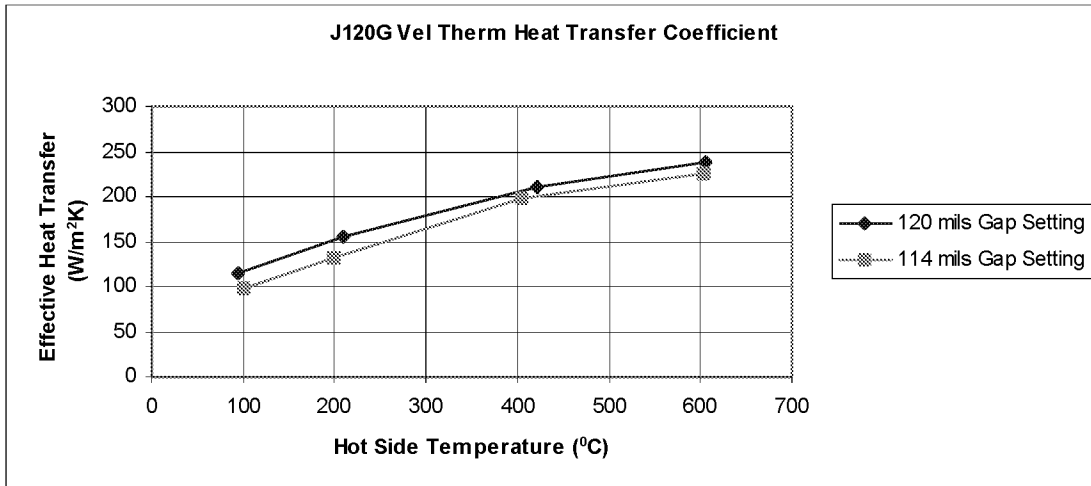


Figure 5. J80G VEL-THERM Heat Transfer Coefficient vs. Hot Side Surface Temperature

The data for the J80G is presented as a function of the hot side temperature and initial gap size. Data was recorded at four temperatures, ranging from 100 to 600 $^{\circ}C$. The cold surface temperature was maintained between 35 and 40 $^{\circ}C$. In the first run (55 mil gap size), the fibers are bent to conform to a gap size that is almost half of the fibers' length. It was supposed that increasing the compression could theoretically result in an increase in effective heat transfer coefficient. As the gap shrinks relative to the fiber length, more of the fiber is bent over. The result would be increased surface contact between the fiber the hot side surface and possibly increased contact pressure due to bending the fibers. This increased area and pressure could increase contact conductance. Results for the 55 mil gap size case, however, were actually lower than the second run which had a larger gap size, indicating that h might actually increase with an increasing gap size. The 55 mil gap could have been excessive, damaging some of the fibers.

The gap size for the second run was set to 95 mils such that the fibers were in contact with the hot copper but not bent to the naked eye. Both cases show significant dependence on temperature. This fact could have arisen from increased radiation at elevated hot surface temperatures.

The following sets of curves summarize the results obtained for the second VEL-THERM type tested, the J120G. Figure 6. J80G VEL-THERM Heat Transfer Coefficient vs. Hot Side Surface Temperature



Now, we can see that the data indeed shows a trend indicating that the effective heat transfer coefficient increases as gap size increases. It is not intuitive why this is happening and further testing is needed to investigate this trend. Again, the results indicate temperature dependence. Comparing the different Vel-Therm types, the J80G's performance is superior.

Error Assessment

To provide an error assessment, the heat transfer measured across the water was compared to the heat provided by the power supply. Attempts were made to quantify the heat loss from the heater that occurred in places other than the felt interface. The only significant conduction heat paths were those from the heater leads and the Hot Side Support Structure. Hand calculations were done to quantify the heat loss in this area.

The J80Gf at 600 °C run was chosen for comparison as a worst case scenario. Comparing the wattage from the power supply to the q into the water, the heater power was 119 W higher. The heat transfer down the two heater leads accounted for 27 W. The heat transfer down the four support rods accounted for another 30W.

The only significant radiation heat transfer was that emitted by the Hot Side Assembly. The test setup configuration employs molybdenum radiation shields to insulate the Hot Side Assembly. In addition, the copper block encasing the heater element was polished reducing the emissivity and the radiative losses further.

Radiation from the hot copper, support rods and shields was calculated using the equation for infinite concentric

$$q_{12} = \frac{\sigma A_1 (T_1^4 - T_2^4)}{[1/\epsilon_1 + 1 - \epsilon_2/\epsilon_2]} (r_1/r_2)$$

cylinders. This identified another 19 W of heat loss.

The heater leads were encapsulated with insulation to exclude interference with the base plate. This insulation provided a heat leak that accounts for 6W. Another possible source of heat loss is into the copper tubing that connects the fluid loop to the flexible tubing of the water pump. Also, radiation from the exposed portions of the surfaces of the copper cylinder where the VEL-THERM is applied may contribute. This accounted for approximately 5 W. This still leaves approximately 30 watts unaccounted for. A possible explanation may be error associated with the measurement devices, either measuring the water flow or the heater output. The unidentified heat loss is less than 10% of the calculated heat transfer into the water. This error may relate to the curve discussed earlier which indicates that heff actually increases as gap size increases. This issue is under investigation.

In addition to the hand calculations, the modeling effort is on going to investigate this heat loss. The test setup is well instrumented, therefore, we are looking at temperatures at various locations to find where the energy loss is occurring. Insights gained from this error assessment will aid in a redesign of the test setup.

Conclusions

Overall, the performance J80G VEL-THERM was in performance, as it had been in the room environment testing. Also, significant temperature dependence was observed in both Vel-Therm types. The results do seem to suggest that the effective heat transfer coefficient increases as gap size increases. Therefore, lower compression rates would be recommended. This trend is not fully understood and will be investigated further. One benefit of utilizing lower compression rates is decreasing the possibility of damaging the fibers. Another benefit of using the lower compression rates is avoiding the misalignment problems caused between the interior surface of the furnace bore and the exterior surface of the SACA during the high processing temperatures when material properties change and expansion occurs.

A possible explanation of the surprising results is the lack of fiber density control. The fiber packing fraction would impact performance by affecting the amount of contact area provided. If it varies from one batch to another more than slightly, the ability to repeat earlier performance is lost. This raises the question of how to control or test each batch before accepting it into inventory. This is an important area of concern and will require future work to resolve.

A great deal of work remains to be done to characterize the heat extraction capability of VelTherm. Namely, resolving the energy balance problem and possibly redesigning the test fixture. Also, examination of the trend indicating that h increases with gap size, since this is not intuitive.

ACKNOWLEDGEMENTS

The author(s) wish to acknowledge the contributions of Phillip Bryant, Kevin Burks, Myscha Crouch and Doug Westra of the Marshall Space Flight Center.

REFERENCES

Quench Module Insert Preliminary Design Review Thermal Design Data Book, NASA-MSFC, TecMaster Inc., Sverdrup Tech., Huntsville, Al, March 1999

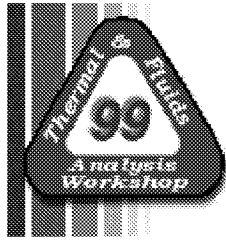
Fundamentals of Heat and Mass Transfer, Second Edition, Frank P. Incropera & David P. DeWitt, Purdue University, 1985

Thermophysical Properties of High Temperature Solid Materials, Vol. 1: Elements, Purdue University, The MacMillan ComVel-Thermy, New York

Introduction to Thermal Analysis Using MSC/THERMAL, PAT312, Exercise Workbook, Release 7.5, April, 1998

Satellite Thermal Control Handbook, David G. Gilmore, The Aerospace Corporation Press, El Segundo, California, 1994

Sample Ampoule-Cartridge Assembly For Microgravity Crystal Growth, ESLI, San Diego, CA



Dean S. Schrage
Dynacs Engineering Company Inc.
Glenn Research Center Group
Brook Park, OH 44142
dean.schrage@grc.nasa.gov

On the Application of ADI Methods to Predict Conjugate Phase Change and Diffusion Heat Transfer

In this paper, the process of phase change heat transfer is investigated. To simplify the representation of the interface between phases, a standard phase-quality based method (equivalent to an enthalpy method) is implemented to describe the energy conservation process. This equation describes an equivalence of the time-rate of change of the continuous phase-quality x to the diffusive energy transport via a Laplacian of the continuous temperature field T . Because of the mixture of terms (x , T), relaxation techniques are usually employed to solve the discretization of the energy equation for a continuous geometry. In this manner, the quality is solved iteratively and applied to a constitutive relationship for temperature in order to survey the temperature field and reveal the diffusive heat flow term. In the present study these equations are extended for implementation of alternating direction implicit (ADI) techniques in a direct solution with the main goal of decreasing computational wall-clock time. The formulation allows a discretized model to possess both phase change nodes and solid diffusion nodes, the former defaulting to basic diffusion above and below the melt point of the material in question. This expands the utility in conjugate heat transfer modelling, e.g. as in heat exchangers employing phase change materials. In the present study, one set of equations is used to represent all diffusion nodes. By relating the temperature to the phase quality with two coefficients which adjust as a function of x and physical properties, the discretized equations are converted to the form $\mathbf{A} \mathbf{x} = \mathbf{f}$ where \mathbf{x} is the phase quality vector, thus producing the sought-after conversion from a temperature solution to a quality based solution. The equations are developed for both the 3D *splitting* and 3D *Brian* ADI methods. Because the overall heat transfer process involves transient solidification or melting, the time-space variations in the quality field cause the diagonals of \mathbf{A} to change in time. In this fashion, the tri-diagonal matrix that is extracted from the thermal diffusion network of laterally connected nodes in a sweep direction must be computed at every time step. This forces and additional LDU decomposition at each time step. These incremental expenses of an ADI implementation can be significant; however, for the case study presented, the overall ADI technique is nearly x30 faster than conventional relaxation methods. The current method is validated against analytical solutions of 2D flat and cylindrical solidification front propagation. A pseudo code is presented to assist the reader in algorithmic implementation.

NOMENCLATURE

| | |
|-------------------|---|
| A, B | linear temperature coefficients |
| C_i | heat capacity, specific to phase f or g |
| h_{fg} | latent heat of fusion |
| ρh_{fg} | specific latent heat of fusion $\rho h_{fg} = \rho_g h_g - \rho_f h_f$ |
| r | radius of solidification front |
| r_o | radius of solidification front, time initial value |
| r^* | radius of solidification front, nondimensional $r^* = \frac{r}{r_o}$ |
| \dot{S}_i | heat generation applied to node |
| t | time |
| t^* | time, nondimensional, $t^* = \frac{\tilde{\alpha}}{r_o^2} t$ for cylindrical geometry and $t^* = \frac{\tilde{\alpha}}{\Delta X^2} t$ for flat front geometry |
| T | temperature |
| T_{fg} | two phase equilibrium temperature |
| $\hat{T}(x)$ | temperature conversion function |
| ΔT | subcooling |
| ΔT^* | subcooling, nondimensional, $\Delta T^* = \frac{\Delta T}{T_{fg}}$ |
| $x^{(n-1)}, U, V$ | succession of intermediate states applied in ADI equation splitting en route to solution $x^{(n)}$ |
| Δn | node thickness, $n = X, Y, Z$ |
| X, Y, Z | Cartesian coordinate directions |
| x | phase quality, $x = 0$ implies 100 % phase f , $x = 1$ implies 100 % phase g |
| δv_i | volume of node i |

GREEK

| | |
|------------------|--|
| $\tilde{\alpha}$ | effective thermal diffusivity, $\tilde{\alpha} = \frac{k_s T_{fg}}{\rho h_{fg}}$ |
| δ | thickness of solidification front |
| δ^* | thickness of solidification front, nondimensional $\delta^* = \frac{\delta}{\Delta X}$ |
| ρ | density |

VECTORS AND TENSORS

| | |
|-----|---------------------------------|
| A | tri-diagonal coefficient matrix |
|-----|---------------------------------|

| | |
|----------|---------------------------------|
| f | forcing vector |
| G | conductance tensor |
| q | heat flux vector |
| r | spatial domain |
| T | temperature in spatial domain |
| x | phase quality in spatial domain |
| ∇ | gradient operator |

1. INTRODUCTION

Phase change heat transfer processes are common in many industrial applications. Generally speaking, phase-change processes do not proceed unconstrained. Rather, they occur in contact with some solid structure such as a heat exchanger case or conductive fin. These solid diffusive structures can be thought of a thermal shunt which brings the boundary conditions to bear on the phase change materials. These diffusive components interact with the phase change material creating a conjugate heat transfer process - conjugate in the sense that there is a coupling between diffusive-diffusive and diffusive-phase-change mechanisms. The need for efficient numerical techniques to simulate the conjugate heat transfer processes has stimulated the development of many models. These are reviewed in [1]. In many cases, the complexities of tracking the interface can be collapsed by adopting a homogeneous model and applying a phase quality to represent the fractional content of a two-phase region. This is more commonly referred to as the enthalpy-porosity method and appears to have established a satisfactory level of acceptance within the thermal community.

There are several forms to the discrete enthalpy-porosity equations. The energy equations can be parabolized with temperature as the primary state, carrying along phase quality to apply to a logical model to assess the heat capacity in the field. As the temperature penetrates a narrow bandwidth around the discrete melting point, the heat capacity of a control volume is set to near infinite values, hence emulating the nature of latent energy takeup (e.g. see [2, 3]). In another form, the continuous enthalpy field is parabolized and the time-rate of the quality field is carried as a source term, activated with a Heaviside operator on the quality (e.g. see [4]). These discretized forms are cumbersome to work with because of the multiplicity of states, variables and logical elements in assessing thermal properties and switched source terms for each node. A residual form is usually applied to represent each thermal control volume. The residual describes an excess energy content of the node, basically an numerical energy imbalance which is driven to near-zero values through the application of successive over relaxation (SOR) methods. The functional dependence of the phase change aspect can be coded quite readily with this approach and tends to reinforce a marriage between enthalpy-porosity models and iterative solution methods.

In most instances, the application of SOR methods for large node-count 3D problems incurs slow transient solution rates, and the addition of phase change phenomenon degrades matters worse, if only through the additional computations described above. The emergence of *direct inversion techniques* such as alternating direction implicit (ADI) methods would appear to be an attractive approach. However, it is not entirely clear how ADI methods, which require the discretized equations in vector form $\mathbf{Ax} = \mathbf{f}$ with a single definitive state \mathbf{x} for which to solve, are to be adopted to the enthalpy-porosity model. Indeed, relevant studies of ADI adaptations to phase change heat transfer are uncommon in comparison to ADI treatments of diffusion transport alone. Voller [4] presented a discretized enthalpy representation which was solved with a tri-diagonal matrix algorithm. Voller describes the regeneration of matrix \mathbf{A} at each time step; however, the particular algorithm, whether splitting, conventional, Douglas etc, was not specified. Mampaey [5] described a Peachman and Rachford ADI method to predict multidimensional solidification. The temperature field was parabolized and phase change was modelled by adjusting the specific heat of the melt at the onset of solidification. Temperature oscillations were observed at the onset of a prediction, thought to be the effect of extreme temperature gradients between a melt and a sand casting boundary; this led to the development of a revised scheme for 3D simulations which was effective in predicting total solidification times for a casting. More recently Ismail and Goncalves [1] describe the application of an ADI method to enthalpy-based equations to predict the performance of a cylindrical phase change storage unit. The specific method, equations and implementation were not presented, the paper, instead, focusing on parametric results.

Rationale and Approach

An ADI implementation to predict phase change heat transfer appears to be practical but within these studies, the following deficiencies are noted. First, the matrix inversion routine requires a single target state; the selection of this state, be it phase quality x or other variable, and subsequent modification of the conservation equations is not well described. Second, the coefficient matrix A will adjust when a thermal node transfigures from a single-phase to a two-phase and back to a single-phase state; the algorithmic approach to the reconfiguration induced by these *regime shifts* is not described systematically. Third, the unconditional solution stability obtained with a diffusionally-designed ADI method may be compromised by these regime shifts; the extent or existence of this stability degradation has not been studied. Fourth with the ensemble of ADI methods available, there is little mention of a best method to use. Fifth, a systematic validation of an ADI-derived phase-change simulation is lacking. Sixth, the motivation for ADI implementation - computational expedience compared to relaxation methods - has not been established in a practical application study.

The objectives of the present study echo these. The discretized energy equation is derived in §2 and using a temperature conversion function derived in §2.1, is converted to a quality-based equation in §2.4. This equation is adapted to both 3D *splitting* and 3D *Brian* ADI methods in §3, further summarized by extracting the tri-diagonals and forcing coefficients in §3.1. A pseudo-code is presented in §3.2, along with a discussion of regime-shift stability issues and a suggested approach to recomputation of the coefficient matrix A , the forcing vector f . The solutions derived with the 3D splitting method is compared to analytical solutions of flat front solidification in both one and two dimensions, and to a cylindrical two dimensional solidification in §4.1 and §4.2, respectively. The computational performance of the both ADI methods is compared to a SOR-derived solution of a 3D conjugate heat transfer problem in §5.

2. GOVERNING EQUATIONS

In this paper, the terms *control volume* and *node* are synonymous. Each describes a fixed geometric volume, a Cartesian-based six sided parallel-piped, which exchanges energy with adjoining nodes through Fourier-originated thermal diffusion. An enthalpy-quality method will be adopted to predict the transient energy content in a thermal node. The primary state will be the phase quality x which will range continuously from negative to positive values. The energy equation for a node i is written as an equivalence between the substantial derivative of enthalpy, to thermal diffusion and

$$\int_{CS} -\mathbf{q} \cdot d\mathbf{A} + \int_{CV} \dot{s}_i dv = \frac{\partial}{\partial t} \int_{CV} \rho \left(h - \frac{P}{\rho} \right) dv + \int_{CS} \rho h \mathbf{V} \cdot d\mathbf{A}$$

a source heating term:

Neglecting the advection of enthalpy by a velocity field V , kinetic and potential energy changes, and assuming the material to be incompressible, the energy equation for a node of fixed volume is simplified:

$$-\int_{CS_j} \mathbf{q}_{ji} \cdot d\mathbf{A}_j + \dot{s}_i = \rho_i \delta_{V_i} \frac{\partial h_i}{\partial t}$$

where the left side terms read as the total heat flow by diffusion into node i and the source heating. The integration of the heat flux vector \mathbf{q}_{ji} over the control surfaces residing about node i can be rewritten as a heat flow into node i :

$$\delta Q_i = - \int_{CS_j} \mathbf{q}_{ji} \bullet \mathbf{d}A_j$$

Next, the enthalpy is referenced to a continuous function of the phase quality and the f -phase enthalpy and latent heat of fusion:

$$h = h_f + x h_{fg}$$

where h_f and h_{fg} are understood to depend on pressure through a coexistence curve. Taking the time-partial derivative

$$\begin{aligned} \frac{\partial h}{\partial t} &= \frac{\partial}{\partial t} (h_f + x h_{fg}) \\ &= h_{fg} \frac{\partial x}{\partial t} \end{aligned}$$

and observing the compressibility constraint:

$$\rho_i h_{fg} \delta v_i \frac{\partial x_i}{\partial t} = \delta Q_i + \dot{S}_i$$

which when combined with the heat flow rate and the original expression, yields:

2.1 Temperature Conversion Function

The phase quality is related to temperature through the conversion function $\hat{T}(x)$. To derive this function, a range of constraints must be observed. The function must return the unique equilibrium melting temperature $\hat{T}(x) = T_{fg}$ for $0 \leq x \leq 1$. Outside this quality range, the function must return subcooled and superheated

$$h_f + C_{P_f}(T - T_{fg}) = h_f + x h_{fg}$$

temperatures. In the subcooled region ($x < 0$) the temperature follows the approximation:

$$h_g + C_{P_g}(T - T_{fg}) = h_f + x h_{fg}$$

and in the superheated region ($x > 1$):

which upon combining and inverting yields the following linear relationship:

$$\hat{T}(x, i) = A_i x + B_i$$

$$A_i = \begin{pmatrix} \frac{h_{fg}}{C_{P_f}} & x < 0 \\ 0 & 0 \leq x \leq 1 \\ \frac{h_{fg}}{C_{P_g}} & x > 1 \end{pmatrix}$$

$$B_i = \begin{pmatrix} T_{fg} & x < 0 \\ T_{fg} & 0 \leq x \leq 1 \\ T_{fg} - \frac{h_{fg}}{C_{P_g}} & x > 1 \end{pmatrix}$$

for which the coefficients are defined:

Coefficients A and B are subscripted with the node index number, indicating they are unique for each node. These vary in two ways. First, a model may possess different phase change materials; each node may be associated with a different set of phase change properties $T_{fg}, h_{fg}, C_{P_f}, C_{P_g}$ ¹. Second, during the course of a thermal simulation, the quality field will evolve naturally and A and B will change from node to node, reflected by the composite nature of the function.

2.2 Diffusion Term

The thermal diffusion between adjoining nodes is specified by a thermal conductance, itself determined by thermal conductivity of the material in question and the geometry of the two nodes. As described in Appendix A, the conductance between two adjoining nodes is determined by the geometric mean of the respective half-node conductances, enabling nodes of dissimilar thermal conductivity to be modelled. The heat flux vector is determined by a product of a *conductance tensor* G (made up of these values) and a unit vector, either $\pm e_x, \pm e_y, \pm e_z$, proportional to the temperature difference between respective nodes:

¹ Because both phase-change and conventional diffusion nodes can be grouped and solved together, the ADI solution requires that each node have a defined set of phase change properties. For conventional diffusion nodes, these properties are meaningless, basically reflecting the fact that the phase change process is out of reach of the temperature penetrating the node. In this case, the values $T_{fg}, h_{fg}, C_{P_f}, C_{P_g}$ can be set to 1. Practical experience shows that this has no effect on the solution.

$$\mathbf{q}_{ji} = \frac{1}{A_{ji}} \mathbf{G} \mathbf{e}_j (T_i - T_j)$$

In the present study, the use of Cartesian-based nodes restrict the j -indices from 1 to 6, i.e. the six faces of a three dimensional parallel-piped. Thus, at node i , and in a particular direction, \mathbf{e}_X for example, the value of heat flux across X -

$$\begin{aligned} \mathbf{q}_{Xji} &= \frac{1}{A_{ji}} \mathbf{G} \mathbf{e}_X (T_i - T_j) \\ &= \frac{G_{ji}}{A_{ji}} (T_i - T_j) \mathbf{e}_{Xj} \end{aligned}$$

directed faces is derived:

which when applied in the control surface integration, yields the amount of X -directed heat flow into the node:

$$\begin{aligned} \delta Q_i(T, \mathbf{e}_X) &= - \sum_{j=1}^2 \frac{G_{ji}}{A_{ji}} (T_i - T_j) \mathbf{e}_{Xj} \cdot \mathbf{A}_{ki} \mathbf{e}_{kj} \\ &= \sum_{j=1}^2 G_{ji} (T_j - T_i) \end{aligned}$$

That is, the first 2 j -indices of the conductance tensor are reserved for X -directed sweeps. This can be written in the more familiar form, referencing forward and backward directed nodes in the \mathbf{e}_X direction:

$$\delta Q_i(T, \mathbf{e}_X) = G_{i+1_X, i} (T_{i+1_X, i} - T_i) + G_{i-1_X, i} (T_{i-1_X, i} - T_i)$$

The notation $i \pm I_X$ indicates nodes which adjoin node i on the $\pm \mathbf{e}_X$ directions. A similar notation is to be presumed for sweeps in the Y and Z directions.

2.3 General Flow Term

The conductance tensor, specified by both material and geometry, can be treated as a fixed quantity. As such, the process of heat flow can be extended to a *flow* of any general field quantity. In this manner, a flow of an arbitrary general source term ϕ , as effected by the conductance tensor, can be written:

$$\delta Q_i(\phi, \mathbf{e}_n) = \mathbf{e}_x \bullet \mathbf{e}_n \sum_{j=1}^2 G_{ji} (\phi_j - \phi_i) + \mathbf{e}_y \bullet \mathbf{e}_n \sum_{j=3}^4 G_{ji} (\phi_j - \phi_i) + \mathbf{e}_z \bullet \mathbf{e}_n \sum_{j=5}^6 G_{ji} (\phi_j - \phi_i)$$

That is, field property ϕ induces a net flow into node i , in the \mathbf{e}_n direction. As presented below, this convention will allow the basic ADI equations to be streamlined and simplified for the various methods. As described below, the flow term will operate on the temperature coefficients A, B . Thus, flow terms will be presented in the form $\delta Q_i(B, \mathbf{e}_x)$ which read as the flow caused by the coefficient B , affected and controlled by the conductance tensor, directed in the \mathbf{e}_x direction. The form of these terms and there operative direction depend ultimately on the sweep direction and the specific ADI method.

2.4 Discretized Quality Equation

Upon collecting the above equations, the final form of the discrete energy equation at node i is given by the following:

$$\rho_i h_{fg} \delta v_i \frac{\partial x_i}{\partial t} = \delta Q_i(T, \mathbf{e}_x) + \delta Q_i(T, \mathbf{e}_y) + \delta Q_i(T, \mathbf{e}_z) + \dot{S}_i$$

As discussed above, this equation is a function of both T and x , not of a form suitable for the ADI implementation. By referencing heat flow terms through the temperature conversion function, this equation can be rewritten:

$$\rho_i h_{fg} \delta v_i \frac{\partial x_i}{\partial t} = \delta Q_i(\hat{T}(x), \mathbf{e}_x) + \delta Q_{\text{subi}}(\hat{T}(x), \mathbf{e}_y) + \delta Q_i(\hat{T}(x), \mathbf{e}_z) + \dot{S}_i$$

with the phase quality now appearing throughout the left and right hand sides. Because the diffusion function δQ_i is a linear operator, the conversion to a quality-based equation is made by combining this equation with the linear temperature conversion function (9):

$$\rho_i h_{fg} \delta v_i \frac{\partial x_i}{\partial t} = \delta Q_i(A_i x_i, \mathbf{e}_x, \mathbf{e}_y, \mathbf{e}_z) + \delta Q_i(B_i, \mathbf{e}_x, \mathbf{e}_y, \mathbf{e}_z) + \dot{S}_i$$

While the coefficients A, B themselves depend on the quality state, the goal of isolating a single target state is achieved with this equation. It is this basic equation which will be adapted to the various methods.

3. ADI IMPLEMENTATION

The basic ADI equations are adapted from the Chang et al. [6] paper which describes the splitting and Brian ADI methods (in addition to conventional, Douglas and modified splitting methods). In the following equations, as identified in the nomenclature, three successive ADI sweep levels operate on the intermediate quality states, $\mathbf{x}^{(n-1)}, U, V$, en route to the solution of the future-time quality, $\mathbf{x}^{(n)}$.

Splitting Method: The splitting method operates on time levels offset by $\frac{\Delta t}{3}$. In Equation 19, the source term is combined with the diffusive transport of the B coefficient. The diffusive transport of the quality term is then split into respective X, Y, Z components creating the three implicit equations:

$$(X - \text{Sweep}) \quad \rho_i h_{fg} \delta v_i \frac{U_i - x_i^{(n-1)}}{\frac{\Delta t}{3}} - 3 \delta Q_i(A_i U_i, \mathbf{e}_x) = \delta Q_i(B_i, \mathbf{e}_x, \mathbf{e}_Y, \mathbf{e}_Z) + \dot{S}_i$$

$$(Y - \text{Sweep}) \quad \rho_i h_{fg} \delta v_i \frac{V_i - U_i}{\frac{\Delta t}{3}} - 3 \delta Q_i(A_i V_i, \mathbf{e}_Y) = \delta Q_i(B_i, \mathbf{e}_x, \mathbf{e}_Y, \mathbf{e}_Z) + \dot{S}_i$$

$$(Z - \text{Sweep}) \quad \rho_i h_{fg} \delta v_i \frac{x_i^{(n)} - V_i}{\frac{\Delta t}{3}} - 3 \delta Q_i(A_i V_i, \mathbf{e}_Z) = \delta Q_i(B_i, \mathbf{e}_x, \mathbf{e}_Y, \mathbf{e}_Z) + \dot{S}_i$$

Brian Method: The Brian method operates on levels of $\frac{\Delta t}{2}$. As opposed to splitting the diffusion of the quality, the Brian method applies the intermediate quality states in the following manner:

$$(X - \text{Sweep}) \quad \rho_i h_{fg} \delta v_i \frac{U_i - x_i^{(n-1)}}{\frac{\Delta t}{2}} - \delta Q_i(A_i U_i, \mathbf{e}_x) = \delta Q_i(A_i x_i^{(n-1)}, \mathbf{e}_y, \mathbf{e}_z)$$

$$(Y - \text{Sweep}) \quad \rho_i h_{fg} \delta v_i \frac{V_i - x_i^{(n-1)}}{\frac{\Delta t}{2}} - \delta Q_i(A_i V_i, \mathbf{e}_y) = \delta Q_i(A_i U_i, \mathbf{e}_x) + \delta Q_i(A_i$$

$$(Z - \text{Sweep}) \quad \rho_i h_{fg} \delta v_i \frac{x_i^{(n)} - V_i}{\frac{\Delta t}{2}} - \delta Q_i(A_i x_i^{(n)}, \mathbf{e}_z) = \delta Q_i(A_i U_i, \mathbf{e}_x) + \delta Q_i(A_i$$

3.1 Coefficient Extraction

A general tri-diagonal sweep equation can be extracted from each of these sweep equations:

$$b_i \psi_{i-1} + a_i \psi_i + c_i \psi_{i+1} = f_i \quad \text{for } n = X, Y, Z$$

where ψ represents either $U, V, x^{(n)}$, respective to X, Y, Z sweep directions. Table 1 summarizes the coefficient extraction of A and f for each sweep direction, method-specific. The convention $(\cdot)_{iX}$ reads, the coefficient value (\cdot) at node i , in sweep direction X . Similarly, the indexing notation $i-1_X$ reads as the west-facing node connecting node i , while $i-1_Y$ reads as the south-facing node connecting node i , and so forth.

| Splitting Method | b_i | a_i | c_i | f_i |
|------------------|-------------------|--|-------------------|---|
| <i>X-sweep</i> | $-3 G_{i-1_X, i}$ | $\frac{\rho \delta v_i h_{fg_i}}{\Delta t/3} + 3 A_i (G_{i-1_X, i})$ | $-3 G_{i+1_X, i}$ | $\dot{S}_i + \frac{\rho \delta v_i h_{fg_i}}{\Delta t/3} x_i^{(n-1)} + 3 \sum_l^6 G_{i, l}$ |
| <i>Y-sweep</i> | $-3 G_{i-1_Y, i}$ | $\frac{\rho \delta v_i h_{fg_i}}{\Delta t/3} + 3 A_i (G_{i-1_Y, i})$ | $-3 G_{i+1_Y, i}$ | $\dot{S}_i + \frac{\rho \delta v_i h_{fg_i}}{\Delta t/3} U_i + 3 \sum_l^6 G_{i, l}$ |
| <i>Z-sweep</i> | $-3 G_{i-1_Z, i}$ | $\frac{\rho \delta v_i h_{fg_i}}{\Delta t/3} + 3 A_i (G_{i-1_Z, i})$ | $-3 G_{i+1_Z, i}$ | $\dot{S}_i + \frac{\rho \delta v_i h_{fg_i}}{\Delta t/3} V_i + 3 \sum_l^6 G_{i, l}$ |

| Brian Method | b_i | a_i | c_i | f_i |
|----------------|-------------------|---|-------------------|---|
| <i>X-sweep</i> | $-G_{i-1x,i} A_i$ | $\frac{\rho \delta v_i h_{fg_i}}{\Delta t/2} + A_i (G_{i-1x,i} + G_{i+1x,i})$ | $-G_{i+1x,i} A_i$ | $\dot{S}_i + \frac{\rho \delta v_i h_{fg_i}}{\Delta t/2} x_i^{(n-1)} + \sum_1^6 G_{si} + \sum_3^6 G_{ji} (A_j x_j^{(n-1)} - A_j x_j^{(n-2)})$ |
| <i>Y-sweep</i> | $-G_{i-1y,i} A_i$ | $\frac{\rho \delta v_i h_{fg_i}}{\Delta t/2} + A_i (G_{i-1y,i} + G_{i+1y,i})$ | $-G_{i+1y,i} A_i$ | $\dot{S}_i + \frac{\rho \delta v_i h_{fg_i}}{\Delta t/2} x_i^{(n-1)} + \sum_1^6 G_{si} + \sum_1^2 G_{ji} (A_j U_j - A_j U_j^{(n-1)}) + \sum_5^6 G_{ji} (A_j x_j^{(n-1)} - A_j x_j^{(n-2)})$ |
| <i>Z-sweep</i> | $-G_{i-1z,i} A_i$ | $\frac{\rho \delta v_i h_{fg_i}}{\Delta t/2} + A_i (G_{i-1z,i} + G_{i+1z,i})$ | $-G_{i+1z,i} A_i$ | $\dot{S}_i + \frac{\rho \delta v_i h_{fg_i}}{\Delta t/2} V_i + \sum_1^6 G_{si} + \sum_1^2 G_{ji} (A_j U_j - A_j U_j^{(n-1)}) + \sum_3^4 G_{ji} (A_j V_j - A_j V_j^{(n-1)}) + \sum_5^6 G_{ji} (A_j x_j^{(n-1)} - A_j x_j^{(n-2)})$ |

Table 1. Summary of coefficient extraction for general sweep matrix equation.

3.2 Solution Algorithm

The following text block describes a pseudo code to execute a thermal solution over one time step. As alluded to above, regime shifts require that the tri-diagonals be recomputed on each time step. The second step in the p -loop (denoted with \blacktriangleright) indicates that the temperature coefficients are to be recomputed using the current available sweep level state, i.e. X -sweep has available the $x^{(n-1)}$ quality state and is applied to the functions for coefficients A, B . Similarly, the U quality state is applied in the Y -sweep and V for the Z -sweep. This can be arranged in the coding by creating a simple sub-pointer as shown in the pseudo code. It has been found that simulations using the $x^{(n-1)}$ quality state to compute the coefficients just once, to apply to all three sweeps, will produce temperature oscillations. This is apparent from Figure 1 which shows a simple time-space representation of a temperature field for a 1D slab which is melting under the imposition of hot wall boundary conditions, as the normally isothermal field, post melting, is littered with standing temperature oscillations. The adjoining contour plot shows the stable melting of the solid derived using updated coefficients. The temperature oscillations are more extensive with the Brian method, apparently due to the more complex arrangement for the forcing coefficients f_i in comparison to splitting. Even so, both methods are shown to benefit from using current quality level information for the update.

```

step 2 | set the initial conditions on first quality level  $x^{(n-1)}$ 
step 3 | for p = 1 to 3   (levels corresponding to X, Y, Z)
        |
        | •           point to ADI sub level  $\theta[p] = [x^{(n-1)}, U, V]^T$ 
        |
        | •           compute temperature coefficients  $A = \hat{A}(\theta[p])$  and  $B = \hat{B}(\theta[p])$  specific
        |  $\blacktriangleright$           to ADI sub level
        | •           compute diffusion matrix coefficients  $b, a, c$  per Table 1 specific to sweep direction
        | •           perform the LDU decomposition of matrix  $A$ 
        | •           compute the forcing vector coefficients  $f$  per Table 1 specific to sweep direction
        | •           apply Thomas algorithm to arrive at ADI solution  $\psi[p] = [U, V, x^{(n)}]^T$ 
        | •           if (p = 2 or 3) renumber ADI sub levels  $\theta[p] = [U, V]^T$  consistent with  $X$  sweep
        |               node numbering
        |
        | next p
step 4 | recalculate the temperature coefficients  $A = \hat{A}(x^{(n)})$  and  $B = \hat{B}(x^{(n)})$  based on final

```

4. VALIDATION of ADI METHOD

The ADI phase change model is validated by comparing the numerical simulation to an analytical solution of freezing fronts in two simple geometries. Table 2 presents the details for the numerical-analytical model comparisons. The analytical models are derived by simplifying the transient solidification-diffusion process by assuming a non-capacitive diffusion process across the accumulating solidified region. Under these conditions, a control volume formulation can be applied to predict the time-dependent size of the solidification region as a function of an effective thermal diffusivity $\tilde{\alpha}$ and the subcooled temperature of the boundary. As derived in Appendix B, the transient

$$\delta^* = \sqrt{2 \Delta T^* t^*}$$

propagation of the flat and a cylindrical solidification fronts is determined, respectively:

$$\frac{1}{2} r^{*2} \ln(r^*) - \frac{1}{4} (r^{*2} - 1) = \Delta T^* t^*$$

| solidification front: geometry and thermal physical properties | | numerical simulation model | |
|---|------------------------------------|----------------------------|--|
| material | water | $\Delta X, \Delta Y,$ | node size 1 cm |
| h_{fg} | $333.7 \times 10^3 \text{ J/kg K}$ | Δt | 2000 s |
| C | 4220 J/kg K • | t_f | 5×10^5 |
| k_f, k_g | 0.566 W/m C • | $x(r, 0)$ | initial quality field set to 1.0, corresponding to saturated liquid |
| T_{fg} | 273.15 K | $T(r, 0)$ | initial temperature field set to 273.15 K |
| ρ | 1000 kg/m ³ | $T(0, t)$ | cold wall boundary temperature maintained at $\Delta T = 10 \text{ }^\circ\text{C}$ below T_{fg} . |
| <ul style="list-style-type: none"> • both phases set equal for comparison to analytical model - note this is for convenience only and not required by the method | | x_{front} | node represents solidification front when $x_i \leq 0.5$ |
| | | ADI scheme | 3D splitting method applied in respective 2D domains, Z-direction split included in solution |

Table 2. Description of parameters applied in numerical prediction of solidification front and comparisons to analytical models.

4.1 Flat-Front Solidification

The flat-front geometries applied in the simulation are depicted in Figure 2. The fundamental geometry is a one-dimensional mesh. A two-dimensional variation is created by rotating the 1D mesh by 45 degrees. Figure 3 presents a comparison of the ADI-numerical and analytical solutions for these model variants. The linear 1D and rotated 2D node configurations should yield the identical numerical prediction of the advance of the solidification front. However, the rotated mesh invokes diffusion in both directions, testing the solutions of the intermediate quality states at the time levels

$t + \frac{1}{3}\Delta t, t + \frac{2}{3}\Delta t$. As shown, the results compare to within 5 percent of the flat front analytical solution. The

numerical predictions fall below the predictive line, suggested to result from including finite capacitance in the solidifying regions in the numerical model which retards the discharge of the energy accumulated in the solid to the cold wall boundary condition. Equivalently speaking, the analytical model predicts a higher propagation rate because capacitance in the solid phase is nullified. The quality field for the rotated slab is presented in Figure 4. The adiabatic edges of the slab model and notched discretization creates a slight disturbance which causes the solidification front, expectantly flat, to exhibit a slight curvature near the adiabatic boundaries.

4.2 Cylindrical-Front Solidification

The cylindrical front simulation is performed by approximating a cylinder with a select number of Cartesian nodes. Figure 5 illustrates the Cartesian node geometry applied to the vary node densities. The corresponding predictive comparison is presented in Figure 6. As shown, the ADI model predicts the position of the solidification front to within 5 percent, despite the apparently crude discretization of the initial cylinder forming the cold wall boundary condition.

In contrast to retardation of the growth for the flat front (owed to neglect of capacitance in the analytical model), the cylindrical front data lie above the predictive line and are explained on the basis of the conversion of the discrete field problem from a linear to a cylindrical geometry with increasing node density. Basically, in the limit of one center node, the numerical model *nearly* represents a flat front solidification, however, not exactly because diffusion still occurs in both X, Y directions. With increasing node density, the quasi-flat front solidification is incrementally converted to a cylindrical expanse. With this incremental conversion, the data form increasingly better comparisons with the analytical predictions. Eventually, at some point, the capacitive terms retained in the numerical prediction tend to offset this aspect as is the case in the flat front prediction. The quality field is presented in Figure 7, displaying a sharp transition from solid to liquid across the solidification front and showing the expected circular expanse of solidification.

5. APPLICATION STUDY

Figure 8 illustrates the geometry applied in this conjugate problem, which consists of an aluminum-cased phase change module (PCM) which is coupled between a simulated electronics heat source and a temperature boundary condition. The boundary condition varies sinusoidally from ± 10 °C above and below the melting point of 0 °C with a period of 10 seconds. The simulated electronics apply a total of 9 Watts over the 9 nodes. A quarter-symmetry section is modeled with each node described by a cube, measuring 2 mm on edge. Figure 9 describes the evolution of wall clock time versus the simulation time. The wall clock time is normalized using the end-value of wall clock time measured with the ADI-Brian method in order to offer results of a general nature which are to an extent, independent of processor speed and coding techniques. The ADI simulation proceeds at about a factor of x30 faster than the SOR-derived solution. Figure 10 shows the time-temperature trace of several points in the solution domain and also the temperature field at time $t = 100$ s, derive with the ADI-Brian method. These results indicate the computational savings offset the expense of recomputing A and f by a significant factor.

6. CONCLUSION

The present study presents an adaptation of the splitting and Brian ADI methods to effect a direct solution of the quality-based conservation equations to predict phase change heat transfer. It has been shown that the equations can be constructed with a single target state. The application of a temperature conversion function allows both conventional diffusion nodes and phase change nodes to be mixed in a simulation with no special considerations or restrictions. The method appears to be numerically stable for 3D simulations, compares well with analytical solutions and is significantly faster than conventional relaxation methods. The incremental expenses introduced by the quality representation, i.e. matrix recomputation, LDU decomposition, can be readily forfeited given a near two order of magnitude increase in algorithmic speed obtained with the new method.

REFERENCES

- 1 Ismail, K. A. R., and Goncalves, M. M., "Thermal Performance of a PCM Storage Unit," *Energy Conversion and Management*, Vol. 40, pp 115-138, 1999.
- 2 Runnels S. R., and Cary, G. F., "Finite Element Simulation of Phase Change Using Capacitance Methods," *Numerical Heat Transfer, Part B*, Vol. 19, pp 13-30, 1991.
- 3 Busko, W., and Gross, I. R., "New Finite Element Method for Multidimensional Phase Change Heat Transfer Problems," *Numerical Heat Transfer, Part B*, Vol. 19, pp 31-48, 1991.
- 4 Voller, V. R., "Fast Implicit Finite-Difference Methods for the Analysis of Phase Change Problems," *Numerical Heat Transfer, Part B*, Vol. 17, pp 155-169, 1990.
- 5 Mampaey, F., "A Stable Alternating Direction Method for Simulating Multi-Dimensional Solidification Problems," *International Journal for Numerical Methods in Engineering*, Vol. 30, pp 711-728, 1990.
- 6 Chang, M. J., Chow, L. C., and Chang, W. S., "Improved Alternating-Direction Implicit Method for Solving Transient Three Dimensional Diffusion Problems," *Numerical Heat Transfer, Part B*, Vol. 19, pp 69-84, 1991.

Appendix A
Determination of Thermal Conductance Values

From Figure B.1, the thermal conductance between two nodes is determined by the following half-node

$$G_{i,i+\%o} = \frac{k_i A_{y z_i}}{\frac{\delta x_i}{2}}$$

conductance values:

The half-node conductance values for any two connecting nodes are combined in a geometric average to represent the overall thermal conductance between nodes:

$$G_{2,1} = \frac{1}{\frac{1}{G_{1,1+\%o}} + \frac{1}{G_{2,2-\%o}}}$$

Appendix B
Analytical Model of Propagation of Solidification Front

In this analysis, a transient control volume is used to capture the energy conservation of an expanding solidification front. As illustrated in Figure B.1, the control volume encompasses and expands with the solidified region.

$$\int_{CS} -\mathbf{q} \cdot d\mathbf{A} = \frac{\partial}{\partial t} \int_{CV} \rho \left(h - \frac{P}{\rho} \right) dv + \int_{CS} \rho h \mathbf{V} \cdot d\mathbf{A}$$

The energy equation can be expressed as:

For simplification the following constraints and stipulations are placed: the density is constant across the two phases; the substances are incompressible; the capacitance of the accumulating solid phase is neglected in the time-partial integral. Because the control volume contains the entire solid region, the enthalpy flux is determined by the portion of the liquid

$$\int_{CS} \rho h \mathbf{V} \cdot d\mathbf{A} = -\rho h_g A(t) \dot{\xi}$$

phase advecting into the surface:

$$-k_f \Delta T(\xi \rightarrow \xi_o) A_o(t) = \rho h_f \frac{\partial v}{\partial t} - \rho h_g A(t) \dot{\xi}(t)$$

The energy equation can be simplified applying a Fourier term for the heat flux vector:

As shown below, the final solution to the cylindrical front degenerates to the flat front when the initial radius is made very large. Exploiting this generality, the analysis will proceed specific to the cylindrical geometry to avoid the redundant

$$\frac{\partial v}{\partial t} = H 2\pi r \dot{r}$$

analysis. The time-partial of volume can be simplified:

$$k_f \Delta T(r \rightarrow r_o) 2\pi r_o = \rho h_{fg} 2\pi r \dot{r}$$

which when combined with the energy equation, produces the following ODE:

Prior to separating and integrating this equation, the temperature gradient at r_o , i.e. the gradient imposed by the cold wall boundary condition. As stipulated that the solid or f -phase is non-capacitive, the temperature distribution throughout the solid must be conducive to preserving the total heat flow through the differential rings which comprise the cylinder. A simple analysis will show that the contraction of the the cross sectional area nearing the inner cold wall cylinder forces the temperature profile to follow a logarithmic distribution of the form $T(r) = m \ln(r) + b$.

Applying the two boundary conditions across the extent of the solid phase yields two equations which with to solve for m and b :

$$T_{fg} = m \ln(r) + b$$

$$T_{fg} - \Delta T = m \ln(r_o) + b$$

Upon solving these equations, the gradient at r_o is expressible:

Equations B.5 and B.8 are then combined with an expression for the effective thermal diffusivity to yield the following

$$\frac{r \ln\left(\frac{r}{r_o}\right) \dot{r}}{\Delta T (r \rightarrow r_o)} = \tilde{\alpha} \frac{\Delta T}{T_{sub} l} \frac{1}{r_o \ln\left(\frac{r}{r_o}\right)}$$

ODE:

$$\frac{l}{2} r^2 \ln\left(\frac{r}{r_o}\right) - \frac{l}{4} (r^2 - r_o^2) = \tilde{\alpha} \frac{\Delta T}{T_{sub}} fg t$$

which upon separating can be integrated to yield:

$$\frac{l}{2} r^{*2} \ln(r^*) - \frac{l}{4} (r^{*2} - l) = \Delta T^* t^*$$

and nondimensionalized according the definitions put forth in the nomenclature:

For the analysis of cylindrical fronts, this analytical solution is solved numerically to yield the time-dependent radial position of the freezing front.

For flat fronts, the analytical objective is instead the determination of the front thickness δ . By making the

$$\frac{l}{2} \left(\frac{\delta}{r_o}\right)^2 + \text{Order} \left(\frac{\delta}{r_o}\right)^3 = \Delta T^* \left(\tilde{\alpha} \frac{t}{r_o^2}\right)$$

substitution $r^* = l + \delta^*$ and expanding, in Taylor series, terms of δ^* , Equation 11 can be approximated:

As the inside cold wall radius tends to infinity $r_o \ll l$ the geometry becomes a flat front. Balancing terms of like-order

$$\delta \approx \sqrt{2 \tilde{\alpha} \Delta T^* t}$$

requires that $\delta \ll \sqrt{t}$ and the front thickness δ can therefore be approximated:

The flat front solution (in the absence of a convection boundary condition) lacks a characteristic length scale suitable for the nondimensionalization. Thus, in the flat front simulations and data comparisons, the removal of length

solution with A B coefficients derived with current sweep level pointer $\theta[p]$

$$A = \hat{A}(\theta[p])$$

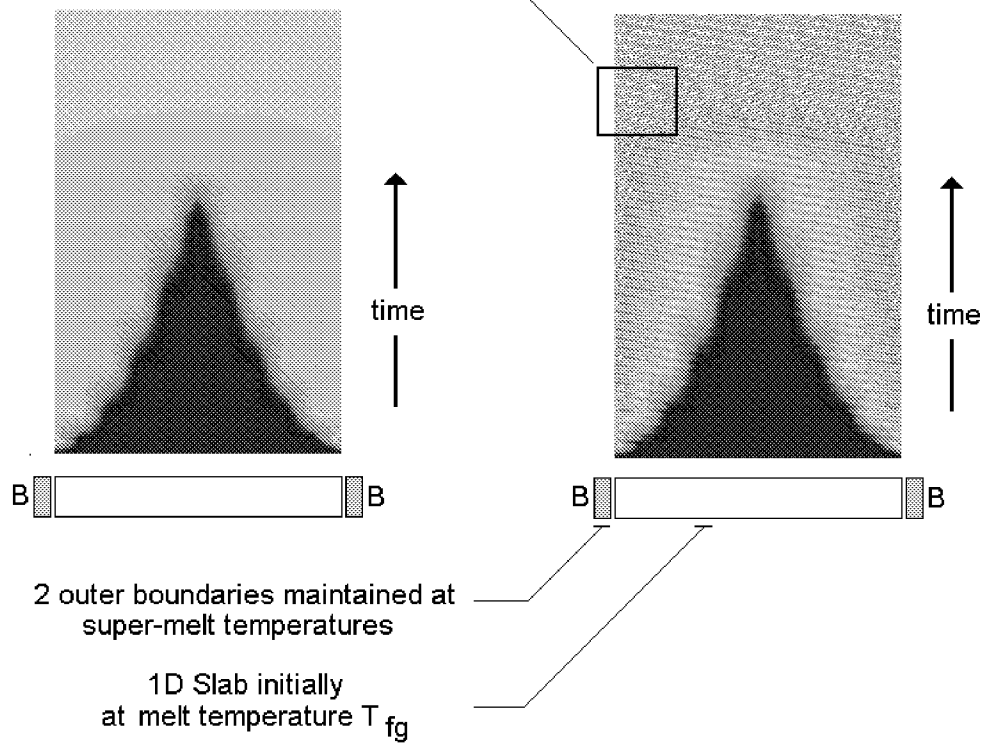
$$B = \hat{B}(\theta[p])$$

solution with A B coefficients derived with first sweep level pointer $\theta[1]$

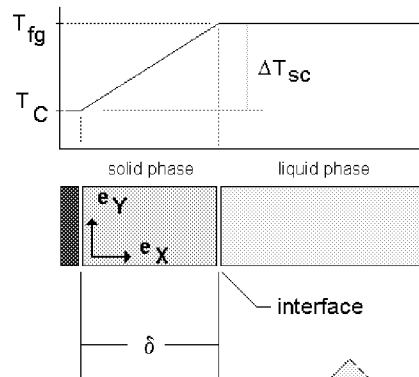
$$A = \hat{A}(x^{(n-1)})$$

$$B = \hat{B}(x^{(n-1)})$$

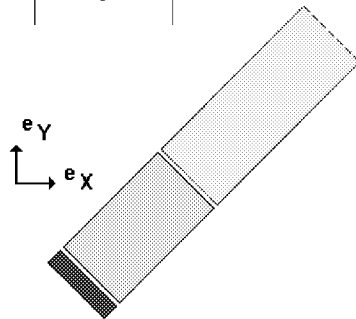
produces spatial temperature variations which emanate from front and rebound continuously off boundaries



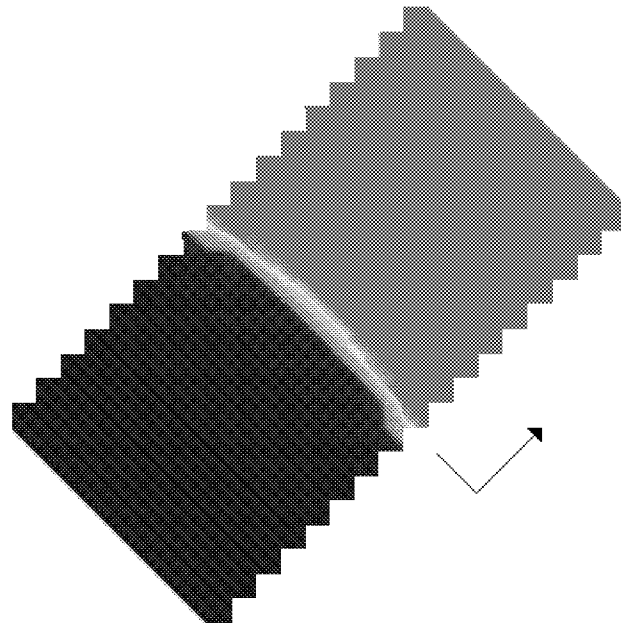
and time units is affected by applying the discrete node thickness ΔX used in the simulation, producing the following expression:



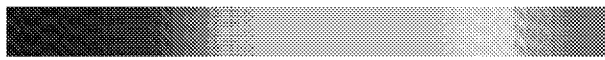
slab (1D): solidification front propogates in e_x direction only



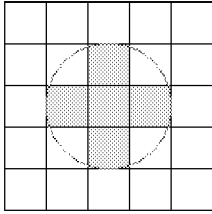
slab (1D) rotated (45 degrees) creates 2D grid, solidification front propogates in e_x and e_y directions



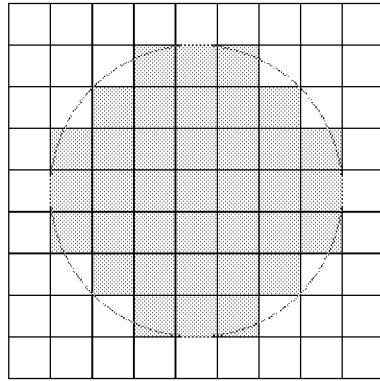
quality x



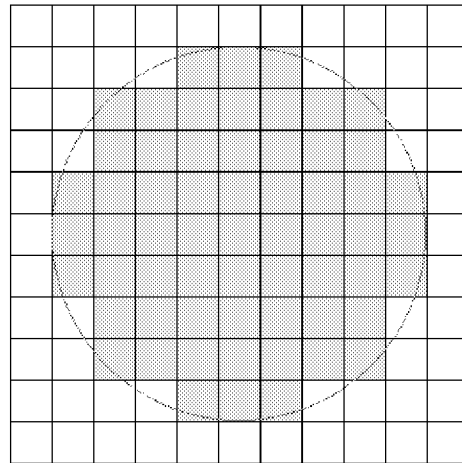
-0.13 0.01 0.15 0.29 0.43 0.58 0.72 0.86 1



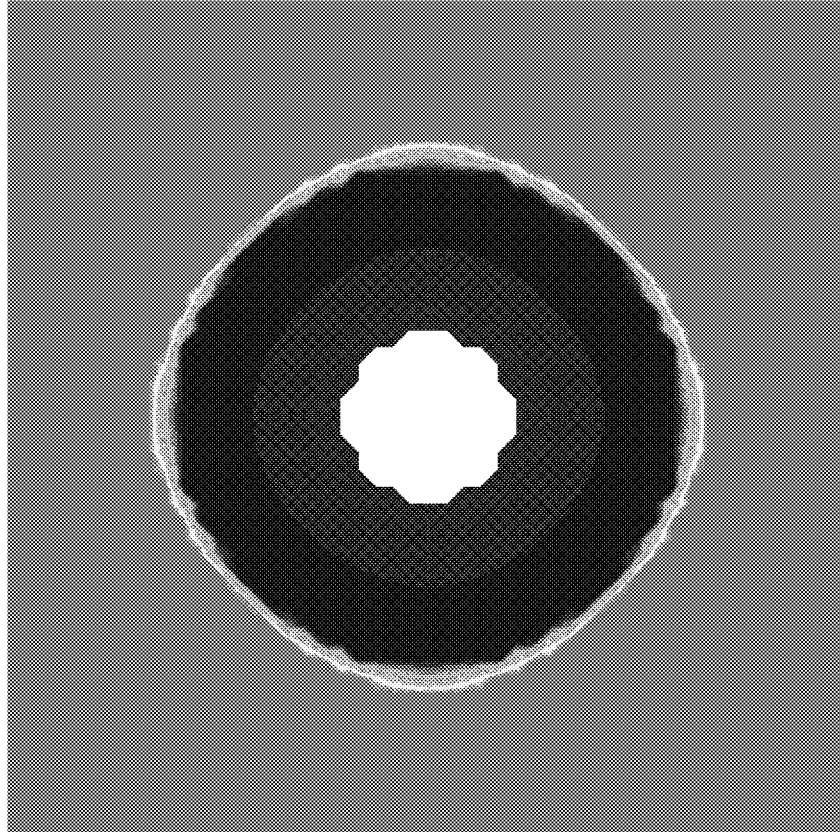
$1.5 \cdot \Delta n$



$3.5 \cdot \Delta n$



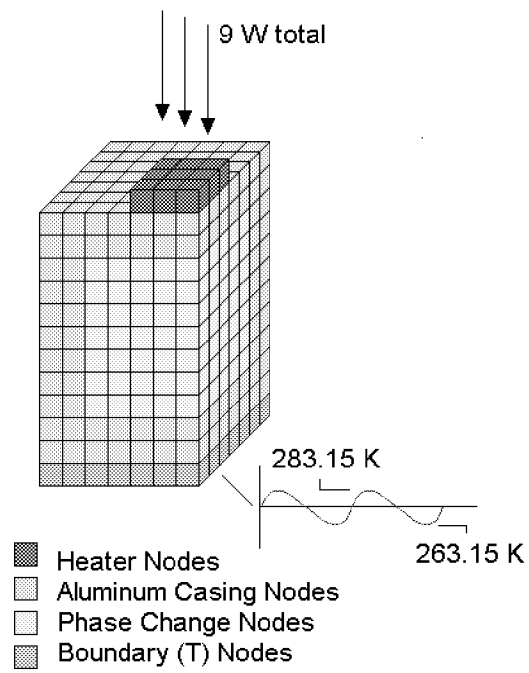
$4.5 \cdot \Delta n$



quality x



-0.13 0.01 0.15 0.29 0.43 0.58 0.72 0.86 1

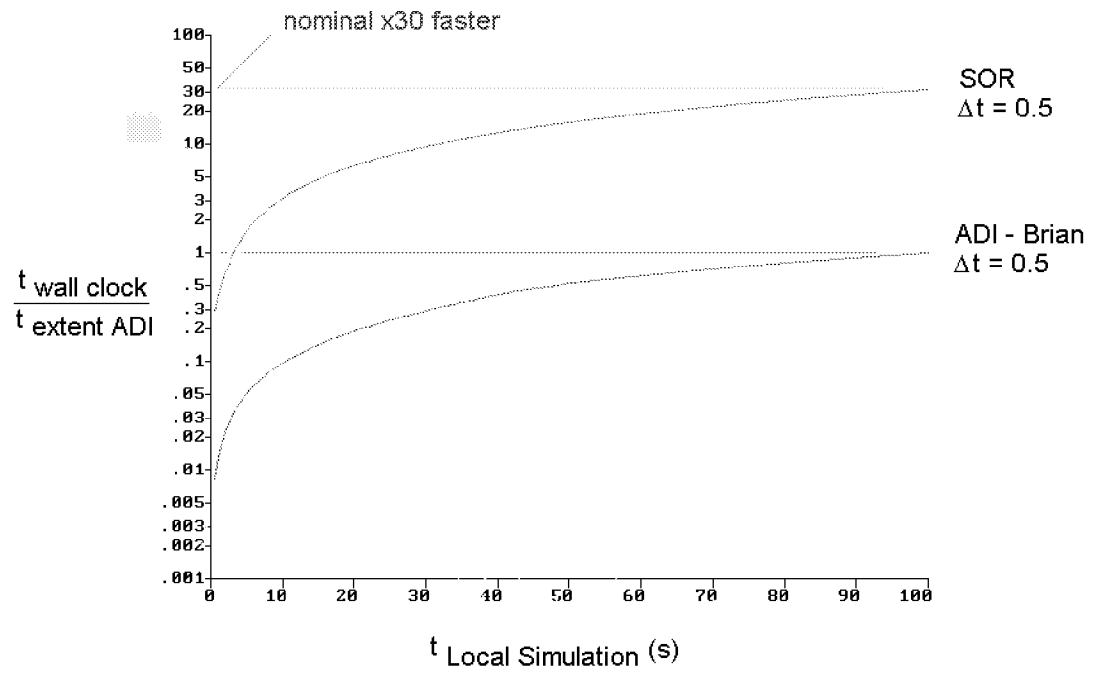


Phase Change Nodes

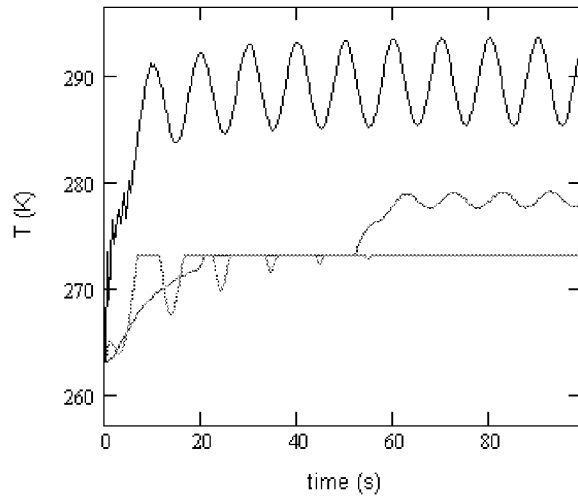
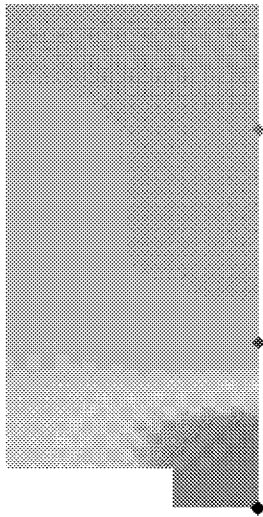
$k = 1.080 \quad \text{W/m C}$
 $\rho = 1000 \quad \text{kg/m}^3$
 $C = 1000 \quad \text{J/kg C}$

$T_{fg} = 273.15 \quad \text{K}$

$h_{fg} = 70.26\text{E}3 \quad \text{J/kg}$

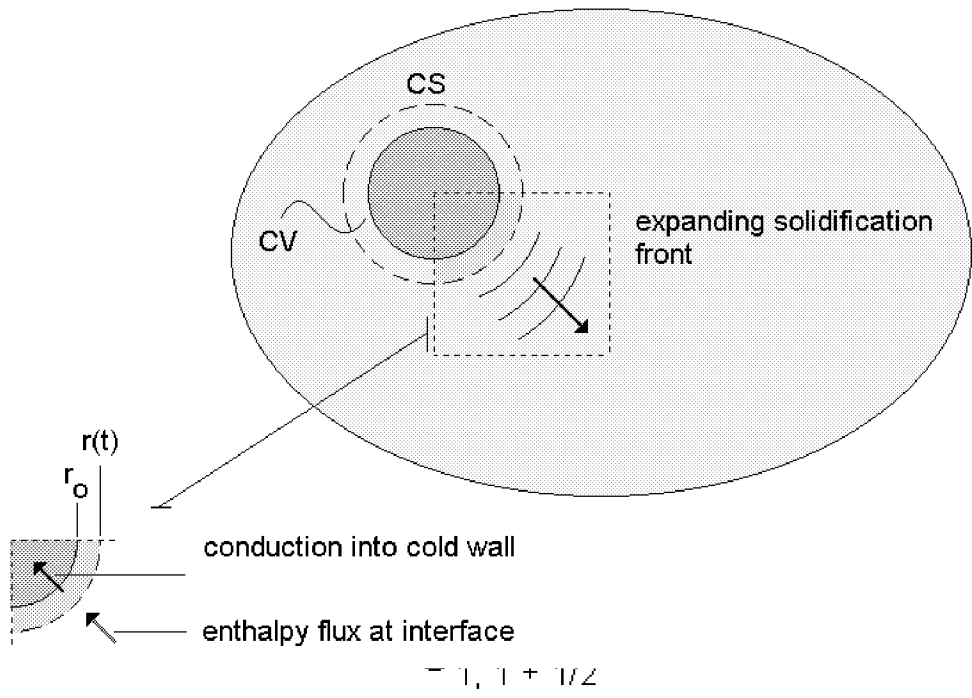


t = 100



Min = 259.842

Max = 293.65



REUSABLE SOLID ROCKET MOTOR NOZZLE JOINT -4 THERMAL ANALYSIS

J. Louie Clayton
National Aeronautics and Space Administration
Marshall Space Flight Center
Huntsville, Alabama

Abstract

This study provides for development and test verification of a thermal model used for prediction of joint heating environments, structural temperatures and seal erosions in the Space Shuttle Reusable Solid Rocket Motor (RSRM) Nozzle Joint-4. The heating environments are a result of rapid pressurization of the joint free volume assuming a leak path has occurred in the filler material used for assembly gap close out. Combustion gasses flow along the leak path from nozzle environment to joint O-ring gland resulting in local heating to the metal housing and erosion of seal materials. Analysis of this condition was based on usage of the NASA Joint Pressurization Routine (JPR) for environment determination and the Systems Improved Numerical Differencing Analyzer (SINDA) for structural temperature prediction. Model generated temperatures, pressures and seal erosions are compared to hot fire test data for several different leak path situations. Investigated in the hot fire test program were nozzle joint-4 O-ring erosion sensitivities to leak path width in both open and confined joint geometries. Model predictions were in generally good agreement with the test data for the confined leak path cases. Worst case flight predictions are provided using the test-calibrated model. Analysis issues are discussed based on model calibration procedures.

List of Symbols

| | |
|-------|-----------------------------|
| A | normal surface area |
| C | specific heat |
| D | passage hydraulic |
| e | Euler constant |
| f | Moody friction factor |
| g_c | gravitational constant |
| h | convection film coefficient |
| H | enthalpy |
| L | flow path length |
| M | molecular weight |

| | |
|---|-----------------|
| m | mass |
| p | pressure |
| Q | heat rate |
| R | gas constant |
| T | temperature |
| U | internal energy |
| t | time |
| V | volume |
| W | work |

Greek

| | |
|----------|---------------------|
| Δ | difference operator |
|----------|---------------------|

Subscripts

| | |
|---|-------------------|
| g | gas |
| i | inlet |
| o | outlet |
| p | constant pressure |
| w | wall |
| v | constant volume |

Summary

First, an overview of the RSRM nozzle joint-4 configuration and process history will be presented. JPR¹ methodology fundamentals are covered next by providing a cursory look at governing equations and modeling techniques used for computation of heating environments. Incorporation with SINDA² as a finite element thermal solver is briefly discussed. Results of model calibration with data obtained from test program "ETP-1385 Joint-4 Hot Gas Test"³ are discussed. Finally, the test calibrated joint-4 model will be used for prediction of worst case flight results using nozzle joint-4 boundary conditions and current gland geometry. In closing analysis issues, results and conclusions are presented.

Introduction

Nozzle Joint-4 Information

RSRM Nozzle Joint-4, Fig. 1, is located aft of the throat in the supersonic region of the nozzle. Liner materials at this location are a carbon phenolic ablator backed by glass phenolic insulator, which is secondarily bonded to a steel housing. Operational environments are estimated to be ~150 psia static pressure at a local recovery temperature of ~5100°R. The primary O-ring is a face seal housed in a glass phenolic gland and the opposing sealing surface is the aft end of the steel throat assembly. The joint-4 secondary O-ring is a bore seal and contained entirely in the aft end of the throat housing structure.

Contributions to joint free volume come from the primary and secondary gland, the chamfer region and assembly gaps in the liner materials. After the housings are bolted together, the assembly gaps are back-filled with room temperature vulcanizing silicon (RTV). The RTV is injected radially penetrating the length of the assembly gap typically with depth irregularities adjacent to the primary O-ring gland. Post-flight observation of typical RTV penetration depths has allowed for an average assembly gap volume contribution to be estimated at ~0.5 in³. Nominal primary gland volume is ~2.2 in³, chamfer region is estimated at 5.5 in³ and secondary gland has a nominal volume of ~4.2 in³. As an assembly aid HD-2 grease is applied to mating surfaces and has the effect of a volume filler. Based on the post-flight data, about one cubic inch of grease typically occupies joint volume. Accounting for all individual contributions, total joint-4 free volume on a nominal basis is about 11.4 in³.

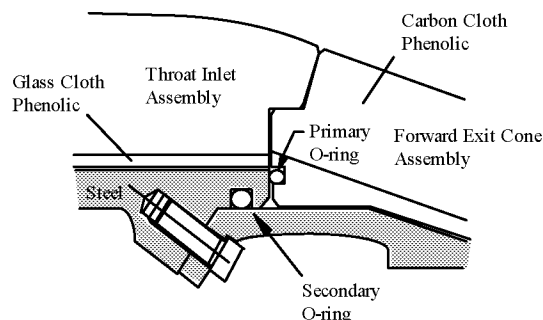


Fig. 1. RSRM Nozzle Joint-4 Cross Section

Nozzle Joint Back-Fill Process

There are two ways of dealing with assembly gaps that can potentially communicate motor environments with joint sealing surfaces. The first is to vent the joint. No back-fill materials are used in the gaps. Pressurization of the primary gland is rapid and heating to the sealing surfaces a result of compression of the gases at the stagnation point. This design is used in many solid rocket motor joints with perhaps addition of a permeable “slag barrier” to trap hot particulate matter. The second method fills the assembly gaps with a “filler” material, which is the process used in the RSRM program. Early in the motor program, application of RTV was a one-step procedure involving radial injection into the assembly gap. The procedure had the characteristic of producing “tail voids” at the circumferential location where the injection process began. It was determined voids were a result of the close-out phase of the back-fill process. When the injection process clocked 360 degrees and was “closing-out”, air was being trapped and compressed. Over time the trapped air would work its way out of the joint through the uncured RTV. Tail voids are formed extending from gland inboard to flame surface. If the void terminates before it reaches the free surface, it has potential for being exposed during motor operation. For this scenario, a confined leak path pressurizes the primary gland usually resulting in local heat affects and seal erosion. This specific anomaly happened in nozzle joint-3 of motor flight sets 44 and 45 where minor amounts of primary seal erosion occurred.

Programmatic evolution of the back-fill process has led to qualification of a two-step procedure. The joint gaps are filled, partially excavated, and then re-filled. Due to the geometry involved in joint-4, the excavation (a digging process) is performed to the first turn. The excavated portion of the gap is then re-filled with RTV. A vacuum close-out procedure is used to minimize trapped air. This process change transpired on RSRM-48 nozzle flight set and since that time, there has been no evidence of gas penetration into the joints as a result of a tail void.

A problem with the current procedure is that excavation can only be performed in the first leg to the inflection point. If a void exists in the second leg of the assembly gap, there is a finite chance of exposure resulting in a confined jet pressurization of the primary gland. Based on

liner char/erosion statistics at this nozzle station, the 3- σ char line passes the inflection point at ~104 seconds into motor operation. At this time chamber pressures are over 400 psia - thus there is potential for primary seal damage should this condition occur.

Gas Dynamic/ Thermal Modeling

Environment Prediction

Determination of the pressurization-heating environment was accomplished with the NASA JPR computer program. Calculation strategy is based on a detail inlet simulation (leak path) connected to a pressurizing volume (O-ring gland). This scheme has sufficed for the majority of gland filling problems due to characteristics of the heat transfer and influence on the overall pressurization transient. Most heat transfer occurs near the inlet while gland pressurization takes place with relatively cool gasses. The JPR method is efficient in terms of nodalization in that a detail grid is used to resolve thermal gradients where necessary and a course grid where heat transfer is not as significant. The JPR numerical scheme is based on a resistor-capacitor (R-C) formulated flow network, Fig. 2, which solves concurrently with a detail SINDA conduction grid. This scheme allows for flow-thermal-structural couplings to be simulated.

JPR uses the Lapple Tables⁴ for computation of compressible gas flow rates based on flow path inlet-exit conditions. The basic form of the flow equation for constant area is given as;

$$\dot{m} = p_i A \sqrt{\frac{g_c M}{eRT_i}} f\left(\frac{L}{D}, \frac{p_o}{p_i}\right) \quad (1)$$

where; $f\left(\frac{L}{D}, \frac{p_o}{p_i}\right)$ is a table lookup factor

During the volume filling process, instantaneous values of inlet-exit pressure and temperature constitute the known conditions of the state variables in Eq. (1). Evaluation of flow rates by this method assumes that pressure and friction forces control flow rate magnitude at any instant in time (quasi-steady solution).

The limitation of constant flow path area in Eq. (1) necessitated formulation of a procedure that solves for a system of connected paths. By applying continuity of mass and energy at path

inlet-exit, Eq. (1) expands into a system of equations that can be solved simultaneously to describe the system flow rate. This method of solution allows for inclusion of secondary head loss terms such as turns, expansion/contractions in proper serial order in the direction of flow.

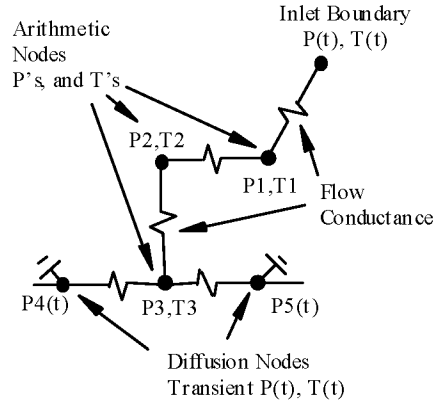


Fig. 2. Gas Flow R-C Network Formulation

Calculations of the thermodynamic conditions in the volumes are based on bulk formulation of the unsteady form of the mass and energy conservation equations. They are given as:

$$\frac{dm}{dt} = (\dot{m}_i - \dot{m}_o) \quad (2)$$

$$\dot{Q} + H_i = \frac{d}{dt}(mU) + H_o + W \quad (3)$$

where; $\dot{Q} = \bar{h}A(T_g - T_w)$

$$\Delta U = C_v \Delta T$$

$$\Delta H = C_p \Delta T$$

$$pV = mRT \quad (4)$$

Eqs. (2) and (3) are finite differenced by fully implicit methods and applied to the number of volumes involved in the simulation. Temperature and composition dependent specific heats are used for enthalpy and internal energy terms in Eq. (3). Gas compositional chemistry was assumed frozen below 2500°F and in equilibrium above this value. Aluminum Oxide (Al_2O_3) contributions to mixture properties were excluded below 3700°F. There was no attempt at modeling constituent deposition along the flow path. The ideal gas law, Eq. (4), was used

to relate total pressure to volumetric mass and bulk temperature. Equivalent molecular weights were used in the evaluation of the gas constant.

JPR internally solves for volumetric heat loss by using convective boundary conditions coupled to a 1-D conduction grid. The built-in conduction grid allows for efficient calculation of heat loss in gland regions away from the leak path inlet. Details of JPR computational procedures are found in Ref. [1].

Detail Temperature Prediction

A feature of JPR is the concurrent solution of a detail conduction grid describing heat transfer along the inlet leak path. For this study a 3-D finite element grid, Fig. 3., was constructed using MSC/PATRAN⁵. The grid region contained thermal mass sufficient to capture the heat transfer events associated with joint pressurization. Along the inlet to the primary gland, heat losses to the lateral sides were sub-modeled with a finite difference grid. Lateral heat transfer (z-direction) was accounted for and a numerically simplified treatment of flow path ablation easily implemented. Given path rectangular aspect ratio's and duration of a typical filling event, conduction corner effects have a second order influence on gas temperature prediction.

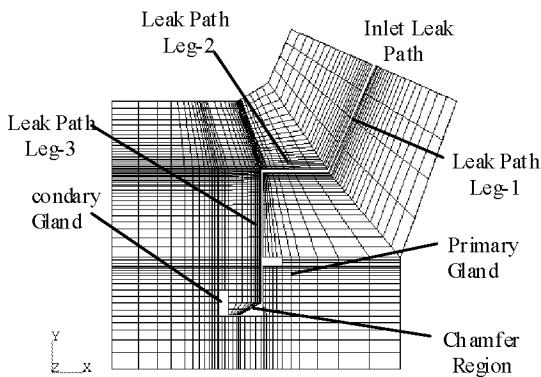


Fig. 3. Nozzle Joint-4 Finite Element Grid

Conductivity and heat capacitances for liner materials were temperature and density dependent. The material was assumed to be fully charred at temperatures above 1000°F and no accounting for kinetic decomposition rate was considered. Directional conductivities were used and ply angles fixed at 45° from nozzle centerline. Steel and O-ring material properties were input as

functions of temperature. The O-ring material is elastomeric fluorocarbon (V1115) and has an ablation temperature of ~805°F. Surface erosion rates have been measured⁶ and correlated in terms of heat transfer coefficient. Model predictions of O-ring erosion are performed on a fine grid sub-model using internally calculated environments and the 1-D surface erosion data.

Jet Spreading and Computational Fluid Dynamics (CFD) Sub-Modeling

Several test configurations include regions where the leak path is not confined. The flow is free to spread laterally before entering an O-ring gland. Several of the primary gland tests were configured with leg-3 open over the length of the article. Gas flows along a confined rectangular path in legs-1 and -2 and enters the unconfined leg-3 where a partial free jet forms. The width of the jet increases and centerline velocity decreases in the direction of flow⁷. There is a generally a reduction in centerline mass velocity accompanied by lower gas temperatures at the impingement point.

For the secondary gland cases, jet spreading occurs in the chamfer region outboard of the primary seal. Leakage past the primary seal will result in pressurization of both chamfer and secondary gland. Assuming flow past a leaking primary is localized, flow enters the chamfered region and spreads laterally before entering the secondary gland. It was determined by CFD analysis most of the flow traverses the chamfer paths before entering the secondary groove. Three-dimensional CFD models of both leg-3 and joint chamfer-secondary regions were constructed using the Finite Difference Navier-Stokes (FDNS 3-D) code.⁸

An approximate method of quantifying relative amounts of flow involved in heat transfer in a spreading region was devised and based on CFD sub-modeling. The rate of gland pressurization and inlet mass flow can be sufficiently calculated with traditional 1-D internal flow equations. Spreading regions are treated as a secondary loss (sudden expansion) in the global flow solution. The globally computed mass flow, temperature and pressure of gas entering a spreading region provide in-flow boundary conditions for a CFD sub-model. The technique involves capturing time slices of the inlet conditions and performing steady CFD solutions of the flow field. Results are tabulated where the dependent variable is the ratio of centerline mass velocity versus mass flow rate

and distance from origin of jet. This method of correlation is incorporated into a transient SINDA thermal model to determine time based flow fractions used in specific locations of the conduction grid.

Results

Work performed under Engineering Test Plan (ETP)-1385 "Tortuous Path Thermal Test Bed" generated usable results for most testing performed. Early tests were developmental in nature and results considered not highly reliable. Fig. 4 depicts a cross section of the test article showing centerline measurement locations.

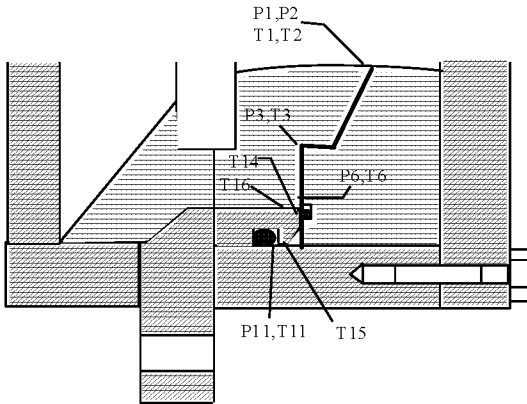


Fig. 4. Test Article Measurement Locations

The assembly measured eight inches in the lateral direction and to simulate O-ring glands of a flight joint, 55-mil ID tubes were attached to the sides of the test article. This set-up allowed for flow impingement inside the detail section of the assembly and traversal of gas flow in two lateral directions. The tubes were 5 feet long, made of stainless steel, and had fill bottles attached to the end. The fill bottles contained the additional free volume necessary to match the free volume contained in a flight-configured joint-4. Original intent of the tubing was to simulate flow friction and heat transfer associated with a pressurizing gland.

Delivered environments were consistent with inlet pressure measurements averaging ~200 psia. Several attempts were made at measurement of inlet gas temperature but were generally considered unsuccessful. The test article grain was cast from shuttle propellant TP-H1148 thus theoretical flame temperatures and combustion

gas thermochemistry was considered comparable to flight. Details of hardware, measurements and results are found in Ref. [3].

The following section provides a brief description of the test configuration followed by a comparison of analysis results versus test measured data.

Configuration-1

The leak path was machined and width fixed at 150 mils confined to the primary gland. Gaps along the path ranged from 50-60 mil, at the entrance, to 30-40 mils adjacent to the gland. Total volume was ~3.8 in³. Shown in Fig. 5-7 are predicted and measured pressures, temperatures and erosion.

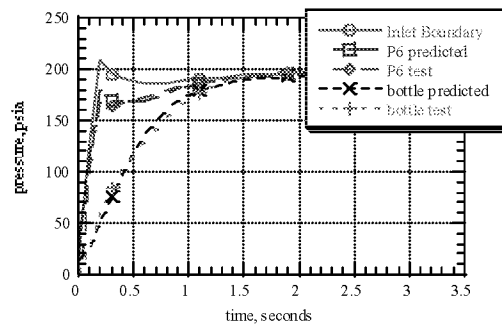


Fig. 5. Configuration-1, Leak Path and Fill Bottle Pressure Comparison

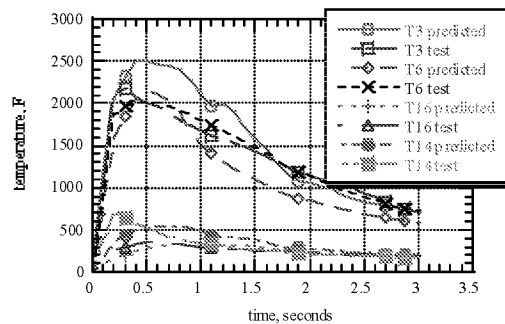


Fig. 6. Configuration-1, Leak Path Gas and Metal Temperature Comparison

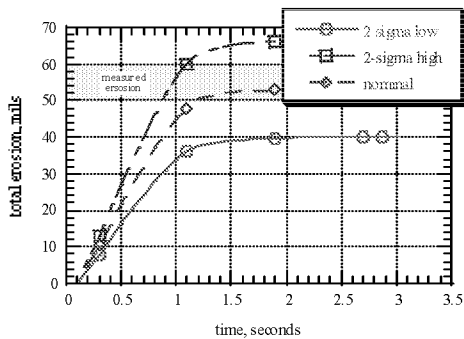


Fig. 7. Configuration-1, Primary O-ring Erosion Comparison

Pressure transients, thermocouple data and primary seal erosions compare well. There is generally less than 20% error in the predicted versus measured temperatures. Nominal erosion prediction was within scatter of measured erosion.

Configurations-2.6

Fill volumes and inlet gaps are nominal. Path width has been reduced to 100 mils. Configuration-6 uses an RTV formed inlet. Provided in Figs. 8-10 are results for test configuration-2. Fig. 10 shows the nominal erosion for configuration-6.

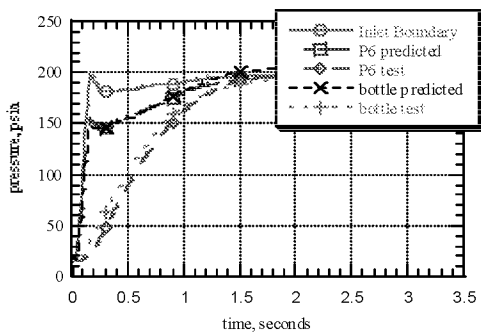


Fig. 8. Configuration-2, Leak Path and Fill Bottle Pressure Comparison

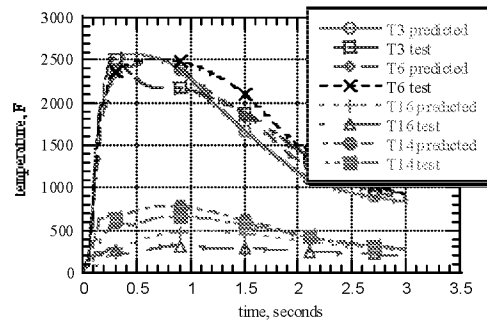


Fig. 9. Configuration-2, Leak Path Gas and Metal Temperature Comparison

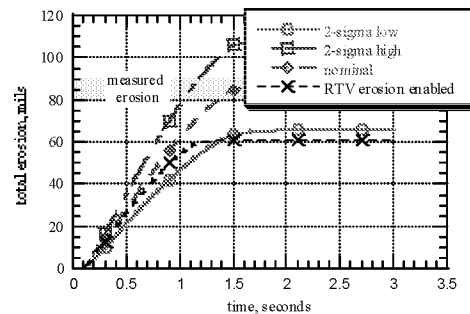


Fig. 10. Configuration-2/6, Primary O-Ring Erosion Comparison

Pressure transients, thermocouple data and seal erosions compare well. In-depth bond line temperatures are cooler than predicted but gas temperature comparison is good. Nominal erosion prediction was within scatter of measured erosion.

Configurations-3.4.11.14

For these configurations leg-3 is open in the lateral direction. Joint gaps and fill volumes are nominal. Varied were leg-1/2 widths and path materials. Two tests with 150 mil inlet (one machined and one RTV'ed) and two tests with a 100 mil inlet. All results for these cases are similar - thus comparisons for only one configuration are presented. Shown in Figs. 11-13 are results for configuration-4.

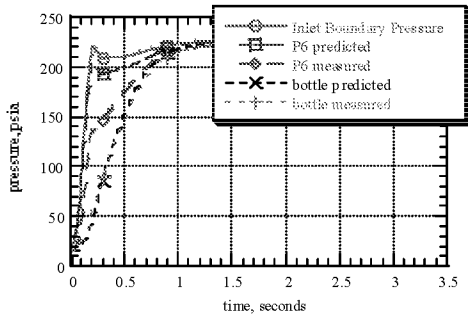


Fig. 11. Configuration-4, Leak Path and Fill Bottle Pressure Comparison

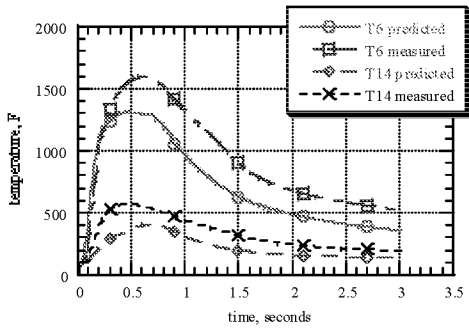


Fig. 12. Configuration-4, Leak Path Gas and Metal Temperature Comparison

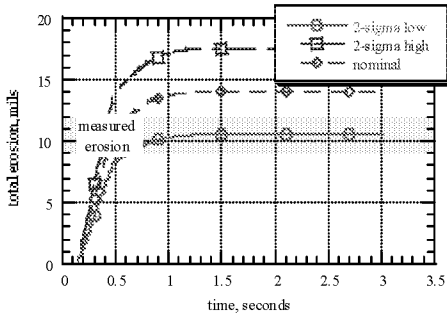


Fig. 13. Configuration-4, Primary O-Ring Erosion Comparison

For the unconfined cases predicted bottle pressures compare well, implying that computed mass flow rates are accurate. Centerline pressures in leg-3 did not compare well. Temperature predictions were generally lower than measured by 20-40%. The lower 2- σ erosion prediction is the best match with the measured data.

Secondary Gland Filling Cases

Four tests were conducted with a flawed primary seal, allowing pressurization of the chamfer and secondary gland. Results for configuration-8 are presented. Geometry is similar to a flight-configured joint-4 and measurable secondary O-ring erosion was produced. Configuration-8 had a confined 150 mil machined path to the primary. The primary seal had a “dog-bone” defect aligned with the inlet path. Fill volume for the primary gland was nominal. The chamfer contained $\sim 5.41 \text{ in}^3$ and secondary $\sim 4.21 \text{ in}^3$. Leading into the secondary gland, the metal gap measured 5 mils. Shown in Figs. 14-17 are comparisons for bottle pressures, inlet gas/metal housing temperatures and secondary O-ring erosion.

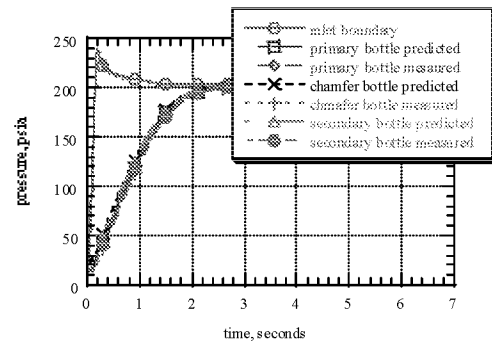


Fig. 14. Configuration-8, Secondary Gland Case Fill Bottle Pressure Comparison

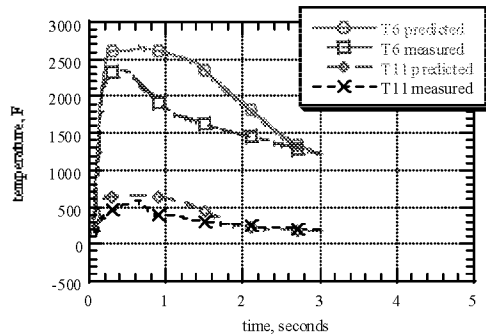


Fig. 15. Configuration-8, Secondary Gland Case Gas Temperature Comparison

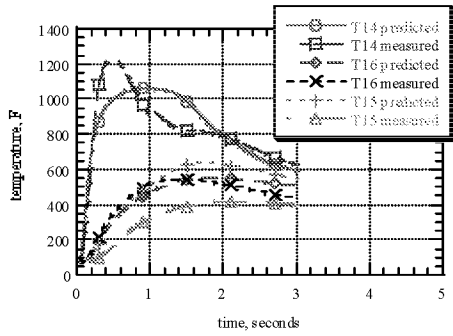


Fig. 16. Configuration-8, Secondary Gland Case Metal Temperature Comparison

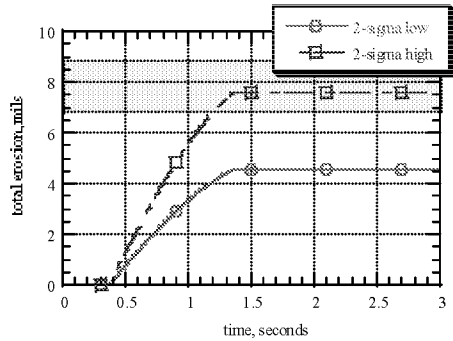


Fig. 17. Configuration-8, Secondary Gland Case Secondary O-ring Erosion Comparison

Flight Configured Joint Modeling

To account for differences between the test article and full-scale joint, the following modeling modifications were made. Effective joint-4 gland flow areas, hydraulic diameters, flow path lengths and volumes were calculated using current configuration data. These calculations accounted for curvature of a seated O-ring and effect of assembly grease. Full-scale nozzle environments adjusted for the joint-4 location were used. Early in motor operation static pressures at the joint are ~150 psia. A temperature of 5100°R was assumed for gas available for pressurization. Standard chamber data was used for adjustment of local pressure and temperature as a function of time.

Two cases were investigated. The first assumes a pre-existing leak path to the secondary at motor ignition. Geometry of the leak path was the same as test configuration-8. For this case, pressures, temperatures and secondary seal total erosion is presented. The second case deals with the smart void scenario. Analysis begins at 104 seconds when the char line has penetrated the first turn and exposes a smart void. For this case, pressures, temperatures and primary seal erosions are presented for various leak path widths.

Provided in Figs. 18-20 are results for the secondary gland pressurization. The analysis assumes a 150 mil leak path and 150 mil dog-bone in the primary at motor ignition.

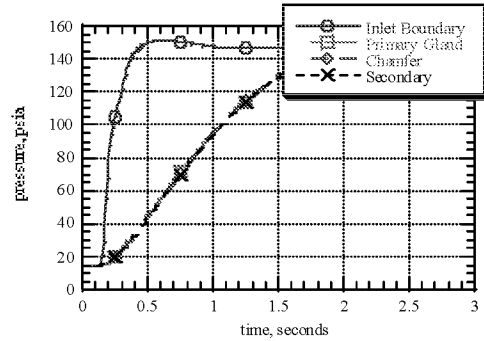


Fig. 18. Leak Path to Secondary @ Ignition Flight Case Gland Pressures

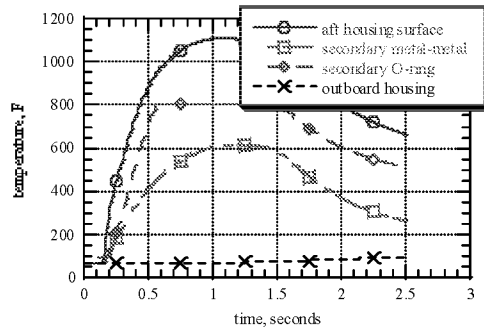


Fig. 19. Gas Path to Secondary @ Ignition Flight Case Temperatures

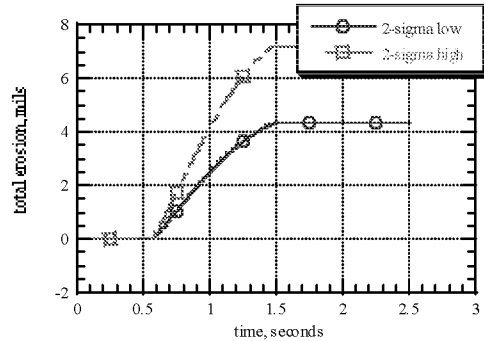


Fig. 20. Gas Path to Secondary @ Ignition Secondary O-ring Erosion

Gland pressure response is similar to test results. The joint volume fill time is ~3 seconds. Metal surface temperatures adjacent to the gas path range from 1100°F next to the primary to 600°F in the secondary metal gap. Outboard surfaces

remain ambient. Secondary seal erosion is predicted to be 5 mils.

Shown in Figs. 21-23 are parametric results for primary gland pressurization assuming a 30, 50 and 100 mil smart void. Inlet pressures are approximately 80 psia. Filling of the gland occurs in less than two seconds for all cases. Peak housing temperatures are generally less than 500°F for all cases. Maximum primary seal erosion of 20 mils is predicted with a 50 mil leak path.

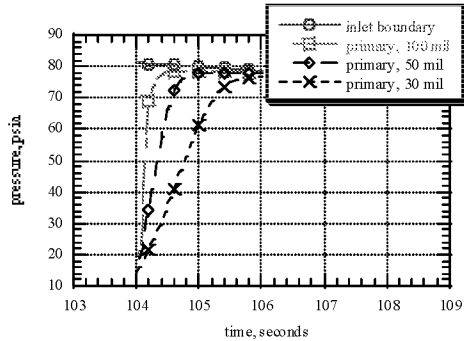


Fig. 21. Smart Void Case, Predicted Primary Gland Pressures

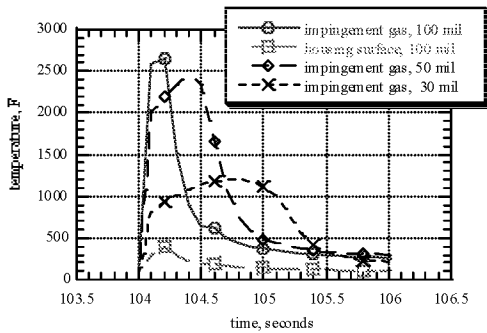


Fig. 22. Smart Void Case, Predicted Gas And Metal Temperatures

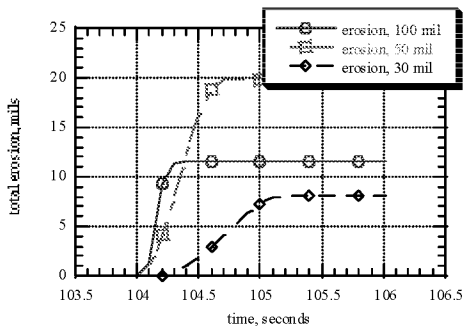


Fig. 23. Smart Void Case, Predicted Primary Seal Erosion

Conclusions

Based on results presented in this study, the following conclusions / observations are made;

- (1) Test configurations-1,-2 provided calibration benchmarks for inlet gas temperature. By machining the leak path, flow areas remained constant over time. There was no flow spreading to be accounted for in determination of mass velocities at the jet origin. These configurations provided the least amount of guesswork in quantifying the effect of impingement gas temperature on seal erosion. Inlet gas temperature of $\sim 5100^{\circ}\text{R}$ gave the best fit to erosion and thermocouple data.
- (2) Methodologies used for prediction of fill bottle pressurization rates were accurate without use of empirically derived factors to account for comparison mismatches. The gas flow network global method of solution provided good estimates of total mass flow and hence a solid basis for the sub-model procedures used.
- (3) Temperature comparisons were acceptable given the nature of the measurements, e.g., large gradients, tiny gaps and millisecond time scales. Gas temperature measurements were difficult to match and required sub-modeling of the thermocouple junction. Sub-model results indicate gas temperatures may be in error as much as 1000°F during peak flow rate conditions.
- (4) Seal erosion predictions were in good agreement for the confined jet cases. Erosion coefficients for a planar jet⁹ best fit the measured data. Nominal predictions usually were bounded within the scatter of the data. The impingement film coefficient relationships contained in Ref. [6] were slightly modified to account for 2-D velocity decay dependencies.
- (5) Largest comparison inaccuracies occurred in non-confined geometry where the flow field is multidimensional and CFD sub-modeling required. The analysis tendency was to over-predict seal erosions with CFD computed flow fractions. Based on nominal geometry, the fractions were reduced by a factor of 2-3 to best fit the data. Parametric CFD analyses shows that varying the

secondary metal gap from the nominal 5 mils to 3 mils yields approximately the right magnitude for the flow fraction. The over-prediction tendency may be an artifact of assembly tolerances or soot / condensable deposition all of which contribute to off-nominal geometry.

- (6) Primary O-ring erosion for all “unconfined” configurations ranged between 5 and 12 mils. Model results suggest that venting leg-3 complete circumference and adding this volume back into total system volume would result in double the primary erosion (10-25 mil range). Model response indicated peak flow rate magnitudes remained about the same, occurred at the same time but fill times increased. The time increase was proportional to the volume increase, which was proportional to the erosion increase (about double). Recall the 100 mil confined test produced seal erosion on the order of 90-100 mils, about 10 times the erosion amount of the spreading cases. This observation suggests that a vented leg-3 is more tolerant of seal erosion in the worst case scenarios.
- (7) The issue of inlet leak path width and what is considered “worst case” was assessed. For the smart void case, it was determined that a maximum primary seal erosion of 20 mils occurred with a 40-50 mil initial leak path size. Below this threshold, total erosions decreased as a function of decreased width. Albeit fill times are longer, decreasing impingement gas temperatures are controlling seal erosion rates at the smaller gas path widths.
- (8) Test results provided in ETP-1385 are conservative due to the following; test free volumes were larger, gland geometry more constrictive and source pressures were high. The results are non-conservative due to the lack of testing at smaller leak path widths. Parametrics were performed to evaluate the relationship between inlet leak path width and secondary seal erosion. Findings indicate a maximum secondary erosion of 16 mils occurs at path widths of 40-50 mils. Again, as path widths decrease below 40 mils, gas temperature reduction effects on seal erosion rate control total erosion and not the overall fill time.

References

1. “Joint Pressurization Routine (JPR) Theoretical Development and Users Manual”, J. Louie Clayton, NASA-MSFC Internal Memorandum, ED66 (95-01), 1995
2. Systems Improved Numerical Differencing Analyzer (SINDA), J.D. Gaski, Network Analysis Associates Inc., Version 1.8
3. “Tortuous Path Thermal Analysis Test Bed ETP-1385”, Thiokol Corporation final report TWR-66623, Mar-04, 1999
4. “Isothermal And Adiabatic flow of Compressible Fluids”, C.E. Lapple, American Institute of Chemical Engineers, 1963
5. MSC/PATRAN, Version 7.5, McNeal Scheindler Corporation, Cosa Mesa California, 1998
6. “O-Ring2: Volume Filling And O-ring Prediction Code, Improved Model Description And Validation, Part I Improved O-ring Erosion Model”, M. O’Mally, Thiokol Corporation TWR—17030, 1988
7. “Boundary Layer Theory”, Herman Schlichting, Seventh Edition, McGraw Hill Book Company, 1979
8. Finite Difference Navier-Stokes (FDNS3D), CFD code, Y.S. Chen, NASA contract NAS8-37408, 1990
9. “Prediction of Pressurization and Erosion of the SRB O-Rings During Motor Ignition (Part II): Parametric Studies of Field and Nozzle Joints, M. Salita, Thiokol Corporation TWR-15186, July 1985

Thermal / Pyrolysis Gas Flow Analysis of Carbon Phenolic Material

J. Louie Clayton
Thermodynamics and Heat Transfer Group
Marshall Space Flight Center / NASA
Redstone Arsenal, Alabama

ABSTRACT

Provided in this study are predicted in-depth temperature and pyrolysis gas pressure distributions for carbon phenolic materials that are externally heated with a laser source. Governing equations, numerical techniques and comparisons to measured temperature data are also presented. Surface thermochemical conditions were determined using the Aerotherm Chemical Equilibrium (ACE) program. Surface heating simulation used facility calibrated radiative and convective flux levels. Temperatures and pyrolysis gas pressures are predicted using an upgraded form of the SINDA/CMA program that was developed by NASA during the Solid Propulsion Integrity Program (SPIP). Multi-specie mass balance, tracking of condensable vapors, high heat rate kinetics, real gas compressibility and reduced mixture viscosity's have been added to the algorithm. In general, surface and in-depth temperature comparisons are very good. Specie partial pressures calculations show that a saturated water-vapor mixture is the main contributor to peak in-depth total pressure. Further, for most of the cases studied, the water-vapor mixture is driven near the critical point and is believed to significantly increase the local heat capacity of the composite material. This phenomenon if not accounted for in analysis models may lead to an over prediction in temperature response in charring regions of the material.

NOMENCLATURE

| | | | |
|-----------|--------------------------------------|---------------|--|
| A | -area | Z | -diffusional driving potential |
| B' | -dimensionless mass loss rate | α | -surface total absorptivity |
| C_H | -Stanton Number, Heat Transfer | β | -pre-exponential factor |
| C_M | -Stanton Number, Mass Transfer | ε | -surface total emissivity |
| C | -specific heat | Γ | -resin volume fraction |
| E | -activation energy | μ | -dynamic viscosity |
| F | -1 st generic coefficient | ϕ | -porosity |
| G | -2 nd generic coefficient | ρ | -density |
| h | -enthalpy | γ | -coefficient for Forchheimer extension |
| J | -mass source/sink rate | | |
| k | -thermal conductivity | | |
| K | -permeability | Subscripts: | |
| m | -mass | c | -carbon |
| \dot{m} | -mass flow rate | cn | -condensation |
| mf | -mass fraction | e | -edge |
| n | -number of reactions | f | -final |
| M | -Molecular weight | g | -gas |
| P | -total pressure | i,j | -free indices |
| Q | -heat transfer rate | o | -original |
| R | -gas constant | p | -constant pressure |
| \dot{X} | -recession rate | r | -recovery |
| S | -source term | rad | -radiation |
| t | -time | s | -solid material |
| T | -temperature | sc | -solid conduction |
| u | -velocity | t | -total |
| V | -volume | v | -virgin |
| w | -weight fraction | vp | -vaporization |
| x | -spatial coordinate | w | -wall |
| z | -compressibility factor | | |

INTRODUCTION

The Space Shuttle Reusable Solid Rocket Motors (RSRM) have now provided the main propulsion source for over 95 missions. During this time a very extensive database of motor operational performance has been amassed which includes parameters such as nozzle insulation erosion rates. These data are understood statistically to the extent that variations on the order of tenths of an inch are indicators that a change has occurred in either materials and/or processes used in their refurbishment. The left hand nozzle of the RSRM-56 flight set displayed anomalous erosion (pocketing) aft of the throat (Fig. 1) affecting the full circumference of the motor and measuring as much as 0.5" deeper than expected mean values. Based on statistics, the event was approximately a 6- σ occurrence and thus could not be discarded without further understanding.

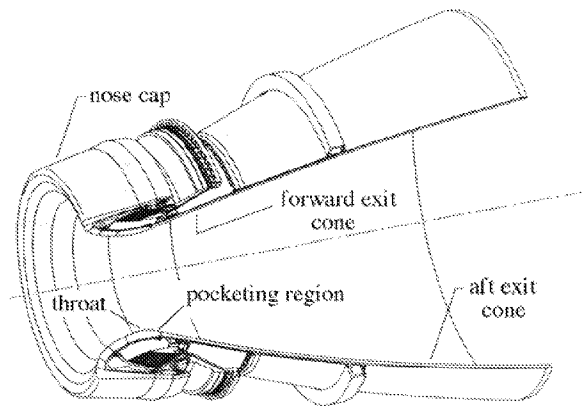


Fig. 1. RSRM Nozzle Showing Pocketing Region

The degraded material performance was believed to be attributable to the “pocketing” phenomenon that is distinctly different from typically occurring thermochemical erosion. At this location in the nozzle throat ring material ply angles are 45° to motor centerline and about 70° to the conducted isotherms. It is known that in-plane (with ply) fibers oriented orthogonal to the isotherms are more likely to pocket. It was therefore suspected that for the RSRM-56 nozzle, process variation had produced fiber orientations approaching 90° to the flame surface and was likely the primary cause of the increased erosion. Additionally, other factors related to materials and/or process variation were considered potential contributors thus it was decided to initiate a comprehensive test program aimed at gaining a better understanding of material thermostructural behavior.

The resources of the Laser Hardened Material Evaluation Laboratory (LHMEL) facility were utilized to examine pocketing activity as a function of fiber orientation and other material variations such as resin content, moisture content and ply distortions. LHMEL has the major advantages of a relatively large spatially flat surface heating distribution of precise magnitude, rapid turn-around test time and direct measurement of surface temperature. Disadvantages of the LHMEL are total pressures, thermochemistry and surface recession does not compare well with the actual RSRM. Average recession rates are about one-fourth of that experienced in the RSRM nozzle at the location of interest. There is some debate and conflicting data ^[1] that seems to suggest that the effect of active surface thermochemistry may be important in terms of suppression of pocketing. Notwithstanding these data, the decision was made to test at LHMEL based on the belief that pocketing is an “in-depth” phenomena and not strongly dependent on surface recession.

The following provides a description of modifications incorporated into the SINDA/CMA computer code which was developed by the author ^[2] during the Solid Propulsion Integrity Program (SPIP). Upgrades include multi-specie mass balance, real gas equation of state using generalized compressibility data, reduced mixture viscosity, resin weight fraction Arrhenius formulation, high rate TGA coefficients and a condensation/ vaporization simulation for vapors in the pyrolysis gas mixture. Basic formulations of the energy and momentum equations remain essentially unchanged but will be covered for completeness.

Governing Equations

In-depth temperature and pyrolysis gas pressure calculations are based on simultaneous solution of 1-D conservation equations for mass, momentum and energy along with a real gas equation of state and kinetic rate equation. The following basic assumptions were incorporated into the math model:

- 1) Local thermal equilibrium exists between pyrolysis gas and solid thus one energy equation can describe thermal response of both.
- 2) Pyrolysis gas motion is governed by the Darcy-Forcheimer equation. Permeability and porosity data was correlated as a function of degree of char. Data was assembled from Clayton^[3] and Stokes^[4].
- 3) Temperature and pressure gradients are 1-dimensional thus material anisotropy can be simulated by use of effective properties. Rule of mixtures was used for determination of properties in the charring region.
- 4) Transport of condensable species through the pore network occurs in the vapor phase. Liquid occupying pore volumes was assumed to be stationary and in equilibrium with its respective vapor in the mixture. Condensation and vaporization rates are governed by the amount of a specie that can be thermodynamically accommodated in the mixture relative to saturation over a given time step.
- 5) Condensed phase species residing together in a pore volume are assumed not to interact with each other chemically or physically. Gas phase permeability remains unchanged due to the presence of liquid in the pore volumes.
- 6) Mixture specie concentrations, in the pore free volumes, were determined by "origin" generation, condensation/vaporization rates and upstream advection. Equilibrium and/or kinetic rate reactions within the gas and reactions with the char layer are currently not modeled.

Surface Energy Balance

Surface heating conditions are determined by consideration of combined convective, radiative and thermochemical loading. The LHMEI is unique, and different from the RSRM in that surface response is driven by the incident radiation emitted from a CO₂ laser and is convectively cooled by air flow. Oxidation of carbon in the char layer is present and averages about one mil/sec depending on incident heat rate and location on the sample. Components of the surface heat flux are depicted in Fig. 2.

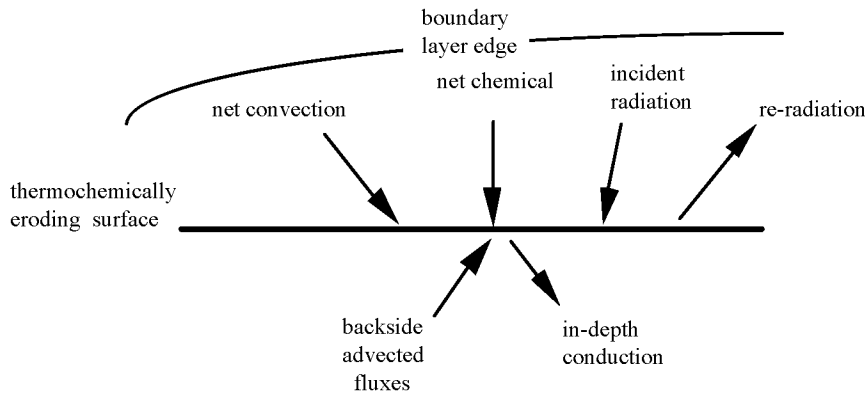


Fig. 2. Thermochemically Eroding Surface Boundary Conditions

During testing, surface radiometer data was collected and used for model calibration of surface optical properties. Backfitting model response to measured data across the range of incident flux levels, surface absorptivity was found to be independent of temperature while re-radiated energy levels were controlled by a temperature dependent emissivity. The backfit suggested that $\alpha \sim 0.97$ and ϵ was ~ 0.85 @ 3000°F and increased linearly to ~ 0.96 @ 5000°F. Forced convective cooling of the sample was imposed by a 0.5 Mach air flow directed parallel to the heated surface. Facility airflow calibration data was used for determination of convective heat and mass transfer coefficients and average values of these quantities input into the SINDA/CMA model. Surface oxidation rate was correlated in familiar b-prime table format and estimated by an ACE^[5] solution for standard air environment. Surface recession rates average about one

mil/sec and vary substantially along the heated surface with the leading edge having the greatest erosion. Arithmetic summation of respective fluxes identified in Fig. 2. gives the following expression for the surface energy balance:

$$\rho_e u_e C_H (h_r - h_{e_w}) + \rho_e u_e C_M \left[\sum (Z_{i_e}^* - Z_{i_w}^*) h_i^{T_w} - B' h_w \right] + \dot{m}_c h_c + \dot{m}_g h_g + \alpha_w q_{rad} - F \sigma \epsilon_w T_w^4 - q_{sc} = 0 \quad (1)$$

Terms left to right are identified as free stream convection, surface thermochemical, backside advective fluxes, radiation incident/emitted and conduction into the material. Numerical solution for the surface energy balance^[2] is implicit with respect to temperature calculations but explicit in time relative to mass flow calculated quantities. Net flux values are loaded into the source term of the surface node during iterative convergence of the global temperature and pressure calculations. This numerical method is different from the standard CMA approach but the two methods compare well with a difference of less than 1/2 % in computed surface temperature^[2].

In-Depth Thermal Solution

Invoking the assumption of gas-solid equilibrium, leads to the standard CMA^[6] formulation for energy conservation given by Eq. 2. For this study an additional term that accounts for pyrolysis gas capacitance has been added to the equation per the general formulation provided by Keyhani^[7]. Inclusion of gas capacitance has heretofore been considered unnecessary due to order of magnitude considerations however based on findings presented in this study, it is believed this term can become significant in charring regions of the material. Terms left to right are energy storage, conduction, decomposition, grid movement, pyrolysis gas flow and latent phase change rates. The last two terms were added to account for the phase energy of saturated water and phenol compounds.

$$\left(\rho_s C_s + \phi \rho_g C_g \right) \frac{\partial T_s}{\partial t} = \frac{1}{A} \frac{\partial}{\partial x} \left(kA \frac{\partial T}{\partial x} \right) + (h_g - \bar{h}) \frac{\partial p}{\partial t} + \dot{s} \rho C_p \frac{\partial T}{\partial x} + \frac{\dot{m}_g}{A} \frac{\partial h_g}{\partial x} + Q_{cn} - Q_{vp} \quad (2)$$

A finite element scheme was used for discretization of the energy equation. The computational grid consist of one dimensional first order elements with applied front/back face boundary conditions, Fig. 3.

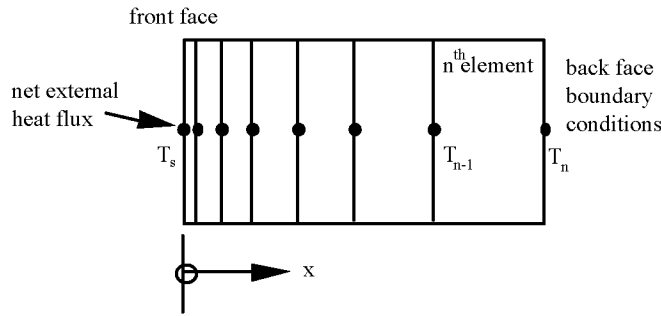


Fig. 3. One Dimensional Finite Element Grid

Surface recession is accommodated by movement of the grid relative to a fixed coordinate and applying a correction term to account for the induced advected energy into the element(s). As with the baseline CMA technique, the last element (furthest from the heated surface) shrinks to accommodate surface recession. If eroded total depth exceeds elemental thickness it is dropped from the active network and the adjacent element now absorbs the recession and so on. Determination of the elemental "stiffness" matrix is based on trapezoidal rule numerical quadrature which evaluates material heterogeneous and temperature dependencies explicitly in time. Temperature and pressure elemental integration points are coincident with a density field "nodlet" grid. Use of a nodlet grid for the density calculations is similar to the CMA technique and is generally necessitated by the exponential behavior of the Arrhenius equation.

In-Depth Pyrolysis Gas Pressure Solution

Pyrolysis gas pressure distributions are calculated using a Darcy-Forcheimer form of the momentum equation substituted into the conservation of mass equation. Real gas effects for the mixture are simulated by application of a generalized compressibility factor to the ideal gas law. Pseudocritical temperatures and pressures^[8] are calculated for the mixture based on mole fractions and the individual specie data. These “reduced” properties are used as independent variables for table lookup to determine the z factors. Mixture viscosity calculations^[9] incorporate the effects of pressure, temperature and molecular polarity and are functions of mole fraction data and the pseudocritical reduced properties. Expression of gas properties in terms of mixture equivalents, i.e., gas constant, viscosity’s, etc., permits use of Darcys equation for computation of total gas pressures. Specie partial pressures are simple functions of the mole fraction data which result from the multi-component mass balance. Terms left to right in Eq. (3) are functionally identified as gaseous mixture storage, total diffusive mass flux, total rate of pyrolysis gas generation, coordinate set movement correction, total multi-specie vaporization and condensation.

$$\frac{\partial}{\partial t} \left(\frac{\phi MA}{zRT} P \right) = \frac{\partial}{\partial t} \left[\left(\frac{K}{\mu \gamma} \right) (\rho_g) A \frac{\partial P}{\partial x} \right] - A \frac{\partial \rho_s}{\partial t} + \dot{s} \frac{\partial (\phi \rho_s)}{\partial x} + J_{vp} - J_{cn} \quad (3)$$

Eq. (3), the “pressure” equation, is analogous in formulation to the energy equation and is thus numerically solvable by the same finite element techniques used for temperature calculation. Assembly of the pressure elemental stiffness matrix relies on explicit quadrature of spatially dependent properties using the same procedure derived for the thermal calculations. Details of discretization of the diffusive term, treatment of source/sink terms and numerical degree of coupling are developed and discussed in Ref. [2].

In-Depth Kinetic Decomposition

A resin based weight fraction formulation of the Arrhenius equation was employed for the in-depth material decomposition simulation. Kinetics coefficients were developed by Clayton^[10] and computed from high rate TGA data derived by Southern Research Institute (SoRI). The weight loss curve fit considered three reactions and was based on the 3000°C/minute data. The Arrhenius relationship used in the SINDA/CMA code has the following form:

$$\frac{dw_i}{dt} = \sum_{i=1}^n -w_{o_i}^{1-n_i} (w_i - w_{f_i})^{n_i} \beta_i e^{\frac{-E_i}{RT}} \quad (4)$$

A thermal decomposition “nodlet” grid was implemented for refined description of variation in material density along the 1-D coordinate. This grid is fixed and contains time based composite material density resulting from integration of Eq. (4). A simple Euler scheme was applied in which integration time steps are set equal to the transient solution time step for the temperature and pressure calculations. Updating of temperature in the calculation occurs explicitly and the resultant pyrolysis gas flow rates are used explicitly in temperature and pressure calculations (loosely coupled). Quadrature involved in evaluation of stiffness matrices assumes a piecewise linear distribution of density described by integration of Eq. (4) at the fixed nodlet sites. Conversion of resin weight fraction data to composite density was based on the following relationship

$$\rho_s = \Gamma \rho_v \left(\sum_i w_i \right) + (1 - \Gamma) \rho_v \quad (5)$$

Multi-Component Mass Balance

A multi-component mass balance allows for tracking of individual molecular species evolved during the in-depth thermal decomposition process. The procedure utilizes a control volume aligned with elements in the pressure grid, Fig. 4. Total rate of decomposition and thus pyrolysis gas generation is determined by Eq. (4) and is assumed strictly a function of temperature and local char state. Mole fraction data that describes molecular species evolved as a function

of degree of char taken from Clayton^[3] was used to determine the “origin” generation rate. A total of eight molecular species were considered; water, carbon dioxide, carbon monoxide, methane, hydrogen, phenol, cresol and xylenol. Of these eight, water and phenol have critical temperatures high enough and occur in sufficient concentrations that condensation and vaporization has to be considered if accurate total pressure magnitudes are to be calculated.

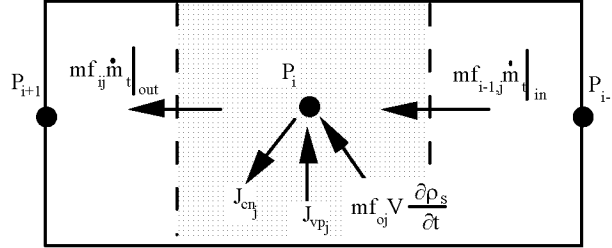


Fig. 4. Multi-Component Mass Balance

At the boundaries of the control volume are the advected fluxes of the individual species. Depending on computed direction of flow upstream contributions contribute to a weighted average type calculation of pore volume specie concentration. Equivalent molecular weights, gas constants, mixture viscosity's, specific heats are all functions of the mixture mole fraction calculations. Tracking partial pressures of individual species allows for simulation of condensation and vaporization. The computational procedure involves comparing specie partial pressure to its saturation pressure for the local temperature, Fig. 5. Below critical temperatures for the given specie, if its partial pressure tries to exceed the saturation pressure, an instantaneous rate of condensation is calculated that will keep the specie partial pressures equal to its saturation pressure (T_2^* to T_3). Time integration of the rate of condensation gives the total amount of liquid that has accumulated in the open pore volumes. This liquid is available for vaporization when conditions are such that the mixture can thermodynamically accommodate its presence. Vaporization rates are computed based on the premise that the gas mixture remains saturated until all the liquid in the pore volume is removed (T_5^* to T_5). Above critical temperatures gas mixture PVT behavior is described by the ideal gas law using generalized compressibility factors. The technique employed is similar to that used by Clayton^[3].

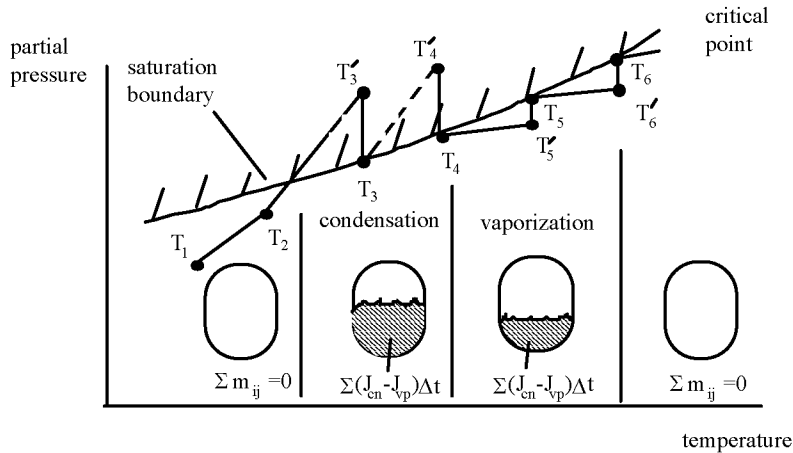


Fig. 5. Condensation and Vaporization Simulation

NUMERICAL SOLUTION

As previously discussed, discretization of energy and mass conservation equations was based on a finite element formulation employing a nodlet grid for integration of the Arrhenius equation. Time integration of the non-steady behavior of the diffusion equations, i.e., pressure and temperature, was performed by a Crank-Nicholson procedure. Eqs. (2) and (3), are cast into the following generic form:

$$F_i \frac{\Delta\Phi_i}{\Delta t} = \sum G_{ij} \left(\left(\Phi_j + \frac{\Delta\Phi_j}{2} \right) - \left(\Phi_i + \frac{\Delta\Phi_i}{2} \right) \right) + S_i \quad (5)$$

where; Φ is temperature or total pressure

Eq. (5) is solved by iteration for the dependent variable $\Delta\Phi_i$. A successive point (Gauss-Seidel) scheme is applied which uses dependent and source term damping. Coupling is fully implicit between pressure, temperature and surface energy balance meaning that all quantities are converged together along with their respective coefficients and source terms at every time step. The Arrhenius equation is not iterated with temperature and pressures. A simple explicit updating is performed using “old” time step data values. The global method of solution is described in detail by Clayton^[2] but will be summarized here to include the phase change logic. The overall numerical procedure goes as follows:

- 1) Initialize temperature, pressure, density and nodal coordinates. Compute coefficients in Equation (5).
- 2) Increment boundary information and solve for temperatures and pressures by iteration.
- 3) Using converged data in Variables 2, interpolate temperatures onto density grid and integrate Arrhenius equation across the time step. Store decomposition data into an array versus position.
- 4) Recalculate coefficients in Eqn. (5) based on new properties data, i.e., conductivity's, permeability's, mass-energy source and sink rates, coordinate system location, etc...
- 5) Perform nodal mass balance as function of converged flow conditions for current time step. Compute mass and mole fractions, partial pressures, mixture equivalent properties.
- 6) Compare partial pressures with saturation pressure @ temperature for condensable species. If partial pressure is greater, using real gas law compute amount of mass removal necessary to make the two equal. Accumulate this mass as liquid in the control volume. If partial pressure is less than saturation, using real gas law compute amount of mass necessary to saturate mixture and vaporize accumulated liquid (if there is any). Adjust mass source terms in pressure network to reflect local rates of condensation/vaporization.
- 7) Perform grid movement logistics, if current time is less than end time return to step #2

Steps #3-#7 are performed in Variables 2 of the SINDA/CMA model thus all procedures described in these steps are explicitly coupled in time to the pressure and temperature calculations in step #2.

RESULTS

Spatial distributions for in-depth temperature and pyrolysis gas pressure for various incident radiant heating rates are presented in Figs. 6-14. For these cases ply angles are fixed at 90° and time slices at 3, 10 and 20 seconds are provided. For clarity, partial pressures of only major contributors such as water vapor, carbon dioxide and monoxide are presented. For the 300 Watt case, surface temperatures range from 2900°-3700°F and increase monotonically during the test. Peak total pressures range from 140-180 atmospheres with the maximum occurring at the 10 second time slice. Water vapor is the dominant pyrolysis gas specie in the charring regions of the material with mixture mole fractions approaching 99%. Gas flows are driven in-depth and to the heated surface depending on proximity relative to the peak pressure location. In the cooler material, carbon dioxide becomes the dominant specie. As the mixture is driven in-depth, the water vapor is condensed out leaving only species with critical temperatures low enough to exist as a gas at the given total pressure and temperature. For the 500 Watt cases, Figs. 9-11, surface temperatures range from 3600°-4300°F, increasing during the test. Peak total pressures range from 130-190 atmospheres with the maximum occurring at 3 seconds (earlier in test compared to 300 Watts). Specie distributions follow the same general trends. Looking at the 1000 Watt cases, Figs. 12-14, surface temperatures now vary from 4600°-5100°F and increase during the test. Peak total pressures range from 200-220 atmospheres with the maximum occurring at 10 seconds. Clearly observable trends in Figs. 6-14 are overall increase in material temperatures and total pressures with increasing surface heat flux.

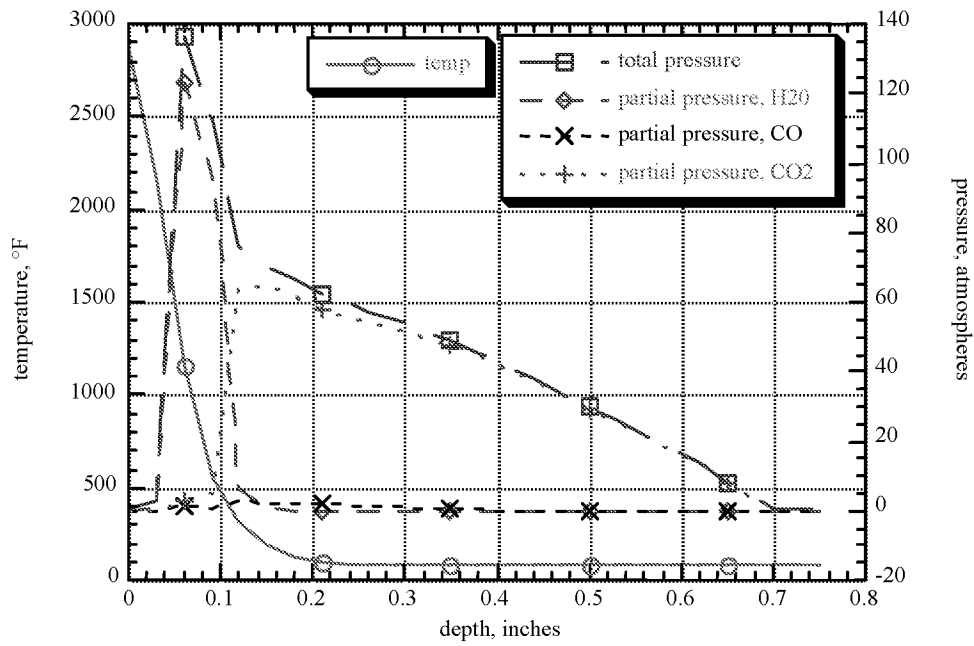


Fig. 6. Temperature and Pressure Distributions @ 3 Seconds
300 Watt Case, 90° Ply

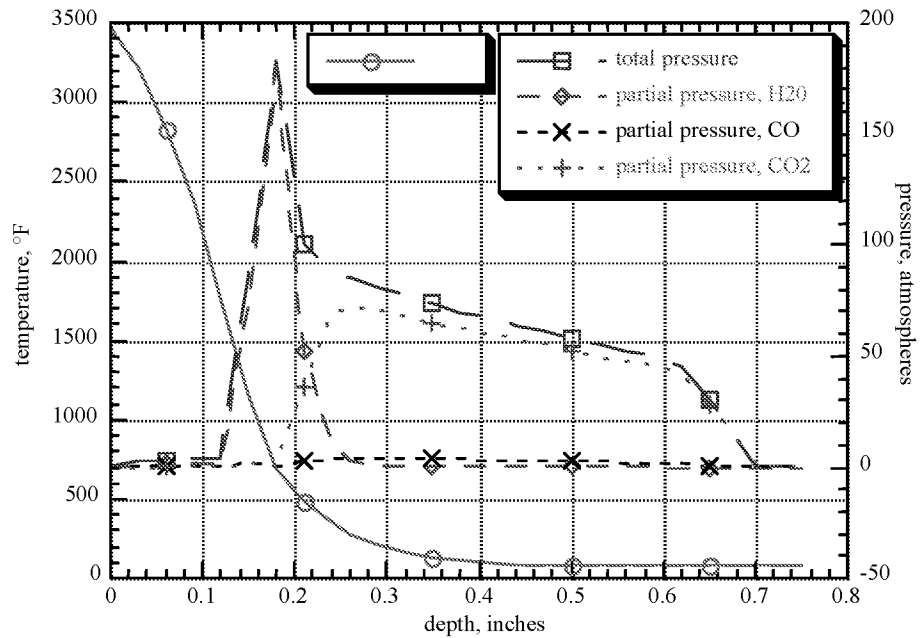


Fig. 7. Temperature and Pressure Distributions @ 10 Seconds
300 Watt Case, 90° Ply

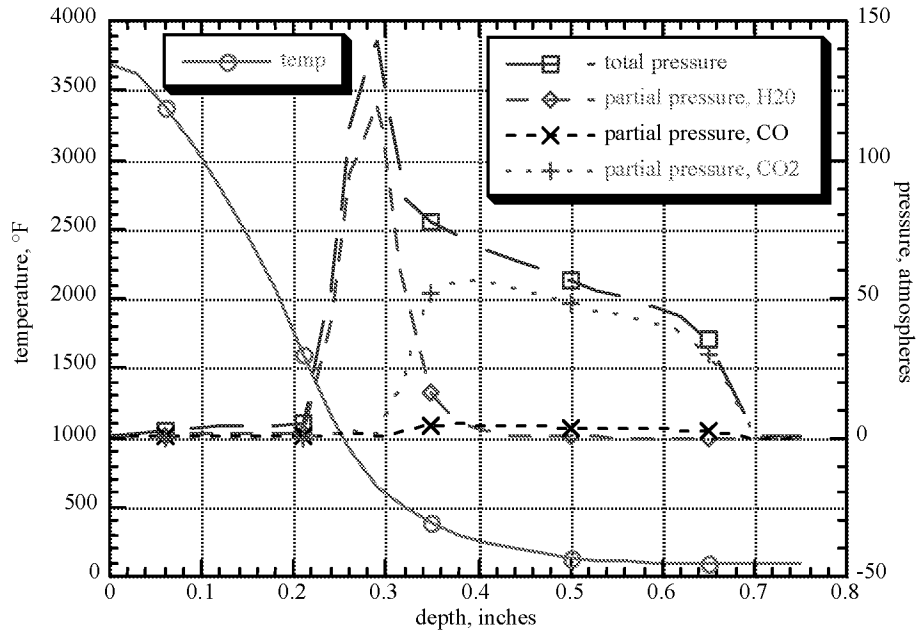


Fig. 8. Temperature and Pressure Distributions @ 20 Seconds
300 Watt Case, 90° Ply

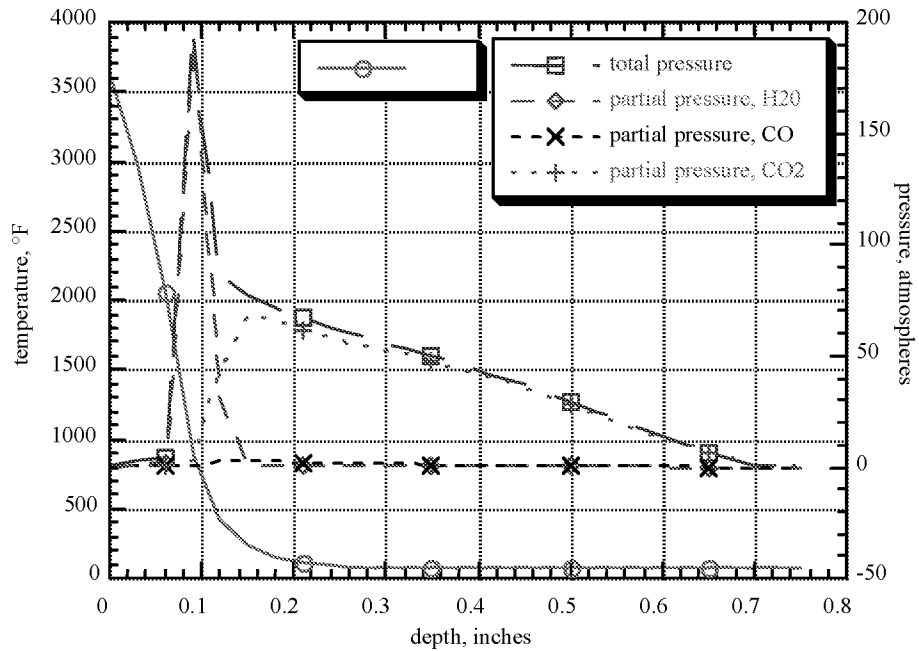


Fig. 9. Temperature and Pressure Distributions @ 3 Seconds
500 Watt Case, 90° Ply

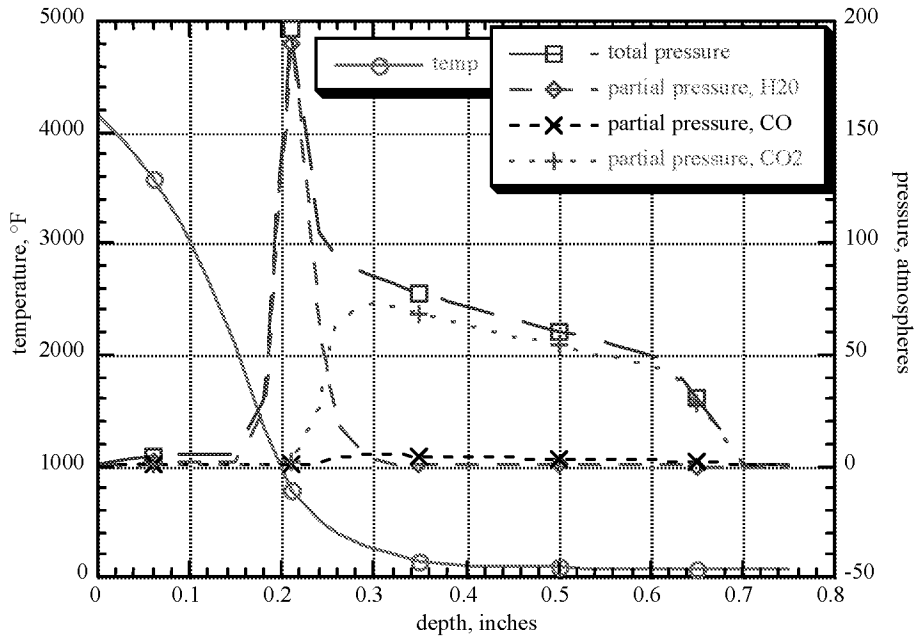


Fig. 10. Temperature and Pressure Distributions @ 10 Seconds
500 Watt Case, 90° Ply

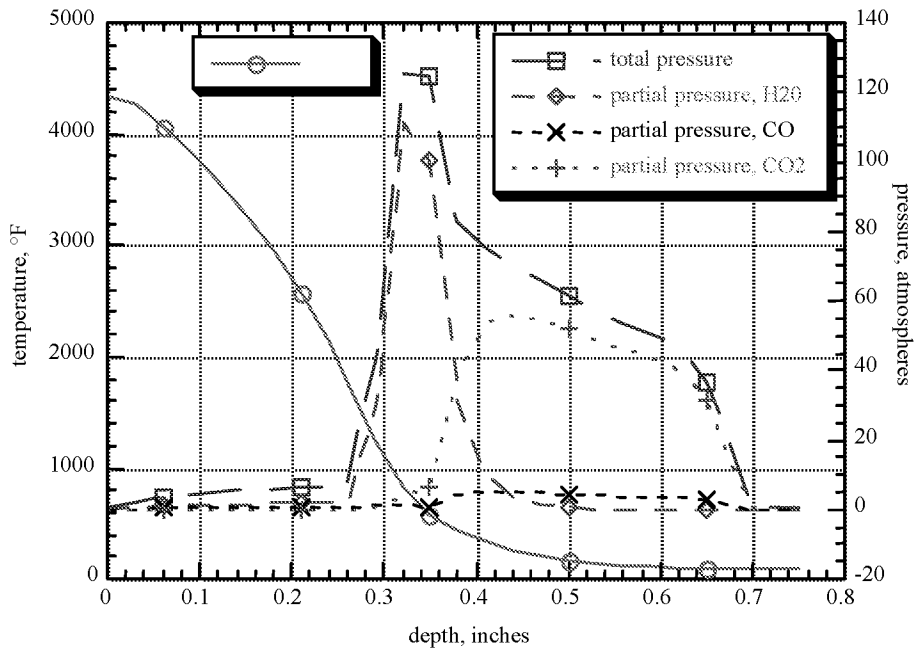


Fig. 11. Temperature and Pressure Distributions @ 20 Seconds
500 Watt Case, 90° Ply

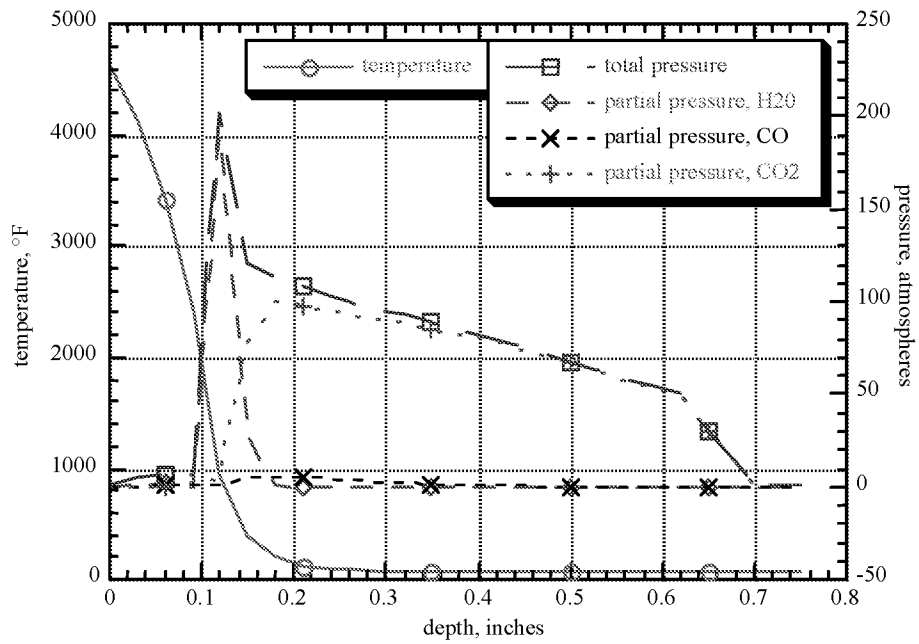


Fig. 12. Temperature and Pressure Distributions @ 3 Seconds
1000 Watt Case, 90° Ply

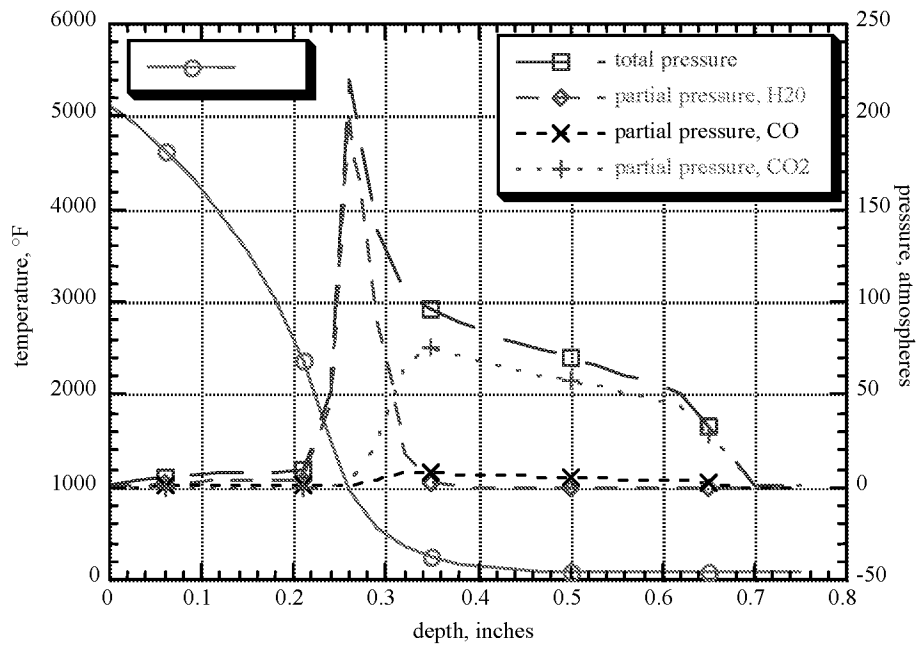


Fig. 13. Temperature and Pressure Distributions @ 10 Seconds
1000 Watt Case, 90° Ply

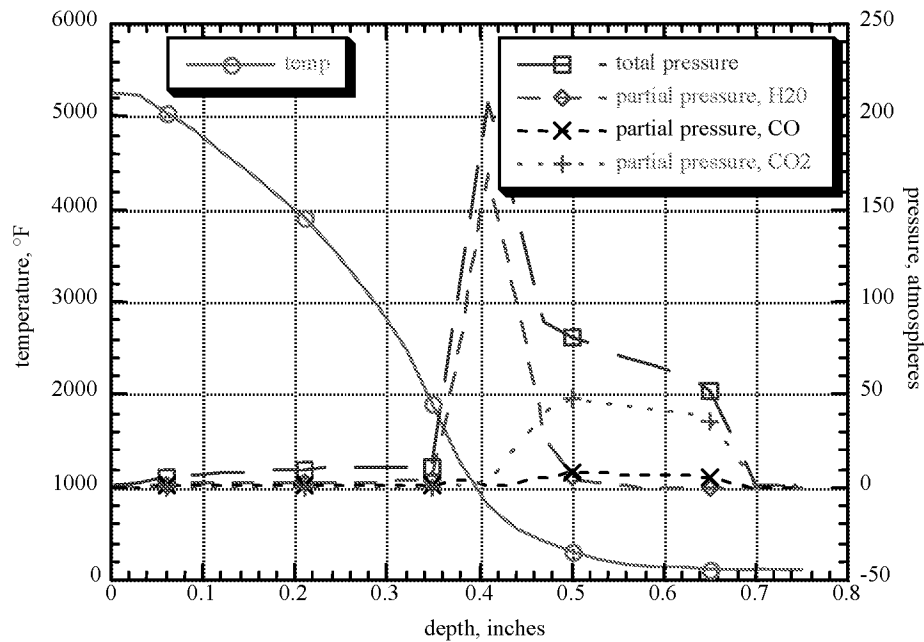


Fig. 14. Temperature and Pressure Distributions @ 20 Seconds
1000 Watt Case, 90° Ply

Provided in Figs. 15 and 16 are comparisons of predicted material thermal response to the laboratory measured data. Surface temperature data was obtained by radiometry while in-depth measurements were gathered by secondarily bonded thermocouples. Thermocouple depths were 0.125, 0.250 and 0.375 inches; a constant spacing of one-eighth inch. Adjustment of surface optical properties, per the discussed procedure, allowed for very good correlation in predicted response to the measured data. A good temperature match at the surface is a necessary starting point for understanding comparisons made at the in-depth locations. In general, the in-depth calculated quantities compare well with measured data and some discernible trends were evident. For the 300 Watt case at the 0.25" location, the measurement strays from the prediction at ~10 seconds. Comparisons at locations on both sides of this thermocouple are very good thus it is believed that the measurement may be inaccurate to some extent. High surface heating rate (1000 Watt case) comparisons are provided in Fig. 16. Unfortunately, lower capability thermocouples were used for this test and the in-depth measurements fail at ~2100°F. A general tendency for this test, and others in a series of ~1100 tests, is that model predictions lead measurements in the 700-1500°F range. Laboratory measured specific heats, for virgin and char material, were used for results presented in Figs. 15 and 16 to demonstrate this over prediction trend. Addition of saturated water pressure and temperature dependent specific heats into the energy equation would produce a better temperature comparison at the in-depth locations.

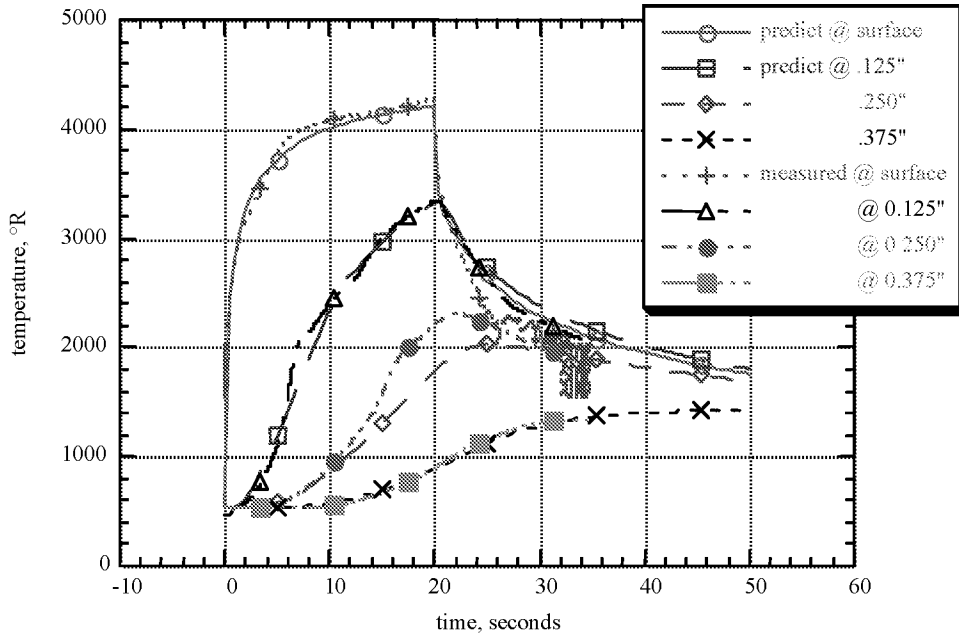


Fig. 15. Temperature Prediction versus Measured Data
300 Watt Case, 90° Ply

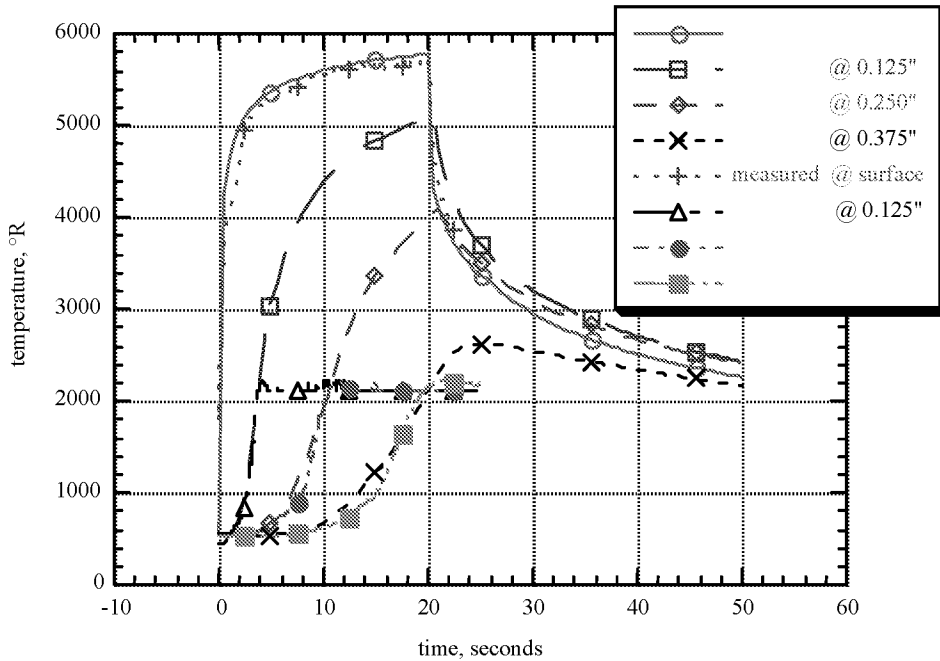


Fig. 16. Temperature Predicted Versus Measured Data
1000 Watt Case, 90° ply

CONCLUSIONS

Based on findings presented in this study the following conclusions are made:

- 1) Surface thermal simulation was best backfit by assuming a constant absorptivity and temperature dependent emissivity. At surface temperatures approaching 6000°R the two are equal at ~ 0.97 while at the lower temperatures, emissivity values were estimated to be ~ 0.85 . It is recognized these backfit values are sensitive to the assumed radiometer values used during testing.
- 2) In-depth thermal response is not strongly dependent on detail calculation of the pyrolysis gas flow field. Somewhat satisfactory results have been obtained for years assuming gas flow is always directed to the heated surface and vapor condensation not a factor. The reason for the “weak” coupling is that in-depth thermal response is driven primarily by conduction into the material. Pyrolysis gas flow contributions to the overall energy balance are second order effects.
- 3) The trend of increasing total pressures with increasing surface heat rate is attributable to material “kinetic shift” meaning basically that at the higher heat rates, the material has a tendency to be less charred at higher temperatures. Trapped volatile’s and initially evolved gases are dealing with higher temperatures and logarithmically smaller shifts in permeability thus pressure build up is greater.
- 4) Not accounting for pyrolysis gas reactions with carbon in the char layer seems to be a reasonable approximation at temperatures < 2000 - 2500°F . This premise is supported by findings presented by April^[11] where specie concentration data was obtained for gas flow through char layers at various temperatures. Peak magnitudes of pyrolysis gas pressure build up, see Figs. 6-14, take place in partially decomposed material where local temperatures are in the 700 - 1100°F range. Water-carbon reactions within the char layer could potentially increase local permeability and thus affect pressure magnitude and distribution obtained from the global solution. The exact extent of influence is unknown at this time and suggest that permeability may be correlated versus actual material density rather than the degree of char parameter. This method of correlation could potentially capture the effect of residual char density changes due to heat rate dependence and/or enhanced pyrolysis gas reactions with carbon.
- 5) For a given heat flux, calculated gas pressures for ply angles less than 90° are greater than pressures calculated for the 90° case. This is a result of the across-ply permeability component coming into play in the effective 1-D property calculations, i.e., across-ply \ll in-plane permeability’s at temperatures less than $\sim 750^{\circ}\text{F}$. Gas generation rate is essentially unchanged while flow resistance has increased thus in-depth pressure build-up is greater. This trend is based on the premise that permeability is a function of degree of char only which is how the data was correlated in the thermal model. It is known that permeability can be a function of compressive load which has the implications that the overall solution will necessarily have to couple thermal and structural response.
- 6) Formulation of the energy equation includes the local heat capacity of pyrolysis gas as contributing to the storage of energy in the material. The advective terms have always been included in CMA type codes but storage terms neglected on the premise of being second order. Results provided by the multi-specie calculations indicate that a liquid water-vapor mixture can exist during the decomposition process and that the mixture can be driven near critical conditions. In theory, a substance at the critical point has an infinite heat capacitance^[12] and the asymptotes, near the singularity, are finite and are thermodynamically obtainable to a fixed extent. Historically, there has been a tendency to over predict in-depth temperature response using laboratory measured thermal properties. Many theories have been proposed to explain the differences which include kinetics, dynamic conductivity’s, instrumentation, but it is believed by findings presented herein that part of the in-accuracy may be a result of not considering the thermodynamic state of water and implications of its pressure and temperature history.

REFERENCES

- ¹ Ross R., Strobel F., Fretter E., 1992, "Plasma Arc Testing and Thermal Characterization of NARC FM5055 Carbon-Phenolic", Document Number HI-046F1.2.9, Prepared For NASA Sponsored by the Solid Propulsion Integrity Program Nozzle work Package.
- ² Clayton J.L., 1992, "SINDA Temperature and Pressure Predictions of Carbon-Phenolic in Solid Rocket Motor Environment", in the Proceedings of the JANNAF Rocket Nozzle Technology Subcommittee Meeting, CPIA publication.
- ³ Clayton F.I., 1992, "Influence of Real Gas effects on the Predicted Response of Carbon Phenolic Material Exposed to Elevated Temperature and Pressure Environments", in the Proceedings of the JANNAF Rocket Nozzle Technology Subcommittee Meeting, CPIA publication.
- ⁴ Stokes Eric, 1997, "Room Temperature As-Cured In-Plane Permeability of MX4926 From Several Post Fired RSRM Throat Rings", Southern Research Corporation, SRI-ENG-97-281-9115.16
- ⁵ Powers, Charles and Kendal, Robert, "Aerothermal Chemical Equilibrium Program (ACE)", May 1969, Aerotherm Corporation, Mountain Valley California
- ⁶ Strobel, Forest and Ross, Robert, "CMA90S Input Guide and Users Manual, December 1990, Aerotherm Corporation, Huntsville Operations, Huntsville, Alabama
- ⁷ Keyhani, Majid and Krishnan, Vikran, "A One-Dimensional Thermal Model with Efficient Scheme for Surface Recession", in the Proceedings of the JANNAF Rocket Nozzle Technology Subcommittee Meeting, CPIA publication, Mechanical And Aerospace Engineering Department University of Tennessee.
- ⁷ Clayton , F.I., 1992, "Predictions of the Thermal Response of the SPIP 48-2 MNASA Ground Test Nozzle Materials", in the Proceedings of the JANNAF Rocket Nozzle Technology Subcommittee Meeting, CPIA publication
- ⁸ Van Wylen and Sontag, "Introduction to Thermodynamics: Classical and Statistical" , John Wiley and Sons, Inc., 1970
- ⁹ Bird, Stewart and Lightfoot, "Transport Phenomena", Department of Chemical Engineering, University of Wisconsin, John Wiley and Sons, Inc. 1960.
- ¹⁰ Clayton , F.I., 1994, "Derivation of New Thermal decomposition Model For Carbon-Phenolic Composites", Science Applications International Corporation, DN. HI-065F/1.2.9, Contract Number NAS8-37801, Subtask:3.1.1.2
- ¹¹ April, G., Pike R. and Valle, E., "Modeling Reacting Gas Flow in the Char Layer of an Ablator", Louisiana State University, Baton Rouge, La., AIAA Journal Vol. 9, No. 6, June 1971
- ¹² Eckert, E.R.G. and Drake, R.M., "Analysis of Heat and Mass Transfer", Hemisphere Publishing Corporation, 1987



LOX SYSTEM PRESTART CONDITIONING ON X-34

Brian K. Goode

Marshall Space Flight Center

ED25 Thermodynamics and Heat Transfer Group

ABSTRACT

The X-34 is a reusable launch vehicle that will be carried underneath an airplane to altitude of 35000 feet where it will be launched. It utilizes a single Fastrac 60K rocket engine for propulsion. This engine burns RP-1 and Lox as propellants and has a single shaft Lox and RP-1 turbopump. With these features there are three important requirements that must be met during the prestart thermal conditioning of this engine and feed system. First, the Lox temperature prior to starting the engine must be cold enough to be in the predefined start box at that pressure. Second, the RP-1 in the single shaft turbopump in close proximity to the lox must not freeze significantly where it effects turbopump or engine operation. Third, the chill phase of the prestart countdown has been allocated 700lb of Lox which if exceeded starts to effect mission performance. Extensive testing and analysis has been performed to evaluate the chill characteristics of the Fastrac Engine as well as test facilities and X-34 Lox feed and bleed systems.

INTRODUCTION

The captive carry phase of the X-34 launch is the period that the X-34 is attached to the L1011 aircraft and the aircraft is airborne. During development of the Fastrac engine, it has been thermally conditioned before start, using many different procedures and with many different facility configurations. None of which have exactly duplicated the X-34 captive carry flight conditions. The X-34 feed line is smaller than any in the ground test program. The flight environment as well as the helium supply to the turbopump buffer seal is expected to be much colder. A thermal model is being developed to assist in determining the flight chill procedure and to show that the requirements can be met given the vehicle configuration and the colder conditions.

Experiments have been performed to characterize the RP-1 freezing hazard and to determine Lox and LN2 boiling heat transfer coefficients. A thermal model using SINDA has been created that simulates the chill down of all the mass in the feed system, turbopump, and bleed system. An integral flow model of the Lox is included to get the transient flow rate through the system. Logic is included which will simulate each of the ground test facilities and X-34, Lox or LN2, and with actual valve sequences and tank pressure profiles.

FUNDAMENTAL TESTING

RP-1 FREEZING CHARACTERISTICS

Simple tests were performed to provide an experimental basis for some aspects of this problem. All that was known of frozen RP-1 was the freezing temperatures listed in text books and property books. RP-1 was

frozen in an aluminum tray using liquid nitrogen and as the RP-1 thawed the temperature was measured and physical properties were observed. The results indicated that there is no freezing temperature but a transition that occurs between the temperatures of 400 R and 350 R. As temperature is reduced below 350 R the solid wax increases in hardness. These temperatures are approximate because during thaw there were many phases, and temperatures existing simultaneously in the tray. This test showed conclusively that 400 R would be a safe lower limit, and that 335 R represents a significant risk to turbopump operation. RP-1 is shown in figure 1 with a temperature of 373 R (-87 F). Table 1 lists the temperatures and corresponding physical observations.



Figure 1: Freezing RP-1 In a Tray

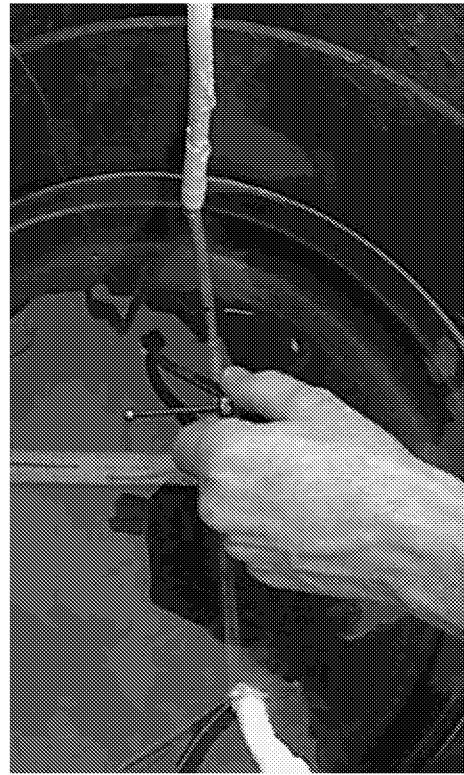


Figure 2: Freezing RP-1 on Tube Wall

A second test was performed to determine how much frozen RP-1 would accumulate on a cold wall submerged in warm RP-1. LN₂ flowed through the tube, and the wall temperature was measured to be 160 R. Again there was no solid liquid boundary but a transition that occurred as the distance from the wall increased. This made thickness measurements rather subjective. This test showed that if bulk RP-1 temperatures remained warm no significant buildup of solid RP-1 can take place. A conservative approach to calculating frozen thickness was developed. Figure 2 shows a thickness measurement being taken in this experiment and table 2 shows the values for four separate measurements and an average.

Table 1: Frozen RP-1 Observations

| Temperature | Description |
|-------------|-------------------------------------|
| 302 R | Hard wax |
| 335 R | Solid wax, softening some |
| 350 R | Soft wax |
| 355 R | Gel |
| 380 R | Gel, thick liquid, rapid warm up |
| 420 R | Liquid RP-1 with some solid present |

Table 2: Steady State Thickness Values

| Measurement | Value |
|-------------|--------------------|
| A. | .044 inches |
| B. | .082 inches |
| C. | .074 inches |
| <u>D.</u> | <u>.024 inches</u> |
| average | .056 inches |

BOILING HEAT TRANSFER COEFFICIENTS

Two experiments were performed to investigate Boiling Heat Transfer Coefficients (HTC). The first test measured 17 impeller surfaces as it was chilled in liquid nitrogen. Figure 3 shows a chilled impeller in a vertical orientation. Figure 4 shows the impeller being submerged in liquid nitrogen in a horizontal orientation. The second test measured the surface temperatures of two steel plates chilled in liquid oxygen. Figure 5 shows the plates in lox and figure 6 shows the instrumented plates on the table. A one dimensional thermal model was used to derive the boiling HTC as a function of surface temperature from the measured data. The impeller test showed no significant variation with orientation. This test shows that when LN2 envelopes the impeller that all surfaces were chilled in 140 seconds. Figure 7 shows the measured data from an impeller test. Figure 8 shows predicted impeller surface temperatures for metal of different thickness using the derived LN2 boiling HTC curve. Figure 9 shows the derived curves for Lox and it is an average of these lox curves that is used in the thermal model. The critical boiling characteristics apparent from testing were the film boiling HTC and the transition region from minimum to maximum heat flux.

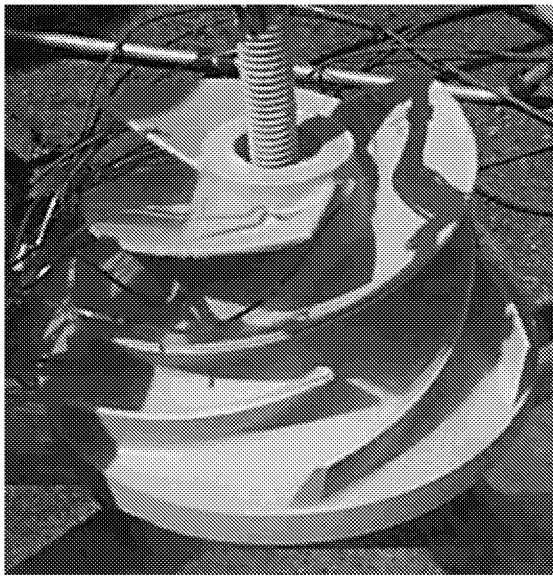


Figure 3: Chilled Lox Impeller



Figure 4: Chilling Lox Impeller in LN2

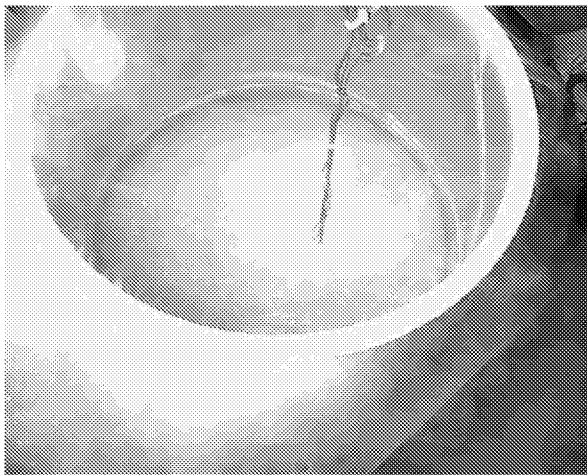


Figure 5: Chilling Steel Plates in Lox

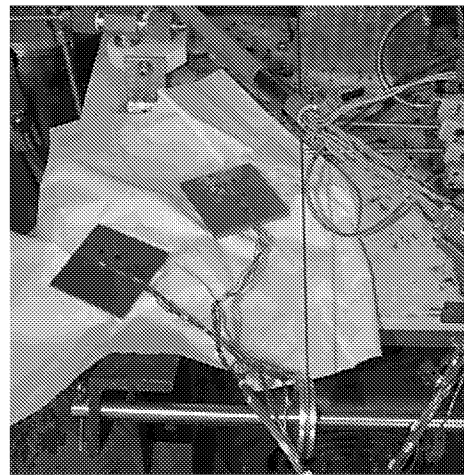


Figure 6: Instrumented Steel Plates

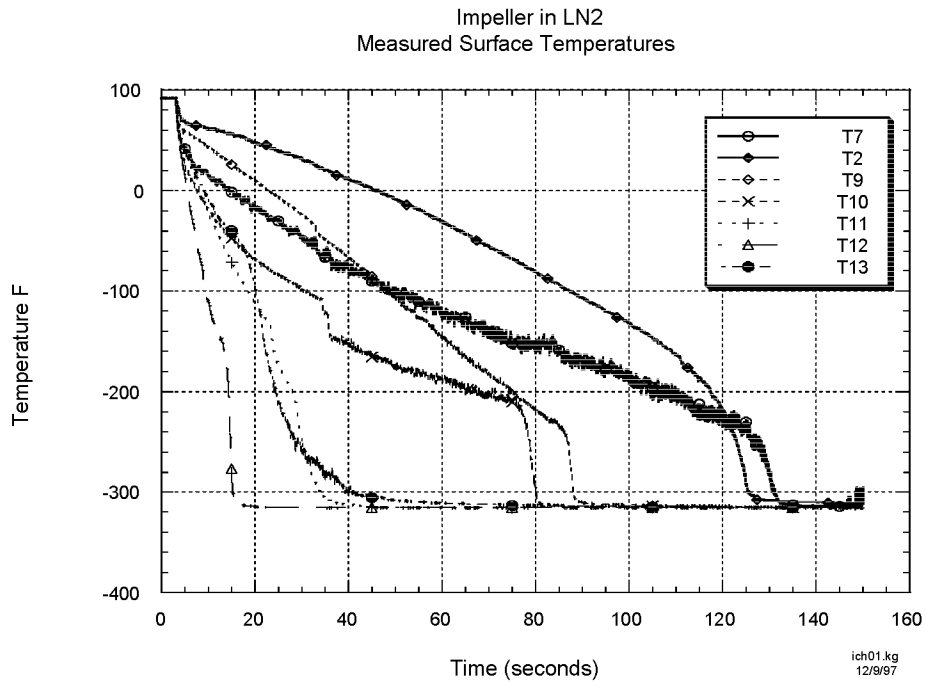


Figure 7: Measured Surface Temperatures, LN2 Impeller Test

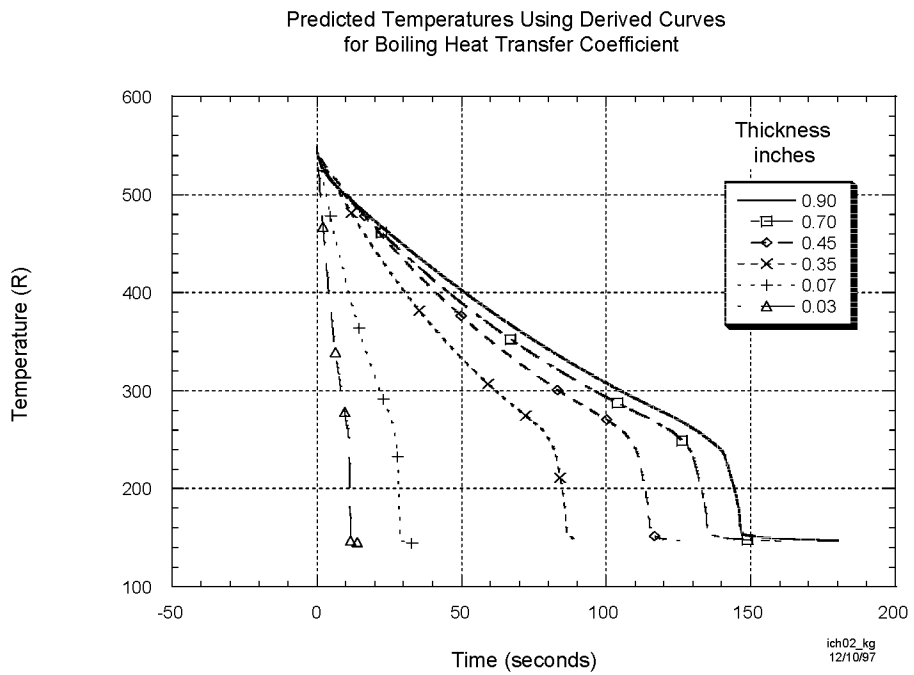


Figure 8: Predicted Impeller Surface Temperatures from Derived HTC Curve

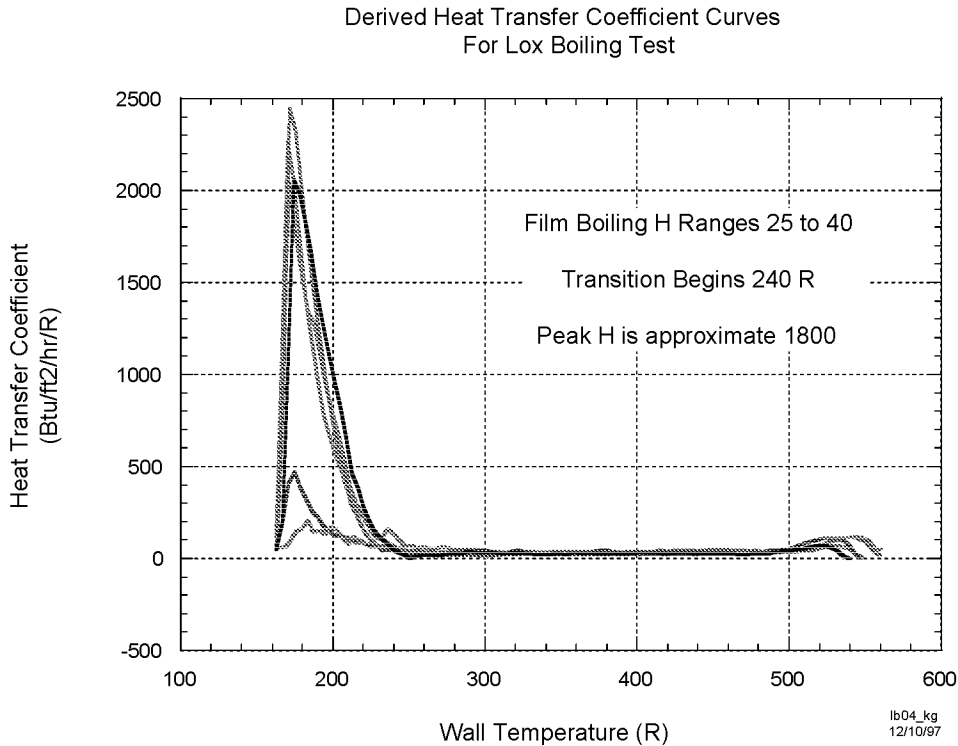


Figure 9: Derived HTC Curves from Steel Plates in Lox

COMPONENT AND ENGINE TESTING

The first component test series had the turbopump only with an upper lox line bleed and a turbopump bleed for thermal conditioning prior to start. There were many pressure and temperature measurements in the lox system and on the external surfaces of the turbopump. There was no flow meter installed which could measure the low bleed flow rates during chill. The first attempt to chill through the turbopump bleed was much too slow so an alternate plan to chill through the Lox throttle valve was incorporated. This valve at 40% open and a 4.5 inch diameter line simulates the main oxidizer valve on the engine. There was a temperature probe installed in the fuel bearing coolant line to measure the fuel temperature behind the impeller. Many changes were made to the model after this first series. The tests revealed that the 9 tooth Kel-F labyrinth seal ring and the warm helium are important in maintaining warm fuel temperatures. External thermocouples on the IPS housing matched well with the model predictions.

The first engine level testing occurred on the Horizontal Test Facility. This series provided the first flow rate data through the engine bleed which was critical information for model correlation. This facility also had many pressures and temperatures measured in the lox system. The 9 tooth labyrinth seal ring material changed to nickel 200 which had a larger operating clearance than the Kel-F. To maintain warm fuel temperatures helium cavity pressure was raised in the Inter Propellant Seal (IPS). Another significant chill test was performed on HTF where the engine and lower feed line were chilled with flow through the main oxidizer valve only. The actual flow rate was 43 lbm/sec which was lower than expected. There was an unexpected 30 psi pressure drop between pump inlet and discharge which happened when the pump spun to

2000 rpm. Turbomachinery provided the negative head portion of the pump map and it was incorporated into the thermal model. Another unexpected result was the slow rate at which the main injector lox dome temperature decreased after dropping below the saturation temperature. Horizontal test facility and the component testing has supplied vast amounts of data for model correlation. Figure 10 shows the turbopump.

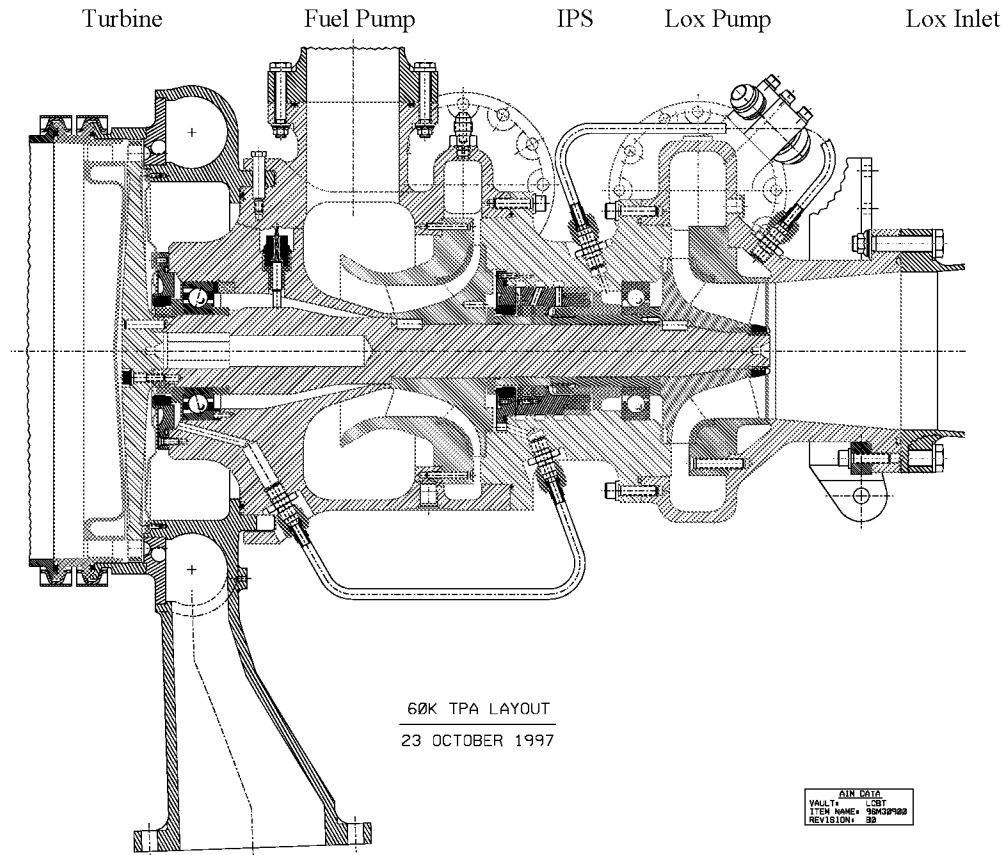


Figure 10: Turbopump Cross Section

X-34 SYSTEM AND ENVIRONMENTS

There are significant differences between the flight and ground test experience in terms of configuration and environments. The flight lox feed line has much less mass and is shorter than HTF or the Component Stand. The bleed line on X-34 has an inner diameter of 0.62 inches and is 5 to 6 feet long. At the end is a check valve with an Equivalent Sharp Edge Orifice Diameter (ESEOD) of .43 inches. On HTF the Engine bleed line is 0.884 inner diameter and 20 feet long with no check valve. The engine with the HTF bleed configuration flows approximately 3.5 lbm/sec of lox with 67 psia at the engine interface. Helium, Fuel and ambient air temperature has always been warm in ground testing. The flight cold case helium temperature is 417 R, fuel temperature 460 R and engine compartment purge temperature reaches a low of 449 R at engine start. Bleed exit pressure on the ground has been 14.7 psia where flight will be 3 psia at an altitude of 35000 feet. To alleviate some of the cold environments the X-34 will have a warm purge on the ground. In addition, a turbopump heater will add 200 watts to the IPS fuel side flange on the ground and 100 watts during the captive carry phase.

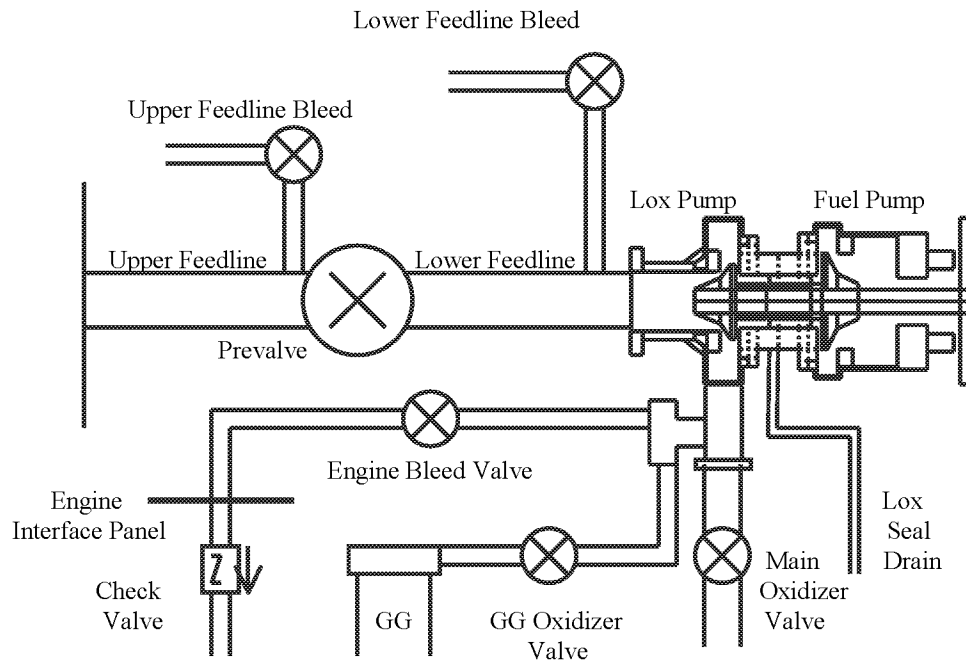


Figure 11: Typical Lox Feed and Bleed System

THERMAL MODEL

A thermal model was created to determine the important parameters that drive the thermal conditioning of the turbopump prestart. It encompasses the feed line, bleed lines, and most of the turbopump. There is detailed modeling of the lox also since transient flow rates and lox quality are such important aspects of this problem. The approach taken is to model the ground test hardware, environments, valve sequences, pressures and correlate the model. Only then can the X-34 condition be predicted with confidence. As more test data has been produced the model has evolved to be more complex to match the data. The following major changes to the model have taken place in chronological order. The first improvement was the detailed modeling of the Inter Propellant Seal to match the warm fuel seal drain temperature that was seen on the component stand. These changes include a variable clearance in the 9 tooth labyrinth seal and fluid nodes with heat transfer for the helium. Then heaters were added along with logic to simulate the flight designed thermostat set points and tolerances. Then the necessary logic to model all facilities with all the flow circuits was added with the capability to run complicated pressure and valve position profiles. Properties and lox temperatures are determined from calculated enthalpy to better model the saturated and subcooled fluid and the heat transfer occurring in the lox system.

INTEGRAL FLUID MODEL

The fluid in the lox feed and bleed system has been divided in to approximately 60 nodes. At each location the state of the lox is dependent on the energy balance including the stored energy, energy in and out from mass flow, and the convective energy transferred to the fluid in the volume. The enthalpy is calculated and

used to determine the fluid properties. For nodes which contain saturated liquid and vapor, all properties are calculated based on volume fraction of vapor, and saturated vapor and liquid properties. The approach to calculating heat transfer coefficient (HTC) is to calculate a vapor and liquid HTC and then average the two based on the vapor fraction by volume.

The flow rate calculation has proven to be the most difficult. The first approach was simple and used loss factors and Bernoulli's equation to iterate on a flow rate in each bleed path. The difficulty has come from the fact that there are large variations in density and HTC that occur, causing the flow rate prediction to be unstable. At a pressure of 50 psia saturated liquid is 77 times more dense than vapor. Nucleate boiling HTC is as high as 1800 btu/ft²/hr/F and film boiling HTC is as low as 20 btu/ft²/hr/F. The flow calculation was stabilized and a good correlation was achieved for an engine bleed only chill on HTF. Correlation to the MOV chill on HTF however has been difficult. The current version of the chill model has a more complicated solution that includes conductors for choked flow and cavitation. It is incomplete at this time.

HARDWARE TEMPERATURE PREDICTIONS

All the mass which must be chilled or that may transfer heat to any of the lox flow circuits is included in the model. The turbopump is modeled in greater detail in order to address the fuel side temperature requirements as well as match any IPS and turbopump surface temperatures measured in the ground test program. The feed lines and bleed lines are modeled simply with approximately 60 nodes, each with the correct surface area and mass. External heat transfer is included or disabled if the line is insulated.

RESULTS FOR HTF AND X-34

The results presented in this paper are from a version of the model which correlated well with an engine bleed test on HTF and then was used to predict the X-34 chill. This version of the model did not correlate well with the HTF test where the engine, feed and bleed system were chilled through the Main Oxidizer Valve (MOV). The results presented here are for illustration of what the model capabilities are, recognizing that more features are required to match all the test data.

On HTF the chill sequence typically involves a low pressure chill of the upper feed line through the upper feed line bleed. When cold liquid is evident upstream of the pre valve, the pre valve is opened beginning the chill of the lower feed line through the lower feed line bleed and engine bleed. Shortly after pre valve opening the upper feed line bleed is closed and the tank is pressurized taking the engine interface pressure from 18 psia to 68 psia. Figures 12 shows the predicted mass flow rate. The first hump in this curve is the low pressure upper feed line chill. The second hump is lower feed line chill with both lower valves open and engine interface pressure at 80psia. Flow rate drops in half to 4.5 lbm/sec when the lower lox line bleed is closed. The next drop in flow rate occurs when the tank is vented. While vented the lower lox line bleed is opened again and at approximately -1700 seconds the tank is pressurized to 68 psia. Shortly after pressurization the lower lox line bleed is closed again. Figures 13 and 14 show analysis and test data respectively for engine interface temperature and how it compares to saturation temperature at that pressure. Figures 15 and 16 show predicted and measured gallons of lox in the tank. Figures 17 and 18 show predicted and measured fuel seal drain temperature. It is interesting to note how this temperature rises at -3200 seconds when tank pressure is reduced and how it drops again at -1700 seconds when the tank pressure is increased again.

The X-34 analysis is much more simple in terms of tank pressurization and valve sequences. Tank pressure starts at 13 psia and the pre valve and engine bleed are opened at 0 seconds. Soon the tank pressure is ramped to 58 psia which is the start pressure for the engine. Figure 19 shows the engine interface temperature as well as the saturation temperature at the interface pressure. The plot shows the engine interface temperature constraint being met at 410 seconds. The lox consumption curve is shown in figure

20 and with this chill procedure shows 700 lb consumed at 710 seconds. The start window then will occur between 410 and 710 seconds. Figure 21 shows that in this window the fuel seal drain temperature at an acceptable level and consistent with the ground test experience of 400 R. Figure 22 shows the predicted transient flow rate for the X-34 bleed line at the low exit pressure.

FUTURE TESTING AND ANALYSIS

There is a planned test on HTF with a simulated X-34 bleed line. Downstream of the Engine Interface Panel there currently is a bleed line 20 feet long with inner diameter of .884 inch. The last 5.5 feet of this line is to be modified to inner diameter of .62 inch and with an orifice at the end with diameter of .43 to simulate a check valve which is in the X-34 bleed line. The X-34 vehicle itself is scheduled to ground tested with an engine firing included so there will be chill data for the flight feed and bleed system prior to first flight.

The thermal model is currently being modified to include flow conductors to calculate choked flow and cavitating flow for valves and orifices in the lox feed and bleed system. Once that version is operational and predicting stable flow rates, correlation to test data will begin.

Analysis, HTF Test, Lox Mass Flowrate

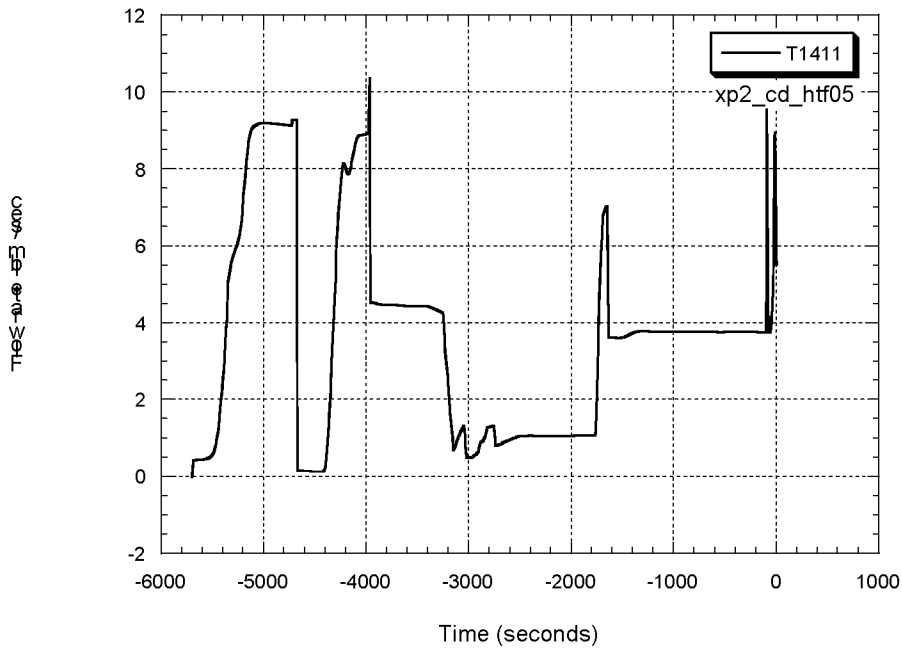


Figure 12: Predicted Feed line Flow rate

Analysis, HTF Test, Engine Interface Temperature

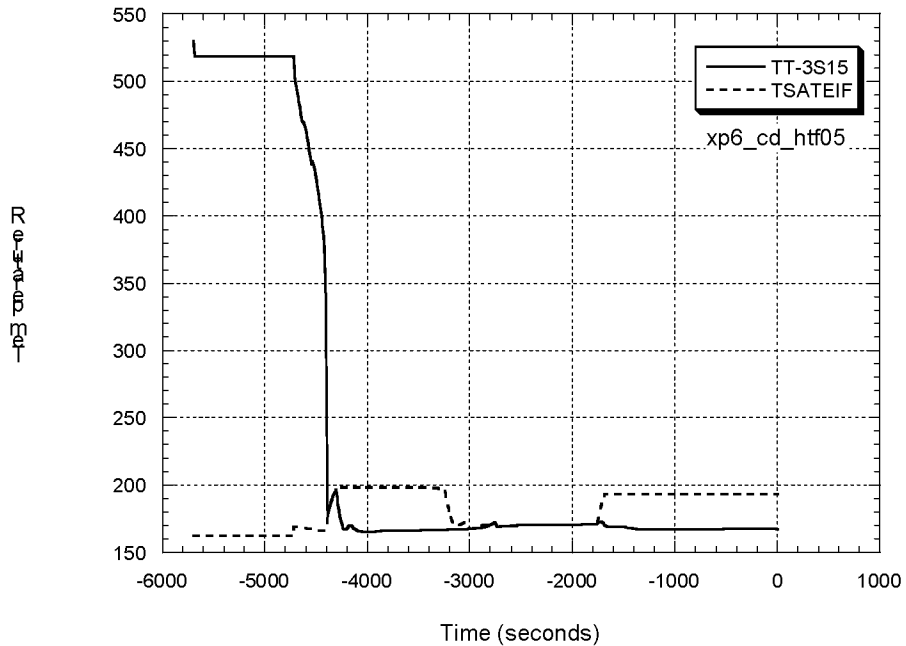


Figure 13: Predicted Engine Inlet Temperature

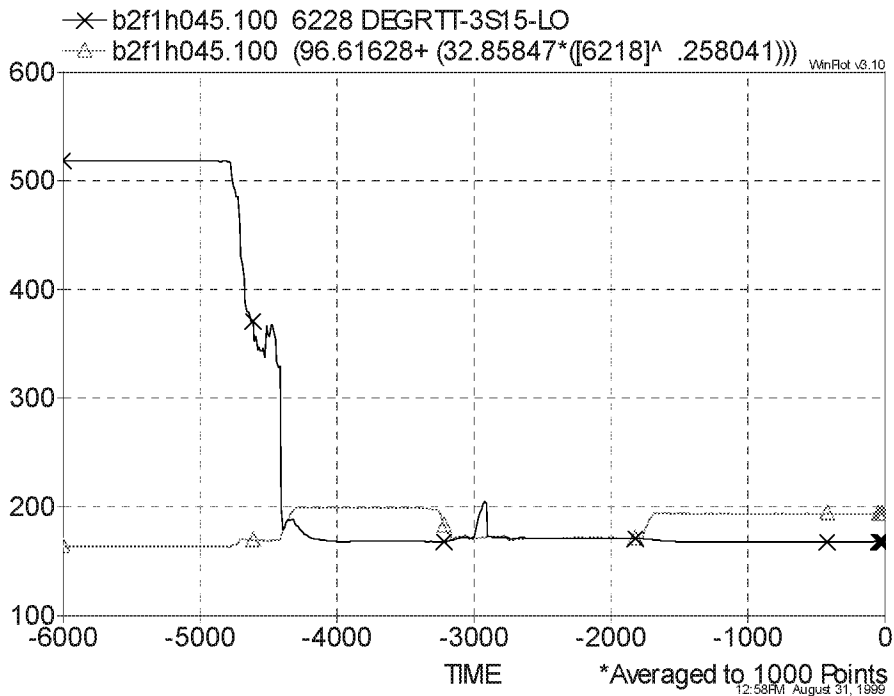


Figure 14: Measured Engine Inlet Temperature

Analysis, HTF Test, Lox Volume Gallons

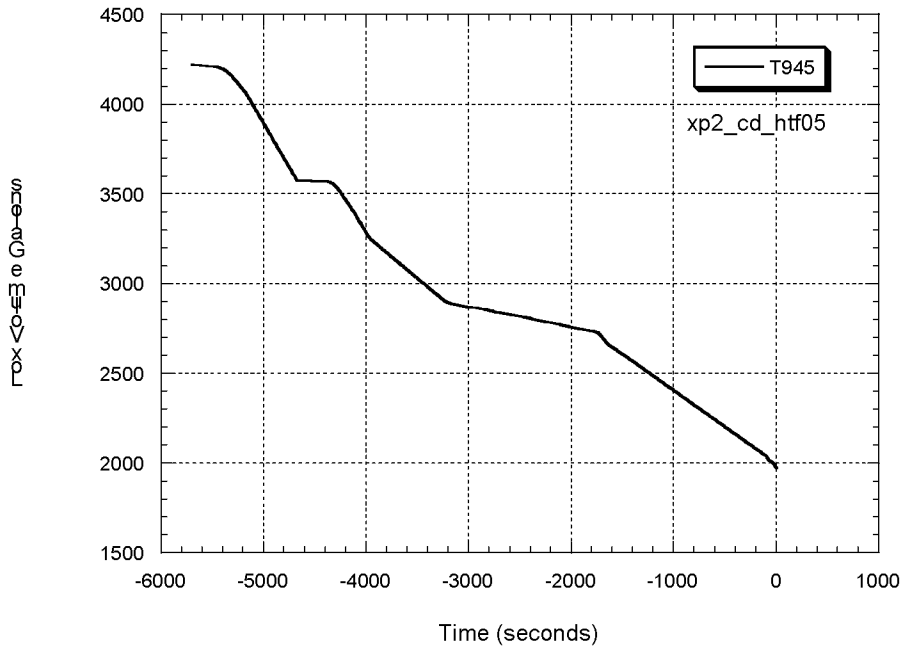


Figure 15: Predicted Lox Volume in Gallons

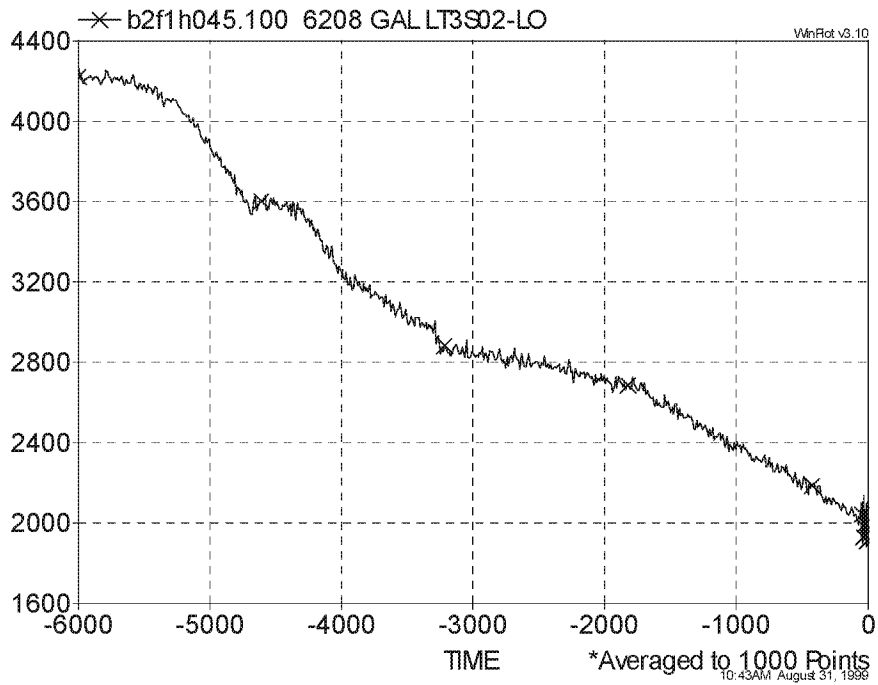


Figure 16: Measured Lox Volume in Gallons

Analysis, HTF Test, Fuel Seal Drain Temperature

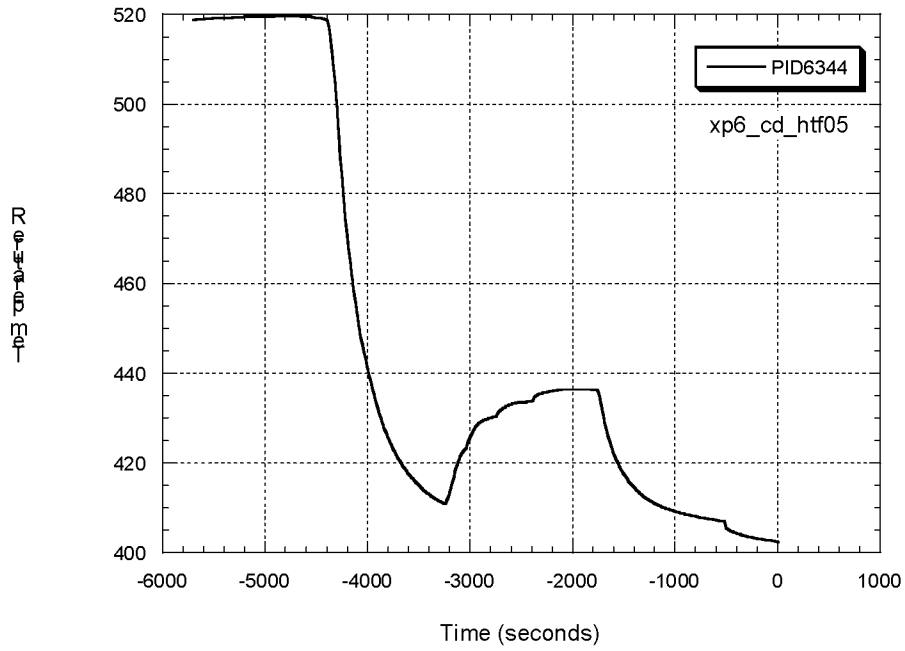


Figure 17: Predicted Fuel Seal Drain Temperature

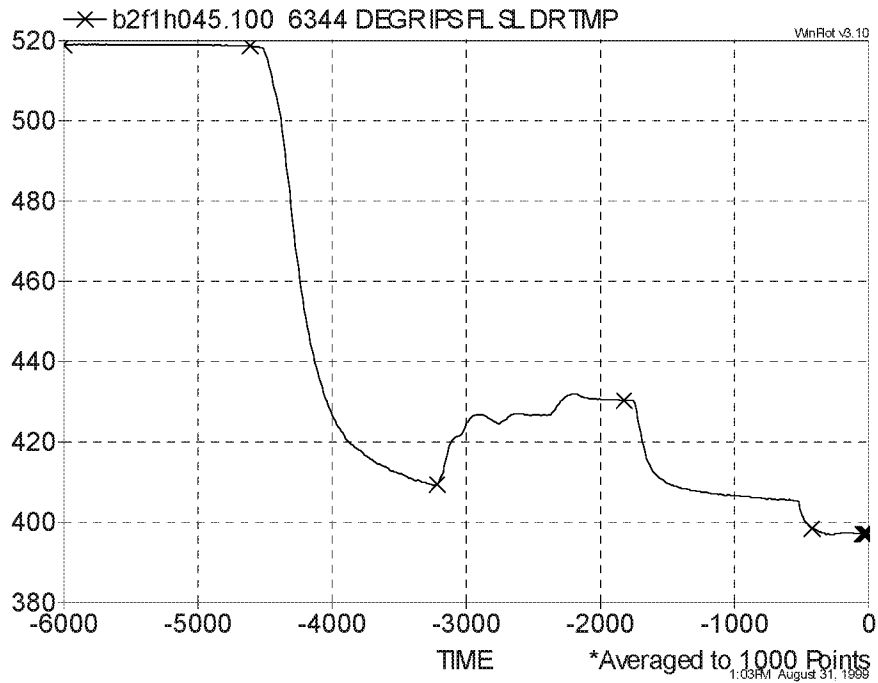


Figure 18: Measured Fuel Seal Drain Temperature

Analysis, X-34 Cold Case, Engine Interface Temperature

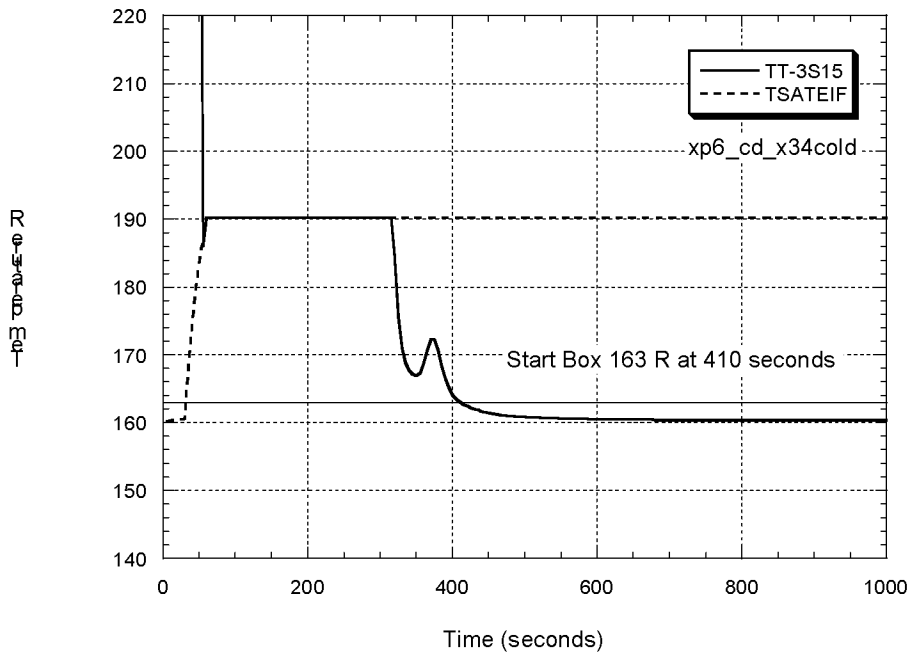


Figure 19: Predicted X-34 Engine Inlet Temperature

Analysis, X-34 Cold Case, Lox Consumption

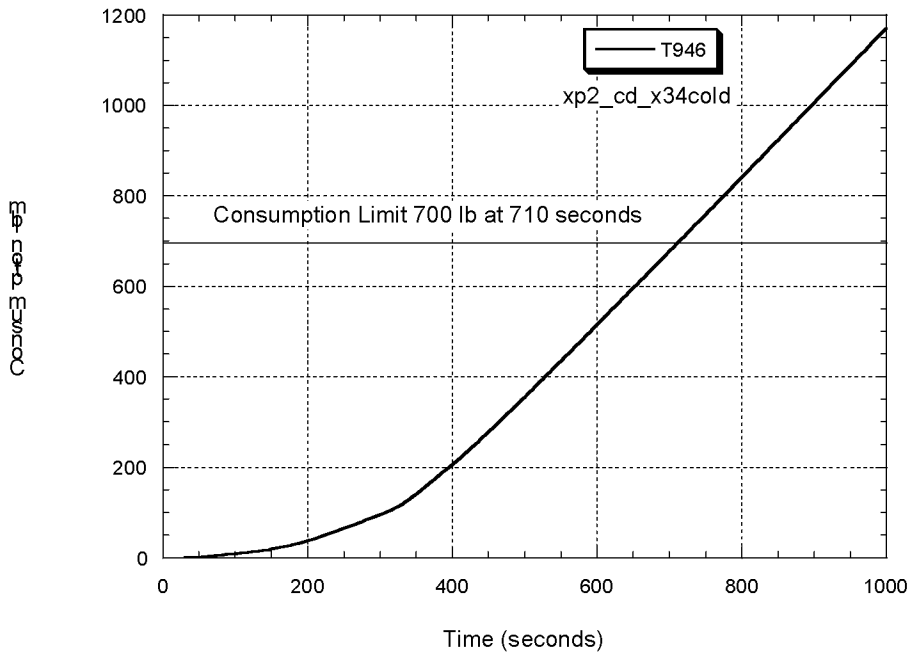


Figure 20: Predicted X-34 Lox Consumption

Analysis, X-34 Cold Case, Fuel Seal Drain Temperature

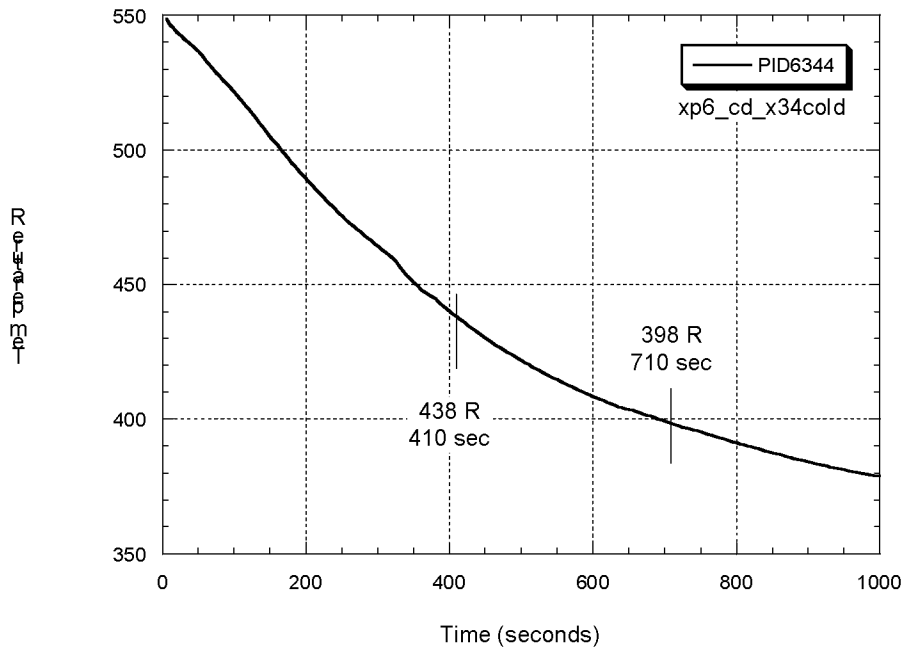


Figure 21: Predicted X-34 Fuel Seal Drain Temperature

Analysis, X-34 Cold Case, Lox Flowrate

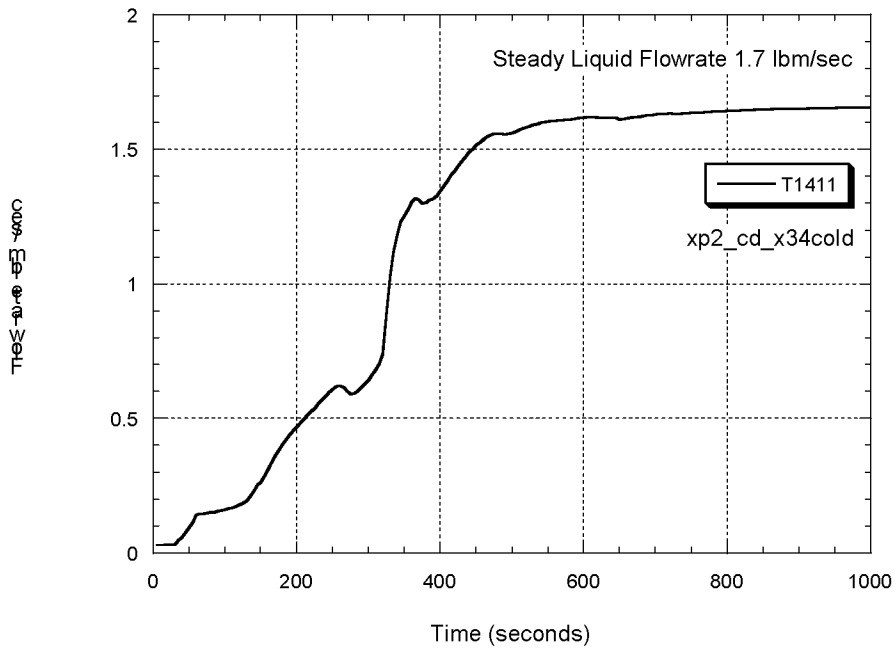


Figure 22: Predicted X-34 Lox Flowrate

CONCLUSIONS

Current analysis indicates that all the prestart thermal conditioning requirements can be met although the exact procedure and timing for the start window can't exactly be determined. There is some flexibility in the procedure in that the MOV can be opened to accelerate the opening of the start window. Also, once the liquid starts flowing in the bleed line the tank pressure can be reduced to reduce consumption and delay the closing of the window.

ACKNOWLEDGEMENTS

The author wishes to acknowledge the contributions of the following people and organizations.

Richard Cooper and the component test team for performing the work necessary in the RP-1 Tray freezing test, the Impeller chill test in LN2 and the modifications performed on the component test stand as well as special chill tests on the component test stand for the purpose of model correlation.

Phil Hall for performing the work necessary in the lox boiling heat transfer coefficient testing.

Bruce Tiller and Wayne Gamwell for performing the work necessary for the RP-1 freezing on the cold tube wall testing.

Mike Ise, Tom Byrd and the Fastrac Engine Horizontal Test Facility team for hardware modifications and dedicated chill testing with the engine.

STS-93 SSME NOZZLE TUBE RUPTURE INVESTIGATION

W. Dennis Romine, Senior Engineering Specialist
Rocketdyne Propulsion & Power
Space & Communications Group
Boeing Corporation

INTRODUCTION

STS-93 was launched on July 23, 1999. There was an anomaly at the end of the launch in that the Space Shuttle Main Engines (SSME) shut down 0.16 second early because sensors detected a low level of oxidizer in the LOX tank (actually the duct from the tank to the vehicle). This resulted in a cutoff velocity for the vehicle that was 16 ft/sec low. It should have been 25872 ft/sec. An investigation was immediately initiated into the cause of this LOX tank low level cutoff.

It was noticed during the launch that the turbine temperatures for Main Engine 3 (E2019) were approximately 100°F higher than the preflight prediction. Linear Engine Model matching of the data indicated that a nozzle leak best fit the data. Post launch review of the data showed, that at approximately five seconds into the start, numerous parameters indicated small anomalous shifts. These shifts were all consistent with a rupture of nozzle tubes.

Post launch review of the films showed that just after SSME ignition and just prior to liftoff a streak is seen in the exhaust plume of E2019. Just after liftoff the streak can be seen emanating from the nozzle wall. This photo confirmed that a leak was coming from the nozzle tubes. Based on the photo, the axial location of the leak was estimated to be 28" from the aft end of the nozzle. The streak continued to be visible during the launch (Figure 1).

Almost immediately upon landing a visual inspection was made of the nozzle. It was confirmed that three nozzle tubes were ruptured at the suspected location (Figure 2). The focus then turned to the cause of the tube ruptures. Prior to landing, a hardware review revealed that two main injector LOX posts had been deactivated prior to the flight. This is done by inserting pins in the orifices located in the interpropellant plate of the main injector (Figure 3). Therefore, once the engine was available, a high priority was to inspect for these pins. Indeed one of two pins was missing. A pin is approximately 0.9" long by 0.1" in diameter, weighs 1.5 grams, and is gold plated. Also, there was a ding in the Main Combustion Chamber (MCC) in line with this post at a location 2.5" upstream of the MCC throat. The tube ruptures are located approximately 30° in the azimuthal direction from the post with the missing pin.

The ruptured tubes were sectioned from the nozzle and subjected to an evaluation in the Materials laboratory. The overall length encompassed by the tube ruptures was consistent with the size of a deactivation pin. The key finding from this investigation was

that the discoloration noted at the ruptures was indeed gold and had a chemical composition identical with that of the gold plating used on the pins. The same gold was also found at the dent in the MCC wall. The other significant finding was that the rupturing of the tubes occurred during the impact and was not a delayed event. This evaluation confirmed that the ejected pin caused the tube ruptures.

As a result of this conclusion, the following aerothermal questions were generated with regard to the pin.

- What is the trajectory of the pin?
- What is the velocity of the pin as it impacts the nozzle?
- What is the probability that an ejected pin will impact the nozzle?
- What is the probability that the pin will damage the nozzle if it hits the nozzle?
- Was this the worst damage that the pin could cause?
- Would the pin hit the nozzle if it is ejected from a different location on the face of the injector?
- How much damage can the pin do to the MCC?

At first it would seem to be a difficult task to answer these questions for a seemingly random event. However, it was found that a relatively simple computer model using basic flow principles could be developed to provide reasonable first order answers to these questions.

TRAJECTORY CALCULATION METHODOLOGY

In order to attempt any type of trajectory analysis for the pin, the combustion gas flow field must be defined. This information was generated when the chamber and nozzle contours were initially developed. These parameters are

- The combustion chamber and nozzle contour profiles.
- The combustion gas Mach number.
- The combustion gas velocity.
- The combustion gas static pressure.
- The combustion gas static temperature.
- The combustion gas density.

With this information, a simple model can be set up for calculating the pin trajectory. The fundamental equation for this model is the equation for the drag force on the pin.

$$F = C_D * A_N * \rho (V_G - V_P)^2 / 2$$

Using this fundamental equation, the following procedure is used to calculate the axial component of the pin trajectory.

1. The initial coordinates of the pin are selected (axial and radial location).
2. An initial pin velocity (speed and angle or, equivalently axial and radial components of velocity) is selected.
3. Values for the axial and radial drag coefficients are selected.
4. Values for the pin area normal and parallel to the combustion chamber axis are determined.
5. An incremental axial position is selected (initial $X + \Delta X$).
6. The combustion gas density and axial speed are determined for the average axial position (initial $X + \Delta X/2$).
7. An initial guess is made for the pin axial speed after it has traversed the axial length increment.
8. The average axial speed of the pin for the axial increment is calculated by taking the average of the starting and ending speeds.
9. From the relative axial speed and the density, the pressure $[\rho(V_{GX}-V_{PX})^2/2]$ acting on the pin in the axial direction is calculated.
10. The average axial force over the axial length increment is calculated from the axial pressure acting on the pin, the drag coefficient, and the pin area normal to the chamber axis.
11. From the initial axial speed, the average force, the pin mass and the axial length increment, the time for the pin to traverse the axial length increment is determined.
12. From the initial axial speed, the time increment, the mass of the pin, and the average axial force on the pin, the axial speed of the pin at the end of the axial increment is calculated.
13. Using this axial speed at the end of the axial increment, Steps 8 through 12 are repeated until the axial speed converges.
14. Steps 5 through 13 are repeated until the desired final axial position is reached.

Once the axial component of the trajectory has been calculated, the radial component can be calculated using the following similar procedure.

1. Starting at the initial position of the pin and the initial axial increment, the average radial component of the combustion gas velocity is determined.
2. An initial guess is made for the pin radial speed after it has traversed the axial length increment.
3. The pin radial speed at the average axial position is calculated by averaging the starting and ending radial speeds.
4. From the relative radial speed and the density, the pressure $[\rho(V_{GR}-V_{PR})^2/2]$ acting on the pin in the radial direction is calculated.

5. The average radial force over the axial length increment is calculated from the radial pressure acting on the pin, the drag coefficient, and the pin area parallel to the chamber axis.
6. From the initial radial speed, the time increment, the mass of the pin, and the average radial force on the pin, the radial speed of the pin at the end of the axial increment is calculated.
7. Using this radial speed at the end of the axial increment, Steps 3 through 6 are repeated until the radial speed converges.
8. Using the average radial speed and the time for traversing the axial increment, the change in radial position is calculated and added to the radial position at the start of the increment to get the radial position at the end of the increment.
9. Steps 1 through 8 are repeated until the desired final axial position is reached.

Using this procedure, starting parameters can be iterated to determine the values required to impact the nozzle as a specific location.

DRAG COEFFICIENT

To make the above calculations, the drag coefficients for the pin in both the axial and radial directions must be determined. The drag coefficient is a function of the Mach number, the Reynolds number, the object shape, and the orientation of the object within the flow field. The Reynolds number for the pin as it travels in the combustion gas flow field is calculated to be in the range from 10^3 to 10^5 . The two extreme positions for the pin orientation are for the pin axis to be either normal or parallel to either the axial or radial component of the combustion gas velocity.

For the pin axis normal to the flow field, the pin can be approximated as a cylinder in cross flow. The drag for this configuration has been studied extensively for an infinitely long cylinder and is available as a function of Reynolds number in standard texts. For this configuration in the Reynolds number range of interest, the drag coefficient is between 0.9 and 1.2. For a cylinder of finite length the drag coefficient will be lower. For a cylinder with an aspect ratio of 9:1 (approximately that of the pin), the drag coefficient is approximately 2/3 that for an infinitely long cylinder. Applying this ratio to the infinitely long cylinder results gives a drag coefficient range from 0.6 to 0.8. The area of the pin normal to its axis is approximately 0.09 in^2 . This will result in a maximum drag coefficient times area of 0.072 in^2 .

For the pin axis parallel to the flow field, the pin can be approximated as either a square ended cylinder or a projectile depending on which way the pin is oriented. The projectile will have the lower drag coefficient. The minimum drag coefficient for a projectile is 0.2. Multiplying this by the pin approximate cross sectional area of 0.015 in^2 gives a minimum drag coefficient times area of 0.003 in^2 .

The pin could also be rotating and/or tumbling. Rotation can create lift. However, calculations indicate that the pin would have to develop a significant rotation rate to generate an appreciable lift. It is not expected to do this. Any tumbling will cause the drag coefficient times area value to vary with time. The calculated range of values for the drag coefficient times area (0.003 in^2 to 0.072 in^2) are intended to provide a general range of the values that can be expected for the pin as it is traveling through the combustion gas flow field.

TRAJECTORY TO MCC IMPACT

Once the pin dislodges from the orifice it will travel down the LOX post until it exits the injector. From the LOX pressure and the geometry, the force on the pin can be estimated and the velocity calculated. From the Materials evaluation it is known that the tubes ruptured when the pin hit them. The data indicates that the tubes ruptured at approximately five seconds after ignition, which is one second into 100% power level operation. Therefore, the pin was dislodged during 100% power level operation. From a number of calculations it was determined that a reasonable estimate for the velocity of the pin as it exits the post is 100 ft/sec. The pin initial radial position will be approximately 0.4" from the MCC wall. Most likely it will be traveling with the pin axis parallel to the flow. Its drag coefficient times area in the axial direction should be close to the minimum calculated value 0.003 in^2 . In the normal direction it will be close to the maximum value of 0.072 in^2 .

A parametric analysis was made to determine the conditions required for the pin to impact the MCC at a location 2.5" forward of the throat. Parameters varied were the axial drag coefficient times area, radial drag coefficient times area, initial velocity, and exit angle from LOX post. The following conclusions were made from this parametric analysis.

- The most significant result was that the minimum initial trajectory angle for the pin had to be approximately 10° in order for the pin to impact 2.5" forward of the throat. This minimum angle was independent of the combination of other conditions required. Any angle less than 10° will cause the pin to impact more forward of the throat.
- For an initial velocity less than 100 ft/sec, the axial drag coefficient times area becomes smaller than what appears to be a minimum realistic value. This would imply that the 100 ft/sec is a reasonable value for the initial speed of the pin when it exits the LOX post.
- A pin in one of the outer two rows of elements (rows 12 or 13, which are most likely to have a pin) of the main injector will have a high probability of striking the MCC.
- The impact angle of the pin relative to the MCC wall is shallow (less than 10° with a typical value of 5°). This is consistent with the observed damage to the MCC.
- The velocity of the pin when it hits the MCC is primarily a function of the initial velocity. This is because the acceleration of the pin is relatively small up to the time

it hits the MCC. The axial velocity at impact is less than 50 ft/sec greater than the initial velocity for the range of conditions analyzed.

- The time from expulsion of the pin to impact with the MCC will be a function of the axial velocity which, in turn, is a primarily a function of the assumed initial velocity. For an initial velocity of 100 ft/sec, the time is approximately 10 milliseconds.

TRAJECTORY FOR NOZZLE IMPACT

After the pin impacts the MCC, it continues traveling in the combustion gas flow field until it impacts the nozzle at a location 28" forward of the aft manifold. It is not known precisely how the impact of the pin with the MCC affects the pin trajectory. It can be expected there will be a reduction in the pin velocity as a result of it hitting the MCC. The shallow impact angle suggests that the pin trajectory angle when it leaves the MCC will be similar to that of the MCC wall at the point of impact (25°). It is known that the pin impacted the nozzle at an azimuthal angle 30° from the MCC impact point. This could imply that the impact with the MCC gave the pin a velocity component in the azimuthal direction.

A parametric analysis was also made for the trajectory of the pin from when it grazed the MCC to when it impacted the nozzle. Parameters varied were the axial drag coefficient times area, radial drag coefficient times area, initial speed and angle after grazing the MCC. The following conclusions were made from this analysis.

- For reasonable values of the initial speed and angle after grazing the MCC, these parameters do not significantly affect the trajectory (Figure 4).
- The pin velocity at impact is on the order of 700 to 900 ft/sec depending on the assumed set of conditions. This is roughly an order of magnitude less than the combustion gas velocity. A structural analysis estimated that an axial component of the velocity of 300 ft/sec and a radial component of 600 ft/sec are required to produce the observed damage to the nozzle tubes. This is equivalent to a pin velocity of about 700 ft/sec. The calculated velocities are consistent with this structural evaluation.
- The pin impacts the nozzle at an angle of typically 13° to 15° relative to the nozzle wall.
- The time from impact with the MCC to impact the nozzle is on the order of 20 to 30 milliseconds depending on the assumed set of conditions.

PROBABILITY OF PIN HITTING THE NOZZLE

Using the trajectory calculation model, the combination of conditions required for the pin to hit the nozzle can be determined. This is done by first determining the combination of conditions (radial and axial drag coefficient time area) that will result in the pin hitting at the aft end of the nozzle. This set of conditions represents the dividing line between impacting and not impacting the nozzle (Figure 5). Any combination of

axial drag coefficient times area and radial drag coefficient times area below the line will result in the pin hitting the nozzle.

Next the range of axial drag coefficient times area and radial drag coefficient times area that can occur for the pin can be determined. This was discussed earlier. The minimum axial drag coefficient times area that can be expected is 0.003 in^2 . For this condition the radial drag coefficient times area would be at its maximum value of 0.072 in^2 . The maximum value for axial drag coefficient times area would be the 0.072 in^2 value. For this condition the radial drag coefficient time area could range from the minimum of 0.003 in^2 to the maximum of 0.072 in^2 depending on the pin orientation. These ranges result in a triangular region of possible axial and radial drag coefficient times areas (Figure 5). If there is an equal probability of any point within the triangle, then the probability of the pin hitting the nozzle is the ratio of the hit area of the triangle to the total area of the triangle. This ratio is 12%, which is equivalent to a one in eight chance of the pin hitting the nozzle.

However, rather than an equal probability of any condition within the triangle occurring, it is expected that there will be a probability distribution for both the axial and radial components. The pin should want to align its axis generally to that of the nozzle centerline. This would cause a skewed probability distribution where the axial drag coefficient times area would most probably be at the low end of its range and the radial drag coefficient times area would most probably be at the high end of its range.

A log normal distribution applied to both the axial drag coefficient times area and the radial drag coefficient times area can be used to approximate this expected skewness (Figure 4). When these probability distributions are factored into the calculation, the probability of the pin hitting the nozzle increases to 64% or approximately two in three.

PROBABILITY OF PIN RUPTURING A NOZZLE TUBE

Starting with a set of conditions that results in the pin impacting the nozzle at the aft end, the axial drag coefficient times area can be incrementally reduced to result in the pin impacting farther and farther forward in the nozzle. The velocity of the pin at the various impact locations is a part of the trajectory calculation. As expected, the impact velocity of the pin decreases as the impact location moves forward. The kinetic energy of the pin as it impacts the nozzle is expected to be the primary factor in determining if the pin will rupture a nozzle tube. Simplistically, since the square of the velocity is proportional to the kinetic energy of the pin, there should be a minimum pin velocity required to cause a tube to rupture. In reality, other factors need to be considered such as pin orientation at impact, the radial and axial components of the velocity, the tube geometry at the impact location (tube diameter and wall thickness decreases going forward in the nozzle), and the tube temperature (increases going forward in the nozzle).

Lines of constant velocity can be determined and then overlaid on the parametric analysis results (Figure 5). The area within the triangle between a constant velocity line

and the line of demarcation between hitting and not hitting the nozzle, is the set of conditions that will result in the pin impacting at or greater than a given velocity. Assuming an equal probability for any point, the probability of the pin hitting at or greater than a given velocity is the ratio of areas. Again, the probability distributions can also be factored in. These probabilities can then be plotted as a function of velocity (Figure 6).

The structural evaluation indicated that minimum required pin velocity to cause the ruptures is on the order of 700 ft/sec. Applying a 50 ft/sec uncertainty to this calculation results in a range from 650 ft/sec to 750 ft/sec. The hot fire experience is that one in eighteen (5.6%) ejected pins caused a rupture of nozzle tubes. Because of the small sample, the 95% confidence limits for this statistic are 1.4% to 27%. This box of conditions can be overlaid on the calculation (Figure 6). From this it can be seen that, despite the simplifications and assumptions that went into the model, the model can make reasonable probability assessments.

CONCLUSIONS

In summary, a simple generic model for determining the trajectory and other conditions of an object in the combustion chamber and nozzle hot gas flow field of a rocket engine has been developed. This model (process) can be used for any analysis of a rocket engine where it is desired to estimate the implications of a solid contaminant that has been introduced into the combustion gas flow field.

For the specific case of the LOX post deactivation pin that was ejected during the launch of STS-93, it was found that the results of the model were consistent with the hardware observations. Additionally, the model was used to make probability predictions, which were also consistent with the hot fire experience.

NOMENCLATURE

| | |
|------------|--|
| A_N | = Area normal to flow |
| C_D | = Drag coefficient |
| F | = Force |
| LOX | = Liquid oxygen |
| MCC | = Main Combustion Chamber |
| SSME | = Space Shuttle Main Engine |
| STS | = Space Transportation System |
| V_G | = Velocity of combustion gas |
| V_{GR} | = Component of combustion gas velocity in radial direction |
| V_{GX} | = Component of combustion gas velocity in axial direction |
| V_P | = Velocity of particle |
| V_{PR} | = Component of particle velocity in the radial direction |
| V_{PX} | = Component of particle velocity in the axial direction |
| X | = Axial position |
| ΔX | = Axial position increment |
| ρ | = Density |



Figure 1. Nozzle Leak During Launch

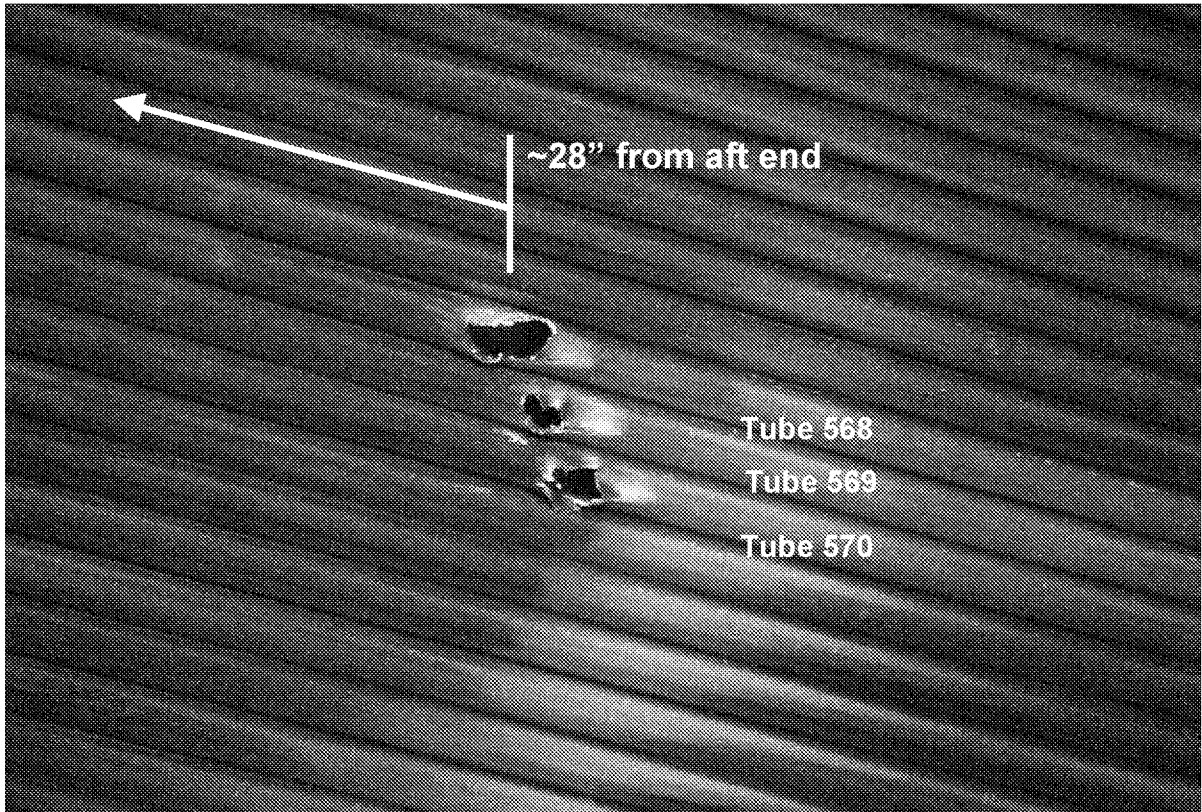


Figure 2. Nozzle Tube Ruptures

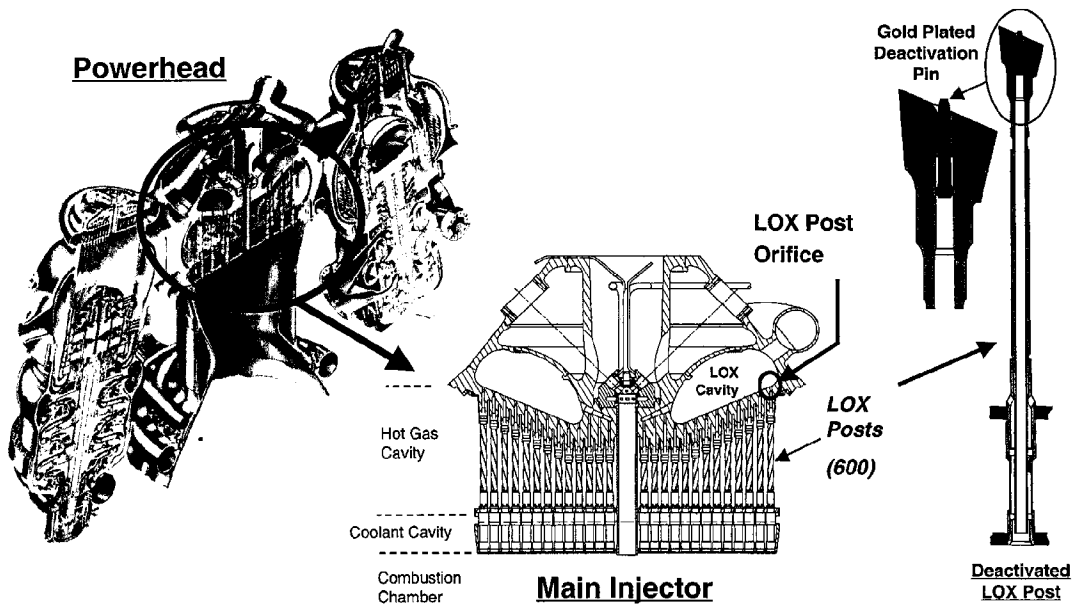


Figure 3. SSME Main Injector LOX Post Deactivation

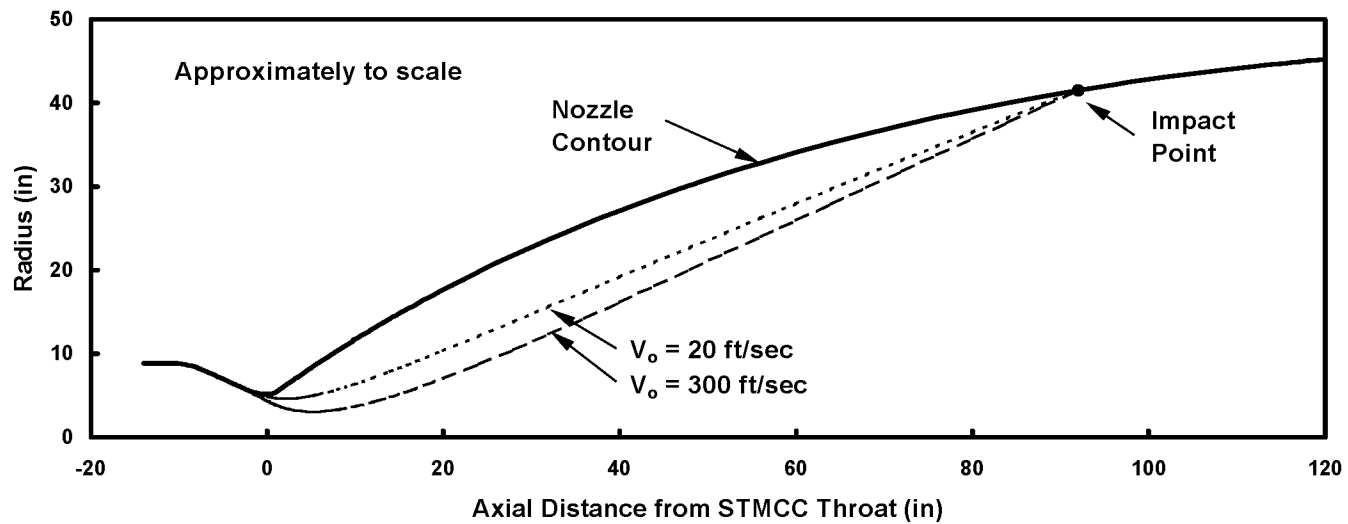


Figure 4. Example Pin Trajectories

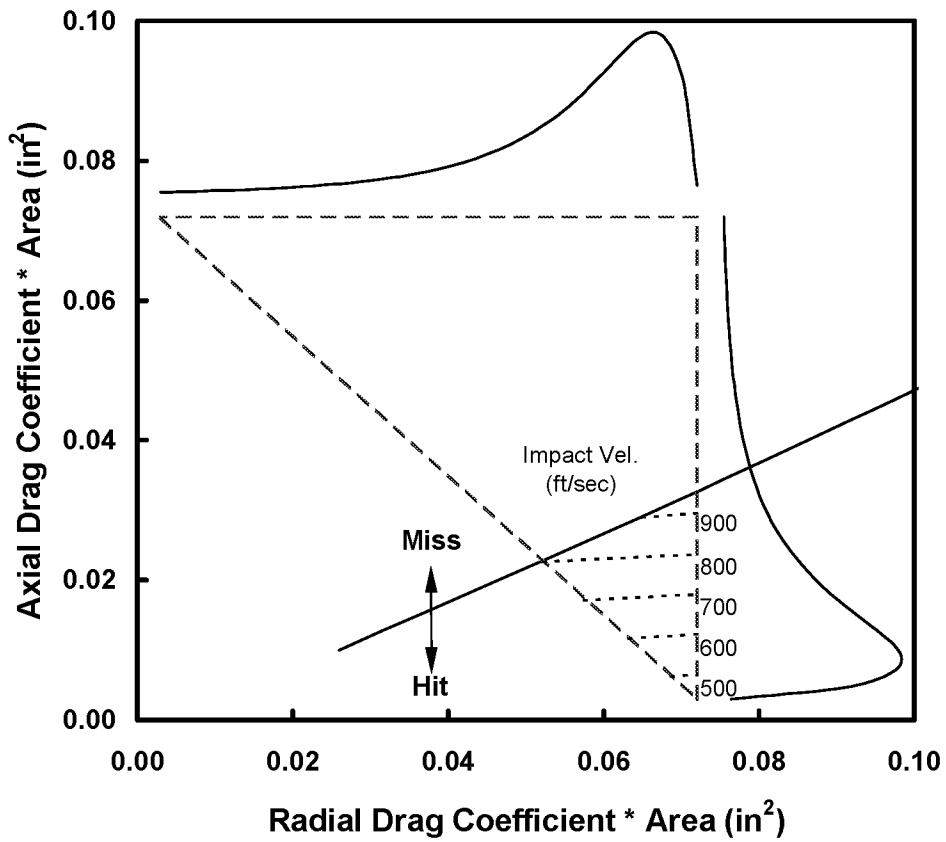


Figure 5. Flow Conditions for Pin Impacting Nozzle

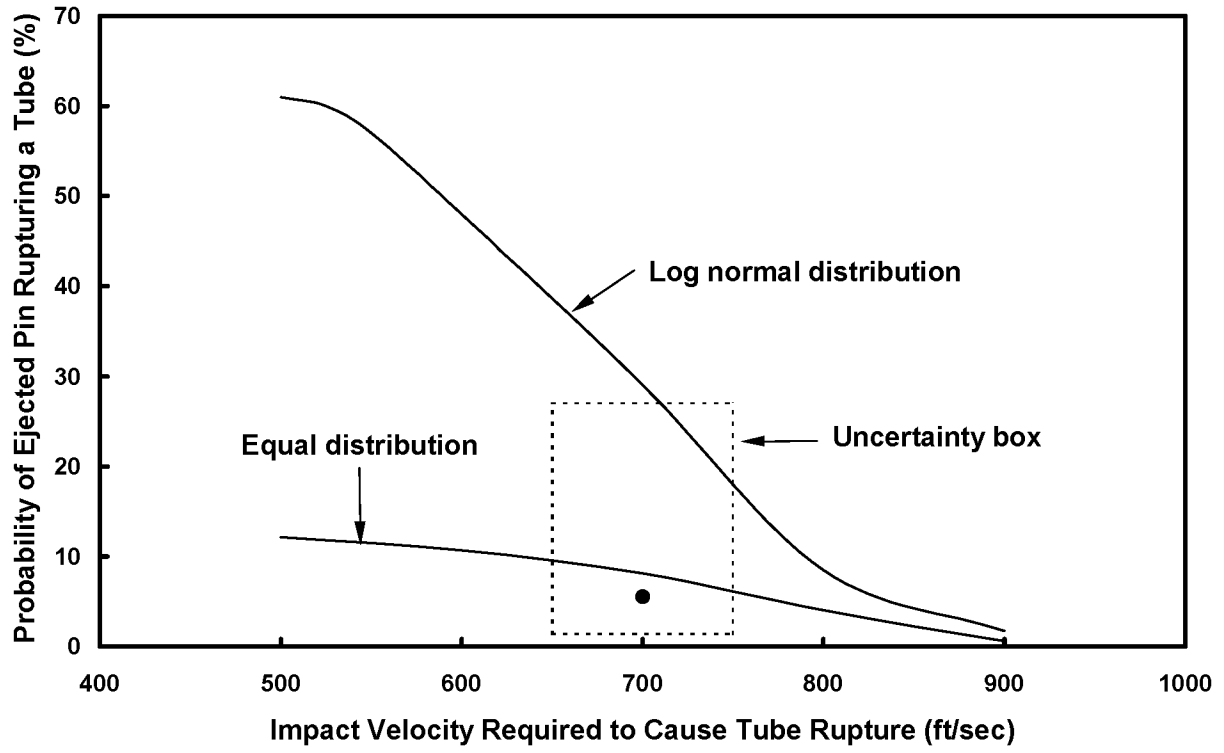


Figure 6. Probability of Tube Rupture



ZERO GRAVITY CRYOGENIC VENT SYSTEM CONCEPTS FOR UPPER STAGES

Robin H. Flachbart

James B. Holt

Leon J. Hastings

Space Transportation Directorate
NASA- Marshall Space Flight Center

ABSTRACT

The capability to vent in zero gravity without resettling is a technology need that involves practically all uses of sub-critical cryogenics in space, and would extend cryogenic orbital transfer vehicle capabilities. However, the lack of definition regarding liquid/ullage orientation coupled with the somewhat random nature of the thermal stratification and resulting pressure rise rates, lead to significant technical challenges. Typically a zero gravity vent concept, termed a thermodynamic vent system (TVS), consists of a tank mixer to destratify the propellant, combined with a Joule-Thomson (J-T) valve to extract thermal energy from the propellant. Marshall Space Flight Center's (MSFC's) Multipurpose Hydrogen Test Bed (MHTB) was used to test both spray-bar and axial jet TVS concepts. The axial jet system consists of a recirculation pump heat exchanger unit. The spray-bar system consists of a recirculation pump, a parallel flow concentric tube heat exchanger, and a spray-bar positioned close to the longitudinal axis of the tank. The operation of both concepts is similar. In the mixing mode, the recirculation pump withdraws liquid from the tank and sprays it into the tank liquid, ullage, and exposed tank surfaces. When energy extraction is required, a small portion of the recirculated liquid is passed sequentially through the J-T expansion valve, the heat exchanger, and is vented overboard. The vented vapor cools the circulated bulk fluid, thereby removing thermal energy and reducing tank pressure. The pump operates alone, cycling on and off, to destratify the tank liquid and ullage until the liquid vapor pressure reaches the lower set point. At that point, the J-T valve begins to cycle on and off with the pump. Thus, for short duration missions, only the mixer may operate, thus minimizing or even eliminating boil-off losses.

TVS performance testing demonstrated that the spray-bar was effective in providing tank pressure control within a 6.89 kPa (1psi) band for fill levels of 90%, 50%, and 25%. Complete destratification of the liquid and ullage was achieved at these fill levels. The axial jet was effective in providing tank pressure control within the same pressure control band at the 90% fill level. However, at the 50% level, the system reached a point at which it was unable to extract enough energy to keep up with the heat leak into the tank. Due to a hardware problem, the recirculation pump operated well below the axial jet design flow rate. Therefore, it is likely that the performance of the axial jet would have improved had the pump operated at the proper flow rate. A CFD model is being used to determine if the desired axial jet performance would be achieved if a higher pump flow rate were available. Testing conducted thus far has demonstrated that both TVS concepts can be effective in destratifying a propellant tank, rejecting stored heat energy, and thus, controlling tank pressure.

NOMENCLATURE

| | |
|------------|------------------------------------|
| CdA | equivalent flow area |
| h_{fg} | heat of vaporization |
| h | enthalpy |
| $Lohm$ | viscojet flow resistance |
| \dot{m} | mass flow rate |
| P | pressure |
| \dot{Q} | heat leak rate |
| S | specific gravity at viscojet inlet |
| T | temperature |
| t | time |
| U | internal energy |
| X | viscojet exit quality |
| ΔP | pressure drop across viscojet |

INTRODUCTION

The development of high-energy cryogenic upper stages is essential for the efficient delivery of large payloads to various destinations envisioned in near term chemical propulsion programs. Also, many advanced propulsion systems, including solar thermal and nuclear fission, use hydrogen as a working fluid. Some of these systems are intended for long duration missions. A key technology challenge for all of these applications is cryogenic fluid management (CFM) advanced development, specifically, the long term storage of cryogenics in space. In response to this challenge, MSFC has initiated an advanced

development/technology program to broaden the CFM experience/data base. Due to the cost of, and limited opportunities for, orbital experiments, ground testing is being employed to the fullest extent possible. Therefore, a major objective of the MSFC program has been to perform ground based advanced development testing on CFM systems for space transportation applications.

A significant challenge associated with long term storage of cryogenics in space is maintaining propellant tank pressure control while minimizing propellant boiloff loss. Auxiliary thrusters are traditionally used to settle the propellants in order to accomplish tank venting. Such systems incur increasing weight penalties associated with the propellant and hardware required to perform the settling burns. In addition, tank venting may become necessary at an inopportune time in the mission timeline. The thermodynamic vent system (TVS) concept enables tank pressure control through venting without resettling. A TVS typically includes a Joule-Thompson expansion device, two-phase heat exchanger, and a mixing pump to destratify and extract thermal energy from the tank contents without significant liquid losses.

However, TVS implementation has been constrained by the lack of opportunities for on-orbit experience, mainly due to funding constraints. Analytical modeling of such systems is difficult due to the complex combination of micro-gravity heat transfer, thermodynamic, and fluid mechanic phenomena involved, and is further complicated by the lack of on-orbit data to correlate with the models.

SPRAY-BAR CONCEPT

The spray-bar TVS concept, developed by Boeing (Reference 1), was the first TVS concept tested in MSFC's Multipurpose Hydrogen Test Bed (MHTB) (Reference 2). An illustration of spray-bar TVS concept is provided in Figure 1. One advantage of this concept is that the active components (J-T expansion valve, subsystem pump, and isolation valve) are located outside of the tank. Such an approach simplifies component installation and enables modification or changeout of TVS components without entering the tank. Also, this configuration supports feed line and engine thermal conditioning during micro-gravity coast. The second, and perhaps more important advantage, is the longitudinal spray-bar, which is used to achieve both liquid bulk and ullage gas thermal destratification through mixing. Since the liquid bulk and ullage are destratified regardless of position, and the self induced heat transfer mechanisms are based on forced convection, the spray-bar concept lends itself to verification in normal gravity. Therefore, there is the potential for minimizing the dependence on costly micro-gravity experimentation.

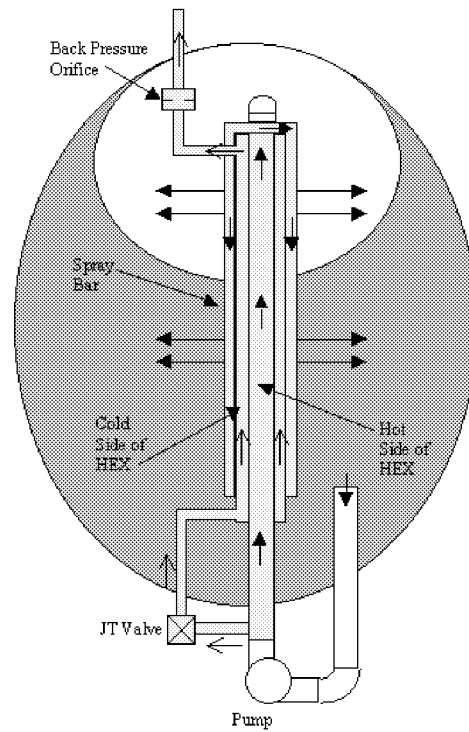


Figure 1: Spray-Bar TVS Concept

In the mixing mode, fluid is withdrawn from the tank by the pump and flows back into the tank through a spray-bar positioned along (or near) the tank longitudinal axis. The fluid is expelled radially back into the tank through the spray-bar, which forces circulation and mixing of the tank contents regardless of liquid and ullage position, assuring destratification and minimum pressure rise rate. For missions lasting from a few days to weeks, depending on the insulation performance, tank mixing may be sufficient to control the tank pressure with no propellant loss. When pressure control can no longer be achieved with mixing alone, a portion of the circulated liquid is passed through the J-T valve, where it is expanded to a lower temperature and pressure, passed through the heat exchanger element of the spray-bar, and finally is vented to space. Therefore, the vented fluid removes thermal energy from, and thus cools, the bulk fluid circulated through the mixing element of the spray-bar.

In an orbital propellant transfer scenario the spray-bar concept can be used to assist tank refill. By filling through the spray-bar/heat exchanger, the in-flowing fluid can be cooled and used to mix the tank contents, thus resulting in a "no-vent fill" process with minimal propellant losses. Additionally, if capillary liquid acquisition devices (LAD) are used for micro-gravity propellant expulsion, the liquid within the LAD can be conditioned by the spray-bar TVS. By withdrawing liquid from the capillary liquid acquisition device,

cooling it through the J-T device, and returning it to the LAD, thermal conditioning of the LAD liquid is achieved. Thus heat entrapment within the LAD can be minimized or perhaps eliminated.

AXIAL JET CONCEPT

The axial jet TVS system, provided by the Glenn Research Center, was the second TVS concept tested in the MHTB. A schematic of the axial jet concept is included in Figure 2. The advantage of this concept is simplicity. For the most part, the hardware does not require precise and complicated design and fabrication, as with the spray-bar concept.

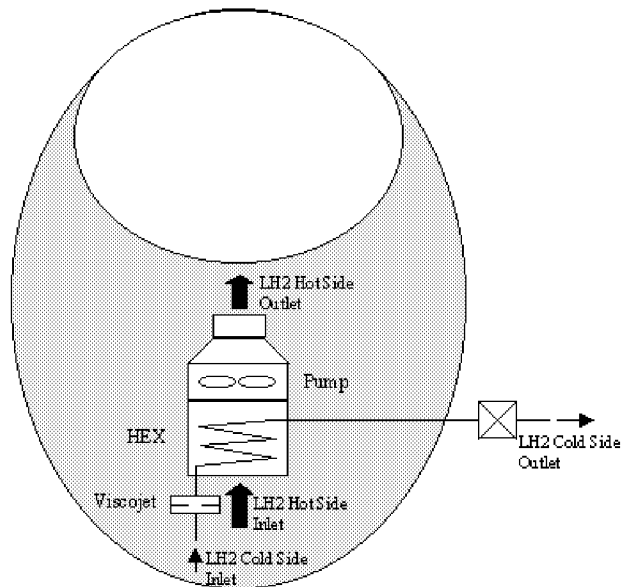


Figure 2: Axial Jet TVS Concept

The operation of the axial jet concept is very similar to that of the spray bar concept. The main differences are the configuration of the heat exchanger and the way the cooled bulk liquid is returned to the tank (axially versus radially). As with the spray-bar concept, the axial jet TVS can be used to condition the propellant within the LAD. Such a configuration, with an axial jet TVS, was recently tested in Boeing's Solar Thermal Upper Stage Test Demonstrator (STUSTD) ground test at MSFC (Reference 3). During the testing, the axial jet TVS was able to subcool the liquid within the LAD. A similar configuration is proposed to fly aboard the Solar Orbit Transfer Vehicle (SOTV).

TEST SET UP

The major test article elements consist of the test tank and environmental shroud with supporting equipment, cryogenic insulation subsystem, and test article instrumentation. The technical description of each of these elements is presented in the following sections.

TEST TANK AND SUPPORTING EQUIPMENT

The MHTB aluminum tank is cylindrical with a height of 3.05 m, a diameter of 3.05 m and 2:1 elliptical domes as shown in Figure 3. It has an internal volume of 18.09 m³ and a surface area of 34.75 m². The tank is ASME pressure vessel coded for a maximum operating pressure of 344 kPa and was designed to accommodate various CFM concepts. The low heat leak composite legs and other tank penetrations are equipped with LH₂ heat guards so that more accurate measurement of the tank insulation performance can be made.

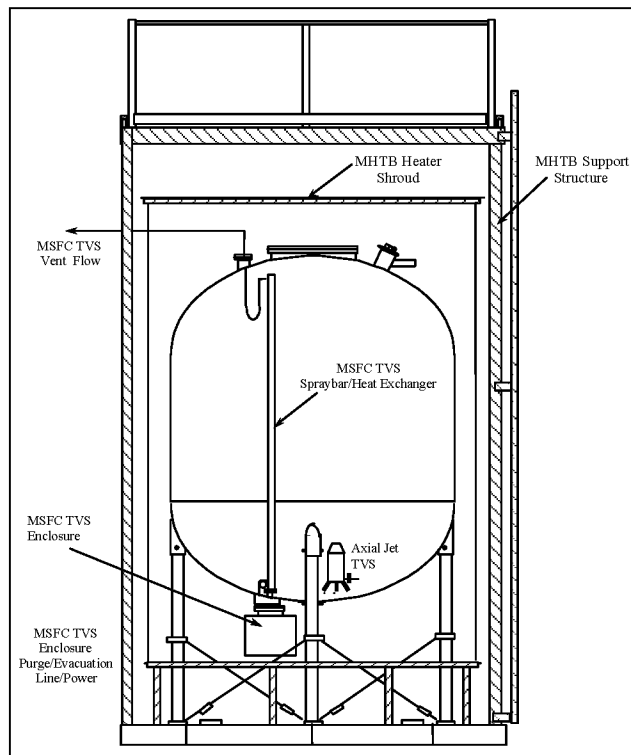


Figure 3: MHTB Tank and Support Equipment

The tank is enclosed within an environmental shroud which contains a ground hold conditioning purge, (similar to a payload bay) and imposes a range of uniform temperatures on the insulation external surfaces during orbit hold simulations. The shroud is 4.57 m high with a diameter of 3.56 m, and contains a purge ring for distributing dry nitrogen.

CRYOGENIC INSULATION SUB-SYSTEM

The MHTB insulation consists of a “spray-on” foam/multilayer combination. The foam element enables the use of a payload bay type purge during ground hold periods and the 45 layer multilayer insulation (MLI) provides thermal protection while at vacuum conditions in orbit. As reported in Reference 4, which describes the insulation performance in more detail, the combined effects of the MLI variable density, large vent hole pattern, and installation technique yield substantial performance improvements. However, in this application, the insulation system is compromised by the TVS hardware installation and taken “as is” as part of the MHTB tank configuration.

INSTRUMENTATION

The tank instrumentation consists primarily of thermocouple and silicon diodes to measure insulation, fluid, and tank wall temperatures. The MLI interstitial pressure is measured at the SOFI/MLI interface using a thin walled probe that penetrates the MLI. The probe is also equipped with a port for both dew point and gas species sampling. Two of the four composite legs, the vent, fill/drain, pressurization, pressure sensor probe, and manhole pump-out penetrations are instrumented to determine the solid conduction component of heat leak. The tank is internally equipped with two silicon diode rakes, which provide temperature gradient measurements within both ullage and liquid. The TVS systems are instrumented with pressure and temperature measurements throughout, in order to determine the pump flow rate, gas state in the vent lines, and vent gas mass flow rate. These measured values are used to quantify the performance of the two TVS concepts.

TEST FACILITY

Testing was performed at the MSFC East Test Area thermal vacuum facility, Test Stand 300. The cylindrical vacuum chamber has usable internal diameter of 5.5 meters and height of 7.9 meters. The chamber pumping train consists of a single stage gaseous nitrogen (GN_2) ejector, three mechanical roughing pumps with blowers, and two 1.2 meter diameter oil diffusion pumps. Liquid nitrogen cold walls surround the usable chamber volume providing cryopumping and thermal conditioning. The facility and test article shroud systems in combination enabled simulation of orbital conditions (vacuum levels as low as 10^{-8} torr and insulation surface temperatures ranging from 80 to 300 K).

A key facility capability was the test article pressure control subsystem used to maintain the steady-state tank ullage pressure necessary during the boiloff tests, which are described in the next section. The subsystem was composed of several flow control valves (located in the MHTB vent line), each of which

was regulated through a closed loop control system. This control system adjusted the valve positions based on a comparison between the measured tank ullage pressure and a desired set point.

TEST PROCEDURES

Two types of tests were performed with the TVS system in the MHTB. The first type was referred to as the boiloff test, and the second was the TVS performance test. A more detailed description of each type of test is provided in the following subsections.

BOILOFF TESTING

Boiloff testing was conducted to determine the ambient heat leak into the MHTB tank and to set up consistent initial conditions for each of the TVS tests. The first test series was conducted with the vacuum chamber LN₂ cold walls operating to produce a minimum heat leak condition. The second series was run without the LN₂ cold walls, thereby providing a high ambient heat leak condition. Details relating to the performance of boiloff testing were reported in Reference 4. Maintenance of constant ullage pressure and steady state insulation temperatures was necessary during this test. The boiloff vent flow rate was typically recorded for 6 hours after steady state was achieved.

The ambient heat leak is expressed as an energy balance across the tank boundary where the boiloff heat transfer is equal to the sum of the heat transfer through the insulation, the tank penetrations, and the rate of energy storage, if any, as seen in the following equation:

$$\dot{Q}_{boiloff} = \dot{Q}_{insulation} + \dot{Q}_{penetrations} + \frac{\Delta U_{system}}{\Delta t}.$$

The terms $\dot{Q}_{boiloff}$ and $\dot{Q}_{penetrations}$, are defined using the test data. Specific calculation of these parameters can be found in Reference 4. The thermal storage term $\Delta U_{system} / \Delta t$ represents the energy flow into or out of the test tank wall, insulation, and fluid mass. It is driven by the fluid saturation temperature, which varies as ullage pressure varies. Since the ullage pressure is held within a tight control band (+/- 0.0069 kPa), this term is considered negligible. The $\dot{Q}_{insulation}$ term can then be determined using the defined quantities listed above.

TVS PERFORMANCE TESTING

The spray-bar was evaluated at 90%, 50%, and 25% fill levels in the first test series. In the second series, both the spray-bar and axial jet concepts were tested at 90% and 50% fill levels, but with an elevated heat leak condition. The ambient heat leak was elevated during Series 2 due to the axial jet TVS hardware addition, and because the facility cold walls were not operated.

For each fill level, after boiloff testing was complete, the tank was locked up and allowed to self pressurize until the ullage pressure (P4) reached the maximum tank pressure set point of 138 kPa. Upon reaching this pressure, the recirculation pump was turned on, and mixing continued until the ullage pressure reached 131 kPa, the tank minimum set point. Upon reaching the minimum set point, the pump was turned off and the tank would self pressurize for the next cycle. This automated operation continued until the tank liquid saturation pressure (PSA1) reached the lower pressure set point. At this point, the J-T device was used to extract heat energy from the liquid whenever the pump operated. Both TVS system concepts operated in this manner until the tests concluded. This TVS control logic is illustrated in Figure 4.

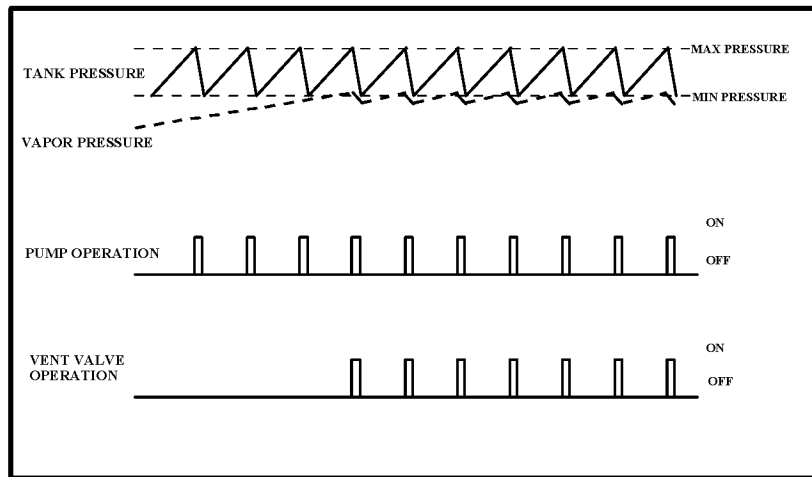


Figure 4: TVS Control Logic Illustration

RESULTS AND DISCUSSION

The baseline heat leak, mixing or destratification performance, and thermal energy removal, for both TVS concepts, are discussed in the following sections.

TANK HEAT LEAK

The results from the boiloff tests, presented in Table 1, indicated that the ambient heat leak for Series 1 was less than half that of Series 2. The heat leak for Series 2 was greater due to additional heat leak through the axial jet TVS hardware (not present during series 1), and because the vacuum chamber cold walls were not operating. As one would expect, the heat leak magnitude had a significant influence on the vent cycle operation, which was discussed in some detail, for the spray-bar configuration, in Reference 5.

Table 1: Ambient Heat Leak Data From Boiloff Tests

| Fill Level (%) | Ambient Heat Leak, Test Series 1, (Watt) | Ambient Heat Leak, Test Series 2, (Watt) |
|-----------------------|---|---|
| 90 | 20.2 | 54.1 |
| 50 | 18.7 | 51.0 |
| 25 | 18.8 | ---- |

PROPELLANT TANK DESTRATIFICATION

Spray-Bar

The test data confirmed that the spray-bar was effective in destratifying the tank ullage and liquid, as can be seen from the plot of the silicon diode rake temperatures in Figure 5. The percentages listed with each silicon diode designation represent the liquid fill level. During tank lock-up, the ullage became significantly stratified. When the spray-bar was activated, the ullage rapidly destratified, regardless of fill level. For the 50% fill level in Series 1, the tank destratified such that the liquid and gas temperatures were within 0.4 K of each other. These results were significant since they represented the worst case gravity environment of 1-g. In micro-gravity, the spray-bar would be even more effective in mixing the tank contents, since there would be no significant gravitational force to pull the sprayed fluid out of the ullage. The spray-bar was also effective in chilling down warm tank walls regardless of propellant position, which would be beneficial in tank fill operations. For example, during the 50% fill test illustrated in Figure 5, the tank dome cooled approximately 2 K during spray-bar operation.

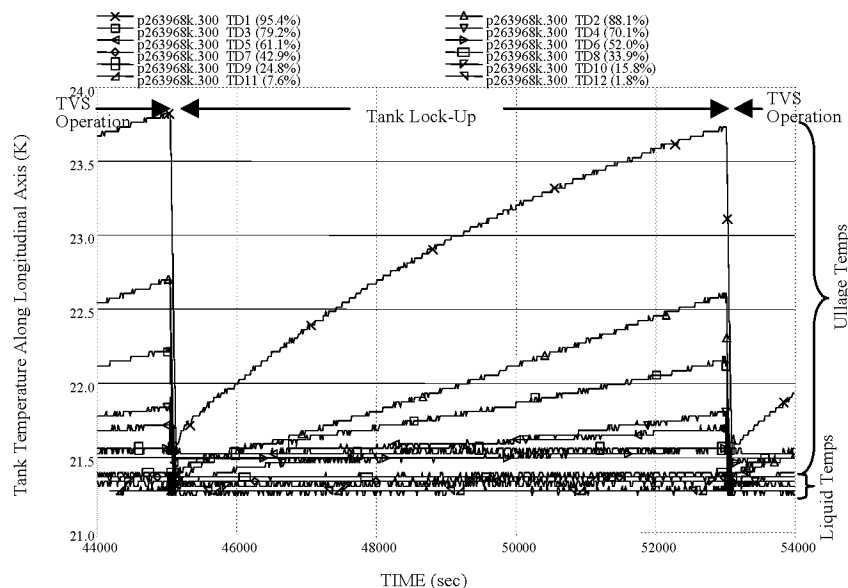


Figure 5: Plot Illustrating Tank Stratification/Destratification for the Spray-Bar, 50% Fill, Series 1

Axial Jet

The axial jet did not appear to destratify the ullage as can be seen by the plots in Figures 6 and 7. However, there was not a significant rise in temperature during the tank lock-up between TVS cycles. One explanation for the lack of destratification was that the liquid jet did not penetrate the liquid/ullage interface, and thus was unable to cool the ullage. However, due to a hardware problem, the axial jet recirculation pump operated at approximately 38 lpm, one third of its rated flow rate of 114 lpm. A CFD model of the axial jet was constructed in order to investigate whether or not, the higher flow rate would have significantly improved the axial jet performance. Preliminary results from that model are discussed later in this paper.

One observation that was counter-intuitive, was the tank lock-up time between TVS cycles, for the axial jet versus the spray-bar. The tank lock-up time for the axial jet was expected to be less than for the spray-bar since it was not as effective in cooling the ullage as the spray-bar. It was expected that the warm, stratified ullage would lead to a pressure rise rate much greater than for the cool, destratified ullage created by the spray-bar. However, the tank lock-up times for the axial jet were actually longer for both fill levels tested in Series 2. Some potential causes for this phenomenon have been identified, and are being investigated. Potential causes include: larger ullage volume (lower fill level) during axial jet tests, evaporation of liquid deposited on tank surfaces by the spray bar, and less efficient destratification of the tank liquid by the spray-

bar compared to the axial jet. CFD models planned for both TVS concepts will clarify this phenomenon, and the results of these analyses will be published at a later date.

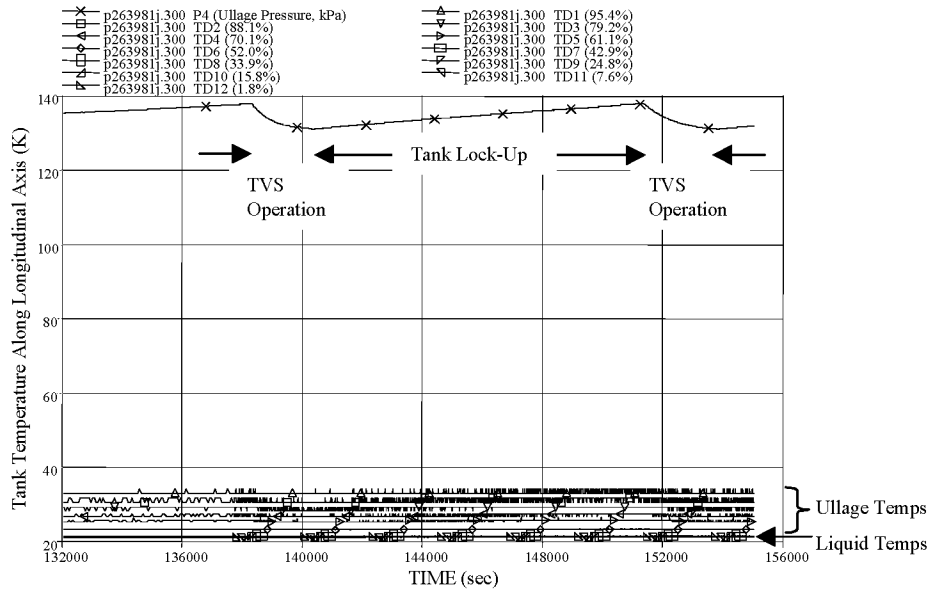


Figure 6: Plot of Tank Stratification for Axial Jet, 50% Fill, Series 2

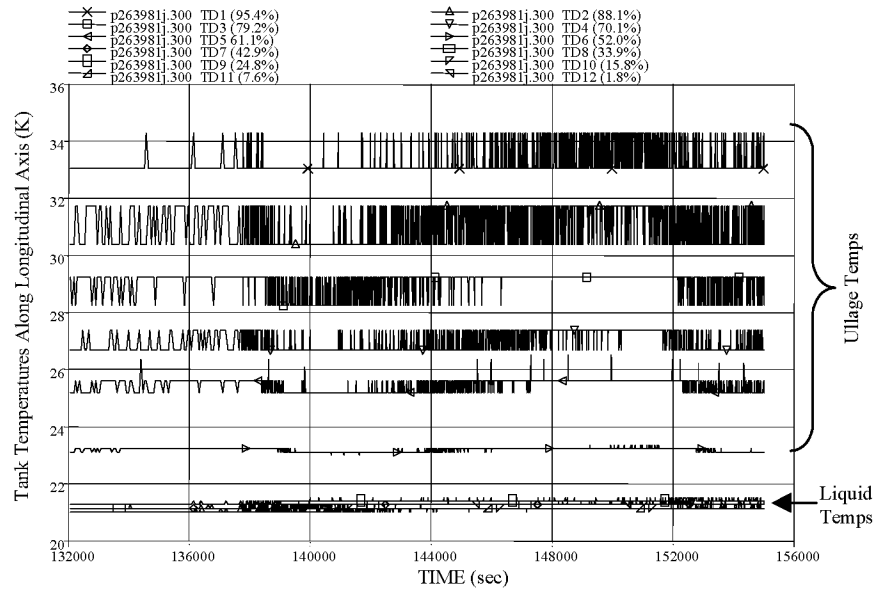


Figure 7: Enlarged Plot of Tank Temperatures in Figure 6

HEAT ENERGY EXTRACTION

The most important measure of TVS performance is its ability to extract thermal energy from the tank propellant. Once the propellant has reached the saturation temperature at tank operating pressure, the TVS system must be able to extract enough energy to offset the ambient heat leak into the tank and maintain tank pressure control. The heat extracted by the vent flow is calculated by the following equations:

$$\dot{Q}_{vent} = \dot{m}_{vent}(h_{out} - h_{in})$$

$$\dot{Q}_{ave} = \dot{Q}_{vent}\left(\frac{t_{open}}{t_{total}}\right)$$

Given the duty cycle (valve open time divided by the sum of valve open plus valve closed time) for a particular test, the value of vent heat extraction is averaged (\dot{Q}_{ave}) over a selected interval, during steady state operation, of each test in order to yield valid comparisons of TVS performance from test to test.

Table 2: Calculated Heat Extraction and Mass Flow Rates for Both TVS Concepts

| Test Series | Mixer Type | Fill Level (%) | \dot{Q}_{vent} (Watt) | \dot{Q}_{ave} (Watt) | \dot{m}_{vent} (kg/s) |
|-------------|------------|----------------|-------------------------|------------------------|-------------------------|
| 1 | Spray Bar | 90 | 1444 | 15.9 | 0.0034 |
| 1 | Spray Bar | 50 | 1486 | 16.3 | 0.0035 |
| 1 | Spray Bar | 25 | 1507 | 17.5 | 0.0036 |
| 2 | Spray Bar | 90 | ** | ** | ** |
| 2 | Spray Bar | 50 | 2108 | 40.6 | 0.0048 |
| 2 | Axial Jet | 90 | 215.8 | 109.3 | 0.000485 |
| 2 | Axial Jet | 50 | 223.4 | 77.3 | 0.000499 |

** Hardware problem, not enough J-T cycles to calculate heat extracted.

Spray-Bar

The vent mass flow rate for the spray-bar TVS is calculated using the compressible flow equation for a gas through a sonic orifice shown in the following equation:

$$\dot{m}_{vent} = \frac{0.14(CdA)P}{\sqrt{T}}.$$

The assumption that gas was flowing through the orifice was verified with the test data, which indicated that the heat exchanger completely vaporized the two-phase mixture exiting the J-T valve.

Table 2 summarizes the average heat extraction rates for all of the spray-bar tests conducted, both in 1996 and 1998. When comparing \dot{Q}_{ave} values to the ambient heat leak values for the same test, in all cases, the \dot{Q}_{ave} value is lower than the corresponding ambient heat leak value. The maximum difference, 21%, occurred in test Series 1 at the 90% fill level. In reality, the thermal energy removed by the TVS equaled the ambient heat leak into the tank. Otherwise, the tank pressure would not have remained within the prescribed pressure control band and the liquid saturation pressure would have continued to rise.

Potential sources for the difference between the heat extraction rate and the ambient heat leak were investigated. One source considered, but ruled out, was instrumentation uncertainties. The error in measured quantities would had to have been much larger than the instrumentation uncertainties to yield the additional enthalpy necessary to raise the heat extraction rate to the ambient heat leak value. The small magnitude of the vent mass flow rate and its calculation sensitivities made it the most likely candidate to account for any difference between the ambient heat leak and the TVS heat extraction calculation.

Axial Jet

The vent flow rate for the axial jet was calculated using an the following equation for the mass flow rate through the viscojet:

$$\dot{m}_{vent} = 0.9\left(\frac{10000}{Lohm}\right)(\Delta P * S)^{1/2}(1 - X).$$

Further detail on this flow rate equation is supplied in Reference 6. The comparison of the heat extraction calculations for the axial jet in Table 2, to the ambient heat leak values in Table 1, reveals a 102% difference for the 90% fill case, and a 52% difference for the 50% fill case. These differences are even greater than those observed for the spray-bar configuration. As with the spray-bar tests, the most likely candidate for these differences lies again in the vent mass flow rate calculation. The equation was originally formulated for a liquid or two phase mixture flowing through the viscojet. Temperature and pressure data at

the viscojet exit indicated that the state was a gas, the quality of which is $X=1$. Since at $X=1$, the vent flow rate becomes zero, the $(1-X)$ term was discarded and the vent flow rate was calculated based on a liquid state. This would lead to a much larger calculation for mass flow rate, and thus a greater heat extraction rate. As with the spray-bar cases, the heat extraction calculation is irrelevant if the TVS is able to maintain the propellant tank pressure within the subscribed control band. One can conclude that the TVS is able to remove heat energy at a rate equal to the ambient heat leak. Such was the case for the axial jet at the 90% fill level. However, at the 50% fill level, the TVS was unable to remove enough heat energy to maintain the tank ullage pressure within the control band. As the TVS continued to operate, tank ullage pressure continued to increase.

CFD MODELING

Since the axial jet concept, due to a hardware problem, ran at less than its designed capacity, any comparison of the test data alone is incomplete. In order to gain a more valid comparison of the two concepts, a CFD model of the axial jet configuration was assembled. The tool used was CFX-4, a CFD code distributed by AEA Technology, Inc. In addition to the fluid dynamics modeling, CFX is capable of modeling ambient heat leak into, as well as heat and mass transfer within, a system.

Two CFX cases were modeled, at the 50% fill level, with pump flow rates of 114 lpm (30 gpm) and 38 lpm (10 gpm). Ambient heat leak and mass transfer within the tank were not taken into account. The initial temperature conditions for each case were identical and based on actual test data. Temperature contours from the two cases were included in Figures 8 and 9. The preliminary results show that the liquid jet barely penetrated the liquid/ullage interface for the 38 lpm case, as seen in Figure 8. The temperature contour indicated a stratified ullage, which is unaffected by the jet. This was confirmed by the ullage temperature data, which remained stratified and almost constant, as shown in Figure 7. For the case run at the rated flow rate of 114 lpm, the liquid jet penetrated the liquid/ullage interface and hit the tank dome, as shown in Figure 9. The temperature contour indicated that some ullage cooling took place, although the very top of the ullage was still quite warm. Therefore, it is reasonable to assume that the axial jet performance would have been improved had the mixer been able to run at the rated flow rate. However, the performance cannot be quantified at this time since the CFD case modeled the fluid dynamics only. Results with ambient heat transfer and mass transfer effects will be published at a later date.

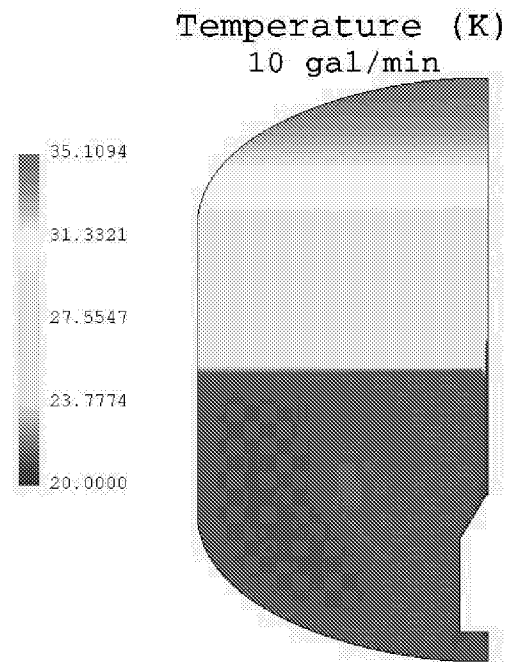


Figure 8: Temperature Contour in Tank, Axial Jet, 50% Fill, 10 gpm

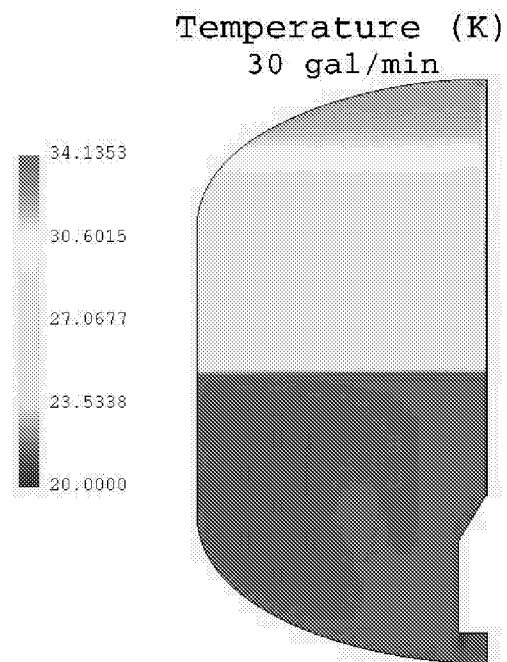


Figure 9: Temperature Contour in Tank, Axial Jet, 50% Fill, 30 gpm

CONCLUSIONS

The test data dramatically illustrate that the spray-bar TVS configuration was very effective in destratifying, and removing heat energy from, the propellant tank contents. This was evidenced by the fact that the spray-bar maintained ullage pressure within the prescribed control band, for all fill levels and heat leak values tested. The axial jet was ineffective in destratifying the tank ullage, and failed to maintain the tank ullage pressure within the control band for the 50% fill case. Preliminary CFD models indicated that the hardware problem limiting the mixer flow rate to almost 1/3 of its rated value, was a factor in the reduced performance of the axial jet. Had the mixer liquid jet penetrated the ullage, some destratification would have taken place. Unfortunately, that amount of destratification is difficult to quantify at this time. However, future CFD modeling with heat and mass transfer should provide some insight into whether or not the axial jet would have performed nominally at the rated mixer flow rate.

ACKNOWLEDGEMENTS

The authors would like to thank the MSFC East Test Area personnel, especially Kevin Pedersen, for their dedicated work in testing both the spray-bar and axial jet concepts. The authors would like to extend their appreciation to Tibor Lak and Han Nguyen at Boeing for the spray-bar design, hardware delivery, and test support. The authors would also like to thank personnel at Glenn Research Center for providing the axial jet hardware and test support.

REFERENCES

1. Lak, Tibor; Wood, Charles, "Zero-G Thermodynamic Vent System Final Report", Rockwell Aerospace Report Number: SDD 94M0038, Contract Number: NAS8-39202, 1994.
2. Fox, E. C.; Kiefel, E. R.; McIntosh, G.L.; Sharpe, J. B.; Sheahan, D. R.; Wakefield, M. E.; "Multipurpose Hydrogen Test Bed System Definition and Insulated Tank Performance, Final Report", Martin Marietta Astronautics, Contract Number: NAS8-39201, July 1993.
3. Olsen, A.D.; Cady, E.C.; Jenkins, D.S.; Hastings, L. J.; "Solar Thermal Upper Stage Cryogen System Engineering Test", AIAA/SAE/ASME/ASEE 35th Joint Propulsion Conference and Exhibit, June 20-23, Los Angeles, CA, 1999.

4. Hastings, Leon J., Martin, James J., "Experimental Testing of a Foam/Multilayer Insulation (FMLI) Thermal Control System (TCS) For Use On a Cryogenic Upper Stage", 1st Conference on Orbital Transfer Vehicles, Space Technology and Applications International Forum (STAIF), 1998.
5. Flachbart, Robin H.; Hastings, Leon J.; Martin, James J., "Testing of a Spray-Bar Zero Gravity Cryogenic Vent System For Upper Stages", AIAA/SAE/ASME/ASEE 35th Joint Propulsion Conference and Exhibit, June 20-23, Los Angeles, CA, 1999.
6. Papell, Stephen S.; Nyland, Ted W.; Saiyed, Naseem H., "Liquid Hydrogen Mass Flow Through a Multiple Orifice Joule-Thomson Device", 27th AIAA Thermophysics Conference, July 6-8, Nashville, TN, 1992.



THERMAL ANALYSIS OF THE FASTRAC CHAMBER/NOZZLE

Darrell Davis
Marshall Space Flight Center

ABSTRACT

This paper will describe the thermal analysis techniques used to predict temperatures in the film-cooled ablative rocket nozzle used on the Fastrac 60K rocket engine. A model was developed that predicts char and pyrolysis depths, liner thermal gradients, and temperatures of the bondline between the overwrap and liner. Correlation of the model was accomplished by thermal analog tests performed at Southern Research, and specially instrumented hot fire tests at the Marshall Space Flight Center. Infrared thermography was instrumental in defining nozzle hot wall surface temperatures. In-depth and outboard thermocouple data was used to correlate the kinetic decomposition routine used to predict char and pyrolysis depths. These depths were anchored with measured char and pyrolysis depths from cross-sectioned hot-fire nozzles. For the X-34 flight analysis, the model includes the ablative Thermal Protection System (TPS) material that protects the overwrap from the recirculating plume. Results from model correlation, hot-fire testing, and flight predictions will be discussed.

INTRODUCTION

The Fastrac program provides a low-cost, 60,000 lb (60K) thrust, rocket engine to the aerospace community. Part of this low-cost design is an ablative chamber/nozzle assembly that is actively film-cooled with RP1. The chamber/nozzle is designed for one time use only and will be replaced after every flight. The baseline chamber/nozzle consists of a tape-wrapped silica phenolic liner with a filament-wound carbon epoxy overwrap added for extra strength. A filament wound glass phenolic overwrap is also being tested as part of a parallel verification effort. The flight nozzles will have a 30:1 area ratio. However, most of the nozzles that have been ground tested have a 15:1 area ratio since the 30:1 nozzle is underexpanded at sea level.

The concerns during the design phase included: effects of the film cooling, degree of surface recession and the ability to maintain the liner to overwrap bondline below 300 F. The insulative properties of the silica phenolic protect the bondline during firing (typically 150 seconds), however the "soakback" effect causes the bondline to exceed the limit after shutdown and to potentially create a debond. The soakback effect was mentioned as a design problem at the Preliminary Design Review. To address this, as well as the other desing concerns, extra tests were added to the test plan to assist in gathering data to refine the thermal model. As the design progressed, it was obvious that the liner had to be thicker to protect the bondline. This was an undesirable solution since it increased the weight of the nozzle. The solution was to thicken the liner as much as possible only at the attach rings and add to shear pins to distribute the load into the nozzle in case the rings still came loose. This resulted in the baseline configuration shown in Figure 1. Table 1 presents the design thicknesses at key locations.

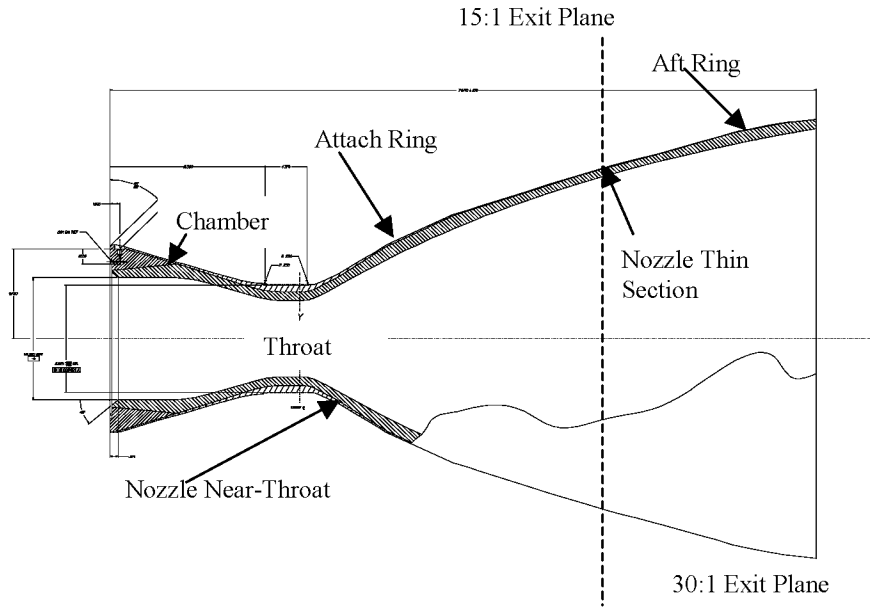


Figure 1: Fastrac Chamber/Nozzle Baseline Configuration.

| | Silica Phenolic Thickness | Graphite Epoxy Thickness |
|---------------------|------------------------------|-----------------------------|
| Chamber | 0.987 | 0.253 |
| Throat | 0.850 | 0.807 |
| Nozzle Near-Throat | 0.852 | 0.316 |
| Attach Ring | 1.349 | 0.123 |
| Nozzle Thin Section | 0.801 | 0.072 |
| Aft Ring | 1.194 | 0.062 |

Table 1: Fastrac Chamber/Nozzle Design Thickness.

MODEL DESCRIPTION

A one-dimensional SINDA model was developed to predict in-depth temperature response and bondline temperatures for ground tests and for flight conditions. The SINDA model consisted of 45 finite element nodes across the thickness of the silica phenolic liner and 5 nodes through the graphite epoxy overwrap. A non-linear grid was used to capture the high gradients near the surface while minimizing the overall number of nodes. Material properties for the virgin and charred silica phenolic were obtained through testing at Southern Research, Inc. (SORI) in Birmingham, AL. Preliminary hot gas temperature predictions were provided by the CFD group at the Marshall Space Flight Center. SINDA/CMA¹, a kinetic decomposition routine, based on the Arrhenius equation, was added to account for the effect of material decomposition and pyrolysis gas formation. Cork was added to the external nozzle surfaces to protect the graphite epoxy from the plume recirculation environments during flight. ABL², an in-house developed code that can be coupled with SINDA, was used to size the cork. ABL uses an empirically derived recession rate versus heat rate curve to calculate surface recession of the cork while tracking thermal capacitance and conduction path lengths to calculate heat transfer through the receding material. This is the first model generated at MSFC that has incorporated SINDA/CMA and ABL to account for material decomposition of two different materials experiencing two different environments.

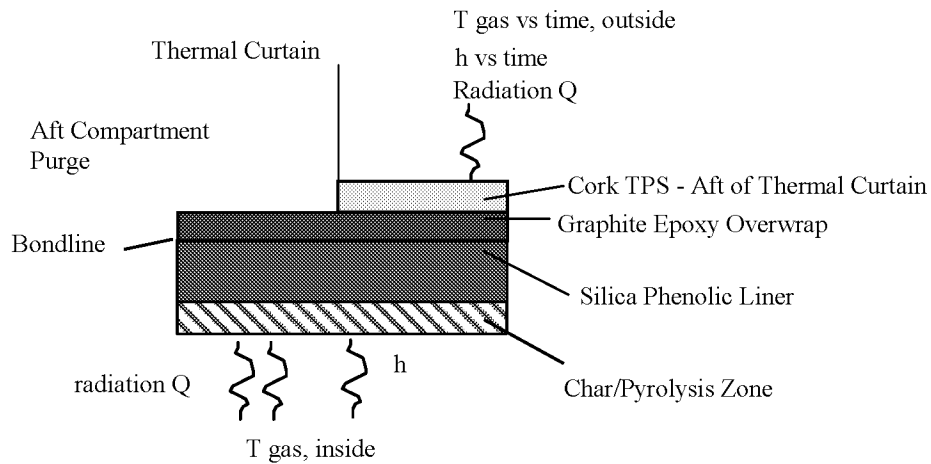


Figure 2: Schematic Representation of SINDA Model

TESTING

Preliminary material testing was performed at MSFC's Improved Hot Gas Facility (IHGF) and Wright Patterson Air Force Base's Laser Hardened Material Evaluation Laboratory (LHMEL). These tests did not provide much data that could be used to validate the in-depth model predictions, however they verified the assumption that the surface would not recede at the expected hot-fire conditions. The first data used to correlate the model came from Thermal Analog tests performed at SORI³. The test provided one-dimensional heating of a 2.0" x 2.0" x 0.85" coupon of silica phenolic/graphite epoxy lay-up by exposing the coupon surface to a resistively heated graphite heater. The coupon surface was heated at rates that simulated actual engine firings. A schematic of the basic facility is shown in Figure 3.

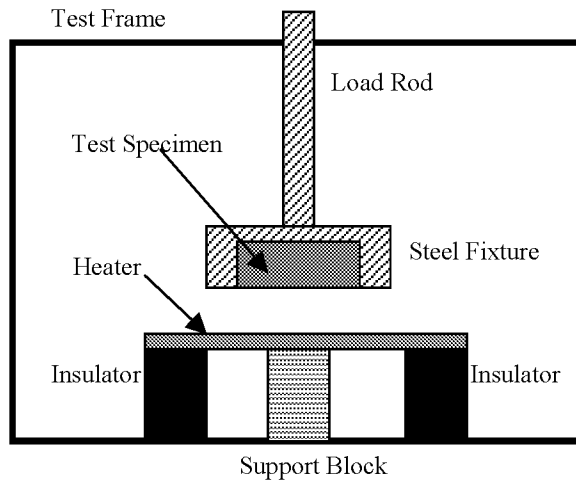


Figure 3: Schematic of SORI Analog Tests

A total of three samples were tested. The first two tests runs were for 150 seconds and the third was for 230 seconds. Temperature of the surface, backside, and five in-depth locations were recorded with thermocouples. Depths of the imbedded thermocouples were determined by CT techniques. The recorded surface temperature was used as an input to the SINDA model and temperatures were predicted at the measured thermocouple depths. Because of uncertainty in the char properties, and the unknown material properties in the pyrolysis region, material properties were adjusted until the SINDA model results matched the results from the Thermal Analog Tests. Char and heat-affected depths were also taken from these samples. This data was used to anchor the kinetic decomposition routine.

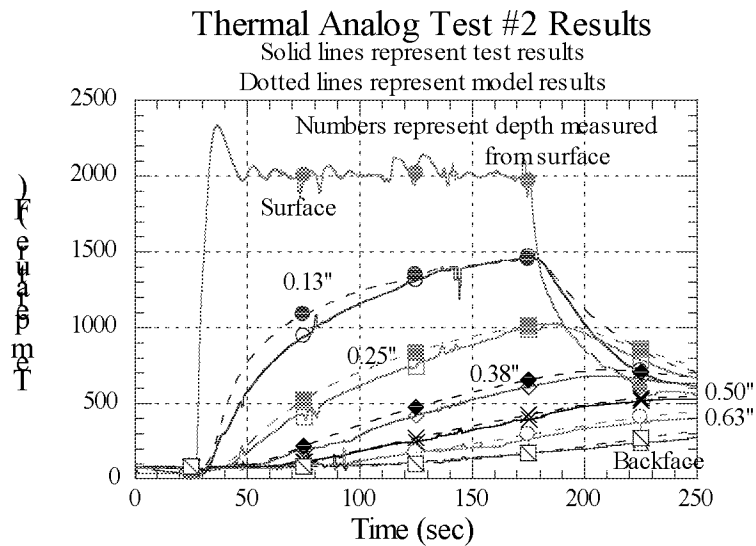


Figure 4: Model Comparison to SORI Analog Tests

A significant amount of data was gathered from hot fire component testing performed at MSFC's Test Stand 116. These were static tests to verify the design of the Thrust Chamber Assembly (TCA). The propellants were pressure-fed instead of using the actual Fastrac turbomachinery. During this series of tests, an attempt was made to gather as much data as resources would allow. This data would prove valuable to the validation of the thermal math model.

All static tests had two thermocouples installed in holes drilled through the aft-facing surface of the silica phenolic. One was a bare Type C thermocouple mounted flush with the liner surface to measure surface temperature, the other was a shielded Type C thermocouple mounted with the bead about 0.125" into the flow to measure the local hot gas temperature. An infrared scanner was also used to determine the interior surface temperature. The results from these two methods matched well and enabled the surface temperatures used in the model to be lowered.

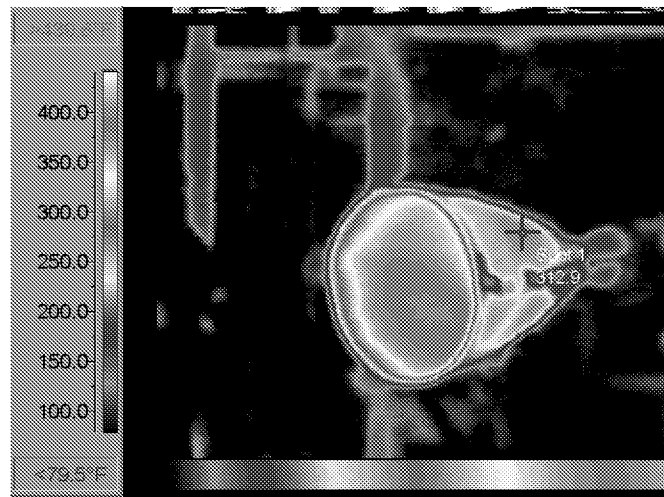


Figure 5: Infrared Image of Fastrac Nozzle Showing Soakback Effect

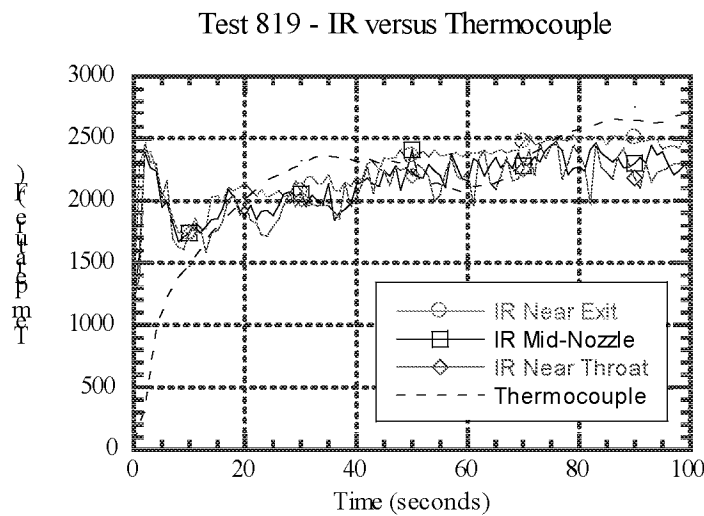


Figure 6: Comparison of Temperatures from Thermocouples and Infrared

In two of the early tests, designated 60K #1 and 60K #2, thermocouple plugs were used to measure in-depth temperature response. This process was developed during earlier technology development programs at MSFC. The plugs were 0.25" silica phenolic cylinders into which were imbedded three thermocouples.

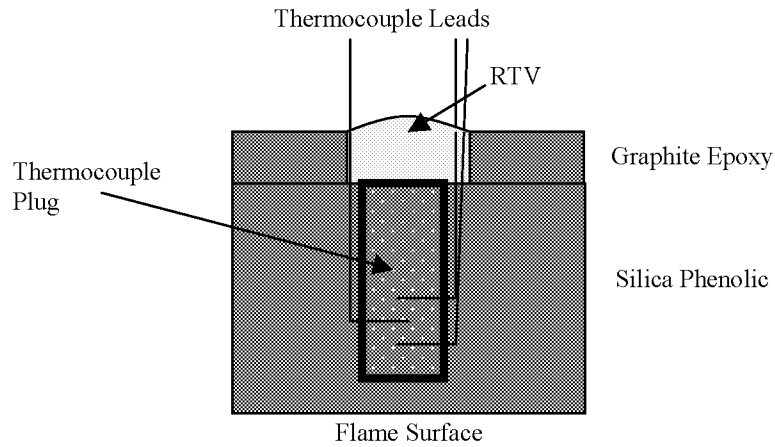


Figure7: Schematic of Thermocouple Plug

The plugs were laid up in the same manner as the liner material. Care had to be taken during installation to ensure proper placement of the thermocouple leads within the plug. A hole was drilled into the silica phenolic liner from the backside to within a nominal 0.100" from the surface and the plugs were installed into these holes. Plugs were placed at four axial locations and two radial locations for each axial location.

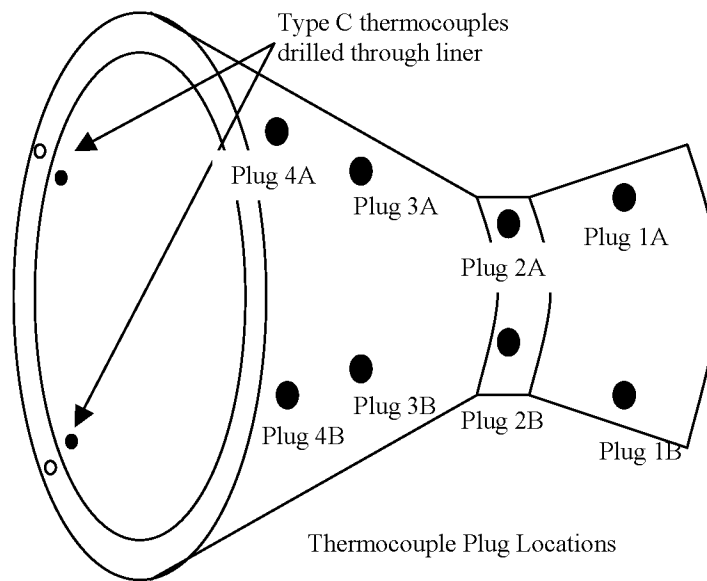


Figure8: Thermocouple locations on 60K #1 and 60k #2

All of the thermocouples in the A plugs were Type S while the B plugs used a combination of Type K and Type S. Because of the low conductivity of the silica phenolic, a steep thermal gradient exists in the liner and it was necessary to know the exact depths of the thermocouples. Depths of these thermocouples were again obtained by using CT techniques. However, the Type K thermocouples were invisible to CT. The Type K thermocouple data also tended to have more noise in the data and tended to open during the firing. Therefore the data from the Type S thermocouples in the A plugs was used in model verification. In the 60K #1 test, two Type S thermocouples failed, and during the 60K #2 test, a leak path developed around plug 2A and invalidated the thermocouple readings from that plug. Both tests were planned 150 second duration tests, however due to test anomalies, 60K #1 ran for 28 seconds and 60K #2 ran for 130 seconds. Thermocouple measurements versus model predictions are presented in the figures below

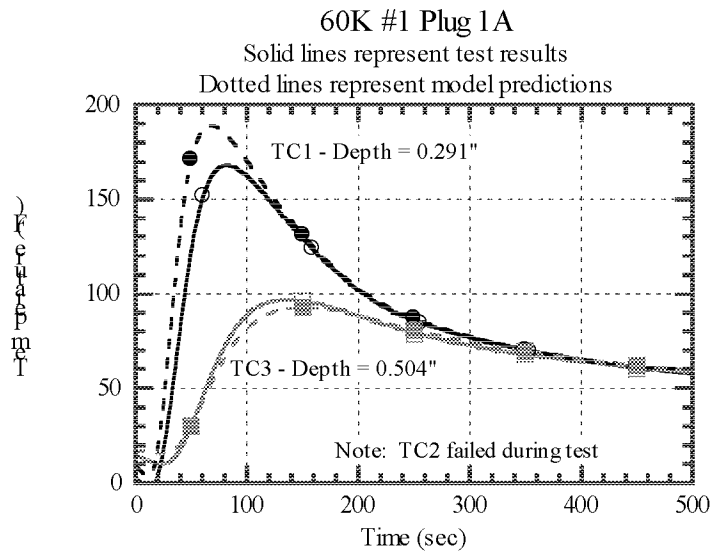


Figure 9: Model versus Test Data for Test 60K #1, Plug 1A

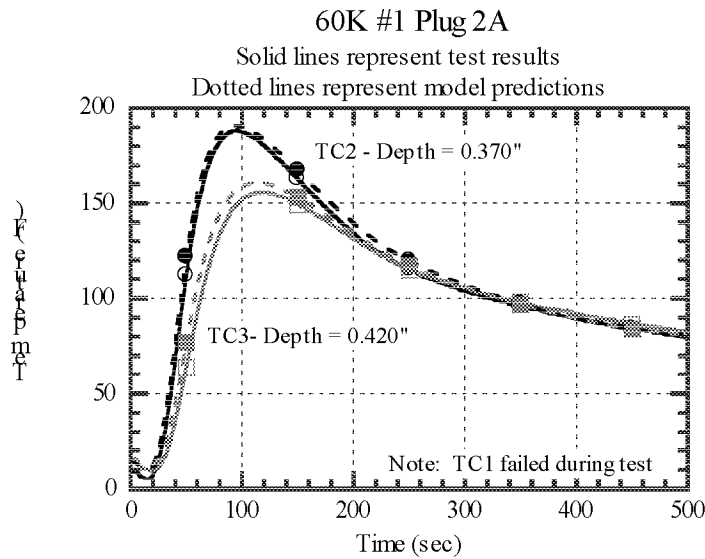


Figure 10: Model versus Test Data for Test 60K #1, Plug 2A

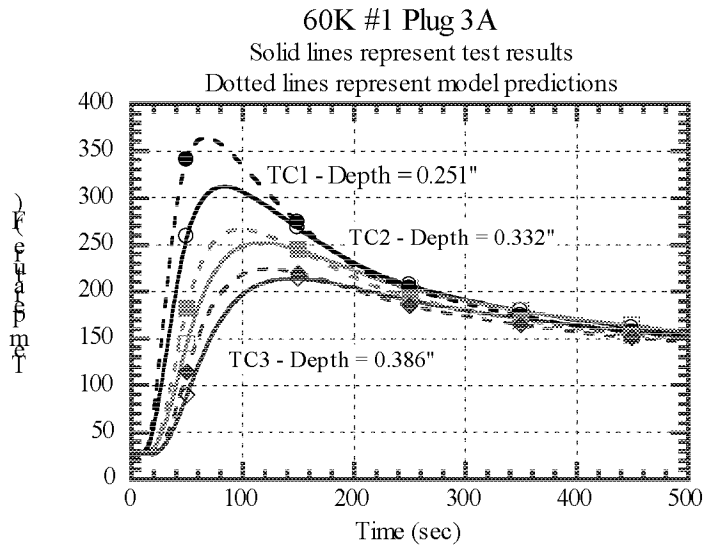


Figure 11: Model versus Test Data for Test 60K #1, Plug 3A

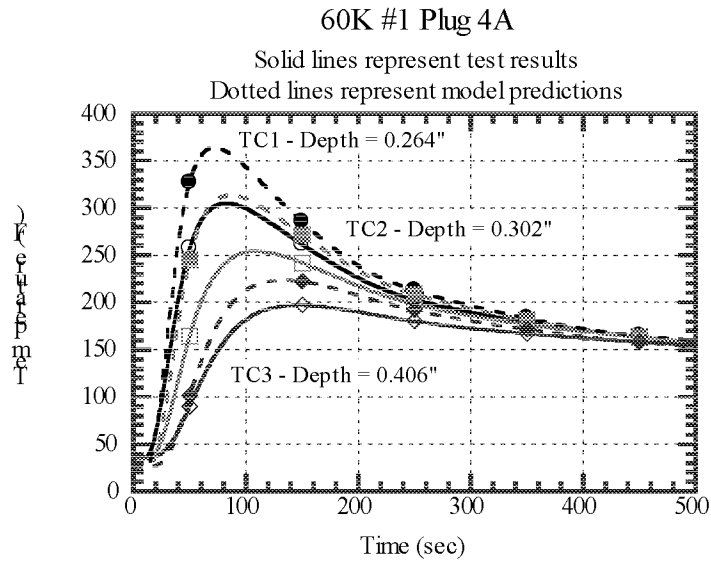


Figure 12: Model versus Test Data for Test 60K #1, Plug 4A

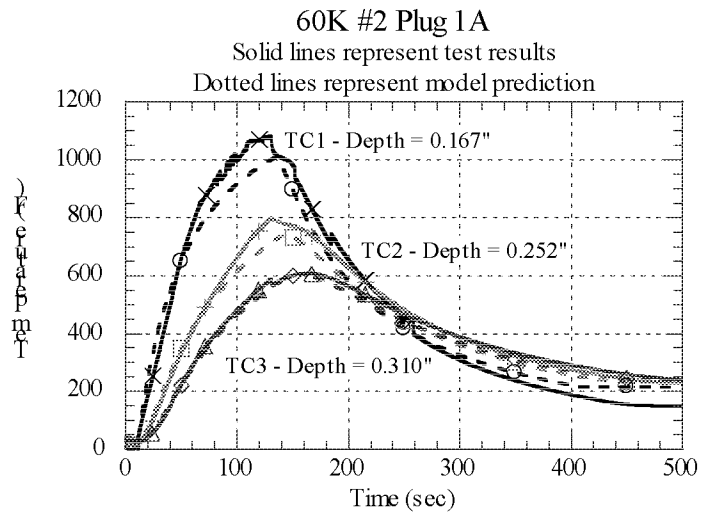


Figure 13: Model versus Test Data for Test 60K #2, Plug 1A

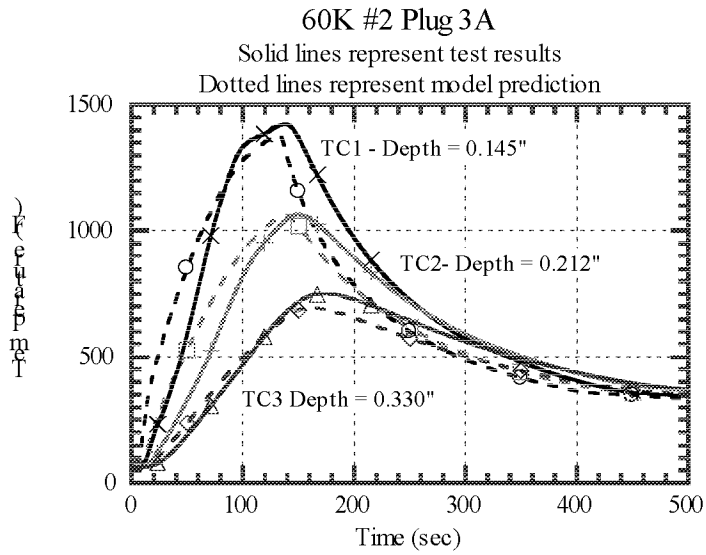


Figure 14: Model versus Test Data for Test 60K #2, Plug 3A

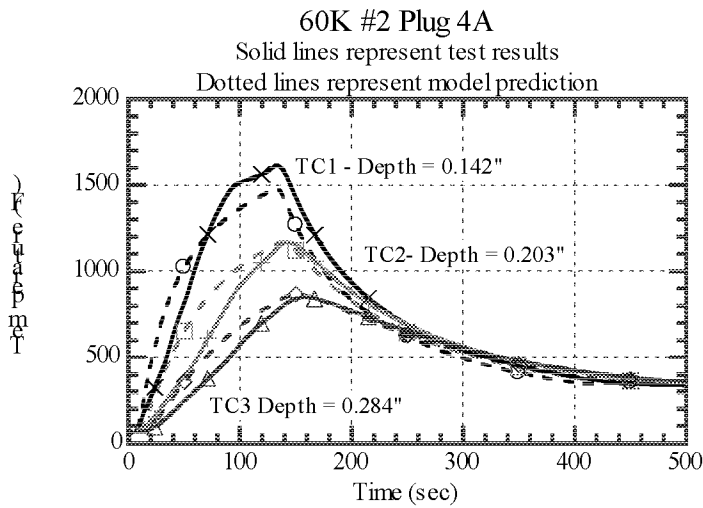


Figure 15: Model versus Test Data for Test 60K #2, Plug 4A

The 60K #1 and 60K #2 nozzles were sliced axially and post-test char and heat-affected depths were measured. Data from these tests also confirmed that there was no surface recession of the silica phenolic even during a 130-second test.

Since multiple short-duration tests were to be performed on each nozzle, the model was relied upon to verify that the bondline had not exceeded its temperature limit, and could be tested again. Therefore all static tests also had exterior thermocouples placed at key axial locations. These thermocouples provided data to anchor the model for each test and ensured reliable bondline predictions.

The next series of tests performed on the Fastrac nozzle occurred at the Stennis Space Center (SSC) in Pascagoula, Mississippi. These tests were system level validation tests that incorporated the turbomachinery with the TCA. Since drilling was not allowed on these nozzles, and the test stand does not provide adequate placement for the infrared scanner, external thermocouples are the only source of data on the tests at SSC.

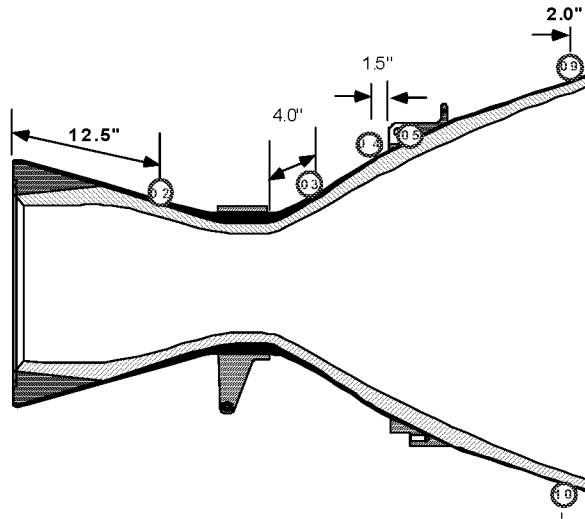


Figure 16: Thermocouple Placement on the H2 Series Tests at SSC

The H2 series tests were performed on a 15:1 nozzle with a glass phenolic overwrap. Results from thermal analysis and test data showed that the glass phenolic and graphite epoxy overwraps would perform very similarly thermally. Test H2A-2B and Test H2B-2 both ran for the planned full duration of 24 and 155 second, respectively. Comparison of model results with exterior thermocouple data is presented in the figures below. The model predictions tend to agree well with the thermocouple data. Most of the disagreements are caused by purges on the test stand cooling the nozzle surface after shutdown. While the model can account for this effect, the timeline and temperatures of these purges are not easily obtained.

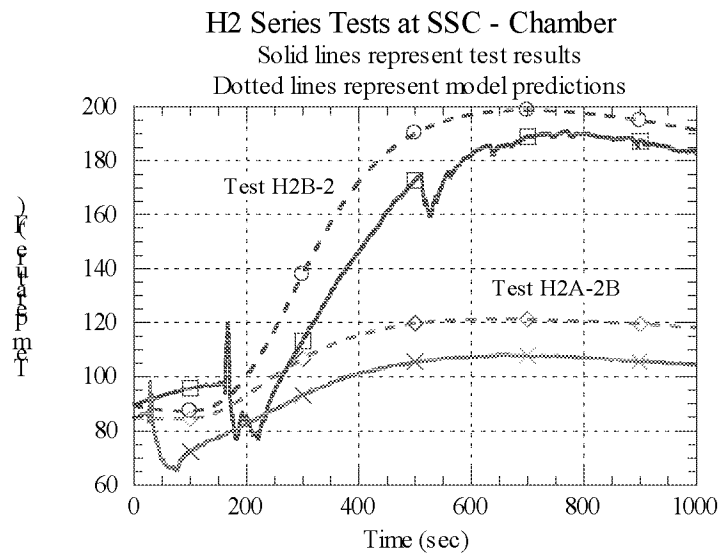


Figure 17: Fastrac Chamber Model Results versus Test Data for H2 Series Testing

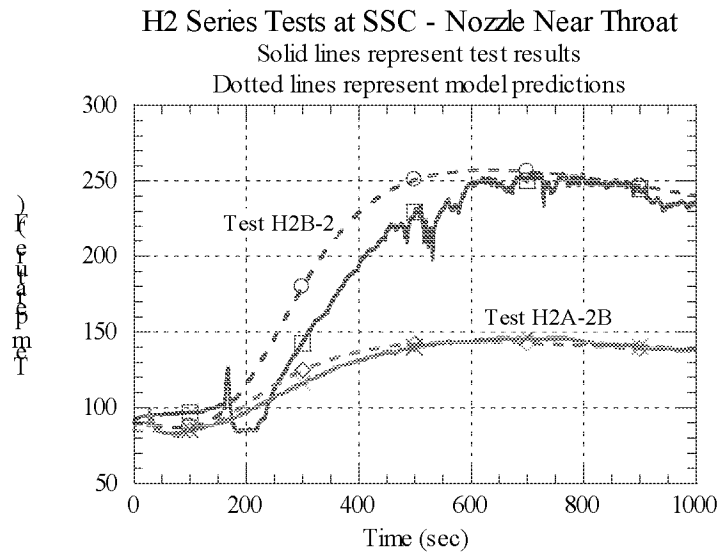


Figure 18: Fastrac Nozzle Near-Throat Model Results versus Test Data for H2 Series Testing

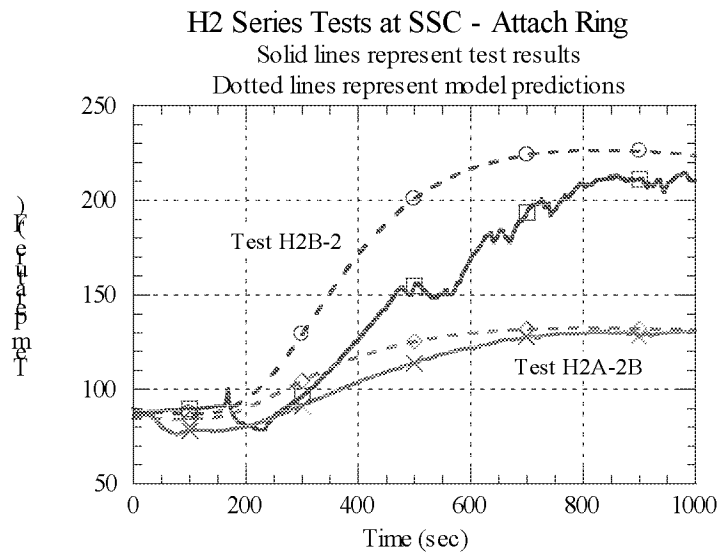


Figure 19: Fastrac Attach Ring Model Results versus Test Data for H2 Series Testing

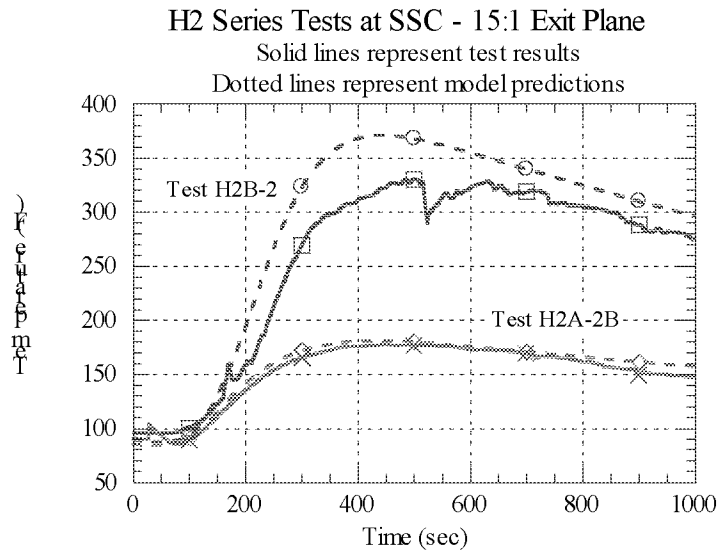


Figure 20: Fastrac Exit Plane Model Results versus Test Data for H2 Series Testing

These nozzles are also instrumented with strain gauges to allow structural analysts to verify their models. Data from these strain gauges can show where a debond has occurred. Figure 19 shows strain gauge and thermocouple data plotted together at the exit plane, where a visual examination confirmed a debond.

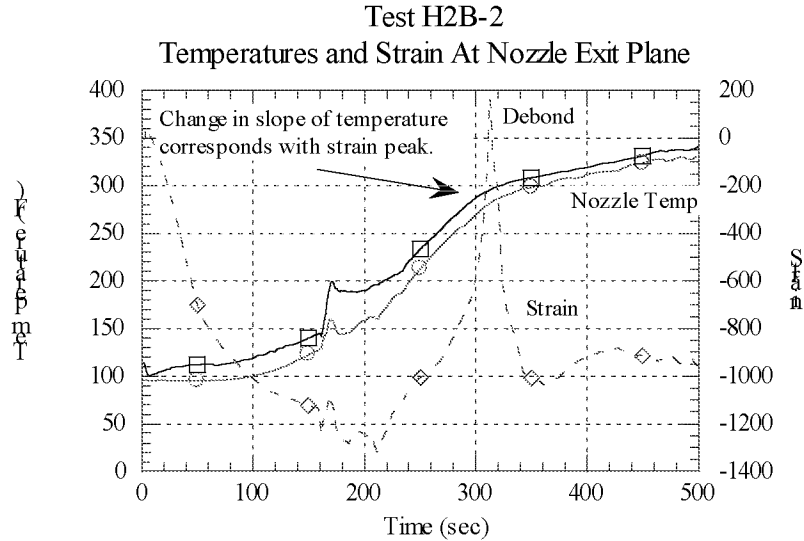


Figure 21: Thermocouple and Strain Gauge Data From Test H2B-2

The spike in the strain gauge data indicates a debond occurred at that time. At the same time, the thermocouple data changes slope. This is also an indication of a debond. When the graphite epoxy overwrap debonds from the liner, the conduction path from the liner to overwrap is broken. The overwrap is then more heavily influenced by convective cooling from the ambient temperature than by the radiant heating now produced by the liner. This causes a change in slope in the thermocouple response.

The nozzle near-throat region is an area of concern for potential debonding. In this section, the overwrap is becoming thinner due to an increase in local area ratio and the liner is not as thick as it is further downstream at the attach ring. Visual observations cannot reveal a debond in this region, and on-pad non-destructive evaluation (NDE) methods have not been developed to a point where they are feasible to use in small, tight spaces. Strain gauge data from the near-throat region of Test H2B-2 seems to indicate a debond. When the thermocouple data is plotted alongside the strain gauge data, Figure 20, it may also show indications of a debond by the change of slope in the temperature trace.

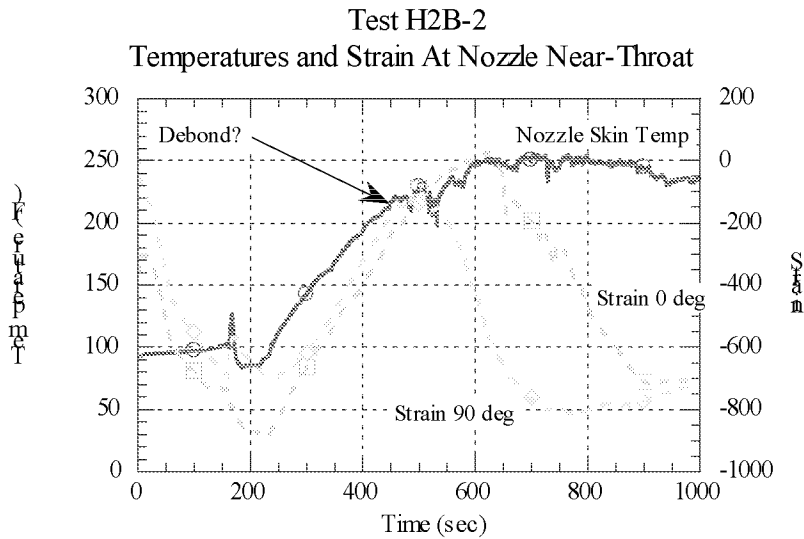


Figure 22: Thermocouple and Strain Gauge Data from Test H2B-2

Post test laboratory NDE could not positively declare a debond at this location, but did reveal a low-density area. It is possible that this configuration of thermocouples and strain gauges could be used for health monitoring of the nozzle during ground tests.

THERMAL PREDICTIONS FOR STRUCTURAL ANALYSIS

Once the model had been proven reliable and able to match test results, it was used to provide two-dimensional thermal distributions to structural analysts. The kinetic decomposition routine could not be adapted to a two-dimensional grid. Since there was very little difference in local plume temperatures and therefore no ΔT to drive axial conduction, it was determined that an interpolation of 1-D results would provide the necessary data. The analytical nozzle was separated into 28 1-D slices as shown in Figure 21.

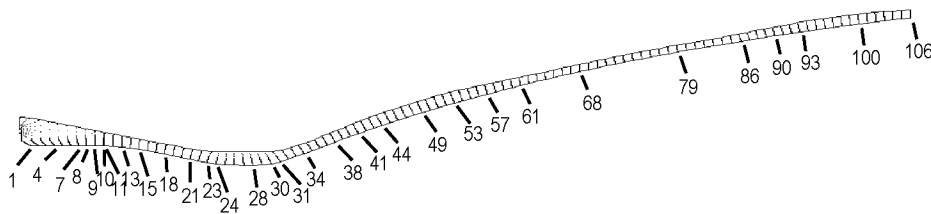


Figure 23: Locations of 1-D Slices Used to Generate 2-D Thermal Distributions

Each slice was run with its corresponding gas temperature, heat transfer coefficient, silica phenolic thickness, graphite epoxy thickness to provide a thermal gradient profile at that location. The results were interpolated onto a 2-D PATRAN finite element mesh. Results provided for structural analysis included hot and cold extremes for both ground and flight.

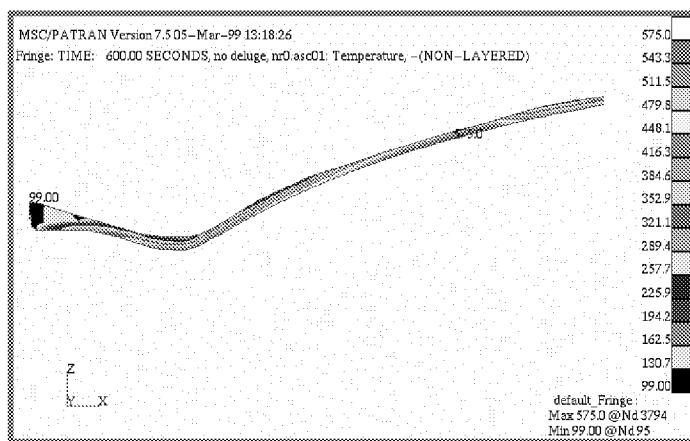


Figure 24: Example of Two-Dimensional Thermal Distribution

FLIGHT PREDICTIONS

During flight, the overwrap forward of the heat shield will be exposed to environments generated inside the aft compartment. The nozzle itself will contribute to this environment, especially post-firing. Flight exterior nozzle temperatures were provided to Orbital Sciences Corporation for inclusion to their aft compartment model. Aft of the heat shield, the nozzle will be exposed to recirculation of the plume. MSFC's CFD group provided plume recirculation environments. ABL, an in-house code that runs concurrently with SINDA, was used to size the thermal protection system (TPS) materials. Two materials were selected for analysis; cork, Marshall Convergent Coating (MCC-1). MCC-1 is a sprayable ablator developed at MSFC containing cork, glass ecospheres and an epoxy resin. It is currently used as the main acreage TPS on the Solid Rocket Boosters. Results from the analysis showed that 0.25" of either material would protect the graphite epoxy overwrap to 300 F. Since MCC-1 is sprayable, it requires the

programming of a computer to follow the specific geometry of the nozzle. This made the MCC-1 more expensive for a short production run, so the program decided to use cork as the external TPS material. RT-455, a K5NA substitute, will be used as a closeout material and the entire TPS system will be covered with Acrymax paint.

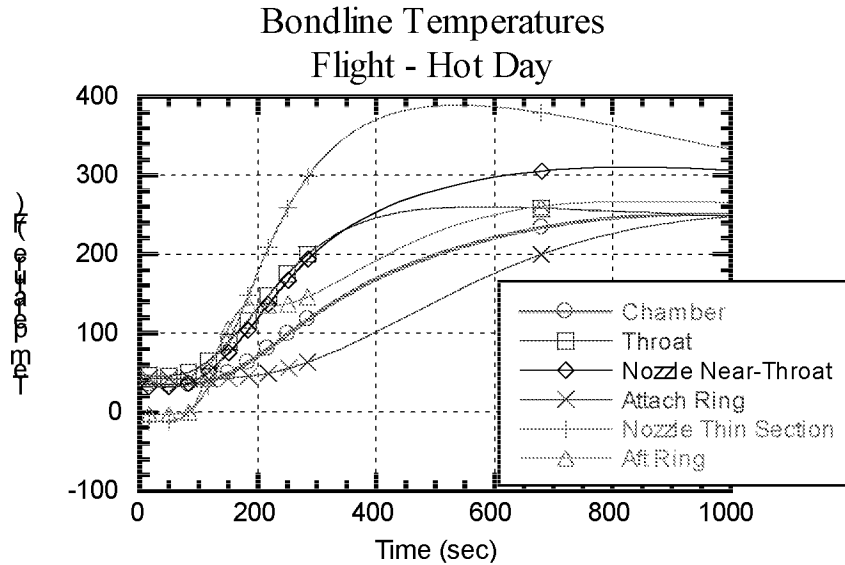


Figure 25: Flight Predictions

CONCLUSIONS

Because of an extensive test program that generated data used to correlate the model, the model can be trusted to give reliable results. These results indicate that during a 150-second engine burn, all bondlines will remain below 150F. However, this bondline limit will be violated during the soakback and will potentially cause a debond.

ACKNOWLEDGEMENTS

The author wishes to acknowledge the contributions of Louie Clayton for help with the SINDA/CMA routine, Donald Bryan for help with the infrared imaging, and Bruce Tiller for guidance.

REFERENCES

1. "SINDA Temperature and Pressure Predictions of Carbon-Phenolic in a Solid Rocket Motor Nozzle Environment", 1992 JANNAF Conference, Moffat Field, Palo Alto, CA, J. Louie Clayton
2. "SINDA/ABL Solution Routine Updates", J. Louie Clayton, NASA Internal Memorandum, ED63(25-96), 1996

3. "Thermal Analog Testing of Fastrac MX2600 Silica Phenolic, Final Report to MSFC", Michael D. Johns, SRI-ENG-98-26-8657.15, 1998



METHOD IMPROVEMENTS IN THERMAL ANALYSIS OF MACH 10 LEADING EDGES

Ruth M. Amundsen

National Aeronautics and Space Administration

Langley Research Center

Hampton VA 23681-2199

ABSTRACT

Several improvements have recently been made in the thermal analysis methods for leading edges of a hypersonic vehicle. The leading edges of this vehicle undergo exceptionally high heat loads that incorporate extreme spatial gradients as well as severe transients. Due to the varying flight conditions, complex geometry, and need for thermal loads at many points along the trajectory, full computational fluid dynamics (CFD) analysis of the aeroheating loads is not feasible. Thus, engineering methods must be used to determine the aeroheating on the vehicle surfaces, and that must be utilized in the thermal analysis. Over the last year, the thermal analysis of a hypersonic vehicle has been enhanced in several ways. Two different engineering codes are used to predict aeroheating loads: one over the curve near the stagnation point, and the other on flat surfaces downstream of the leading edge. These two are matched together at the intersection point using a method that allows closer approximation of CFD results. User-developed FORTRAN, which is part of the thermal solver PATRAN Thermal, is used to accomplish this. The customizable FORTRAN code also allows use of many different time- and space-dependent factors, interpolation of the heat load in time and space, and inclusion of both highly swept and unswept grid structures. This FORTRAN is available to other PATRAN users who may want to accomplish a similar objective in analysis. Flux, rather than convective coefficient, is used to define heat loads, which allows more accurate analysis as well as better application of margins. Improvements have also been made in more efficient utilization of imported CAD geometry, by creating faces on solids to facilitate load application.

INTRODUCTION

Earlier work by the author in the thermal analysis of hypersonic leading edges has been described elsewhere.^{1,2} This paper will describe improvements in the methodology that have been made recently. Several hypersonic leading edges of varying geometries have been analyzed. The thermal solver used is MSC/PATRAN Thermal. The aeroheating loads for the hypersonic trajectory are generated in other software, and output in a text file format. The challenge is to import these aeroheating loads into PATRAN, interpolate in time and space to allow application to the PATRAN thermal model, and apply factors to the loads that are both time and spatially dependent. The main improvements that have been made in the last year are: to import and interpolate heat flux rather than the convective coefficient and recovery temperature; add flexibility so that the code can correctly interpolate from swept grid structures with varying directionality; incorporate time- and space-dependent factors; and alter the aeroheating loads at specific points on the geometry. The method for applying heat loads on the leading edge that are dependent on nodal temperature has been fully developed. Also, the method for verifying the interpolation has been optimized.

HEAT FLUX IMPORT

A change was made in the interpolation software to import aeroheating flux, rather than the convective coefficient h_c and the fluid temperature. This was done for several reasons. First, the flux is the value actually calculated by the aeroheating software. The other two values were determined from flux, introducing possible inaccuracies. The fluid temperature is of questionable value at the range of Mach numbers encountered in this analysis. Second, the flux depends not only directly on the nodal temperature (as it also was in the original method using h_c), but also indirectly. This indirect or second-order dependence of flux on the nodal temperature was not fully handled by importing h_c and computing flux based on a temperature difference. Third, the question of applying factors to the flux becomes more complex when h_c was used. When h_c was the value imported, any uncertainty factors could only be applied to h_c . This would lead to different temperatures at later times than when run without factors, and thus to a different (lower) flux. Thus, the factor was not really being applied to the total input flux. When flux is the imported value, any factor applied is actually increasing the flux by the correct amount at any given time.

In order to import flux rather than h_c , a different subroutine in the PATRAN ulib files was required. The `uhval.f` subroutine was used for import of h_c and fluid temperature. For import of flux, the `umicro.f` subroutine was utilized. The logic in the two subroutines is very similar. However, different variables are passed to, and used within, the two subroutines. In `umicro.f`, many of the internal PATRAN variables and arrays, such as `ITLIST`, `IFLIST`, and `MFID`, must be initialized with the correct sizes. Then, within `umicro.f`, the solution time and nodal position are evaluated and used for the time and spatial interpolation. A separate subroutine is called to perform the interpolation. Since the interpolation is based only on the nodal position in PATRAN, this method can be applied equally well to structured (brick) or unstructured (tetrahedral) meshes. It can also be applied to surface meshes.

Since the aeroheating flux is dependent on the temperature of the surface, surface temperatures at each time point must be output to the aeroheating program for calculation of flux. With new predicted fluxes, the PATRAN thermal solution is re-run, and temperatures again transferred for new calculation of aeroheating. This iteration normally only requires about three cycles to achieve closure (matching of input and output temperatures).

IMPORT GRID PARAMETERS

The interpolation from one grid set to another would be fairly simple if the grids were both orthogonal to the same axes, and the gradients were small relative to the grid spacing. However, in the aeroheating grid, there are several parameters that make interpolation difficult.

First, the leading edge is sometimes swept at a severe angle, by as much as 70 degrees from normal to the flow. The vehicle is normally modeled with one axis parallel to the flow, and thus the leading edge is not in general parallel with an axis, but can be at a large angle to an axis. The grid of the aeroheating model usually follows the vehicle lines, and thus is swept with the leading edge, although the sweep angle is not constant and decreases substantially toward the aft end of the part. The steep gradient in heating that occurs on a hypersonic leading edge is normal to the line of the leading edge: i.e., the fall-off in heat flux is very abrupt in the direction directly away from the leading edge. If interpolation were done directly on the spatial coordinates of x and y , the flux could be interpolated incorrectly, since the gradient is dependent on the distance from the leading edge and not specifically on x or y . The sweep also makes it difficult to select the correct set of grid points to interpolate between. Using either x or y alone to select the grid point is not sufficient. It is also not enough to base it on the closest aeroheating point, since the point that is physically closest may have a very different flux based on its distance from the leading edge. In the software, an iterative set of equations is used to find the correct starting point in the aeroheating grid. Then, effective coordinates based on the distance from the leading edge are used for interpolation.

An example mesh is shown in Figure 1. The aeroheating grid is represented by closed circles, and two example nodes in the PATRAN mesh by open circles. The PATRAN mesh is much denser than the aeroheating grid, so for clarity only two example nodes are shown. The solid lines indicate the lines of

nodes in the aeroheating grid. One can see that for any given line of y points, the values are not constant, and for any given line of x points, the values change substantially for each change in y . Looking at example PATRAN node A, one can see that going only by the x coordinate would result in selecting a grid line much farther from the leading edge than is correct. Looking at example PATRAN node B, one can see that the y coordinate cannot be used as the sole criteria either. In fact, due to the relative coarseness and sweep angle of the aeroheating grid, the position of each PATRAN node must be determined based on an equivalent line, parallel to the aeroheating grid at that point. The dashed line in the figure indicates this equivalent line for node A. Then, the true grid cell containing the node can be determined, and the interpolation can be performed based on the equivalent position.

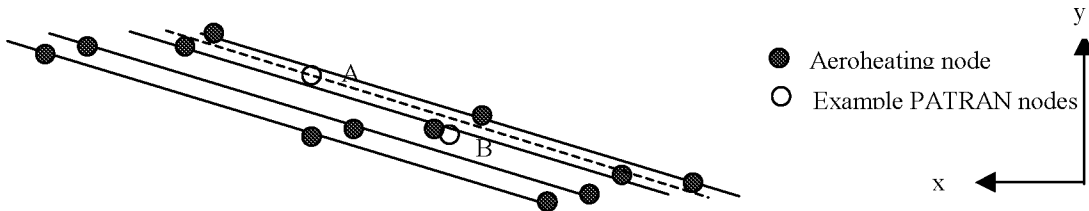


Figure 1. Example interpolation mesh (viewed in 2D).

Second, the aeroheating gridding does not follow a prescribed physical direction. The grid is ordered in the aeroheating program so as to conform to the sweep angle. On a part where part of the leading edge is swept back along positive z , and the other swept along negative z (as illustrated below in Figure 3), the physical ordering of the grid when brought into PATRAN will not be constant. The grid may be ordered such that the array increases in x and decreases in y , or the other way around. Or both values may increase or decrease together in the array. In the y axis (normal to the swept lines), the lines are close to constant value, but not quite. A line of nodes at some given position in the array (say, at the second value of y in each row) may not even be monotonic in y . The FORTRAN needs to be flexible enough to handle these changes in directionality.

Also, the aeroheating grid may not be oriented with the same x and y , and may not have the origin in the same place as the PATRAN model. The software handles changes in the axis orientation and origin position by modifying the values read in from the array, before they are used for interpolation.

ALTERATIONS TO HEAT FLUX

The `umicro.f` subroutine is where factors can be applied to the heat flux value. There are several different conditions where factors are required. Effects on trailing edges, outer edges, coves, and gap regions, are all not completely predicted by the aeroheating code. Thus, factors must be applied to the loads in these regions to achieve an accurate thermal prediction. Regions that will all receive the same factor can be grouped, and a separate boundary condition applied. Then, the identification number of the boundary condition is used as the flag in `umicro.f` to trigger application of a given factor. The position in any of three axes can be used as a trigger for applying a set factor, or as a variable in calculating a spatially dependent factor to apply. The time in a transient solution can also be used as a trigger for changing factors.

In some cases, the region where a factor is required is not a discrete part of the solid geometry. In most cases, the solid geometry is electronically imported from Pro/Engineer. There are often cases where a region is not broken out as a geometric entity on the solid that is imported, but due to aerodynamic considerations it must be treated with a separate factor. This can be done by manually selecting the affected elements, or by setting up a complex logic network of the spatial variables to define the region in question. These methods are somewhat cumbersome and time-consuming. A more straightforward method is to break the base geometry according to the surfaces that are desired. The base geometry will still exist as a solid, and can be handled as such for application of loads and boundary conditions. Faces may be added to the solid that facilitate loads application. One way to accomplish this is by breaking the solid (for example, with a plane), but this leaves multiple solids instead of the original one. A more elegant method is to break

the solid into its constituent surfaces, and split whichever surfaces are necessary for efficient load application. The solid can then be re-assembled from the desired surfaces, leaving a single solid containing all the required faces for loads application.

The aeroheating flux prediction is not reliable at the forward tangency point where the flat section meets the round of the leading edge. A method was developed to make this flux more consistent with CFD predictions. For sections where the aeroheating grid extends to the forward leading edge, the value of each point along the tangency line was replaced by a value calculated using Fay-Riddell methods. This substitution is done using logic in the subroutine where the array is read in.

LEADING EDGE METHOD

The leading edge heating requires another method entirely, since the aeroheating code used for the flat acreage sections is not used on the leading edge. The value of heating is dependent on the trajectory, the leading edge geometry, the angular position on the leading edge, and on the temperature at the leading edge. The code uses basic Fay-Riddell methods to calculate stagnation heating, then modifies those values by the specified sweep angle and body angle. See Figure 2 for an illustration of the angular position (body angle). The Fay-Riddell calculation must be done for each time point in the trajectory. For swept leading edges, the temperature of all nodes at a given angular position may not be constant. Thus, in order to use a correct heat flux for all nodes, the heat flux must be altered based on the local temperature.

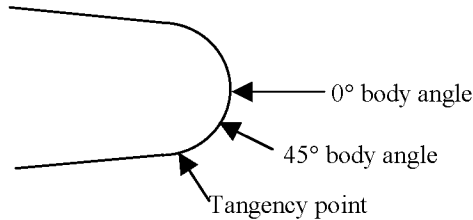


Figure 2. Body angle definition.

For nodes other than the reference node used to calculate heat flux, the flux into the node was factored using the following:

$$Q_{node} = Q_{ref} \frac{T_{stag} - T_{node}}{T_{stag} - T_{ref}} \quad [1]$$

where T_{node} and Q_{node} are the temperature of and flux into the given node, and T_{ref} and Q_{ref} are the temperature of and flux into the node whose temperature is used for heat flux calculation. This was done in PATRAN by making the heat into the leading edge nodes a product of three functions:

$$[Q_{ref}] * \left[\frac{1}{T_{stag} - T_{ref}} \right] * [T_{stag} - T_{node}] \quad [2]$$

VERIFICATION OF FLUX INTERPOLATION

The verification of the interpolation of the flux would at first seem to be a simple matter of evaluating the flux in PATRAN versus the flux from the text formatted input file. However, a difficulty arises in that PATRAN Thermal does not plot flux as one of the standard parameters. The parameter that can be plotted directly from the nodal results file is nodal heating, which is the heat per node. This can be changed to flux

by dividing by the nodal sub-area. To accomplish this, one first needs to generate a file of the nodal sub-areas for each node that receives heating. One simple way to do this is to import the qmacro.dat file into any spreadsheet program, such as Microsoft Excel. The file can be reformatted to give only node number and nodal sub-area. Then, nodes that receive heating via more than one boundary condition must be summed to find their total sub-area. Once this is done, the file can be filtered so that each node appears only once.

The heat per node can be output from PATRAN into a text file by doing a Create_Report from the Results menu, on only the surface nodes (those receiving aerodynamic heating). This text file can then be pulled into the same spreadsheet described above. Once the nodes are in the same order, it is a simple matter to calculate flux by dividing the heat by the nodal sub-area. The sheet of node number versus heat flux can be saved as a text file and pulled into PATRAN via PATRAN's shareware spreadsheet function. A result case can be created from the spreadsheet data, and the flux plotted on the model. The flux from the original text-formatted aeroheating file can be compared graphically by plotting it in Tecplot or a similar plotting program. The flux on an example PATRAN model is shown in Figure 3. This model utilizes 12 separate boundary conditions for acreage heat flux, to capture the discrete regions on the geometry, as well as five regions for leading edge heat flux. The mesh on the PATRAN model is not shown since it is such a dense mesh that it would completely obscure the flux contours (in this model there are more than 45,000 nodes). The flux directly from the aeroheating code, plotted in Tecplot, is shown in Figure 4. The units and scale are withheld due to concerns with data export; however, when the plots are evaluated in their original color format, on the same scale and units, the interpolation and factor application can be directly verified.

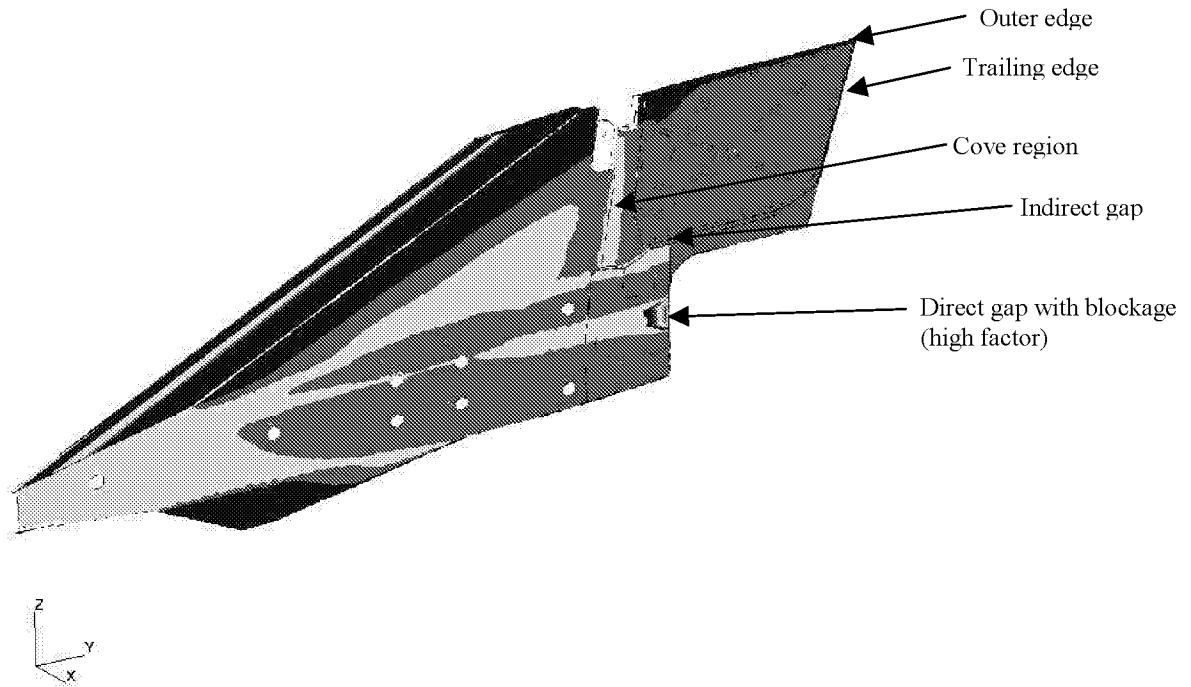


Figure 3. Flux interpolated onto PATRAN model, with factors applied.

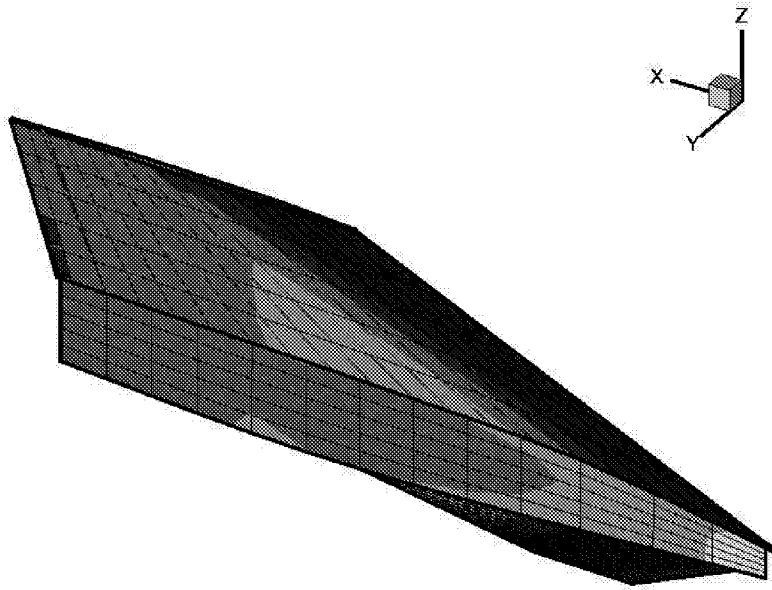


Figure 4. Aeroheating load on original grid.

The flux can also be evaluated versus x, y and z, to obtain a quantitative comparison. The flux from the original file and as interpolated within PATRAN can be output versus x, y and z. Differences between the two can be determined, versus each variable, to assess the interpolation. Exact comparisons of the interpolation can be performed in this manner.

CONCLUSIONS

The prediction of thermal behavior of hypersonic leading edges using PATRAN has been accomplished by development of the user-customizable FORTRAN available. Performance of accurate thermal analysis requires consideration of many factors. Interpolation of the heating loads from an aerodynamic code must be done carefully due to the highly swept and directional nature of the grid, as well as the steep gradients in heat flux away from a leading edge. Interpolation of heat flux, rather than convective coefficient, has been found to make the aeroheating prediction more accurate, as well as facilitating the application of factors. Leading edges with various sweep angles, grid directionality, and grid orientation are all handled by the FORTRAN developed for this interpolation. Factors that are constant, spatially dependent or time dependent can be applied to discrete areas of the geometry. Discrete areas for load application can be created as needed by breaking the original geometry prior to meshing or load application. A method for robust application of the stagnation point heating at the leading edge has been developed. A method for verifying the flux interpolation by plotting flux on the PATRAN model has been established.

ACRONYMNS AND SYMBOLS

| | |
|-----------------------|---|
| CFD | computational fluid dynamics |
| h_c | convective coefficient |
| $Q_{ref, node}$ | Flux at a reference node, and at a given node, respectively |
| $T_{stag, ref, node}$ | Temperature at the stagnation point (fluid), at a reference node, and at a given node, respectively |

ACKNOWLEDGEMENTS

The author wishes to acknowledge the contributions of Phil Yarrington in providing the original software, Chuck Leonard and Vince Cuda for assistance with aeroheating, and Mike Lindell for general modeling assistance.

REFERENCES

1. Ruth M. Amundsen, "Comparison of Integrated Analysis Methods for Two Model Scenarios," Ninth Conference, Workshop and Product Presentation on Thermal and Fluids Analysis Tools and Methods, Cleveland, Ohio, August 31--September 4, 1998.
2. R. M. Amundsen, A. O. Torres, C. P. Leonard, Thermal Analysis Of The Hyper-X Research Vehicle Wing: Mach 7 Design, 1997 Joint Army NAVY NASA Air Force (JANNAF), West Palm Beach, Florida, October 30, 1997.



A STEADY STATE AND QUASI-STEADY INTERFACE BETWEEN THE GENERALIZED FLUID SYSTEM SIMULATION PROGRAM AND THE SINDA/G THERMAL ANALYSIS PROGRAM

Paul Schallhorn and Alok Majumdar
Sverdrup Technology, Inc.
Huntsville, Alabama

Bruce Tiller
NASA Marshall Space Flight Center
MSFC, Alabama

ABSTRACT

A general purpose, one dimensional fluid flow code is currently being interfaced with the thermal analysis program SINDA/G. The flow code, GFSSP, is capable of analyzing steady state and transient flow in a complex network. The flow code is capable of modeling several physical phenomena including compressibility effects, phase changes, body forces (such as gravity and centrifugal) and mixture thermodynamics for multiple species. The addition of GFSSP to SINDA/G provides a significant improvement in convective heat transfer modeling for SINDA/G. The interface development is conducted in multiple phases. This paper describes the first phase of the interface which allows for steady and quasi-steady (unsteady solid, steady fluid) conjugate heat transfer modeling.

INTRODUCTION

Accurate conjugate heat transfer predictions for complex situations require both proper modeling of the solid and flow networks and realistically modeling the interaction between these networks. Proper modeling of the solid network can be easily performed using either classical analytical techniques or with established numerical model tools, such as SINDA/G. Proper modeling of the flow network, however, requires a numerical tool that account for multiple different flow paths, a variety of flow geometries, an ability to predict flow reversal, the ability to account for compressibility effects and ability to predict phase change.

THERMAL CODE

SINDA/G¹ (Systems Improved Numerical Differencing Analyzer / Gaski) is a code that solves the diffusion equation using a lumped parameter approach. The code was developed as a general purpose thermal analysis program which uses a conductor-capacitor network to represent a physical situation; however, SINDA can solve other diffusion type problems. The code consists of two components: a preprocessor and a library. The library consists of a series of subroutines necessary to solve a wide variety of problems. The preprocessor converts the input model deck into a driver FORTRAN source code, compiles and links with the library, then executes the model and generates an output file. One of the main advantages of SINDA

over other thermal codes is that it accepts FORTRAN statements, developed by the user, in the input deck which allow the user to tailor the code to suit a particular problem. It is this ability to add FORTRAN coding to the SINDA input deck which easily allows for an interface with other codes, specifically in the case at hand, a general purpose fluid network flow code.

FLUID CODE

CODE

The Generalized Fluid System Simulation Program² (GFSSP) was developed for the Marshall Space Flight Center's Propulsion Laboratory for the purpose of calculating pressure and flow distribution in a complex flow network associated with secondary flow in a liquid rocket engine turbopump. The code was developed to be a general purpose, one-dimensional flow network solver so that generic networks could be modeled. Capabilities of the GFSSP are summarized below:

- Modeling flow distributions in a complex network;
- Modeling of compressible and incompressible flows;
- Modeling real fluids via embedded thermodynamic and thermophysical properties routines and tables;
- Mixing calculation of real fluids;
- Phase change calculation of real fluids;
- Axial thrust calculations for turbopumps;
- Calculation of buoyancy driven flows;
- Calculation of both steady and unsteady flows (both boundary conditions and geometry can vary with time);
- Choice of first or second law approach to solving the energy equation.

The GFSSP uses a series of nodes and branches to define the flow network. Nodes are positions within the network where fluid properties (pressure, density, etc.) are either known or calculated. Branches are the portions of the flow network where flow conditions (geometry, flow rate, etc.) are known or calculated. The code contains 18 various branch options to model different geometries. These branch options include classical pipe flow with and without end losses, flow with a loss coefficient, non-circular duct, thick orifice, thin orifice, square expansion, square reduction, face seal, labyrinth seal, valves and tees, pump using pump characteristics, pump using horsepower and efficiency, and a Joule-Thompson device.

The GFSSP has additional options including the ability to model gravitational effects, rotation, fluid mixture, a turbopump assembly, the ability to add mass, momentum and heat sources at any appropriate point in the model, and the ability to model multidimensional flow (two and three dimensional flow field calculation).

The GFSSP uses a finite volume approach with a staggered grid. This approach is commonly used in computational fluid dynamics schemes (Patankar³, Patankar and Karki⁴).

OVERVIEW OF SOLID/FLUID INTERFACE

In order to run the two codes concurrently, GFSSP was converted into a subroutine called from an interface subroutine. Figure 1 schematically illustrates the interface call sequence. This interface subroutine, called from SINDA, uses the surface temperature and area of the adjacent solid node along with the flowrate and upstream temperature of the adjacent fluid branch to calculate the heat exchange between the solid and fluid. The interface routine calculates, or has specified, the convective heat transfer coefficient (h). The interface subroutine calculates and distributes the heat back to the solid node and to the downstream fluid node using a technique called "upwinding." Upwinding models the effect of heat addition to the fluid

manifesting downstream of the point of the addition, from a bulk flow perspective. This technique is commonly used in CFD codes to model fluid inertia. Figure 2 illustrates the convective heat transfer calculation scheme.

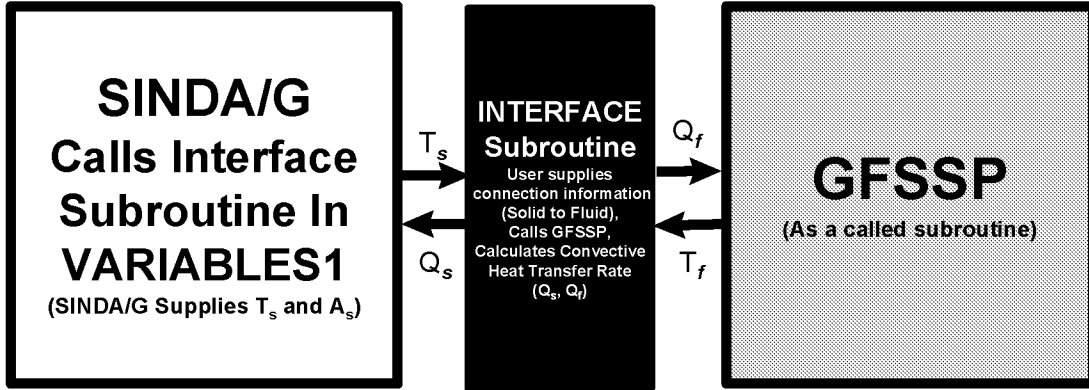


Figure 1: SINDA - GFSSP Interface

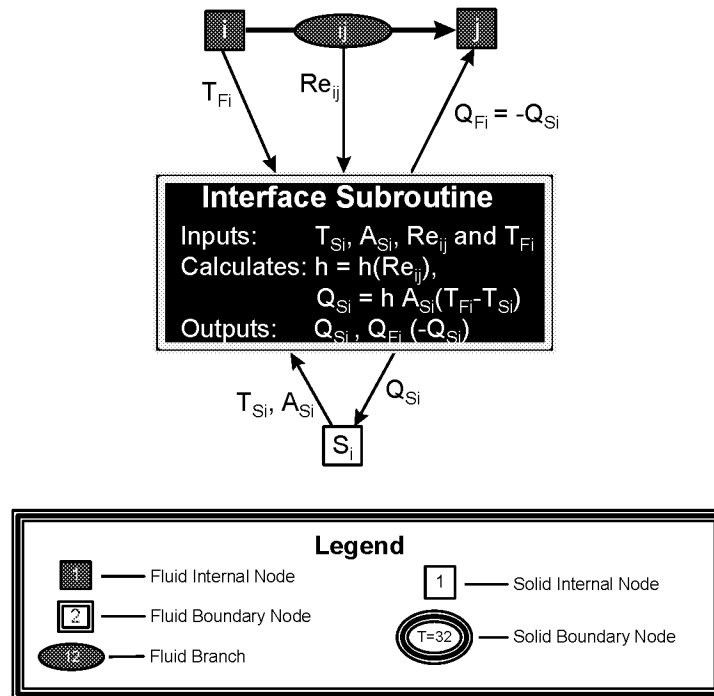


Figure 2: Convective Heat Transfer Scheme Within The SINDA - GFSSP Interface

From the point of view of the two codes involved, therefore, only heat sources/sinks are added at discrete nodes and these heat sources/sinks are updated with every SINDA iteration.

The interface is generalized so that the solid and fluid models can have different levels of discretization, resulting in three different scenarios: multiple solid nodes for a given fluid branch, one solid node for a given fluid branch, and one solid node for multiple fluid branches. These three scenarios are illustrated in Figure 3.

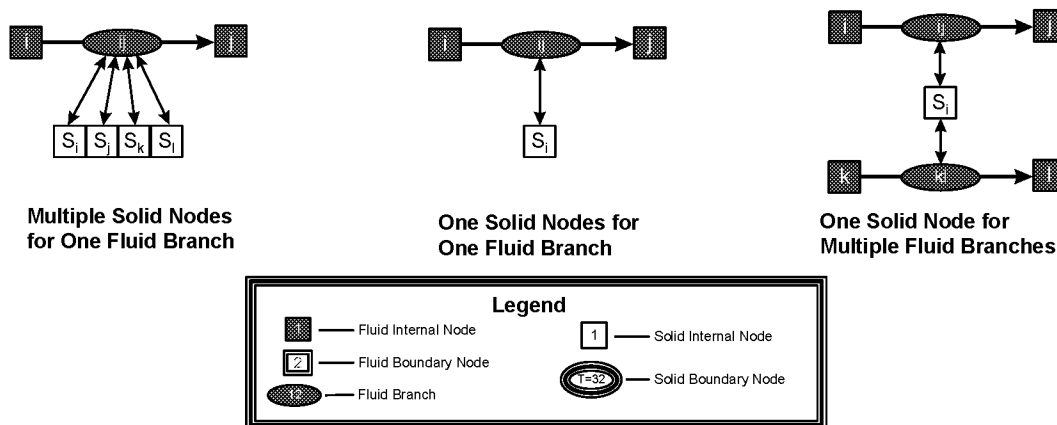


Figure 3: Possible Solid/Fluid Discretization Scenarios

The entire GFSSP common block has been placed into the interface subroutine to allow the user to update the fluid network at every iteration/time-step via this subroutine. The number of solid nodes that connect to the fluid network, the names, temperatures, areas exposed to the fluid network and corresponding heat sources are passed back and forth from SINDA/G and the interface subroutine.

BENCHMARKING

In order to debug and validate the interface, a simple textbook example was chosen as a benchmark case. The benchmark case is a circular rod between two walls with convective heat transfer. The walls are held at 32°F and 212°F, respectively. The rod has a thermal conductivity of 9.4 BTU/ft-hr°R (2.611×10^{-3} BTU/ft-sec°R). The convective heat transfer coefficient between the rod and the fluid is 1.14 BTU/ft²hr°R (3.167×10^{-4} BTU/ft²sec°R), with the fluid temperature set at 70°F. The rod has a diameter of 2.0 inches (0.167 ft) and has a length of 2.0 ft.

The SINDA/G model consists of 10 nodes - 8 diffusion nodes and 2 boundary nodes. The GFSSP model consists of 5 nodes - 3 internal nodes and 2 boundary nodes - and 4 branches. For every four nodes in the solid model, a corresponding fluid branch is assigned. Water was chosen as the working fluid with a sufficient pressure differential between the boundary nodes to supply a flowrate that would allow for an approximately constant temperature without appreciable temperature rise due to shear. The convection coefficient was provided directly to the interface so as to make a direct comparison to an analytical solution. The benchmark case and combined model is shown schematically in Figure 4.

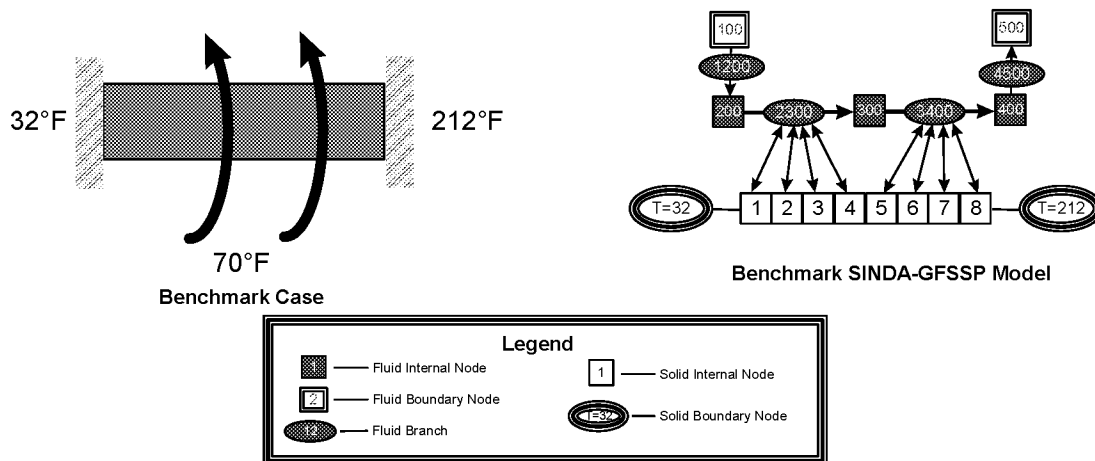


Figure 4: SINDA/G - GFSSP Benchmark Case

The closed form solution of the benchmark case is given in Equation 1, below, and derived in the Thermal Analysis Workbook⁵.

$$T(x) = T_{\text{fluid}} + 4.653e^{1.714x} - 42.650e^{-1.714x} \quad (1)$$

where, x = distance from the cold wall in feet and
 $T_{\text{fluid}} = 70^\circ\text{F}$.

The results of the benchmark combined models are shown with the analytical solution in Figure 5 below. As Figure 5 illustrates, the SINDA/G - GFSSP interfaced prediction lies on the curve of the analytical solution, thus providing a first level validation of the interface.

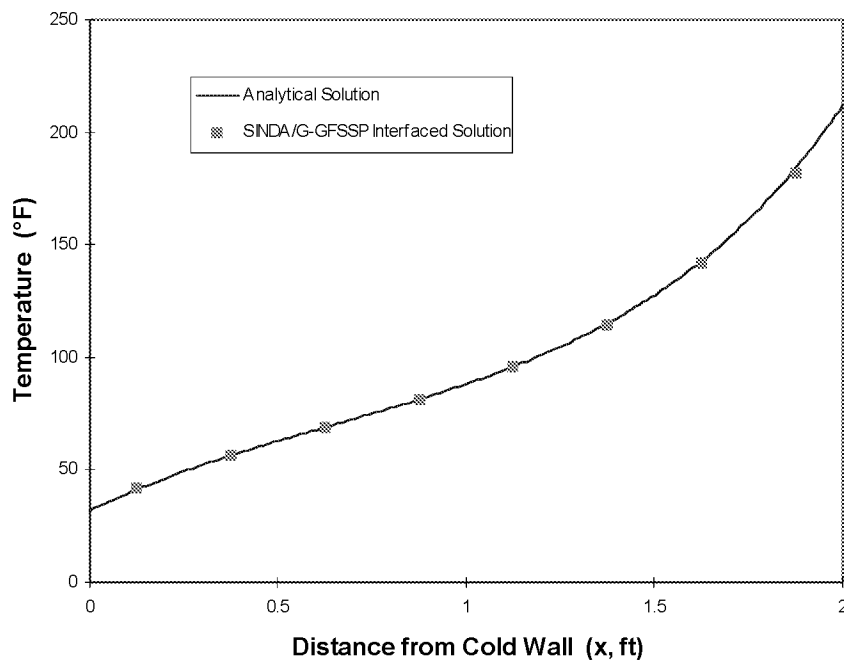


Figure 5: Benchmark Case Results for SINDA/G-GFSSP Model with Analytical Solution

ADDITIONAL TEST CASES

In order to exercise the interface between SINDA/G and GFSSP, three additional test cases were identified which exploit different aspects of the interface.

The goal of the first of the additional test cases (the second test case) was to predict phase change in the fluid model due to heat transfer to the solid. In this case, steam at 215°F and 14.705 psia enters a flow path and flows over a solid bar and exits at 14.700 psia. The back face of the bar is held at 32°F. For simplicity, the convective heat transfer coefficient is set in the interface at a constant value (3.167×10^{-3} BTU/ft²sec°R, an order of magnitude higher than the benchmark case). It should be noted that Figure 6 illustrates the physical situation and the SINDA/G - GFSSP combined models. The results of the modeling effort for case 2 is shown in Figures 7 and 8. Figure 7 illustrates the temperature profile for both the solid and the fluid. Note that the temperature of the fluid remaining constant during the phase change. Figure 8 illustrates the quality of the fluid as a function of location downstream of the inlet. The fluid temperature is superimposed on this figure to show the constant temperature during the phase change.

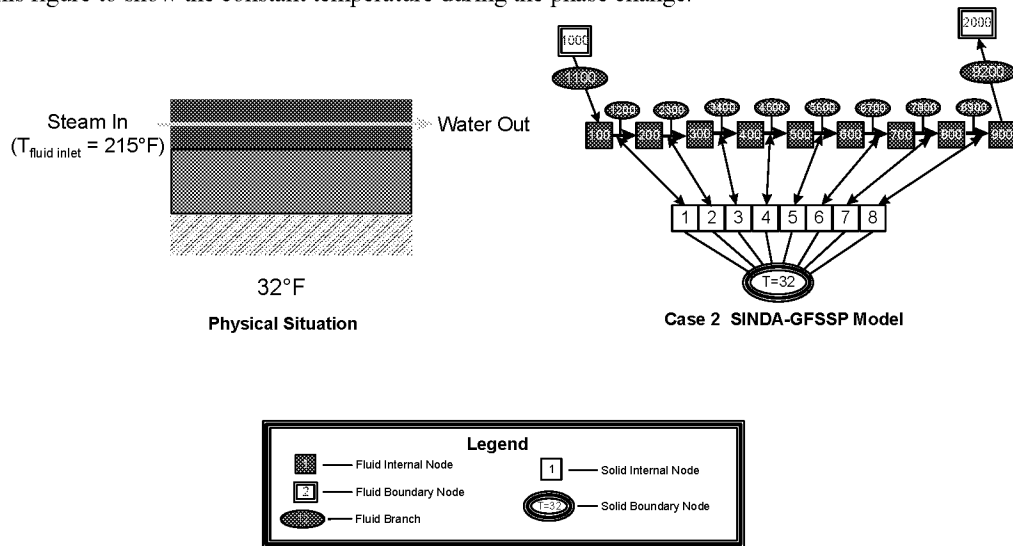


Figure 6: Test Case Two - Physical Situation and Combined Models

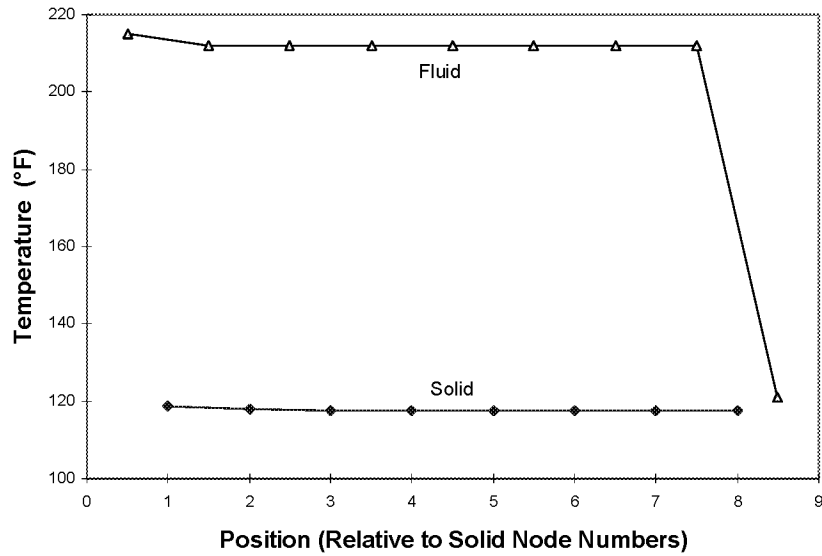


Figure 7: Test Case Two - Temperature vs. Location for both Solid & Fluid Models

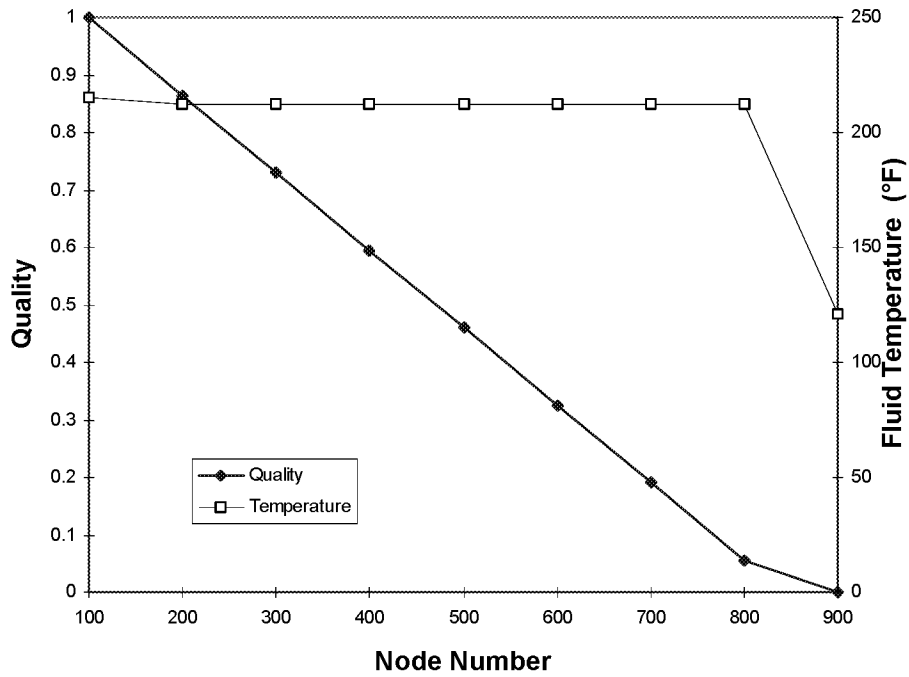


Figure 8: Test Case Two - Fluid Quality vs. Location

The goal of the second of the additional test cases (the third test case) was to control the area of an orifice using a temperature supplied by SINDA/G. In this case, a metal bar is bounded by two fluid streams (one cold, the other hot) in steady state operation as illustrated in Figure 9, below. The bar is 0.25 feet thick, with a thermal conductivity of 18.8 BTU/ft-hr°R (5.22×10^{-3} BTU/ft-sec°R). The bar has been discretized into 35 solid nodes. The cold fluid stream consists of water entering at boundary node 1 with boundary conditions of 70°F and 45.5 psia, and exiting at boundary node 8 with a boundary pressure of 45.0 psia.

The cold stream entrance branch (branch 12) is an orifice with a cross-sectional area of 0.25 square inches and loss coefficient of 0.6. The remainder of the cold stream has a cross-sectional area of 0.5 square inches. The hot stream consists of steam entering at boundary node 11 with boundary conditions of 250°F and 14.75 psia, and exiting at boundary node 18 with a boundary pressure of 14.70 psia. The hot stream entrance branch (branch 1112) is an orifice whose area is a function of the temperature of the adjacent solid node (node 105). The functional relationship between the orifice cross-sectional area and solid node temperature is provided in Equation 2, below.

$$A_{\text{Orifice}} = 0.15 + [0.01 * (T_{\text{solid}} - 155.0)] \quad (2)$$

where, A = Area in square inches
T = Temperature in °F

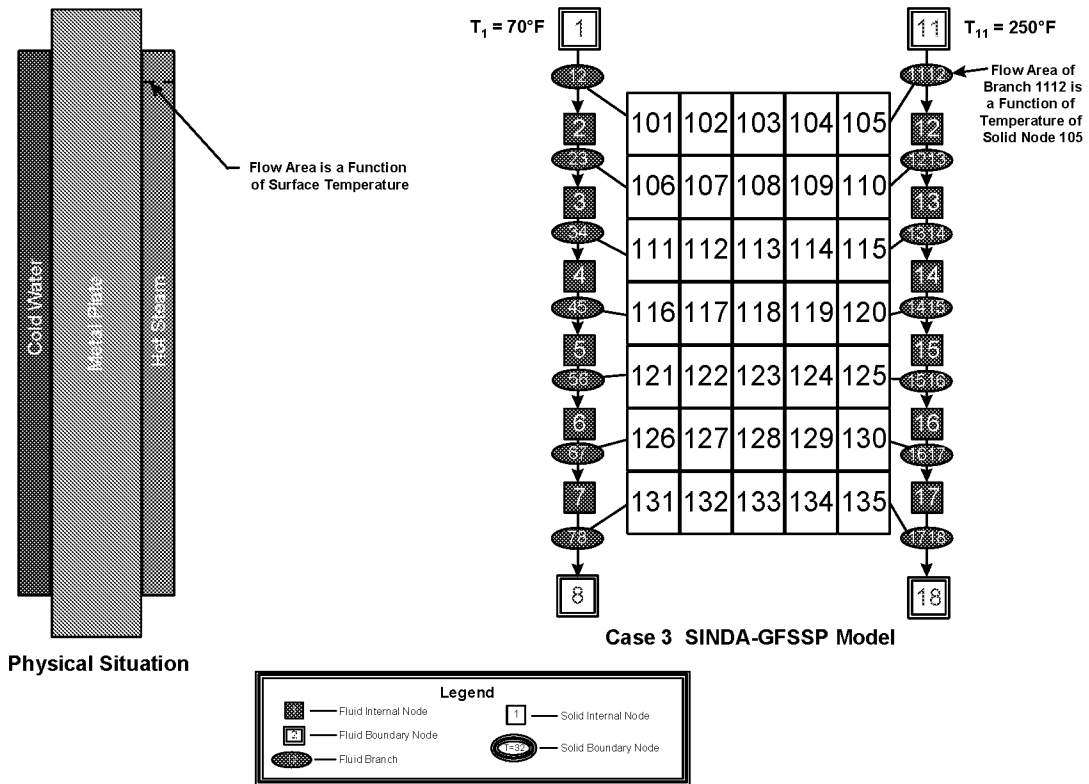


Figure 9: Test Case Three - Physical Situation and Combined Models

For simplicity, the heat transfer coefficient for each stream was set at a constant value: 5.0×10^{-3} BTU/ft²sec°R for the cold stream and 2.5×10^{-3} BTU/ft²sec°R for the hot stream. The results of the modeling effort for case 3 are shown in Figures 10 and 11. Figure 10 illustrates the temperature profile in the bar at the fluid entrance location (solid nodes 101-105), midline (solid nodes 116-120) and fluid exit location (solid nodes 131-135). Figure 11 illustrates the convergence characteristics of the area for fluid branch 1112 as a function of the solid model iteration.

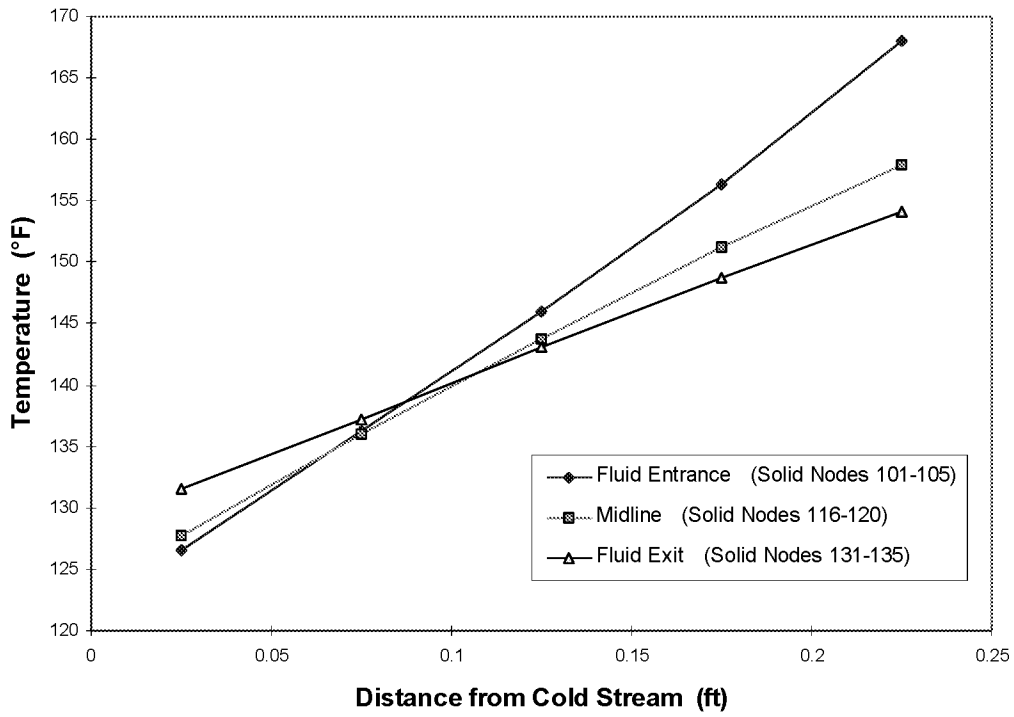


Figure 10: Test Case Three - Temperature Profile in the Solid at Three Locations

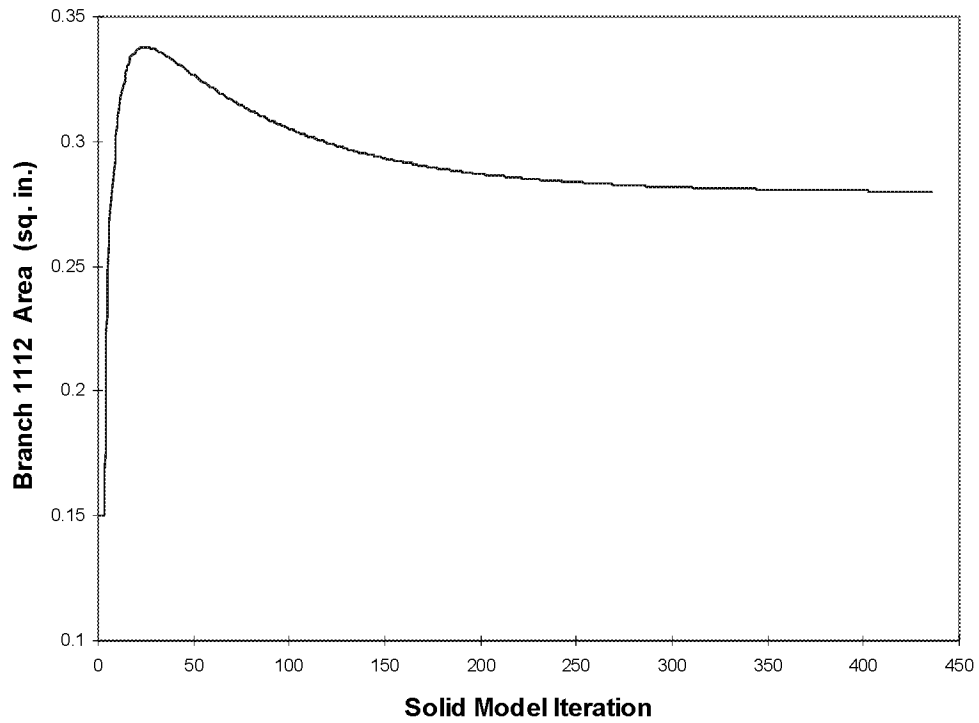


Figure 11: Test Case Three - Fluid Branch 1112 Orifice Area vs. Solid Model Iteration

The final additional test case (test case four) had the goal of a “quasi-steady” operation in which the SINDA model is run in an unsteady mode, and the time step controls the boundary conditions of the fluid loop operating in steady state mode. The physical situation modeled is nearly identical in geometry to test case three, except that the fluid networks’ geometries remain constant (i.e. area of branch 1112 is 0.15 in² and not a function of the temperature of solid node 105). The metal bar is initially at an uniform temperature of 155°F. The cold fluid stream boundary node 1 is initially at 70°F and 45.5 psia; whereas, the cold fluid stream boundary node 8 pressure is set at 45.0 psia. The hot fluid stream boundary node 11 is initially at 250°F and 14.75 psia; whereas, the hot fluid stream boundary node 18 pressure is set at 14.70 psia. The thermal conductivity and convective heat transfer coefficients are the same as used in test case three. The total model run time is 20 hours, with the first 10 hours used to establish a steady state prediction. After 10 hours, the inlet temperature of the two fluid boundary nodes (fluid nodes 1 and 11) become a function of time. Equations 3 and 4 provide the functional relationship between temperature and time for fluid nodes 1 and 11, respectively. Figure 12 illustrates the physical situation and combined models.

$$T_1 = \begin{cases} 70^\circ\text{F} \\ 10t \text{ (}^\circ\text{F)} \end{cases} \quad (3)$$

$$T_{11} = \begin{cases} 250^\circ\text{F} \\ 280 - 4t \text{ (}^\circ\text{F)} \end{cases} \quad (4)$$

where, T = Temperature in °F
 t = time in hours

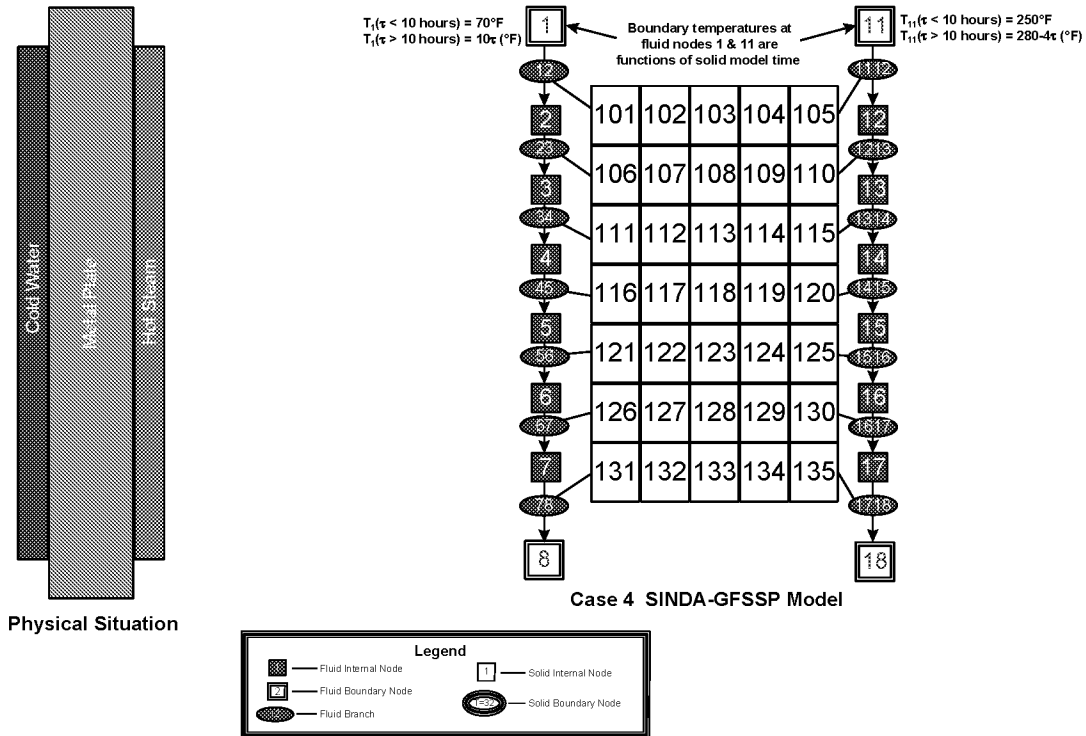


Figure 12: Test Case Four - Physical Situation and Combined Models

The results of the modeling effort for case 4 are shown in Figures 13 and 14. Figure 13 illustrates the temperature/time profile for three solid nodes (116, 118, and 120) and the two inlet fluid boundary nodes.

Figure 14 illustrates the temperature profile in the bar for solid nodes 116 - 120 at several time steps. These figures illustrate the solid temperature following the inlet fluid temperature.

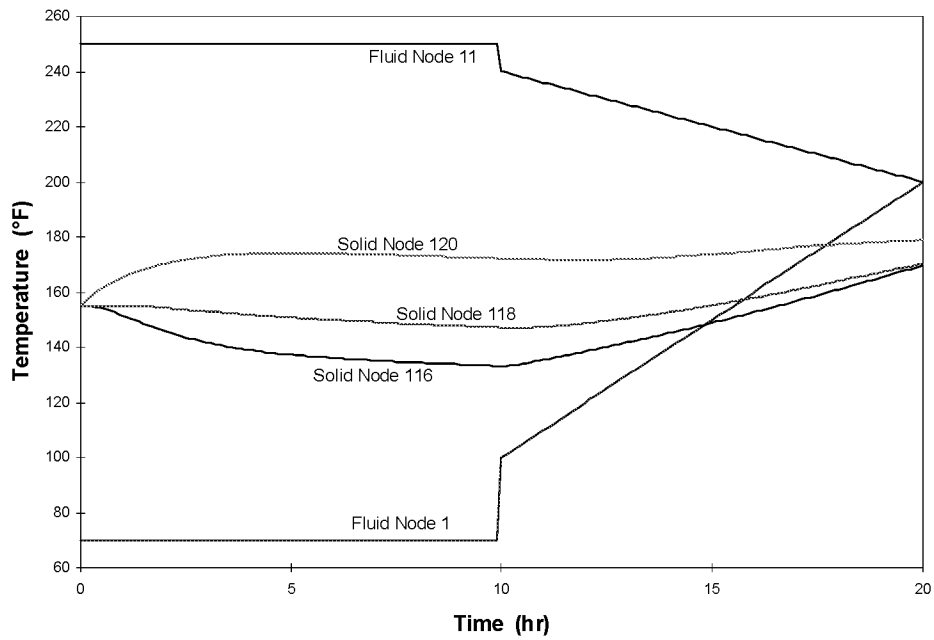


Figure 13: Test Case Four - Temperature vs. Time

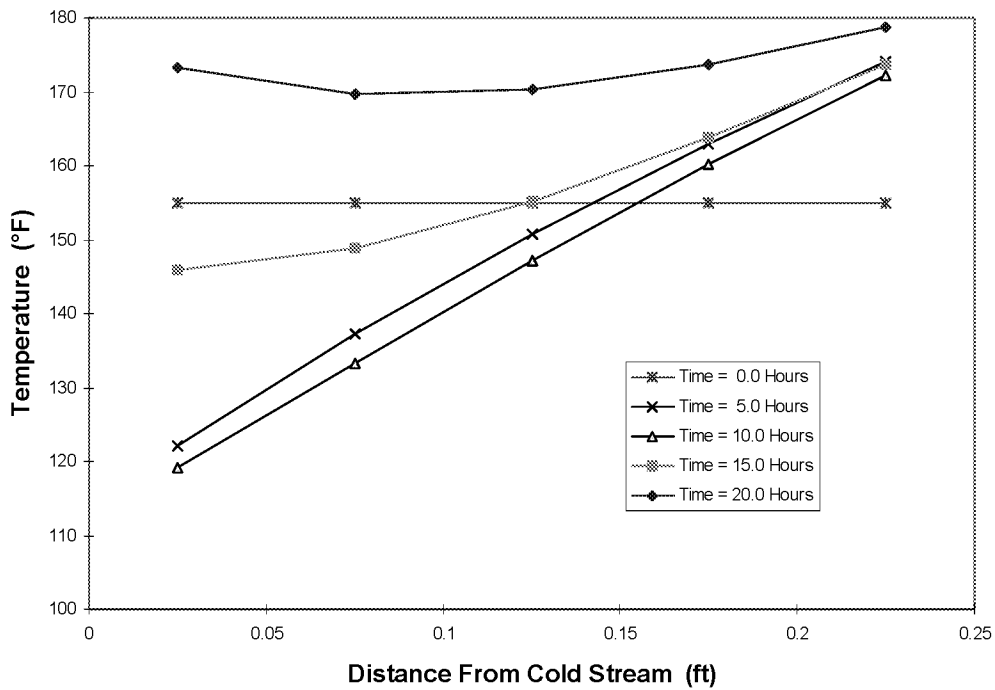


Figure 14: Test Case Four - Midline Temperature Profile

IMPLEMENTATION STATUS

To date, the interface subroutine has been developed to allow for modeling of steady state flow networks with steady or unsteady solid modeling. Development is currently underway for fully unsteady modeling in which the time step for the fluid model may be different than that of the solid model.

CONCLUSIONS

A general purpose fluid network code has successfully been interface with a general purpose thermal analysis code for steady state flow models and both steady and unsteady thermal models. A benchmark case was identified, combined models were constructed and executed. The predictions from the combined benchmark models provided an accurate prediction of the temperature profile in the solid when compared to the analytical, closed form solution. Three additional cases demonstrated fluid phase prediction and control of the fluid model by the solid model's information via the interface subroutine. A status of the implementation was also provided.

ACKNOWLEDGEMENTS

The authors wish to acknowledge the contributions of Mr. Randy Lycans of Sverdrup Technology and Dr. Barry Battista of Tec-Masters.

This work was performed for the George C. Marshall Space Flight Center under contract NAS8-40386, Task Directive 661-007.

REFERENCES

1. Behee, R.: *SINDA/G User's Guide*, Version 1.81, Network Analysis, Inc., 1998.
2. Majumdar, A.K.; Bailey, J.W.; Schallhorn, P.A.; Steadman, T.: *A Generalized Fluid System Simulation Program to Model Flow Distributions in Fluid Networks*, (User's Manual) SvT Report No. 331-201-97-005, NASA MSFC Contract No. NAS 8-40836, October 1997.
3. Patankar, S., *Numerical Heat Transfer and Fluid Flow*, Hemisphere Publishing Co., New York, 1980.
4. Patankar, S., Karki, K., *Documentation of COMPACT-2D Version 3.1*, (User's Manual) Innovative Research, Inc., 1993.
5. Owen, J.W. (ed.): *Thermal Analysis Workbook*, NASA TM-103568, p.1-3-2, January 1992.



A COLLABORATIVE ANALYSIS TOOL FOR THERMAL PROTECTION SYSTEMS FOR SINGLE STAGE TO ORBIT LAUNCH VEHICLES

Reginald Alexander
NASA/Marshall Space Flight Center
MSFC, AL USA 35812

Thomas Troy Stanley
International Space Systems, Inc.
Huntsville, AL USA 35816

ABSTRACT

Presented is a design tool and process that connects several disciplines which are needed in the complex and integrated design of high performance reusable single stage to orbit (SSTO) vehicles. Every system is linked to all other systems, as is the case with SSTO vehicles with air breathing propulsion, which is currently being studied by the National Aeronautics and Space Administration (NASA). In particular, the thermal protection system (TPS) is linked directly to almost every major system. The propulsion system pushes the vehicle to velocities on the order of 15 times the speed of sound in the atmosphere before pulling up to go to orbit which results in high temperatures on the external surfaces of the vehicle. Thermal protection systems to maintain the structural integrity of the vehicle must be able to mitigate the heat transfer to the structure and be lightweight. Herein lies the interdependency, in that as the vehicle's speed increases, the TPS requirements are increased. And as TPS masses increase the effect on the propulsion system and all other systems is compounded. To adequately calculate the TPS mass of this type of vehicle several engineering disciplines and analytical tools must be used preferably in an environment that data is easily transferred and multiple iterations are easily facilitated.

INTRODUCTION

Developing the next generation of launch vehicles is a primary focus of the National Aeronautics and Space Administration (NASA). Several concepts have been proposed, many of which are fully reusable single stage to orbit (SSTO) vehicles. Lowering the cost of placing a payload into orbit drives this idea of a fully reusable vehicle.

Analysis of these concepts is essential to determining which to carry forward into more detail design. According to Malone [1] in the current development process, 90% of the cost is committed in the first 10% of the development cycle. Thus, more design knowledge is needed in the design process to minimize changes. Also, the fidelity of the analyses is critical due to the strong interaction between each of the systems (Figure 1). This interaction is most notable in the SSTO concepts that involve air-breathing propulsion. In these concepts the thermal protection system (TPS) is a critical system. The TPS must protect the air frame structure of a vehicle which flies at 15 to 20 times the speed of sound in the atmosphere before the vehicle pulls up and goes into orbit. The TPS mass affects the mass of the vehicle which affects the propulsion system, the vehicle's ascent trajectory, structure, aerosurfaces and other vehicle subsystems. The TPS can not just be added to vehicle but must be an integral part of the vehicle's mission scenario definition.

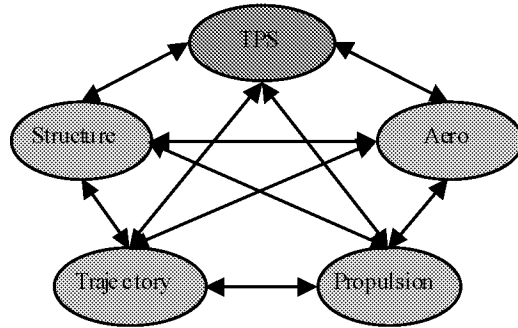


Figure 1. Interaction of Vehicle Systems

THERMAL ANALYSIS

Several engineering disciplines are involved in vehicle analysis and design. This work will focus on the thermal protection system (TPS) analysis. Directly involved in TPS sizing are trajectory analysis and aerothermal heating analysis. To begin assessing the TPS mass requirements for a vehicle the trajectory analyst generates a trajectory that delivers the required payload to the specified orbit. Similarly the analyst calculates the trajectory required for a vehicle’s reentry from orbit. Next the aerothermal analyst calculates the convective heating rates on defined “body points” of the vehicle. TPS materials are selected based on the surface temperatures due to the heating on each defined surface. Finally the thermal analyst calculates the thickness of the TPS material and derives a mass. This process is iterated as often as necessary (time allowing) to achieve an optimum design.

TOOLS

Several disciplines (on different computing platforms and maybe even in different locations) use tools specific to their disciplines to provide input to the analysis process. The Program to Optimize Simulated Trajectories (POST) is used to calculate trajectories and vehicle ascent and reentry performance. The output of this code is a single large text file containing the numerical results for the run. The Miniature Version of the JA70 Aerodynamic Heating Computer Program (MINIVER) is used to calculate aerothermal heating. Its output also is a large set of data containing various information relative to understanding the heating environment of a launch vehicle. The program Systems Improved Numerical Differencing Analyzer (SINDA) is used to calculate the TPS thickness at each body point. It is a numerical solver used to calculate the temperatures of a thermal network of nodes set-up by the user. All of these programs are UNIX based although there are personal computer (PC) versions of SINDA. Other tools used are text editors and spread sheet programs used on desktop PC’s.

PROCESS

The problem with the process described is that those codes often reside on different computing platforms, and have output formats that are not compatible with the data input format required by other tools. Figure 2 shows the process used in the Preliminary Design Office at NASA Marshall Space Flight Center. The vehicle’s ascent or reentry trajectory is generated using POST. Data specifically needed for input into the aeroheating model is extracted and passed via e-mail or by hand to the aeroheating analyst. The aerothermal heating analyst receives this data and uses a spreadsheet program to remove any unnecessary data points. Once this is completed the data is formatted (in the spreadsheet) and transferred from the PC to a UNIX based machine using a File Transfer Protocol (FTP) program. This part of the process is important since

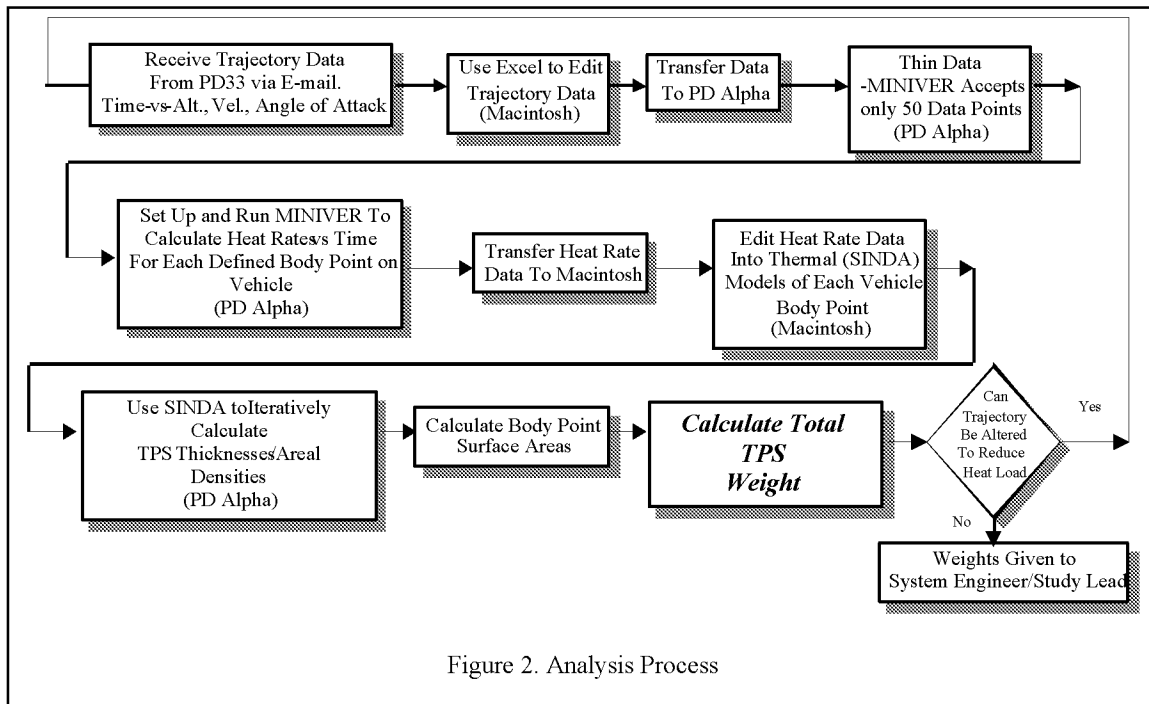


Figure 2. Analysis Process

the aeroheating program, MINIVER, only accepts 50 trajectory points. The data is further thinned using a computer program THINDATA on the UNIX machine that also formats the trajectory data to be used in the MINIVER model. This thinned trajectory file is now transferred to the aeroheating analysts via e-mail or by hand. The aeroheating analysts inputs the geometry of the vehicle and the heat transfer options that will be used to calculate the convective heat rates on the defined number of areas of the vehicle, known as body points. The properly formatted trajectory data is added to the MINIVER input file, and the analyst then executes the program. The program generates much useful information, including the surface temperature, the convective heating rates, and pressure all as a function of time. The thermal analyst only needs the convective heating rate data for his SINDA model of the TPS material at each body point. The temperature data is desired because the temperature of the surface helps the thermal analyst select the TPS material to use at each body point. With these time varying heat rates the thermal analyst calculates the thickness of the TPS material. These heat rates are added into the SINDA models of each of the body points as defined earlier in the analysis. The SINDA models are now used to calculate the insulation thickness at each body point that is required to maintain the structure below its maximum temperature limits. These material thicknesses are then transferred back to the PC using the FTP program where a spreadsheet is used to compile the data. Using these thicknesses and the material density, the spreadsheet calculates the mass of TPS for each body point and sums all of the body point masses into a total vehicle mass. Further iterations of the complete process may be necessary because the TPS mass may be lowered by altering the trajectory to produce a lower total integrated heat load, or a different TPS material may be used that may be superior. If the vehicle moldline is changed, additional runs in trajectory and TPS process are required.

Described in the previous paragraph is what Acton [2] has labeled a *loosely integrated* analysis. This methodology relies heavily on legacy codes and provides very little electronics integration. A goal of this effort is to produce what Acton [2] calls a *tightly integrated* analysis. In this framework the engineers still use the codes with which they are familiar, but these codes are linked or have interfaces between them such that data is easily exchanged between them. Described in the following paragraphs is a tightly integrated analysis tool called RECIPE[®].

A COLLABORATIVE TOOL

Collaboration between these disciplines is essential to adequately size the TPS for this type of vehicle. To increase the fidelity of the models and reduce cycle time for design the vehicle, there must be better interaction and exchanging of data. The development of a tool that interfaces with all of the tools and provides the output in the format necessary to be used by the other codes is desired. This tool would enable the usage of legacy tools such as SINDA, MINIVER, and POST. These codes are well understood by engineers and have become standards in the industry. That is important when trying to establish a very cohesive collaborative environment. This tool would also have to be cross-platform, meaning that it would be usable on and can transfer data between UNIX-based, PC, and Macintosh machines. This is again essential because all engineers have different computing platforms and tools that they use in their analysis.

A solution to the aforementioned problem is RECIPE[®]. This software tool is a cross-platform application capable of hosting a number of engineers and designers across the Internet for distributed and collaborative engineering environments. It provides an interface between the engineering tools of a particular discipline and the other tools that need the data that it provides. The data is provided in the input format required by the designated receiving tool(s). The program allows the user to select from a suite of stand-alone programs that would be used for the desired analysis. For example, in the case of the TPS analysis described above, the users may choose POST as the trajectory analysis tool. But, if any other trajectory programs have been integrated into to the suite of programs, the user may choose it. Once he has executed his program and is satisfied with his results he can publish the data to be used by the analyst who is producing the aerothermal results.

According to Stanley [3] the user interfaces for the RECIPE[®] framework preserve the standard user interaction with the legacy codes while also providing the ability to use the Internet to exchange data and work in collaborative environments. This framework allows the single user to optimize his results from within his discipline and then “publish” them for the world to use in their models. The user interface consists of a graphical user interface (GUI) to direct a portion of the design process. Shown in Figure 3 is the RECIPE[®] executive GUI.

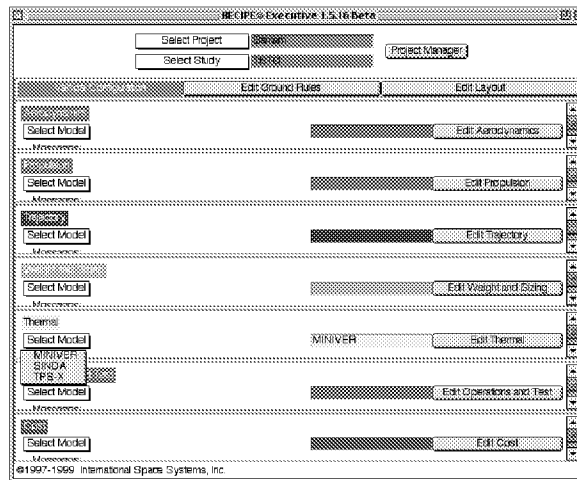


Figure 3. RECIPE[®] Executive GUI

To determine its effectiveness in saving time and achieve a collaborative environment, a Thermal Analysis Test Bed (TATB) was developed that connected only the trajectory analysis, the aeroheating analysis and the thermal analysis. The goal of this activity was to demonstrate the effectiveness of the collaborative environment and show the time savings attained by eliminating much of the data manipulation performed by the users of the programs mentioned.

In the TATB, RECIPE[®] will be performing all of the functions that the user would have to perform with the exception of “building” the initial analytical models. That function is left to the analyst. Figure 4 is a simplified schematic of the TATB analysis process. All of the functions in the boxes are RECIPE[®] functions, while the circles are entry points where the user can assess the calculations of the analysis codes. These entry points are not necessary except to ensure that the inputs are being used properly and that the engineer has confidence that data being generated are correct. Once an iteration is completed and the TPS masses have been calculated, this process may be iterated to approach an optimum design. For example, if the masses are excessive and pose a threat to the vehicle feasibility changes may be made. One of these is altering the trajectory; another may be selecting a more technologically advanced TPS material. Using the previously outlined process, another iteration would likely be too time consuming and labor intensive. But, using this collaborative tool much of the labor has been removed making iterations more attractive. So several trajectories may be analyzed considering the thermal implications, and several different TPS materials may be analyzed to examine the technology implications.

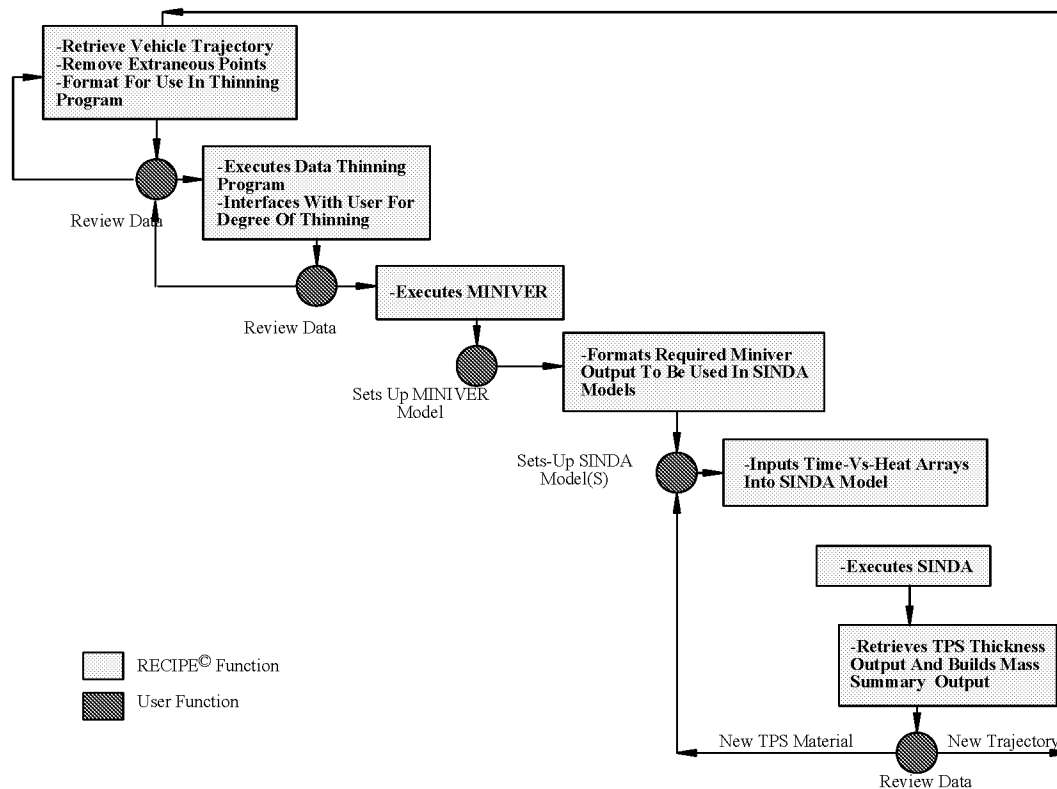


Figure 4. TATB Simplified

PROGRAM EXECUTION/TEST CASE

A sample analysis of an SSTO vehicle TPS was performed to determine the effectiveness of the TATB process. The object of this test was to compare the actual time required to complete the analyses described earlier. The vehicle uses air-breathing propulsion to help it achieve its mission requirements. As stated earlier, this requirement puts a severe burden on the TPS not only during reentry from orbit, but also on ascent where the vehicle may accelerate up to speeds 15 times the speed of sound before going to orbit. For this test case the computer platforms are a UNIX-based DEC ALPHA (on which MINIVER, SINDA, THINDATA and the RECIPE[®] server were run) and an Apple Power Macintosh 9600 (on which the RECIPE[®] client and spreadsheet were run).

First a baseline analysis time was established using the process shown in Figure 2. As stated earlier this process is very labor intensive and requires considerable interaction from the analysts to manipulate the data to be used by the specified tools. Next the process shown in Figure 2 was executed. Figure 3 shows the Executive Graphical User Interface (GUI) for RECIPE[®]. In this Executive GUI under thermal the button “Edit Thermal” was selected. Another set of GUI’s is now available. One in which the MINIVER models may be set up and edited and another where the SINDA models are set up and edited.

In the MINIVER GUI the POST trajectory data that will be used is selected. RECIPE[®] retrieves the specified data and executes the thinning program. This program required some interaction from the user to determine the degree of thinning required to minimize the data to 50 sets. From this point in the process the MINIVER model is set up and run. The engineer is in full control of where and how the data will be executed and used. RECIPE[®] provides model connectivity, file transfer, and data manipulation. In the process of running MINIVER, the vehicle is divided in 40 body points, 20 leeward and 20 windward. There will be a separate output file of convective heat rates and radiation equilibrium temperature both as functions of time. The TATB database enables the correlation of the MINIVER output files with the SINDA models of each body point TPS for which these output files will be input. As is shown in Figure 5 of the MINIVER GUI there is a number of text files that contain the heat rate data for each particular project. The database allows the user to store several projects’ output files. The user next selects the SINDA GUI. The desired MINIVER output file is selected and the corresponding SINDA model is selected. With the MINIVER data edited into the SINDA model program can be executed and the TPS thickness for the selected body point can be calculated. Each body point SINDA model is executed until all of the TPS thicknesses are calculated. For these test cases the SINDA models of each body point will be run in series as the MINIVER data is linked to the SINDA models and the user selects “Run” in the SINDA GUI (Figure 6). Later versions of the code will enable the user to link all of the MINIVER output with the SINDA models and the models will be run with no user interaction.

Finally with all of the TPS sized for the whole vehicle the mass is calculated using a spreadsheet. The output from each of the SINDA runs is linked directly in the spreadsheet and the vehicle TPS mass is calculated based on the area that is represented by the body point and the density of the TPS material.

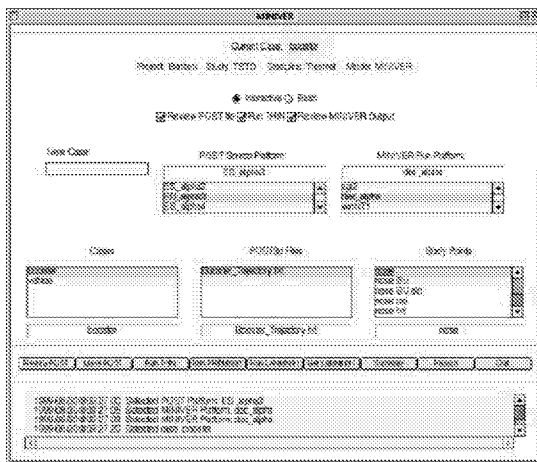


Figure 5. MINIVER GUI

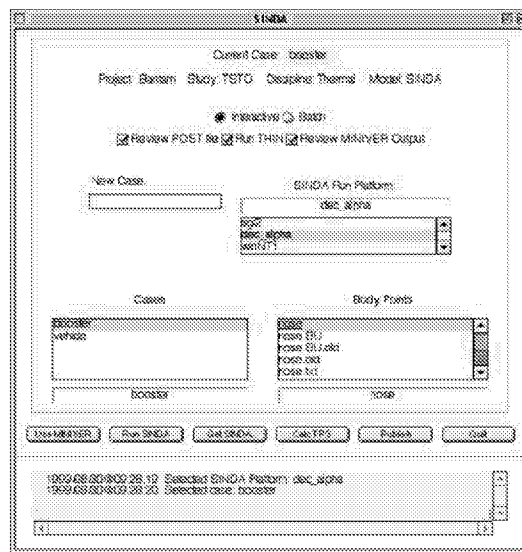


Figure 6. SINDA GUI

RESULTS/COMPARISON

A benchmark was established by executing the process as described in Figure 2 and measuring the time required to complete each step. For this work the process was executed once with no extra iterations. The process is now well understood and can be performed more easily now than in the initial runs when the process was being developed. The data shown in Table 1 is the amount of time required to complete the TPS conceptual analysis of a vehicle before the TATB. The length of time to complete the initial analysis was probably 3 to 4 times the values shown in the tables. But as the users became more familiar with the tools for data manipulation, the length of time to complete the processes became shorter.

The results of using the RECIPE[®] code in the first steps of the TATB process shows that there is about a 20% reduction in the time taken to complete the steps to edit the POST data and to thin it. This reduction is due mainly to the decrease in the time required to move and format data for each of the analysis tools. This tool does not remove the responsibility of the analysts to utilize the legacy codes, but it enables them to integrate the tools to achieve a better set of results more quickly. An even greater reduction in the total time to complete the analysis is expected when file management system portion of the code is completed which will be used to connect the aeroheating data to the thermal models. A conservative estimate of 50% is the anticipated reduction in the analysis cycle time.

| Process Step | Manual | |
|------------------------------------|------------------|------------------------|
| | Step Time (min.) | Cumulative Time (min.) |
| Edit Trajectory | 13 | 13 |
| Thinning Data | 7 | 20 |
| Executing MINIVER | 7 | 27 |
| Editing MINIVER Output | 7 | 34 |
| Editing SINDA models | 2.5 | 36.5 |
| Executing SINDA models | 3.5 | 40 |
| Time To Complete 40 Body Points | | 527 min./9.12 hr. |

Table 1. Time to Complete TPS Analysis Benchmark

BENEFITS

The benefits of this type of tool in concept design are numerous. First, because the tool is cross-platform the designers may use the type computers with which they are most familiar. The information is easily exchanged between disciplines regardless of the platform. The tools will eliminate mistakes in the transfer of input and output files. Also several engineers may be accommodated in the collaborative environment. Thus better designs may be attained sooner. Design/analysis time will be reduced due to increased communication and reduced efforts by the engineers to format the data and pass it on the next user of the information. These factors should enable the team to perform more design iterations thereby reaching an optimum design. Finally it allows the engineer to concentrate on engineering rather than data manipulation. Thus more time can be spent considering the design of the thermal protection system of the vehicle rather than developing the models or formatting the data.

CONCLUSION

Wurster [4] states that the TPS of the entry vehicle, as much as any other vehicle component, requires integrated design at the vehicle system level. The TATB is a demonstration of such a system level tool that will allow users to evaluate TPS concepts, trajectories, structure and how they interact and affect the feasibility and cost of a SSTO vehicle. It is important to note that this test bed is only a part or module in a suite of tools that may be integrated to be used for vehicle design and analysis. Having these integrated these tools gives engineers the ability to collaborate on designs and analyses can only make for higher fidelity designs and analyses that should eventually lead to better and lower cost designs. It has been shown that integrating the tools reduces the amount of time to complete a discipline iteration. This implies that

given the original amount of time for analyses more iterations should be completed which help the designers optimize a vehicle design.

REFERENCES

- [1] Malone, John B., "Intelligent Synthesis Environment." <http://ise.larc.nasa.gov/>
- [2] Acton, D. E., Olds, J. R., "Computational Frameworks for Collaborative Multidisciplinary Design of Complex Systems." AIAA 98-4942, Symposium on Multidisciplinary Analysis and Optimization Sept. 2-4, 1998.
- [3] Stanley, Thomas T., Christenson, R. L., "Integrated Design Modeling in a Design-to-Cost Environment." The Pennsylvania State Propulsion Engineering Research Center 10th Annual Symposium, NASA/MSFC, October 26-27, 1998.
- [4] Wurster, Kathryn E., "Lifting Entry Vehicle Mass Reduction through Integrated Thermostructural/Trajectory Design." *Journal of Spacecraft*, Vol. 20, No. 6 Nov.-Dec. 1983.



COMPUTATION OF COUPLED THERMAL-FLUID PROBLEMS IN DISTRIBUTED MEMORY ENVIRONMENT

H. Wei, H. M. Shang, Y. S. Chen
Engineering Sciences Inc., Huntsville, AL
Phone: (256) 883-6233, fax: (256) 883-6267, e-mail: hwei@esi-al.com

ABSTRACT

The thermal-fluid coupling problems are very important to aerospace and engineering applications. In stead of analyzing heat transfer and fluid flow separately, this study merged two well-accepted engineering solution methods, SINDA for thermal analysis and FDNS for fluid flow simulation, into a unified multi-disciplinary thermal-fluid prediction method. A fully conservative patched grid interface algorithm for arbitrary two-dimensional and three-dimensional geometry has been developed. The state-of-the-art parallel computing concept was used to couple SINDA and FDNS for the communication of boundary conditions through PVM (Parallel Virtual Machine) libraries. Therefore, the thermal analysis performed by SINDA and the fluid flow calculated by FDNS are fully coupled to obtain steady state or transient solutions. The natural convection between two thick-walled eccentric tubes was calculated and the predicted results match the experiment data perfectly. A 3-D rocket engine model and a real 3-D SSME geometry were used to test the current model, and the reasonable temperature field was obtained.

INTRODUCTION

Modeling of the thermal-fluid coupling effects plays an important role in the design and problem diagnostics of liquid rocket engine systems and the sub-systems, such as combustion chamber regenerative cooling channels compatibility, cryogenic fluid management with passive recirculation, etc. The heat transfer between different material and fluid media is also commonly encountered in the engineering practices. The applications include the cooling of electric equipment, material processing and compact heat exchangers. Conventional approach for the thermal-fluid coupling solution very often requires two separate analyses that involve different ways of practice and complexity in each discipline. This study is to merge two well-accepted engineering solution methods, SINDA and FDNS, into a unified multi-disciplinary thermal-fluid analysis method with the aid of patched grid and parallel computing techniques. In the resulting method, the thermal simulating by SINDA and the flow fields calculating by FDNS are fully coupled to get the steady state or transient solutions.

SINDA (Systems Improved Numerical Differencing Analyzer) [1] is a widely accepted thermal analysis software for simulating solid components energy balance using method of conductor-capacitor networks. Other models such as wall radiation heat transfer and one-dimensional fluid flow equations are used to provide boundary conditions for complex systems. On the other hand, many practical applications in rocket engine flow analysis require CFD models, such as the FDNS (Finite Difference Navier-Stokes) code [2], for better predictions of the flow fields which can not be modeled properly with the simplified method used in SINDA. Therefore, merge of these two disciplines into one unified analytical model will enhance the productivity and prediction capability of the thermal-fluid design community.

Since the grids for CFD and SINDA are generated independently, the grid lines of two adjoining regions may align (continuous grids) or may not align (discontinuous grids) with each other. Generally, the CFD model requires finer grids to accurately predict flow fields than the grids used for thermal analyses. So, the grid lines are mostly discontinuous at the interface for most applications. The boundary solution translation procedure must be conservative, stable, and robust for the integrated system. The patched grid approach [3] was used for interface linkage between SINDA and FDNS. We keep all the grid lines and collect the smallest cells. When the heat flux or temperature are exchanged across the interface, the local energy conservation is achieved by integrating upon cell areas. In the iterative procedure, SINDA and FDNS communicate and exchange boundary conditions through the boundary heat transfer coefficient and temperature.

A unique feature of this method is the usage of implicit coupling of SINDA and FDNS by the parallel computing technique. It makes this method better efficiency and stability, and applicable for both steady state and transient solutions. In the integrated SINDA and FDNS system using the PVM library [4], SINDA is run as the master (parent) process, and can initialize several FDNS copies for the slave (children) processes. Both SINDA and FDNS are run with their own input and control data, and are communicating and exchanging boundary conditions with each other through PVM.

The developed numerical method is first tested by a benchmark problem. A 2-D case of the natural convection between two thick-walled eccentric tubes has been simulated. The predicted results match the experiment data perfectly. Then, a 3-D rocket engine model and a real 3-D SSME geometry are used to test the current model. The nozzle flow, the solid wall and the cooling channel flow are all coupled together during the computation.

NUMERICAL METHODS

A FULLY CONSERVATIVE PATCHED GRID INTERFACE ALGORITHM

For 2-D cases, the interface boundary is determined by all of the face grid points of both adjoining zones as shown in Fig. 1. This enables that all the individual points from both zones lie in the interface line and then the interface is unique and accurate.

For 3-D cases, the cell elements are defined using the original grid points in both zones plus the intersection points. So, all of the grid points are used to construct the interface surface. The intersection point of these two set of grid meshes is defined as the intersection of one grid mesh with the image of the nearby cells of another grid mesh on it. For higher accuracy, the finer mesh is selected as the base mesh and the image of the other mesh is calculated based on every cell of the base mesh. If the interface is planar surface, the image can be calculated only once based on the base surface.

Figure 2 shows that a planar surface structured mesh intersect with another unstructured mesh. We keep all the grid lines and collect the resulting cells. They may be no longer quadrilaterals or triangular, but polygons with the edge number less than eight (the maximum edge number of a polygon is eight in the case of two structured grids mesh interface). The polygon doesn't need to be triangulated under the memory and speed consideration. Figure 3 is a cylinder face as a simple example of curved interface in 3-D application. The 6x6 mesh (dark lines) is the base mesh and the 4x4 mesh (light lines) is projected based on every cell of the base mesh to construct the interface mesh.

We use the unstructured grid data format to manage cell element at the interface. The surface in 3-D domain should first be translated into x-y plane by translation and rotation processes. Then cell elements (polygon) are detected. The process includes calculating the intersect point, determining the vortex of polygon, calculating the cell area, defining a pointer to indicate its corresponding cell ID in the original interface meshes of two zones respectively. When communicating across the interface, the local mass and energy conservation is enforced through integration upon cell areas.

ACCELERATE PATCH GRID GEOMETRIC SEARCH BY USING BINARY SEARCH TREE ALGORITHM

In order to construct interface elements, every cell in one mesh must be checked with every cell in another mesh to see if they have intersections. The number of search is the first mesh cell number times the second mesh cell number, $n_1 \times n_2$. However, if we build a binary tree [5] to organize the geometric domain of one mesh, and search the intersected cell by using tree traverse technique, the search effort will be tremendously reduced. Assume every terminal node of the tree holds five cells, then the comparison times needed for one cell in mesh 1 to get the interested cell group in mesh 2 is only $\log_2(n_2/5)$.

Here we use the two end points coordinates of the block diagonal as the key to build the geometric binary search tree. First find out minimum and maximum x, y, z over all the grids in mesh 2. The root represents the cube A(min x, min y, min z)-B(max x, max y, max z). This block is bisected across the x axis and the region for which $X_a < X < (X_a + X_b)/2$ is assigned to left son and the region for which $(X_a + X_b)/2 < X < X_b$ is assigned to the right son.

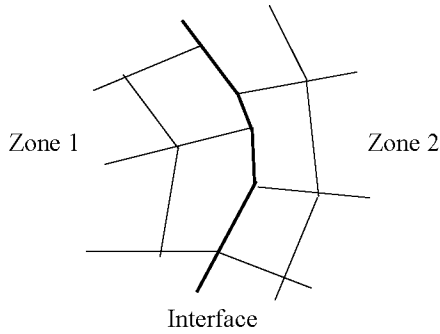


Figure 1. Interface is defined by all of the grid points in 2-D case

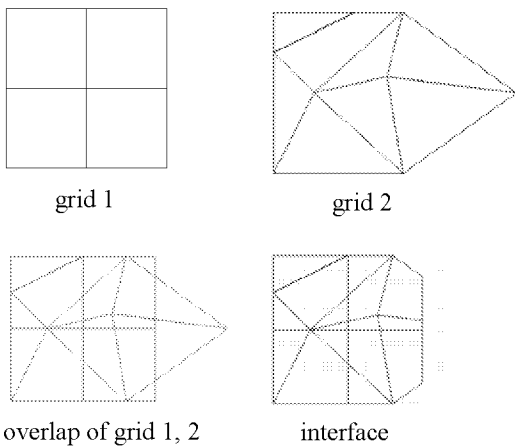


Figure 2 : Patched grid planar surface interface

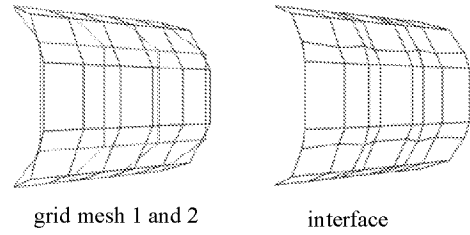


Figure 3. Patched grid curve surface interface

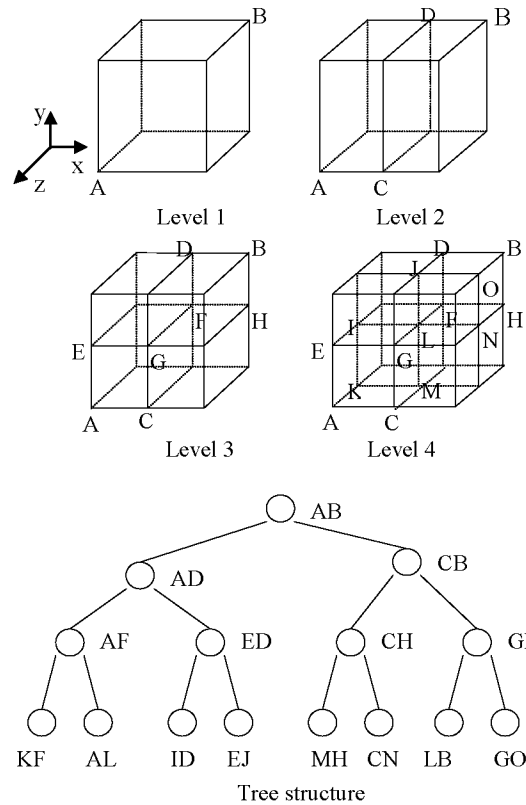


Figure 4. Geometric binary search tree structure.

For each of the node, repeat the process across Y-axis, and then do it across Z-axis. The process is continued by choosing X Y Z in cyclic order. Figure 4 shows the procedure.

Since the region represented by son node is covered by the region represented by its parent, so if a cell is not overlapped with a region represented by a node, the complete set of the regions stored in the sub tree of this node can be disregarded from the search. The geometric search algorithm can be displayed by a recursive procedure as:

1. Check if the cell overlapped with the region represented by the root.
2. If the cell overlapped with the left sub region, search the left tree.
3. If the cell overlapped with the right sub region, search the right tree.

The binary search tree is implemented by using C++ language and coupled with the patch grid subroutine in FORTRAN. For the 3-D nozzle case, there exist two interfaces between nozzle flow and solid wall. One interface is 231 cells in fluid side and 56 cells in solid side, another interface is 891 cells in fluid side and 56 cells in solid side. On IRIS workstation, the CPU time used for constructing the interface is 2.13s with binary search tree and 4.08s without binary search tree. The patched grid process is greatly speed up, and the larger the grid size, the more efficient of this method.

SINDA/FDNS PRE-PROCESSOR

The comprehensive CFD techniques including geometry modeling, grid generation, flow solver and post-processor have been well developed at Engineering Sciences. For the SINDA input file, it generally requires tedious hand calculations of nodal capacitance and conductance. To couple CFD model with SINDA, a preprocessor must be developed first to generate a SINDA input deck for subsequent finite difference analyses. We developed a preprocessor that has two main tasks. The first task is to detach interface boundary grids from SINDA domain grids to prepare boundary grid data for the patched grid manipulation as described above. The second task is to generate SINDA input file, which includes calculation of nodal capacitance and conductance for SINDA network model, setting boundary conditions, taking the CFD-SINDA communication subroutines and finally, writing out the SINDA input file according to its required format. Our preprocessor can take both structured and unstructured grids. It can also take the grid and boundary information directly from the PATRAN neutral file to generate the SINDA input file. And, the post-processor can print out SINDA temperature field in plot3d format, to be viewed through the CFD post-processor.

SINDA AND FDNS COUPLING WITH PVM

The communication between SINDA and FDNS will be achieved through parallel computing approach. In the integrated SINDA and FDNS system using PVM libraries, SINDA will run as master (parent) process, and can initialize several FDNS copies as other slave (children) processes. Both SINDA and FDNS run with their own input and control data, and communicate and exchange boundary conditions each other through PVM. SINDA calculates the conduction heat flux and temperature within the wall nodes, based on the boundary heat transfer coefficient provided by the CFD model. On the other hand, the CFD model uses the SINDA-calculated wall temperatures as fixed boundary temperatures, and solves the energy equation to calculate the fluid temperatures, heat flux and heat transfer coefficient at the boundary. This process is coupled and repeated for steady state or transient solutions.

The program communications between SINDA and FDNS are shown in Fig. 5. After starting PVM daemon, executing SINDA code will automatically start FDNS. The whole process will stop when the iteration number for steady state solution or time progressing for transient calculation exceed the specified values.

ENHANCEMENT OF THERMAL-FLUID COUPLING

In the iterative procedure, SINDA and FDNS communicate and exchange boundary conditions through the boundary heat flux or temperature. We have experienced convergence problem when passing heat flux directly from fluid side to solid side if the thermal conductivity is very small compared to fluid side's effective thermal conductivity. The temperature fields close to solid-fluid interface oscillate during the iteration procedure unless small time step is used. It is found that the numerical stability can be enhanced if we pass the heat transfer coefficient and temperature instead of heat flux.

The heat flux calculated in fluid side can be expressed as:

$$q = h(T_f - T_w)$$

and

$$q = k(T_f - T_w) / \Delta_s$$

where q is the heat flux, h is the heat transfer coefficient, T_f is the fluid temperature at the grid adjacent to the wall, T_w is the wall temperature, k is the thermal conductivity and Δ_s is the normal distance between the grid and wall. So the heat transfer coefficient of laminar flow can be calculated as

$$h = k / \Delta_s$$

where, for turbulent flow, h is given by the turbulence model.

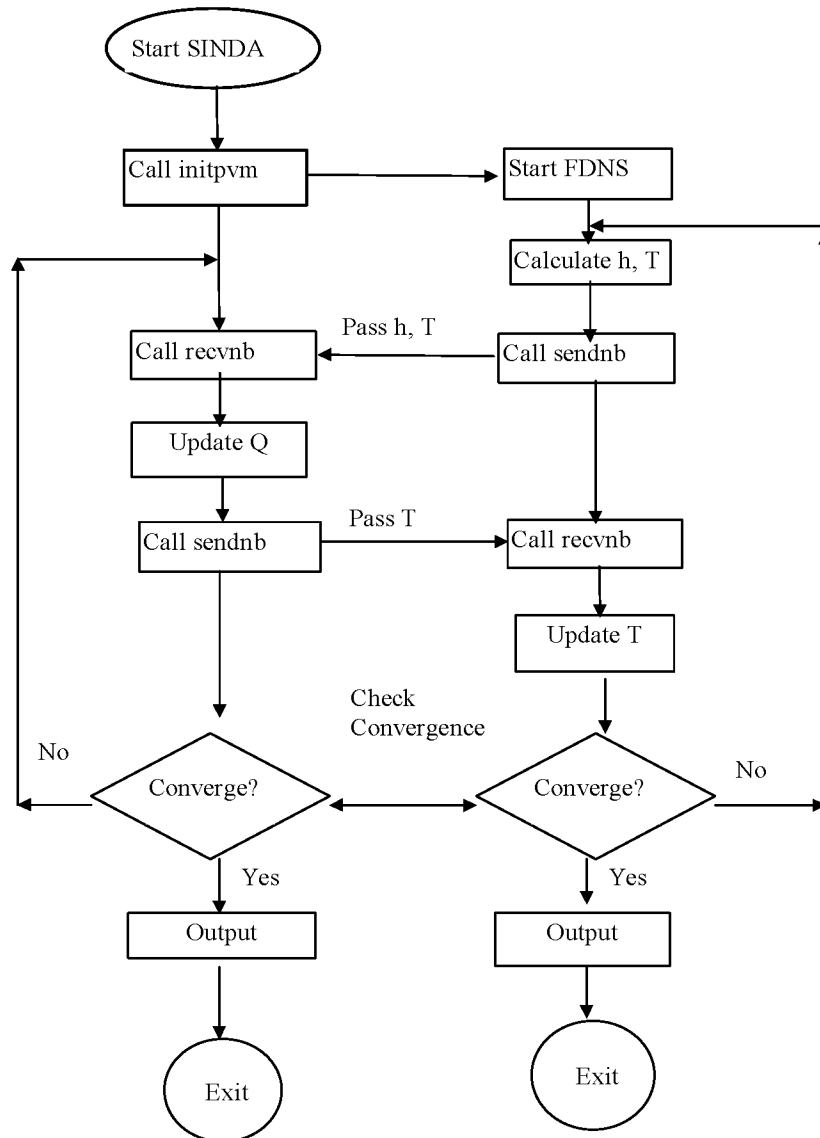


Figure 5. Communication between SINDA and FDNS

NUMERICAL RESULTS

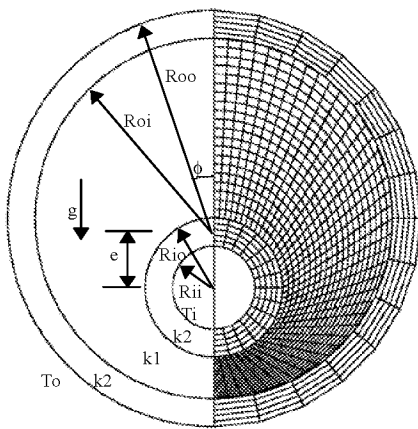
THICK-WALLED ECCENTRIC TUBES CONJUGATE HEAT TRANSFER

The conjugate heat transfer between eccentric tubes is calculated by the integrated CFD-SINDA model, where the FDNS code is used to solve the natural convection and SINDA is used to solve the tube wall heat conduction. Figure 6 gives the geometry and the boundary conditions for this problem. The inner surface of the inner tube and the outer surface of the outer tube are kept at different fixed temperatures, T_i and T_o . The flow between the tubes is induced through the buoyancy force caused by temperature gradient. According to the experiments conducted by Kuehn and Goldstein [6], the Prandtl number of the fluid is 0.7, the Rayleigh number based on the length scale $(R_{oi}-R_{io})$ and the temperature difference (T_i-T_o) is taken to be 4.93×10^4 .

Two types of grid systems denoted as Grid 1 and Grid 2 are used. In Grid 1, the grid mesh is 41×21 for the fluid and 41×6 for inner and outer tube walls respectively. The grid lines are continuous at the interface. In Grid 2, the grid size is 41×21 for the fluid but 15×6 is used for the solid walls. The grid lines at the interface are discontinuous for Grid 2 and the patched grid technique is utilized.

For very large conductivity ratio C between solid and fluid (i.e. $C=10^4$ for copper: air), the tubes are indicated to be isothermal. The numerically predicted temperature distributions at $\phi=0^\circ$ and $\phi=180^\circ$ are compared with the experimental data of Kuehn and Goldstein [6] in Fig. 7. η represents the distance from the innermost tube wall, which is normalized by the distance between the outermost and the innermost walls. The dimensionless temperature is defined as $(T-T_o)/(T_i-T_o)$. From the figure we can see that the Grid 2 can give same results as Grid 1 and all are in good agreement with experimental data.

We simulated two different conductivity ratio cases, one for C equals to 1 and another for C equals to 10^4 , the latter one corresponding to copper and air. Figure 8 shows the streamlines and the temperature contours. It is clear that the bigger the conductivity ratio the smaller the temperature gradient across the wall. When the C value is very large, the Bi number (defined as thermal conductivity ratio of solid to fluid) is very small and the wall is almost isothermal. That is the case for copper and air. This is verified in both Fig. 7 and Fig. 8 for different conductivity ratios. For the case of $C=1$, the transient solutions at $t=1s, 5s, 10s$ are shown in Fig. 9.



$$\begin{aligned} R_{oi}/R_{io} &= 2.6, & R_{ii}/R_{io} &= 0.6, \\ R_{oo}/R_{io} &= 3.0, & e/(R_{oi}-R_{io}) &= 0.623 \end{aligned}$$

Figure 6. Geometry and Grid 2 for thick-walled eccentric tubes conjugate heat transfer.

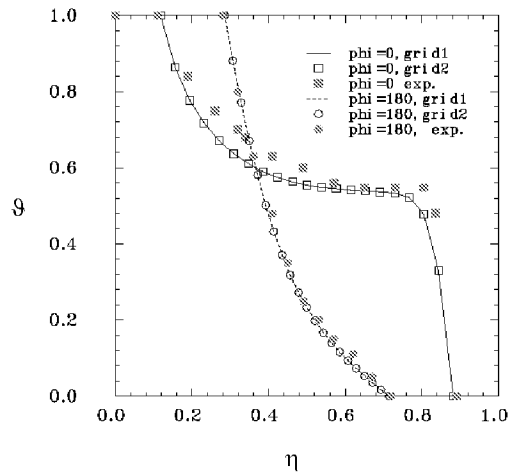


Figure 7. The dimensionless temperature vs. normalized distance between the tube walls for $\phi=0^\circ$ and 180° .

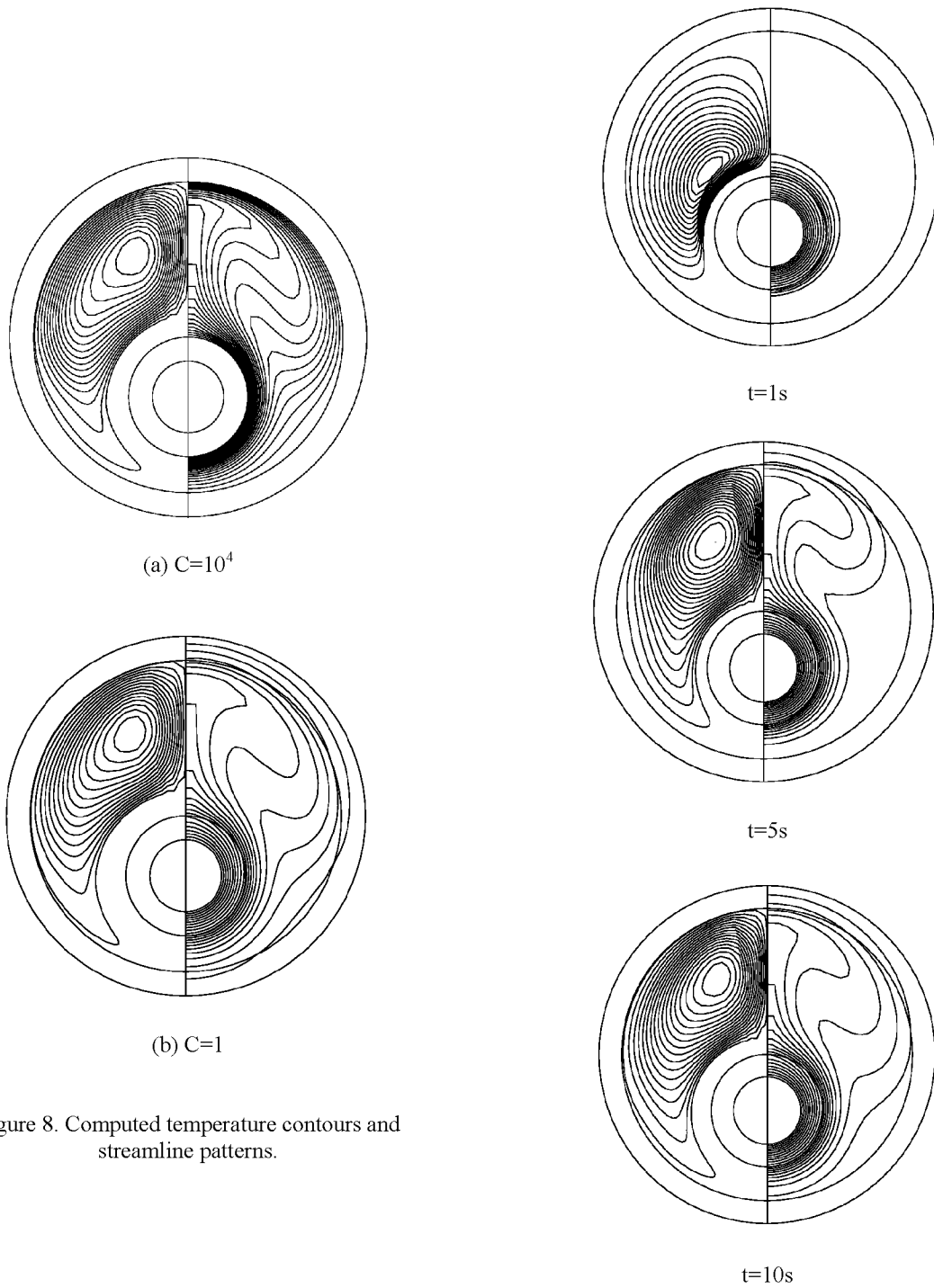


Figure 8. Computed temperature contours and streamline patterns.

Figure 9. Flow pattern and temperature field developing transient process for $C=1$.

3-D ROCKET ENGINE

Development of the algorithm for running multiple copies of FDNS for flow fields with a SINDA model for heat conduction is the solid component. The 3-D rocket engine model is selected as a test case. As shown in Fig. 10, this model consists of a hot gas flow part for FDNS nozzle flow model, a solid metal wall part for SINDA thermal model and two outer flow passages for FDNS cooling channel model. The nozzle gas flow is a compressible flow, and the cooling channel water flow is an incompressible flow. The grid size and initial conditions for each model are shown in Fig.10. For better observation, solid wall and cooling channel is showed apart from the nozzle.

SINDA runs with two copies of FDNS simultaneously. SINDA and each copy of FDNS use their own input and control data. SINDA runs as a master process and initialize two FDNS children processes. Figure 11 (a) shows the overall view of the temperature field including the hot gas nozzle flow solved by FDNS, the solid wall block solved by SINDA, and the outer cooling channel flow solved by FDNS. Enlarged views near location b, c, and d, indicated in Fig. 11(a), are shown in Fig. 11(b), 11(c), and 11(d) respectively. The gapes shown in Fig. 11 are caused by the differences in grid densities between the FDNS model and the SINDA model. Computationally, there is no gapes between these two models. The patched grid interface model enforces the energy conservation across arbitrarily patched interface grids between FDNS model and SINDA model. Reasonable temperature contours and variations across the fluid-solid interfaces are observed in Fig. 11.

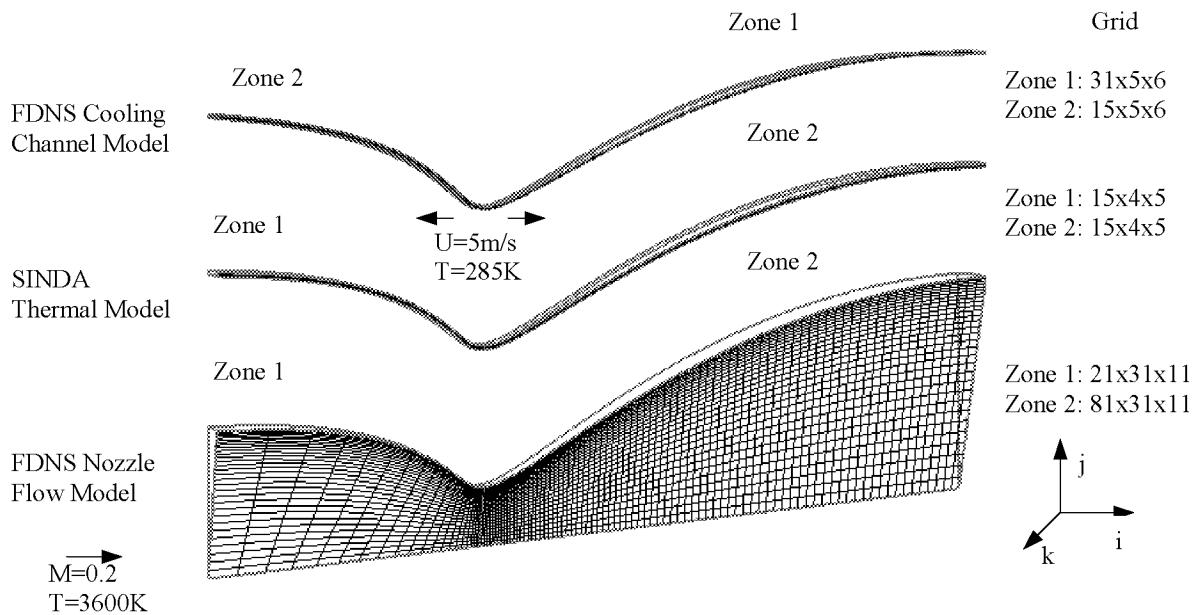


Figure 10: SSME nozzle and coolant channel flow configuration

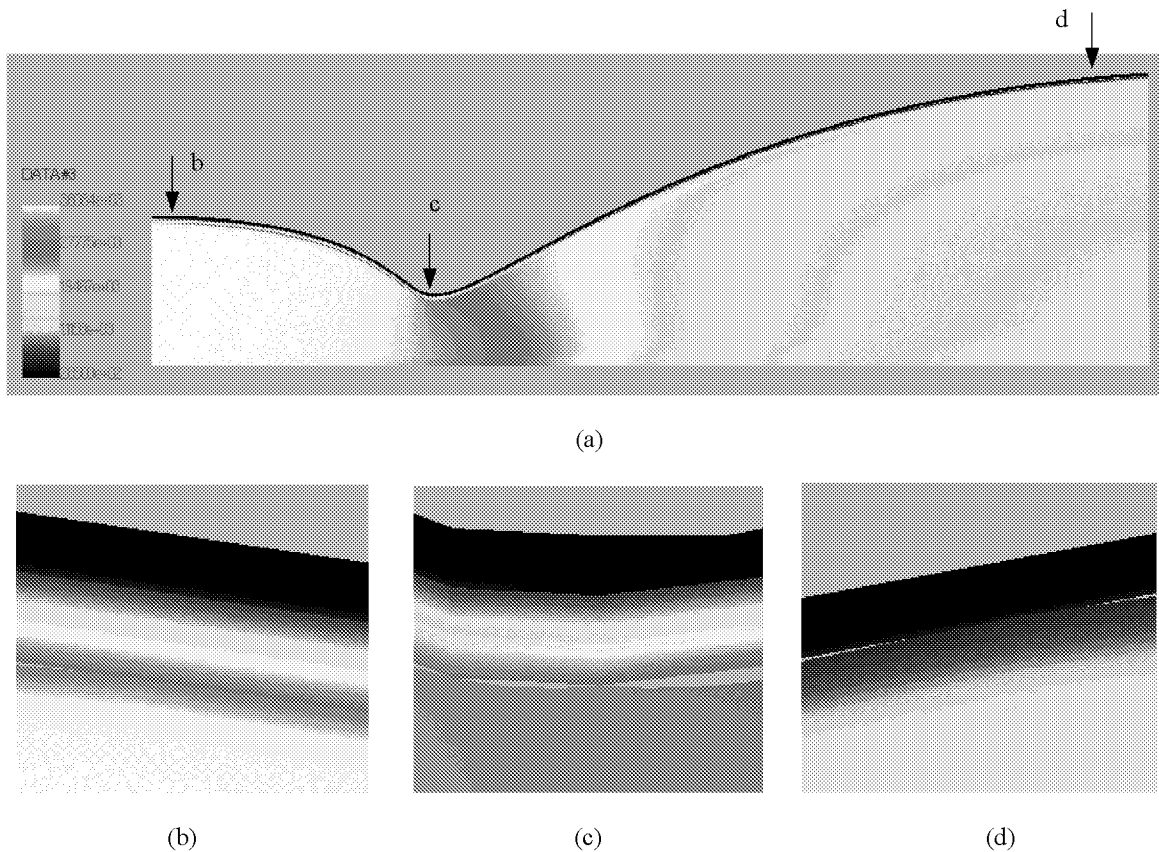


Figure 11: Temperature field of a 3-D SINDA/FDNS coupled solution.
 (a). Full view. (b) (c) (d): Coolant, solid and main flow interfaces at different sections.

3-D SSME

A real geometry SSME nozzle flow with coolant channel flow and channel solid heat conduction is calculated using the new developed SINDA/multiple-FDNS simulation tool. Figure 12 shows the system configuration and grid mesh distribution. The coolant channel is showed apart from the SSME nozzle for clear observation. The hot gas flows in at uniform velocity with the Mach number of 0.2 and temperature of 3600K. Liquid hydrogen enters the coolant channel at velocity of 0.51m/s, which results in the coolant mass flow rate of 29.45lb/s for the 550-channel design. The hydrogen properties at pressure of 5000 psia and temperature of 54K are used in the calculations.

Figure 13 shows the temperature fields of 3-D SSME hot gas flow, coolant flow and coolant channel wall heat conduction by SINDA/multiple-FDNS coupled solution. Where, Fig. 13(a) is the full view in the middle cut of x-y plane. Fig. 13(b) gives the enlarged view of coolant, solid and main flow interfaces at the location (b) indicated in Fig. 13(a). Fig. 13(c) is the cross section temperature contours (in y-z plane) at the location (c). Due to the grid lines are discontinuous at the interfaces of coolant flow and channel wall, the temperature contour lines also show some discontinuity by the graphics package. The gape between hot gas flow and the channel wall is because of the x-location of the hot gas cross section and x-location of the channel wall and coolant flow cross section are not exactly the same.

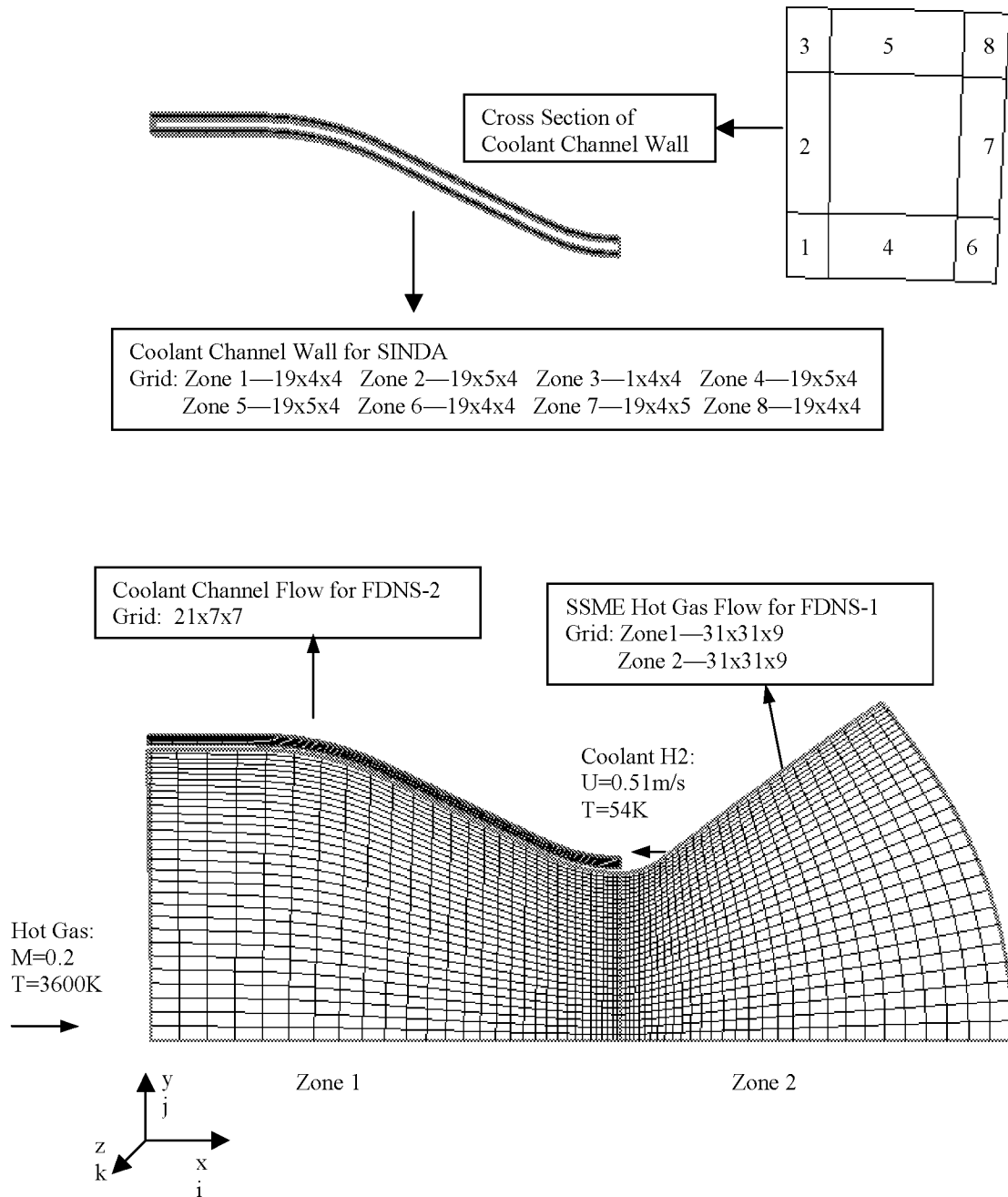
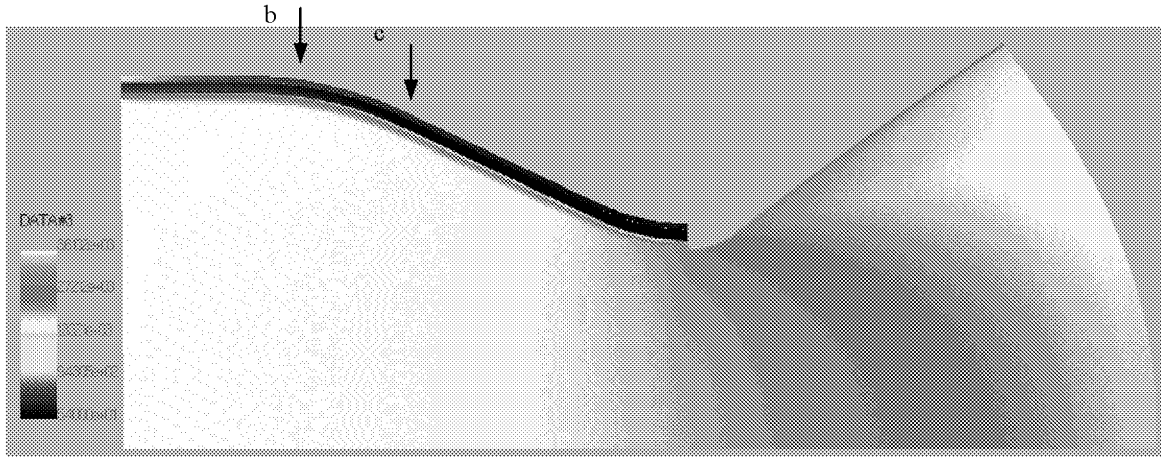
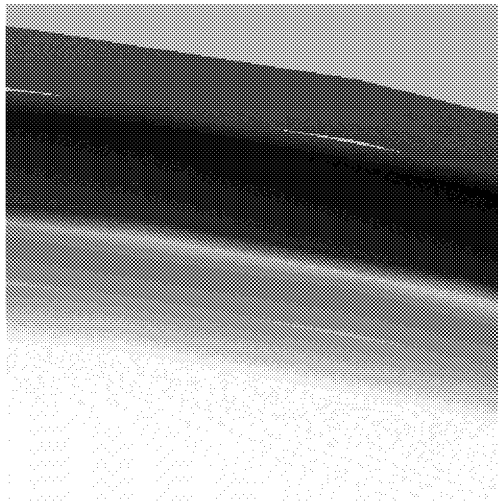


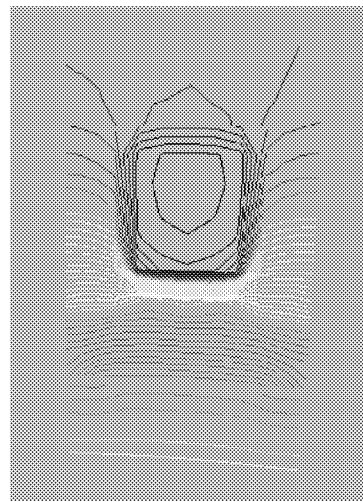
Figure 12. 3-D SSME nozzle flow with coolant channel configuration for SINDA/multiple-FDNS simulation.



(a)



(b)



(c)

Figure 13: Temperature fields of 3-D SSME hot gas flow, coolant flow and coolant channel wall heat conduction by SINDA/multiple-FDNS coupled solution.
 (a) Full view. (b) Coolant, solid and main flow interfaces. (c) cross section temperature contours

CONCLUSIONS

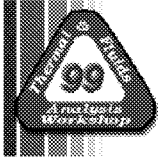
The integrated SINDA-FDNS model can effectively solve the coupled thermal-fluid problems. The fully conserved patched grid algorithm can ensure the energy conservation across the solid-fluid interfaces. The state-of-art parallel computing technique makes SINDA and FDNS running and exchanging information every time step. The successful implementation of SINDA model starting multiple copies of FDNS completed the entire model building. The resulted thermal-fluid model will be used for typical liquid rocket engine thermal-fluid analysis. It can serve as a reliable modeling tool in the aerospace and civil engineering industry.

ACKNOWLEDGMENT

This work is performed under the support from NASA Marshall Space Flight Center with the contract NAS8-98066. The authors would like to acknowledge the technical suggestions from Dr. T. S. Wang of NASA Marshall.

REFERENCES

1. SINDA/FLUINT-Systems Improved Numerical Differencing Analyzer and Fluid Integrator, Version 2.6, NASA/Cosmic Library.
2. Y.S. Chen: "FDNS-a General Purpose CFD Code, User's Guide, Version 3.0," ESI-93-01, May 1993.
3. G. H. Klopfer and G. A. Molvik: "Conservative Multizonal Interface Algorithm for the 3-D Navier-Stokes Equations," AIAA-91-1601.
4. Geist, A., Beguelin, A., Dongarra, J., Jiang, W., Manchek, R., and Sunderam, V., "PVM: Parallel Virtual Machine - A Users' Guide and Tutorial for Networked Parallel Computing," The MIT Press, Cambridge, MA, 1994.
5. J. Bonet and J. Peraire: "An Alternating Digital Tree (ADT) Algorithm for 3D Geometric Searching and Intersection Problem," International Journal for Numerical Methods in Engineering, Vol. 31, pp. 1-17, 1991.
6. Kuehn, J.H., and Goldstein, R.J., "An Experimental Study of Natural Convection Heat Transfer in Concentric Horizontal Cylindrical Annuli," *Journal of Heat Transfer*, Vol. 100, pp. 635-640, 1978.



MULTI-DISCIPLINARY COMPUTING AT CFDRC

W.J. Coirier, A.J. Przekwas, and V.J. Harrand

wjc@cfdr.com; ajp@cfdr.com; vjh@cfdr.com

CFD Research Corporation

215 Wynn Dr.

Huntsville, AL 35805

ABSTRACT

This paper describes two methodologies to perform Multi-Disciplinary simulations involving coupled fluid, thermal, structural, and electromagnetic interactions. The two approaches taken, termed tightly-coupled and loosely-coupled, yield two very different numerical and resultant software implementations. The tightly-coupled approach follows a more traditional integration strategy, where the different application modules (flow, heat, structures) are bound tightly together in a single package. This approach has distinct advantages for problems that are computationally stiff and require a more tightly-coupled/implicit solution strategy. The loosely-coupled approach defines a heterogeneous, distributed computing framework within which the different applications operate, allowing not only data exchange, but also invocation of functionality amongst the different applications. Unique interfacing procedures permit the rapid introduction of new applications into the framework, and allow independent, multi-disciplinary integration of different vendor-supplied software. Both approaches are being actively pursued at CFD Research Corporation. This paper briefly describes the two approaches and presents example applications of both to Aerospace and Micro-Electro-Mechanical Systems (MEMS).

SECTION I. INTRODUCTION

It is becoming widely recognized that Multi-Disciplinary Analysis, Design and Optimization is necessary to extract the highest possible performance for Aerospace vehicles [Goldin, et al., 1998; Singhal, et al., 1999]. This also holds true for a number of other areas, such as Automotive products, Bio-Medical devices, and especially for Micro-Electro-Mechanical Systems (MEMS) [Stout et al., 1999; Przekwas, et al. 1999]. Due to the explosive increase in computing power and resultant decrease in cost, computationally intensive applications unrealizable just a few years ago are now viable. Work in the improvement of algorithms for uni-disciplines will always be important and necessary, but the near term growth in the application of scientific computing based analysis will be through the software integration of existing technologies. This paper describes two approaches being taken to perform Multi-Disciplinary simulations involving coupled fluid, thermal, structural, and electromagnetic interactions. The two approaches, loosely termed tightly-coupled and loosely-coupled, yield two very different numerical and resultant software implementation strategies.

The tightly-coupled approach, used in the CFD-ACE+ system, follows a more traditional integration strategy, where the different application modules (flow, heat, structures) are bound tightly together in a single package. This approach has distinct advantages for problems that are computationally stiff/ill-conditioned, and require a more tightly-coupled/implicit solution strategy.

The loosely-coupled approach, used in the Multi-Disciplinary Integrated Computing Environment (MDICE), defines a distributed computing framework within which the different applications operate, allowing not only data exchange, but also invocation of functionality amongst the different applications. This permits the rapid introduction of new applications into the framework, and allows independent, multi-disciplinary integration of different vendor-supplied software.

Both approaches are being actively pursued at CFD Research Corporation. This paper briefly describes the two approaches and presents example applications of both to Aerospace and Micro-Electro-Mechanical Systems (MEMS).

SECTION II. TIGHTLY-COUPLED ANALYSIS: CFD-ACE+

The tightly-coupled approach to solving Multi-Disciplinary problems is represented by the CFD-ACE+ system. This system solves the governing equations for a variety of physical processes, including:

- Mass and Momentum Transfer
- Heat Transfer
- Structural Mechanics
- Electrostatics
- Electromagnetics

Each of these phenomena are represented by different governing equation sets, and exhibit elliptic, parabolic and hyperbolic characteristics. Therefore, dependent upon the particular discipline, different discretization strategies are taken, including Finite-Volume, Finite-Element and Boundary-Element methods. Coupling between the different disciplines is implicit when they share the same discretization strategy, and is explicit for those disciplines that do not. In this context, explicit coupling employs a relaxation (steady state), or sub-iterative (unsteady) procedure. Implicit coupling, also called tight coupling, then implies a fully-coupled approach, which by necessity, also means discretization scheme. For example, conductive heat transfer problems are solved fully coupled to fluids problems, as they both share the same finite-volume formulation, and hence, can share the same algorithmic implementations. For fluids-structures interactions, the coupling is based upon a sub-iterative procedure for temporally varying solutions, and is a relaxation-based coupling for steady problems. The key to the tightly-coupled approach is the use of common data representations as well as functionality within the core solver.

The CFD-ACE+ system is built around a collection of core physics solvers, using the CFD-DTF common file format as a persistent storage mechanism and static data transfer path (Data Bus). The CFD-DTF common file format and library defines a common set of data definitions and access mechanisms useful for Finite-Volume (FVM), Finite-Element (FEM) and Boundary-Element Methods (BEM)-based scientific applications. This allows the complete definition of most CFD and CSD problems by providing sufficiently complete data definitions and their corresponding file access mechanisms. The library and accompanying common file format permit such features/data as:

- Structured, Unstructured, Polyhedral Grids
- Extensible Boundary and Volume Condition Data
- Platform Independent Data Exchange
- Consistent, Complete and Efficient Connectivity independent of grid type
- Fortran, Fortran90, C and C++ interfaces

The CFD-ACE+ system is comprised of a geometry modeler/mesh generator, graphical based pre-processor/model setup, physics solvers and graphical post processor. These modules are:

- CFD-GEOM: A geometry modeler, mesh generator
- CFD-GUI: A graphical user interface for pre-processing the solver
- CFD-ACEU: A parallel, pressure-based, polyhedral unstructured solver
- CFD-VIEW: A visualization package/post-processing tool.

These application modules are all integrated via the CFD-DTF common file format and library. This publicly available common file format/library enables many important features in the unstructured flow solver, allowing the treatment of multiple-domained grids containing structured, unstructured and polyhedral-unstructured meshes in a fully implicit manner, as if they were consolidated into a single "virtual" zone. Figure 1 illustrates the components of this system showing the data transfer mechanism (CFD-DTF) that allows the model definition, preprocessing, solver and postprocessing to be procedurally integrated.

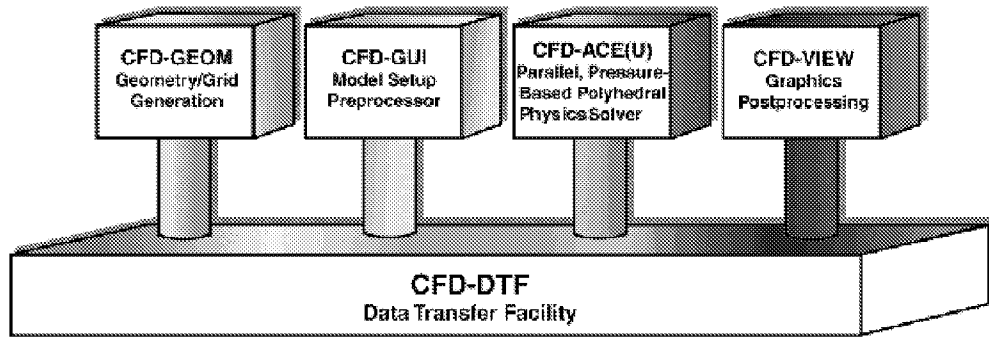
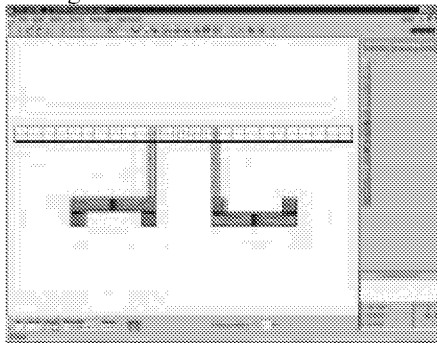
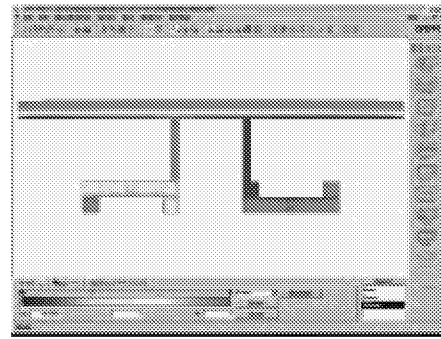


Figure 1. CFD-ACE+ SoftwareSystem

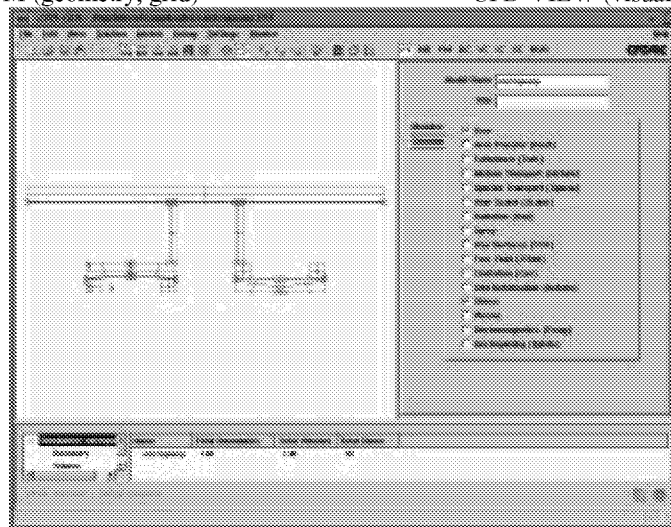
The geometry modeler/mesh generator, coupled to the graphical preprocessor and post processor package via the CFD-DTF common file format and library is an open simulation architecture applicable to a wide variety of other solution modules. By making a solver module DTF-compliant, it can leverage the pre- and post-processing capabilities available with the CFD-ACE+ system. A complete description of each component of the system is beyond the scope of this paper; Figure 2 illustrates each of the components of the system by showing a snapshot of the graphical interfaces for the geometry modeling, pre- and post-processing modules.



CFD-GEOM (geometry, grid)



CFD-VIEW (visualization)



CFD-GUI (model setup)

Figure 2: Sample Screenshots for Micro-Pump Analysis showing CFD-GEOM, CFD-GUI and CFD-VIEW

The core physics solver is comprised of 3 separate applications:

- CFD-ACE(U): FVM flow, heat, mass transfer module
- CFD-FastBEM: A fast BEM solver
- CFD-FEMSTRESS: A FEM structural analysis package

Each of these is described briefly below.

SECTION IIA. CFD-ACE(U)

CFD-ACEU is a finite-volume, pressure-based, unstructured transport equation solver. It supports conservation volumes comprised of arbitrary polyhedra, including the more commonly used types, such as hexahedra, tetrahedra, prisms, quadrilaterals and triangles. It uses a fully implicit procedure based upon the SIMPLE/PISO algorithm, and employs first-, second- and third-order spatial discretizations, as well as first- and second-order temporal schemes. In addition to the traditional Reynolds Averaged Navier-Stokes equations, it is used to solve a wide variety of transport/conservation equations, including:

- Two- and One-equation Turbulence Models
- Multi-component Diffusion of reacting and non-reacting dilute gases, including PDF models.
- Surface Chemistry.
- Radiation and Conjugate Heat Transfer

Discretization of the equations is made using a finite-volume formulation, which relates the conservation-law form of the Navier-Stokes equations to a collection of flux integrations over the surfaces of a set of discrete control volumes, or cells. The equations are solved sequentially and implicitly, meaning that each equation, such as say a momentum equation, is linearized about the current time/iteration level. The physics solver has been parallelized upon distributed and SMP architectures using the MPI message passing library. The parallelization of the code has been performed in such a manner that the convergence rate and robustness of the code is not degraded relative to the serial mode of operation.

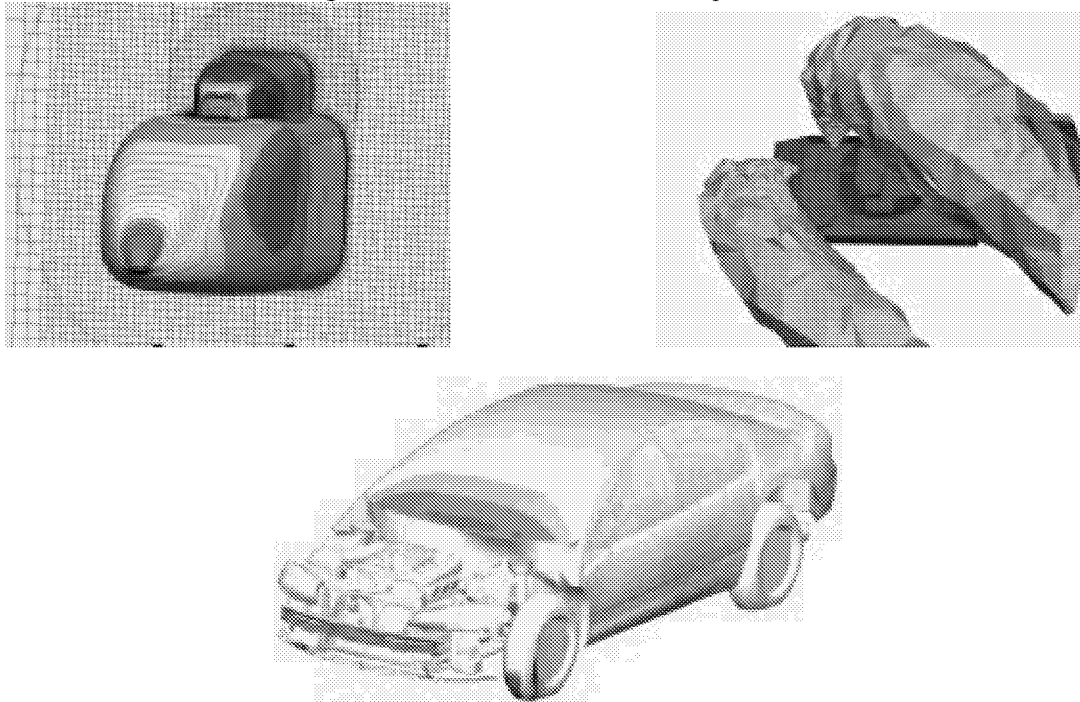


Figure 3. Parallel Computations of Selected Aerospace, Automotive and Defense-Related Problems using CFD-ACE+

The Finite-Volume formulation used in developing the physics solver allows it to be applied to meshes of arbitrary polyhedra, permitting the solution on all mesh types, including

- structured grids
- unstructured grids of triangles, quads, tetrahedra, pyramids, prisms and hexahedra
- polyhedral grids, obtained via cartesian mesh, and mesh refinement.

Figure 3 shows an illustration of recent applications of CFD-ACE+ to rotorcraft aerodynamics, underhood cooling and combat vehicle exhaust/gun-fume modeling.

SECTION IIB. CFD-FEMSTRESS

FEMSTRESS is a finite-element structural analysis developed at CFDRC. It solves the structural mechanics equations in finite-element form derived from the principle of virtual work. In this approach, a balance is formed between the externally applied loads and the internally generated loads. Convergence is obtained when the stress field resulting from the calculated deformations is such that the externally applied loads are balanced. For linear problems, this results in the standard linear equations obtained using the Galerkin or Energy formulations. For linear transient problems, a modal analysis option is also available. For nonlinear problems, a Newton-Rhapson iterative scheme using the tangent stiffness matrix is used to converge to the balance of external and internal forces.

Input to FEMSTRESS consists of surface forces (e.g. pressure loads) and body forces (e.g. gravity, thermoelasticity), as well as the fixed boundary conditions and the solid properties. Output includes displacements of all the node points, the Cartesian stress tensor, and the principal stresses.

The current capabilities of FEMSTRESS include:

- static and dynamic analysis
- modal analysis
- thermolasticity
- material and geometric nonlinearity
- plasticity
- anisotropy
- elastic/rigid and elastic/elastic contact

The elements supported by FEMSTRESS are:

| 2D Elements (plane stress, plane strain, and axisymmetric): | 3D Elements: | Special Elements |
|--|---|--|
| <ul style="list-style-type: none"> • 3-node triangle • 6-node triangle • 4-node quadrilateral • 8-node quadrilateral | <ul style="list-style-type: none"> • 4-node Tetrahedral • 10-node Tetrahedral • 6-node Prism (wedge) • 15-node Prism (wedge) • 8-node hexahedral • 20-node hexahedral | <ul style="list-style-type: none"> • Rectangular Beam • 3-node triangular shell • 6-node triangular shell • 4-node quadrilateral shell • 8-node quadrilateral shell |

SECTION IIC. CFD-FASTBEM

CFD-FastBEM is a Boundary Element Method (BEM) solver that is may be used to solve such problems as:

- Electrostatics
- Low Re Fluid Flows
- Acoustics/EM Waves

The BEM solver is capable of solving different equation types including Laplace/ Poisson, Navier, Stokes, and Hemholtz at low frequency. Boundary conditions BEM supports include Dirichlet, Neumann, and third

kind (convective for Laplace and spring support for Navier). Multi-domains, each with different set of properties, are supported. Continuity of the primary variable (temperature, electric potential, displacement) as well as the secondary variable (fluxes and tractions) are automatically handled across the interface. A new method (developed within CFDRC) is used to evaluate the boundary integrals. The method is similar to the multipole method, but is applicable to any boundary integral equation, including the 3-D Navier equation. Sources terms (terms typically placed on the right-hand side of the equations and are not a function of the primary variable solved) are approximated by particles. Fast summations of the sources terms are used. The time complexity is $O(\log M)$ for each summation of the contribution of M particles. A “matrixless” generalized minimal residual (GMRES) method is used to solve the linear equation systems iteratively. A diagonal preconditioner is used everywhere except on the interfaces, where a 2×2 submatrix preconditioner is used. The overall time complexity is $O(N)$ without sources and $O(N \log M)$ with sources for each iteration. The total time also depends on the number of iterations of the GMRES method. This number is in turn problem dependent and preconditioner dependent. In general, about $N^{0.05 \sim 0.25}$ iterations are needed. Therefore, the time dependence is roughly $O(N^{1.05 \sim 1.25})$ or $O(N^{1.05 \sim 1.25} \log M)$. The spatial dependence is $O(N+M)$. For small problems (with up to a few hundred elements), conventional $O(N^2)$ BEM can be faster than accelerated BEM. The conventional BEM solver can be activated by a simple parameter setting. The BEM libraries are accessible through C function calls. The user can print the results in CFD-VIEW format or VRML.

SECTION IID. EXAMPLES OF MULTI-DISCIPLINARY ANALYSIS USING CFD-ACE+

CFD-ACE+ has recently been used to investigate a variety of micro-scale devices that must be modeled using Multi-Disciplinary analysis. The following shows a subset of some of the devices being analyzed, indicating the different analysis modules being used to perform the analysis.

Micropump (Unsteady, fluid-structure-electrostatics)

This illustrates the unsteady flow-structures-electrostatics interaction present for the modeling of a micro-scale pump. This pump is piezo-electrically activated, which when the voltage is applied, draws the pump membrane (see Figure 4) up. This membrane is modeled as a plate fixed up at both ends, which deforms according to the electrostatically applied voltage. Upon voltage application, this membrane deflects upwards, imposing a pressure gradient, which pulls fluid from the inlet reservoir (on left), filling the volume created by the deflection of the upper membrane. Once the voltage is turned off, the membrane returns to its original shape, pumping fluid out of the outlet membrane, on right. Figure 4 shows two snapshots in time of this unsteady process. The grid, model setup and post-processing for this problem are illustrated in Figure 2.

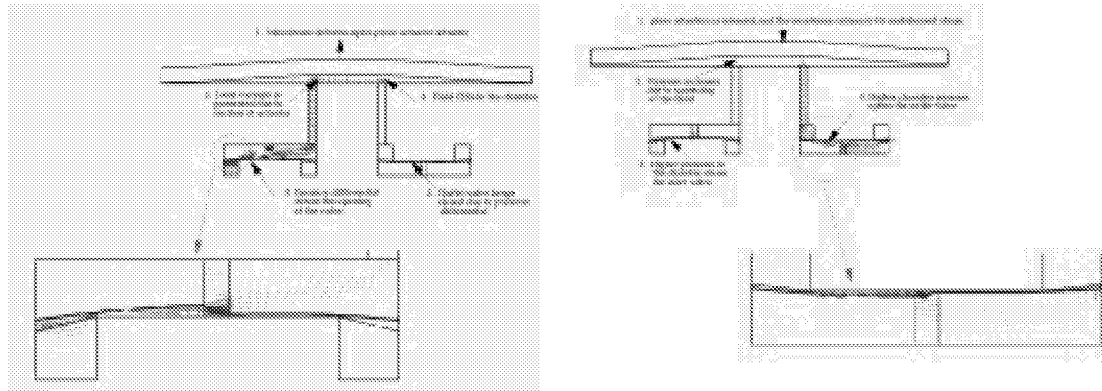


Figure 4. Micropump Simulation using Coupled Fluid-Structures-Electromagnetic Disciplines

Accelerometer (Electrostatics)

This problem simulates an electrostatically driven accelerometer. The electrostatic model calculates the electrostatic pressure force on the elastic beam. The structural model is used to calculate the stresses, strains, and displacements on the elastic beam. As seen in Figure 5 when 10 V is applied to the upper beam

the deflection toward the rigid body is small, with a maximum displacement of $0.055 \mu\text{m}$ at beam center. With an applied voltage of 20 V the beam deforms onto the rigid body.

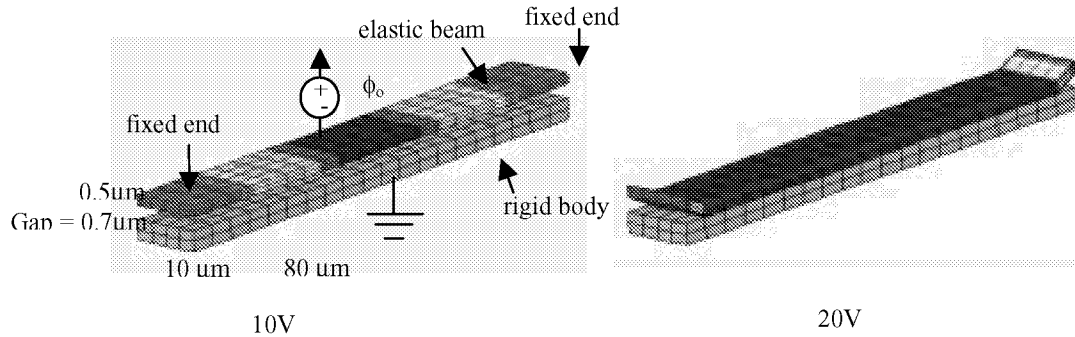


Figure 5. Doubly Clamped Beam Under an Electrostatic Load, with an Applied Voltage $\phi_0 = 10$ or 20 V

Another problem shown in Figure 6(a) is an electrostatically loaded plate. This is an example of an accelerometer. A large plate with an applied voltage of 20 V is clamped by four beams. The whole upper elastic structure has a Young's Modulus of $1.69 \times 10^9 \text{ Pa}$, Poisson's Ratio of 0.3 , and no residual stress. The upper plate is $2.0 \mu\text{m}$ above a ground plane. Figure 6(b) shows the calculated displacement contours on the upper plate due to the electrostatic load. With 20 V applied to the upper plate a maximum deflection in the center of the plate of $1.83 \mu\text{m}$ toward the ground plane is calculated.

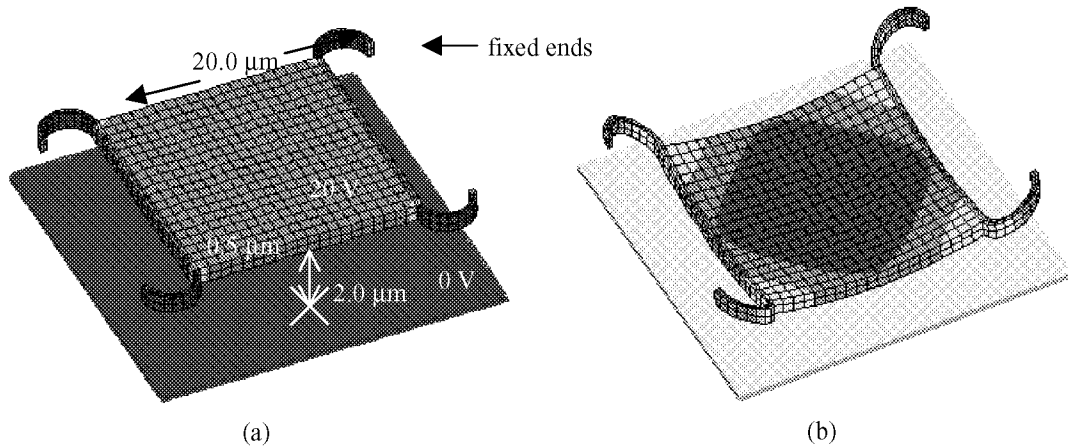
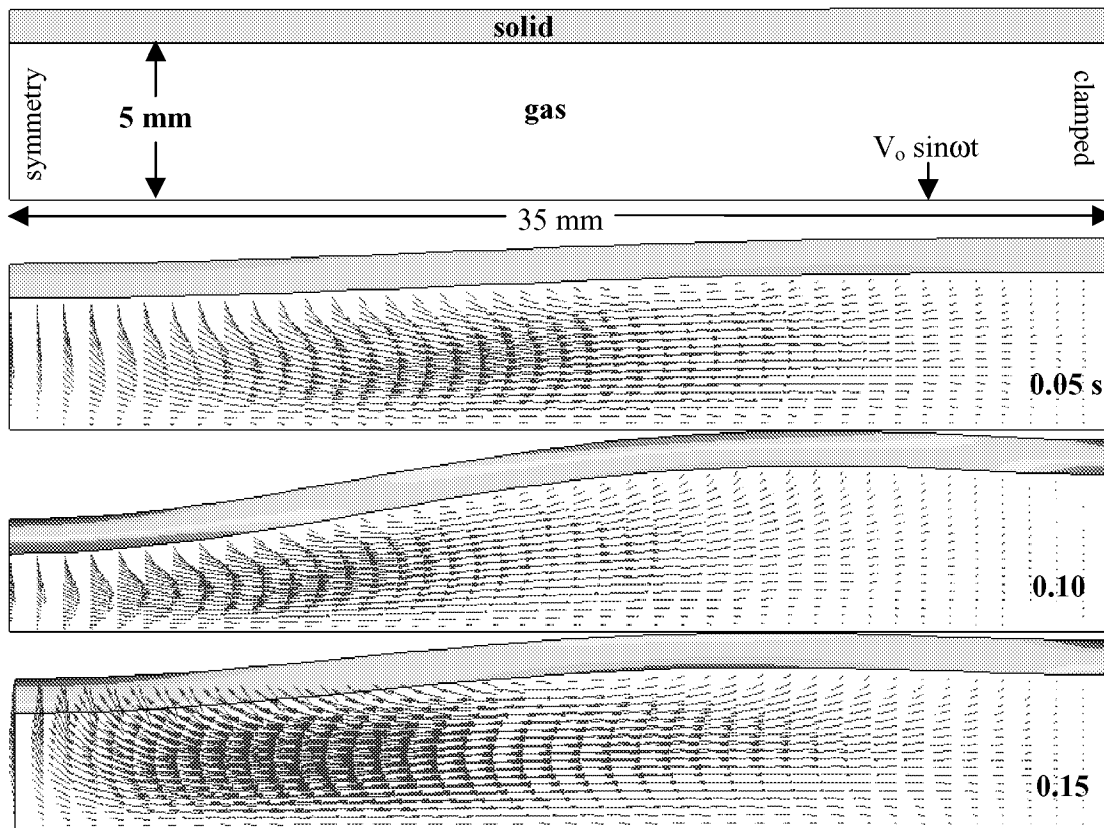


Figure 6. Accelerometer Under an Electrostatic Load. (a) The geometric dimensions and problem set-up. (b) The calculated displacement of the plate due to the electrostatic load. The displacement of the plate toward the ground plane is maximum ($1.83 \mu\text{m}$) at the center of the upper plate.

Fluidicly-damped Beam under Electrostatic Load (Fluid-Structures-Electrostatics)

The coupled thermal-fluid-structural-electrostatic capability in CFD-ACE+MEMS was tested on a simple demonstration problem. The problem setup is shown in Figure 7. The geometry consists of a closed chamber, 5 mm high and 70 mm long, which contains a compressible gas of viscosity equal to $0.0171 \text{ Pa}\cdot\text{s}$ at an initial pressure $P_0 = 10 \text{ Pa}$ and temperature $T_0 = 300 \text{ K}$. The chamber is bounded at the top by a flexible beam clamped at each edge, and by adiabatic walls on the other three sides. The beam is 1 mm thick, and has a modulus of elasticity of 4000 Pa . From symmetry considerations, half of the geometry is modeled, with symmetry conditions applied to the left edge.



$$P_0 = 10 \text{ Pa}$$

Figure 7. Doubly Clamped Fluid Damped Beam Under a Sinusoidal Electrostatic Load. Shown is a time sequence of the beam displacement, fluid velocity field (vectors), and normal axial stress (contours on beam) for the $P_0 = 10 \text{ Pa}$ case.

A sinusoidal voltage is applied ($12000 \sin 5\pi t \text{ V}$) to the bottom wall, and the beam on top of the chamber is grounded. The sinusoidal varying electrostatic force deflects the beam downward compressing the gas. As the gas is compressed, the pressure increases, applying an upward force to the beam to counteract the electrostatic force. At each time step the resulting deformation is obtained from a balance of the electrostatic, pressure, and inertial forces.

The result of the analysis was to determine the transient response of the fluid pressure, temperature, electrostatic field, and the deflection and stresses of the beam. To accomplish this, the governing equations for the four models (flow, heat, electrostatic, and structural analysis) are coupled and solved implicitly at each time step. The time sequence of Figure 7 shows the deflection of the beam, the gas flow as vectors, and the normal axial stress as contours on the beam. The snapshots were taken before, at, and after the voltage maximum. As the beam moves downward the gas is forced into the clamped corner pushing the elastic beam upward. The energy equation was also solved but the temperature increases were minimal (only 0.1 K) due to the small number of cycles simulated.

Buoyancy-Driven Flow of a Conductive Fluid (Flow-Electromagnetics)

The Lorentz force is demonstrated by the calculation of buoyancy driven flow of a conducting fluid in a uniform magnetic field. The bottom boundary rotates with a specified angular velocity and has a uniform temperature. The inner part of the top boundary rotates in the opposite direction of the lower boundary and has a uniform temperature lower than that of the bottom boundary. The outer part of the top boundary is a

free surface. The temperature difference between the boundaries creates a buoyancy-driven flow pattern in addition to the rotation imposed by the walls. A uniform magnetic field in the opposite direction of gravity damps the flow through the Lorentz force. Figure 8 shows contours of the temperature and velocity in the vertical direction with and without the magnetic field. The velocity magnitude is much smaller when the magnetic field damps the flow.

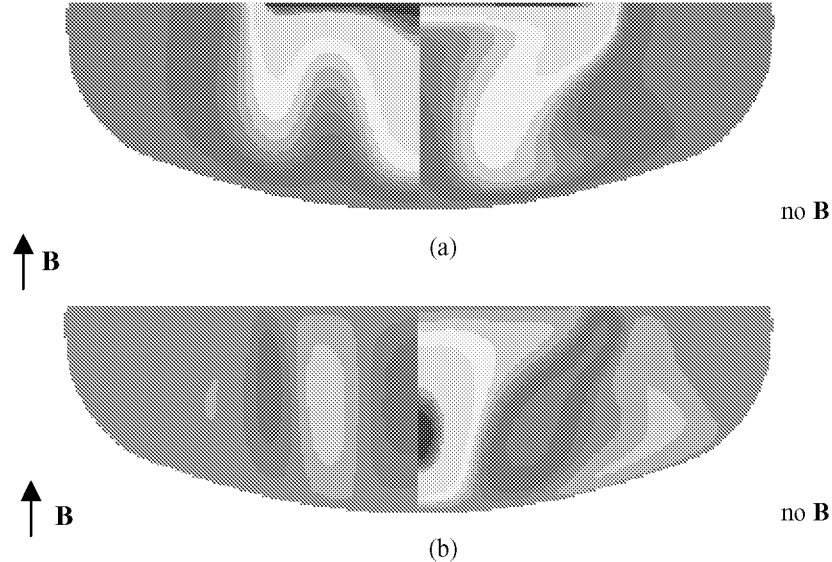
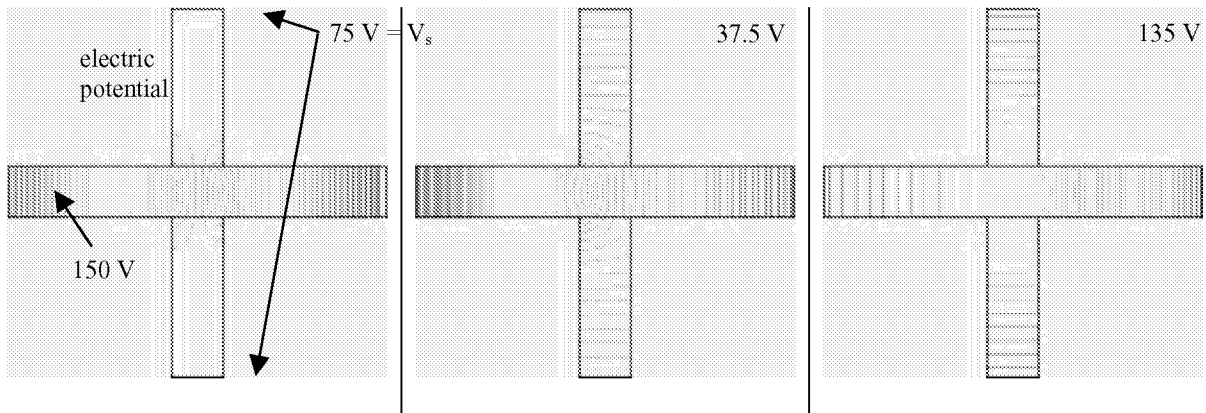


Figure 8. (a) Temperature and (b) Vertical Velocity Contours for Coupled Flow/Magnetics Solution. Right Half is without the Magnetic Field, Left Half is with the Magnetic Field

Electro-Osmosis (Fluid-Electromagnetics)

Electroosmosis techniques are widely used for transport of charged fluids in microfluidic systems. Shown in Fig. 9 is a cross channel device used for sample injection and separation. The flow of material in the device is controlled by static fields. Depending on the voltage V_s applied to the upper and lower reservoir of the cross channels, the flow of charged specie can be suppressed (0V), flowed into (37.5V), or flowed out (135V) the cross channels.



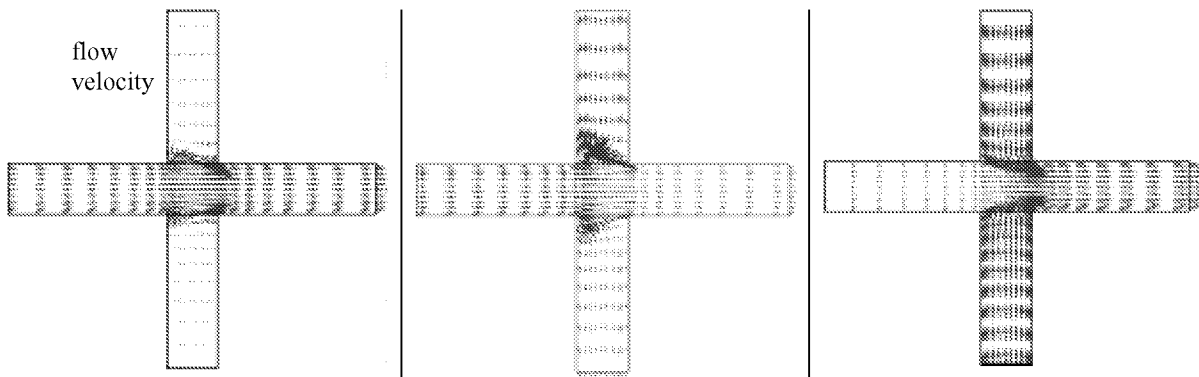


Figure 9. Electric Potential in Flow Velocities for a Cross Channel Device

SECTION III. MDICE: MULTI-DISCIPLINARY INTEGRATED COMPUTING ENVIRONMENT

The Multi-Disciplinary Integrated Computing Environment (MDICE) provides a distributed computing framework that is suitable for Multi-Disciplinary analysis, design and optimization. This approach allows separately developed and maintained analysis packages to be integrated within a dynamic, distributed and heterogeneous computing environment. The MDICE architecture allows not only data exchange amongst applications, but also functionality exchange: Applications may invoke certain functions in other applications through the MDICE environment. The different applications communicate through a rich set of pre-defined, MDICE supplied interfaces, which perform all necessary data manipulations as well as interface specific function invocation. This environment is constructed of three separate components: a central controller, a library of MDICE communication and control functions, and lastly, the MDICE-compliant application modules themselves, which include a variety of structural, fluid and heat transfer solvers.

The central controlling process provides network and application control, serves as an object repository, executes remote procedure calls and coordinates and synchronizes the execution of the application modules. It communicates via a message passing library (PVM), and provides the overall control via a Graphical User Interface and strongly typed scripting language. Figure 10 shows the GUI for the MDICE-AE (AeroElastic) controller.

The next component, the MDICE library, provides an extensible object definition that is used to define and instantiate all data passed to and from the application modules. This library also contains the interface objects, which perform the very necessary data exchange and data manipulations between the application modules. The development of a rich set of interface objects is crucial to the application of the MDICE environment to a wide variety of Multi-Disciplinary problems. Contained within this environment are:

Fluid/Structure Interfaces:

- Conservative and Consistent interfacing (force and virtual work conservation)
- Arbitrary grid coupling and alignment (e.g. structured to unstructured grids)
- Multi-Dimensional coupling (e.g. structural beam models coupled to three-dimensional fluids flow models)

Fluid/Fluid Interfaces

- Arbitrary grid coupling and alignment (e.g. structured to unstructured grids)
- Multi-Dimensional coupling (e.g. axisymmetric-3D or 2D to 3D)
- Mixing Plane interfacing (circumferential averaging)

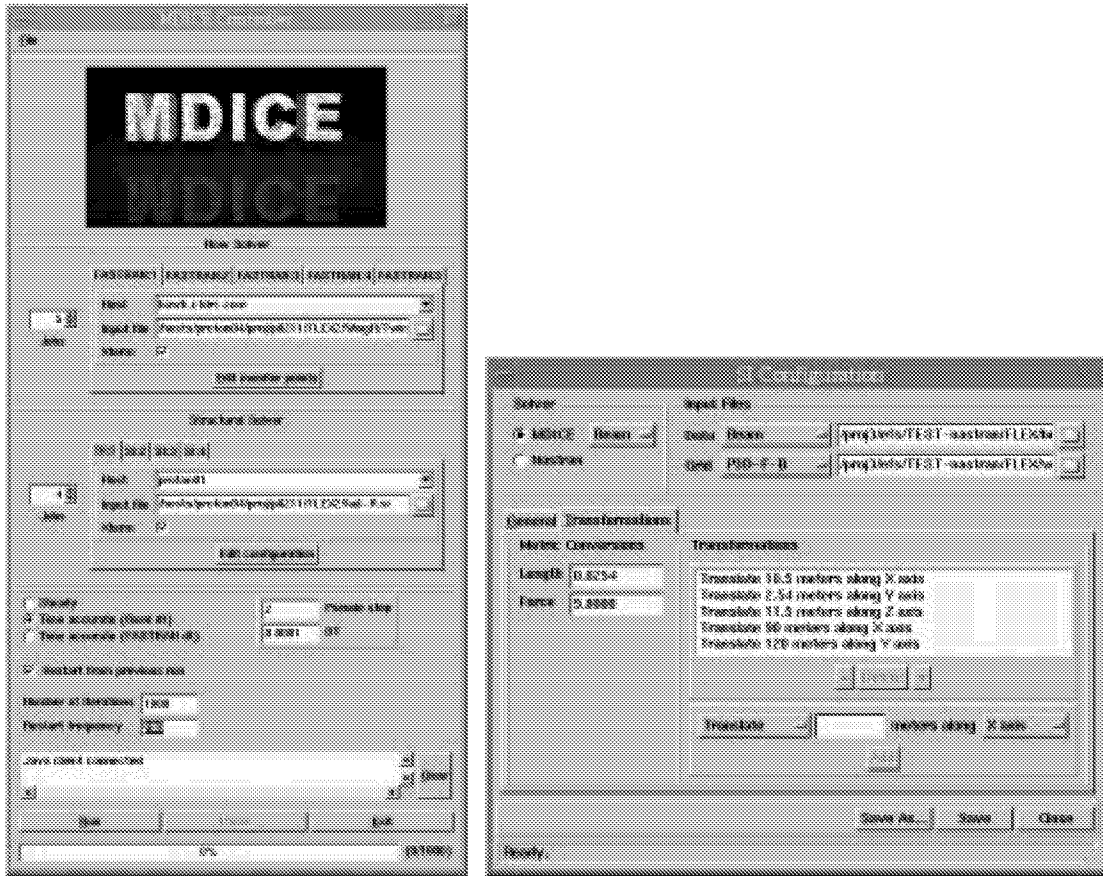


Figure 10. MDICE-AE Users Interface Structures Interface Panel

Overset/Chimera Interfaces

- Automated hole cutting for structured, unstructured, polyhedral grids
- Automatic Data Conversion
- Units, Axes, dimensionality

These interfaces allow different fidelity models to communicate across different disciplines. This allows, for example, a beam structural model to be used with a three-dimensional Reynolds Averaged Navier-Stokes (RANS) solver, or a two-dimensional RANS to be coupled with a three-dimensional structural analysis module. Since the interfaces provide self describing data exchange, applications such as visualization packages may also be driven within the environment. As an example, consider Figure 11, which shows a circumferential averaging interface for turbomachinery applications, and Figure 12 showing a 2D/3D interface used for gas turbine combustor calculations.

In the context of tight and loose coupling procedures, the MDICE environment uses a loose coupling approach, but since it is operating in a heterogeneous/distributed environment, the modules may run in parallel. For instance, for a fluid structures interaction problem, the structural analysis modules and flow solver modules are computing simultaneously, and are synchronized by the central controlling MDICE process. This also allows parallel physics solvers, such as CFD-ACE+, to perform independently threaded parallel calculations while being treated as a single module in the MDICE environment (multi-level parallelization).

Each application module in the environment communicates to others through the interface objects, allowing a wide variety of module combinations to be constructed to approach a given Multi-Disciplinary problem.

This allows the retrofitting of legacy applications into a Multi-Disciplinary environment, permitting discipline specific tools to be used where they are best. As an example, for an organization that might be very experienced using, say, MSC/NASTRAN, but not experienced using CFD, this environment would be ideal. In this case, no corporate experience and confidence gained with the structural analysis package would be lost, while functionality to perform high-fidelity aero-structural interaction problems would be gained.

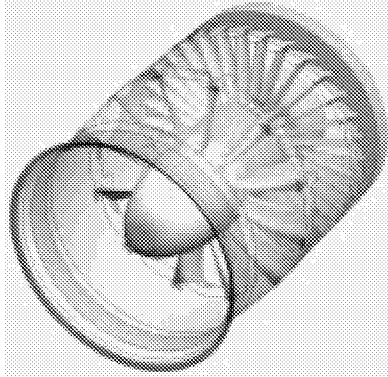


Figure 11. Illustration of Circumferential Averaging Interface (Left, for turbomachinery)

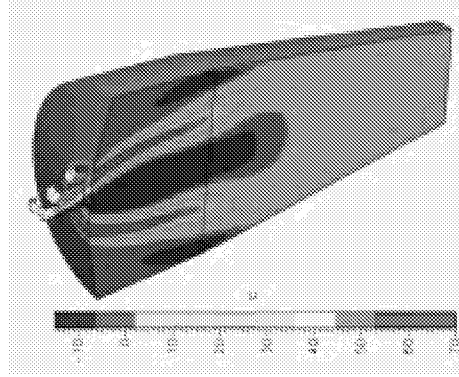


Figure 12. 2D/3D Interface (for Gas Turbine Combustor Swirler to Dome Interface)

Presently, there are a wide variety of applications and organizations using the MDICE environment, primarily for aero-structural interaction problems. Recently, direct interfaces to parametric CAD packages, such as Pro/Engineer have been made, and work is underway integrating other disciplines into the MDICE environment. Table 1 shows a list of Disciplines and Organizations/Applications that are using the MDICE framework.

Table 1.

| Discipline | Code |
|--|--------------------------------------|
| Parametric Computer Aided Design (CAD) | Pro-Engineer (Parametric Technology) |
| | UniGraphics (UniGraphics) |
| | CATIA (IBM) |
| Geometric Modeling/Mesh Generation | CFD-GEOM (CFDRC) |
| Computational Fluid Dynamics | CFD-ACE (CFDRC) |
| | CFD-ACE+ (CFDRC) |
| | CFD-FASTRAN (CFDRC) |
| | GCNSfv (Northrop-Grumman) |
| | NISTAR (Pratt & Whitney) |
| | NASTAR (Pratt & Whitney) |
| | Corsair (Pratt & Whitney/NASA-Lewis) |
| | NPARC (NASA Glenn) |
| | Cobalt (AFRL) |
| | (CFD)ENS3D-AE (ARFL) |
| | Splitflow (Lockheed-Martin) |
| | ADPAC (NASA-Glenn) |
| Finite Element Analysis (FEA), Linear Structures Solvers (Modal, Influence Coeff.) Beam Models | LSS (CFDRC) |
| | NG LSS (Northrop-Grumman) |
| | MSC/NASTRAN ANSYS |
| | CFD-FEMSTRESS (CFDRC) |
| 3D Graphical Visualization | CFD-VIEW (CFDRC) |
| Line Plotting Package | XMGR (Public Domain) |
| Screen Snapping/Moving Making | ImageMagick (Public Domain) |

SECTION IIIB. SAMPLE MDICE EXAMPLES

Two examples of the Multi-Disciplinary Integrated Computing Environment are shown here for solving coupled aero-structural interaction problems. Also, an example is shown illustrating Chimera mesh capability coupled with CFD-ACE+ to perform a moving body, 6DOF, fluid-structures low speed flow.

F-16 Wing/Body

This example shows MDICE being applied to compute the steady state aeroelastic deflections of a F-16 wing/body structural/aero model. The LSS solver was used for the structural model, which consisted of a rigid fuselage and strake, and flexible wing. The aerodynamics model was constructed using the CFD-FASTRAN compressible flow solver. The flight conditions correspond to a Mach number of 1.2 and an angle of attack of 5.116 degrees.

The computed wing tip deflection (65 mm) compared favorably to the experimentally measured deflection (68 mm).

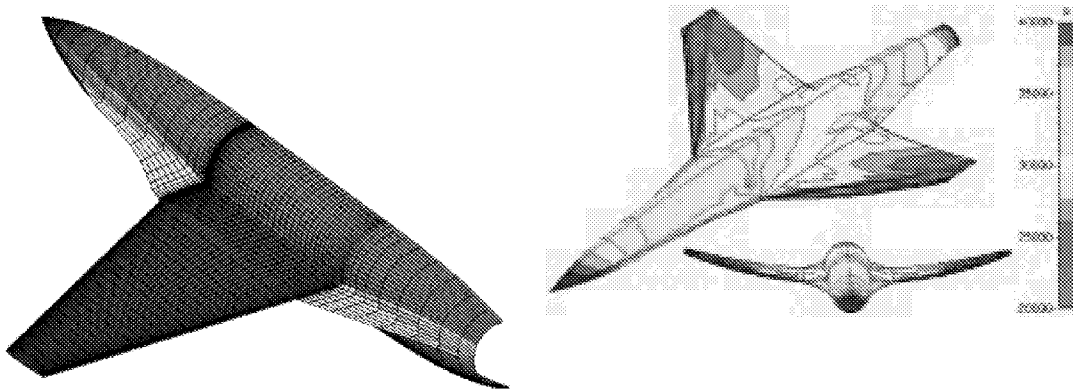


Figure 12: F-16 Wing/Body Deformation due to Aero Loads

Twin-Tail Buffet

This example shows how the MDICE environment has been used to compute the unsteady, coupled, aero-structural response of a twin tail delta wing configuration at angle of attack. This configuration can experience an unsteady buffeting caused by interaction of the wing leading edge vortex with the flexible vertical stabilizers. For this subsonic flow, the tail deflections cause pressure perturbations to the flow field that are fed upstream, altering the vortex structure. The results computed here [Sheta, et al., 1999] have been compared favorably with experimental data in [Washburn, et al., 1993].

The fluids model used is the CFD-FASTRAN flow solver, coupled to the LSS structural module. The flow equations solved are the compressible RANS equations using a 2nd-order upwind scheme, with a 1st-order temporal scheme. The structural model used is a beam model, where the tails are modeled as cantilevered beams, fixed at the root, and allowed to oscillate in both bending and torsional modes. The MDICE interface for this run is shown in Figure 13. This configuration was run at 4 angles of attack, and the results compared to experimental data. Figure 14 shows a selection of the computed results at the 4 angles of attack, illustrating the asymmetrical, unsteady vortex breakdown, interacting with the tail torsional/bending modes.

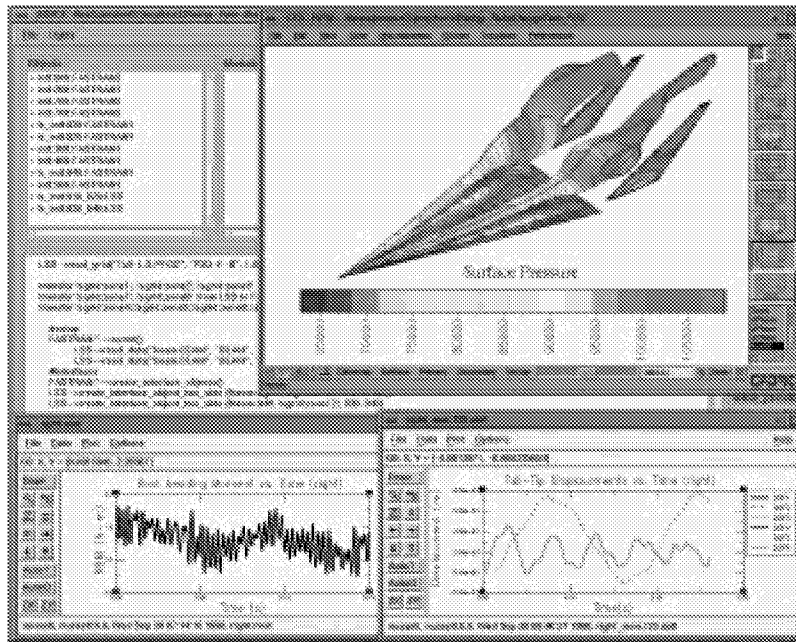


Figure 13: MDICE Control of Coupled Fluid/Structures Interaction Problem

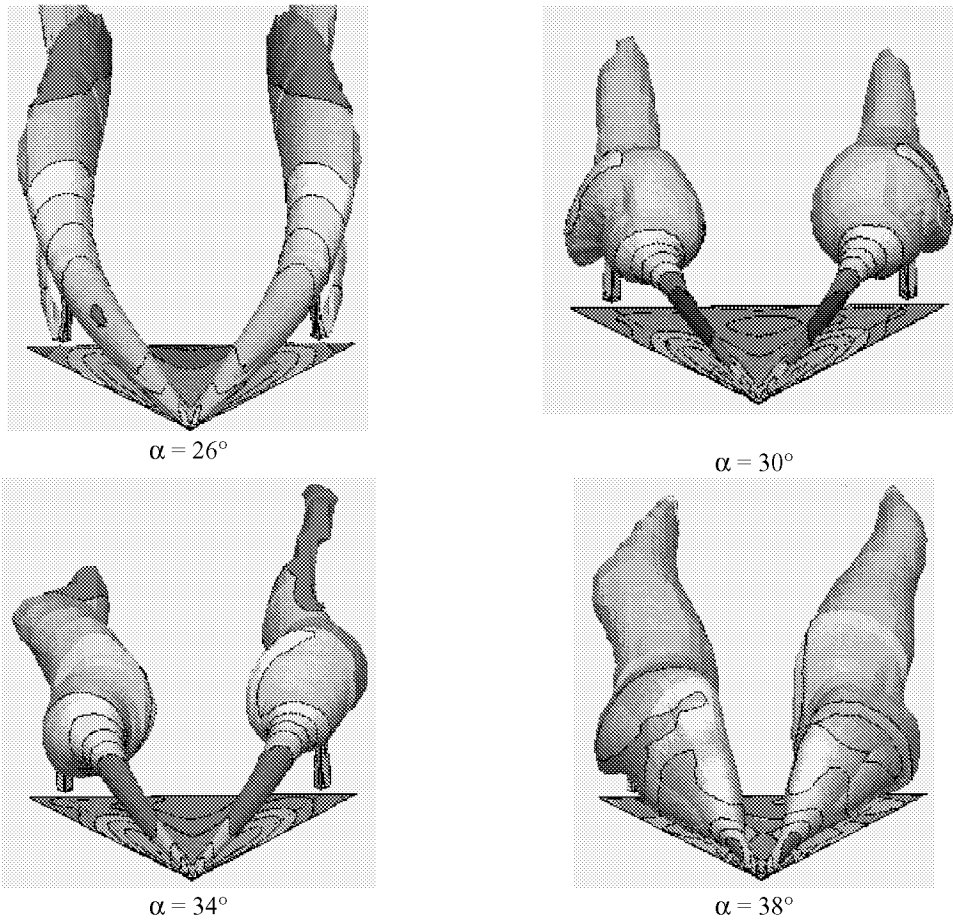


Figure 14: Unsteady, Coupled Aero-Structural Analysis of Twin-Tail Buffeting using MDICE-AE

As seen in these figures, at the lowest angle of attack, the leading edge vortices are symmetric, and do not burst until past the vertical stabilizers. At 30 degrees, some asymmetry is noted, and the vortices are seen to burst near the tails. This asymmetry causes an unsteady pressure load on the tails, causing (asymmetric) bending and torsional modes of vibration. These unsteady modes then feed upstream, further coupling with the asymmetric behavior of the vortex structure. At higher angles of attack, this asymmetric, unsteady behavior is further excited, as shown by the contours at 34 and 38 degrees. The computed bending moments, torsional moments and frequencies compared very well with the experimental data, and are shown more completely in [Sheta, et al., 1999].

Transient Analysis of a Butterfly Valve Closure (MDICE + CFD-ACE+)

For this example, the unsteady flow and solid stresses induced during the closing of a butterfly valve are simulated. The MDICE environment is used to drive CFD-ACE+ (flow-structures), along with the MDICE library's Chimera mesh module and interfaces, as well as MDICE's 6 Degrees-of-Freedom (6DOF) module and interfaces. This unsteady calculation begins with the steady solution of the valve in the open position, and progresses to fully closed in 3 seconds. The valve motion is defined via the 6DOF model, and the MDICE environment generates the unsteady results, viewed in real time. Figure 15 shows the overset mesh, the initial (steady) conditions at fully opened, and the a snapshot of the transient simulation near closing, showing the induced stresses in the valve.

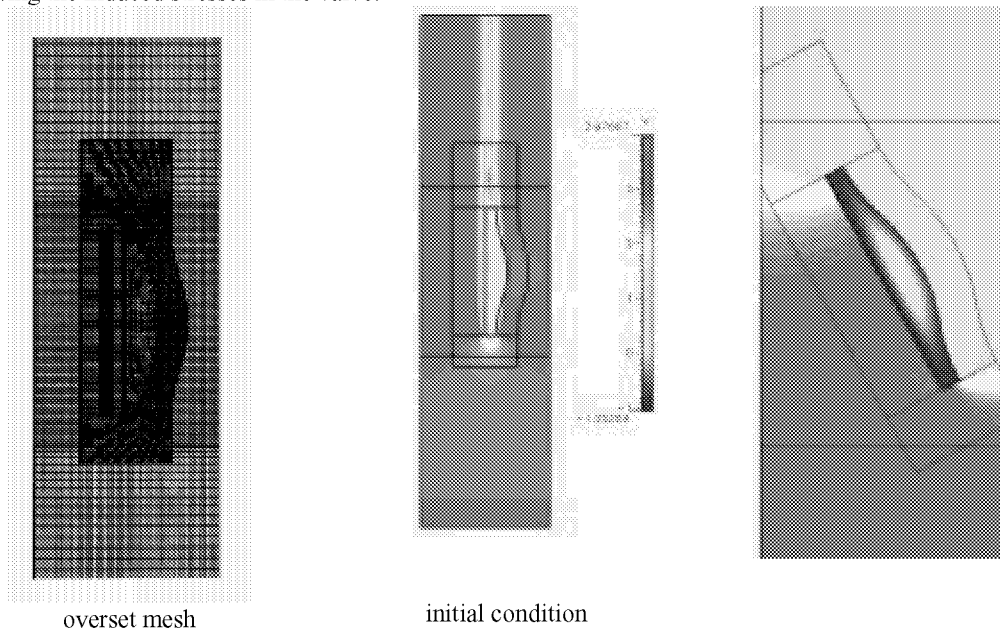


Figure 15. Transient Butterfly Valve Closing Process: Unsteady, Overset, Fluid-Structures using MDICE+CFD-ACE+

SECTION IV. CONCLUSIONS

Two approaches suitable for Multi-Disciplinary Analysis have been presented, and the corresponding software suites described. For each of these approaches, a limited selection of examples have been shown, illustrating the different disciplines and ranges of applicability. These two approaches have been termed "tightly-coupled" and "loosely-coupled". The tightly-coupled approach has been represented by the CFD-ACE+ system, while the loosely-coupled approach has been represented by the Multi-Disciplinary Integrated Computing Environment. A brief description of the CFD-ACE+ system has been given, describing the implicit coupling procedures used for like discretization schemes, relaxation-based coupling for dissimilar discretization schemes, the common data access mechanisms via the CFD-DTF common file format and library, and the different modules that make up the system. A limited set of examples of this approach have been shown. The loosely-coupled approach has been represented by the MDICE

environment. The different components that make up this heterogeneously distributed, Multi-Disciplinary environment have been described, the interfacing technology addressed, and a number of sample applications shown.

SECTION V. ACKNOWLEDGEMENTS

The authors would like to acknowledge a number of very important contributors to the capability that has been outlined in this paper. For the CFD-ACE+ system, we would like to particularly acknowledge the continuous support and encouragement of Dr. Ashok Singhal/President CFDRC, as well as the entire CFD-ACE+ development team, including; Milind Talpallikar, Dr. H.Q. Yang, Dr. Yu Jiang, Dr. Mahesh Athavale, Dr. Philip Stout, and Dr. Giridharan. For the MDICE environment, external support via AFRL/VA and NASA GRC is greatly appreciated, as well the internal support via CFDRC IR&D. In particular, we would like to thank Dr. Vijayan Parthasarthy, Dr. Essam Sheta and Dr. Charles Warren for their contributions to the development and further application of the MDICE environment.

REFERENCES

- Goldin, D.S., Venneri, S.L. and Noor, A., (1998), "NASA's ISE (Intelligent Synthesis Environment)," presentation.
- Przekwas, A.J., Yang, H.Q. and Athavale, M.M., (1999), "Computational Design of Membrane Pumps with Active/Passive Values for Microfluidic MEMS," SPIE, Paris, France.
- Sheta, E.F., Siegel, J.M., Golos, F.N., and Harrand, V.J., (1999), "Twin-Tail Buffet Simulation Using a Multi-Disciplinary Computing Environment," NASA/CP-1999-209136, CEAS/AIAA/ICASE/NASA Langley International Forum on Aeroelasticity and Structural Dynamics, Williamsburg, VA, June 22-25.
- Singhal, A.K., Parthasarathy, V., Siegel, J.M., and Reich, A., (1999), "Coupled Fluid-Structural-Thermal Simulations of Industrial Problems; Requirements, Approaches and Examples - Keynote Lecture," Keynote Lecture ASME, Pressure Vessels and Piping Conference, August 1-5, 1999, Boston, MA.
- Stout, P.J., et al., (1999) "A CAD System for Simulation and Modeling of MEMS,;" SPIE , Paris, France.
- Washburn, A.E., Jenkins, L.N., Ferman, M.A., (1993), "Experimental Investigation of Vortex Fin Interaction," AIAA-93-0050.



Overview of Fluid Dynamic Activities At the Marshall Space Flight Center

Roberto Garcia
Lisa Griffin
Ten-See Wang
Applied Fluid Dynamics Group

Presented at:
The 10th Thermal and Fluids Analysis Workshop
Huntsville, AL
September 13-17, 1999



Overview



- **Organizational Changes at MSFC**
- **Recent Program Support & Technology Development**
 - Analysis & cold flow testing
 - Fastrac, X-34, X-33, RLV, LFBB
- **Ongoing Activities**
 - RLV focused technology, RBCC concepts development, methodology & code development
- **Future Activities and Direction**
 - Hardware design and development
 - Tools Development
- **Concluding remarks**
 - Constraints, cooperation, opportunities



Organizational Changes at MSFC



- **Center Reorganization Completed in May 1999**
 - Increase focus on the center's assigned roles and missions
 - Center of Excellence for Propulsion
 - Space Transportation Systems Development
 - Microgravity Research
 - Space Optics Fabrication, Metrology, & Testing
 - Strengthen MSFC Product Lines
 - Space Transportation, Flight Projects, Science
 - Maintain Strong Engineering Capability
- **Product Line Dedicated Functions Assigned to Product Line Directorate**
- **Maintained Focused, Cross Functional Engineering Disciplines in Engineering Directorate**



Organizational Changes at MSFC



- **Fluid Dynamics in Space Transportation Directorate**
 - Discipline primarily supports space transportation product line
 - TD63: Fluid Physics and Dynamics Group (bldg. 4203)
 - Acoustics, aerothermal analysis, dynamic data reduction and analysis, plume induced environments, cold-flow testing PIs
 - TD64: Applied Fluid Dynamics Analysis Group (bldg. 4203)
 - Develop and apply computational fluid dynamics (CFD) analysis
 - TD74: Experimental Fluid Dynamics Group (bldg. 4732)
 - Maintain, operate, & develop cold-flow experimental facilities
- **Other Disciplines (Thermal, Stress, etc.) in Engineering Directorate**
 - Support broadly distributed among product lines



Recent Program Support & Tech. Dev.



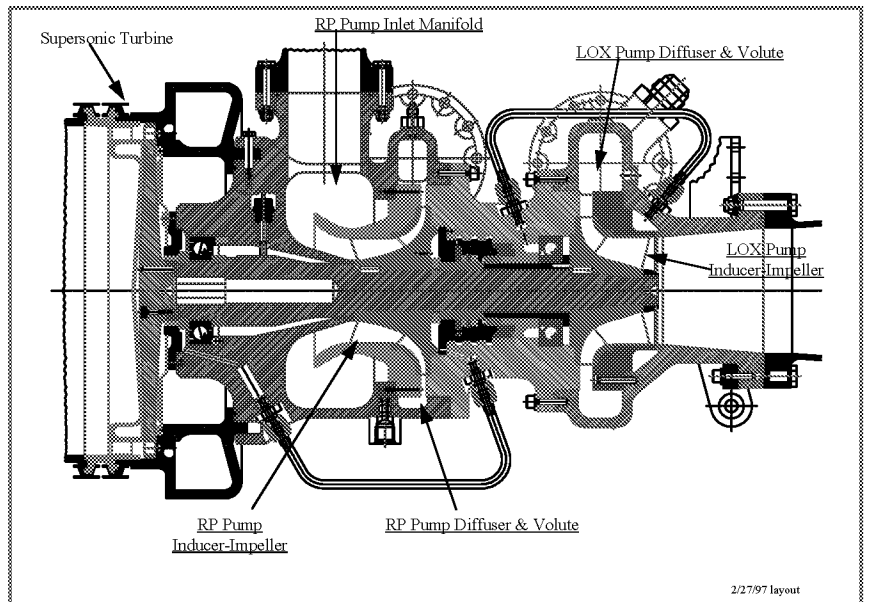
- **Fastrac Low-Cost Engine Technology Demonstrator**
 - Primary propulsion for X-34 vehicle
 - Hydrodynamic design and analysis of both pumps
 - All the primary flow paths in the LOX and RP-1 pumps
 - Water flow test of LOX pump
 - **Verify non-cavitated performance, determine suction capability**
 - **Steve Skelley presentation Tuesday morning (Fluids 3a)**
 - Aerodynamic design and analysis of the turbine
 - Single stage supersonic turbine w/ exit guide vanes
 - First time accurate, full NS, rotor stator analysis
 - **Lisa Griffin presentation Tuesday morning (Fluids 3b)**
 - TCA and GG performance and environments predictions
 - Injector patternization water tests
 - Finite rate combustion devices analysis
 - **CFD baselined as performance prediction method**



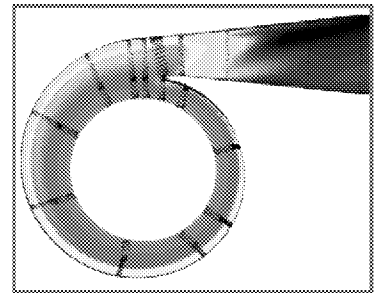
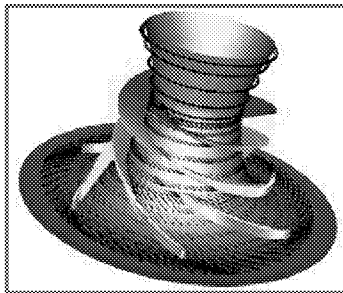
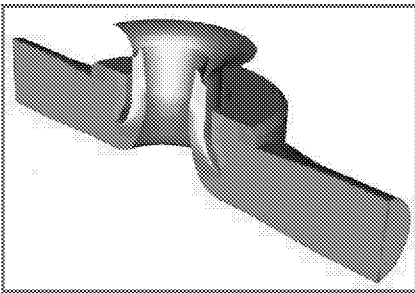
Recent Program Support & Tech. Dev.



Fastrac Turbopump Cross-section

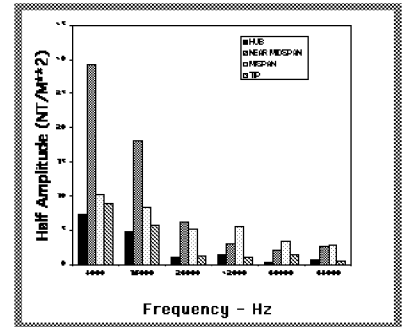
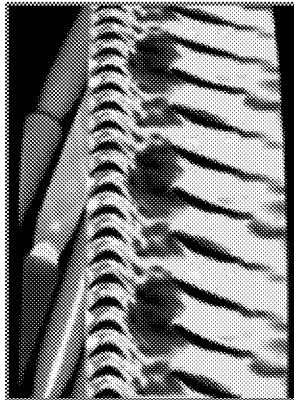
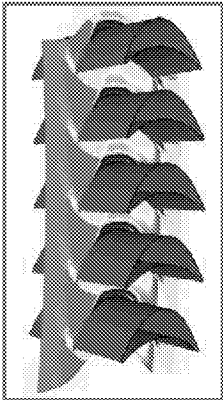


Recent Program Support & Tech. Dev.

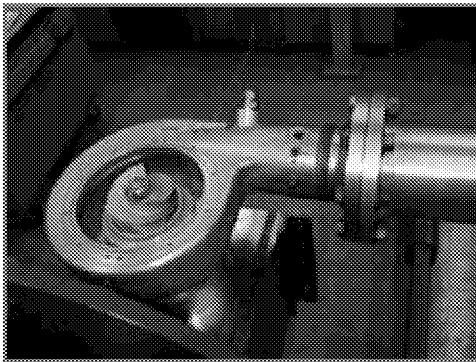


Pump flow path design and analysis

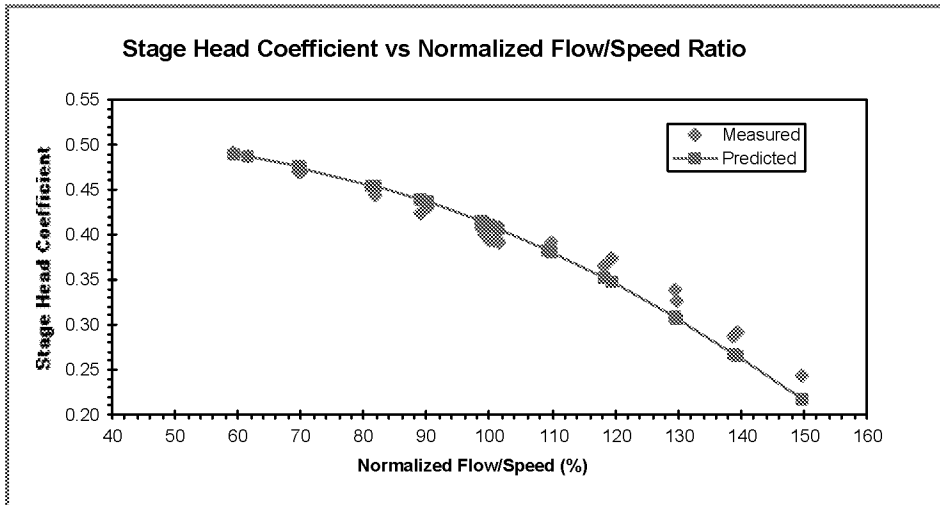
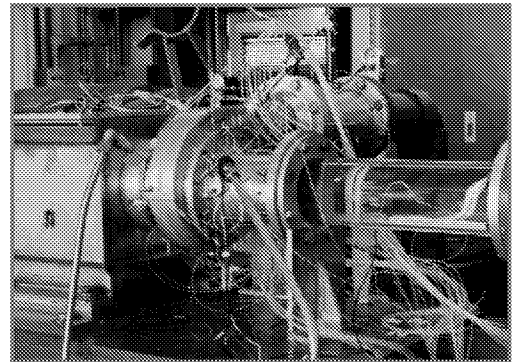
Turbine flowpath design and time accurate analysis



Recent Program Support & Tech. Dev.

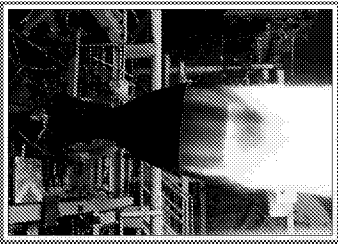


Fastrac LOX pump
cold flow testing

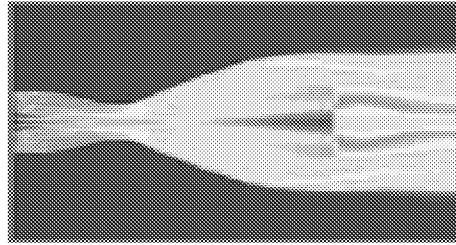




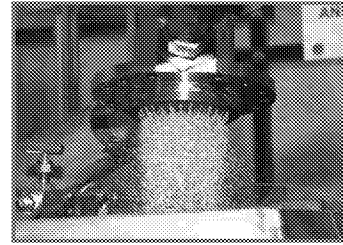
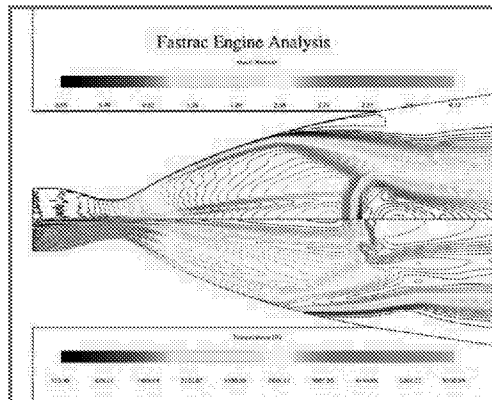
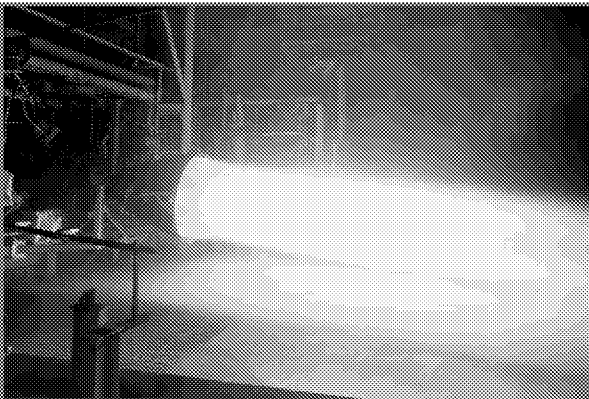
Recent Program Support & Tech. Dev.



Fastrac TCA performance prediction with 15:1 nozzle



Fastrac TCA performance prediction with 30:1 nozzle



Patternization tests and performance prediction





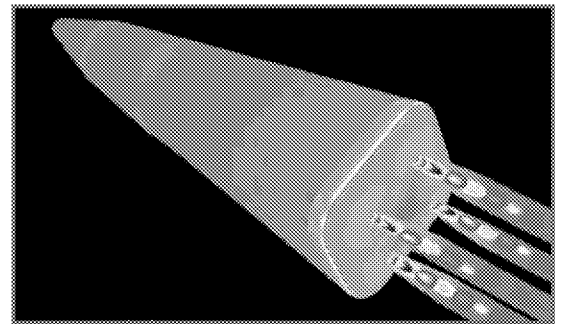
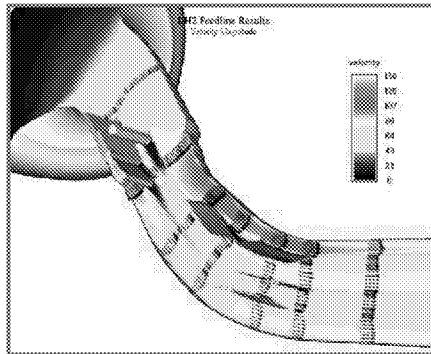
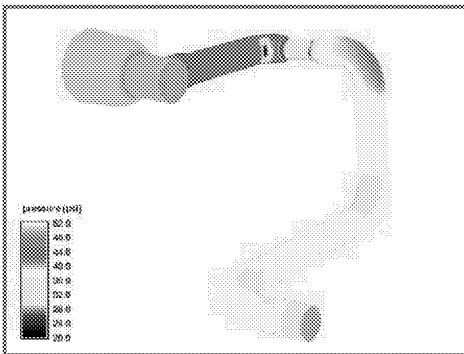
Recent Program Support & Tech. Dev.



- **X-34 Pathfinder Vehicle Design Support**
 - Propulsion system feedlines flow analysis
 - Assure pump inlet flow distortion within acceptable limits
 - Plume induced heating on the vehicle
 - Initial predictions refined with component test data
 - Sonic boom prediction for environmental impact statement
- **X-33 / RLV Vehicle Design Support**
 - Assessment of 3 phase-1 concepts: lifting body, winged body, Delta-Clipper
 - Extensive wind tunnel tests for aerodynamic configuration development
 - Critical impact on resolving transonic pitching moment issue

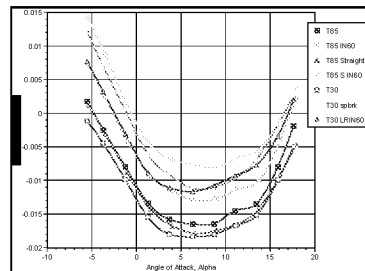
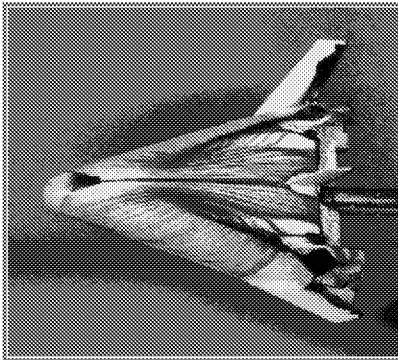


Recent Program Support & Tech. Dev.

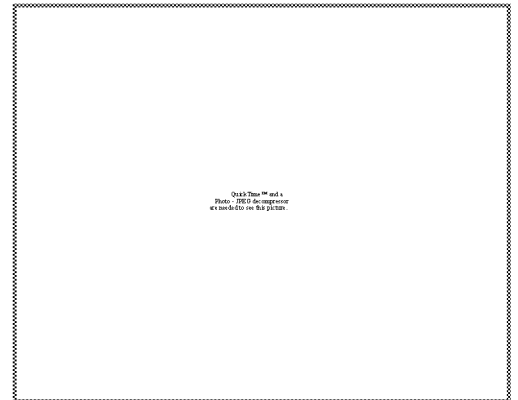


X-34 and X-33 feedline analysis

RLV Phase-1 Concepts



X-33 and RLV Aerodynamic Testing





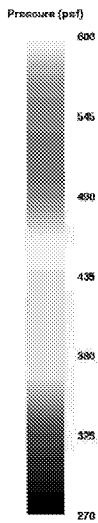
Recent Program Support & Tech. Dev.



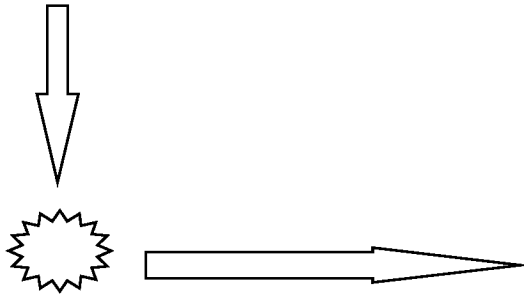
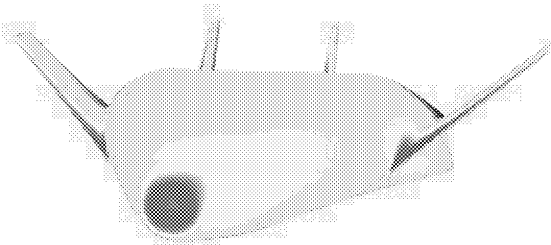
- **X-33 / RLV Vehicle Design Support (continued)**
 - Ascent loads with and without plume
 - Aerodynamics load benchmark with LaRC jet-effects tests
 - Plume induced thermal loads
 - **CFD used to supplement empirical data base**
 - Base heating hot-fire short duration tests
 - LH2 feedline hydrodynamic design, analysis, & cold flow test
 - Tight packaging, close-coupled valve, J-2 turbomachinery
 - X-33 sonic boom prediction for environmental impact statement
- **Liquid Fly-Back Booster Wind Tunnel Tests**
 - Fly-back, liquid propulsion boosters under consideration for Shuttle upgrades
 - Support aerodynamic configuration development
 - Using wind tunnel data for CFD code assessment



Recent Program Support & Tech. Dev.

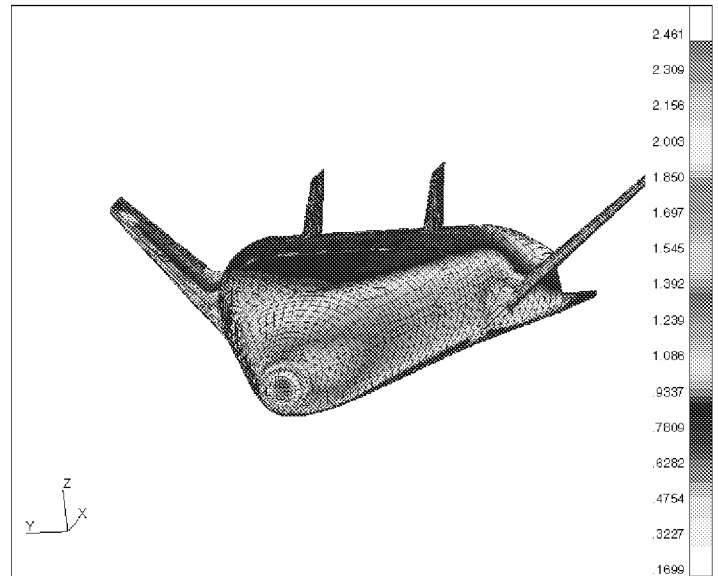


CFD External Pressures



Interpolate CFD onto Finite Element Model

External Applied CFD Pressures onto Finite Element Model

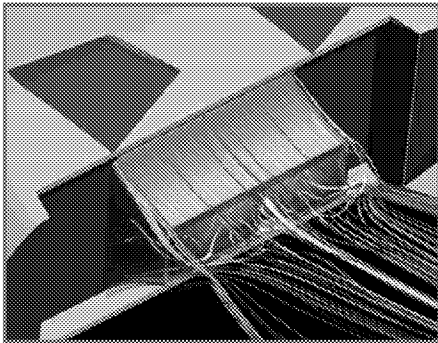




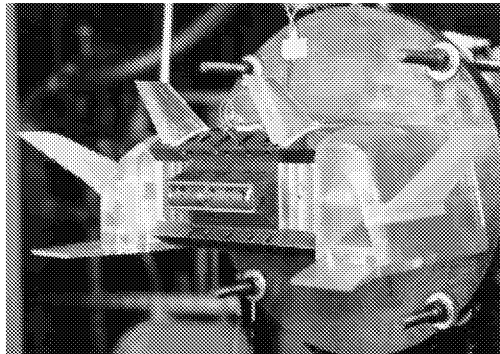
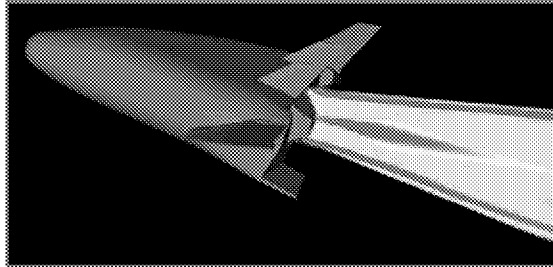
Recent Program Support & Tech. Dev.



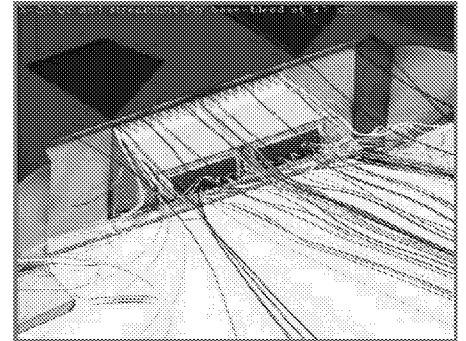
Linear Aerospike Plume-Induced X-33 Base-Heating



Sea level, no bleed



Short Duration hot-fire of base flows



At an altitude of 3.7km w/ base bleed



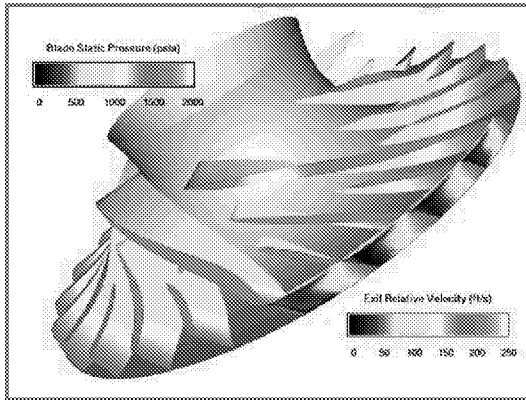
Ongoing Activities



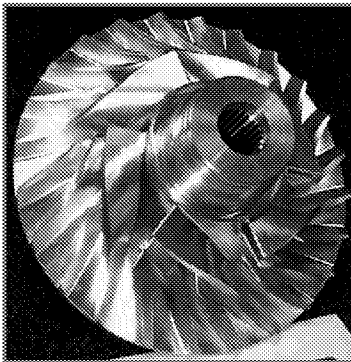
- **RLV Focused Technology**
 - Awarded two tasks to develop RLV turbomachinery technology
 - Turbine optimization task
 - Eliminate dependence on availability of composites &/or increase Isp
 - **Daniel Dorney presentation Tuesday morning (Fluids 3a)**
 - Unshrouded impeller technology development task
 - Increase stage loading without sacrificing efficiency
 - **George Prueger presentation Tuesday morning (Fluids 3a)**
- **Rocket Based Combined Cycle Concepts Development**
 - Trailblazer LOX-LH2 and DRACO LOX-Hydrocarbon concepts
 - Code benchmark for ejector mode operation
 - **Joe Ruf presentation later this morning (Fluids 1b)**



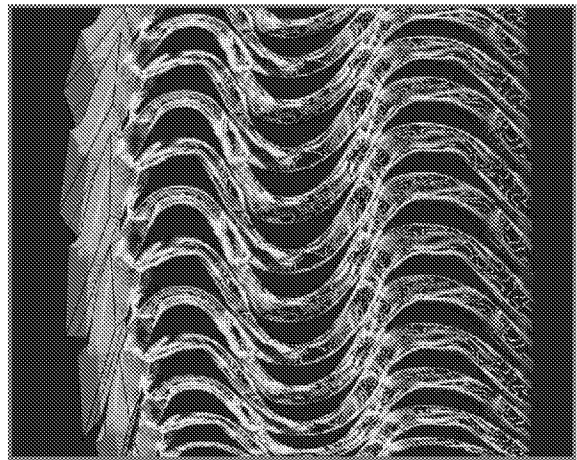
Ongoing Activities

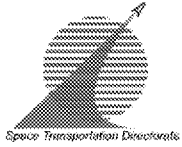


RLV Focused Technology
Unshrouded Impeller Tech.



RLV Focused Technology
Turbine Optimization

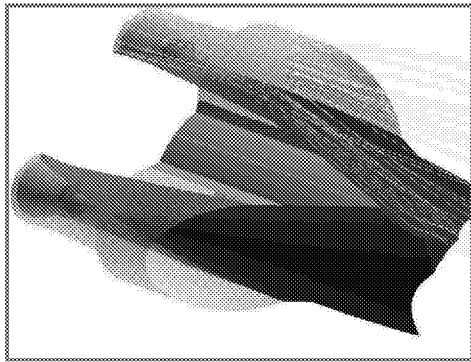




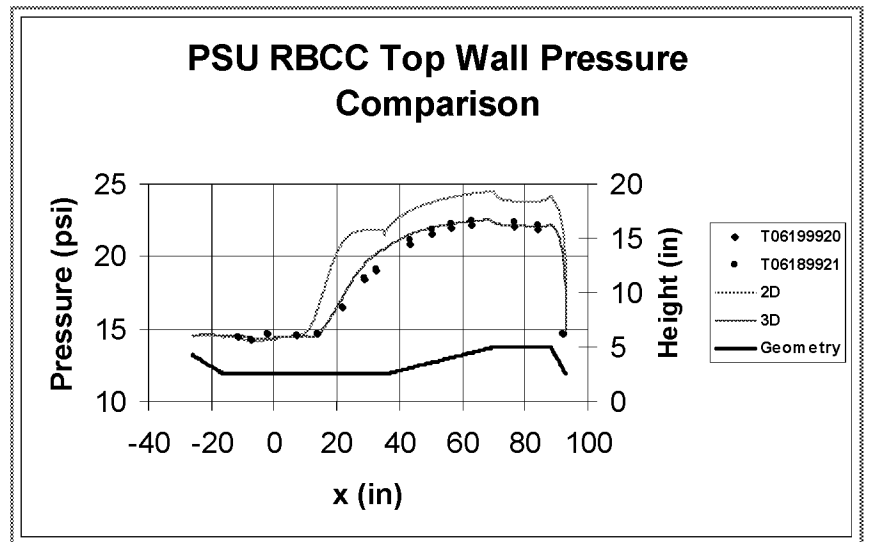
Ongoing Activities



Ejector concept parametrics



Trailblazer nozzle concept assessment



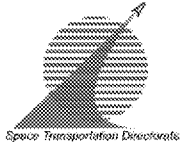
Ejector mode code benchmark
Using Penn State data



Ongoing Activities



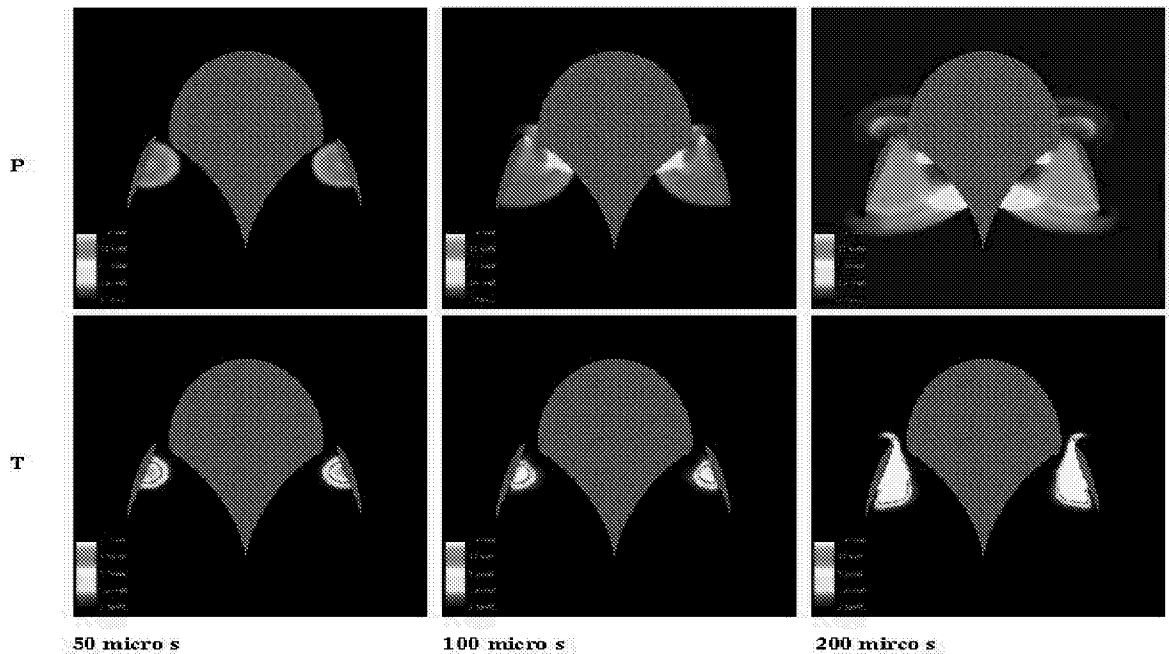
- **Methodology and Code Development**
 - Assessing & developing codes to support advanced propulsion concepts
 - Pulse detonation wave engine code assessment
 - Laser-light craft performance prediction code development
 - Defining requirements for high temperature, ionized flows
 - Demonstrating coupled fluids-thermal analysis capability in support of RBCC concept development
 - Assessing available unstructured grid generation capability
 - Developing optimization techniques
 - **Kevin Tucker presentation this afternoon (Fluids 2a)**
 - Assessing and demonstrating CART3D
 - Inviscid, Cartesian vehicle aerodynamic code
 - **Michael Aftosmis presentation later this morning (Fluids 1b)**



Ongoing Activities

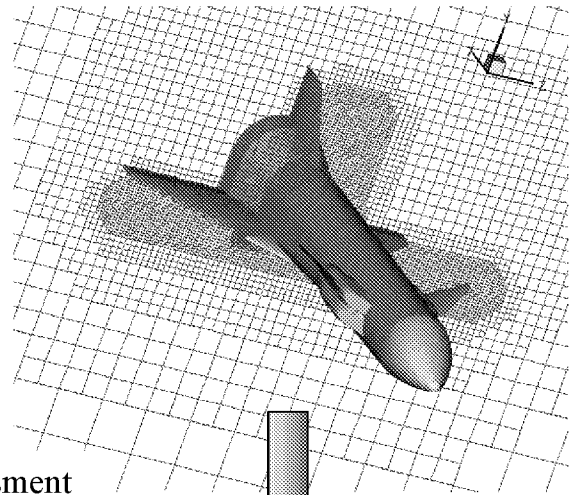
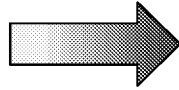
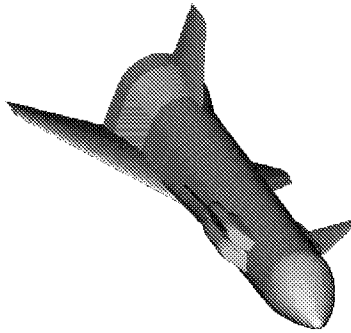


Performance Modeling of Laser Light Crafts

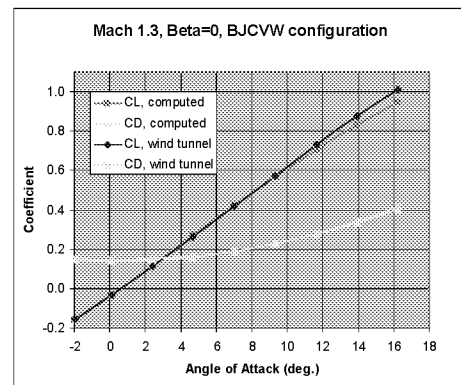
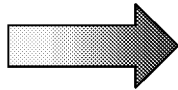
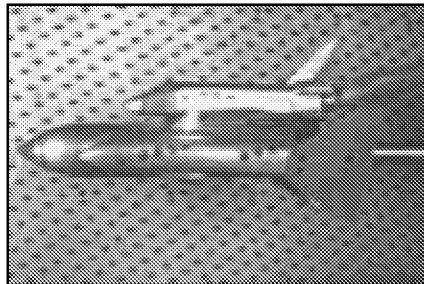
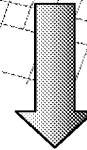


NASA/MSFC/ED32 Laser Lightcraft Thermo-Fluid Field Simulation

Ongoing Activities



LFBB used for CART3D Assessment





Future Activities and Direction



- **Hardware Design and Development**
 - RLV engine preliminary design (next 12 months)
 - Aerodynamic design and cold flow tests
 - Propulsion system environments
 - Support detail design of RBCC concepts (next 3 years)
 - DRACO flow path development and flight experiment
 - Trailblazer detail design
 - Combustion devices and turbomachinery supporting technologies
 - **Long life, wide flow range capabilities, low weight**
 - Spaceliner 100 Technology Roadmap
 - 5, 10, and 20 year goals
 - Hardware and supporting code technology
 - RBCC part of roadmaps 10 year goals
 - Laser light crafts part of 20 year goals



Future Activities and Direction



- **Tools Development**

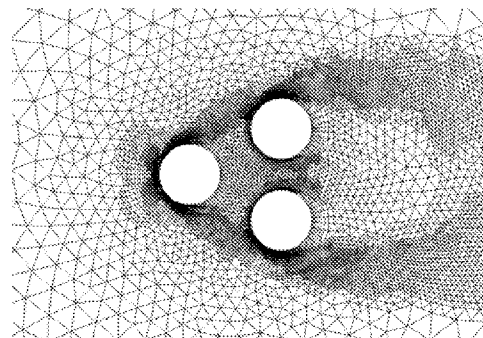
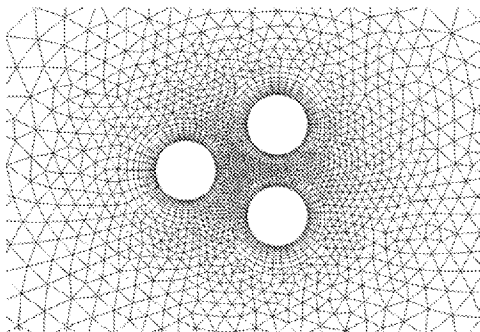
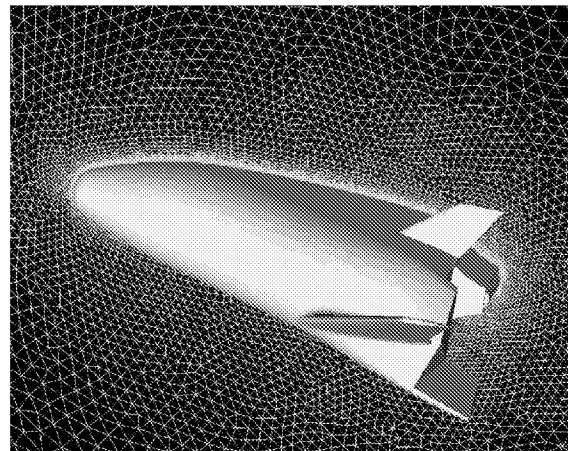
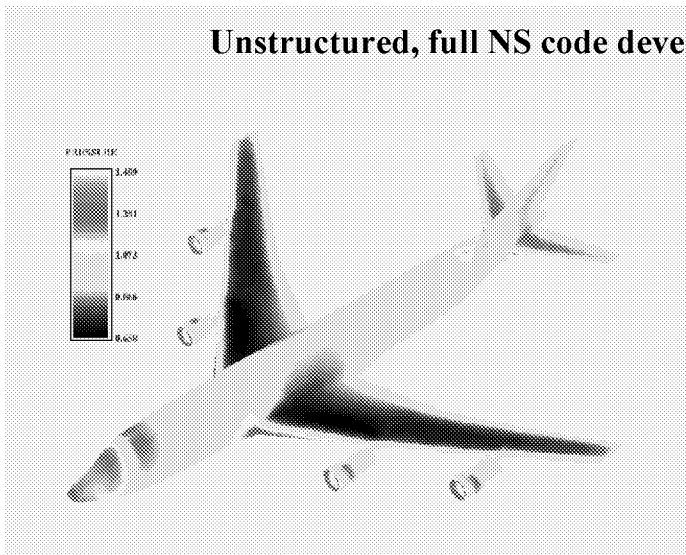
- Fast, efficient incompressible flow analysis code (Pearl)
- Time accurate, rotor-stator incompressible flow analysis capability
 - **Cetin Kiris presentation Tuesday morning (Fluids 3a)**
- Improvements to hydrocarbon combustion modeling capability
 - Increase code efficiency, expand physics
- Increase flexibility and capability at cold flow test facilities
 - On-rotor measurements, broader speed range for pump testing, allow nearly simultaneous testing of turbine and nozzle test facility
- Unstructured, full NS code development w/ finite rate capability
 - **Y. S. Chen presentation this afternoon (Fluids 2a)**
- Advanced Engineering Initiative (AEI)
 - Code improvements, automation, & integration into design system
 - Develop, demonstrate, and implement MDO capability



Future Activities and Direction



Unstructured, full NS code development w/ finite rate capability





Concluding remarks



- **Constraints**
 - Budget situation currently tenuous
 - New starts will suffer if budget cuts not addressed
- **Cooperation**
 - Leveraging from each others activities necessary
 - Maximum benefits from invested funds, builds political support
- **Opportunity**
 - Future hardware development becoming more reliant on high fidelity analysis
 - Required to achieve the necessary system operational characteristics
 - Budget constraints, public relations (political) consequences of failure
 - In the midst of major leap forward in fluid analysis capabilities

Aerothermodynamics At NASA – Langley Research Center

K. James Weilmuenster
Senior Research Engineer
Aerothermodynamics Branch
NASA Langley Research Center
Hampton, VA

INTRODUCTION

The Aerothermodynamics Branch at NASA – Langley Research Center is tasked with developing, assessing and applying aerothermodynamic technologies to enable the development of hypersonic aircraft, launch vehicles, and planetary/earth entry systems. To accomplish this mission, the Branch capitalizes on the synergism between the experimental and computational facilities/tools which reside in the branch and a staff that can draw on five decades of experience in aerothermodynamics.

The Aerothermodynamics Branch is staffed by 30 scientists/engineers. The staff, of which two-thirds are less than 40 years old, is split evenly between experimentalists and computationalists. Approximately 90 percent of the staff work on space transportation systems while the remainder work on planetary missions. The Branch manages 5 hypersonic wind tunnels which are staffed by 14 technicians, numerous high end work stations and a SGI Origin 2000 system. The Branch also utilizes other test facilities located at Langley as well as other national and international test sites. Large scale computational requirements are met by access to Agency resources.

AEROTHERMODYNAMIC PROCESS

Aerothermodynamics is a blend of aerodynamic forces and moments, pressure/shear loading, heating and fluid dynamics across the speed range. This information is obtained from ground based experiments, engineering/computational analysis and flight test results and becomes the basis for the aerothermodynamic process.

The aerothermodynamic process is the road map that defines the steps necessary to turn mission requirements into a flight vehicle. A systems analysis, based on mission requirements, will define an initial concept. The configuration is then screened using parametric ground-based testing to determine whether or not the vehicle is flyable (aerodynamics) and survivable (aeroheating) throughout the reference trajectory. If the vehicle passes this test, then the flight characteristics of the vehicle are optimized using detailed ground based testing and CFD codes. Ultimately, the outer mold lines are frozen.

At this point, high fidelity testing and “benchmark” CFD codes are used to develop a flight data book and establish aerodynamic/aeroheating flight margins.

This process has been developed and refined through Langley’s involvement in the design and analysis of hypersonic vehicles beginning with the X-15 and currently the NASA family of X planes. During that time, the Branch has dealt with blunt to very slender vehicles such as the high energy Jovian entry vehicle, Galileo, the Shuttle Orbiter, DOD missile programs, Mars micro probes, NASP, Hyper X and the X-33.

ANALYSIS TOOLS

Up until the mid 1980’s, aerothermodynamic analysis was based on engineering tools, data obtained from ground based facilities and a very limited amount of flight data. At this time, Computational Fluid Dynamics (CFD) began to contribute to the knowledge base, primarily as a tool to characterize real-gas effects at flight conditions. As CFD has matured, it has taken on an increasingly larger role in the analysis of hypersonic vehicles. Currently, for a given vehicle, CFD accounts for approximately 25% of the aerothermal data base. In another decade that percentage should double due to increased computer speed/size, radical improvements in surface modeling/grid generation and improved solution techniques. However, ground based facilities will always be a major contributor to the aerothermodynamic data base due to their ability to quickly generate large amounts of data.

Ground Based Testing

The Aerothermodynamic Facilities Complex¹ (AFC) represents all of NASA’s experimental aerothermodynamic testing capability via conventional-type (as opposed to impulse-type) hypersonic blowdown-to-vacuum wind tunnels. The five facilities of the AFC provide a Mach number range from 6 to 20 using three different test gases. The 20-Inch Mach 6 Air Tunnel can provide unit Reynolds numbers from 0.5 to 8 million per foot in perfect air (i.e. $\gamma = 1.4$ in the freestream and within the model shocklayer) via reservoir stagnation pressures from 30 to 500 psia at a temperature of approximately 950 °R. The 15-Inch Mach 6 Hi Temp Tunnel provides essentially the same Reynolds number in air, but at an increased total temperature capability (to 1500 °R). The 20 –Inch Mach 6 CF₄ Tunnel simulates real-gas effects at Mach 15 – 20 by using a gas three times heavier than air which provides a relatively low value of γ within the shocklayer of the model; thereby simulating the low γ aspect of a dissociated gas. . The 31-Inch Mach 10 Tunnel can provide unit Reynolds numbers of .5 to 2 million per foot at reservoir stagnation pressures of 350 to 1450 psia at a temperature of 1850 °R. The 22-Inch Mach 15/20 He Tunnel provides a high Mach number test capability using an unheated gas as helium can be expanded from ambient temperature to Mach 26 without liquification. Over the past decade, these facilities have been upgraded to improve data quality and to implement a common instrumentation and data acquisition system among the facilities.

Standard measurement and visualization techniques, strain gauge balances to obtain aerodynamics, oil-flow for surface streamlines, thin film resistance gauges for discreet surface temperature/heat flux measurements, electronically scanned pressure models and

schlieren are available. In addition, Langley has developed phosphor thermography² technology to obtain global surface heat transfer measurements. Work is continuing to enhance the quality of the experimental data by implementing rapid model fabrication³ and 3-dimensional optical scanning⁴ QA processes to reduce time from design to test as well as improved measurement and data analysis techniques. Model coatings⁵ capable of providing simultaneous global temperature and pressure distributions will undergo tunnel testing by the end of this year. In addition, a technique⁶ designed to rapidly extrapolate ground based heating data to flight surface temperatures has shown great promise.

CFD and Grid Generation

Grid Generation: One of the major impediments to the timely inclusion of CFD analysis in the design process has been the long lead time required to generate grids. The Aerothermodynamics Branch has made a large investment in the development of a state-of-the-art, robust grid generation process based on commercial and in-house developed software for both structured⁷ and unstructured⁸ grid generation. Given a surface definition, block decomposed, viscous, structured grids can be generated in 1-5 days depending on the complexity of the configuration while parametric geometry changes and regriding can take as little as ½ day. Currently, the Branch's unstructured grid generation is based on the FELISA⁹ system and limited to grids for inviscid flow. A viscous capability based on the VGRID¹⁰ software is being developed. In general, the unstructured grid generation is less cumbersome than the structured grid generation and it is much easier to handle parametric geometry changes. It is still time consuming due to required initial preprocessing of the surface geometry. Limited grid adaptation for structured grids is imbedded in the flow solver with some additional refinement capability available through the grid generation tools while unstructured grid adaptation resides in the grid generator.

Computational Tools: The Branch has several codes at its disposal. Some are designed for specific tasks or flow regimes while others are general in nature.

The Langley Approximate Three-dimensional Convective Heating¹¹ (LATCH) and Solution of the Axisymmetric Boundary Layer Equations¹¹ (SABLE) are engineering codes designed to quickly assess a vehicle's thermal environment. LATCH can rapidly compute the approximate heating along inviscid surface streamlines on complex three-dimensional vehicles based on the axisymmetric analog for 3D boundary layers. The SABLE code computes axisymmetric and two-dimensional boundary layer flows on reentry vehicles and can be interfaced with the LATCH code to compute approximate 3D boundary layer solutions along streamlines on complex vehicles. Each of these codes has a turbulent option and can handle perfect gas, CF₄ and equilibrium air chemistry flows. In each code, edge conditions are obtained from an existing 3D inviscid flowfield solution. LATCH can work with solutions on both structured and unstructured grids while SABLE is currently restricted to working with structured grids. Both of these codes can compute the global heating in a matter of minutes on a SGI R10000 work station.

The FELISA⁹ code is an inviscid flow solver for unstructured grids that is multigrid accelerated for subsonic/ supersonic flows, TVD upwinded for hypersonic flows and can

handle perfect gas, CF₄ and equilibrium air chemistry flows. The code is used extensively for parametric aerodynamic analysis and trade studies and to generate input solutions for the LATCH code. The Langley Aerothermodynamic Upwind Relaxation Algorithm¹² (LAURA) code also has an inviscid option for structured grid computations.

The LAURA code is the “benchmark” flow solver used by the Branch. It is a finite-volume code based on Roe’s averaging and TVD limiters. It has options for chemical and thermal nonequilibrium flow in Earth and Mars atmospheres, laminar or turbulent flow and finite catalytic wall models. This code has been extensively validated against ground based and flight data and has been the workhorse CFD code in the development of Mars entry vehicles and the NASA’s current family of X planes. The commercially available GASP code was also used in parts of the X33 and X34 programs.

The Viscous Shock Layer¹³ (VSL) code provides the Branch with a tool to quickly assess high energy entry flows over axisymmetric bodies using detailed thermodynamic and chemistry models and accounting for surface ablation, radiation and shock slip.

The Direct Simulation Monte Carlo¹⁴ (DSMC) method is based on the statistical simulation of molecules as they collide with themselves and a vehicle moving through a fluid. DSMC is used to simulate flows under highly rarified conditions where conventional continuum methods such as Navier-Stokes analysis are not valid. The applications can range from RCS jet interactions to on orbit contamination studies.

With the exception of the VSL code, all of the flow solvers used by the Branch have a vector and MPI implementation. The codes are routinely run on C-90 and SGI Origin 2000 mainframes as well as single and clustered workstations. The Branch is also investigating a shared memory multi-level parallel implementation of the LAURA code on a 256 processor Origin 2000.

CFD is still a maturing technology which offers many opportunities for large productivity gains. The Aerothermodynamics Branch is looking to the following areas to elevate the quality and timeliness of CFD in the aerothermodynamic design process. The grid generation process can still be improved. In particular, by tying the grid generator directly to the configuration’s CAD representation. This can improve the structured grid generation process, but the big impact is on the time required to generate an unstructured grid, which can be reduced by an order of magnitude, and at the same time improve the quality of the surface grid. The Branch has a prototype for such a system working and will continue the development of this software. To take advantage of this enhanced unstructured grid generation capability, the Branch is building a new “benchmark” flow solver based on unstructured grids the will maintain all of the functionality of the current LAURA code and include grid adaptation based on error estimates from the adjoint equations. In addition, the Branch will continue to search for improved engineering prediction technology that will speed the analysis process over the hypersonic portion of a trajectory and the rapid integration of flight thermal environments with TPS sizing programs.

FLIGHT DATA

Hypersonic flight data is very scarce, but it represents a unique opportunity to benchmark prediction techniques, both experimental and computational, against flight values. Historically, the Branch has utilized all available flight data in this manner. For example, confidence in the Branch's analysis tools being used in today's X plane programs is directly linked to Shuttle Orbiter flight data which is almost 20 years old. There will soon be new opportunities for benchmarking against flight data as the X planes begin to fly. These vehicles represent new configurations and TPS systems relative to vehicles that have flown in the past. Also, on board measurements should be of a higher quality than those available in the past and there is also a potential to get global surface temperatures from ground based measurements. As with the Orbiter flight data, this new set of data will drive significant improvements in both experimental and computational aerothermodynamic analysis tools.

FUTURE PROGRAMS

With the emphasis on space transportation systems and reduction in the cost of access to space, aerothermodynamics is in the critical path of NASA's high profile programs. While the X-33/X-34 programs are nearing flight status, The X-37, 2nd generation RLV(Lockheed Martin) and 3rd generation space transportation system programs are being initiated. An exciting growth area for aerothermodynamics is the renewed interest in high energy planetary entry probes such as the Mars Sample Return, Comet Sample Return and Human Exploration and Development of Space (HEDS) programs.

SUMMARY

The Aerothermodynamics Branch has developed a well defined process for aerothermodynamic analysis and design based on five decades of experience. As NASA's lead Center for aerothermodynamics, the Branch has the personnel, experimental facilities and computational tools to effectively carry out its mission while continuously upgrading its analysis capabilities. NASA's current focus on access to space activities will keep aerothermodynamics in the critical path of these programs. However, renewed interest in high energy planetary entry missions is a growth area for this discipline.

1. Michael DiFulvio, (757) 864-5229, m.difulvio@larc.nasa.gov
2. Norman R. Merski, Jr., (757) 864-7539, n.r.merski@larc.nasa.gov
3. Norman R. Merski, Jr., (757) 864-7539, n.r.merski@larc.nasa.gov
4. Gregory M. Buck, (757) 864-5240, g.m.buck@larc.nasa.gov
5. Gregory M. Buck, (757) 864-5240, g.m.buck@larc.nasa.gov
6. Norman R. Merski, Jr., (757) 864-7539, n.r.merski@larc.nasa.gov
7. Steve J. Alter, (757) 864-7771, s.j.alter@larc.nasa.gov
8. K. James Weilmuenster, (757) 864-4363, k.j.weilmuenster@larc.nasa.gov

9. Karen L. Bibb, (757) 864-8005, k.l.bibb@larc.nasa.gov
10. Shahyar Z. Pirzadeh, (757) 864-2245, s.z.pirzadeh@larc.nasa.gov
11. H. Harris Hamilton, II, (757) 864-4365 h.h.hamilton@larc.nasa.gov
12. Peter A. Gnoffo, (757) 864-4380, p.a.gnoffo@larc.nasa.gov
13. Roop N. Gupta, (757) 864-4385, r.n.gupta@larc.nasa.gov
14. James N. Moss, (757) 864-4379, j.n.moss@larc.nasa.gov



COMPUTATIONAL AERODYNAMIC DESIGN AND ANALYSIS OF A COMMERCIAL REUSABLE LAUNCH VEHICLE

M. R. Mendenhall, H. S. Y. Chou, and J. F. Love
Nielsen Engineering & Research

ABSTRACT

Aerodynamic analysis tools ranging from semiempirical engineering methods to Euler and Navier-Stokes CFD methods have been used with wind tunnel tests in an integrated design approach to accomplish the aerodynamic design and analysis of the Kistler Aerospace K-1 reusable launch vehicle. It was shown that traditional engineering missile aerodynamic prediction methods are not adequate for this unconventional RLV design, and it was necessary to rely heavily on applied CFD for the aerodynamic characteristics over a wide range of Mach numbers and angles of attack. The practical and economical uses of computational aerodynamic results for performance, stability and control, stage separation, trajectory simulations, and structural analysis are described.

NOMENCLATURE

| | |
|----------|---|
| C_N | Normal force coefficient |
| D | Reference diameter |
| LAP | Launch Assist Platform |
| OV | Orbiter vehicle |
| p | Static pressure |
| q | Dynamic pressure |
| X_{cp} | Center of pressure location, positive aft |
| (inf) | Free stream value |

INTRODUCTION

The need for commercial satellite launches is due in no small part to the large Low-Earth-Orbit constellations of communications satellites.¹ The projected launch needs for the next ten years far exceeds the current capabilities. As a consequence, the scarcity of future launch vehicles is encouraging new launch service providers to enter the market with new vehicles.

Kistler Aerospace is in the midst of the commercial development of a fully reusable launch vehicle, and NEAR has been tasked to provide the computational and experimental aerodynamic analyses to assist in the development of this unique vehicle. The K-1 vehicle is a two-stage RLV in which both stages are returned to the launch point; stage one immediately after separation from stage two, and stage two after a trip to orbit to release its payload.² To further

complicate the aerodynamic analysis, this real-world commercial venture is defined by a compressed development schedule with cost playing an important role. In an effort to tailor the aerodynamic analysis to the overall development program, it was necessary to accomplish the aerodynamic analysis using both computational methods and wind tunnel testing in an efficient integrated approach.

Engineering methods, CFD, and wind tunnel testing were used in a coordinated effort to provide the various levels of aerodynamic detail required by the various disciplines involved in the design. The purpose of this paper is to document some experiences using computational aerodynamic methods for the K-1 launch vehicle analyses. Evaluations of empirical, engineering, and CFD methods, their relative usefulness, their availability, and their reliability are described, and a discussion of practical problems involving computational aerodynamics for the K-1 vehicle are presented.

BACKGROUND

NEAR has provided aerodynamic support for a variety of commercial launch vehicles, including the Kistler K-1 RLV, Orbital's Pegasus³ and Taurus, and the Beal BA-2. Each of these projects required the selection of appropriate prediction methods. Factors of cost and schedule were considered along with accuracy and reliability when selecting the aerodynamic prediction methods. The objective is to minimize uncertainties in the aerodynamics, but the analyst must always consider what solution is adequate for each specific requirement to avoid using higher level methods than necessary thus increasing the analysis costs.

Depending on the design phase, conceptual, preliminary, or detailed, selection of the level and type of computational method to use is dictated by the type of results needed and the acceptable margins and error bounds for the results. This process has been accomplished at each step of the analysis to maintain control of the analysis costs while providing the best possible results to the disciplines using the aerodynamic characteristics. For example, general aerodynamic forces and moments are required over a wide range of Mach numbers and flow angles for use in performance and trajectory analyses as well as GN&C system design. Detailed pressure distributions are required at a more limited set of flight conditions for structural design and analysis and other studies such as venting and access door loads.

MISSION REQUIREMENTS

The general characteristics of the K-1 mission profile are shown in Figure 1. At launch (**1** in Fig. 1), the stack configuration is similar to traditional launch vehicles, and detailed analysis has been accomplished with both wind tunnel tests and computational methods. After stage 1 separation (**2** in Fig. 1), the aerodynamic requirements for the booster stage are unique because of the innovative flight requirements and unconventional configuration. The first stage shown in Figure 2(a) must rotate and fly at a very high angle of attack ($\alpha > 90^\circ$) in the wake of the orbiter vehicle (**2** in Fig. 1) in preparation for the return to the launch site. During the reentry phase, the first stage rotates 180 degrees and reenters the atmosphere with the nozzles forward.

The orbiter vehicle (OV) shown in Figure 2(b) continues the ascent into orbit where it deploys its payload (**4** in Fig. 1). During reentry, the computational aerodynamic challenges begin again. As part of the aerodynamic design and analysis of the OV, aerodynamic characteristics for a wide range of Mach numbers (subsonic, supersonic, and hypersonic) and a high angle of attack range (0 to 25 deg) are required. Because of the critical nature of the trim characteristics, it is important that the lift, drag, and center of pressure be known to a high degree of accuracy. In addition, the OV will deploy parachutes; therefore, the wake characteristics of the OV must be known to reasonable accuracy for parachute design.

TECHNICAL APPROACH

The aerodynamic design and analysis of the K-1 configurations described above require creative use of analytical methods, CFD, and wind tunnel testing in an integrated design effort. Many different prediction methods are available for application to launch vehicles, ranging from engineering methods^{4,5} to CFD.^{6,7,8} Those described herein are not the only codes available, but they are the methods that have been validated at NEAR, and there is an experience base to provide some confidence about the accuracy and reliability for specific flow conditions. It is also important to understand the influence of configuration characteristics on the resulting aerodynamics so that the proper code selection is made for the specific configuration of interest. Because of the compressed schedule dictated by the commercial effort, it is important that results be available on a timely basis and that the accuracy of the individual results be assessed. As noted above, it is important that the analytical results be 'good enough' without being 'too good' because of the additional time and costs associated with using a higher-level prediction method than necessary.

The initial technical approach was to obtain preliminary aerodynamic characteristics with an engineering prediction method.^{4,5} Because of the critical nature of the center of pressure on the orbiter vehicle, it was soon determined that the engineering methods were not adequate to this task. It was determined that Euler⁶ solutions were the minimum acceptable level of prediction method which would provide the required accuracy in center of pressure for the range of Mach numbers of interest. Consequently, as the configuration changed during preliminary design, the aerodynamic characteristics were updated through iteration between Euler solutions and wind tunnel tests. As the configuration converged, solutions of the Navier-Stokes equations were used to provide detailed aerodynamic characteristics for those conditions for which viscous effects are important. As part of the CFD effort, grids and solutions from independent sources^{7,8} were used to evaluate the quality of the predicted results.

PRELIMINARY DESIGN

For purposes of this discussion, many codes with varying levels of fidelity have been classified as preliminary design methods. In earlier work, this classification was reserved for semiempirical and lower level engineering methods, and engineering and panel methods were classified as higher fidelity methods. However, with the advances in computer power and the use of higher fidelity methods during preliminary design, all of these methods have been grouped under preliminary design. They will be discussed in order of increasing fidelity.

M3HAX⁵ is a semiempirical method which uses a combination of theoretical models and an experimental database for tail fin loads. The method emphasizes high angles of attack and transonic speeds, and M3HAX has been validated extensively by comparison with measured aerodynamic characteristics for a wide range of configurations. Unfortunately, the extremely blunt nose of the K-1 OV and the absence of control surfaces dictate that M3HAX would not be adequate for this analysis.

Missile DATCOM⁴ was developed specifically for preliminary design applications and it has also been validated by numerous comparisons with experimental data. It is a body buildup method which uses prediction methods for each component of the configuration.

INVISCID CFD

OVERFLOW⁶ is usually run as a Navier-Stokes viscous solver; however, it can also be run in Euler mode for inviscid solutions using a coarser grid. The Euler solutions discussed in the Results section are from this code unless otherwise noted.

VISCOUS CFD

OVERFLOW⁶ is a Navier-Stokes CFD solver developed at NASA/Ames Research Center. It has become very efficient for large numbers of CFD simulations of different configurations like those discussed in this paper. It is a very flexible CFD tool for launch vehicle design. The central difference scheme with dissipation in space was used throughout the Kistler project for K-1 CFD analysis, and all CFD runs were obtained on either SUN or HP workstations.

CFL3D⁷ is a Navier-Stokes flow solver for multi-block and structured grids, developed at the NASA/Langley Research Center. It utilizes efficient multigrid and mesh sequencing relaxation schemes for the steady-state solutions. CFL3D provides the most comprehensive list of turbulence models, including 0-equation, 1-equation, and 2-equation models. CFL3D was used as a cross-checking tool for other CFD solutions in the K-1 analysis.

LAURA⁸ is a Navier-Stokes code designed for hypersonic viscous flow simulation developed at NASA/Langley Research Center. In particular, LAURA has comprehensive capabilities for both chemical equilibrium and non-equilibrium flow simulations. It was used in the CFD analysis of the K-1 configuration for Mach numbers greater than 6. NASA Langley Research Center⁹ produced the solutions shown from this code.

RESULTS

The Kistler K-1 orbiter vehicle (OV) has been studied with wind tunnel tests and a number of computational methods at all levels. The special requirements for this vehicle must always be considered when looking at the computational results; that is, it must return from orbit, be stable through the hypersonic and supersonic Mach regimes, and maintain reasonable trim characteristics until the landing parachutes can be deployed. The K-1 OV configuration with its blunt nose, long cylindrical body, and aft flare proved to be a challenge for all the prediction methods investigated. CFD solutions were used to tailor the nose bluntness to move the center of pressure aft for increased static stability at low supersonic speeds. These results were then verified in wind tunnel tests.

Aerodynamic forces and moments were obtained using all levels of methods, including Missile DATCOM and CFD solutions for both Euler and Navier-Stokes equations. The version of M3HAX available during the preliminary design phase was not capable of handling the OV flare with reliability, so it was not considered for this analysis. Wind tunnel data were also available for the range $0.8 \leq M_{\infty} \leq 20$ for use in validation of the methods. As the design evolved, the results from the computational methods could be used with greater confidence and reduced uncertainties based on the comparisons between experiment and computations for the previous configurations.

The geometry and mass characteristics of the K-1 OV are such that the vehicle trims at a positive angle of attack over the entire Mach range. The normal force coefficient and the longitudinal center of pressure at a constant $\alpha = 8$ deg is shown as a function of Mach number in Figure 3. In this figure, the wind tunnel results shown are from several different test programs and different tunnels. The data for $M_{\infty} \geq 6$ are from NASA/Langley Research Center.¹⁰ Though there is some roughness in the data from the tests at $M_{\infty} \leq 4.4$, the general character of the data for the entire Mach range is consistent.

The predicted normal force coefficients from the different computational methods are shown in Figure 3. The Missile DATCOM results are greater than the measurements, and the agreement seems to deteriorate at the higher supersonic Mach numbers. This may be caused by a problem with the aerodynamic contribution of the flare and the inability to handle nonlinear effects. The Euler solution is not available for $M_{\infty} < 1$, but above Mach 3, the results are in good agreement with the experiments to about Mach 10. Finally, the viscous Navier-Stokes solutions from OVERFLOW through the transonic range and the supersonic range to about Mach 2.5 are in very good agreement with the experimental data.

Results from the LAURA aerothermodynamics CFD code were provided by NASA/Langley.¹⁰ The differences between the LAURA and the OVERFLOW results have been attributed to the use of real gas effects and a slightly coarser grid for the LAURA calculations. CFL3D and OVERFLOW provide nearly identical results for calculations on the same grid.

Because of the importance of the static stability on the return flight of the OV, the centers of pressure for the above flight conditions are also shown in Figure 3 for the wind tunnel data and the computational results. These comparisons demonstrate that Missile DATCOM is not able to produce acceptable results for longitudinal center of pressure. At $M_{\infty} < 1$, DATCOM predicts the center of pressure to be forward of that measured in the wind tunnel by approximately 0.2D. This is a conservative result in that it indicates less static stability than the wind tunnel data. At supersonic speeds, DATCOM predicts the center of pressure to be approximately 0.2D aft of that measured in the wind tunnel. This is an unconservative result that indicates more static stability than the wind tunnel data. While an error of 0.2D in the center of pressure is often acceptable for slender tactical missile configurations, it is not acceptable for a vehicle like the K-1 OV.

Both Euler and Navier-Stokes CFD solutions for center of pressure are in reasonable agreement at supersonic Mach numbers. At hypersonic Mach numbers, the predicted center of pressure is nearly 0.2D forward of that measured in the wind tunnel, but there is some uncertainty about the validity of the measurements at $M = 20$ in the He tunnel at LaRC. The real gas results from the LAURA code and the perfect gas results from the OVERFLOW code are not in as good agreement as expected. The normal force distributions on the OV from both solutions show similar results, but the real gas effects change the loading on the flare and have a large impact on the vehicle center of pressure.

The traditional approach to analyzing vehicle aerodynamics is to look at the variation of normal force and center of pressure as a function of angle of attack at a constant Mach number. The results of the comparison of measurements and predictions for the OV at Mach 2.0 are shown in Figure 4. The predicted normal force on the OV is in good agreement for all levels of computational results, further verification that normal force is relatively easy to predict using lower level methods.

The center-of-pressure results in Figure 4 illustrate the challenge in the selection of a computational method for preliminary aerodynamics design. The engineering method, DATCOM, produced very optimistic stability results at low angles of attack, but above 20 degrees, these results are in reasonable agreement with the wind tunnel results. The inviscid Euler results are much closer to the experimental results, and at low angles of attack where the agreement is poorest, the predicted results are conservative in that they indicate less static stability than exhibited by the vehicle. The viscous results are in good agreement over the entire angle range.

Another interesting application of CFD for the K-1 OV analysis was to define the details of the flow in the wake at supersonic Mach numbers. The LAP must fly in the OV wake for a short time after separation, and a drogue chute will be deployed from the OV at low supersonic Mach numbers. Data for CFD validation purposes are not available at the Mach numbers of interest, but appropriate wake data are available at a higher Mach number; therefore, validation of the computations was conducted at a higher supersonic Mach number to build confidence in the solutions at the lower Mach numbers. These results are shown in Figures 5 and 6.

In Figure 5, the predicted variation of local Mach number and pressure on the centerline of the OV is compared with measurements in the wake of a similar flared body.¹¹ These viscous solutions were obtained at Mach 4.4. Although the data measurements are sparse, the agreement is quite reasonable.

In Figure 6, the predicted dynamic pressure profiles across the OV wake are shown at several downstream locations. The wind tunnel measurements were obtained from measurements of the axial force on the LAP as it was traversed through the wake. The dynamic pressure ratio was assumed to be the ratio of the axial force in the wake to the axial force in the free stream. The predicted details of the wake are in very good agreement with the experiments, including the location of the bow and flare shocks. The locations of these shocks were also validated with shadowgraph measurements during the wind tunnel test.

CONCLUSIONS

Applied CFD has been used extensively during the preliminary design of a reusable launch vehicle. Euler solutions have proved to be useful as a practical design method, and Navier-Stokes solutions have been used for selected conditions for which high accuracy and detailed flowfield results were needed. Wind tunnel data were used to validate the analytical results and assess the aerodynamic uncertainties.

One of the lessons learned in the aerodynamic design and analysis effort is that advanced CFD methods can be used routinely for the prediction of aerodynamic characteristics on unusual and unconventional flight vehicles. It was shown that these methods can provide aerodynamic information on a timely basis while keeping to the cost and schedule of a commercial program.

Though a number of different aerodynamic tools are required for the successful computational aerodynamic design and analysis of advanced launch vehicles, some care must be applied before using the results, particularly if test data are not available. The user must understand the limits and uncertainties involved with the different methods and approaches. Codes should be validated and grids must be examined carefully for convergence, but it is often tempting to accept without question the aerodynamic results from the methods without exercising a bit of healthy skepticism. It is difficult to be critical when caught up in the euphoria of getting a computational solution on a complex configuration. Application of the prediction methods to selected sample cases on similar configurations for which wind tunnel data are available is highly recommended to build up some experience in the use of the individual codes.

Wind tunnel tests are important in the validation of prediction methods, but if they are not available, the aerodynamics analyst should consider the use of multiple independent codes to test the results for consistency. However, even if this is accomplished, the analyst must have a basic understanding of the applicability of the different levels of computational methods before accepting the predicted aerodynamic characteristics. For example, engineering methods usually predict normal force, but they have problems with center of pressure. Xcp is usually forward of the actual location for the simpler methods. Euler solutions provide the same level of quality in normal force predictions, but the center of pressure is generally better. Viscous solutions will provide the best normal force results, and the center of pressure is much more reliable; however, the major disadvantage is the cost required to achieve good solutions.

ACKNOWLEDGEMENTS

The authors acknowledge Kistler Aerospace Corporation for their willingness to use computational aerodynamics in the design and analysis of the K-1 RLV and for permission to discuss the aerodynamics of the K-1 vehicle. Richard Petersen and Ryan Curtis of Kistler worked closely with the authors on the aerodynamics analyses, and they had the difficult task of making practical use of the aerodynamic information produced by the authors. The authors also wish to thank Peter Gnoffo and Frank Greene of the NASA/Langley Research Center for the LAURA CFD and wind tunnel results on the Kistler orbiter vehicle. In addition, many other staff members at NASA/Langley made valuable contributions to the understanding of the aerodynamics of the K-1 vehicle.

REFERENCES

1. Beardsley, T., "The Way to Go in Space," *Scientific American*, Feb. 1999, pp.80-97.
2. Proctor, P., "Kistler Seeks to Create 'UPS of Space,'" *Aviation Week & Space Technology*, Jun. 30, 1997, pp. 53-55.

3. Mendenhall, M. R., Lesieutre, D. J., Whittaker, C. H., Curry, R. E., and Moulton, B., "Aerodynamic Analysis of Pegasus – Computations vs Reality," AIAA 93-0520, Jan. 1993.
4. Burns, K. A., Deters, K. J., Vukelich, S. R., and Blake, W. B., "Missile DATCOM: User's Manual - Revision 6/93," WL TR-93-3043, Wright Lab., Wright-Patterson AFB, OH, Jun. 1993.
5. Lesieutre, D. J., Love, J. F., and Dillenius, M. F. E., "M3HAX Aerodynamic Analysis for Finned Vehicles with Axisymmetric Bodies," NEAR TR 493, Nielsen Engineering & Research, Mountain View, CA, Nov. 1996.
6. Buning, P. G. et al, "OVERFLOW User's Manual, Version 1.6be," Feb. 2, 1996.
7. Krist, S. L., Biedron, R. T., and Rumsey, C. L., "CFL3D User's Manual, Version 5.0", NASA TM-1998-208444, Jun. 1998.
8. Gnoffo, P. A., "LAURA User's Manual, Version 4.1," NASA document, 1998.
9. NASA/LARC CFD analysis of K-1 OV, Frank Greene and Peter Gnoffo private communications.
10. NASA/LARC hypersonic wind tunnel tests of K-1 OV, Frank Greene private communication.
11. Heinrich, H. G. and Hess, R. S., "Pressure Distribution in the Wake of Two Bodies of Revolution at Transonic and Supersonic Speeds," ASD TDR 62-1104, 1963.

Figure 1.- Kistler K-1 Flight Profile

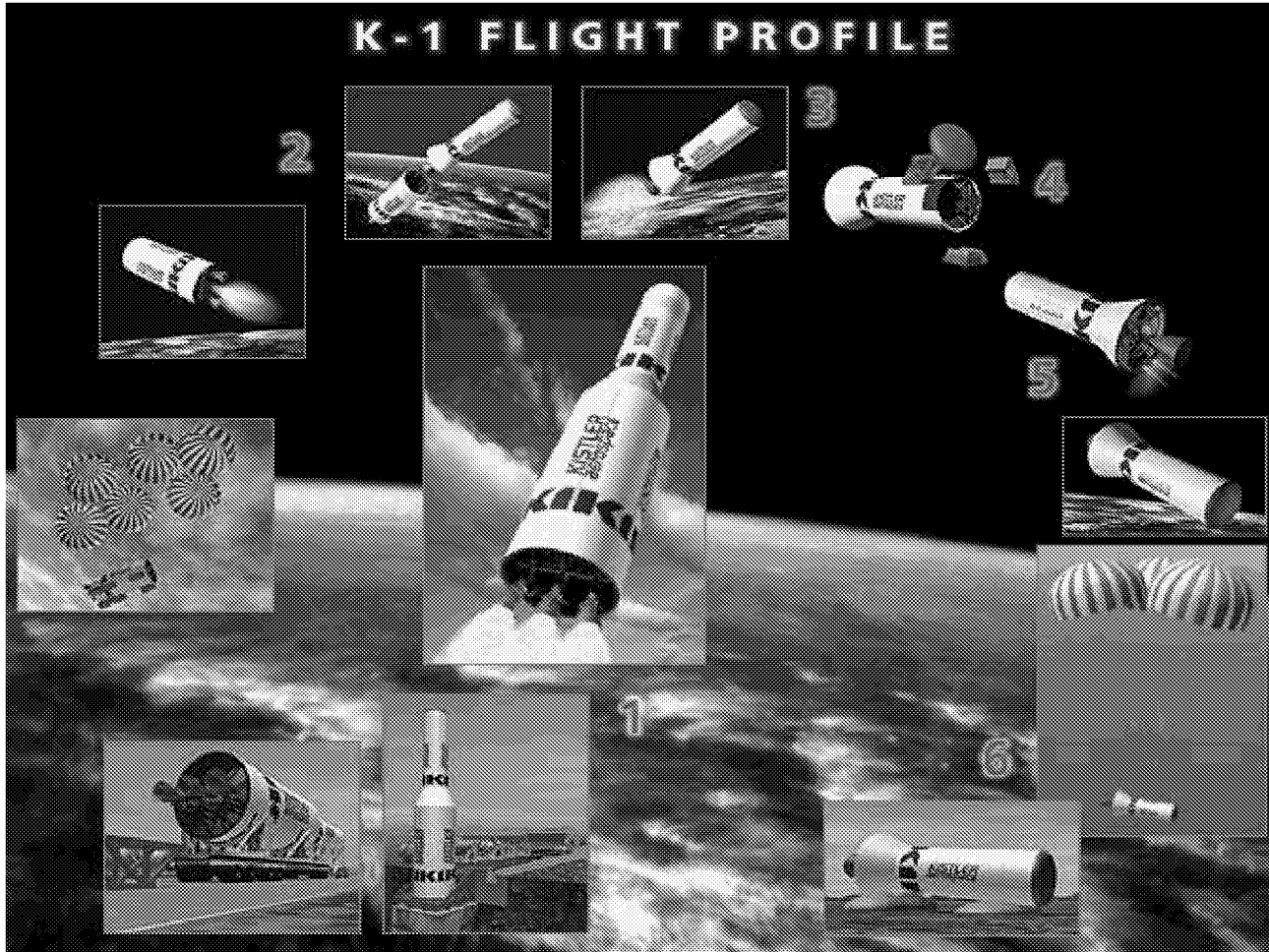


Figure 2(a).- Kistler Aerospace K-1 Stage 1 Booster

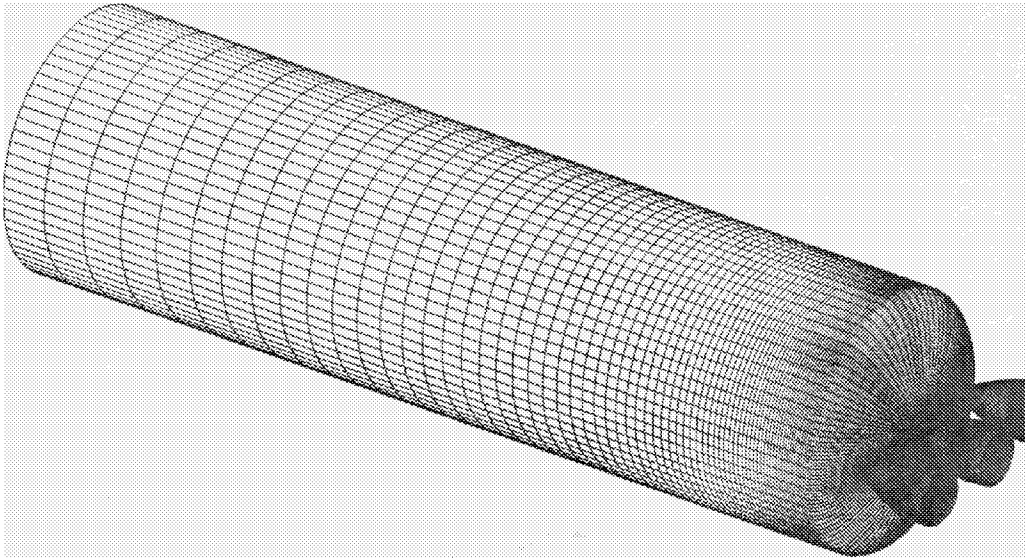


Figure 2(b).- Kistler Aerospace K-1 Orbiter Vehicle

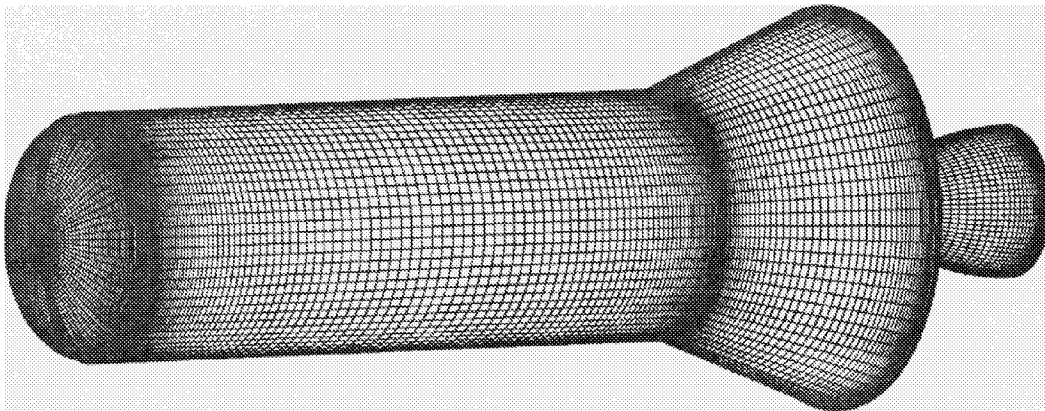


Figure 3.- Measured and predicted aerodynamic characteristics of the K-1 OV at AOA=8 deg.

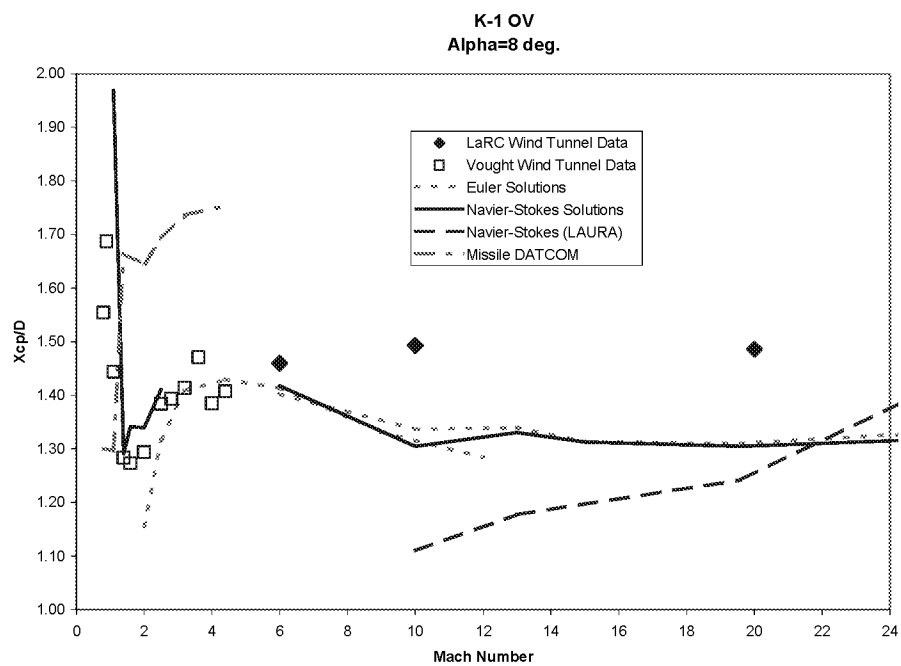
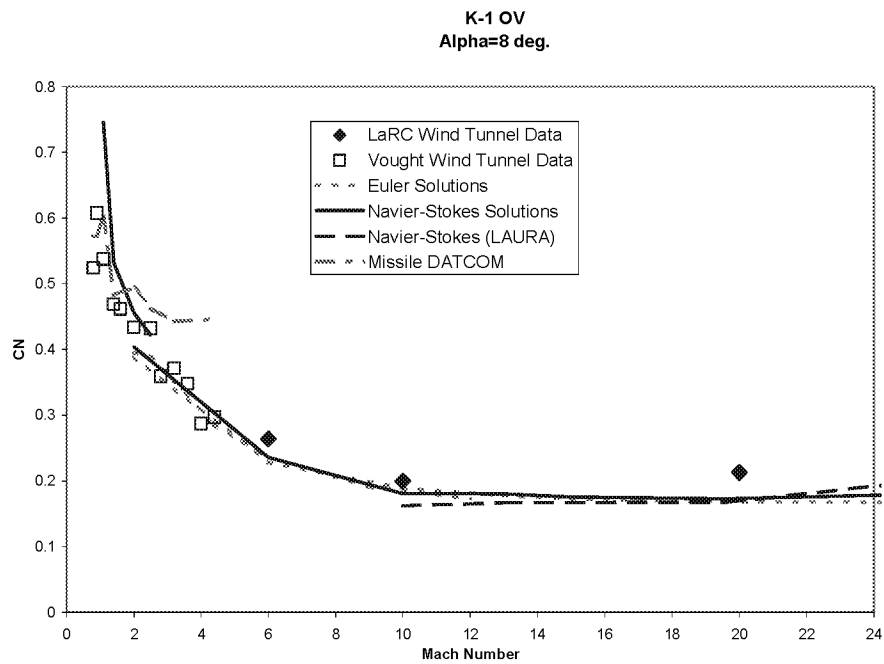


Figure 4.- Measured and predicted aerodynamic characteristics of the K-1 OV at Mach 2.

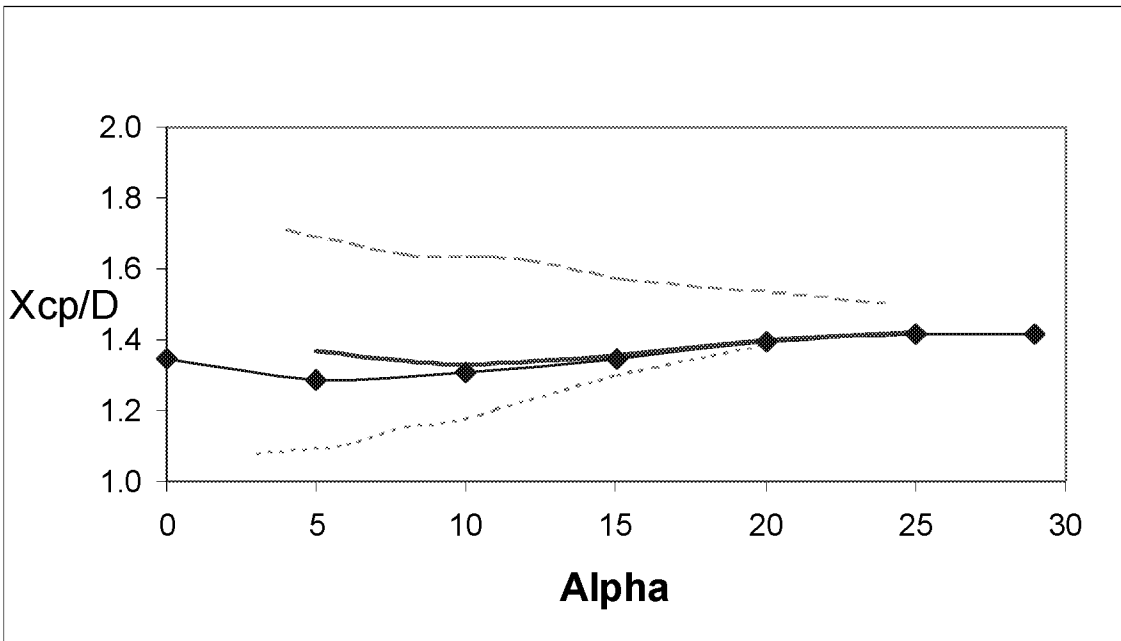
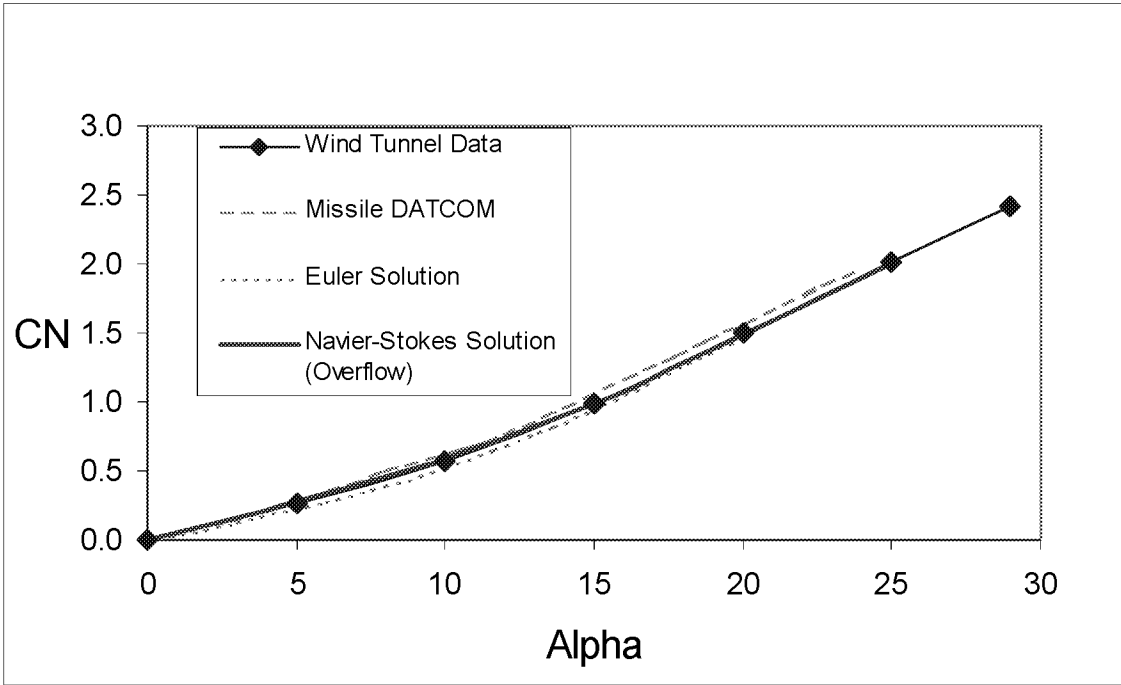


Figure 5.- Measured and predicted K-1 Orbiter wake characteristics

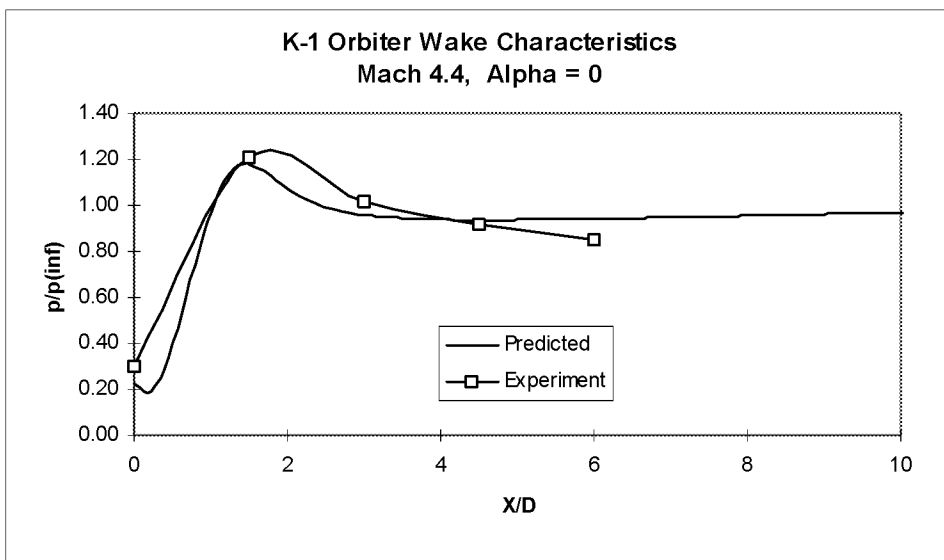
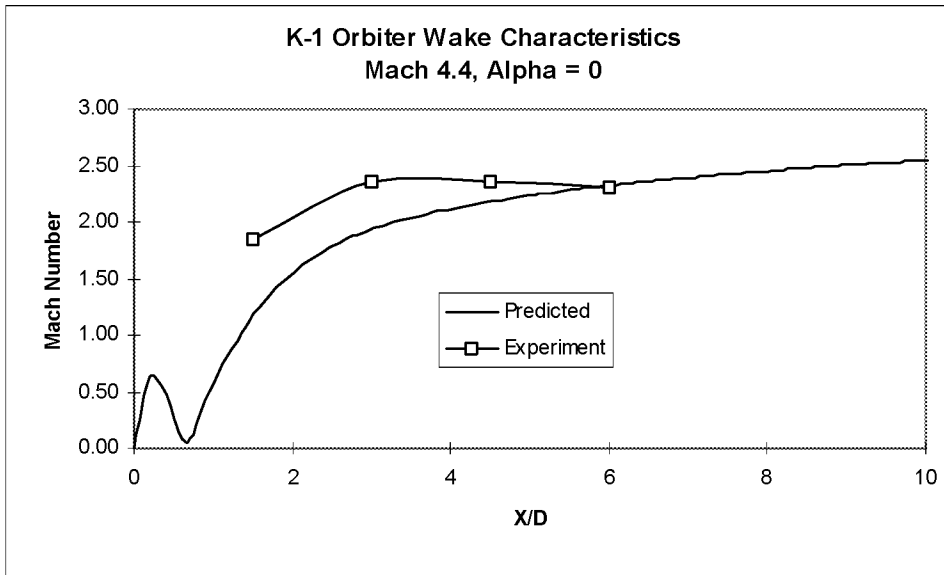
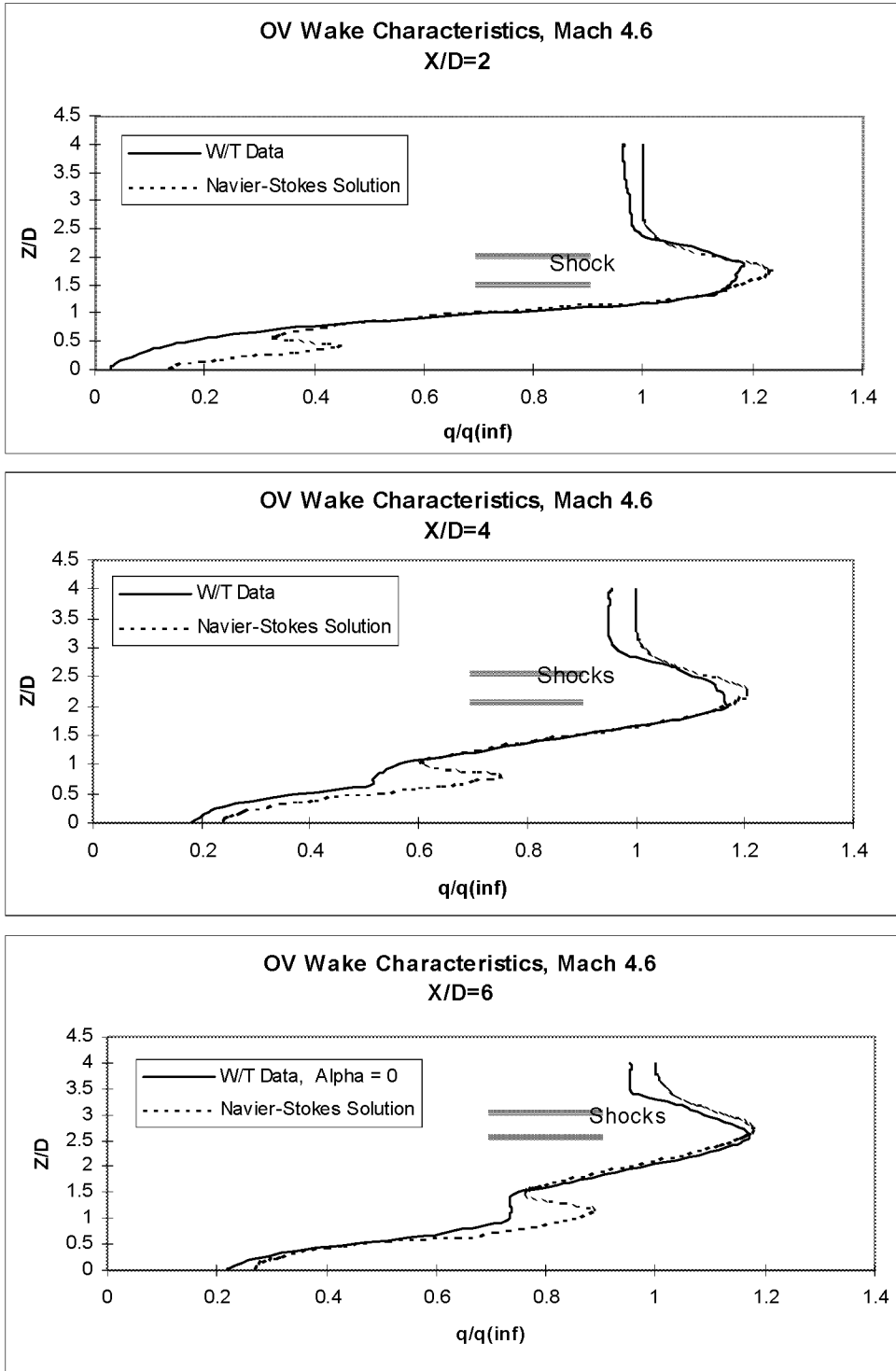
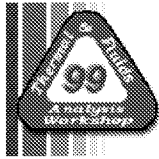


Figure 6.- Measured and predicted K-1 OV wake dynamic pressure profiles





A PARALLEL CARTESIAN APPROACH FOR EXTERNAL AERODYNAMICS OF VEHICLES WITH COMPLEX GEOMETRY

M. J. Aftosis

Mail Stop T27B
NASA Ames Research Center
Moffett Field, CA 94404
aftosis@nas.nasa.gov

M. J. Berger and G. Adomavicius

Courant Institute
12 Mercer St.
New York, NY 10012
berger@cims.nyu.edu

ABSTRACT

This workshop paper presents the current status in the development of a new approach for the solution of the Euler equations on Cartesian meshes with embedded boundaries in three dimensions on distributed and shared memory architectures. The approach uses adaptively refined Cartesian hexahedra to fill the computational domain. Where these cells intersect the geometry, they are cut by the boundary into arbitrarily shaped polyhedra which receive special treatment by the solver. The presentation documents a newly developed multilevel upwind solver based on a flexible domain-decomposition strategy. One novel aspect of the work is its use of space-filling curves (SFC) for memory efficient on-the-fly parallelization, dynamic re-partitioning and automatic coarse mesh generation. Within each subdomain the approach employs a variety reordering techniques so that relevant data are on the same page in memory permitting high-performance on cache-based processors. Details of the on-the-fly SFC based partitioning are presented as are construction rules for the automatic coarse mesh generation. After describing the approach, the paper uses model problems and 3-D configurations to both verify and validate the solver. The model problems demonstrate that second-order accuracy is maintained despite the presence of the irregular cut-cells in the mesh. In addition, it examines both parallel efficiency and convergence behavior. These investigations demonstrate a parallel speed-up in excess of 28 on 32 processors of an SGI Origin 2000 system and confirm that mesh partitioning has no effect on convergence behavior.

INTRODUCTION

Recent years have witnessed the rapid maturation of embedded-boundary Cartesian approaches. The work in references [1]-[7] (among many others) demonstrate that the approach can be used to robustly compute flows around vehicles with a high degree of geometric complexity. This strength is largely due to the underlying observation that cells in these meshes are purely Cartesian (away from geometry) or arbitrarily shaped polyhedra (where initially Cartesian hexahedra are clipped against the body's surface). Figure 1 illustrates the types of cells found in these meshes. Note that *cut-cells* as shown in fig. 1b may be split into any number of unconnected regions by the geometry, such *split-cells* imply that the index space of the Cartesian hexahedra will not, in general, be the same as that of the control volumes integrated by the solver.

The observation that cells in a Cartesian mesh are either cut or un-cut has important implications for both mesh generation and solver efficiency. Since cut-cells are assumed to be arbitrarily shaped, the geometric complexity of a particular configuration does not impact the mesh generation process, and thus mesh gener-

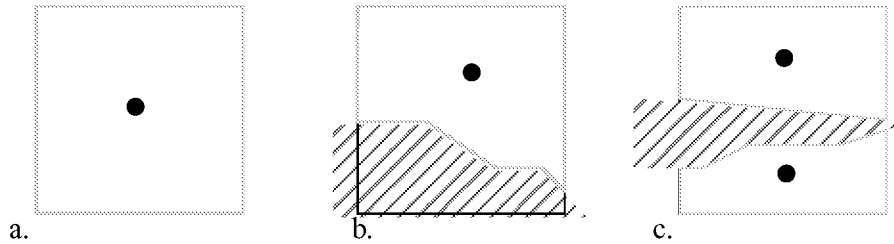


Figure 1: Types of cells in Cartesian meshes with embedded boundaries: a) a *volume cell*, b) a *cut-cell*, c) a *split-cell* cut into two polyhedra.

ation systems – like those in [2], [4], and [6] can be fully automated. Moreover since the vast majority of the domain is discretized with simple hexahedra, the process can be extremely fast. As an example, the mesh generator in ref. [2] produced approximately 1×10^6 cells/minute on moderately powered desktop workstations in 1997^[2].

Advocates of Cartesian approaches often note that solvers which take advantage of these meshes may use simplified discretization formulae in the pure Cartesian cells off-body and yet still take extra care to accurately integrate the cut-cells which have embedded geometry. Such arguments note that un-cut cells fill the volume of space around the geometry. Thus, while a typical mesh may contain $O(N^3)$ off-body cells, only $O(N^2)$ cut-cells actually intersect the body itself. Following this reasoning, one sees that since a simplified form of the spatial discretization operator is applied to the vast majority of the cells in the domain. The net savings in operation count can be dramatic. In addition, throughout much of the domain, the solver operates on pure Cartesian meshes. Without mesh skewing or stretching to hinder performance or stability, the solver therefore may achieve its full order of accuracy in cells with purely Cartesian stencils.

While Cartesian mesh generators have largely overcome an important obstacle in the CFD process, solvers which take full advantage of the approach have been less convincingly documented. Moreover, removal of the mesh generation bottleneck from the analysis cycle places a renewed emphasis on flow solver efficiency. The current research explores the issues of accuracy and efficiency. The approach uses domain-decomposition to target the current crop of shared and distributed memory computing platforms, and multilevel smoothing to enhance convergence. Wherever possible, the solver uses an appropriately simplified operator for the spatial discretization of the pure Cartesian cells. In this workshop paper, we present a brief outline of the finite-volume discretization and multigrid scheme before shifting focus to the domain decomposition and coarse mesh generation. Results are presented for a variety of model problems and 3-D configurations, and these provide a basis for a preliminary assessment of the accuracy and efficiency of the solver.

SPATIAL AND TEMPORAL DISCRETIZATION

Embedded boundary Cartesian approaches discretize the computational domain with either “volume cells” which are the adaptively Cartesian hexahedra filling the space away from boundaries, and “cut-cells” which are formed by the Cartesian cells which actually intersect the surface. As shown by Figure 1, volume cells always have six coordinate aligned faces, while cut-cells are considered to be arbitrarily shaped polyhedra. “Split-cells” refers to a subset of cut-cells which are actually split into multiple, non-communicating, flow polyhedra by the geometry. The solver uses a cell-centered finite-volume scheme for the spatial discretization with the state vector stored at the cell-center of each of the Cartesian hexahedra. In boundary cut-cells, these quantities are stored at the centroid of the actual polyhedron formed by the intersection of the Cartesian cell with the body. The fact that some cut-cells may indeed be split-cells indicates that the index space of the control volumes is not necessarily the same as that of the set of Cartesian hexahedra from which the mesh was constructed.

Within each control volume, the spatial integration scheme proceeds by traversing a face-based data structure to reconstruct a piecewise linear polynomial distribution of each state variable within the cell as in the

linear-reconstruction approach of ref. [8]. A least-squares procedure is used to provide gradient estimates within each cell based on solution of the normal equations of the local mass matrix. State vectors are reconstructed from the cell centroids to the face centroids, and the flux quadrature uses a midpoint integration coupled with either a van Leer flux-vector splitting, or the approximate Riemann solver of Colella^[9].

Evolution is performed using a modified Runge-Kutta scheme to drive a recursively implemented FAS (Full Approximation Storage) multigrid scheme^[10]. This scheme may be used in conjunction with a local block Jacobi preconditioner which requires the inversion of 5×5 matrix for each control volume in the computational domain^[11]. When coupled with the upwind spatial discretization, this preconditioner has been shown to efficiently cluster the residual eigenvalues for rapid annihilation by the multigrid scheme^[13]. Implementation of such a preconditioner is planned in the near future.

Further details of the spatial and temporal operators and aspects of its implementation which impact the overall efficiency of the approach will be presented in an upcoming paper^[12].

DOMAIN DECOMPOSITION

One novel aspect of this work lies in its approach toward domain decomposition. The option exists to apply a commercial grade uni-processor partitioner like the multi-level nested dissection tool in reference ^[14] or its multi-processor variant^[15]. However, an attractive alternative stems from exploiting the nature of Cartesian meshes. We have built-in a partitioner based upon the use of space-filling curves, constructed using either the Morton or Peano-Hilbert orderings^[16]. Both of these orderings have been used for the parallel solution of N -body problems in computational physics^[17], and the later scheme has been proposed for application to algebraic multigrid^[18] in the solution of elliptic PDEs and dynamic repartitioning of adaptive methods^[19]. Figure 2 shows both Peano-Hilbert and Morton space-filling curves constructed on Cartesian meshes at three levels of refinement. In two dimensions, the basic building block of the Hilbert curves is a “U” shaped line which visits each of 4 cells in a 2×2 block. Each subsequent level divides the previous level’s cells by nested dissection, creating subquadrants which are, themselves, visited by U shaped curves as well. This “U-ordering” has locality properties which make it attractive as a partitioner^[19]. Similar properties exist for the Morton ordering which uses an “N” shaped curve as its basic building block. Properties and construction

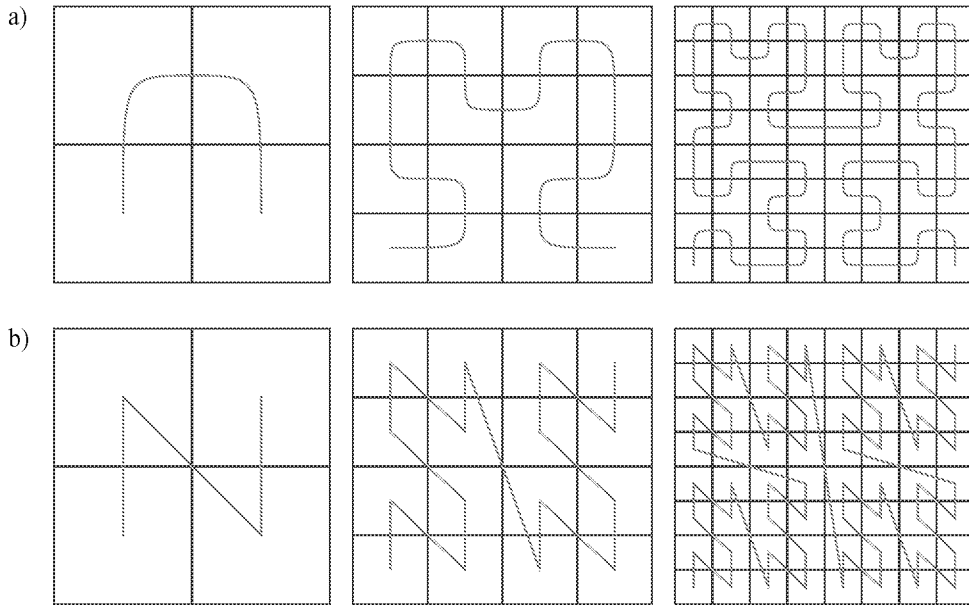


Figure 2: Space-filling curves used to order three Cartesian meshes in two spatial dimensions: a) Peano-Hilbert or “U-ordering”, b) Morton or “N-ordering”.

rules for these space-filling curves are discussed in refs. [20] and [21]. For the present, we note only that such orderings have 3 important properties.

1. **Mapping** $\mathfrak{R}^d \rightarrow U$: The U and N orderings provide a unique mappings from the d -dimensional physical space of the problem domain \mathfrak{R}^d to a one-dimensional hyperspace, U , which one traverses following the curve. In the U-order, two cells adjacent on the curve remain neighbors in this one-dimensional hyperspace.
2. **Locality**: In the U-order, each cell visited by the curve is directly connected to two face-neighboring cells which remain face-neighbors in the one dimensional hyperspace spanned by the curve. Locality in N-ordered domains is almost as good^[16].
3. **Compactness**: Encoding and decoding the Hilbert or Morton order requires only local information. Following the integer indexing for Cartesian meshes outlined in ref. [2], a cell's 1-D index in U may be constructed using only that cell's integer coordinates in \mathfrak{R}^d and the maximum number of refinements that exist in the mesh. This aspect is in marked contrast to other partitioning schemes based on recursive spectral bisection or other multilevel decomposition approaches which require the entire connectivity matrix of the mesh in order to perform the partitioning.

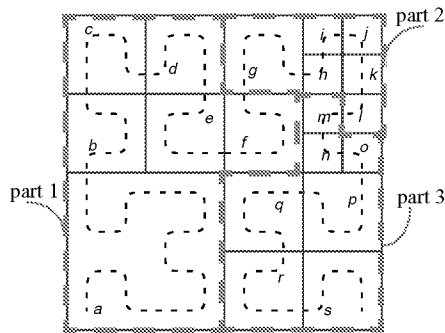
To illustrate the property of *compactness*, consider the position of a cell i in the N-order. One way to construct this mapping would be from a global operation such as a recursive lexicographic ordering of all cells in the domain. Such a construction would not satisfy the property of *compactness*. Instead, the position of i in the N-order may be deduced solely by inspection of cell i 's integer coordinates (x_i, y_i, z_i) .

Assume $(\tilde{x}_i, \tilde{y}_i, \tilde{z}_i)$ is the bitwise representation of the integer coordinates (x_i, y_i, z_i) using m -bit integers. The bit sequence $\{\tilde{x}_i^1 \tilde{y}_i^1 \tilde{z}_i^1\}$ denotes a 3-bit integer constructed by interleaving the first bit of x_i, y_i and z_i . One can then immediately compute cell i 's position in U as the $3m$ -bit integer $\{\tilde{x}_i^1 \tilde{y}_i^1 \tilde{z}_i^1 \tilde{x}_i^2 \tilde{y}_i^2 \tilde{z}_i^2 \dots \tilde{x}_i^m \tilde{y}_i^m \tilde{z}_i^m\}$. Thus, simply by inspection of a cell's integer coordinates, we are able to directly calculate its position in the one-dimensional space U without any additional information. Similarly compact construction rules exist for the U-order^[21].

Figure 3 illustrates these mapping and locality properties for an adapted two-dimensional Cartesian mesh, partitioned into three subdomains. The figure demonstrates the fact that for adapted Cartesian meshes, the hyperspace U may not be fully populated by cells in the mesh. However, since cell indices in U may be explicitly formed, this poses no shortcoming.

The quality of the partitioning resulting from U-ordered meshes have been examined in Ref.[19]. and were found to be competitive with respect to other popular partitioners. Weights can be assigned on a cell-by-cell basis. One advantage of using this partitioning strategy stems from the observation that mesh refinement or

2-D physical space



1-D hyperspace

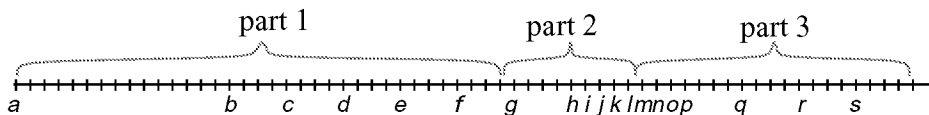


Figure 3: An adapted Cartesian mesh and associated space-filling curve based on the U-ordering of $\mathfrak{R}^2 \rightarrow U$ with the U-ordering illustrating locality and mesh partitioning in two spatial dimensions. Partitions are indicated by the heavy dashed lines in the sketch

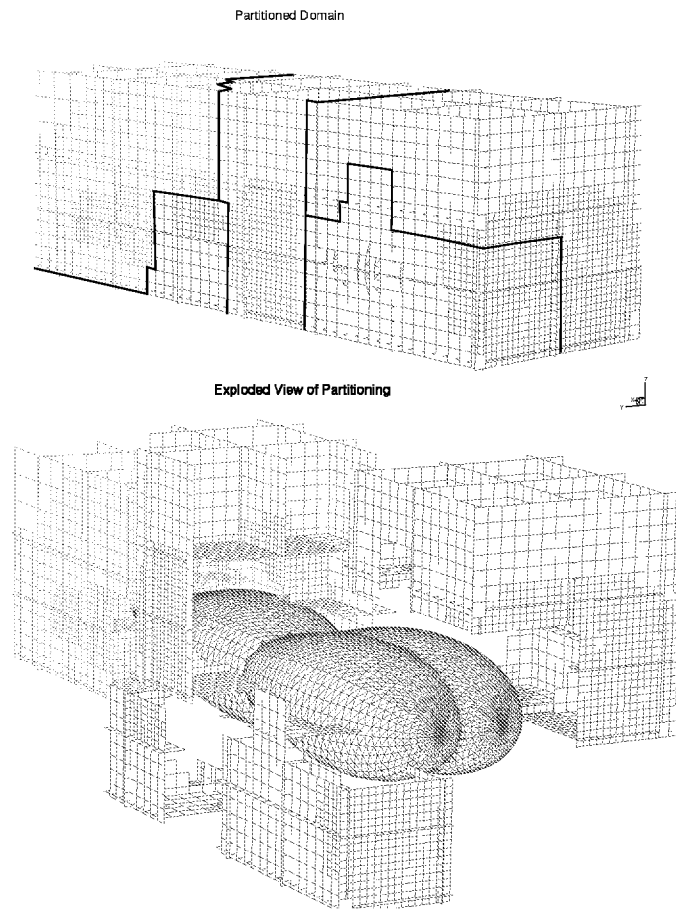


Figure 4: Partitioning of 6 level adapted mesh around a triple teardrop geometry with 240000 cells into 4 subdomains using space-filling curves. The mesh is shown by a collection of cutting planes through each partition.

coarsening simply increases or decreases the population of U while leaving the relative order of elements away from the adaptation unchanged. Re-mapping the new mesh into new subdomains therefore only moves data at partition boundaries and avoids global remappings when cells adaptively refine during mesh adaptation. Recent experience with a variety of global repartitioners suggest that the communication required to conduct this remapping can be an order of magnitude more expensive than the repartitioning itself^[22]. Additionally, since the partitioning is basically just a re-ordering of the mesh cells into the U-order, the entire mesh may be stored as a single domain, which may then be partitioned into any number of subdomains on-the-fly as it is read into the flow solver from mass storage. This approach permits the mesh to be stored as a single unpartitioned file. In a heterogeneous computing environment where the number of available processors may not be known at the time of job submission, the value of such flexibility is self-evident.

Figure 4 shows an example of a three dimensional Cartesian mesh around a triple teardrop configuration partitioned using the U-order. The mesh in this figure contains 240000 cells and is indicated by several cutting planes which have been passed through the mesh, with cells colored by partition number. The upper frame shows the mesh and partition boundaries, while the lower frame offers further detail through an exploded view of the same mesh. In determining partition boundaries in this example, cut-cells were weighted 10x as compared to un-cut Cartesian hexahedra.

SUBDOMAIN CONNECTIVITY MATRIX LOCALITY

Figure 5 illustrates the cell adjacency matrix within a typical subdomain after applying the U-ordering. Each cell face in the subdomain results in a point on this graph whose coordinates are the indices of the neighboring cells. As indicated on the figure, this matrix is block structured, and the regions stemming from the various cell types in the subdomains are labeled. Computation of the residual occurs in the two diagonal blocks labeled “volume cells” and “cut-cells”, while the overlap regions are updated via data-exchange with neighboring subdomains. Examination of the structure of these diagonal blocks indicates high total bandwidth requirements. The face list within each subdomain is sorted by the lowest cell index which the face connects to, and thus a loop over the face lists of either the volume or cut-cells accesses data in these two blocks row-by-row, from the top down. However, since the cells are clustered into “arms” off the main diagonal, memory pages loaded to access one cell will be subsequently hit many times as other nearby cells are requested by subsequent faces. Despite this, further bandwidth reduction and diagonal dominance may still be advantageous on some cache-based computing architectures or for use with some matrix inverters or preconditioners. The standard technique for alleviating this shortcoming is further reordering within each of these blocks^[23].

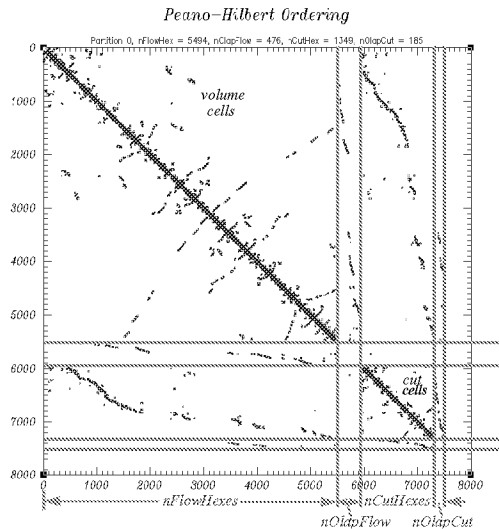


Figure 5: Connectivity matrix of a typical subdomain after partitioning with the U-ordering. Various cell types within the subdomain are labeled.

Provision is included for applying a RCM reordering^[23] to the diagonal blocks in this matrix which produces a matrix with substantially reduced bandwidth. For cache-based machines, further re-ordering is also possible by coloring the data on any given cache-line so that data-dependencies are avoided when loading the data pipes on pipelining architectures, or for constructing short vectors on processors which support short vector processing.

AUTOMATIC CONSTRUCTION OF COARSE GRIDS

A central issue in the implementation of multigrid smoothers on unstructured meshes is the construction of a series of coarse grids for the smoother to act upon. However, since adaptively refined Cartesian grids are based upon successive refinements of an initial coarse grid, there is a natural path for coarse grid construction. A variety of approaches have been suggested in the literature, however, the asymptotic coarsening ratio in some of these has been insufficient to ensure that the method will extract the full benefit of multigrid. Moreover, the approach in ref. [2] permits the cells to divide anisotropically and therefore, we revisit the issue of efficient coarse mesh generation.

In contrast to coarse grid generation problems on unstructured (general) hexahedral, tetrahedral, or mixed element meshes, coarse cells in Cartesian meshes can be designed to nest *exactly* (i.e. cells on the coarse mesh are the precise boolean addition of cells on the fine mesh). In addition, the cells can be organized such that any cell in the mesh may be located uniquely by a set of integer indices^[2]. The combination of these two facts lead to a novel coarse mesh generation algorithm for adaptively refined Cartesian meshes. The asymptotic complexity of this algorithm is $O(N \log N)$, where N is the number of cells in the fine mesh. This result stems from the fact that the central operation is a standard quicksort routine¹, and all other operations may

1. This result could be improved upon through the use of a radix sort, or other sort which has a better time-bound, however, quicksort is fast enough in most cases.

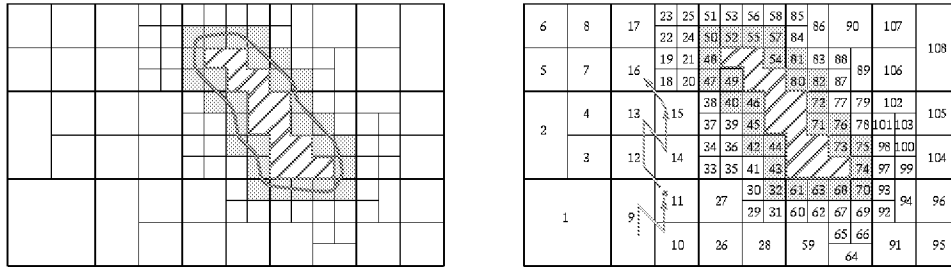


Figure 6: (Left) A two dimensional adaptively refined Cartesian mesh. Cut-cells are shown shaded. (Right) The same mesh, after reordering with a specially designed comparison operator in preparation for coarsening.

be performed in constant time.

Figure 6 displays a two dimensional, directionally refined Cartesian mesh which illustrates the coarse mesh generation strategy. The mesh shown (left) is the input or “fine mesh” which the algorithm coarsens. The boundary of a hypothetical body is indicated, and the crosshatching indicates where there are no cells in the mesh. Gray shaded cells denote cut-hexahedra. To the right of this figure lies a second view of the mesh after it has been sorted using a specially designed comparison operator. The cell indices in this mesh indicate the sorted order, which is further illustrated by a partial sketch of the path shown through cells 9–16.

The comparison operator basically performs a recursive lexicographical ordering of cells which can coarsen into the same coarse cell. Adaptively refined Cartesian meshes are formed by repeated subdivision of an initial coarse mesh (referred to as the *level 0 mesh*), therefore any cell, i , is traceable to an initial “parent cell” in the level 0 mesh. Similarly, if cell i has been refined R times, it will have parent cells at levels 0 through $(R - 1)$. If a cell has never been divided, then it is referred to as a “level 0 cell” and is identical to its level 0 parent.

1. Cells on the level 0 mesh are sorted in lexicographic order using the integer coordinates of their level 0 parents as keys.
2. If a cell has been subdivided, recursively sort its children lexicographically.

This algorithm can be implemented with a single quicksort which uses a comparison operator which examines the integer indices of two input cells on a bit-by-bit basis (see ref. [12]). As noted above, its asymptotic complexity is proportional to that of the sorting method used.

After sorting the fine mesh, coarsening proceeds in a straightforward manner. Cells are processed by a single sweep through the sorted order. If a contiguous set of cells are found which coarsen to the same parent they are coalesced into that parent. Cells which do not meet this criteria are “not coarsenable” and are injected to the coarse mesh without modification.

Figure 7 (left) shows the coarse mesh resulting from one application of the coarsening algorithm, note that fine grid cells on the level-0 mesh are *fully coarsened* and do not coarsen beyond their initial size. The right

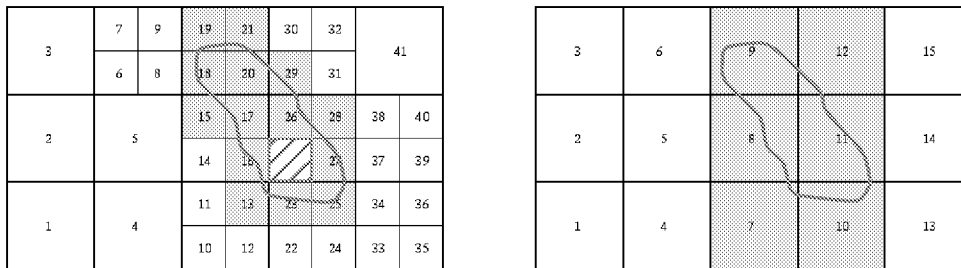


Figure 7: Left: Adapted Cartesian mesh from Figure 6 after one coarsening. Outline of geometry is indicated, and cut-cells are shown in grey. Right: Same mesh after one additional application of the coarsening algorithm

frame in this figure shows the mesh resulting from a second application of the coarsening operator.

Note that with this algorithm, cells won't coarsen in two situations: (1) if they are fully coarsened; or if coarsening is suspended because one (or more) of the children of a given parent is subdivided. Application of this algorithm to a variety of adapted Cartesian meshes on actual geometry (including a 3D wing, a Single Stage to Orbit configuration and a subsonic business jet) revealed that it consistently produces coarse meshes with coarsening ratios greater than 7:1. Finally, note that the coarse cells in fig. 7 are automatically constructed in the sorted order so that further coarsening does not require additional sorting.

One subtlety that the coarsening algorithm must contend with is indicated in Figure 8. The presence of split-cells in the domain implies that, under some coarsening situations, cut-cells on the fine mesh may coarsen into split-cells on the coarse grid. Alternatively, when fine grid split-cells coarsen into the same parent as uncut volume cells, cut- or split-cells may result. This apparent complication stems directly from the fact that the index space of the control volumes is not the same as that of the Cartesian hexahedra from which these control volumes were formed, and in three dimensions, a wide variety of such cases exist. To ensure accurate construction of the coarse mesh, our algorithm insists that two cut/split-cells with the same parent must have at least one common face to coalesce into the same control volume on the coarse grid.

PRELIMINARY RESULTS

The preliminary results presented in this section intend to investigate the global order of accuracy of the flow solver, as well as the parallel scalability of the method using the SFC mesh partitioners. An investigation of the effectiveness of the multigrid scheme will not be presented as such results are still premature. All computations were performed on 1-32 processors of an SGI Origin 2000 equipped with MIPS R10000 processors running at 250Mhz. subdomain boundary information exchange is performed using shared memory programming paradigm, and care was taken to ensure that the memory required to store each subdomain is physically located on boards local to the processor which integrate each subdomain.

VERIFICATION AND GLOBAL ORDER OF ACCURACY

Before examining issues of modeling and parallel scalability, it is necessary to first verify that our implementation correctly solves the Euler equations, and to document the order of accuracy of the solver on a actual meshes. This investigation relies upon a closed-form, analytic solution to the Euler equations for a supersonic vortex model problem^[24]. The presence of an exact solution permits the investigation to examine the truncation error of the discrete solution using a series of telescopic meshes. Since this is a shock-free flow, the measured order of accuracy is not corrupted by limiter action near shocks, and the behavior is indicative of the scheme's performance in smooth regions of a flow. Although this example is only two dimensional, the full three dimensional solver was run using an 3-D geometry made by extrusion.

To investigate the truncation error of the scheme, the domain was initialized to the exact solution and integrated one time step. The residual in each cell then offers a direct measure of the difference between the dis-

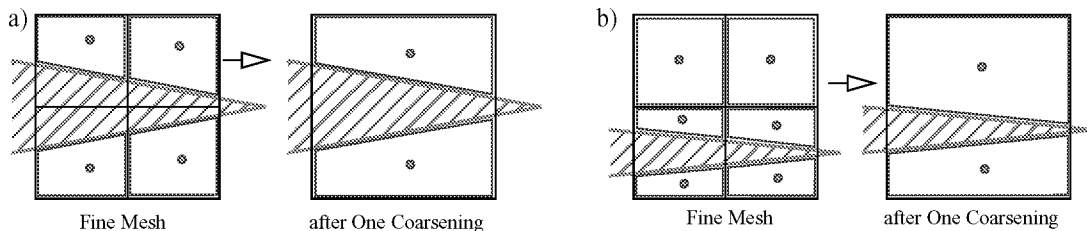


Figure 8: Mesh coarsening examples in which the index space of the control volumes differs from that of the Cartesian hexahedra from which these control volumes are formed. (a) Four cut-cells become 2 split-cells when the mesh is coarsened, (b) 2 volume cells, and 4 split cells become 2 split-cells after coarsening.

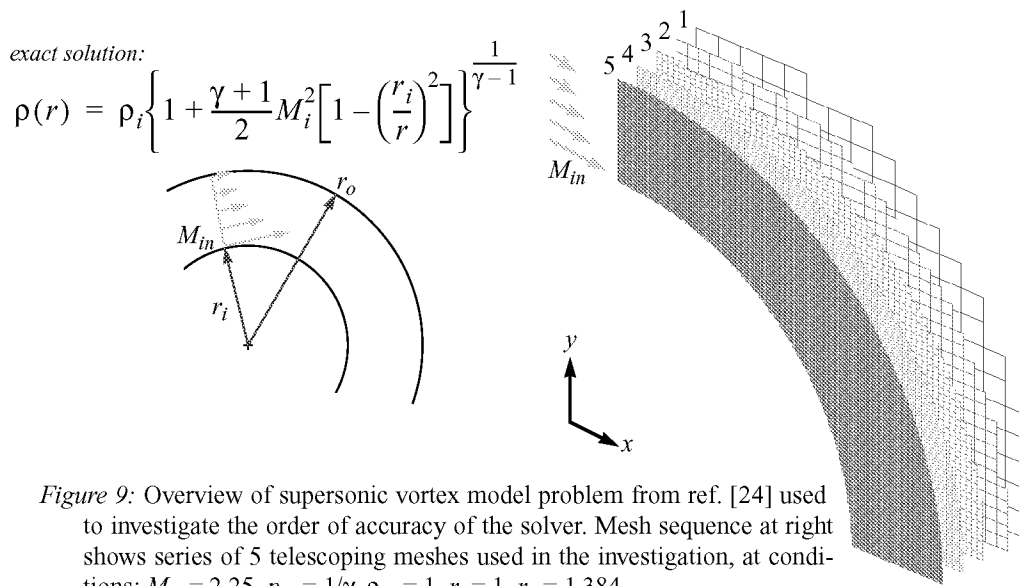


Figure 9: Overview of supersonic vortex model problem from ref. [24] used to investigate the order of accuracy of the solver. Mesh sequence at right shows series of 5 telescoping meshes used in the investigation, at conditions: $M_{in} = 2.25$, $p_{in} = 1/\gamma$, $\rho_{in} = 1$, $r_i = 1$, $r_o = 1.384$.

crete scheme and the governing equations, including the effects of boundary conditions.

Figure 9 presents an overview of the investigation. The sketch at the left shows the inviscid flow between two concentric circular arcs, while the frame at the right shows the sequence of 5 Cartesian meshes used in the investigation. The meshes were created by nested subdivision and while the coarsest of these grids had 105 cells in a 2D slice, the finest had over 21000 cells at the same station.

Figure 10 contains a plot of the L2 norm of density error resulting from this analysis. The error plot is remarkably linear over the first 4 meshes, but shows signs of a slight tailing-off on the final mesh. Over the first 4 meshes, the average order of accuracy is 1.88. If the finest mesh is included, this estimate drops to a value of 1.82. Both of these slopes are comparable to those in the investigation of reconstruction schemes on body-fitted unstructured meshes in ref. [24], and we note that the absolute magnitude of error in the present (Cartesian) scheme is more than a factor of two lower than was reported in that investigation. The slight tailing-off of the results for mesh 5 is believed to be a result of round-off error in computation of the error norm is not surprising considering the extremely low levels of error measured on this mesh. This hypothesis, however, is still under investigation.

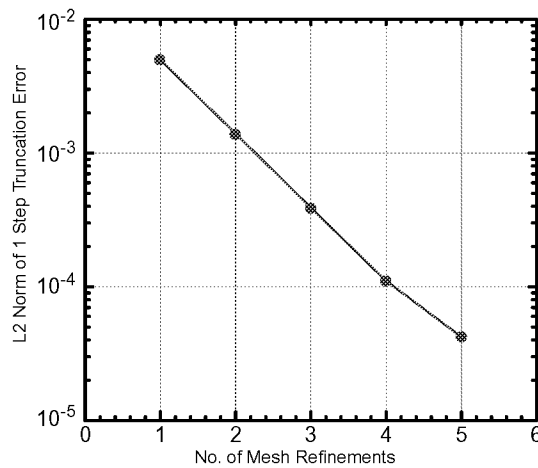


Figure 10: L2 norm of density truncation error for sequence of refined meshes shown in fig. 9.

The results shown in fig. 10 were generated using the Colella flux function, however, results with the van Leer option are essentially identical.

CONVERGENCE ON PARTITIONED DOMAINS

Adopting the domain decomposition with a single overlap cell permits a formulation which ensures that the residuals computed within each cell at every timestep with one partitioning match those for any other partitioning. Figure 11 illustrates this property by documenting convergence of the maximum residual of density for the supersonic vortex problem using a 250,000 cell mesh partitioned into 1, 2, 4, and 8 subdomains. All histories in this figure collapse to the same line to within machine precision. As the legend indicates, this test was performed using both the machine's default arithmetic (SGI Origin 2000, *cc* option *-Ofast*) and IEEE-754 compliant arithmetic.

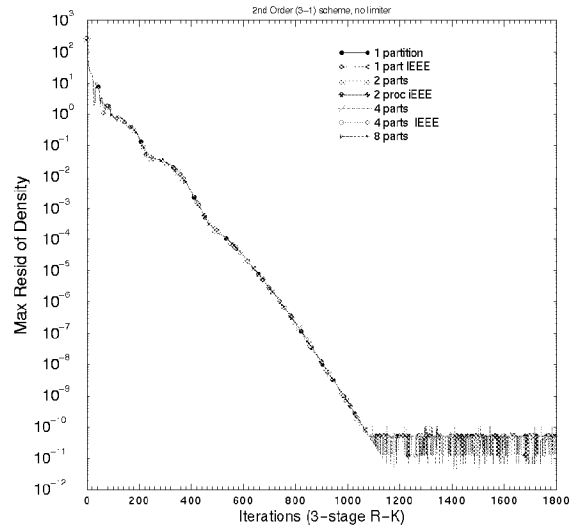


Figure 11: Comparison of convergence history using 1, 2, 4, and 8 subdomains using both default (SGI Origin 2000, *cc* option *-Ofast*) and IEEE-754 compliant arithmetic.

ONERA M6 WING

With the preliminary verification complete, focus shifts to a three dimensional example of an ONERA M6 wing which has been widely cited in the literature. This transonic $M_\infty = 0.84$, $\alpha = 3.06^\circ$ case is often used in the validation of inviscid solution techniques. This test was performed at a relatively high Reynolds number (based on root chord) of 12×10^6 ^[25], which minimizes effects of the displacement thickness making accurate comparisons of sectional pressure distributions possible. Other viscous effects in the experimental data are limited to a slight separation filling in the C_p distribution behind the lambda shock on the lee surface.

Simulation of this test was conducted using the geometry of a wing in free air, with the far-field boundary located 30 chords from the wing. The final mesh contained 525000 control volumes, with 25000 cut-cells and 528 split-cells. The mesh was partitioned into 8 subdomains using the Peano-Hilbert ordering described

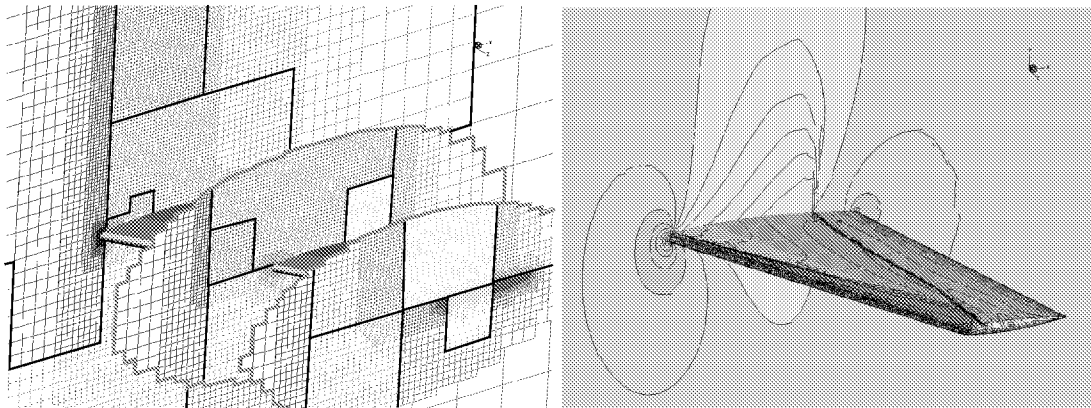


Figure 12: Partitioned mesh and C_p contours for the ONERA M6 wing example. The mesh contains 525000 cells at 9 levels of refinement, mesh partitions are shown by color-coding and outlined in heavy lines. C_p contours are plotted using a cell-by-cell reconstruction of the discrete solution. $M_\infty = 0.84$, $\alpha = 3.06$, van Leer flux.

in the preceding section. Figure 12 displays this mesh by three cutting planes. Cells on each cut plane are color coded by subdomain. Along side the mesh, fig. 12 presents C_p contours on the wing surface, and symmetry plane resulting from a simulation using the van Leer flux option. This image clearly displays the well-known lambda shock structure on the upper surface of the wing. Contours in this image were constructed cell-by-cell, using the computed gradients within each cell. This method of plotting gives a more accurate picture of the discrete solution, since fluxes are formed with this same reconstruction. The slight breaks in the contour lines in some high gradient regions are a by-product of this cell-by-cell plotting. These solution shown was converged 6 orders of magnitude (L1 norm of density) using the van Leer flux option.

Figure 13 provides a quantitative assessment of the solution quality through pressure profiles at six spanwise stations. This figure displays C_p vs. x/c at spanwise stations at 20, 44, 65, 80, 90, and 95% span. The inboard stations correctly display the double-shock on the upper surface, while stations at 90 and 95% confirm accurate prediction of the merging of these shocks. The experimental data at stations 20 and 44% indicate that the rear shock is followed by a mild separation bubble triggered by the shock-boundary layer interaction. As is typical in such cases, the inviscid discrete solution locates this rear shock slightly behind its experimental counterpart.

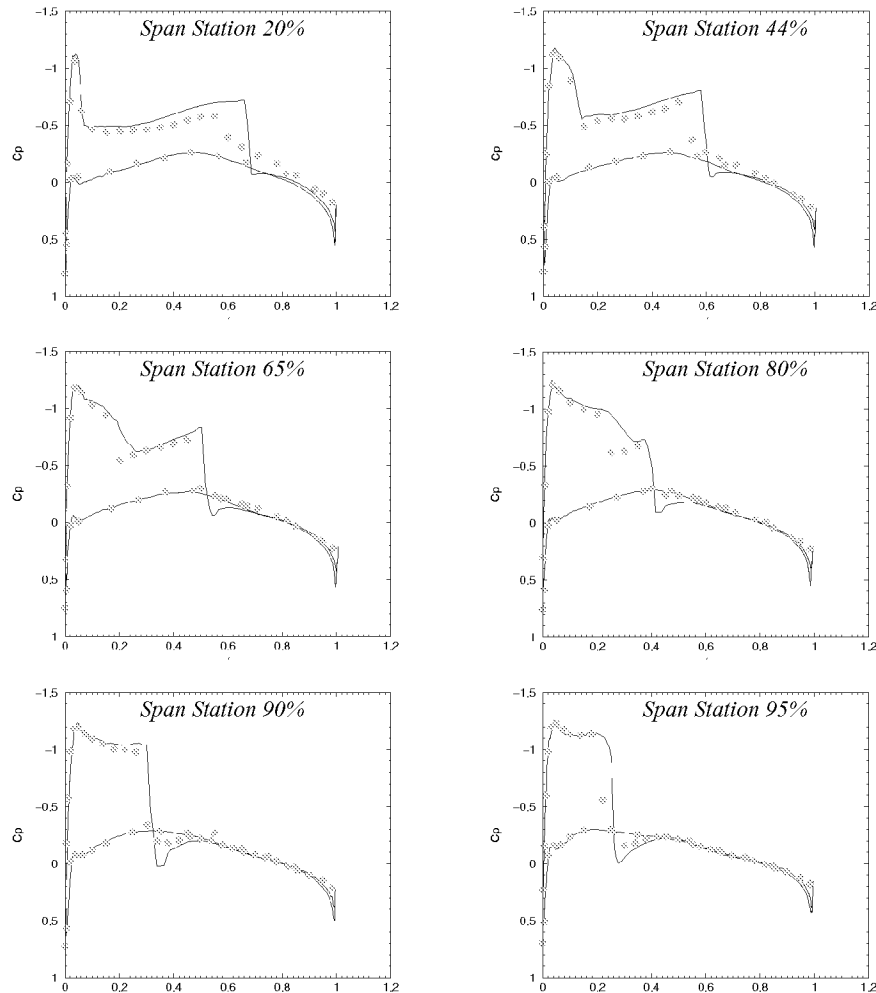


Figure 13: C_p vs. x/c for ONERA M6 wing example at six spanwise locations. $M_\infty = 0.84$, $\alpha = 3.06^\circ$. Experimental data from ref. [25] shown as symbols, inviscid discrete solution shown with solid line.

PARALLEL SCALABILITY AND PERFORMANCE

Figure 14 contains preliminary results from scalability testing. Tests were conducted on from 1 to 32 processors on an Mips R10000 based SGI Origin 2000. The mesh in this test contained 525000 cells. Each processor of this machine has a 4Mb Level 2 cache, and two processors on each board share the same local memory. Examination of this plot shows generally good scalability, however, communication does appear to slow this particular computation on 4 and 8 processors when the problem initially gets spread over several boards within the machine. On 32 processors the timings show a “cache bubble” evidenced by the fact that the results on 32 processors are more than a factor of two faster than the timings on 16 processors. Table 1 shows the per-processor execution rate and parallel speed-up for this example. Results in this table clearly show a 4% increase in per-processor execution rate on 32 processors as each processor’s L2 cache was very nearly sufficient to store the entire subdomain. The table demonstrates no substantial decrease in performance with larger numbers of subdomains, and the communication/computation ratio afforded by the partitioning does not appear to be uncompetitive. Results in Table 1 and in Figure 14 were obtained by averaging the results of 3 separate sets of tests since timings on this machine are known to vary by as much as 10%.

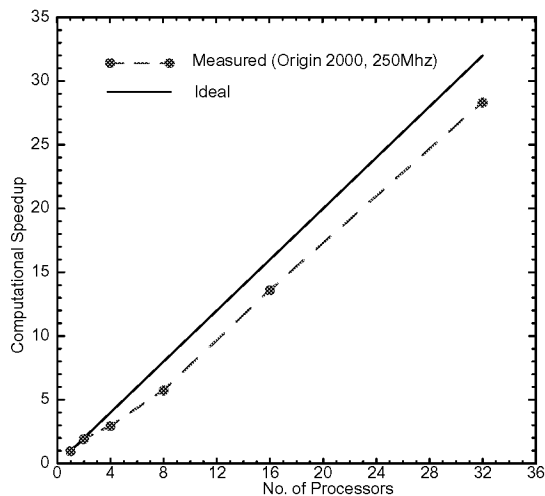


Figure 14: Preliminary investigation of parallel scalability of single mesh (no-multigrid) case. Data reflect average results from 3 runs with each partitioning.

Table 1: Parallel scalability and processing rate per processor. Results for each partitioning reflect average of three runs. 525000 control volumes, 200 iterations per test.

| No. of Processors | CPU time/CPU (sec.) | Parallel Speed-up | Mflops/CPU ^a | Ideal Speedup |
|-------------------|---------------------|-------------------|-------------------------|---------------|
| 1 | 2559 | 1 | 81.4 | 1 |
| 2 | 1315 | 1.94 | 81.9 | 2 |
| 4 | 865 | 2.96 | 72.77 | 4 |
| 8 | 383 | 5.76 | 77.57 | 8 |
| 16 | 188 | 13.61 | 78 | 16 |
| 32 | 90 | 28.37 | 82 | 32 |

a. Mflops counted using R10000 hardware counters on optimized code, with single cycle MADD instruction disabled. Floating-point multiply, add, and divide each counted as one flop.

CONCLUSIONS AND CURRENT WORK

This paper presented preliminary verification and validation of a new, parallel, upwind solver for Cartesian meshes. Comparison of the scheme’s one-step truncation error with an analytic solution demonstrated an achieved order of accuracy between 1.82 and 1.88. Preliminary validation by direct comparison to experimental results on a three dimensional wing configuration was also performed, demonstrating that the discrete solutions were competitive with other solution procedures. Preliminary documentation of a new on-the-fly SFC based partitioning strategy was also presented. This strategy enables reordered meshes to be pre-

sorted and stored as a single domain. This mesh can then be partitioned into any number of partitions at run time. Investigations demonstrated that this decomposition strategy produces a parallel speed-up in excess of 28 on 32 processors with no net decrease in processing rate. Details of a new coarse mesh generation algorithm for multilevel smoothers on Cartesian meshes were also presented. This algorithm generally achieves mesh coarsening ratios in excess of 7 on adaptively refined meshes.

Development of this method continues, and examples on complex configurations at elevated Mach numbers are planned in the immediate future. An investigation of multigrid efficiency for flows with complex geometry at a variety of Mach numbers is on-going.

ACKNOWLEDGMENTS

The authors would like to extend thanks to R. Löhner for pointing to literature on the use of space-filling curves as potentially useful reorderers and partitioners. M. Berger and G. Adomavicius were supported in part by AFOSR Grant F49620-97-1-0322 and DOE Grant DEFG02-92ER25139. Some of this work was performed while M. Berger was at RIACS and this support is gratefully acknowledged.

REFERENCES

- [1] Melton J. E., Berger, M. J., and Aftosmis, M. J., "3D Applications of a Cartesian grid Euler method," *AIAA Paper 95-0853-CP*, Jul. 1993.
- [2] Aftosmis, M.J., Berger, M.J., Melton, J.E.: "Robust and efficient Cartesian mesh generation for component-based geometry." *AIAA Paper 97-0196*, Jan. 1997.
- [3] Charlton, E. F., and Powell, K. G., "An octree solution to conservation-laws over arbitrary regions." *AIAA Paper 97-0198*, Jan. 1997.
- [4] Wang Z.J., "An automated viscous adaptive Cartesian grid generation method for complex geometries." in *Proceedings of the 6th International Conf. on Numerical Grid Generation in Computational Field Simulations*, Eds. Cross, M. *et al.*, Univ. Greenwich, UK., 1998.
- [5] Day, M. S., Colella, P., Lijewski, M. J., Rendleman, C. A., and Marcus, D. L., "Embedded boundary algorithms for solving the Poisson equation on complex domains," Lawrence Berkeley National Laboratory, *LBNL-41811*, May, 1998.
- [6] Karman, S. L., "SPLITFLOW: A 3D unstructured Cartesian/prismatic grid CFD code for complex geometries." *AIAA Paper 95-0343*, Jan. 1995.
- [7] Forrer, H., "Second order accurate boundary treatment for Cartesian grid methods." Seminar for Angewandte Mathematik, ETH Zürich, ETH Research Report 96-13, 1996.
- [8] Barth, T.J., and Jespersen, D.C., "The design and application of upwind schemes on unstructured meshes." *AIAA Paper 89-0366*, Jan. 1989.
- [9] Colella P, Ferguson, R., and Glaz, H., "Multifluid algorithms for Eulerian finite difference methods". Preprint 1996.
- [10] Hackbusch, W., and Trottenberg, U., (eds.), *Lecture Notes in Mathematics: Multigrid Methods*, Springer-Verlag Berlin, Heidelberg, ISBN 0-387-11955-8, 1982.

- [11] Rienslagh, K., and Dick, E., "A multigrid method for steady Euler equations on unstructured adaptive grids." *Proceedings of the 6th Copper Mountain Conf. on Multigrid Methods*, NASA Conference publication 3224, pp. 527-542. 1993.
- [12] Aftosmis, M. J., Berger, M J., and Adomavicius, G. "A domain-decomposed multi-level method for adaptively refined Cartesian grids with embedded boundaries." *AIAA Paper 2000-0808*, Jan. 2000.
- [13] Allmaras, S. R., "Analysis of semi-implicit preconditioners for multigrid solution of the 2-D compressible Navier-Stokes Equations"., *AIAA Paper 95-1651-CP*, Jun., 1995.
- [14] Karypis, G., and Kumar, V., "METIS: A software package for partitioned unstructured graphs, partitioning meshes, and computing fill-reducing orderings of sparse matrices." University of Minn. Dept. of Comp. Sci., Minneapolis, MN., Nov. 1997
- [15] Schloegel, K., Karypis, G., and Kumar, V., "Parallel Multilevel Diffusion Schemes for Repartitioning of Adaptive Meshes." *Tech. Rep. #97-014*, University of Minn. Dept. of Comp. Sci., 1997.
- [16] Samet, *The design and analysis of spatial data structures*. Addison-Wesley Series on Computer science and information processing, Addison-Wesley Publishing Co., 1990.
- [17] Salmon, J.K., Warren, M.S., and Winckelmans, G.S., "Fast parallel tree codes for gravitational and fluid dynamical N-body problems." *Internat. Jol. for Supercomp. Applic.* **8**:(2), 1994.
- [18] Griebel, M., Tilman, N., and Regler, H., "Algebraic multigrid methods for the solution of the Navier-Stokes equations in complicated geometries." *Int. J. Numer. Methods for Heat and Fluid Flow* **26**, pp. 281-301, 1998, also as SFB report 342/1/96A, Institut für Informatik, TU München, 1996.
- [19] Pilkington, J.R., and Baden, S.B., "Dynamic partitioning of non-uniform structured workloads with spacefilling curves." Jan 1995.
- [20] Schrack, G., and Lu, X., "The spatial U-order and some of its mathematical characteristics." *Proceedings of the IEEE Pacific Rim Conf. on Communications, Computers and Signal Processing*. Victoria B.C, Canada, May, 1995.
- [21] Liu, X., and Schrack, G., "Encoding and decoding the Hilbert order." *Software-Practice and Experience*, **26**(12), pp. 1335-1346, Dec. 1996.
- [22] Biswas, R., Oliker, L., "Experiments with repartitioning and load balancing adaptive meshes." NAS Technical Report NAS-97-021, NASA Ames Research Ctr., Moffett Field CA., Oct. 1997.
- [23] Löhner, R., "Renumbering strategies for unstructured-grid solvers operating on shared-memory, cache-based parallel machines." *AIAA Paper 97-2045-CP*, Jun., 1997.
- [24] Aftosmis, M. J., Gaitonde, D., and Tavares, T. S., "Behavior of linear reconstruction techniques on unstructured meshes." *AIAA J.*, **33**(11), pp. 2038-2049, Nov. 1995.
- [25] Schmitt, V., and Charpin, F., "Pressure distributions on the ONERA-M6-Wing at transonic Mach numbers." *Experimental Data Base for Computer Program Assessment*, AGARD Advisory Report AR-138, 1979.



PARALLELIZATION OF THE FLOW FIELD DEPENDENT VARIATION SCHEME FOR SOLVING THE TRIPLE SHOCK/BOUNDARY LAYER INTERACTION PROBLEM

Richard Gregory Schunk
NASA/Marshall Space Flight Center

T. J. Chung
University of Alabama in Huntsville

ABSTRACT

A parallelized version of the Flowfield Dependent Variation (FDV) Method is developed to analyze a problem of current research interest, the flowfield resulting from a triple shock/boundary layer interaction. Such flowfields are often encountered in the inlets of high speed air-breathing vehicles including the NASA Hyper-X research vehicle. In order to resolve the complex shock structure and to provide adequate resolution for boundary layer computations of the convective heat transfer from surfaces inside the inlet, models containing over 500,000 nodes are needed. Efficient parallelization of the computation is essential to achieving results in a timely manner. Results from a parallelization scheme, based upon multi-threading, as implemented on multiple processor supercomputers and workstations is presented.

INTRODUCTION

The Flowfield Dependent Variation (FDV) Method is utilized to analyze a problem of current research interest, the flowfield produced from a triple shock/boundary layer interaction. Flow fields of this nature are often encountered in the inlets of high speed vehicles such as the scramjet engine of NASA's Hyper-X research vehicle. For this analysis, the numerical results are compared to experimental wind tunnel measurements made by Garrison, Settles, and Horstman [1,2]. The objective of the FDV analysis is to resolve the major flowfield structures observed during the experiment while demonstrating an efficient parallelization scheme based upon multi-threaded programming.

FLOWFIELD DEPENDENT VARIATION (FDV) THEORY

The original idea of FDV methods began from the need to address the physics involved in shock wave turbulent boundary layer interactions [3-5]. In this situation, transitions and interactions of inviscid/viscous, compressible/incompressible, and laminar/turbulent flows constitute not only the physical complexities but also computational difficulties. This is where the very low velocity in the vicinity of the wall and very high velocity far away from the wall coexist within a domain of study. Transitions from one type of flow to another and interactions between two distinctly different flows have been studied for many years both experimentally and numerically. Traditionally, incompressible flows were analyzed using the pressure-

based formulation with the primitive variables for the implicit solution of the Navier-Stokes system of equations together with the pressure Poisson equation. On the other hand, compressible flows were analyzed using the density-based formulation with the conservation variables for the explicit solution of the Navier-Stokes system of equations. In dealing with the domain of study which contains all speed flows with various physical properties where the equations of state for compressible and incompressible flows are different, and where the transitions between laminar and turbulent flows are involved in dilatational dissipation due to compressibility, we must provide very special and powerful numerical treatments. The FDV scheme has been devised toward resolving all of these issues.

To this end, let us consider the Navier-Stokes system of equations in conservation form,

$$\frac{\partial \mathbf{U}}{\partial t} + \frac{\partial \mathbf{F}_i}{\partial x_i} + \frac{\partial \mathbf{G}_i}{\partial x_i} = \mathbf{B} \quad (1)$$

In expanding \mathbf{U}^{n+1} in a special form of Taylor series about \mathbf{U}^n , we introduce the variation parameters s_1 and s_2 for the first and second derivatives of \mathbf{U} with respect to time, respectively

$$\mathbf{U}^{n+1} = \mathbf{U}^n + \Delta t \frac{\partial \mathbf{U}^{n+s_1}}{\partial t} + \frac{\Delta t^2}{2} \frac{\partial^2 \mathbf{U}^{n+s_2}}{\partial t^2} \quad (2)$$

where

$$\frac{\partial \mathbf{U}^{n+s_1}}{\partial t} = \frac{\partial \mathbf{U}^n}{\partial t} + s_1 \frac{\partial \Delta \mathbf{U}^{n+1}}{\partial t} \quad 0 \leq s_1 \leq 1 \quad (3a)$$

$$\frac{\partial^2 \mathbf{U}^{n+s_2}}{\partial t^2} = \frac{\partial^2 \mathbf{U}^n}{\partial t^2} + s_2 \frac{\partial^2 \Delta \mathbf{U}^{n+1}}{\partial t^2} \quad 0 \leq s_2 \leq 1 \quad (3b)$$

with $\Delta \mathbf{U}^{n+1} = \mathbf{U}^{n+1} - \mathbf{U}^n$. Substituting (3) into (2),

$$\Delta \mathbf{U}^{n+1} = \Delta t \left(\frac{\partial \mathbf{U}^n}{\partial t} + s_1 \frac{\partial \Delta \mathbf{U}^{n+1}}{\partial t} \right) + \frac{\Delta t^2}{2} \left(\frac{\partial^2 \mathbf{U}^n}{\partial t^2} + s_2 \frac{\partial^2 \Delta \mathbf{U}^{n+1}}{\partial t^2} \right) \quad (4)$$

Notice that s_1 , associated with the first time derivative, is intended to provide variations as appropriate to the convection and diffusion processes of the flowfield, whereas s_2 , involved in the second time derivative, is to control adequate application of artificial viscosity as required in accordance with the flowfield.

In the conservation form of the Navier-Stokes system of equations, \mathbf{F}_i and \mathbf{B} are functions of \mathbf{U} , and \mathbf{G}_i is a function of \mathbf{U} and its gradient $\mathbf{U}_{,k}$. Thus, by the chain rule of calculus, the first and second derivative of \mathbf{U} with respect to time may be written as follows:

$$\frac{\partial \mathbf{U}}{\partial t} = - \frac{\partial \mathbf{F}_i}{\partial x_i} - \frac{\partial \mathbf{G}_i}{\partial x_i} + \mathbf{B} \quad (5a)$$

$$\frac{\partial^2 \mathbf{U}}{\partial t^2} = - \frac{\partial \mathbf{F}_i}{\partial \mathbf{U}} \frac{\partial}{\partial x_i} \left(\frac{\partial \mathbf{U}}{\partial t} \right) - \frac{\partial \mathbf{G}_i}{\partial \mathbf{U}} \frac{\partial}{\partial x_i} \left(\frac{\partial \mathbf{U}}{\partial t} \right) - \frac{\partial \mathbf{G}_i}{\partial \mathbf{U}_{,k}} \frac{\partial^2}{\partial x_i \partial x_k} \left(\frac{\partial \mathbf{U}}{\partial t} \right) + \frac{\partial \mathbf{B}}{\partial \mathbf{U}} \left(\frac{\partial \mathbf{U}}{\partial t} \right) \quad (5b)$$

We denote the convection Jacobian \mathbf{a}_i , the diffusion Jacobian \mathbf{b}_i , the diffusion gradient Jacobian \mathbf{c}_{ik} , and the source Jacobian \mathbf{d} as

$$\mathbf{a}_i = \frac{\partial \mathbf{F}_i}{\partial \mathbf{U}}, \quad \mathbf{b}_i = \frac{\partial \mathbf{G}_i}{\partial \mathbf{U}}, \quad \mathbf{c}_{ik} = \frac{\partial \mathbf{G}_i}{\partial U_{,k}}, \quad \mathbf{d} = \frac{\partial \mathbf{B}}{\partial \mathbf{U}}$$

For the purpose of generality, we assume here that the source terms arise from additional equations for chemical species equations.

The second derivative of \mathbf{U} with respect to time may now be written in terms of these Jacobians by substitution into (5b),

$$\frac{\partial^2 \mathbf{U}}{\partial t^2} = \frac{\partial}{\partial x_i} (\mathbf{a}_i + \mathbf{b}_i) \left(\frac{\partial \mathbf{F}_j}{\partial x_j} + \frac{\partial \mathbf{G}_j}{\partial x_j} - \mathbf{B} \right) + \frac{\partial^2}{\partial x_i \partial x_k} \mathbf{c}_{ik} \left(\frac{\partial \mathbf{F}_j}{\partial x_j} + \frac{\partial \mathbf{G}_j}{\partial x_j} - \mathbf{B} \right) - \mathbf{d} \left(\frac{\partial \mathbf{F}_j}{\partial x_j} + \frac{\partial \mathbf{G}_j}{\partial x_j} - \mathbf{B} \right) \quad (6)$$

Substituting (5a) and (6) into (4), and assuming the product of the diffusion gradient Jacobian with third order spatial derivatives to be negligible, we have

$$\begin{aligned} \Delta \mathbf{U}^{n+1} = & \Delta t \left[-\frac{\partial \mathbf{F}_i^n}{\partial x_i} - \frac{\partial \mathbf{G}_i^n}{\partial x_i} + \mathbf{B}^n + s_1 \left(-\frac{\partial \Delta \mathbf{F}_i^{n+1}}{\partial x_i} - \frac{\partial \Delta \mathbf{G}_i^{n+1}}{\partial x_i} + \Delta \mathbf{B}^{n+1} \right) \right] \\ & + \frac{\Delta t^2}{2} \left[\frac{\partial}{\partial x_i} (\mathbf{a}_i + \mathbf{b}_i) \left(\frac{\partial \mathbf{F}_j^n}{\partial x_j} + \frac{\partial \mathbf{G}_j^n}{\partial x_j} - \mathbf{B}^n \right) - \mathbf{d} \left(\frac{\partial \mathbf{F}_i^n}{\partial x_i} + \frac{\partial \mathbf{G}_i^n}{\partial x_i} - \mathbf{B}^n \right) \right] \\ & + s_2 \left[\frac{\partial}{\partial x_i} (\mathbf{a}_i + \mathbf{b}_i) \left(\frac{\partial \Delta \mathbf{F}_j^{n+1}}{\partial x_j} + \frac{\partial \Delta \mathbf{G}_j^{n+1}}{\partial x_j} - \Delta \mathbf{B}^{n+1} \right) \right. \\ & \left. - \mathbf{d} \left(\frac{\partial \Delta \mathbf{F}_i^{n+1}}{\partial x_i} + \frac{\partial \Delta \mathbf{G}_i^{n+1}}{\partial x_i} - \Delta \mathbf{B}^{n+1} \right) \right] + \mathcal{O}(\Delta t^3) \end{aligned} \quad (7)$$

The variation parameters s_1 and s_2 which appear in (7) may be accorded with appropriate physical roles by calculating them from the flowfield-dependent quantities. For example, if s_1 is associated with the temporal changes (Δ terms, henceforth called *fluctuations*, not meant to be turbulent fluctuations) of convection, it may be calculated from the spatial changes of Mach number between adjacent nodal points so that $s_1 = 0$ would imply no changes in convection fluctuations. Similarly, if s_1 is associated with the fluctuations of diffusion, then it may be calculated from the spatial changes of Reynolds number or Peclet number between adjacent nodal points such that $s_1 = 0$ would signify no changes in diffusion fluctuations. Therefore, the role of s_1 for diffusion is different from that of convection. Similarly, the role of s_1 for the fluctuation of the sources (such as reaction rates and heat generation) should be different from convection and diffusion. For example, we may define the fluctuation quantities associated with s_1 as

$$\begin{aligned} s_1 \left(\frac{\partial \Delta \mathbf{F}_i^{n+1}}{\partial x_i} + \frac{\partial \Delta \mathbf{G}_i^{n+1}}{\partial x_i} - \Delta \mathbf{B}^{n+1} \right) & \Rightarrow s_{1c} \frac{\partial \Delta \mathbf{F}_i^{n+1}}{\partial x_i} + s_{1d} \frac{\partial \Delta \mathbf{G}_i^{n+1}}{\partial x_i} - s_{1s} \Delta \mathbf{B}^{n+1} \\ & = \frac{\sqrt{M_{\max}^2 - M_{\min}^2}}{M_{\min}} \frac{\partial \Delta \mathbf{F}_i^{n+1}}{\partial x_i} + \frac{\sqrt{Re_{\max}^2 - Re_{\min}^2}}{Re_{\min}} \frac{\partial \Delta \mathbf{G}_i^{n+1}}{\partial x_i} - \frac{\sqrt{Da_{\max}^2 - Da_{\min}^2}}{Da_{\min}} \Delta \mathbf{B}^{n+1} \end{aligned} \quad (8)$$

where it is seen that the variation parameter s_1 originally adopted as a single mathematical or numerical parameter has now turned into multiple physical parameters such as the changes of Mach numbers, Reynolds numbers (or Peclet numbers), and Damkohler numbers (Da), between adjacent nodal points. The magnitudes of fluctuations of convection, diffusion, and source terms are dictated by the current flowfield situations in space and time. Similar assessments can be applied to the variation parameter s_2 as associated with its corresponding fluctuation terms of convection, diffusion, and source. Thus, in order to provide variations to the changes of convection, diffusion, and source terms differently in accordance with the current flowfield situations, we reassign s_1 and s_2 associated with convection, diffusion and source terms as follows:

$$s_1 \Delta \mathbf{G}_i \Rightarrow s_{1c} \Delta \mathbf{G}_i = s_3 \Delta \mathbf{G}_i \quad , \quad s_1 \Delta \mathbf{B} \Rightarrow s_{1s} \Delta \mathbf{B}_i = s_5 \Delta \mathbf{B}$$

$$s_2 \Delta \mathbf{G}_i \Rightarrow s_{2d} \Delta \mathbf{G}_i = s_4 \Delta \mathbf{G}_i \quad , \quad s_2 \Delta \mathbf{B} \Rightarrow s_{2s} \Delta \mathbf{B} = s_6 \Delta \mathbf{B}$$

with the various variation parameters defined as

$$s_{1c} = s_1 = \text{first order convection variation parameter}$$

$$s_{2c} = s_2 = \text{second order convection variation parameter}$$

$$s_{1d} = s_3 = \text{first order diffusion variation parameter}$$

$$s_{2d} = s_4 = \text{second order diffusion variation parameter}$$

$$s_{1s} = s_5 = \text{first order source term variation parameter}$$

$$s_{2s} = s_6 = \text{second order source term variation parameter}$$

The first order variation parameters s_1 , s_3 , and s_5 are flowfield-dependent, whereas the second order variation parameters s_2 , s_4 , and s_6 are exponentially proportional to the first order variation parameters, and mainly act as artificial viscosity.

EXPERIMENTAL MEASUREMENTS

The analytical results are compared to experimental measurements for a triple shock interaction obtained by Garrison, Settles, and Horstman [1,2]. The wind tunnel model used to produce the triple shock/boundary layer interaction consists of two vertical fins and a horizontal ramp as shown in Figure 1. The angle of attack for the fins is 15° and the ramp is inclined at an angle of 10° with respect to the inlet flow. The inlet flow is at Mach 3.85 with a stagnation temperature and pressure of 295K and 1500 kPa, respectively. The fins are 82.5 mm high and are separated by a distance of 96.3 mm. The leading edge of the model is located 21 cm in front of the ramp inlet and produces a turbulent boundary layer with a thickness of 3.5 mm at the inlet to the model. Flow through the model is characterized by three oblique shocks originating from the leading edges of the ramp and the fins. Above the oblique ramp shock, the two inviscid fin shocks intersect and reflect as shown in the figure. For the purposes of this analysis, the ramp is assumed to be 120 mm in length, the distance at which the reflected inviscid fin shocks are just incident upon the exit corners of each fin. According to inviscid flow theory, the fin shocks should intersect approximately 92 mm from the combined ramp and fin entrance. Measurements of the flowfield structure in the x-y plane are made via the Planar Laser Scattering (PLS) technique at various depths upstream of, coincident with, and behind the inviscid fin shock intersection [2].

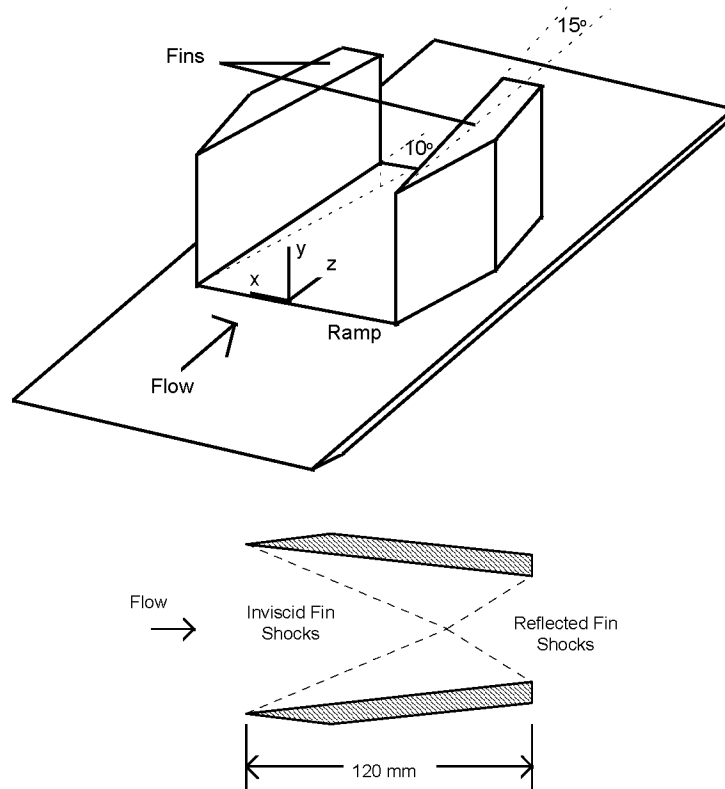


Figure 1: Inviscid Fin Shock Reflection (Top View, X-Z Plane)

Of particular interest in this analysis is the complex shock/boundary layer interaction produced in the x - y planes perpendicular to the flow direction. Upstream of and coincident with the inviscid ramp shock intersection, the fin and ramp shocks are reflected and interact with the fin and ramp boundary layers to produce the shock structures contained in the PLS images of Figure 2. Upstream of the shock intersection (left), the flow is characterized by the inviscid fin and ramp shocks reflecting to form a corner shock. Slip lines separating the shock induced flow regions are also visible in the image. The flow separation from the ramp underneath the embedded fin shock is also visible in the image. At the shock intersection (right), the inviscid fin shocks merge, the ramp shock disappears, and the corner shock is reflected to form the structure shown. The curvature of the fin shocks become more pronounced and a large separation region is observed underneath the reflected corner shocks. This is attributed to the curvature of the inviscid shocks to the finite height of the fins (i.e. there would be no shock curvature with fins of “infinite” height) [1].

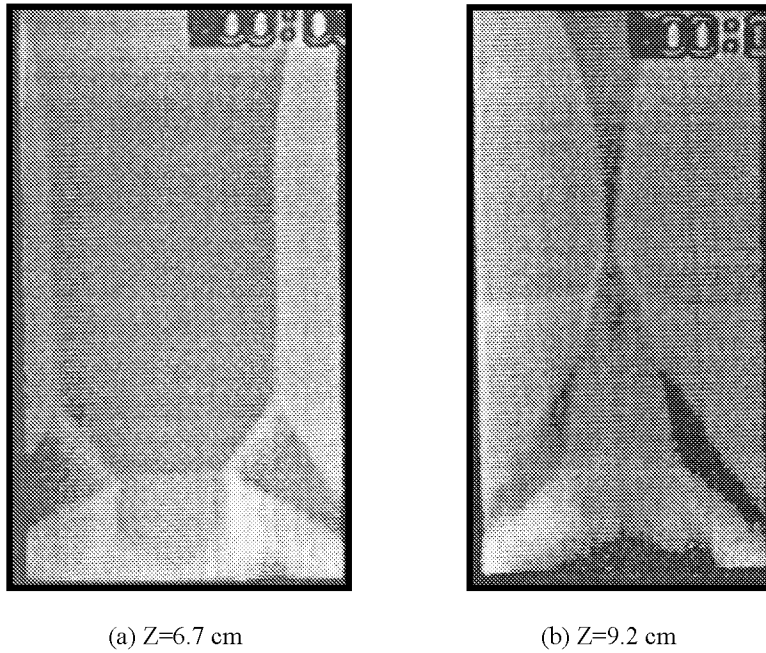
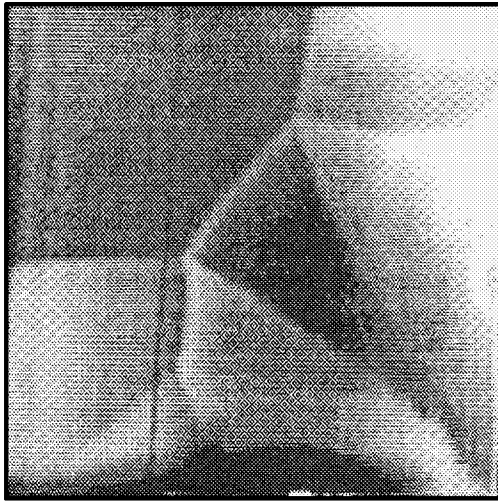
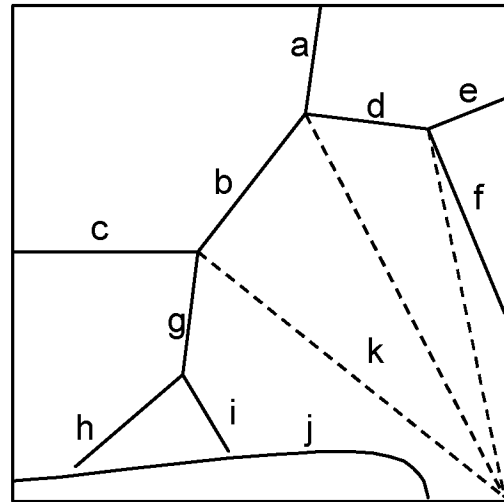


Figure 2: Fin/Ramp Shock Structure in the X-Y Plane Before (Left) and Co-incident (Right) the Inviscid Fin Shock Intersection [1]

A detailed PLS view of the corner shock reflection physics is shown in Figure 3. [1]. As shown in the figure, the inviscid fin (a) and ramp (b) shocks reflect to form the corner (c) shock. Both the embedded ramp (d) and fin (g) shocks split into separation (e,h) and rear (f,i) shocks above the ramp and fin boundary/separation layers. The ramp separated region (j) and the slip lines (k) dividing the different velocity regions as induced by the shock structure are also visible in the image.



PLS Image of Corner Flow



Corresponding Flowfield Structure

Figure 3: Fin/Ramp Shock Structure in the X-Y Plane [1], a) Inviscid Fin Shock, b) Corner Shock, c) Inviscid Ramp Shock, d) Embedded Ramp Shock, e) Ramp Separation Shock, f) Ramp Rear Shock, g) Embedded Fin Shock, h) Separation Fin Shock, i) Rear Fin Shock, j) Separated Region, k) Sliplines

COMPUTER MODEL

Since the two fins are symmetric about the centerline, only half of the wind tunnel model is included in the computational model. Two finite difference computational grids, varying in resolution, are developed for the FDV analysis. The coarse grid model, consisting of a non-uniform nodal resolution of $31 \times 41 \times 55$ (in the x, y, and z directions) is shown in Figure 4. The viscous grid is clustered close to the fin and ramp surfaces. Results from the coarse grid analysis are used as the starting condition for the fine grid model. The fine grid model is obtained by interpolating the flow variables against the coarse mesh. Doubling the number of grid points in each direction produces a fine grid with over 538,000 nodal points ($61 \times 81 \times 109$). Recall that the most important aspect of the FDV theory is that the shock capturing mechanism and the transition and interaction between compressible/incompressible, viscous/inviscid, and laminar/turbulent flows are incorporated into the FDV formulation. No special treatments are required to simulate these physical phenomena. Thus, the finite difference discretization requires no special schemes. Simple central differences can be used to discretize the FDV.

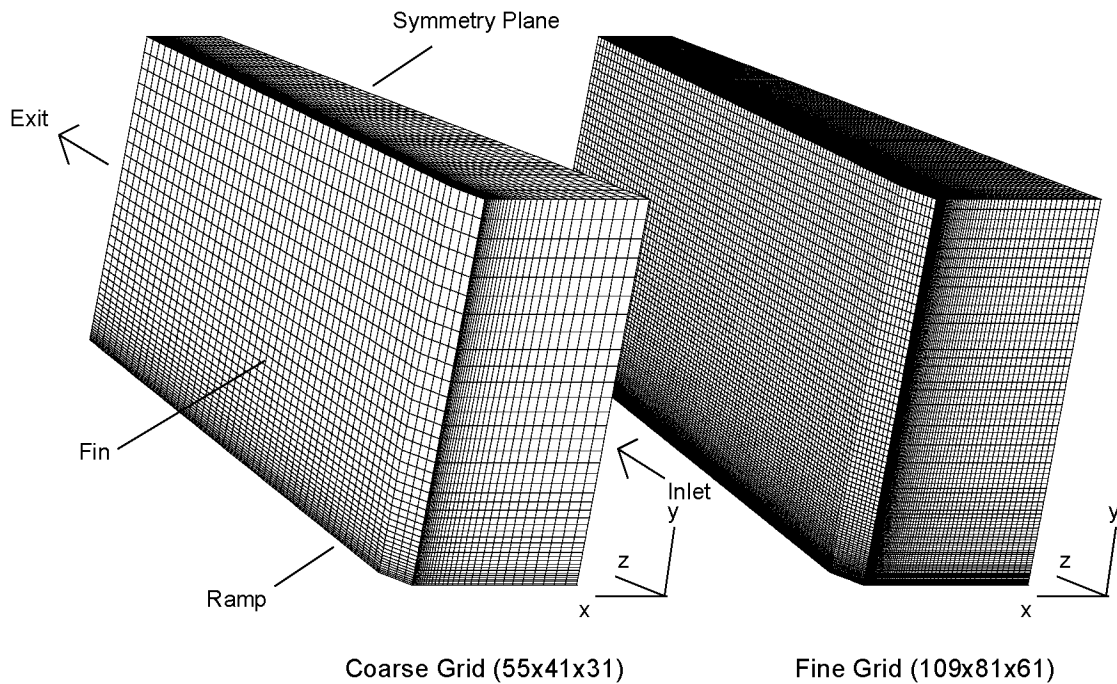


Figure 4: Three Dimensional Finite Difference Models

The inlet conditions to the model are fixed with the freestream conditions described above ($M=3.85$, $P_o=1500$ kPa, and $T_o=295$ K) and include a superimposed boundary layer 3.5 mm in height[1]. At the fin and ramp surfaces, no-slip velocity boundary conditions are imposed and the normal pressure and temperature gradients are set to zero. In the symmetry plane and for the bounding surface on top (x-z plane), all of the flow variables are computed such that the normal gradients vanish except for the normal flux, which is explicitly set to zero. At the exit, all of the flow variables are extrapolated from interior grid points.

PARALLELIZATION STRATEGY: MULTI-THREADED PROGRAMMING AND DOMAIN DECOMPOSITION

Multi-threaded programming is utilized to take advantage of multiple computational elements on the host computer. Typically, a multi-threaded process will spawn multiple threads which are allocated by the operating system to the available computational elements (or processors) within the system. If more than one processor is available, the threads may execute in parallel resulting in a significant reduction in execution time. If more threads are spawned than available processors, the threads appear to execute concurrently as the operating system decides which threads execute while the others wait. One unique advantage of multi-threaded programming on shared memory multiprocessor systems is the ability to share global memory. This alleviates the need for data exchange or message passing between threads as all global memory allocated by the parent process is available to each thread. However, precautions must be taken to prevent deadlock or race conditions resulting from multiple threads trying to simultaneously write to the same data.

Threads are implemented by linking an application to a shared library and making calls to the routines within that library. Two popular implementations are widely used: the Pthreads library [6] (and its derivatives) that are available on most Unix operating systems and the NTthreads library that is available under Windows NT. There are differences between the two implementations, but applications can be ported from one to the other with moderate ease and many of the basic functions are similar albeit with different names and syntax.

Domain decomposition methods [7] can be used in conjunction with multi-threaded programming to create an efficient parallel application. The sub-domains resulting from the decomposition provide a convenient division of labor for the processing elements within the host computer. In this application, an Additive Schwarz domain decomposition [7] method is utilized. The method is illustrated below (Figure 5) for a two dimensional square mesh that is decomposed into four sub-domains. The nodes belonging to each of the four sub-domains are denoted with geometric symbols while boundary nodes are identified with bold crosses. The desire is to solve for each node implicitly within a single sub-domain. For nodes on the edge of each sub-domain this is accomplished by treating the adjacent node in the neighboring sub-domain as a boundary. The overlapping of neighboring nodes between sub-domains is illustrated in Figure 6. Higher degrees of overlapping, which may improve convergence at the expense of computation time, are also used.

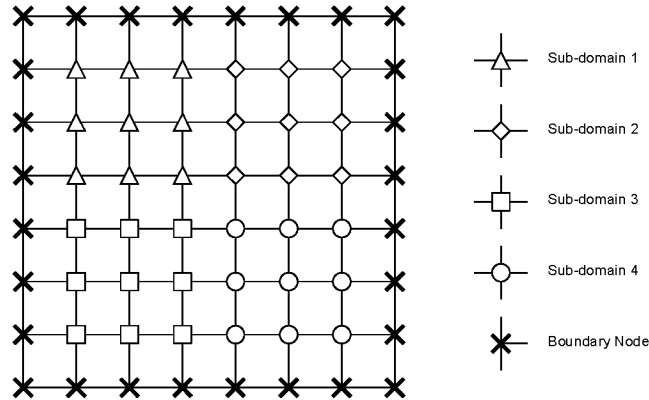


Figure 5: Multiple Subdomains

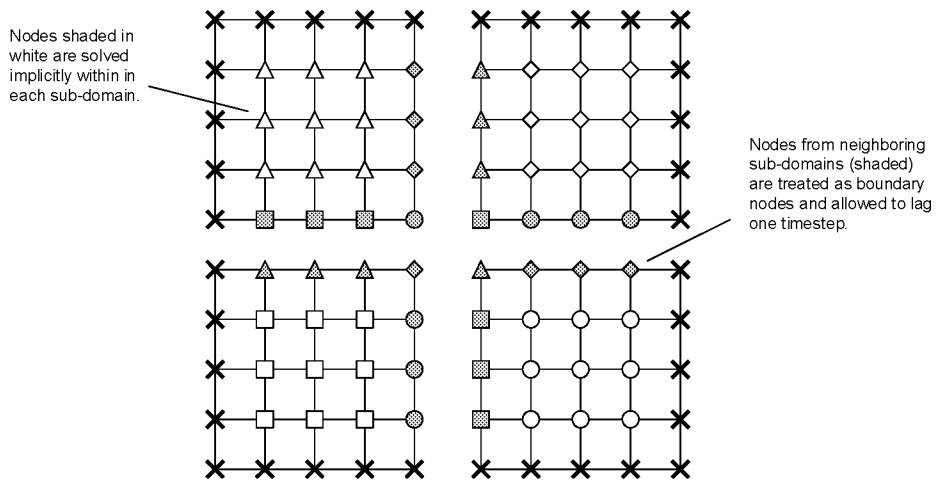


Figure 6: Domain Decomposition

In a parallel application, load balancing between processors is critical to achieving optimum performance. Ideally, if a domain could be decomposed into regions requiring an identical amount of computation, it would be a simple matter to divide the problem between processing elements as shown in Figure 7 for four threads executing on an equal number of processors.

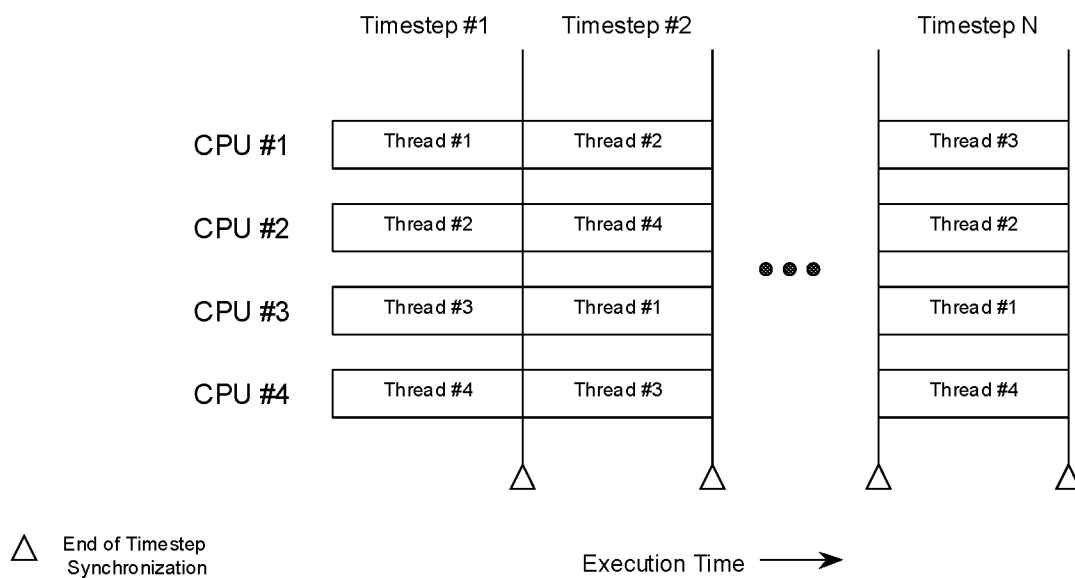


Figure 7: Ideal Load Balancing

Unfortunately, in a “real world” application the domain may not be decomposed such that the computation for each processor is balanced, resulting in lost efficiency. If the execution time required for each sub-domain is not identical, the CPU’s will become idle for portions of time as shown in Figure 8.

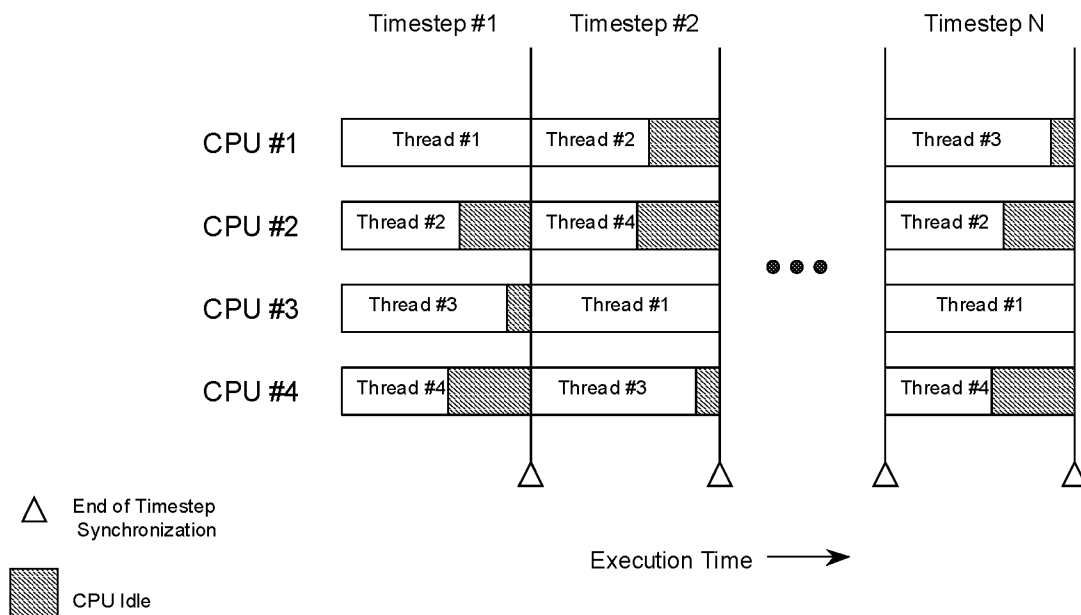


Figure 8: “Real World” Load Balancing

One approach to load balancing, as implemented in this application, is to decompose the domain into more sub-domains than available processors and use threads to perform the computations within each block. The

finer granularity permits a more even distribution of work amongst the available processing elements as shown in Figure 9.

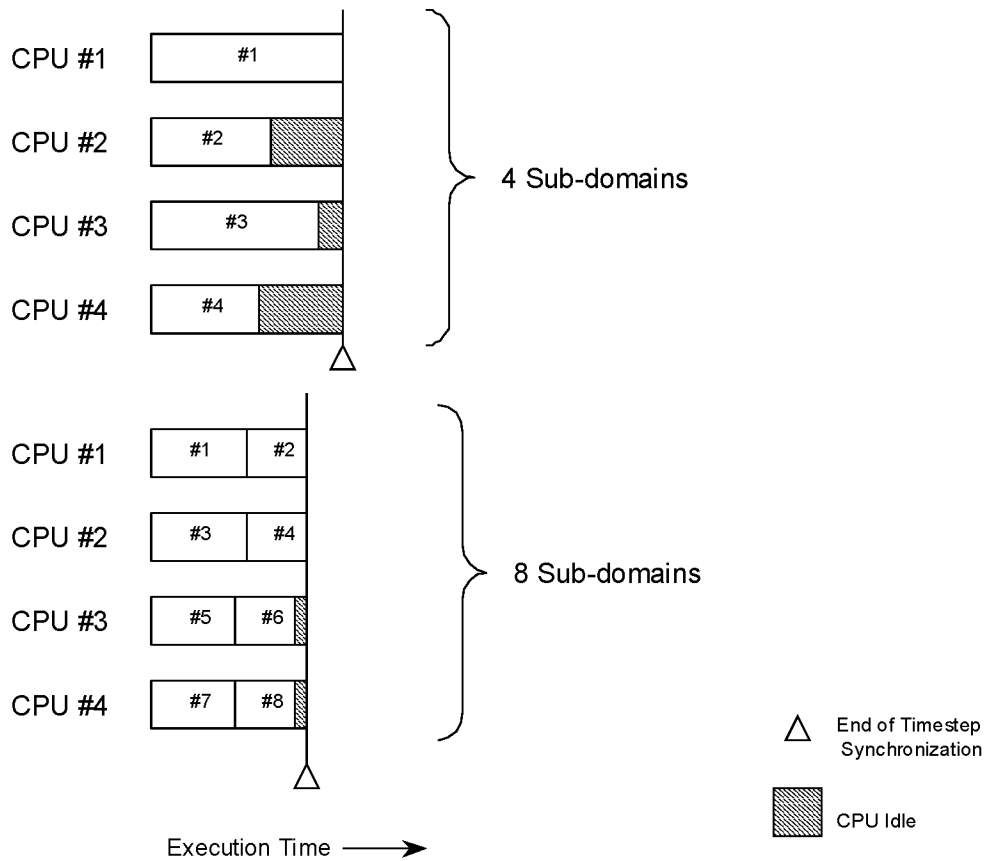
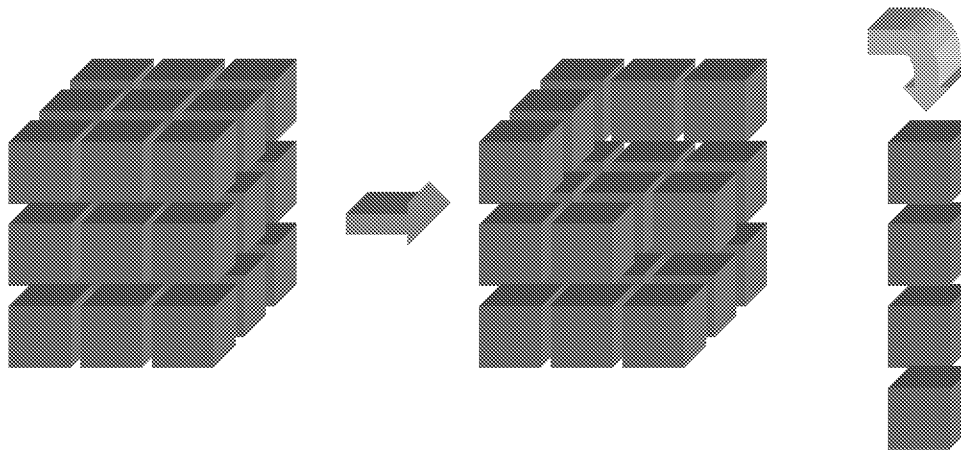


Figure 9: Domain Decomposition Improves Parallelism

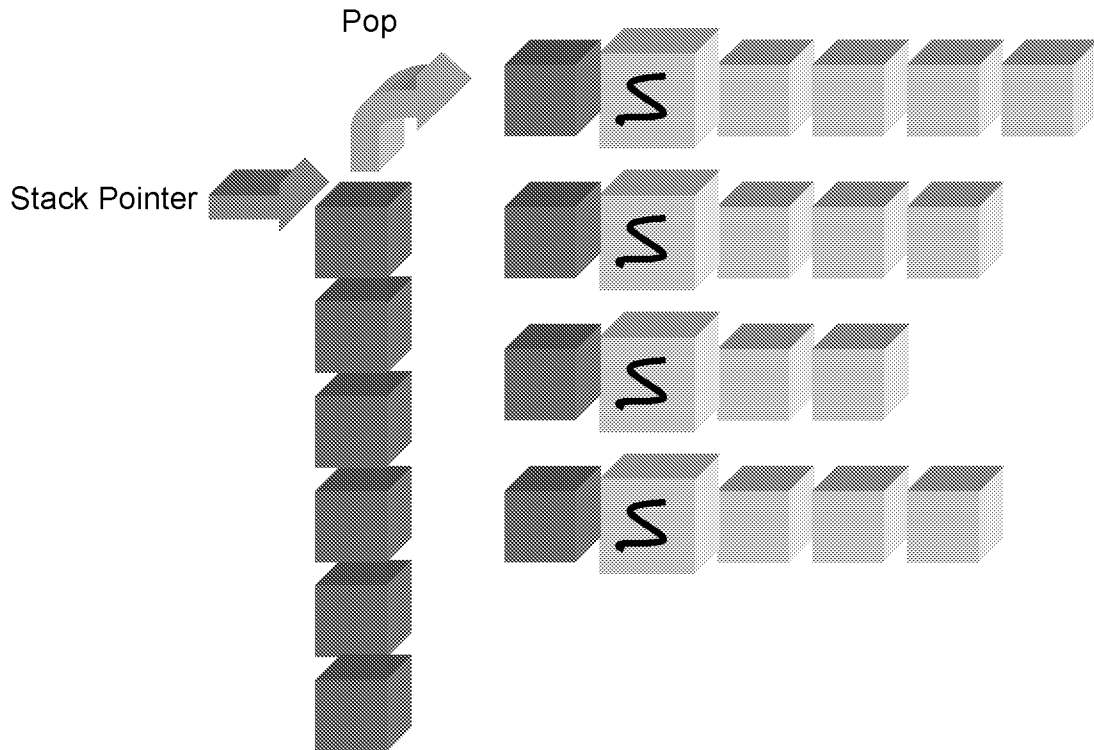
In this approach, the number of threads spawned is equal to the number of available processors with each thread marching through the available sub-domains (which preferably number at least two times the number of processors), solving one at a time in an “assembly-line” fashion. A stack is employed where each thread pops the next sub-domain to be solved off of the top of the stack. Mutual exclusion locks are employed to protect the stack pointer in the event two or more threads access the stack simultaneously. Each thread remains busy until the number of sub-domains is exhausted. If the number of sub-domains is large enough, the degree of parallelism will be high although decomposing a problem into too many sub-domains may adversely affect convergence. This approach is illustrated in Figures 10 and 11.



1) Decompose the domain

2) Push each sub-domain onto a software stack

Figure 10: Decompose the Domain and push onto Stack



3) Spawn threads and execute until stack is exhausted

Figure 11: Allow Threads to Process each Sub-domain

The coarse mesh computations were performed on a four processor Alpha™ based workstation located at the University of Alabama in Huntsville and on a dual processor Pentium™ II workstation located at the Marshall Space Flight Center. The fine mesh computations were conducted on SGI™ Origin 2000 and Power Challenge XL supercomputers (each containing twelve processors) located at the Marshall Space

Flight Center. The FDV application solver is based upon the Generalized Minimum Residual (GMRES) algorithm described by Shakib [8]. The application is coded to be multi-threaded to take advantage parallelism in the host computer. The number of threads is specified at run time and is based upon the expected number of available CPU's. The results for three different architectures are provided in Table 1. Typical utilizations (defined as CPU time/elapsed time) range from 180% to 380% for two to eight threads. It should be noted that both the number of threads and number of processors impose theoretical limits on the maximum performance gain. Obviously, the normalized performance increase can not exceed the number of threads and, aside from tertiary performance issues (such as on processor cache), nor can the normalized performance increase exceed the number of processors. For the coarse mesh model, actual speed increases range from 1.77 to 3.44 for 2 to 4 processors. The results are encouraging when considering the CPU contention between multiple users on the host machines. For the coarse mesh model on a dual processor Pentium II workstation (with no other users) a CPU utilization of 196% is observed with a real time speedup of 1.92. The four processor machine did exhibit a significant amount of overhead when moving beyond a single thread. Utilizing four threads for the fine mesh model resulted in CPU utilizations of 357% and 370% for a domain decomposed into 27 and 64 regions, respectively. The fine mesh model was not run with a single processor or thread so no relative speed-up data is available. The CPU utilization is encouraging considering the high CPU contention on the twelve processor machine.

Table 1. Computational Performance Summary

| Threads | Grid | Decomposition | CPU Time (hours) | Elapsed Time (hours) | CPU Utilization | Speed-up | Processor | Number of Proc |
|---------|-----------|---------------|------------------|----------------------|-----------------|----------|------------|----------------|
| 1 | 55x41x31 | 4x4x4 | 5.05 | 5.05 | 100% | 1.00 | Pentium II | 2 |
| 2 | 55x41x31 | 4x4x4 | 5.13 | 2.62 | 196% | 1.93 | Pentium II | 2 |
| 1 | 55x41x31 | 4x4x4 | 4.69 | 4.72 | 99% | 1.00 | Alpha | 4 |
| 2 | 55x41x31 | 4x4x4 | 5.19 | 2.66 | 195% | 1.77 | Alpha | 4 |
| 4 | 55x41x31 | 4x4x4 | 5.30 | 1.42 | 373% | 3.32 | Alpha | 4 |
| 6 | 55x41x31 | 4x4x4 | 5.30 | 1.40 | 378% | 3.36 | Alpha | 4 |
| 8 | 55x41x31 | 4x4x4 | 5.16 | 1.37 | 377% | 3.44 | Alpha | 4 |
| 4 | 109x81x61 | 3x3x3 | 37.40 | 10.47 | 357% | NA | R10000 | 12 |
| 4 | 109x81x61 | 4x4x4 | 52.76 | 14.25 | 370% | NA | R10000 | 12 |

Density contours for the inviscid shock interaction (x-z plane, as viewed from above the wind tunnel model) are shown in Figure 12. The 15° fins produce inviscid shocks that are predicted to intersect and reflect approximately 92 mm from the ramp entrance. The reflected shock does not intersect with the exit corner of the ramp as expected. Two cross sections, located at 67 mm and 92 mm, respectively, from the entrance are noted on the plot.

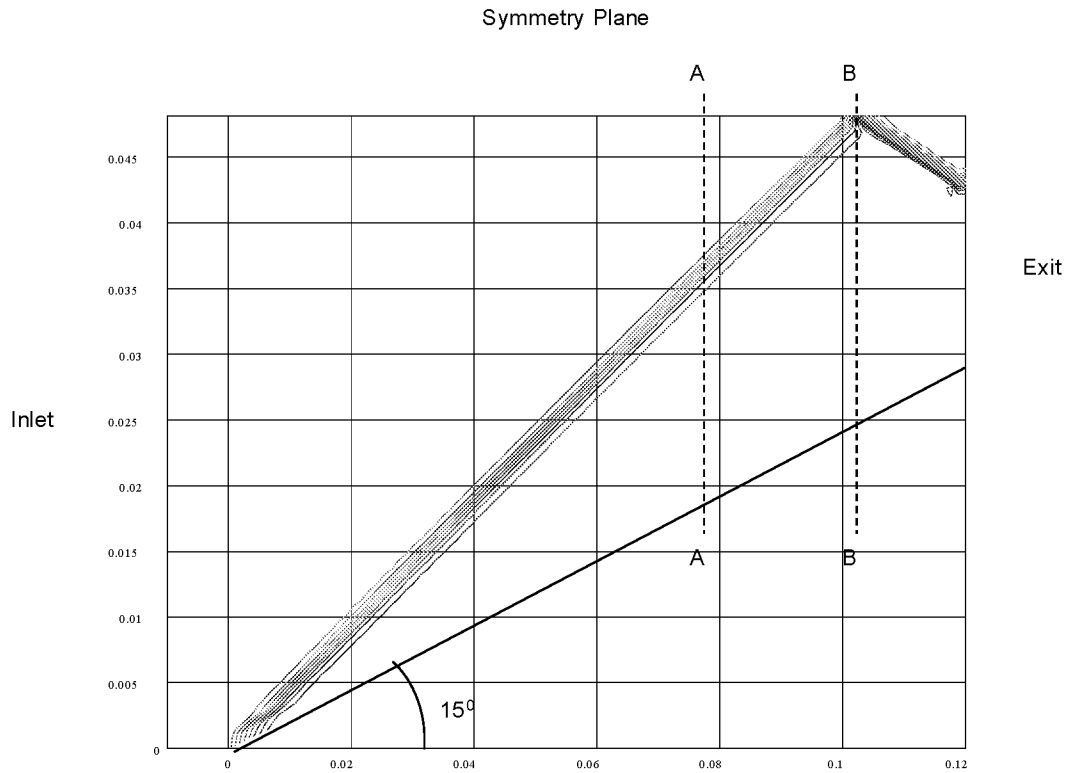
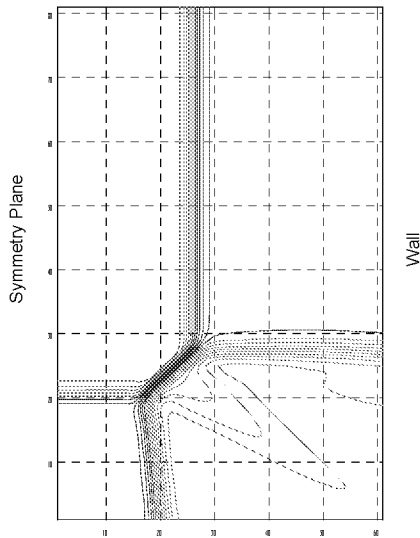


Figure 12: Density Contours for X-Z Cross Section (Top), Slip Boundary

Density contours for the flow in x-y planes located 67 mm (upstream of the inviscid shock intersection) and 92 mm (coincident with the inviscid shock intersection) from the combined fin/ramp entrance are shown in Figure 13. It appears that the upstream predictions correlate well with the experimental images. The inviscid ramp and fin shocks, as well as the corner reflection, are easily discernible in the upstream figure (see left). Interestingly, it appears that the triangular shaped slip lines are present in the numerical results of the upstream plane. Since the slip-lines divide constant pressure regions with differing velocities, this feature is not visible in the static pressure plots. As in the experimental imagery, the inviscid fin shocks merge together in the symmetry plane at the point where the inviscid shocks intersect (see right). No curvature of the inviscid fin shock intersection is observed in the numerical predictions. The reflection of the corner shock about the symmetry plane is observed, but the ramp embedded shock is lower relative to the height of the fin than in the experimental results.

Plane A-A (Ahead of the 15° Fin Shock Intersection)



Plane B-B (At the 15° Fin Shock Intersection)

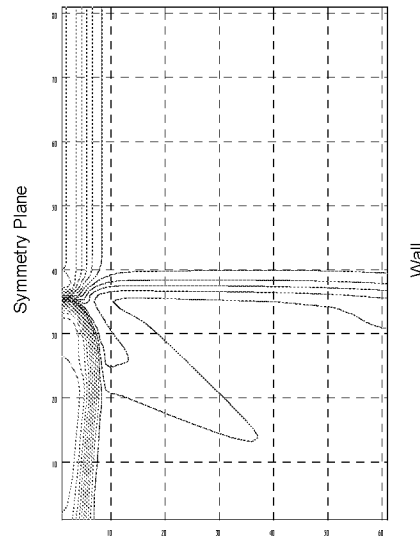


Figure 13: Density Contours for Y-Z Cross Section, Slip Boundary

CONCLUSIONS

The comparison of the FDV method to the actual measured flowfield for the triple shock interaction is encouraging. Many of the flowfield features observed in the experimental imagery are resolved in the computation including the inviscid shock corner reflections. Particularly good results are obtained for the shock structure in the cross sectional x-y planes upstream of the inviscid shock intersection. The numerical results did not exhibit the shock curvatures evident in the experimental images, but this may be rectified through increased grid resolution or a different boundary condition for the top surface (x-z plane) may be required. It is concluded that the multi-threaded domain decomposition approach provides an efficient strategy for parallelizing the FDV code and it is expected to be implemented on problems of increasing size in the future.

ACKNOWLEDGEMENTS

The authors wish to acknowledge Professor Krishna Kavi and members of the “Crash” group at the University of Alabama in Huntsville Electrical and Computer Engineering Department for their support.

REFERENCES

1. Garrison, T. J., Settles G. S., Naranyanswami, N., Knight D. D., and Horstman, C. C., “Flowfield Surveys and Computations of a Crossing Shock Wave/Boundary Layer Interaction”, AIAA Paper 94-2273, June 1994.
2. Garrison, T. J., Settles G. S., and Horstman, C. C., “Measurements of Triple Shock Wave/Turbulent Boundary Layer Interaction”, AIAA Paper 94-2274, June 1994.

3. Yoon, K. T. and Chung, T. J., "Three-dimensional mixed explicit-implicit generalized Galerkin spectral element methods for high-speed turbulent compressible flows", *Computer Methods in Applied Mechanics and Engineering*, 135,343-367 (1996)
4. Yoon, K. T., Moon, S. Y., Garcia, G. A., Heard, G. W., and Chung, T. J., "Flowfield dependent mixed explicit-implicit (FDMEI) methods for high and low speed and compressible and incompressible flows", *Computer methods in Applied Mechanics and Engineering*, 151, 75-104 (1998)
5. Chung, T. J., "Transitions and interactions of inviscid/viscous, compressible/incompressible and laminar/turbulent flows", *Int. J. Numer. Meth. Fluids*, in press.
6. Nichols B., Buttlar D., and Farrell J., "Pthreads Programming", O'Reilly and Associates, Inc., (1996).
7. Demmel, J.W., "Applied Numerical Linear Algebra", SIAM, Philadelphia, 347-351, (1997).
8. Shakib, F., Hughes, T., and Zdenek J., "A Multi-element Group Preconditioned GMRES Algorithm for Non-symmetric Systems Arising in Finite Element Analysis", *Computer Methods in Applied Mechanics and Engineering* (1989).



INTEGRATION OF RBCC FLOWPATH ANALYSIS TOOLS

D.G. Messitt
Gencorp Aerojet
P.O. Box 13222
Sacramento, CA 95813

ABSTRACT

A framework for integration of RBCC flowpath analysis tools is presented which allows for increased modeling flexibility, incorporation of improved engine component models, and integration of disparate computer codes. The interfaces between the engine components are abstracted with a construct which hides the details of the data passing between modules, presenting a standard interface to each component model. This framework facilitates application of different levels of fidelity for analysis of each engine component, which may reflect differing levels of maturity in the component design.

INTRODUCTION

Efforts aimed at integration of flowpath analysis tools have historically resulted in the construction of monolithic codes which contain models of the entire flowpath, from inlet to nozzle. These codes, such as RAMSCRAM,¹ RJPA,² and SRGULL,³ have become industry standards, and have been accepted through an extensive database of established results. They are poorly documented, and careful verification data, where they exist, are not generally available. The models of individual engine components, such as the combustor and nozzle, are tightly integrated within the code framework, cf. Fig. 1. This can make it difficult to add a new model or to analyze a radically different engine design.

The thermodynamic model is usually provided by a version of the CEA code,⁴ although the NOTS routines are used by RJPA, and other codes use custom routines, e.g., SCREAM.⁵ The thermodynamic models are so tightly integrated with the component models, cf. Fig. 1, that it is impossible to update them, or to replace them in order to standardize on a common set of routines.

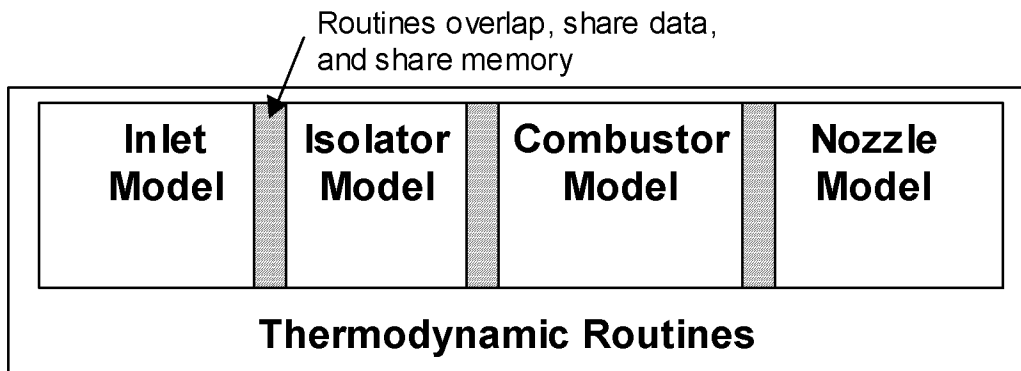


Figure 1 Subroutines share data and cannot be easily improved, replaced, or individually verified.

INTEGRATED FLOWPATH ANALYSIS TOOL

A typical RBCC flowpath may be broken into several parts, as illustrated in Fig. 2. The interface locations are somewhat arbitrary, and are chosen based upon the availability of existing data, or the suitability of available models for the flow processes. Each component has an interface where fluid enters or leaves.

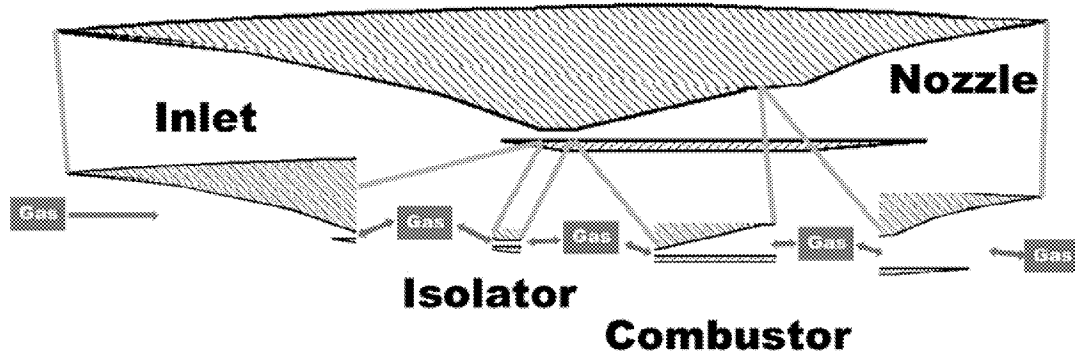


Figure 2 Illustration of RBCC engine flowpath component modelling

A flowpath analysis environment constructed with this philosophy has the ability to use different levels of fidelity for different engine components. This concept is illustrated in Fig. 3, where a 2D inlet simulation provides the inflow properties for the isolator, which is modeled in 1D based upon an experimental correlation. This capability is enabled by the realization that the inlet and isolator interact by the flow of a fluid at the interface. It is important to note that there can sometimes be feedback upstream, as illustrated in Fig. 4, a CFD simulation of inlet unstart.

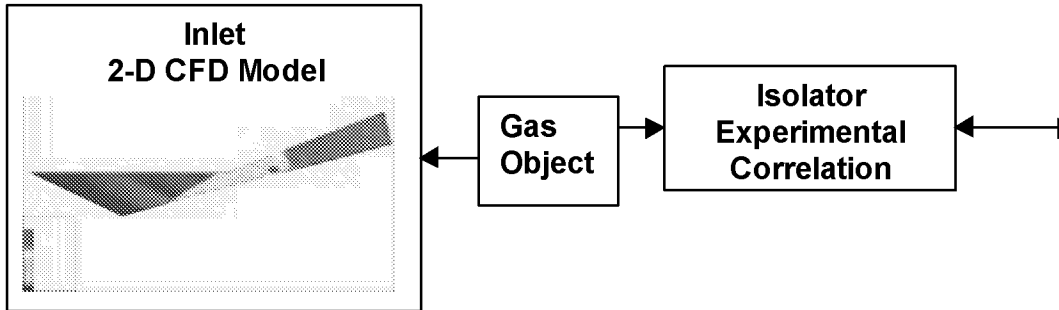


Figure 3 The inlet and isolator interface consists of a gas object which knows the fluid properties at the interface.

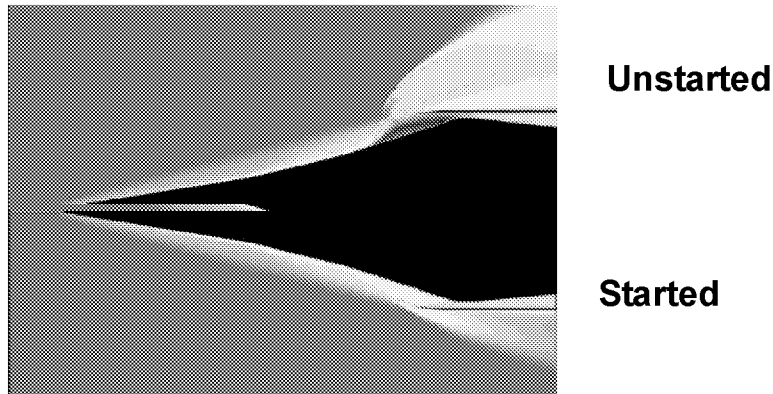


Figure 4 CFD Simulation of an inlet unstart demonstrated feedback from the isolator at Mach 5.

Communication between engine component models is abstracted by using the concept of a gas object. The gas object at the inlet and outlet of each component contains all of the information required to specify the state of the fluid at that point. A conceptual diagram of a gas object may look something like Fig. 5. The gas at the interface has certain properties, such as average pressure, velocity, etc. for a gas generated by a 1D model. The properties may be instead 2D profiles or 3D surfaces, if they were generated by a model with higher fidelity. They may be stored only in the computer memory, and thus be transient, or be persistent, such as a CFD code output file. The data may even physically reside on a different computer and a different operating system.

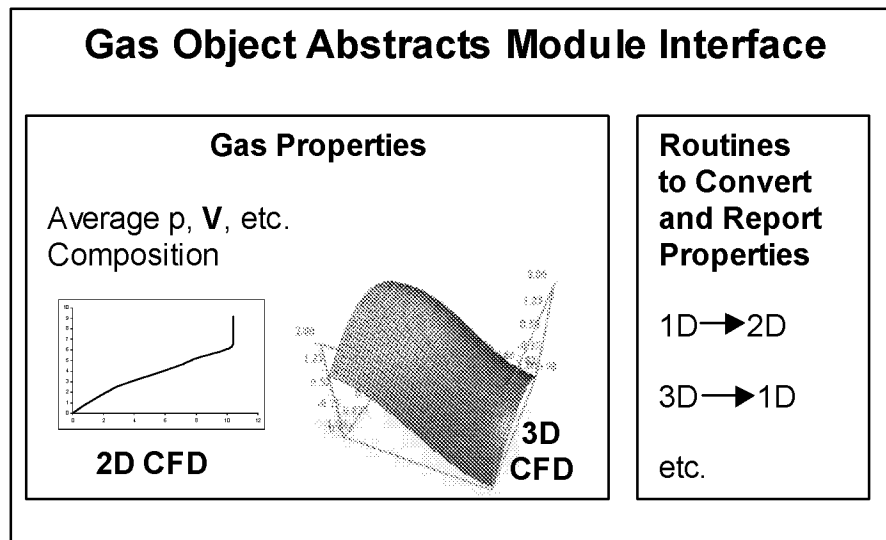


Figure 5 Interface between engine components isolates results from component model details.

The gas object also has the ability to report its properties when queried. For example, the isolator in Fig. 3 needs to obtain the 1D average inflow properties from the product of the 2D inlet CFD analysis. The isolator does this by invoking a subroutine contained in the definition of the gas object, essentially asking the gas “please give me your average pressure, velocity, etc.” The gas object gets the appropriate CFD data file from the network, and then invokes a suitable averaging method for the CFD data. The results of the averaging are reported to the isolator.

In this example, the isolator model has no knowledge of the details of how the properties at the inlet exit were obtained. This important feature is what enables improved or updated component models to be easily incorporated into the overall flowpath analysis procedure. It facilitates the incorporation of experimental data, when the component interfaces can be suitably defined.

The individual conducting the flowpath analysis defines which component models are used and how they are linked together. The interface is abstracted through the use of the gas object concept, outlined above. The framework allows for strongly coupled engine component models, such as a single routine which models the isolator and combustor, cf. Fig. 6. The technique also allows flexibility in assembling engine components to analyze other engine cycles, such as the Dual Combustion Ramjet (DCR)⁶ model illustrated in Fig. 7.

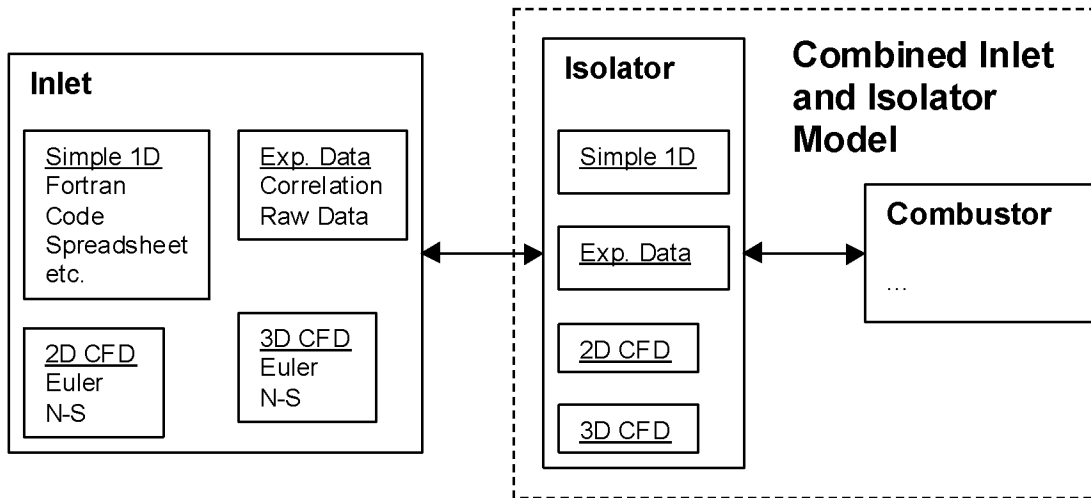


Figure 6 Engine components encapsulate the analysis method.

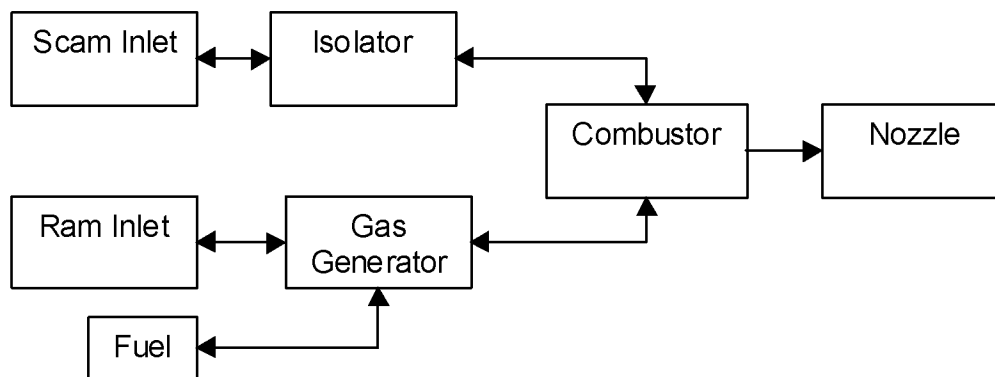


Figure 7 Schematic of a DCR engine analysis using distributed engine component models.

The key benefit of this framework is that the individual component models are isolated from the details of the techniques used to analyze the other engine components. Different engine components may be analyzed to different levels of fidelity, by choosing the appropriate analysis technique for each individual engine component, e.g., 1-D combustor analysis which flows into a 3-D nozzle CFD code.

Distributed computing is also supported. Continuing the example of Fig. 3, the CFD analysis could be conducted on High Performance Computing (HPC) resources, with the subsequent components analyzed on a PC and/or Unix workstations, cf. Fig. 8. The details of the interfaces between the engine component models are hidden by the abstraction of the gas object, which obtains required data from the network transparently.

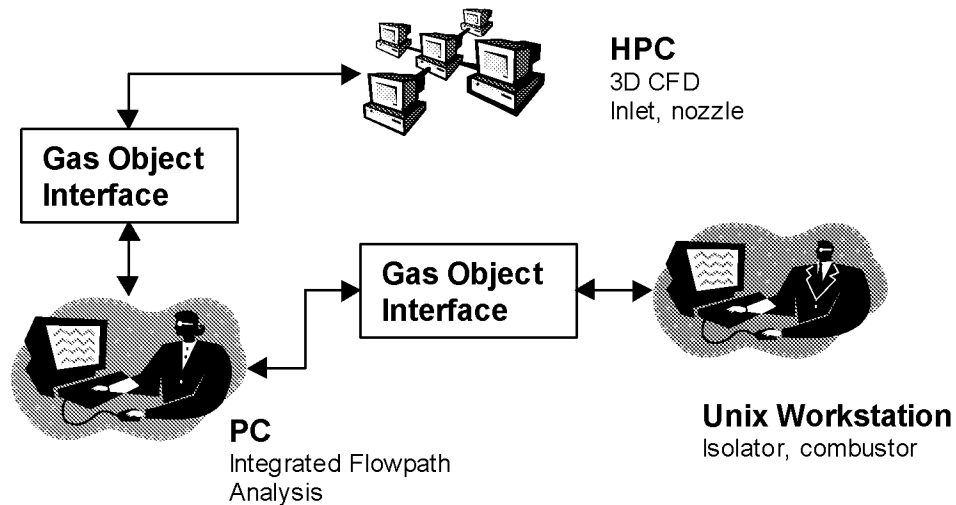


Figure 8 Distributed analysis of RBCC engine flowpath.

INTEGRATION FRAMEWORK ISSUES

There are many important issues which impact the implementation of the flowpath analysis integration framework. The most important of these is the construction of the structure which allows for the building of an engine model from the available component simulation routines. The most straightforward method involves assembling the available component models into a predefined sequence, similar to the existing monolithic codes. The advantages of fidelity zooming, distributed computation, individual model verification and validation, and integration of otherwise incompatible tools (e.g., linking spreadsheets with Fortran code) still exist, but the full potential of the framework is not realized.

INTEGRATION ARCHITECTURE

A better solution would involve constructing an architecture which would allow the graphical layout of engine component models on a canvas, in a manner similar to the schematic of Fig. 7. The architecture would link the models using the gas object abstraction, and collect and store output data for later inspection. This capability does not yet exist for current RBCC engine analysis tools.

Feedback between models, illustrated by inlet unstart in Fig. 4, requires special provisions in the code which assembles the engine component models into a flowpath simulation. The reduction in the level of integration between the component models may increase the time required to obtain a solution in cases where feedback is important.

TRACEABILITY

Another very important issue concerns traceability of the data generated by the flowpath analysis. The individual component models are verified and validated against accepted data, providing confidence in the results of a new analysis.

It is also very important to tag input and output files with information which identifies the component models used, including version information and model assumptions. This capability is included as a property of the gas objects which encapsulate the flowfield information generated by each model. It must also be included in any supplementary information obtained from the model, such as output files containing pressure distributions or other internal information not encapsulated in the gas object which represents the model inflow or outflow.

CONCLUSIONS

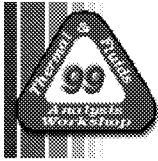
A framework for integration of RBCC flowpath analysis tools has been presented which allows for increased flexibility, incorporation of improved engine component models, and integration of disparate computer codes. The interfaces between the engine components are abstracted with a construct which hides the details of the data passing between modules, presenting a standard interface to each component model. This abstraction of the model interfaces reduces the complications for implementing heterogeneous distributed computing.

ACKNOWLEDGEMENTS

The author wishes to acknowledge the contributions of Mel Bulman and Dick Johnson.

REFERENCES

1. Burkardt, L.A., and Franciscus, L.C., "RAMSCRAM – A Flexible Ramjet/Scramjet Engine Simulation Program," NASA Technical Memorandum 102451, June, 1990.
2. Pandolfini, P.P., Billig, F.S., Corpening, G.P., Corda, S., and Friedman, M.A., "Analyzing Hypersonic Engines Using the Ramjet Performance Analysis Code," *APL Technical Review*, Vol. 2, No. 1, 1990, pp. 34-45.
3. Pinckney, S.Z., Walton, J.T., "Program SRGULL: An Advanced Engineering Model for the Prediction of Airframe-Integrated Subsonic/Supersonic Hydrogen Combustion Ramjet Cycle Performance," NASP TM 1120, Jan., 1991.
4. Gordon, S., and McBride, B.J., "Computer Program for Calculation of Complex Chemical Equilibrium Compositions and Applications I. Analysis," NASA RP-1311, Oct., 1994.
5. Bradford, J.E., and Olds, J.R., "SCCREAM v.5: A Web-Based Airbreathing Propulsion Analysis Tool," AIAA Paper 99-2104, June, 1999.
6. Billig, F.S., Waltrup, P.J., and Stockbridge, R.D., "Integral-Rocket Dual-Combustion Ramjets: A New Propulsion Concept," *Journal of Spacecraft and Rockets*, Vol. 17, Sept.-Oct., 1980, pp. 416-424.



ONGOING ANALYSES OF ROCKET BASED COMBINED CYCLE ENGINES BY THE APPLIED FLUID DYNAMICS ANALYSIS GROUP AT MARSHALL SPACE FLIGHT CENTER

Joseph H. Ruf, James B. Holt, Francisco Canabal
Marshall Space Flight Center

ABSTRACT

This paper presents the status of analyses on three Rocket Based Combined Cycle (RBCC) configurations underway in the Applied Fluid Dynamics Analysis Group (TD64). TD64 is performing computational fluid dynamics (CFD) analysis on a Penn State RBCC test rig, the proposed Draco axisymmetric RBCC engine and the Trailblazer engine. The intent of the analysis on the Penn State test rig is to benchmark the Finite Difference Navier Stokes¹ (FDNS) code for ejector mode fluid dynamics. The Draco analysis was a trade study to determine the ejector mode performance as a function of three engine design variables. The Trailblazer analysis is to evaluate the nozzle performance in scramjet mode. Results to date of each analysis are presented

NOMENCLATURE

A_s = Secondary Flow Area
 A_p = primary thruster exit flow area plus thruster base area
 A_5 = mixer inlet area, $A_s + A_p$
 A_8 = ram burner area
 D = mixer diameter at mixer inlet
 L = mixer length
 R = radius
 y = local radius
 \dot{m} = mass flow rate

SUMMARY

Three analyses related to RBCC concepts are underway in TD64 at MSFC. Each analysis is described in its own section of this paper. The first two analyses deal with the first mode of the RBCC engines or the 'ejector' mode. The ejector mode occurs at Mach numbers less than one while the primary thruster exhaust entrains or 'ejects' air through the engine.

The first analysis is a benchmark of the FDNS CFD code for RBCC ejector mode fluid physics. Penn State University (PSU) is in the process of completing a benchmark quality laboratory experiment of an RBCC

configuration in ejector mode. This benchmark will determine how best to use FDNS to predict ejector mode performance of RBCC engine concepts.

The second analysis used FDNS to predict the ejector mode performance of an early configuration of the Darco RBCC engine. A trade study of 27 engine configurations was performed. Draco is a near term RBCC axisymmetric engine intended to air-breathe up through the ramjet mode.

The third analysis is using FDNS to determine the nozzle performance for the Trailblazer vehicle in the scramjet mode. The computational domain begins inside the engine and includes the freestream flow for the installed performance effects. The Trailblazer vehicle is single-stage-to-orbit RBCC concept with three semi-axisymmetric engines.

FDNS EJECTOR FLOW BENCHMARKING

INTRODUCTION

The PSU RBCC hardware is a two-dimensional design (figure 1) with variable geometry to enable studies of RBCC mixing and secondary combustion phenomena. Gaseous hydrogen and oxygen were used as propellants. The ejector mode configuration had a simple two-dimensional inlet and exhausted to atmospheric pressure. The ejector mode test included measurements for wall static pressure, wall heat flux and overall thrust. Additionally, optical and laser based diagnostics were employed to evaluate mixing and secondary combustion during testing. A primary objective of the PSU ejector mode test was to provide high quality benchmark data for CFD code validation.

OBJECTIVE

The objective of this analysis is to benchmark the FDNS CFD code for RBCC ejector mode operation. The key physical process of interest is the shear layer interaction between and mixing of the primary thruster exhaust with the secondary (air) flow. This process has a significant affect on the amount of secondary flow entrained and, therefore, the performance of the RBCC's ejector mode.

APPROACH

The test conditions modeled are for the primary thruster at 500 psi and an oxidizer-to-fuel (O/F) ratio of eight. The afterburner has a small amount of gaseous hydrogen injected. A semi-3D domain is currently being used to model the test hardware. The symmetry in the hardware allows the domain to contain only 1/4th of the hardware flowpath. The semi-3D domain is fairly dense in the axial and vertical directions, but is coarse in depth. The depth is incorporated to enable the afterburner fuel injection. The analysis is steady state and implements finite-rate chemistry and thermodynamics and the standard k-ε turbulence model.

STATUS

The only test data currently available is the upper wall static pressures for two runs. The complete data should be available with a few weeks. The wall pressures from the current solution are compared to the test data in figure 2. The semi-3D results match the test data very well. The slight drop in pressure in the afterburner is due to the hydrogen injection and afterburning. All hydrogen is consumed before the gases exit the nozzle.

FUTURE WORK

Future work will involve refining the three-dimensional grid and then comparing to the complete experimental data set for O/F of eight. Further benchmarking will be pursued by modeling the same hardware with the primary thruster at an O/F of four.

DRACO EJECTOR/MIXER TRADE STUDY

INTRODUCTION

The first or ‘ejector’ mode of the Draco engine will have a significant impact on the overall engine cycle performance. By their very nature the one-dimensional RBCC cycle performance codes used for RBCC conceptual design do not capture the multidimensional fluid dynamic interactions that may have significant effects on the ejector mode performance. If CFD can be integrated into the design process early the RBCC cycle performance codes would benefit from information on the three-dimensional effects and engine designers would gain additional understanding of RBCC internal fluid dynamics.

An early Draco configuration was chosen to start the CFD trade study on ejector/mixer performance even though significant changes in the Draco design were likely. This trade study was used to get all the CFD related tools in place, working and streamlined so future ejector/mixer configuration trade studies could be tackled much quicker.

OBJECTIVE

The first objective to this analysis was to determine the Draco ejector/mixer performance trends for quiescent freestream for a matrix of engine design variables. The second objective was to get the CFD and related analysis tools in place, working and streamlined for quick turn-around of ejector/mixer configuration trade studies.

APPROACH

The Draco flowpath configuration for this analysis was axisymmetric with a single primary thruster on the engine centerline (figure 3). The primary thruster was housed in a centerbody that created an annular constant area inlet. On the front of the centerbody was an inlet compression spike.

Figure 3 defines some of the Draco design variables. The ejector/mixer inlet plane is defined to be the exit plane of the primary thruster. The mixer length (L) was a function of two of the trade space variables, L/D and A_s/A_p . The mixer diameter (D) was defined as its diameter at the inlet plane. A_s is the area of the secondary flow area and A_p is the area of the primary thruster exit area plus any base area surrounding the thruster. A_5 is the total flow area at the ejector/mixer inlet plane ($A_s + A_p$) and A_8 is the flow area of the ram burner.

The engine design variables that defined the trade space were: ejector/mixer L/D; A_s/A_p , the ratio of secondary to primary flow areas; and A_8/A_5 , ratio of ram burner to ejector/mixer inlet areas. Each variable had three values so that the trade space included 27 cases as shown in table 1. Several of the engine configurations are shown in figure 4.

The performance of the ejector/mixer was measured with the following figures of merit (FOM): By-pass ratio, the ratio of secondary flow to primary flow; ejector compression ratio (ECR), the ratio of total pressure at ejector/mixer exit to total pressure of secondary flow; ejector/mixer thrust efficiency, thrust at the exit divided by thrust at the mixer inlet; ejector/mixer mixing efficiency as defined below.

$$\text{Mixer Mixing Efficiency} \equiv 1 - \frac{\sum_{y=0}^{R_{exit}} |\dot{m}'_{air \text{ ideal}} - \dot{m}'_{air @ y}|_{\text{mixer exit}}}{\sum_{y=0}^{R_{inlet}} |\dot{m}'_{air \text{ ideal}} - \dot{m}'_{air @ y}|_{\text{mixer inlet}}}$$

The mixing efficiency was defined as a measure of how well the mixer achieved perfectly mixed homogeneous flow at the ejector/mixer exit. The mass flow distribution of secondary flow (air) was used to

calculate the mixing efficiency. The difference between homogeneous flow and the air mass flow distribution that existed at the ejector/mixer inlet was determined and normalized to represent zero mixing. A value of 1 would occur only if the entrained air was perfectly mixed with the primary flow and the resulting mixed flow had no gradients ('plug' flow). Values of less than zero were possible if the ejector/mixer increased the striation of the primary and secondary flows.

The geometric definition of the 27 cases was extracted from an engine design spreadsheet. This geometry was passed to Gridgen⁵ to generate the grids. All grids contained the same number of nodes in the freestream, inlet, ram burner and nozzle portions of the domain. The number of nodes in the axial direction of the ejector/mixer varied because of their different lengths. A consistent axial delta-s was used in the ejector/mixer region. The grids contained approximately 33k, 38k and 44k nodes for the L/D=1, 2, and 3 configurations, respectively. Once the Gridgen template was in place for each L/D grids the 24 subsequent grids could be generated in less than five minutes each.

The FDNS CFD code was implemented with a two-specie model: air and a specie of average hot-gas properties. This analysis was non-reacting but future analysis will include finite rate reaction as necessary. The standard k-ε turbulence model was implemented. The benchmarking effort above will indicate if another turbulence model is more appropriate for future work.

The freestream far field boundaries were set to conserve total pressure of one atmosphere. All engine surfaces were set to no-slip adiabatic walls and the centerline of the engine was set to an axisymmetric boundary condition. Primary thruster mass flow rates were the same for all configurations but each A_s/A_p ratio resulted in a different primary thruster area ratio, therefore, a different primary thruster exit pressure. The $A_s/A_p=1$ had the lowest exit pressure and $A_s/A_p=3$ had the highest exit pressure. The primary thruster exit flow properties were calculated with the Reacting and Multiphase Program⁴. These thruster exit flow properties were defined as fixed inlet conditions for the ejector/mixer analysis.

The solution procedure was highly automated by using a series of Unix scripts. The scripting automatically acquired the appropriate grid and initialized the grid and solution in FDNS format. The scripts then ran the solution 15 thousand iterations through a series of CFD inputs increasing the time step while decreasing the damping. The grid was then adapted based on flow field gradients with Self-Adaptive Grid Code⁵, the solutions were run 15 thousand more iterations, and post processed for the FOMs. Subsequent configurations used previously converged restart files where possible. All 27 configurations were run 15k iterations before and after adaptation even though most all were converged much sooner. This scripting procedure allowed the matrix of cases to be run in a 'submit and forget' mode from the end of grid generation to the point of looking at the final post processed answers.

The solutions were run on single processors of an SGI R10000 16-processor computer. Each configuration required about 44 processor hours from start to finish. The 27 cases were submitted on a Friday afternoon with staggered start times over the weekend. The last case was completed on the following Tuesday.

RESULTS

Figure 5 shows Mach number and air mass fraction contours of the Draco internal flow path for two configurations, L/D=1, $A_s/A_p=1.5$ and $A_s/A_p=1$ and 3. The Mach number contours of the $A_s/A_p=3$ configuration indicate the primary flow attached to the mixer wall sooner and incurred significantly stronger shocks than the $A_s/A_p=1$ configuration. The shocks were caused by the primary flow's interaction with the secondary flow and the mixer wall. The Mach contours in the inlet show the $A_s/A_p=1$ configuration had a higher secondary flow rate.

In figure 5 the mixer exit plane is approximately one-third of the distance between the primary thruster exit and the engine exit. The air mass fraction contours indicate that at the mixer exit plane the $A_s/A_p=1$ configuration had slightly better mixing of the primary and secondary flows.

Figure 6 indicates the largest driver in the by-pass ratio was A_s/A_p . This was a result of the different primary thruster area ratios and, therefore, exit pressures. For the range of A_s/A_p studied the lowest primary thruster exit pressure ($A_s/A_p=1$) pumped the most secondary flow. Both L/D and A_8/A_5 had less dramatic but yet significant effects on by-pass ratio.

The ECR (figure 7) was lowest at $A_s/A_p=1$ because the high secondary flow rate diluted the average total pressure of the resultant mixed flow. ECR also was lowest for the largest L/D . This resulted from the increased number of shocks that occurred in the longer mixers.

The mixing efficiency (figure 8) shows that the $A_s/A_p=1$ configuration had the best mixed flow at the mixer exit. There was no significant difference between $L/D=2$ and 3. A_8/A_5 did not significantly effect mixing efficiency. Figure 9 plots the mixing efficiency for all configurations from the mixer inlet to the mixer exit plane. The $A_s/A_p=2$ and 3 decreased the mixing because of the higher primary thruster exit pressures compressed the secondary flow against the mixer walls.

In figure 10 the mixer thrust efficiency is shown versus axial station for the $L/D=3$ configurations. The mixer degraded thrust for all configurations. Note that A_8/A_5 has a significant effect on mixer thrust efficiency, especially for $A_s/A_p=1$.

CONCLUSIONS

In this trade study the $A_s/A_p=1$ configuration clearly had the highest by-pass ratios and mixer mixing efficiencies. The additional length of $L/D=3$ over $L/D=2$ did not significantly enhance the mixer mixing efficiency. The $A_8/A_5=1.5$ configurations had the highest mixer thrust efficiencies.

The CFD and related analysis tools are in place, working and streamlined for quick turn-around of Draco ejector/mixer configuration trade studies.

FUTURE WORK

If the PSU ejector benchmark determines that there is a better turbulence model for ejector flows than the $k-\epsilon$ model these 27 configurations will be re-run with the more appropriate turbulence model.

Response surface methodology⁶ will be incorporated into the solution procedure to determine optimum ejector/mixer configurations.

TRAILBLAZER

INTRODUCTION

The Trailblazer⁷ is a reusable, single-stage-to-orbit vehicle concept, intended to reduce the cost of space access by making optimum use of air-breathing propulsion. The Trailblazer is a hydrogen-oxygen fueled vertical take-off/horizontal landing vehicle with 130,000lb gross lift-off weight and 300lb payload. Figure 11 shows the Trailblazer reference vehicle. The propulsion system operates in four modes including ramjet, scramjet, and rocket modes from lift-off to orbit. A full description of the Trailblazer concept can be found in reference 7.

In scramjet mode the effective specific impulse is very sensitive to the expansion process efficiency, especially approaching the maximum air-breathing Mach number of about 10. To determine the expansion nozzle efficiency the Applied Fluid Dynamics Group is performing CFD analysis of the Trailblazer engine flowpath for the scramjet mode.

OBJECTIVE

The primary objective of this study is to provide estimates of the expansion process efficiency of the Trailblazer nozzle configuration in scramjet mode. The dominant loss mechanisms are to be identified and quantified in order to guide refinements in the nozzle design.

APPROACH

The analysis is being performed with the FDNS CFD code. Finite-rate chemistry and thermodynamics and standard k-ε turbulence model are implemented. The free-stream flow is included to accurately model the altitude compensating effect of the aft-body. Effects of vehicle angle of attack and yaw are neglected. Symmetry is assumed about a plane parallel to the vehicle axis that bisects the engine flowpath such that one half of an engine and 1/6th of the vehicle aft end are in the domain. Figure 12 shows the external portion of the computational domain. The engine inlet boundary conditions for the scramjet mode were provided by a one-dimensional engine performance code. The freestream velocity is set to Mach 10. The expansion process efficiency will be determined by post-processing the three-dimensional CFD solution of the nozzle flowfield

STATUS

Preliminary results are presented in terms of pressure contours in figures 13 through 15. Figure 13 shows the pressure contours along the plane of symmetry. Figures 14 and 15 show surface pressure contours in the neighborhood of the primary thruster and ramp respectively.

FUTURE WORK

After completion of the current scramjet mode analysis two additional engine modes will be analyzed; the ejector mode and the rocket mode. The primary objective will again be to determine the expansion process efficiency of the Trailblazer configuration.

ACKNOWLEDGEMENTS

The authors would like to thank Dr. C. Trefny and Mr. M. D'Agostino for their assistance with this work.

REFERENCES

1. Chen, Y. S., "FDNS - A General Purpose CFD Code, Version 4.0", Engineering Sciences, Inc., ESI-TR-97-01, Huntsville, AL., May 1997.
2. Lehman, M., Pal, S., Broda, J. C. and Santoro, R. J., "Raman Spectroscopy Based Study of RBCC Ejector Mode Performance," AIAA-99-0090, 37th AIAA Aerospace Sciences Meeting, Reno, NV, January 11-14, 1999.
3. Gridgen Version 13 user manual, <http://pointwise.com/>
4. Smith, S.D., "High Altitude Supersonic Flow of Chemically Reacting Gas-Particle Mixtures – Volume 1, LMSC-HREC TR D867400-1, Lockheed Missile and Space Company, Huntsville, AL., October 1984.
5. Davies, C. B. and Venkatapathy, E., "The Multidimensional Self-Adaptive Grid Code, SAGEv2", NASA TM 110350, April 1995.

6. Myers, R. H. and Montgomery, D. C., Response Surface Methodology-Process and Product Optimization Using Designed Experiments, John Wiley & Sons, 1995.
7. Trefny, C., "An Air-Breathing Launch Vehicle Concept for Single-Stage-to-Orbit", AIAA Paper 99-2730, June, 1999.

| | L/D=1 | | | L/D=2 | | | L/D=3 | | |
|-----------|---------|---------|---------|---------|---------|---------|---------|---------|---------|
| | As/Ap=1 | As/Ap=2 | As/Ap=3 | As/Ap=1 | As/Ap=2 | As/Ap=3 | As/Ap=1 | As/Ap=2 | As/Ap=3 |
| A8/A5=1.5 | 1.1.15 | 1.2.15 | 1.3.15 | 2.1.15 | 2.2.15 | 2.3.15 | 3.1.15 | 3.2.15 | 3.3.15 |
| A8/A5=2. | 1.1.20 | 1.2.20 | 1.3.20 | 2.1.20 | 2.2.20 | 2.3.20 | 3.1.20 | 3.2.20 | 3.3.20 |
| A8/A5=2.5 | 1.1.25 | 1.2.25 | 1.3.25 | 2.1.25 | 2.2.25 | 2.3.25 | 3.1.25 | 3.2.25 | 3.3.25 |

Table 1. Draco Ejector Cases

Figure 1. Penn State RBCC Ejector Mode Experimental Hardware

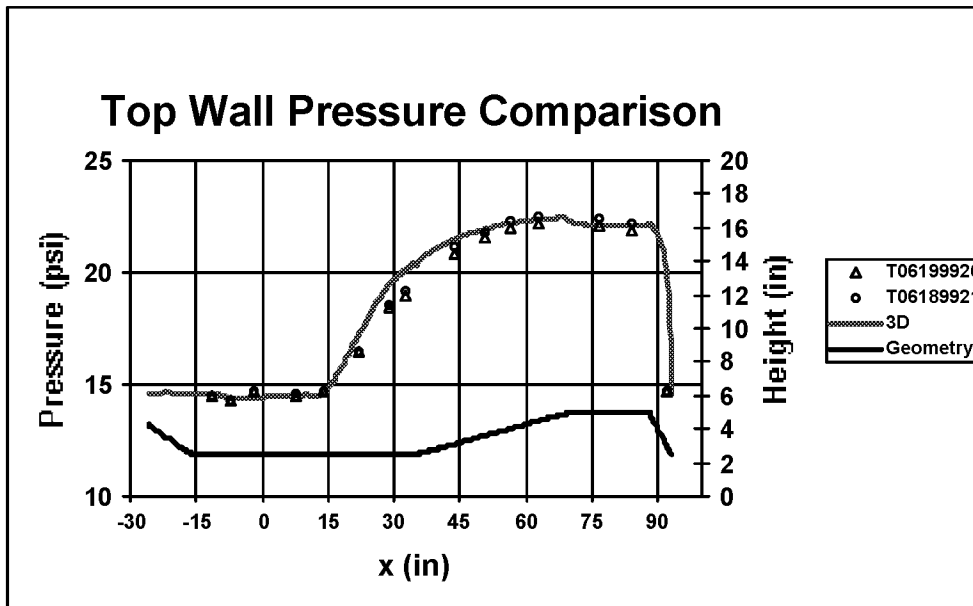
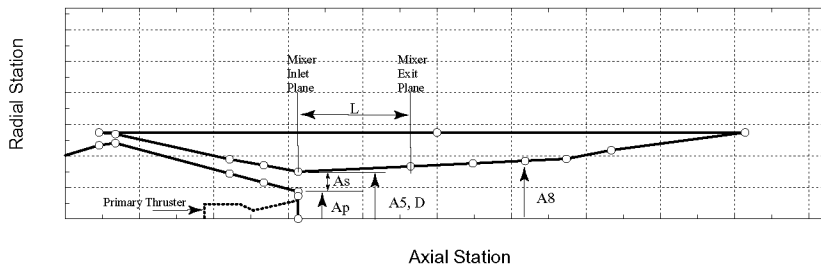


Figure 2. Comparison of FDNS and Test Data Upper Wall Pressures for Ejector Mode



A_s = Secondary Flow Area, Constant Area Inlet
 A_p = Primary Thruster Exit Area + Thruster Base Area
 $A_s/A_p = 1, 2 \text{ or } 3$

L = Mixer Length
 D = Mixer Diameter at Inlet
 $L/D = 1, 2 \text{ or } 3$

A_5 = Mixer Inlet Area
 A_8 = Ram Burner Area
 $A_8/A_5 = 1.5, 2.0, \text{ or } 2.5$

Figure 3. Draco Engine Layout

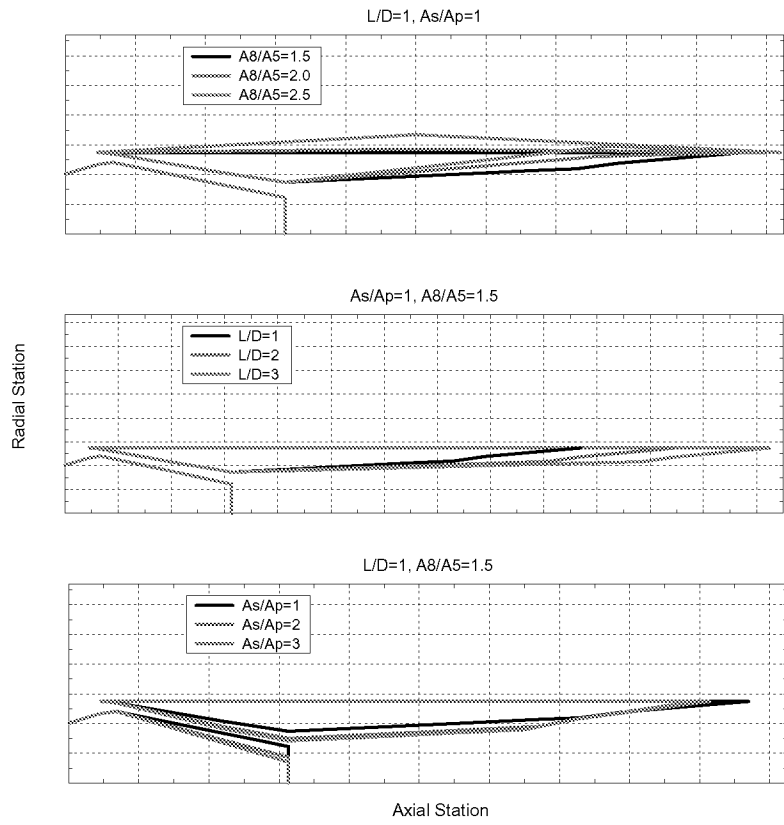
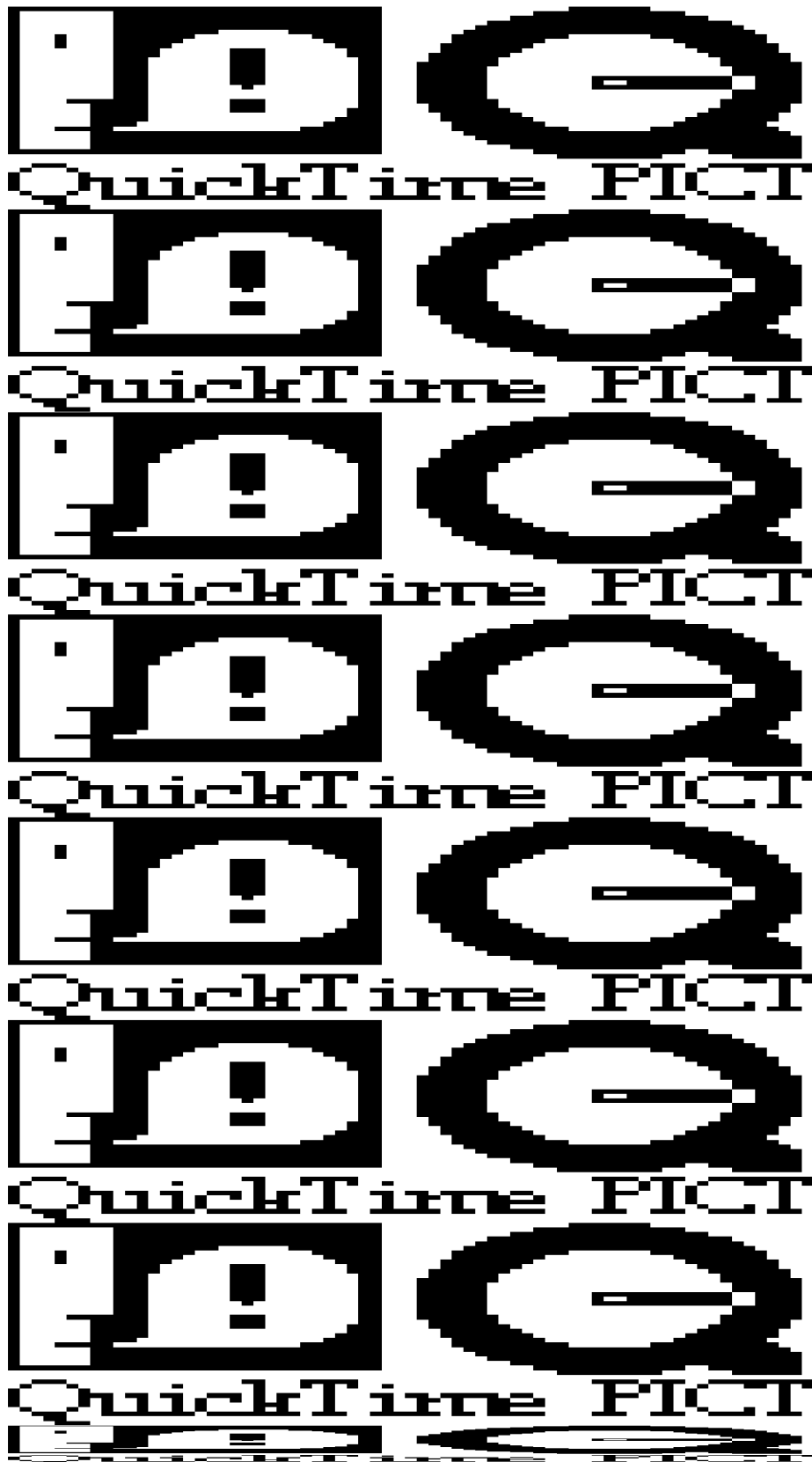


Figure 4. Examples of Engine Layouts in Trade Study



$L/D=1, A_8/A_5=1.5, A_9/A_p=3$

$L/D=1, A_8/A_5=1.5, A_9/A_p=1$

Figure 5. Mach and Mass Fraction Contours for $L/D=1, A_8/A_5=1.5, A_9/A_p=1$ and 3

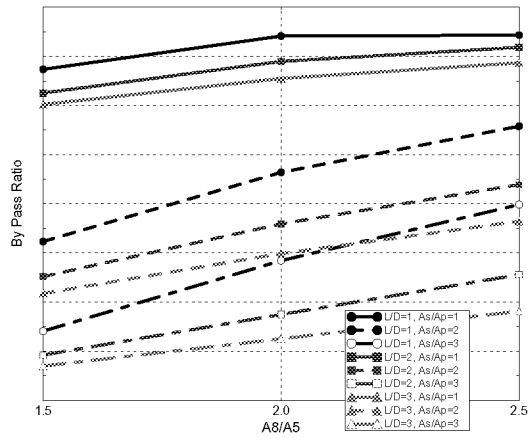


Figure 6. By-Pass Ratio vs. A_8/A_5

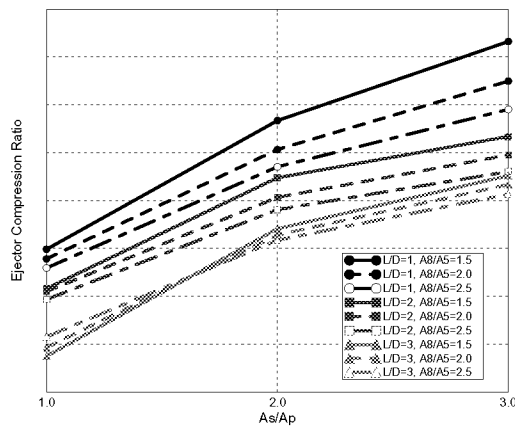


Figure 7. Ejector Compression Ratio vs. A_8/A_p

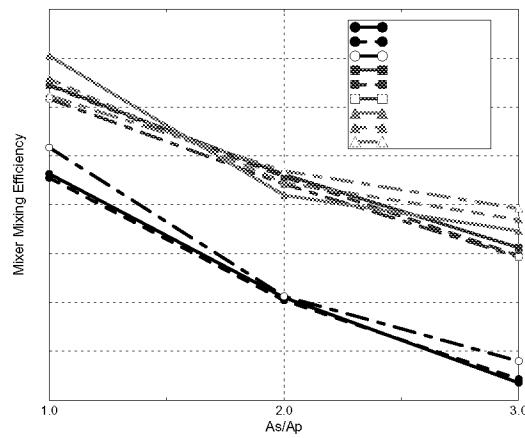


Figure 8. Mixer Mixing Efficiency vs. A_8/A_5

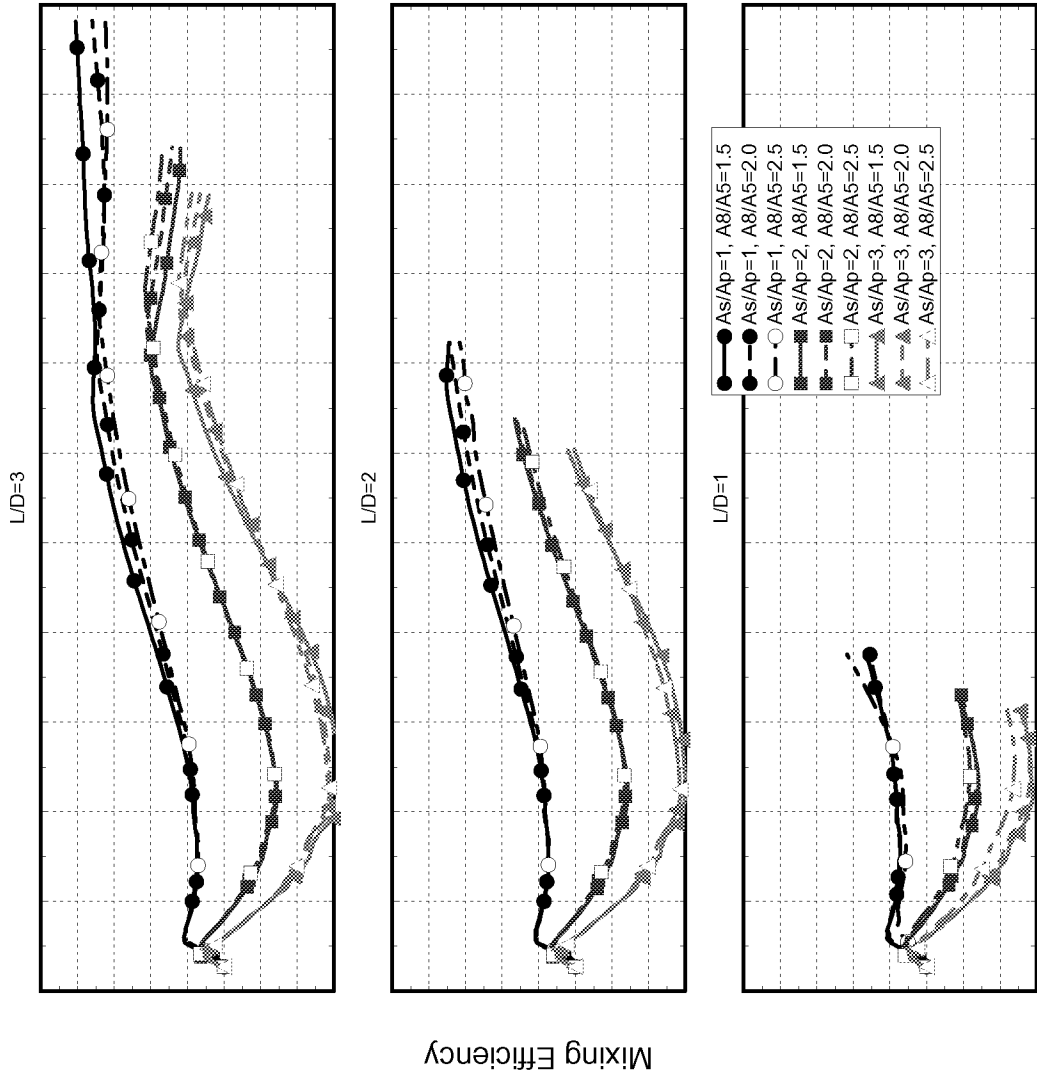


Figure 9. Mixer Mixing Efficiency vs. Axial Station

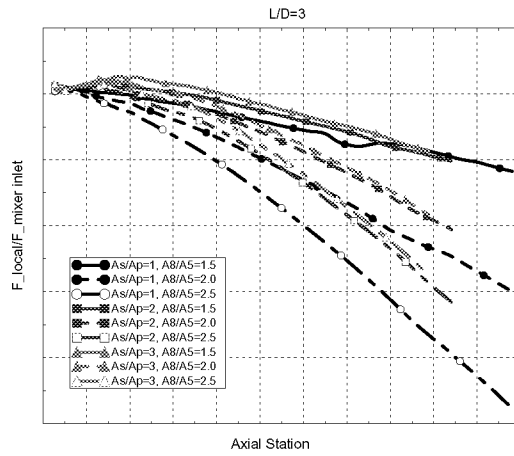


Figure 10. Mixer Thrust Efficiency vs. Axial Station for L/D=3 Configurations

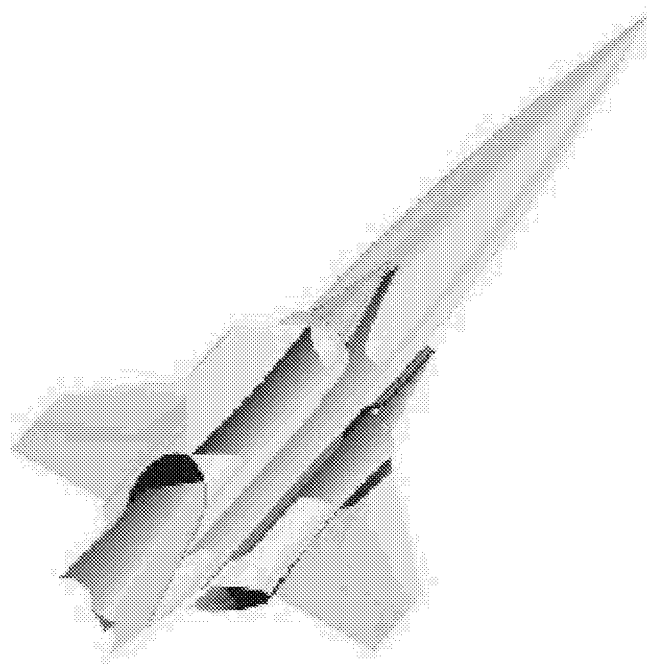


Figure 11. Trailblazer Reference Vehicle

Figure 12. Computational Domain for Trailblazer Nozzle Analysis

Pressure Contour

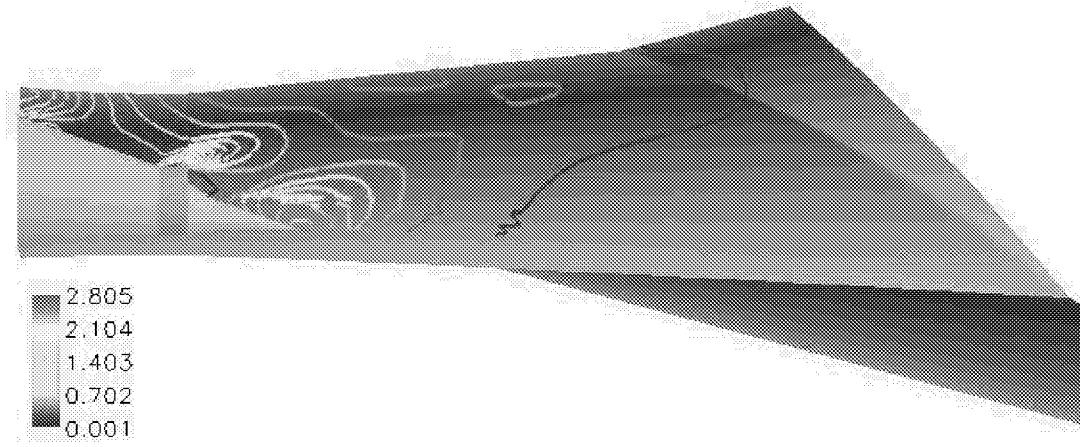


Figure 13. Pressure Contours on Symmetry Plane

Pressure Contour

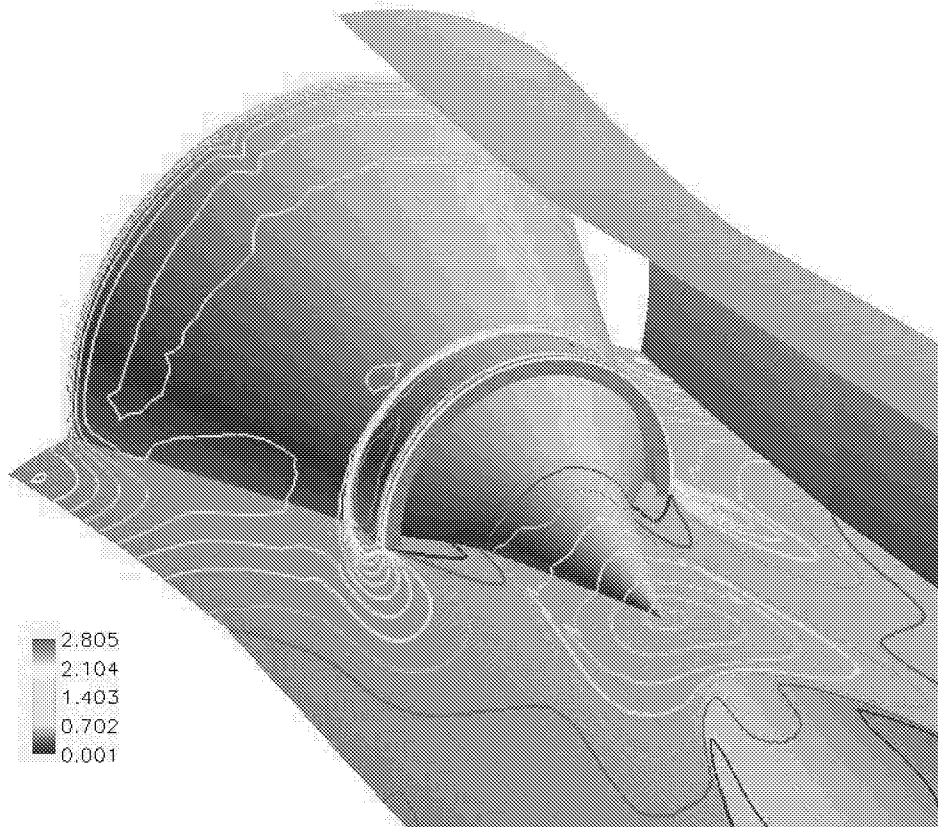


Figure 14. Pressure Contours Near Inlet and Primary Thruster

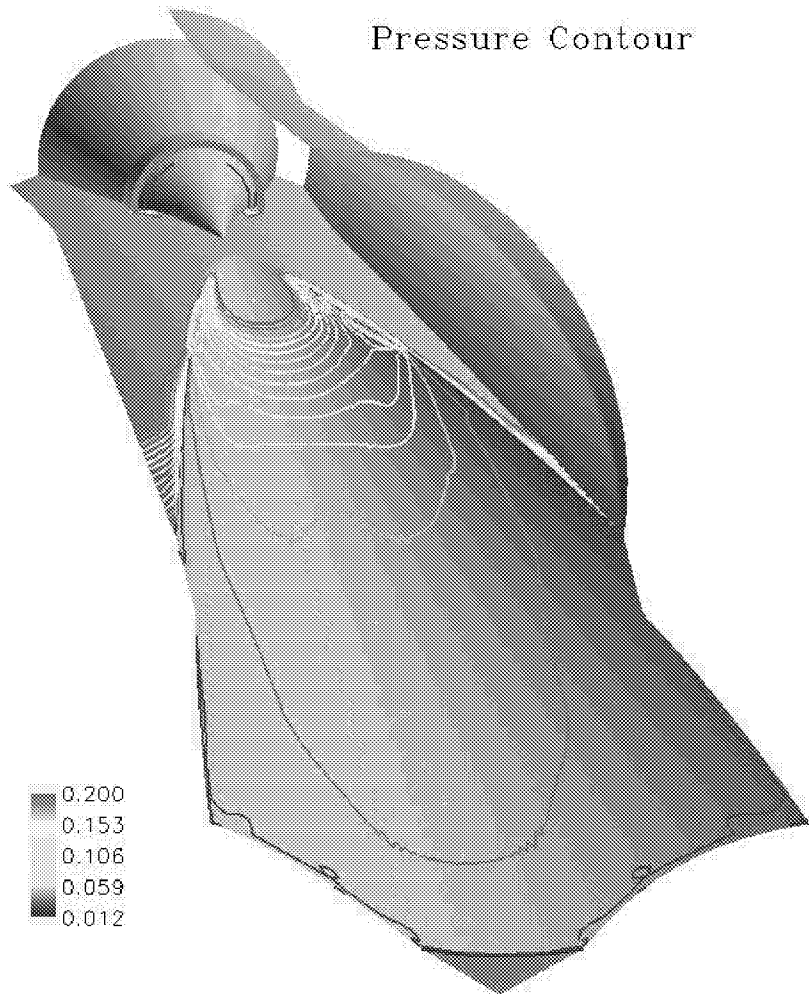


Figure 15. Pressure Contours on the Aft Ramp



OVERVIEW OF THE NCC

Nan-Suey LIU
(216)433-8722, nan-suey.liu@grc.nasa.gov
NASA Glenn Research Center

A multi-disciplinary design/analysis tool for combustion systems is critical for optimizing the low-emission, high-performance combustor design process. Based on discussions between the NASA Lewis Research Center and the jet engine companies, an industry-government team was formed in early 1995 to develop the National Combustion Code (NCC), which is an integrated system of computer codes for the design and analysis of combustion systems. NCC has advanced features that address the need to meet designer's requirements such as "assured accuracy", "fast turnaround", and "acceptable cost". The NCC development team is comprised of Allison Engine Company (Allison), CFD Research Corporation (CFDRC), GE Aircraft Engines (GEAE), NASA Glenn Research Center (LeRC), and Pratt & Whitney (P&W).

The "unstructured mesh" capability and "parallel computing" are fundamental features of NCC from its inception. The NCC system is composed of a set of "elements" which includes grid generator, main flow solver, turbulence module, turbulence and chemistry interaction module, chemistry module, spray module, radiation heat transfer module, data visualization module, and a post-processor for evaluating engine performance parameters. Each element may have contributions from several team members. Such a multi-source multi-element system needs to be integrated in a way that facilitates inter-module data communication, flexibility in module selection, and ease of integration.

The development of the NCC beta version was essentially completed in June 1998. Technical details of the NCC elements are given in the Reference List. Elements such as the baseline flow solver, turbulence module, and the chemistry module, have been extensively validated; and their parallel performance on large-scale parallel systems has been evaluated and optimized. However the scalar PDF module and the Spray module, as well as their coupling with the baseline flow solver, were developed in a small-scale distributed computing environment. As a result, the validation of the NCC beta version as a whole was quite limited. Current effort has been focused on the validation of the integrated code and the evaluation/optimization of its overall performance on large-scale parallel systems.

Acknowledgements

The NASA High Performance Computing and Communications Program (HPCCP) and the Smart Green Engine Program (SGE) have supported this effort.

REFERENCES

- [1] Stubbs, R.M., and Liu, N.-S., "Preview of National Combustion Code," AIAA Paper 97-3114, July 1997.
- [2] Harrand, V.J., Siegel, J.M., Singhal, A.K., and Whitmire, J.B., "Key Components and Technologies for the NCC Computing Framework," AIAA Paper 98-3857, July 1998.
- [3] Ryder, R.C., "The Baseline Solver for the National Combustion Code," AIAA Paper 98-3853, July 1998.
- [4] Brankovic, A., Ryder, R.C., and Syed, S.A., "Mixing and Combustion Modeling for Gas Turbine Combustors Using Unstructured CFD Technology," AIAA Paper 98-3854, July 1998.
- [5] Chen, K.-H., Norris, A.T., Quealy, A., and Liu, N.-S., "Benchmark Test Cases for the National Combustion Code," AIAA Paper 98-3855, July 1998.
- [6] Chen, K.-H., and Liu, N.-S., "Evaluation of A Non-Linear Turbulence Model Using Mixed Volume Unstructured Grids," AIAA Paper 98-0233, January 1998.
- [7] Shih, T.-H., and Liu, N.-S., "A k-epsilon Model for Wall-Bounded Shear Flows," AIAA Paper 98-2551, June 1998.
- [8] Shih, T.-H., Chen, K.-H., and Liu, N.-S., "A Non-Linear k-epsilon Model for Turbulent Shear Flows," AIAA Paper 98-3983, July 1998.
- [9] Nikjoo, M., and Mongia, H.C., "Study of Non-Linear k-epsilon Model for Turbulent Swirling Flows," AIAA Paper 98-3984, July 1998.
- [10] Raju, M.S., "Extension of the Coupled Monte-Carlo-PDF/SPRAY/CFD Computations to Unstructured Grids and Parallel Computing," AIAA Paper 97-0801, January 1997.
- [11] Anand, M.S., James, S., and Razdan, M.K., "A Scalar PDF Combustion Model for the National Combustion Code," AIAA Paper 98-3856, July 1998.
- [12] Kundu, K.P., Penko, P.F., and Yang, S.L., "Simplified Jet-A/Air Combustion Mechanisms for Calculation of NOX Emissions," AIAA Paper 98-3986, July 1998.
- [13] Norris, A.T., "Automated Simplification of Full Chemical Mechanisms: Implementation in National Combustion Code," AIAA paper 98-3987, July 1998.
- [14] Raju, M.S., "Combined Scalar-Monte-Carlo-PDF/CFD Computations of Spray Flames on Unstructured Grids with Parallel Computing," AIAA Paper 97-2969, July 1997.
- [15] Raju, M.S., "LSPRAY-A Lagrangian Spray Solver-User's Manual," NASA CR-97206240, November 1997.
- [16] Kumar, G.N., Mongia, H.C., and Moder, J.P., "Validation of Radiative Heat Transfer Computations Module for National Combustion Code," AIAA Paper 98-3985, July 1998.
- [17] Liu, N.-S., Quealy, A., Kundu, K.P., Brankovic, A., Ryder, R.C., and Van Dyke, K., "Multi-Disciplinary Combustor Design System and Emissions Modeling," NASA CDCP-20011, Proceedings of the 1996 Computational Aerosciences Workshop, May 1997, pp. 49-54.
- [18] Liu, N.-S., Quealy, A., "NCC-A Multi-Disciplinary Design/Analysis Tool for Combustion Systems," NASA Computational Aerosciences Workshop 98, August 1998.
- [19] Liu, N.-S., and Chen, K.-H., "FLUX: An Alternative Flow Solver for the National Combustion Code," AIAA Paper 99-1079, January 1999.
- [20] Guo, Y., He, G., Hsu, A. T., Brankovic, A., Syed, S., and Liu, N.-S., "The Development of a Variable Schmidt Number Model for Jet-in Crossflows Using Genetic Algorithms," AIAA Paper 99-0671, January, 1999.



AN UNSTRUCTURED CFD MODEL FOR BASE HEATING ANALYSIS

Y. S. Chen, H. M. Shang and Jiwen Liu
Engineering Sciences Inc., Huntsville, AL
Phone: (256) 883-6233, fax: (256) 883-6267, e-mail: ychen@esi-al.com

ABSTRACT

This paper summarizes the technical development and findings of a research project for launch vehicle base-heating analysis. An integrated design tool using unstructured grid method with solution-adaptation and parallel computing strategy is employed to predict the base heating and plume radiation. The CFD flow field with solution-adaptation and viscous/turbulence effects is employed for the heat transfer and fluid flow analyses. The present unstructured grid method imports geometry data from computer aided design (CAD) data base and simplifies the grid generation and grid adaptation procedures in the numerical simulation of flow field around complex geometries. Computational efficiency is highly enhanced through parallel computing using multiple CPUs or networked computers. Test cases of fluid flow and radiative heat transfer problems under limited conditions are investigated in this effort. Benchmark base flow test cases are also investigated. Comparisons of the base heating data show reasonably good agreements between the present model and the measured data. Discrepancies in data comparisons can be attributed to the effects of heat loss, fuel mixing and air aspiration that need to be further investigated by using a more complete numerical model. This study also shows the effects of the differences between the subscale model and the real nozzle design. Complex three-dimensional analysis, the solution-adaptation procedure and user friendly graphics interface will be fully integrated with CAD systems in future study. The basic study and development of the present unstructured grid CFD method will enhance the cost effectiveness in the design and evaluation of fluid flow and heat transfer processes of launch vehicles.

INTRODUCTION

With the advent of powerful computers and the development of efficient numerical modeling technology, it is highly feasible to use the advanced computational fluid dynamics (CFD) models as an effective engineering design and analysis tool before the first test program is conducted. One of the critical design issues that must be addressed is the evaluation of the flow conditions in the based region of the launch vehicle during the ascent phase of its trajectory. The engine compartment and aft control surfaces will experience radiative heating due to the hot exhaust plume. At certain flight conditions, the nozzle exhaust gas from the engine may impinge on the aft aerodynamic control surfaces and recirculate within the engine compartment causing a rise in the convective heating. The analysis of radiative base heating from rocket exhaust plumes has attracted considerable attention during the past few decades, since the base has to be protected against radiative heating from rocket exhaust plumes. Theoretically, the properties of gases and particles within exhaust plumes influence the thermal radiation process through absorbing, emitting and scattering characteristics. Therefore, models as well as methods for predicting rocket plume base heating are in high demand.

The Radiative Transfer Equation (RTE) is an integro-differential equation whose exact analytical solution is only possible for very simple and specific settings. The situation worsens even further when this equation is coupled with the energy equation in order to solve for other forms of energy transfer. The resulting expression, under these circumstances has the added difficulty of non linearity. This intrinsic difficulty in the solution of the RTE has resulted in the development of several approximated models such as the zone method, Monte Carlo method, flux method, discrete ordinates method (DOM), finite volume method (FVM) etc. These models have been reviewed, with different degrees of detail, by several authors [1-3]. Currently, two of the most widely used methods in radiative transfer simulation are the DOM and FVM. In the DOM and FVM, the RTE is directly solved numerically along discrete directions or control angles that approximate the angular intensity distribution. As a result, these two

methods are relatively easy to code; they provide accurate results by using higher-order approximations; they can account for spectral absorption by gases and scattering by particles and they are compatible with numerical algorithms for solving transport equations [1,4]. However, the FVM has two salient features that the DOM does not have. One is the freedom of selection of control angle and another is the guarantee of conservation of radiant energy. Liu et al. [5] compared the solutions from these two methods and found that the results from the FVM were more accurate. The GRASP code [6], developed at Engineering Sciences, Inc. (ESI) is a very accurate and efficient code compared to other existing codes, it may still take a large amount of CPU time to simulate most of the practical problems on serial processors due to the characteristics of the RTE. While numerical accuracy, computational efficiency and problem solving robustness through parallel processing have been the key emphases in the today's development of general purpose CFD codes, there has been lack of active exploration of high performance computing for solving RTE. It is this urgent need that motivates us to propose this project. Success of this project will enable us to solve many complex radiative heat transfer problems that are still very challenging today.

The traditional structured grid CFD codes and RTE solvers with multi-zone body-fitted coordinates take the advantage of automatic indexing and are efficient for many applications. However, for very complicated domains, the man-power spent in the grid generation is often the largest portion of the entire effort spent in problem analyses. The CFD applications for complex geometries have achieved significant successes by using unstructured grid (finite element mesh) methods [7-9]. The unstructured grid method has the advantages of automated grid generation in very complex domains and flexible mesh adaptation in high gradient region over structured grid method.

An integrated design tool using unstructured grid method with solution-adaptation and parallel computing strategy is employed in this research project to predict the base heating and plume radiation. CFD solution methods with solution-adaptation and viscous/turbulence effects are used for the heat transfer and fluid flow analyses. The present unstructured grid method imports geometry data from computer aided design (CAD) data base, and simplifies the grid generation and grid adaptation procedures for the numerical simulation of flow field around complex geometries. Computational efficiency is highly enhanced through parallel computing using multiple CPUs or network computers. Test cases of fluid flow and radiative heat transfer problems under specific conditions are investigated in the present study. Complex three-dimensional analysis, the solution-adaptation procedure and user friendly graphics interface will be fully integrated with CAD systems in the follow-on study. The basic study and development of the present unstructured grid CFD method will be used by the designers to enhance the cost effectiveness in the designs and evaluation of fluid flow and heat transfer environment of launch vehicles.

NUMERICAL APPROACH AND IMPLEMENTATION

The procedure of predicting the base-heating environment involves the generation of computational mesh and the solutions of the plume flow and radiative heat transfer equations. The integrated process is illustrated in Figure 1. The governing equations, numerical methodologies, grid generation, solution-adaptation and parallel strategy are described in the following sections.

MATHEMATICAL FORMULATIONS FOR RADIATIVE TRANSFER EQUATION (RTE)

Consider the RTE in a Cartesian coordinate system as shown in Fig. 2a. The balance of energy passing in a specified direction $\mathbf{\Omega}$ through a small differential volume in an absorbing-emitting and scattering medium can be written as [10,11]:

$$(\mathbf{\Omega} \cdot \nabla)I_{\lambda}(\mathbf{r}, \mathbf{\Omega}) = -(\kappa_{\lambda} + \sigma_{\lambda})I_{\lambda}(\mathbf{r}, \mathbf{\Omega}) + \kappa_{\lambda}I_{b,\lambda}(\mathbf{r}) + \frac{\sigma_{\lambda}}{4\pi} \int_{\Omega'=4\pi} I_{\lambda}(\mathbf{r}, \mathbf{\Omega}')\Phi_{\lambda}(\mathbf{\Omega}' \rightarrow \mathbf{\Omega})d\Omega' \quad (1)$$

where the subscript λ represents the wave-number; $I_{\lambda}(\mathbf{r}, \mathbf{\Omega})$ is the spectral radiative intensity, which is a function of position and direction; $I_{b,\lambda}(\mathbf{r})$ is the blackbody radiative intensity at the temperature of the medium; κ_{λ} and σ_{λ} are the spectral absorption and scattering coefficients, respectively; and $\Phi_{\lambda}(\mathbf{\Omega}' \rightarrow \mathbf{\Omega})$ is the scattering phase function from the incoming $\mathbf{\Omega}'$ direction to the outgoing direction $\mathbf{\Omega}$. The term on the left hand side represents the gradient of the intensity in the direction $\mathbf{\Omega}$. The three terms on the right hand side represent the changes in intensity due to absorption and out-scattering, emission and in-scattering, respectively.

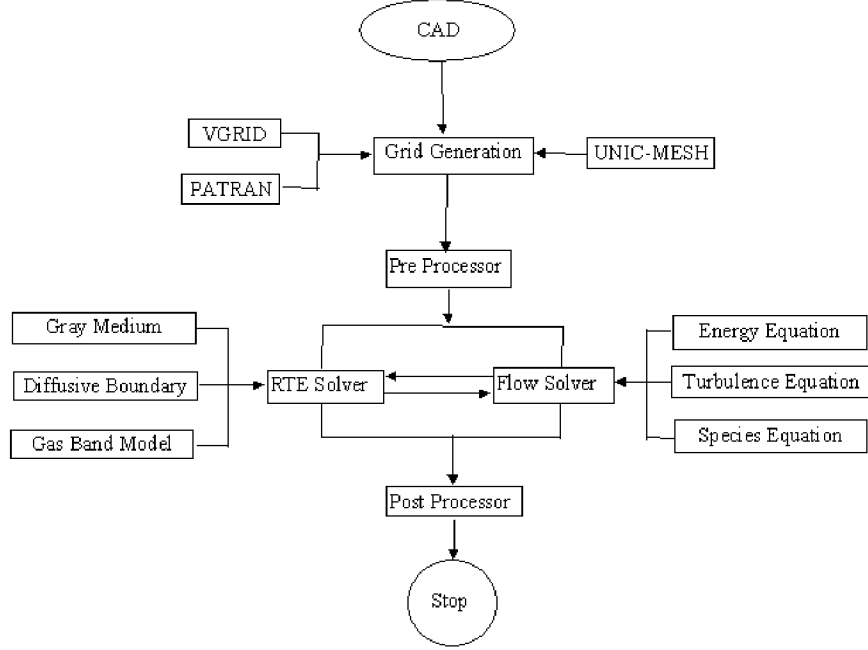


Figure 1. Processes involved in the base-heating analysis.

If the wall bounding the medium emits and reflects diffusely, then the radiative boundary condition for Eq. (1) is given by

$$I_{\lambda}(\mathbf{r}_w, \Omega^+) = \varepsilon_{\lambda} I_{b,\lambda}(\mathbf{r}_w) + \frac{(1 - \varepsilon_{\lambda})}{\pi} \int_{\mathbf{n} \cdot \Omega^- < 0} I_{\lambda}(\mathbf{r}_w, \Omega^-) |\mathbf{n} \cdot \Omega^-| d\Omega^- \quad (2)$$

where Ω^+ and Ω^- denote the leaving and arriving radiative intensity directions, respectively; ε_{λ} is the spectral wall emissivity; \mathbf{n} represents the unit normal vector on the wall.

Equation (1) is a complex integro-differential equation whose exact analytical solution is only possible for very simple and specific settings. This intrinsic difficulty has resulted in the development of several approximated models. In this project, the finite volume method (FVM) will be used to solve the RTE and their numerical analysis procedures are briefly described here. In the following analysis, subscripts λ are dropped for the sake of brevity and they will be added whenever necessary.

In the FVM, the spatial and angular domains are divided into a finite number of control volumes and control angles, respectively. Then Eqs. (1) and (2) are integrated over each control volume and control angle. Since the FVM shares the same computational grid as the CFD approach, the considered spatial domain will be divided into MA control volumes and surfaces by a grid generator. For numerical analysis of the FVM, a representative control volume resulted from the spatial domain division is shown in Fig. 2b. By referring to the division practice for the spatial domain, the angular domain (see Fig. 2c) at a node centered in a control volume is divided into $N_{\theta} \times N_{\phi} = \text{MB}$ control angles with N_{θ} and N_{ϕ} representing numbers of control angle in polar angle θ and azimuthal angle ϕ directions, respectively. These MB discrete solid angles are nonoverlapping and their sum is 4π . Unlike the selection of a quadrature scheme in the discrete ordinates method (DOM), there is no specific restriction in selecting control angles in the FVM. However, the control angles are usually chosen in a manner that best captures the physics of a given problem. This is analogous to the selection of control volumes.

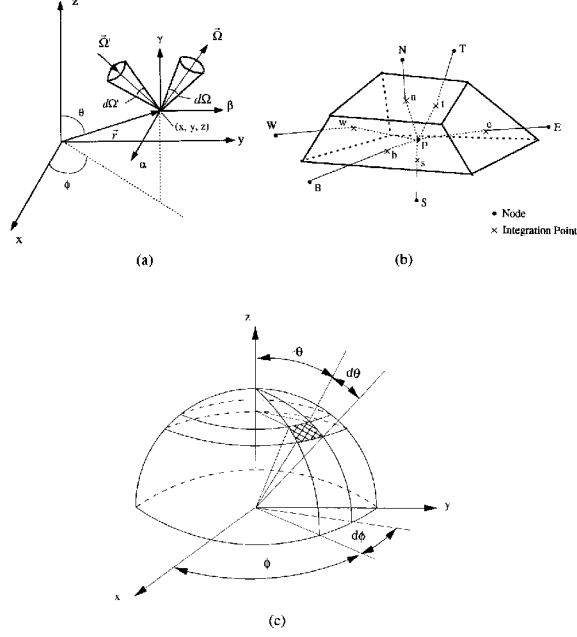


Figure 2. (a) Coordinate system for radiative transfer equation, (b) a representative control volume, and (c) a representative control angle.

GOVERNING EQUATIONS FOR FLUID DYNAMICS

The continuity equation and the Navier-Stokes equation, under the isotropic turbulent viscosity hypothesis, can be written in a Cartesian tensor form:

$$\frac{\partial \rho}{\partial t} + \frac{\partial}{\partial x_j} (\rho u_j) = 0 \quad (3)$$

$$\frac{\partial \rho u_i}{\partial t} + \frac{\partial}{\partial x_j} (\rho u_j u_i) = -\frac{\partial p}{\partial x_i} + \frac{\partial \tau_{ij}}{\partial x_j} \quad (4)$$

where ρ is the fluid density, u_i is the i^{th} Cartesian component of the velocity, and p is the static pressure. The shear stress τ_{ij} can be expressed as:

$$\tau_{ij} = \left(\mu + \mu_t \right) \left(\frac{\partial u_i}{\partial x_j} + \frac{\partial u_j}{\partial x_i} - \frac{2}{3} \frac{\partial u_k}{\partial x_k} \delta_{ij} \right) - \frac{2}{3} \rho k \delta_{ij} \quad (5)$$

where μ is the fluid viscosity and μ_t is the turbulent viscosity defined as:

$$\mu_t = C_\mu \rho \frac{k^2}{\varepsilon} \quad (6)$$

The energy equation for total enthalpy, h_t , is written as:

$$\frac{\partial \rho h_t}{\partial t} + \frac{\partial}{\partial x_j} (\rho u_j h_t) = \frac{\partial}{\partial x_j} \left[\left(\lambda + \frac{\mu_t}{Pr_t} \right) \frac{\partial T}{\partial x_j} \right] + \frac{\partial p}{\partial t} + \Phi \quad (7)$$

where λ is the thermal conductivity, Pr_t is the turbulent Prandtl number, T is the fluid temperature, Φ is the energy dissipation function.

The species conservation equation is expressed as:

$$\frac{\partial \rho Y_i}{\partial t} + \frac{\partial}{\partial x_j} (\rho u_j Y_i) = \frac{\partial}{\partial x_j} \left[\left(\rho D + \frac{\mu_t}{\sigma_Y} \right) \frac{\partial Y_i}{\partial x_j} \right] + \dot{\omega}_i \quad (8)$$

where Y_i is the i^{th} species mass fraction, D is the mass diffusivity, σ_T is the turbulent Schmidt number, and $\dot{\omega}_i$ is the chemical reaction rate for species i respectively.

The standard two-equation k- ϵ model with wall function is employed, and the transport equations are

$$\frac{\partial \rho k}{\partial t} + \frac{\partial}{\partial x_j} (\rho u_j k) = \frac{\partial}{\partial x_j} \left[\left(\mu + \frac{\mu_t}{\sigma_k} \right) \frac{\partial k}{\partial x_j} \right] + \rho(P - \epsilon) \quad (9)$$

$$\frac{\partial \rho \epsilon}{\partial t} + \frac{\partial}{\partial x_j} (\rho u_j \epsilon) = \frac{\partial}{\partial x_j} \left[\left(\mu + \frac{\mu_t}{\sigma_\epsilon} \right) \frac{\partial \epsilon}{\partial x_j} \right] + \rho \frac{\epsilon}{k} (C_1 P - C_2 \epsilon) \quad (10)$$

where P is the rate of production of turbulence kinetic energy and the model constants are $C_{\mu}=0.09$, $C_1=1.44$, $C_2=1.92$, $\sigma_k=1.0$ and $\sigma_\epsilon=1.3$.

The cell-centered scheme is employed here because the control volume surface can be represented by the cell surface and coding structure can be much simplified. The transport equations can also be written in integral form as

$$\frac{\partial}{\partial t} \int_{\Omega} \rho \phi \, d\Omega + \oint_{\Gamma} \vec{F} \cdot \vec{n} \, d\Gamma = \int_{\Omega} S_{\phi} \, d\Omega \quad (11)$$

where Ω is the domain of interest and Γ is the surrounding surface; \vec{n} is the unit normal of Γ in outward direction. A two-dimensional control volume is shown in Figure 3.

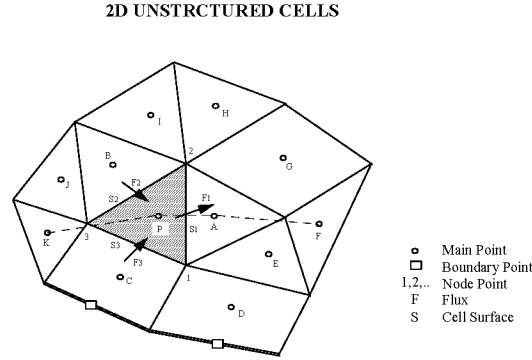


Figure 3. Cell centered control volume for two-dimensional unstructured grids.

The flux function \vec{F} contains the inviscid and the viscous flux vector,

$$\vec{F} = \rho \vec{V} \phi - \mu \nabla \phi \quad (12)$$

The finite volume formulation of flux integral can be evaluated by the summation of the flux vectors over each face,

$$\oint_{\Gamma} \vec{F} \cdot \vec{n} \, d\Gamma = \sum_{j=k(i)} F_{i,j} \Delta \Gamma_j \quad (13)$$

where $k(i)$ is a list of faces of cell i , $F_{i,j}$ represents convection and diffusion fluxes through the interface between cell i and j , and $\Delta \Gamma_j$ is the cell-face area.

A general implicit discretized time-marching scheme for the transport equations can be written as below,

$$\left(\frac{\rho^n}{\Delta t} + A_p \right) \phi_p^{n+1} = \sum_{m=1}^{NB} A_m \phi_m^{n+1} + \frac{(\rho \phi_p)^n}{\Delta t} + S_{\phi} \quad (14)$$

where NB means the neighbor cells of cell P . The high order differencing term and cross diffusion term are treated using known quantities and retained in the source term and updated explicitly.

In an extended SIMPLE [12-14] family pressure-correction algorithm, the pressure correction equation is formulated using the perturbed equation of state, momentum and continuity equations. The simplified formulations can be written as:

$$\rho' = \frac{p'}{RT} \quad u_i' = -D_u \nabla p' \quad u^{k+1} = u^k + u' \quad p^{k+1} = p^k + p' \quad (15)$$

$$\frac{\partial \rho}{\partial t} + \nabla(u_i \rho') + \nabla(\rho u_i') = -\nabla(\rho u_i)^k \quad (16)$$

where D_u is the pressure-velocity coupling coefficient. Substituting Eq.(15) into Eq.(16), and considering $\Delta \rho = \rho^{k+1} - \rho^n = (\rho^{k+1} - \rho^k) + (\rho^k - \rho^n) = \rho' + (\rho^k - \rho^n)$, the following all-speed pressure correction equation is obtained,

$$\frac{1}{RT} \frac{p'}{\Delta t} + \nabla \left(\frac{u_i}{RT} p' \right) - \nabla(\rho D_u \nabla p') = - \left(\frac{\rho^k - \rho^n}{\Delta t} \right) - \nabla(\rho u_i)^k \quad (17)$$

where the superscripts n and k represent the last time step and iterative values respectively. The entire pressure correction step is repeated 2 or 3 times such that the mass conservation condition is enforced.

The momentum equations are solved implicitly at the predictor step. Once the solution of pressure correction Eq.(17) is obtained, the velocity, pressure and density fields are updated using Eq.(15). The scalar equations such as mass fraction, turbulence and energy equations, will be solved sequentially. Then the solution procedure will march to the next time level for transient calculation or global iteration for steady calculation.

LINEAR MATRIX SOLVER

The discretized finite-volume equations can be represented by a set of linear algebra equations, which are non-symmetric matrix system with arbitrary sparsity patterns. Due to the diagonal dominates for the matrixes of the transport equations, they can converge even through the classical iterative methods. However, the coefficient matrix for the pressure-correction equation may be ill conditioned and the classical iterative methods may break down or converge slowly. Since satisfaction of the continuity equation is of crucial importance to guarantee the overall convergence, most of the computing time in fluid flow calculation is spent on solving the pressure-correction equation by which the continuity-satisfying flow field is invoked.

The preconditioned Bi-CGSTAB matrix solver is used to efficiently solve the linear algebra equations [15] resulting from transport equations. An algebraic multigrid method [16] will be used to solve the algebra equation resulting from the pressure correction equation. The algorithm of AMG method is fully introduced in [16].

There are two types of fixed cycle multi-grid sequences, V cycle and W cycle. W cycle is more efficient because each grid level has the chance to pass its residual down to the coarse grid level twice and receive the corrections twice. The paths of V cycle and W cycle are shown in Figure 4, where the restriction process goes down at "d", reach the bottom at "b" and then the prolongation process goes up at "u". In this research, W cycle is used and the coarse grid level is set to no more than six. The bottom level is reached when the mesh cell number is less than 100 or the level is number 6 whichever comes first. The Incomplete Lower Upper (ILU) factorization scheme is used to solve the linear equations. It takes two sweeps in down processes and 3 sweeps in the up processes. At the bottom, GMRES method is used to ensure the accurate solution at the coarsest grid level. Several cycles may be needed to reduce the residual by two orders of magnitude in each time step. For all the calculation in this study, the cycle number is less than 10 and mostly around 5.

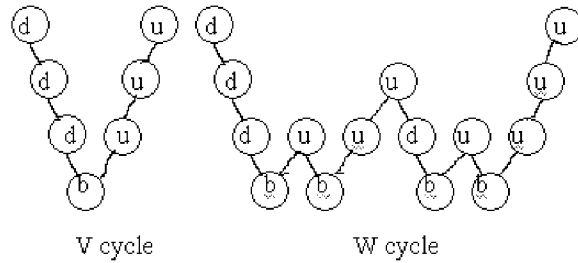


Figure 4. V and W cycle diagram.

GRID GENERATION

The unstructured grid type varies from triangular to quadrilateral for 2D problems and tetrahedral, prism, pyramid, to hexahedral for 3D problems. Grid considered can include either single type or mixed types of grid. The unstructured grids can be generated using PATRAN or VGRID [17]. The former one is a commercial package with CAD capability and the latter one is developed at NANA/LaRC and available in public domain. These grid generation packages are user friendly and can generate high quality unstructured grids. The present unstructured grid method also reads structured grids. Hence, any structured grid generators, such as GRIDGEN, and UNIC-MESH, can also be used to build the base-heating model.

DOMAIN DECOMPOSITION

To implement a parallel computation strategy, the computational domain needs to be partitioned into many sub-domains. Each sub-domain then occupies one processor of a parallel computer. Many partitioning algorithms have been developed to partition an unstructured grid. These algorithms include Recursive Coordinate Bisection (RCB), Recursive Spectral Bisection (RSB), and Recursive Graph Bisection (RGB) methods. A public available package developed at University of Minnesota, METIS [18], can partition high quality unstructured meshes efficiently. Grids with 1 million vertices can be partitioned in 256 parts in under 20 second on a Pentium Pro personal computer.

PARALLEL IMPLEMENTATION

In a parallel computation, the governing equations are solved in all sub-domains, which are assigned to different computer processors [19]. Exchange of data between processors is necessary to enforce the boundary conditions at the divided interfaces. The communication overhead must be kept well below the computational time. Currently, many communication software packages, such as PVM and MPI, have been developed for distributed computing.

The Parallel Virtual Machine (PVM) software system [20] is developed at the University of Tennessee and Oak Ridge National Laboratory (ORNL). It is a standard message passing interface and enables distributed computing across a wide variety of computer types, including massively parallel processors (MPPs). It is built around the concept of a virtual machine which is a dynamic collection of (homogenous or heterogeneous) computational resource managed as a large single parallel computer. PVM is implemented for data communication among processors in this project.

MPI stands for Message Passing Interface[21]. The goal of MPI, simply stated, is to develop a widely used standard for writing message-passing programs. As such interface attempts to establish a practical, portable, efficient, and flexible standard for message passing. The main advantages of establishing a message-passing standard are portability and ease-of-use. In a distributed memory communication environment in which the higher level routines and/or abstractions are build upon lower level message passing routines the benefits of standardization are particularly apparent. Furthermore, the definition of a message passing standard provides vendors with a clearly defined base set of routines that they can implemented efficiently, or in some cases provide hardware support for, thereby enhancing scalability.

VALIDATIONS

VALIDATIONS FOR THE UNSTRUCTURED RADIATION MODEL

Based on the theoretical and numerical analyses described earlier, a computer code has been developed which is capable of modeling multi-dimensional radiative heat transfer using structured, unstructured, or hybrid grids. To investigate the accuracy of the present unstructured method, six selected benchmark problems were investigated which included 2D planar, axisymmetric, and 3D geometries. To test the sensitivity of the unstructured method on the grid, a structured grid and an unstructured grid were used for each problem, and their corresponding solutions were compared against the available other solutions and they were labeled as the unstructured solution and structured solution in the following figures. For a 2D problem, the volume cell type is quadrilateral for a structured grid and triangular for an unstructured grid. For a 3D problem, the volume cell type is hexahedral for a structured grid and prism for an unstructured grid. In each problem, the angular domains for the structured and unstructured grids were divided by the same strategy which was either the Sn-type discretization or azimuthal discretization. All computation was conducted on the IBM RISC/6000 machine and the numerical solution was considered to be convergent when the relative incident radiation change was less than 0.01%. The iteration numbers for different grids were the same for each problem, and they were equal to two for the cases with black walls and not more than ten for other cases with scattering medium or gray walls.

2D PLANAR GEOMETRY NO. 1

The first problem examined is a quarter of a circle with a rectangular region added to the top as shown in Fig. 5a. The curve wall is hot and black and it has an emissive power of unity, while the rest walls are cold and black. The medium is cold and it is transparent for the first case and purely absorbing with $\kappa=1.0 \text{ m}^{-1}$ for the second case. The Monte Carlo method [22] has been used to investigate this problem before and its solution was used to test against the present solutions.

Figure 5b and 5c show the structured and unstructured grids used in the calculation, respectively. The azimuthal discretization strategy was employed for the both grids in which the angular domain was discretized into $N_\theta \times N_\phi = 4 \times 20$ control angles with uniform $\Delta\theta$ and $\Delta\phi$. The results for the radiative heat flux on the right wall from different solutions are presented in Fig. 6. At each case, the structured, unstructured, and Monte Carlo solutions are seen to have a very good agreement, and their maximum difference is within 2%. At the location close to the curve hot wall, the predicted values of radiative wall flux for all solutions are high and they are gradually decreased as the distance from the hot wall is increased.

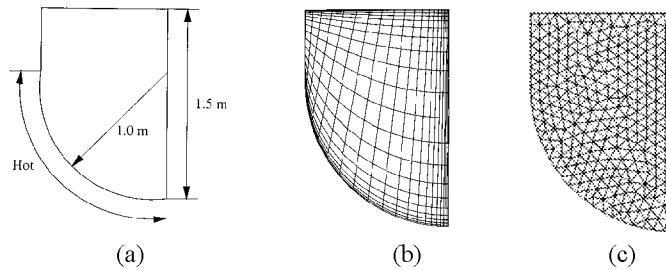


Figure 5. 2D planar geometry No. 1: (a) schematic; (b) structured grid; (c) unstructured grid.

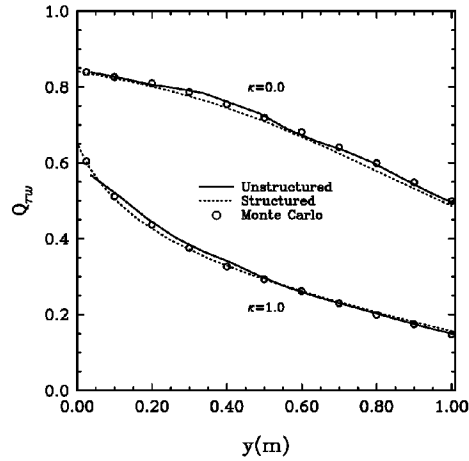


Figure 6. Comparison of radiative wall heat flux distributions on the right wall.

2D PLANAR GEOMETRY NO. 2

The schematic of the second problem is showed in Fig. 7a. The top wall is located at $y=1.0$ m. The bottom wall varies according to the following function

$$y = \frac{1}{2} [\tanh(2 - 3x) - \tanh(2)] 0 \leq x \leq \frac{10}{3}$$

The bottom black wall is maintained at 1000 K while the other black walls are kept at 0 K. The medium is cold (0 K) and it is purely isotropically scattering with $\sigma=1.0 \text{ m}^{-1}$ for the first case and purely absorbing with $\kappa=1.0 \text{ m}^{-1}$ for the second case. Chai et al [23] considered this problem with the FVM and their solution was used to validate the present solutions.

Figure 7a also shows the structured grid used in the calculation while the unstructured grid is presented in Fig. 7b. The angular domain was discretized using the S_8 quadrature scheme. The results of interest are the radiative wall fluxes on the top wall and they are demonstrated in Fig. 8. Both the unstructured and structured solutions are found to be in good agreement with Chai et al's solution. Maximum difference occurs in the left end region of the wall where the structured results are slightly higher for the case with $\kappa=1.0 \text{ m}^{-1}$.

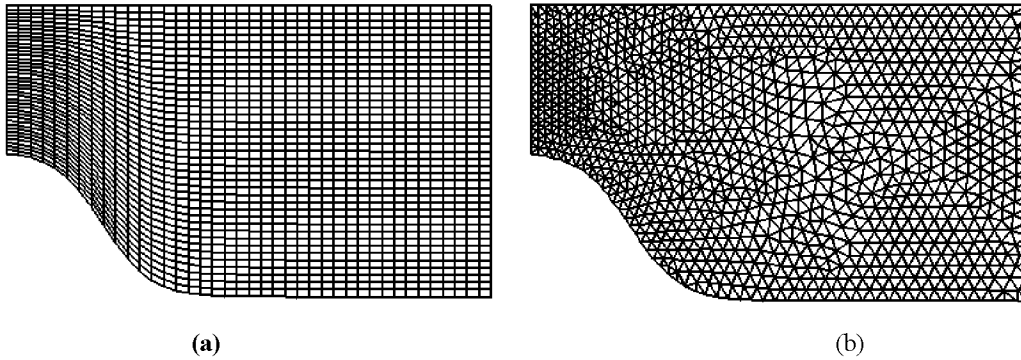


Figure 7. 2D planar geometry No. 2: (a) structured grid; (b) unstructured grid.

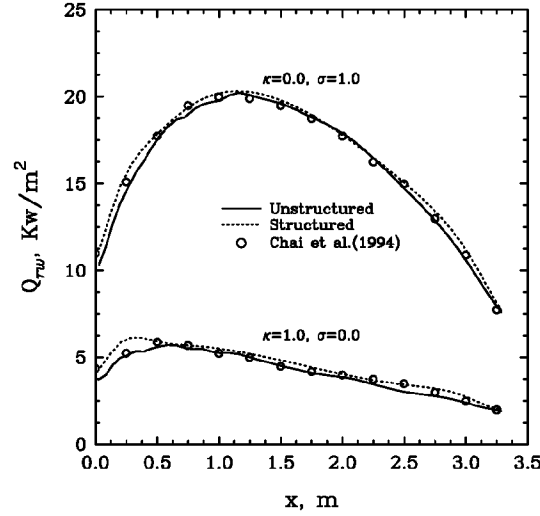


Figure 8. Comparison of radiative wall heat flux distributions on the top wall.

2D AXISYMMETRIC CYLINDRICAL GEOMETRY

The third problem examined is a 2D axisymmetric cylindrical enclosure and its schematic is plotted in Fig. 9a. The radius of cylinder is 1 m and the height is 2m. The enclosure is filled with an absorbing-emitting medium which is maintained at an emissive power of unity. The selected medium absorption coefficient κ varies from 0.1, 1.0 to 5.0 m^{-1} . All enclosure walls are cold and black. This benchmark problem is studied frequently because an exact solution [24] for radiative flux on the lateral wall is available.

Radiative transfer in a 2D axisymmetric geometry is a 3D process but it can be treated in 2D coordinates. Figure 9b and 9c show the 2D computational domains with a structured grid and an unstructured grid, respectively. It is noted that the bottom line of the domain corresponds to the axisymmetric line of the cylinder and the symmetric boundary condition was imposed along this line in the computation. The angular domain discretization was carried out using the S_8 quadrature scheme. Currently, the artifice developed by Carlson and Lathrop (Eq. (6)) has been only used in the Cartesian grid as seen in Fig. 9b, and the curvature coefficients for angular redistribution $\alpha_{m\pm 1/2}$ are the same for all volume cells. However, with the use of the general formulation of $\alpha_{m\pm 1/2}$ (Eq. (8)) for irregular shape of volume cell as seen in Fig. 9c, the values of $\alpha_{m\pm 1/2}$ will be different at different volume cells. This will slightly increase the computational memory of the problem. Figure 10 shows the radiative wall flux distributions along the lateral wall. Both the structured and unstructured solutions are seen to match the exact solution very well for various optical thicknesses.

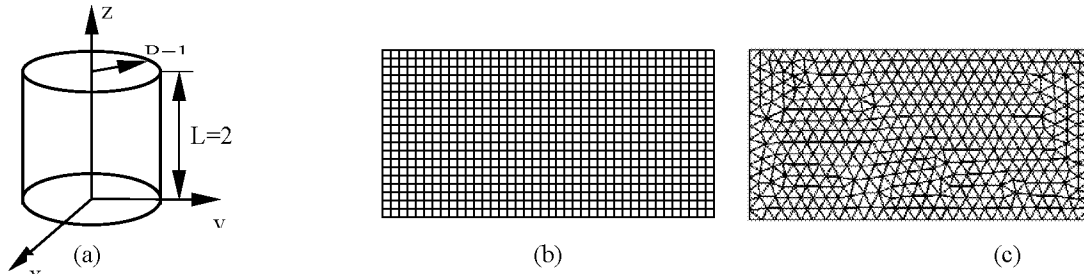


Figure 9. 2D axisymmetric cylindrical enclosure: (a) schematic; (b) structured grid; (c) unstructured grid.

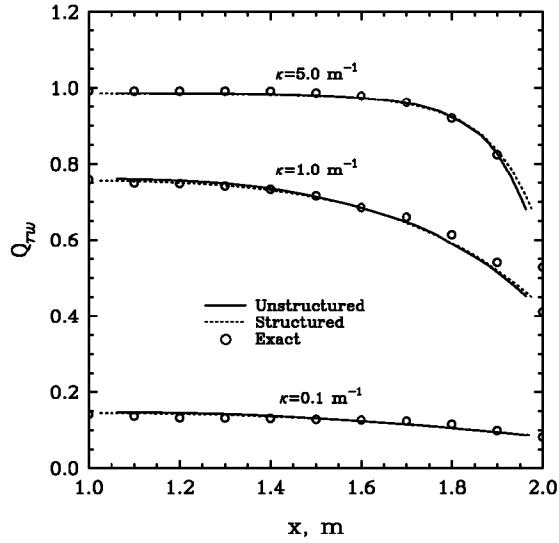


Figure 10. Comparison of radiative wall heat flux distributions on the side wall of a cylindrical enclosure.

2D AXISYMMETRIC TRIANGULAR TOROID

The fourth problem examined is a 2D axisymmetric triangular toroid and Fig. 11a shows the schematic of a cross section of the problem. The length of each equilateral wall is 1 m. The medium in the toroid is maintained at an emissive power of unity and it is assumed to be absorbing-emitting with $\kappa=1.0 \text{ m}^{-1}$. All walls are cold and black. This problem was investigated before and the exact solution [25] for radiative wall flux along the lateral wall is available for the present comparison.

Figure 11b and 11c show the structured and unstructured grids used in the calculation, respectively. Unlike the previous problem which used the Sn-type scheme, the azimuthal discretization strategy with $N_\theta \times N_\phi = 4 \times 20$ was employed to discretize the angular domain in this problem. The artifice developed by Carlson and Lathrop (Eq. (6)) has been mainly applied by the DOM to treat 2D axisymmetric problems. In fact, this artifice can also be used by the FVM which employs azimuthal discretization strategy to discretize the angular domain. One of objective of this problem is to validate the application of Eq. (6) with the azimuthal discretization strategy. Figure 12 presents the radiative wall flux distributions along the lateral wall. It is obvious that the structured and unstructured solutions demonstrate very good agreement with the exact solution. This agreement is consistent with the expectation. The application of the FVM with the artifice shown in Eq. (6) represents a significant simplification over the conventional treatment for FVM where a 2D axisymmetric problem has to be modeled in a way similar to a 3D problem.

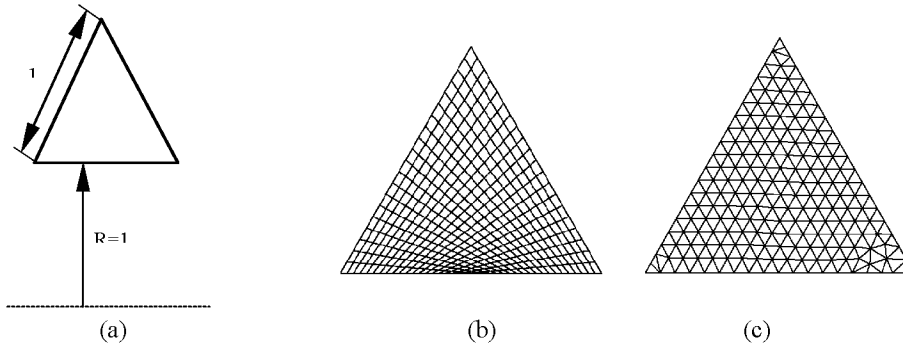


Figure 11. 2D axisymmetric triangular toroid: (a) schematic; (b) structured grid; (c) unstructured grid.

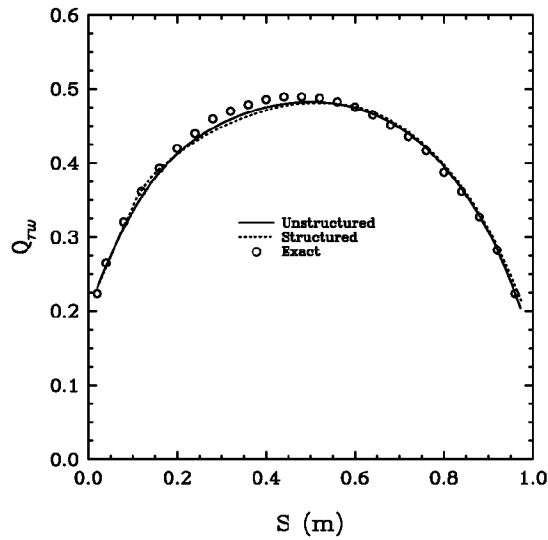


Figure 12. Comparison of radiative wall heat flux distributions on the lateral wall.

3D IDEALIZED FURNACE

The fifth problem examined represents a 3D idealized furnace proposed by Menguc and Viskanta [26] as shown in Fig. 13a. The dimensional size of the geometry is $2 \times 2 \times 4$ m. The furnace is filled with a gray gas with $\kappa = 0.5 \text{ m}^{-1}$ and $\sigma = 0$. The uniform internal heat sources are $q = 5.0 \text{ kW/m}^3$. The six walls are gray walls and their emissivities and temperatures are: $\varepsilon_2 = 0.85$, $T_2 = 1200 \text{ K}$ for wall 2; $\varepsilon_5 = 0.70$, $T_5 = 400 \text{ K}$ for wall 5; $\varepsilon_1 = \varepsilon_3 = \varepsilon_4 = \varepsilon_6 = 0.7$, $T_1 = T_3 = T_4 = T_6 = 900 \text{ K}$ for walls 1, 3, 4 and 6. Due to the internal heat source, this problem requires an iterative solution procedure with the energy equation. Several authors have used the discrete ordinates [27], spherical and zone [28] methods to solve this problem. Different models have predicted similar results. Only zone solution was selected to test against the present results.

Figures 13b and 13c show the structured and unstructured grids used in the calculation. The angular domain was divided using the S_8 quadrature scheme. For the clarity of comparison, the results for temperature and radiative wall flux distributions are only presented along several lines as seen in Figs. 14 and 15. In Fig. 14, the temperature distributions are shown along a line (x-axis direction) with $y = 1.0 \text{ m}$ for three different z locations. At the z locations of 0.4 m and 2.0 m, the predictions from the structured and unstructured solutions are found to be in very good agreement with the zone solution. At the z location of 3.6 m, the unstructured results are slightly higher while the structured results are little lower in comparison with the zone results. However, their maximum difference is not more than 1.5%. Figure 15 demonstrates the net radiative wall heat flux distributions along a line (x-axis direction) with $y = 1.0 \text{ m}$ on the hot wall (wall 2) and cold wall (wall 5). Again, the structured and unstructured solutions are seen very close to the zone solution on each wall.

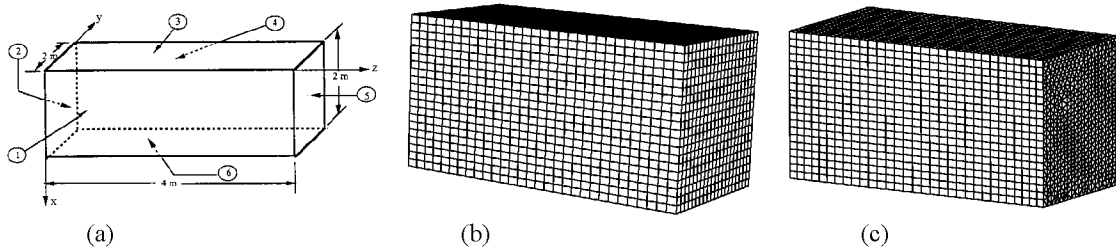


Figure 13. 3D idealized furnace: (a) schematic; (b) structured grid; (c) unstructured grid.

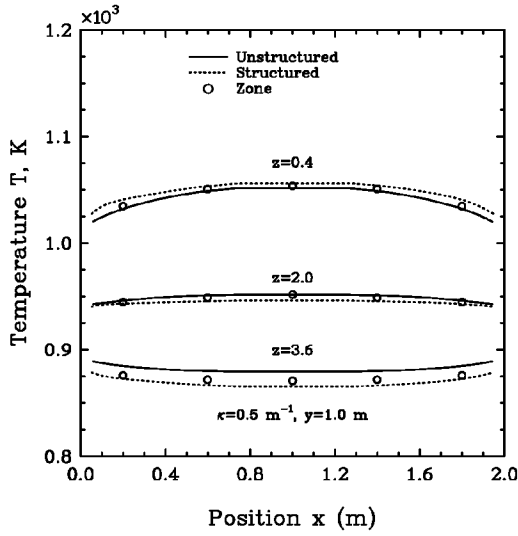


Figure 14. Comparisons of temperature distributions at three z locations.

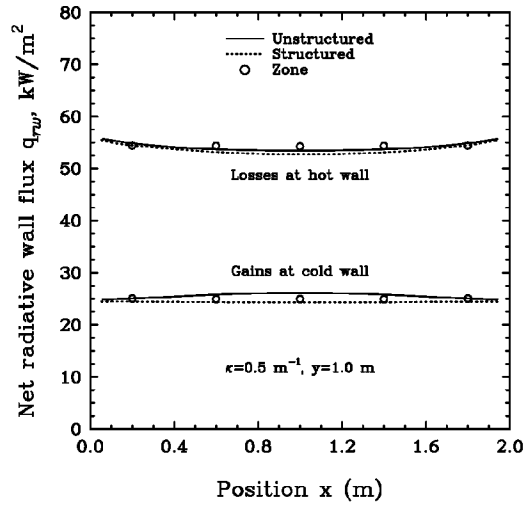


Figure 15. Comparisons of radiative wall heat flux distributions at the hot and cold walls.

3D EQUILATERAL TRIANGULAR ENCLOSURE

The last problem examined is a 3D equilateral triangular enclosure as shown in Fig. 16a. In this problem, all walls are black and cold. The medium is purely absorbing-emitting and maintained at an emissive power of unity. The selected medium absorption coefficient κ varies from 0.1, 1.0 to 10.0 m^{-1} . Chai et al [28] investigated this problem and they obtained the exact solution by integrating the RTE over the spatial and angular domains.

Figure 16b and 16c show the structured and unstructured grids used in the calculation, respectively. The angular domain was discretized by the azimuthal discretization strategy with $N_\theta \times N_\phi = 4 \times 20$. The results of interest are the radiative wall flux distribution along the A-A line (see Fig. 16a) and predictions from different solutions are presented in Fig. 17 for comparison. Due to symmetry, heat fluxes are only plotted for half of the enclosure. Compared to the exact solution, both the structured and unstructured solutions are seen to be very accurate at each case.

In the above six problems considered, an unstructured method was applied to solve the RTE for structured grids as well as unstructured grids. In contrast, a structured method can be only applied for structured grids. In order to investigate the effect of the unstructured method and structured method on the results for the structured grids, the structured method based on Ref. [29] was also used to model the above six problems. The results from the structured and unstructured methods were found to be identical for each problem for the same condition. For the sake of clarity, the results from structured method were not plotted in the previous figures. This identity gives us more confidence on the unstructured method developed in this study.

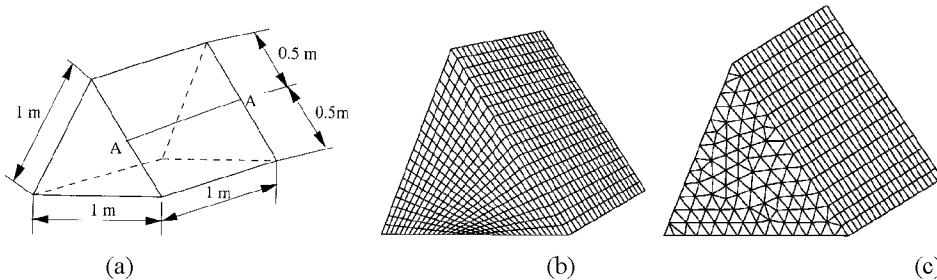


Figure 16. 3D equilateral triangular enclosure: (a) schematic; (b) structured grid; (c) unstructured grid.

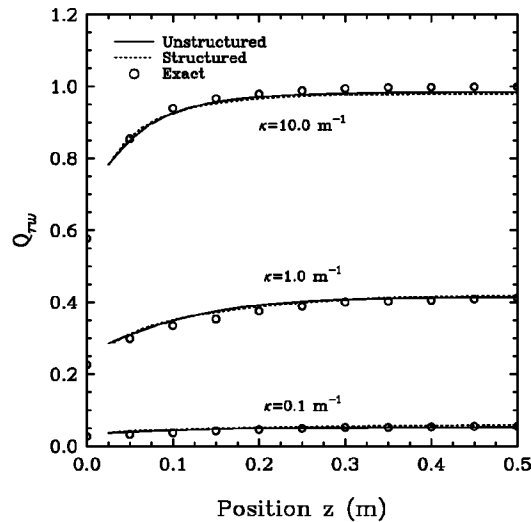


Figure 17. Comparison of radiative wall heat flux distributions along the A-A line.

DEVELOPMENT OF THE UNSTRUCTURED FLOW SOLVER FOR PLUME PREDICTIONS

Free stream boundary condition has been implemented in the unstructured grid flow solver for plume flow predictions. The total pressure and temperature conditions have been enforced at such boundary points for incoming flows, and the flow variables such as pressure, velocity, temperature and species concentrations are extrapolated for outgoing flows. At the exit boundaries, all variables are extrapolated for supersonic flows, but pressure is fixed for subsonic flows. An SSME nozzle plume at sea level conditions is shown in Figs. 18 and 19 by using first-order and second-order schemes respectively. It can be seen the shock is smeared by the first-order scheme while the second-order scheme predicts clear Mach disk structure in the plume.

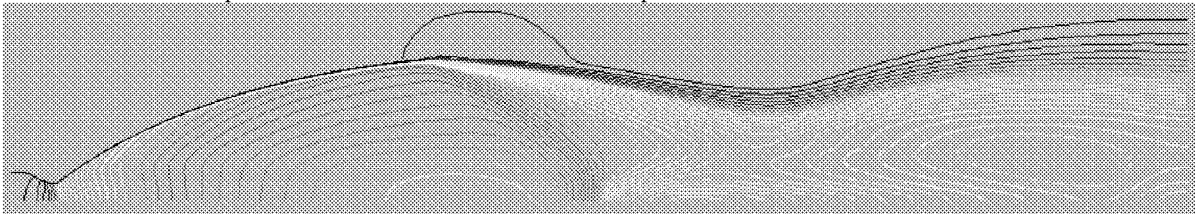


Figure 18. Mach number contours of SSME nozzle plume with first order scheme

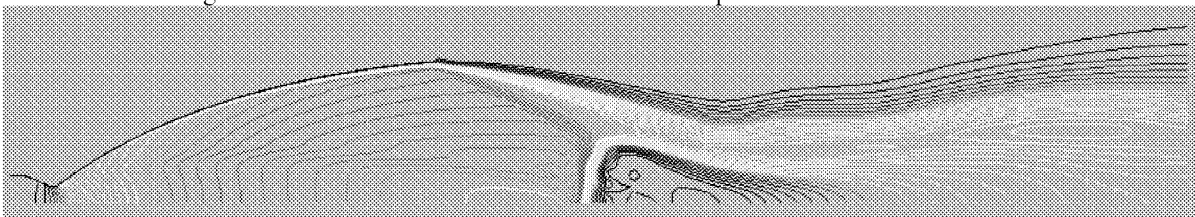


Figure 19. Mach number contours of SSME nozzle plume with second order scheme

IMPLEMENTATION OF DOMAIN DECOMPOSITION USING METIS

To implement the present parallel computation strategy, the computational domain needs to be partitioned into many sub-domains. Each sub-domain then occupies one processor for parallel computing. Many partitioning algorithms have been developed to unstructured meshes. These algorithms include Recursive Coordinate Bisection (RCB), Recursive Spectral Bisection (RSB), and Recursive Graph Bisection (RGB) methods. A publicly available package developed at the University of Minnesota, METIS [18], can partition high quality unstructured meshes efficiently.

Grids with 1 million vertices can be partitioned into 256 parts in less than 20 second on a Pentium Pro personal computer. Figs. 20-21 present 10 partitioned domains for a multi-airfoil grid and the predicted Mach number contours respectively. The partitioned domain surface and the predicted pressure contours are shown for a 3-D Boeing 747 grid in Figs. 22 and 23. About equal grid sizes have been partitioned for each domain, and the total dimension for the zonal interfaces are minimized to reduce the global communication time.

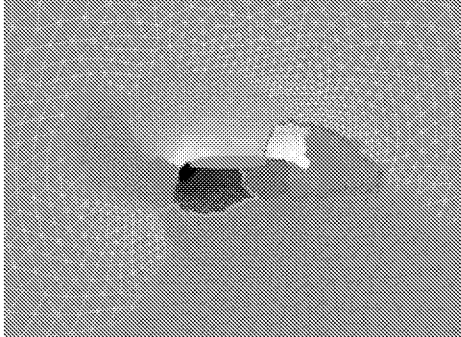


Figure 20. Partitioned grids for a multi-airfoil mesh

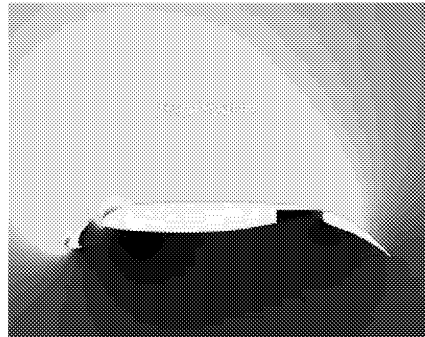


Figure 21. Predicted Mach Number contours.

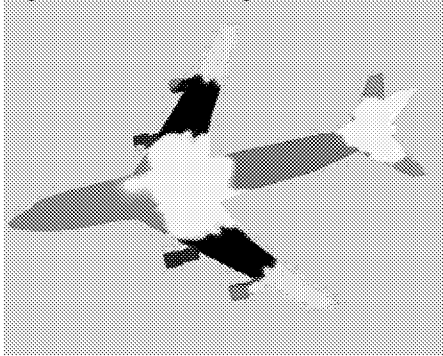


Figure 22. Partitioned domain surface for a three-dimensional Boeing 747 grid.

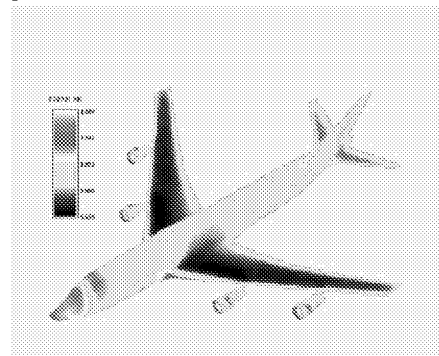


Figure 23. Predicted pressure contours for Boeing 747.

IMPLEMENTATION OF PARALLEL COMPUTING ALGORITHM

Numerical solution has been performed for a turbulent incompressible two-dimensional cascade flow. A four-block grid partition (Fig. 24) was created using METIS. With the explicit block coupling, the solution may diverge in some cases. When the implicit block coupling is used in the algebraic multi-grid (AMG) method, both serial (single CPU) and parallel computing require about the same number of global iterations or time steps to reach a converged solution. Fig. 25 shows the converged pressure contours and Fig. 26 presents the convergence history vs. time steps. Due to the small grid size used in this test case, the parallel efficiency only reaches 60%. The efficiency can be expected to be much higher for large three-dimensional applications.

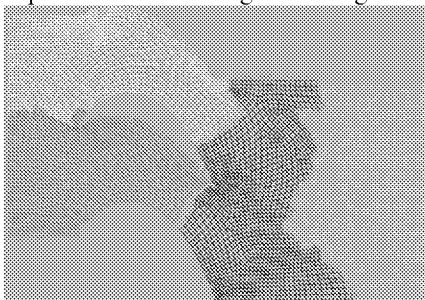


Figure 24. Grid partitions for cascade flow.



Figure 25. Predicted pressure contour

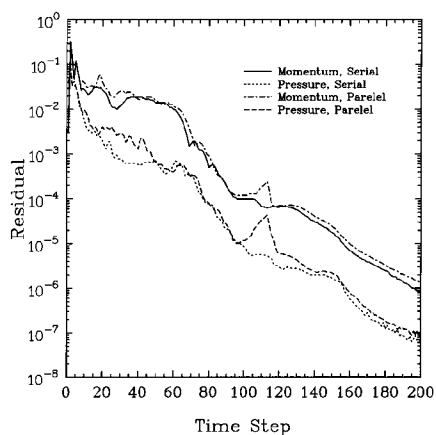


Figure 26. Convergence history for serial and parallel computing

GRID ADAPTATION

An incompressible laminar flow past three circular cylinders is presented to illustrate the grid adaptation procedure. The flow Reynolds number of 40 (based on the free stream velocity and the diameter of the cylinder) is used and the flow is believed to be stable at these flow conditions. The initial **hybrid unstructured mesh** is shown in Fig. 27. Quadrilateral cells are generated at the vicinity of the cylinders to better resolve the boundary layers and achieve high grid qualities.

The initial solution was performed on the initial mesh until it was converged. Then the level-1 adaptive mesh was generated based on the current solution and is shown in Fig. 28. It can be found that the grids closed to cylinders and at the wake region are enriched. The level-2 mesh adaptation is achieved based on the new solution and mesh of level-1 adaptation, and is illustrated in Fig. 29. The final solutions of velocity contours and vectors are presented in Figs. 30 and 31. The flow fields are symmetric about the centerline due to the fact of the symmetric geometry and stable flow conditions. The results obtained indicate the ability to achieve high resolution flow fields through automatic mesh adaptation.

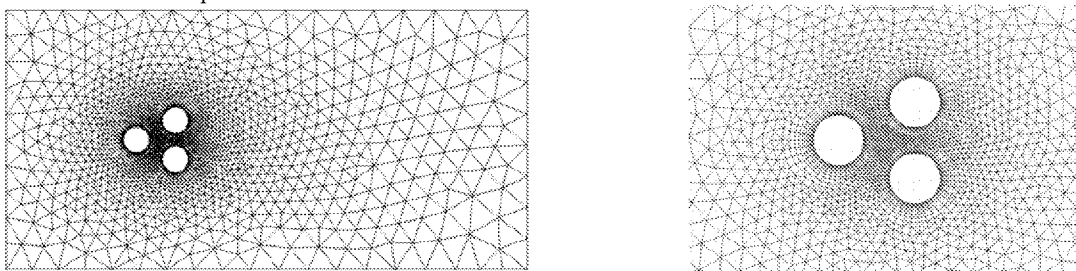


Figure 27. The initial mesh for flow past multiple cylinders.

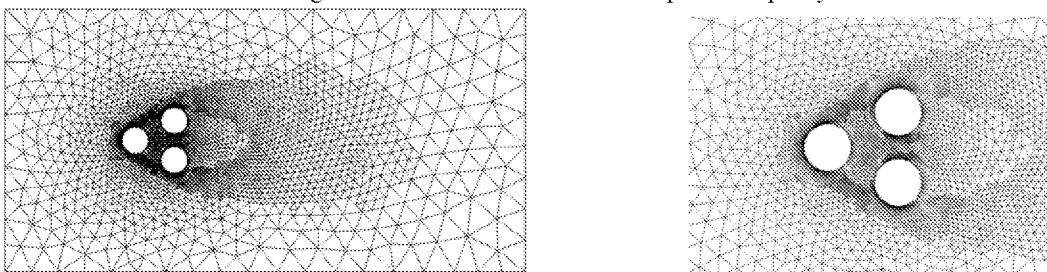


Figure 28. Mesh of level-1 adaptation.

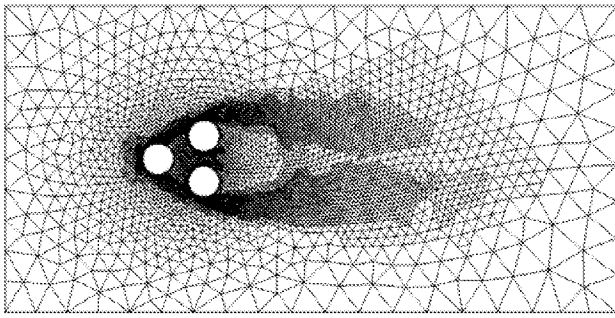


Figure 29. Mesh of level-2 adaptation.

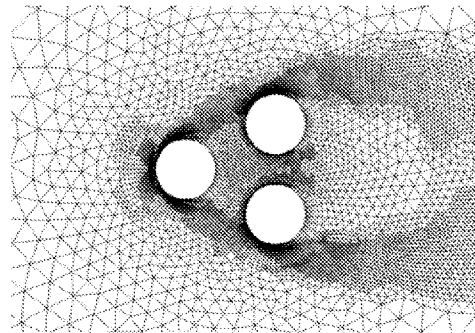


Figure 30. Velocity contours for level-2 mesh adaptation.

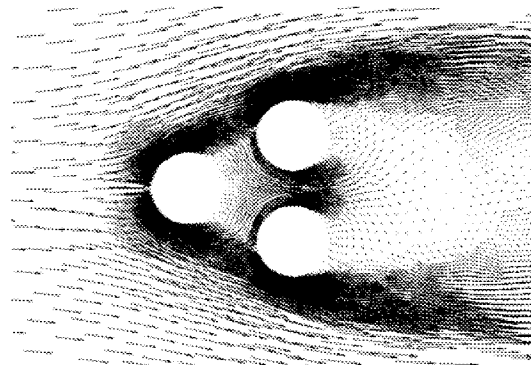


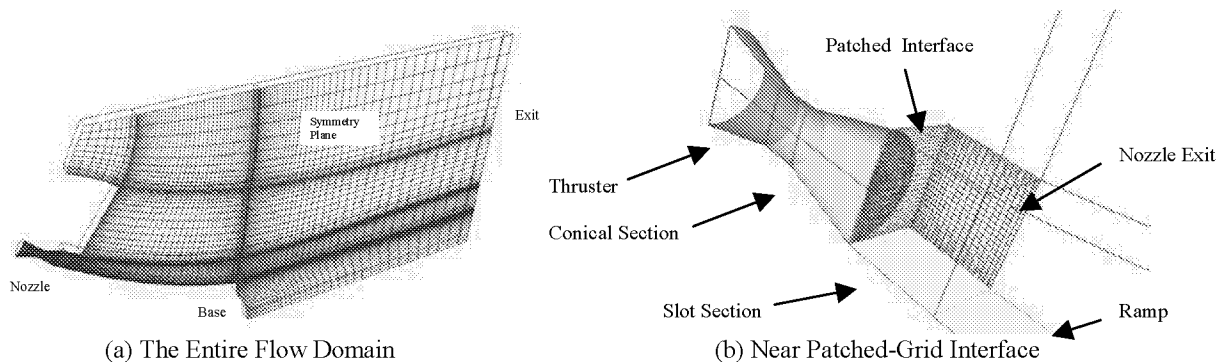
Figure 31. Velocity vectors near the cylinders.

NUMERICAL SIMULATION OF QUALIS/MSFC 2.25% X-33 BASE HEATING MODEL

The model selected jointly by Qualis and NASA MSFC [30], is a 2.25% simulation of the aft third of the X-33 flight demonstration vehicle currently under joint development by NASA and Lockheed Martin Skunk Works, Palmdale, California. The model matches the X-33 propulsion system parameters and produces exhaust gas constituents and external plumes that designed to be a close simulation to the X-33 flight plume shapes and thermodynamic properties. The model is instrumented primarily to monitor propulsion system performance, but also was equipped with base heating instrumentation to measure the base region environments as a secondary objective.

The X-33 vehicle has two rows of rectangular nozzle thrusters; 20 nozzles along the upper aerospike surface and 20 nozzles along the lower aerospike surface respectively. In the current CFD model, only a half of a nozzle region along the upper or lower spike surface is modeled due the cyclic arrangement of the nozzles. This model represents the flow conditions near the center plane of the aerospike engine by ignoring the lateral entrainment effects. Fig. 32a shows the flow domain and grids used in CFD simulations. A patch grid interface is used to connect the nozzle round and square intersection (see Fig. 32b), which is not the exact nozzle geometry of the X-33 design. The grids with 168,000 point are generated by ESI's UMESH package.

The test case of Run 1, 12/03/98, and a latest test case of 669 Psia chamber total pressure are simulated in the present study. For the first case, total pressure of 450 Psia (~30.62 atm) and total temperature of 3456 K have been used as the inlet conditions. The O/F ratio is 5.823 for both cases with equilibrium species concentration specified at the thruster inlet. Numerical solutions are obtained in 5,000 time steps for each case using 10 CPUs at MSFC's Power Challenge and spent 6.1 hours clock time with an average of 75% CPU time fully used. The predicted nozzle pressure, temperature, and Mach number contours of the first case are shown in Fig. 33-35.



(a) The Entire Flow Domain
 (b) Near Patched-Grid Interface
 Figure 32. The flow domain and patched-grid used by the CFD model.

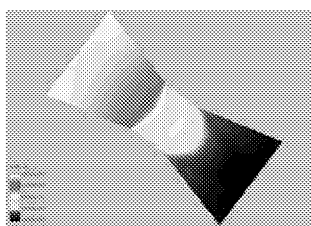


Fig. 33. Predicted pressure (atm).

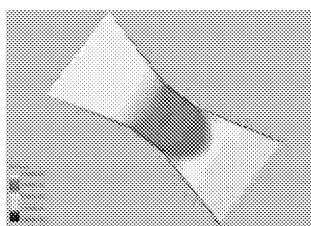


Fig. 34. Predicted temperature (K).

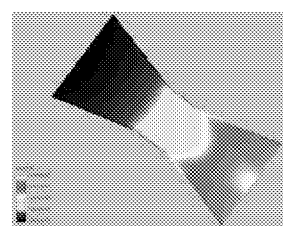


Fig. 35. Predicted Mach number.

The CFD predictions of the velocity vectors, Mach number contours, and temperature contours, on the nozzle symmetry plane, are shown in Figs. 36-38 respectively. A recirculation zone is shown in Fig. 36 near the base region with temperature around 2,100K in the same region (Fig. 38). The predicted convective heat flux near the base center region is around 65 Btu/sft-s, which is over-predicted compared to the measurement heat flux of 51.2 Btu/sft-s.

In the second test case, the entrainment effects and the strength of the recirculating base flow are increased due to the increased chamber pressure and the nozzle flow momentum. The overall plume Mach number is also increased that results in higher flow temperature and convective heat flux in the base region. Figs. 39-41 show the predicted Mach number, Temperature and H₂O mass fraction contours respectively (also on the nozzle symmetry plane). The predicted convective heat flux near the base symmetry plane is around 162 Btu/sft-s. The measured heat flux for this case is about 119 Btu/sft-s. Again, the current model has over-predicted the heat flux. The reasons for this discrepancy can be attributed to:

- (1) the heat loss in the combustion chamber, thruster, along the ramp and base surfaces;
- (2) the fuel/oxidizer mixing and combustion efficiency that may affect the total temperature at the thruster inlet, whereas equilibrium chemistry conditions are used in the CFD model; and
- (3) the heat flux reduction due to the effect of air aspiration from the sides of the linear aerospike engine, which the current numerical model does not consider.

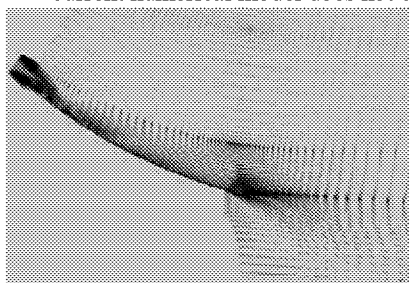


Figure 36. Predicted velocity vectors (450 psia Pc).

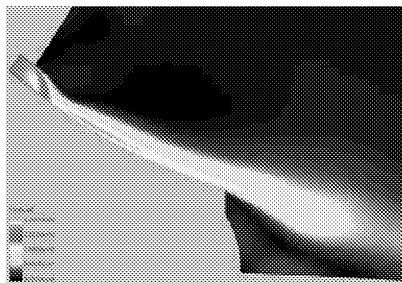


Figure 37. Predicted Mach number contours (450 psia Pc).

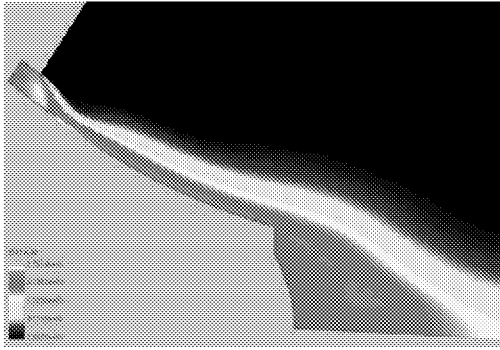


Figure 38. Predicted temperature contours (K) (450 psia Pc).



Figure 39. Predicted Mach number contours (669 psia Pc).

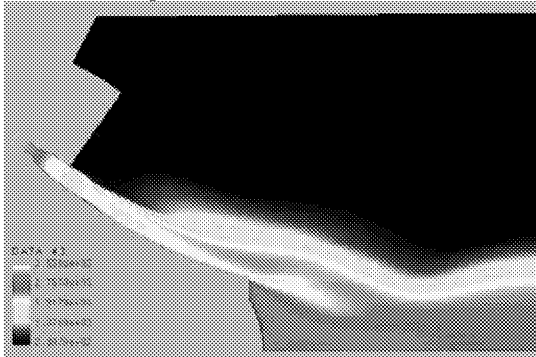


Figure 40. Predicted temperature contours (K) (669 psia Pc)

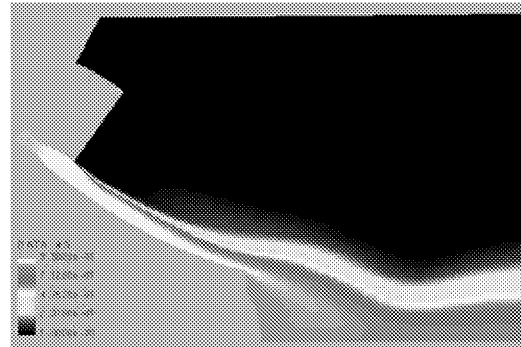


Figure 41. Predicted H2O contours (669 psia Pc).

Finally, there is one more important issue concerning the appropriateness of using the subscale model in simulating the X-33 base flows. As indicated in Qualis' subscale model, the nozzle geometry downstream of the throat is approximated by a conical section and a constant height slot, instead of a nozzle geometry with smooth transition from a circular throat to a rectangular exit (as in the X-33 design). This approximated nozzle geometry creates an oblique shock downstream of the step jump and obstructs the flow expansion down stream of the step. Figs. 42-43 show the Mach number and temperature contours near the region of the step jump. As a result, the nozzle flow is not fully expanded with substantial total pressure loss at the nozzle exit. This may have large effects on the base pressure and base heating levels. One must be very cautious about simulating full-scale launch vehicles using subscale models. Any misrepresented detail may have significant impact on important base flow performance data (such as base pressure and base heating data). These effects could have been discovered using detailed CFD analyses (such as the current model) early on for the subscale model design. Their impact on the base flow performance data can be assessed with confidence before the subscale testing is planned and conducted.

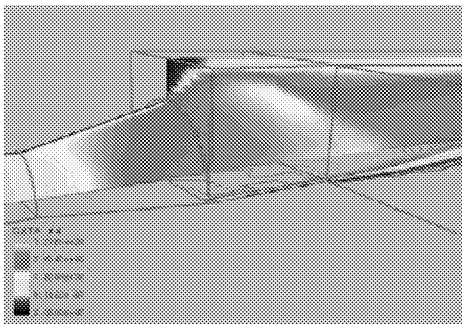


Figure 42. Predicted Mach number contours near the step jump region (669 psia Pc).

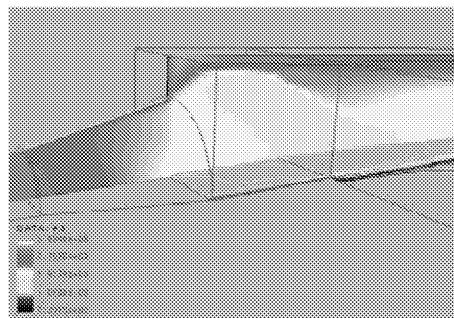


Figure 43. Predicted temperature contours (K) near the step jump region (669 psia Pc).

CONCLUSIONS

The current study has been successfully conducted and established that an integrated design tool using unstructured grid method with solution-adaptation and parallel computing strategy can become a practical analysis tool to predict base heating and plume radiation. An unstructured finite volume method for radiative heat transfer has been developed and they are applicable to any 2D planar, axisymmetric, or 3D problems with unstructured grids. Six benchmark problems, which cover a wide range of geometries and radiative property conditions, have been examined. The present solutions based on a structured grid and an unstructured grid are very close and they all have a very good agreement with available reference solutions. The present study indicates that not only is the developed unstructured radiation model flexible in treating problems with complex geometries but also it is very accurate and efficient.

For plume predictions, free stream (entrainment) boundary condition and plume exit boundary condition have been successfully implemented. Solutions have been obtained for SSME nozzle plume flows and Mach disk has been clearly shown with a flux limited second-order upwind scheme.

To implement a parallel computation strategy, the computational domain needs to be partitioned into many sub-domains. Each sub-domain then occupies one processor of a parallel computer. The domain decomposition using METIS has been implemented in the current flow solver for parallel computing applications.

The parallel-computing algorithm based on domain decomposition has been accomplished in this study. Algebraic multi-grid matrix solver has been paralleled to accelerate the convergence rate of pressure correction equation. Same global convergence rate has been demonstrated for single CPU (domain) and multi-CPU (domain) calculations.

The grid adaptation algorithm based on flow solution has been demonstrated for two-dimensional problem and shows the flexibility of unstructured grid method for solution adaptation. Further extension to three-dimensional applications will be implemented in future study.

Numerical simulation of Qualis/MSFC 2.25% X-33 base heating model has been performed using a sub-domain CFD model with 168,000 grid points and parallel computation. Numerical solution is obtained within 5,000 time steps using 10 CPUs at MSFC's Power Challenge spent 6.1 hours clock time with an average of 75% CPU time fully used. The current CFD model over predicts the base heat flux for two cases with chamber total pressure of 450 psia and 669 psia. Comparisons of the base heating data show reasonably good agreements between the present model and the measured data. Discrepancies in data comparisons can be attributed to the effects of heat loss, fuel mixing and air aspiration that need to be further investigated by using a more complete numerical model.

The present study also reveals the effects of a major difference between the subscale model and the X-33 design in the nozzle geometry. The simplification in the nozzle geometry of the subscale model has been shown to create an oblique shock system in the nozzle, which may have caused obstruction to the nozzle flow expansion and substantial total pressure loss to the nozzle flow. This may have significant impact on the base flow performance data such as the base pressure and the base heat flux. These effects can be investigated using the current CFD model before the design of the subscale model to assess their impact on the base flow performance data.

REFERENCES

1. Viskanta, R. and Menguc, M. P., "Radiation Heat Transfer in Combustion Systems," *Progress in Energy and Combustion Science*, Vol. 13, No. 2, 1987, pp. 97-160.
2. Howell, J. R., "Thermal Radiation in Participating Media: The Past, the Present, and Some Possible Futures," *ASME Journal of Heat Transfer*, Vol. 110, No. 4, 1988, pp. 1220-1229.
3. Modest, M. F., *Radiative Heat Transfer*, McGraw-Hill, New York, 1993.
4. Chai, J. C., Lee, H. S., and Patankar, S. V., "Finite-Volume Method for Radiative Heat Transfer," *Journal of Thermophysics and Heat Transfer*, Vol. 8, No. 3, 1994, pp. 419-425.

5. Liu, J., Shang, H. M., Chen, Y. S., and Wang, T. S., "Prediction of Radiative Transfer in General Body-Fitted Coordinates," AIAA Paper 97-0811, Jan. 1997; Also to be published in *Numerical Heat Transfer, Part B: Fundamentals*.
6. Liu, J., Shang, H. M., Chen, Y. S., and Wang, T. S., "GRASP: A General Radiation Simulation Program," AIAA Paper 97-2559, June, 1997.
7. Shang, H.M., and Chen, Y.S., "Unstructured Adaptive Grid Method for Reacting Flow Computation," AIAA Paper 97-3183.
8. Shang, H.M., Shih, M.H., Chen, Y.S., and Liaw, P., "Flow Calculation On Unstructured Grids With a Pressure-Based Method," *Proc. of 6th Int. Sym. on CFD*, Lake Tahoe, NV, Sep. 4-8, 1995.
9. Shang, H.M., Chen, Y.S., Liaw, P., and Chen, C.P., "A Hybrid Unstructured-Grid Method for Fluid Flow Computation," *Numerical Developments in CFD* Symposium of the Joint ASME/JSME Fluids Engineering Conference, Hilton Head Island, SC, Aug. 13-18, 1995.
10. Liu, J., Shang, H. M., Chen, Y. S., and Wang, T. S., "GRASP: A General Radiation Simulation Program," AIAA Paper 97-2559, June, 1997.
11. Liu, J., Shang, H. M., Chen, Y. S., and Wang, T. S., "Prediction of Radiative Transfer in General Body-Fitted Coordinates," *Numerical Heat Transfer, Part B: Fundamentals*, Vol. 31, No. 4, 1997, pp. 423-439.
12. Patankar, S.V., *Numerical Heat Transfer and Fluid Flow*. Hemisphere, Washington, D.C., 1980.
13. Shang, H.M., Shih, M.H., Chen, Y.S., and Liaw, P., "Flow Calculation On Unstructured Grids With a Pressure-Based Method," *Proc. of 6th Int. Sym. on CFD*, Lake Tahoe, NV, Sep. 4-8, 1995.
14. Shang, H.M., Chen, Y.S., Liaw, P., and Chen, C.P., "A Hybrid Unstructured-Grid Method for Fluid Flow Computation," *Numerical Developments in CFD* Symposium of the Joint ASME/JSME Fluids Engineering Conference, Hilton Head Island, SC, Aug. 13-18, 1995.
15. Shang, H.M., and Chen, Y.S., "Numerical Calculation of Fluid Flow Problems Using Efficient Matrix Solver for Pressure-Correction Equation," *Proceedings of the 1997 ASME Fluids Engineering Division Summer Meeting*, Paper FEDSM97-3508, June 22-26, 1997, Vancouver, British Columbia, Canada.
16. Raw, M., "Robustness of Coupled Algebraic Multigrid for the Navier-Stokes Equations," AIAA Paper 96-0297, January 1996.
17. Parikh, P., Pirzadeh, S., and Lohner, R., "A Package for 3-D Unstructured Grid Generation, Finite-Element Flow Solutions, and Flow-Field Visualization," NASA CR-182090, September, 1990.
18. Karypis and V. Kumar, "METIS, A Software Package for Partitioning Unstructured Graphs, Partitioning Meshes, and Computing Fill-Reducing Orderings of Sparse Matrices," Version 3.0.3, November 5, 1997.
19. Shang, H.M., and Chen, Y.S., "Development of parallel computing algorithm for A pressure-based flow solver," *Proceedings of FEDSM'98 ASME Fluids Engineering Division Summer Meeting*, FEDSM98-4927, Washington, DC, June 21 - 25, 1998
20. Geist, A., Beguelin, A., Dongarra, J., Jiang, W., Manchek, R., and Sunderam, V., "PVM: Parallel Virtual Machine - A Users' Guide and Tutorial for Networked Parallel Computing," The MIT Press, Cambridge, MA, 1994.
21. W. Gropp, E. Lusk, and A. Skjellum, "Using MPI", published by MIT Press, ISBN 0-262-57104-8.
22. G. Parthasarathy, H. S. Lee, J. C. Chai, and S. V. Patankar, ASME HTD-Vol. 276, pp. 191-199, 1994.
23. J. C. Chai, H. S. Lee, and S. V. Patankar, *Num. Heat Transfer, Part B*, **26**, 225-235 (1994).
24. S. S. Dua and P. Cheng, *Int. J. Heat Mass Transfer*, **18**, 245-259 (1975).
25. J. Y. Murthy and S. R. Mathur, *Num. Heat Transfer, Part B*, **33**, 397-416 (1998).
26. M. P. Menguc and R. Viskanta, *JQSRT*, **33**, 533-549 (1985)
27. W. A. Fiveland, *J. Thermophys.* **2**, 309-316 (1988).
28. J. C. Chai, J. P. Moder, and G. Parthasarathy, AIAA Paper 96-1889 (1996).
29. J. Liu, H. M. Shang, and Y. S. Chen, *Num. Heat Transfer, Part B*, **31**, 423-439 (1997).
30. C. D. Engel, R. L. Bender, B. A. Engel and J. M. Sebghati, "NASA SBIR 95-1 Phase II Aerospike Plug Base Heating Model Development Final Report," NASA Contract NAS8-97020, December 31, 1998, Qualis Corporation



OPTIMIZATION OF A GO₂/GH₂ IMPINGING INJECTOR ELEMENT

P. Kevin Tucker

NASA

Marshall Space Flight Center, AL 35812

Wei Shyy and Rajkumar Vaidyanathan

Department of Aerospace Engineering, Mechanics & Engineering Science

University of Florida

Gainesville, Florida 32611

ABSTRACT

An injector optimization methodology, *method i*, is used to investigate optimal design points for a gaseous oxygen/gaseous hydrogen (GO₂/GH₂) impinging injector element. The unlike impinging element, a fuel-oxidizer-fuel (F-O-F) triplet, is optimized in terms of design variables such as fuel pressure drop, ΔP_f , oxidizer pressure drop, ΔP_o , combustor length, L_{comb} , and impingement half-angle, α , for a given mixture ratio and chamber pressure. Dependent variables such as energy release efficiency, ERE , wall heat flux, Q_w , injector heat flux, Q_{inj} , relative combustor weight, W_{rel} , and relative injector cost, C_{rel} , are calculated and then correlated with the design variables. An empirical design methodology is used to generate these responses for 163 combinations of input variables. *Method i* is then used to generate response surfaces for each dependent variable. Desirability functions based on dependent variable constraints are created and used to facilitate development of composite response surfaces representing some, or all, of the five dependent variables in terms of the input variables. Three examples illustrating the utility and flexibility of *method i* are discussed in detail. First, joint response surfaces are constructed by sequentially adding dependent variables. Optimum designs are identified after addition of each variable and the effect each variable has on the design is shown. This stepwise demonstration also highlights the importance of including variables such as weight and cost early in the design process. Secondly, using the composite response surface which includes all five dependent variables, unequal weights are assigned to emphasize certain variables relative to others. Here, *method i* is used to enable objective trade studies on design issues such as component life and thrust to weight ratio. Finally, specific variable weights are further increased to illustrate the high marginal cost of realizing the last increment of injector performance and thruster weight.

NOMENCLATURE

Symbols

| | |
|------------|---|
| <i>A</i> | minimum acceptable value |
| <i>B</i> | target value |
| <i>C</i> | target value |
| <i>D</i> | composite desirability (joint response) |
| <i>E</i> | maximum acceptable value |
| <i>ERE</i> | energy release efficiency |
| <i>H</i> | height |

NOMENCLATURE (Con't)

| | |
|------------|-----------------------------|
| L | length |
| MR | momentum ratio |
| O/F | oxidizer to fuel mass ratio |
| P | pressure |
| d | diameter or desirability |
| m | mass flow rate |
| u | velocity |
| α | impingement half-angle |
| ΔP | pressure drop |

Subscripts

| | |
|-----------|----------------------|
| c | chamber |
| $comb$ | combustor |
| f | fuel |
| fs | freestream |
| $impinge$ | impingement |
| inj | injector |
| ni | normalized injection |
| o | oxidizer |
| rel | relative |
| w | wall |

Superscripts

| | |
|-----|------------------------------|
| s | desirability function weight |
| t | desirability function weight |

INTRODUCTION

In order to meet future launch program goals, the Spaceliner 100 Technology Roadmap¹ specifies very aggressive system goals for safety, life and cost per pound of payload launched into Earth orbit. Spaceliner 100 safety goals would decrease catastrophic events from the current 1 in 200 to 1 in 1,000,000 in 15 years. The life goal would be increased from the current 200 manned missions per year to 2000-5000 per year over the same time period. Concurrently, the cost goal aims to reduce the cost of delivering payloads to Earth orbit from the current \$10,000 per pound to \$1000 per pound in 10 years and to \$100 per pound in 15 years and ultimately to \$10 per pound.

NEED FOR IMPROVED INJECTOR DESIGN METHODOLOGIES

Design and development of advanced propulsion systems will be crucial to meeting these goals. Propulsion systems which meet these requirements must not only have high thrust to weight ratios, but also achieve higher operability and maintainability standards than in previous or current programs. Combustor designs, and injector designs in particular, will be key issues in meeting these goals. The injector design determines performance and stability, and is, therefore, the key factor governing injector face and chamber wall heat transfer/compatibility issues. Injector design also affects engine weight, cost, operability and maintainability.

The injector design methodologies used successfully in previous programs were typically based on large

subscale databases and the empirical design tools derived from them^{2,3,4,5,6}. These methodologies were often guided by extensive sub-and full-scale hot-fire test programs. Current and planned launch vehicle programs have relatively low budgets and aggressive schedules; neither of which is conducive to the large test programs of the past. Also, new requirements for operability and maintainability require that the injector design be robust. Hence, variables not previously included in the injector design now merit consideration for inclusion in the design process. These new programs with compressed schedules, lower budgets and more stringent requirements make the development of broader and more efficient injector design methodologies an worthy goal.

METHOD I

This work demonstrates a new design methodology called *method i*^{7,8} (Methodology for Optimizing the Design of Injectors) which seeks to address the above issues in the context of injector design. Simply put, *method i* is used to generate appropriate design data and then guide the designer through the information toward an optimum design subject to his specified constraints. Since the information generated by *method i* is not linked to any information type or source, it potentially affords the designer the ability to consider any relevant combination of design variables for a wide variety of injector types and propellant combinations. This generality also allows *method i* to use information at varying levels of breadth (i.e., scope of design variables) and depth (i.e., detail of design variables). Hence, *method i* could be useful for both element selection and the preliminary design phase. Once injector selection and preliminary designs are accomplished, *method i* can be used to optimize the injector design. Since *method i* is structured so that any pertinent information source can be used, design data can be obtained from existing databases and empirical design methodologies. If required, new data can be generated with modern experimental techniques or appropriate CFD models.

As implied above, *method i* is comprised of two discrete entities. The first element is the tool used to generate the design data—in this work, an empirical design methodology for GO₂/GH₂ injectors. Injector designs using GO₂/GH₂ propellants serve as a good point for the initial evaluation of *method i* for a number of reasons. First, the physics of the system are relatively simple. Atomization and vaporization do not complicate matters as they do when a liquid propellant is present. Also, an experimental database developed by Calhoon et al.⁹ exists along with an empirical design methodology¹⁰ derived from the data. Finally, should additional information be required, both modern laser-based diagnostic techniques^{11,12,13,14} and CFD modeling^{14,15} have been successfully applied to injector elements using GO₂/GH₂ propellants.

The second entity in *method i* is a group of optimization techniques. It is the optimization capability that extends *method i* beyond previous injector design methodologies. Historically, injectors have been designed, fabricated and tested based on experience and intuition. As the hardware was tested, designers proposed modifications aimed at obtaining an improved design. Despite their experience and skill, these efforts were unlikely to produce the optimal design in a short time frame. Also, as more design variables are considered, the design process becomes increasingly complex and it is more difficult to foresee the effect of the modification of one variable on other variables. Use of an optimization approach to guide the design addresses both of these issues. The optimization scheme allows large amounts of inter-related information to be managed in such a way that the extent to which variables influence each other can be objectively evaluated and optimal design points can be identified with confidence. *Method i* currently uses the Response Surface Method (RSM)¹⁶ to facilitate the optimization. The RSM approach is to conduct a series of well-chosen experiments (i. e., numerical, physical, or both) and use the resulting function values to construct a global approximation (i. e., response surface) of the measured quantity (i. e., response) over the design space. A standard constrained optimization algorithm is then used to interrogate the response surface for an optimum design.

DEVELOPMENT APPROACH AND STATUS

The approach used to develop and demonstrate this new methodology can be divided into three main tasks. Task 1 can be viewed as a proof of concept where the basic methodology is developed and demonstrated on

single element injectors. This task involves demonstration of *method i* in the element selection/preliminary design process. Design data from empirical methodologies is to be generated for three major element types—shear coaxial, swirl coaxial and impinging elements. In addition to the typical design output variable such as performance and heat flux, a goal is to enable the inclusion of additional parameters such as cost and weight early in the design process. This work for the shear coaxial element is essentially complete⁷ and the work for the impinging element is presented below. Generation of design data for the swirl coaxial element will finish the empirical database for Task 1. Then a swirl coaxial element will be optimized in a process similar to what has been done with the other two elements. Finally, to complete Task 1, all the design data, along with the optimization techniques developed to date, will be demonstrated in an element selection/preliminary design process.

Also, any potential “show stoppers” are to be identified and addressed in Task 1. Empirical design methodologies, such as found in Calhoun et al, may allow the designer to generate large quantities of data within a design space. However, due to their empiricism, these methodologies are often sufficiently accurate only over the range of variables for which test data was taken to develop the methodology. For some injector types, propellant combinations or design conditions, this limitation may require that more relevant data be generated to ensure confidence in the design. Historically, this data has been generated in sub- and full-scale test programs. More recently CFD analysis from validated models has been used to augment the test data. The data from test programs and CFD analysis are expensive and time consuming to obtain. Recognition of this fact has direct implications for the usefulness of optimization techniques in injector design methodologies. Although the optimization scheme must be capable of efficiently organizing large amounts of design information generated from empirical design methodologies, it must also be able to make effective use of the relatively small amounts of data available in some cases. An optimization scheme that requires large amounts of data to generate meaningful results will be marginally useful, if at all, when only small amounts of data are available for use. This potential shortcoming was addressed by using Neural Networks to augment the design optimization process⁸. In a process that simulated a case where only a limited amount of design data was available, a radial basis neural network was trained on the available data and then used to generate additional design data. The accuracy of the new data proved to be sufficient to allow it to be used reliably in the design optimization process.

Task 2 involves replacing/augmenting the empirical data with data from physical and numerical experiments (i.e., test data and validated CFD analyses). CFD models will be further validated and applied to selected cases already represented by data from the empirical methodology. Allowance in the optimization process will be made for the differences in depth and breadth of the different types of information since data from physical and numerical experiments are multi-dimensional and allow more design variables to be examined and included in the process. Also, in general, the numerical and physical experiments should be more accurate than the empirical data used to date. The different levels of accuracy must therefore be addressed in Task 2.

Task 3 involves using CFD analyses and empirical methods to design a multi-element injector consisting of 7-12 elements. Optimization will be done in the context of single element variables plus element pattern, element spacing, film cooling, etc.

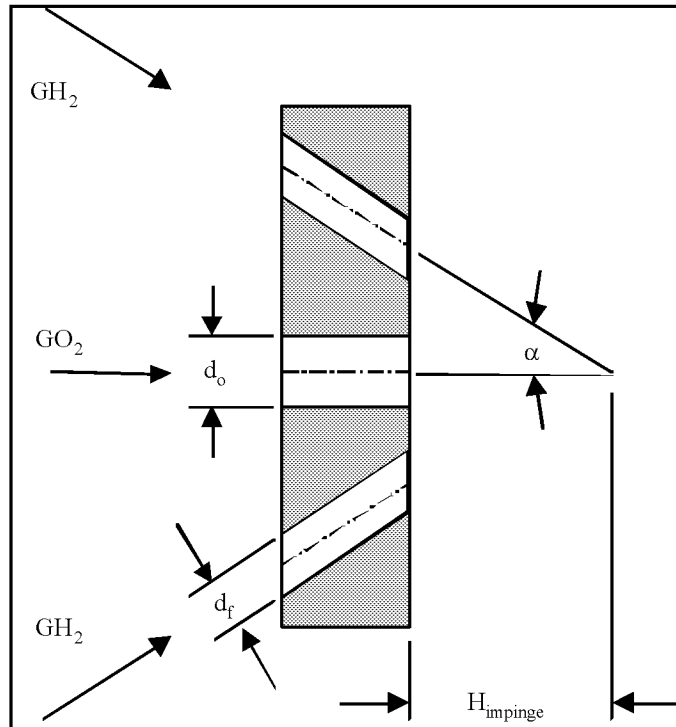
SCOPE OF CURRENT EFFORT

This paper presents the design optimization of a impinging injector—the second element to be evaluated in Task 1. The first element to be evaluated in Task 1 was a shear coaxial GO₂/GH₂ element. Here, an F-O-F triplet element is chosen for the demonstration. This element type is widely used and is capable of operating at high efficiency levels. A schematic of an F-O-F element is shown in Fig. 1.

The empirical design methodology of Calhoun et al uses the oxidizer pressure drop, ΔP_o , fuel pressure drop, ΔP_f , combustor length, L_{comb} , and the impingement half-angle, α as independent variables. For this injector design, the pressure drop range is set to 10-20% of the chamber pressure due to stability considerations. The combustor length, defined as the distance from the injector to the end of the barrel portion of the chamber ranges from 2-8 inches. The impingement half angle is allow to vary from 15-50°.

Dependent variables include ERE (a measure of element performance), wall heat flux, Q_w , injector heat flux, Q_{inj} , relative combustor weight, W_{rel} , and relative injector cost, C_{rel} .

Figure 1. Schematic of F-O-F Injector Element



In the following sections, the injector model and the generation of design data are discussed in some detail. Response surfaces for each of the dependent variables are generated and then combined into a joint surface to facilitate the optimization process. Optimization of the element is then demonstrated by applying equal weights for all dependent variables as they are added to the joint response surface one at a time, by applying unequal weights that might reflect specific design priorities and trades, and finally, over a modified constraint range, by examining the extraction of the last increments of certain variables and the high marginal cost this process levies on other variables.

F-O-F INJECTOR MODEL

This section details the models used to generate the design data for the dependent variables noted above. The process for generating the design data is described and sample results are also presented. The conditions selected for this example are:

$$P_c = 1000 \text{ psi}$$

$$MR = 6$$

$$m_{GO_2} = 0.25 \text{ lb}_m / \text{sec}$$

$$m_{GH_2} = 0.042 \text{ lb}_m / \text{sec}$$

The gaseous propellants are injected at a temperature of 540 R.

MODELS FOR DEPENDENT VARIABLES

As noted above, the empirical design methodology used to characterize the ERE and Q_w was developed by Calhoun et al. This methodology uses a quantity called the normalized injection momentum ratio to correlate the mixing at the different design points for the triplet element. They define this quantity as

$$MR_{ni} = \frac{2.3m_o u_o}{m_f u_f \sin \alpha} \quad (1)$$

The maximum mixing, and thus maximum ERE , occurs at an MR_{ni} of 2.0. Since the propellant mass flowrates are fixed, only the propellant velocities and the impingement half-angle influence the normalized injection momentum ratio. The velocities are proportional to the square root of the respective pressure drops across the injector, ΔP_o and ΔP_f . For the flow conditions and variable ranges considered in this problem, MR_{ni} ranges from 3.2 to 17.8. Accordingly, lowering ΔP_o , raising ΔP_f , increasing α , or some combination of these actions will increase ERE .

The wall heat flux is correlated with the propellant momentum ratio as defined by

$$MR = \frac{m_o u_o}{m_f u_f} \quad (2)$$

For the F-O-F triplet element, the maximum wall heat flux occurs at a momentum ratio of approximately 0.4. High heat flux is the result of over-penetration of the fuel jet which produces a high O/F in the wall region. For the flow conditions and variable ranges considered in this effort, MR ranges from 1.06 to 2.11. Hence, increasing the value of this ratio by either increasing ΔP_o or decreasing ΔP_f lowers the wall heat flux.

The heat flux seen by the injector face, Q_{inj} , is qualitatively modeled by the impingement height, $H_{impinge}$. The notion being that, as the impingement height decreases, the combustion occurs closer to the injector face, causing a proportional increase in Q_{inj} . Thus, for the purposes of this exercise, Q_{inj} is modeled as the reciprocal of the $H_{impinge}$. Impingement height is a function of α and ΔP_f . Reference to Fig. 1 shows that as α is increased, $H_{impinge}$ is shortened. The dependence of $H_{impinge}$ on the fuel orifice diameter, d_f , and thus, ΔP_f , results from making the freestream length of the fuel jet, L_{fs} , a function of $d_f^{1.7}$. For each ΔP_f , L_{fs} was set to six times d_f for an impingement half-angle of 30° . So, as d_f increases (corresponding to decreasing ΔP_f), L_{fs} increases, as does $H_{impinge}$.

The models for W_{rel} and C_{rel} are simple but represent the correct trends. W_{rel} is a function only of L_{comb} , the combustor length from injector face to the end of the chamber barrel section. The dimensions of the rest of the thrust chamber assembly are assumed to be fixed. So, as L_{comb} increases, W_{rel} increases accordingly. The model for C_{rel} is based on the notion that smaller orifices are more expensive to machine. Therefore, C_{rel} is a function of both propellant pressure drops. As the ΔP 's increase, the propellant velocity through the injector increases and the orifice area decreases. So, as either, or both, ΔP_o and ΔP_f increase, C_{rel} increases.

GENERATION OF DESIGN DATA

The system variables given above and independent variables (constrained to the previously noted ranges) are used to generate the design data for element optimization studies. Since propellant momentum ratio is an important variable in the empirical design methodology, a matrix of momentum ratios was developed over the 100-200 psi propellant pressure drop range. The matrix of 49 combinations of fuel and oxidizer pressure drops is shown in Table 1 where momentum ratios range from 1.06 to 2.11. Nine pressure drop combinations, eight around the border and one in the middle, were selected for use in populating the design data base. These nine points are highlighted in Table 1 in bold type.

Table 1. Propellant Momentum Ratio as a Function of Propellant Pressure Drops.

| ΔP_f | ΔP_o | | | | | | |
|--------------|--------------|------|------|------|------|------|------|
| | 200 | 180 | 160 | 150 | 140 | 120 | 100 |
| 200 | 1.49 | 1.42 | 1.33 | 1.30 | 1.25 | 1.16 | 1.06 |
| 180 | 1.57 | 1.50 | 1.41 | 1.37 | 1.32 | 1.22 | 1.11 |
| 160 | 1.67 | 1.59 | 1.50 | 1.45 | 1.40 | 1.30 | 1.18 |
| 150 | 1.73 | 1.64 | 1.54 | 1.49 | 1.44 | 1.34 | 1.22 |
| 140 | 1.79 | 1.70 | 1.60 | 1.55 | 1.50 | 1.39 | 1.27 |
| 120 | 1.93 | 1.83 | 1.72 | 1.67 | 1.61 | 1.50 | 1.37 |
| 100 | 2.11 | 2.00 | 1.89 | 1.83 | 1.77 | 1.64 | 1.49 |

Detailed design results for the case with both ΔP_o and ΔP_f at 200 psi are shown in Table 2. Similar data was generated for the other eight pressure drop combinations. There are 20 combinations of L_{comb} and α for each ΔP combination, making a total of 180 design points selected. Seventeen of these were outside the database embodied by the empirical design methodology, resulting in 163 design points actually being evaluated. The data trends are as expected. *ERE*, for a given ΔP combination, increases with increasing L_{comb} and α . The increased L_{comb} provides more residence time for the propellants to mix and burn. Increasing α increases the radial component of the injected fuel, thus providing better mixing. The wall heat flux is constant for a given ΔP combination. Impingement height increases with increasing α . Relative combustor cost increases with increasing L_{comb} and the relative injector cost is constant for a given ΔP combination.

Table 2. Design Data for ΔP_o and $\Delta P_f = 200$ psi.

| ΔP_o | ΔP_f | L_{comb} | α | ERE | Q_w | $H_{impinge}$ | W_{rel} | C_{rel} |
|--------------|--------------|------------|----------|------|-------|---------------|-----------|-----------|
| 200 | 200 | 2 | 15 | NA | 0.85 | 0.84 | 0.923 | 1.083 |
| 200 | 200 | 2 | 20 | 85 | 0.85 | 0.62 | 0.923 | 1.083 |
| 200 | 200 | 2 | 30 | 92.8 | 0.85 | 0.39 | 0.923 | 1.083 |
| 200 | 200 | 2 | 45 | 95.4 | 0.85 | 0.23 | 0.923 | 1.083 |
| 200 | 200 | 2 | 50 | 95.8 | 0.85 | 0.19 | 0.923 | 1.083 |
| 200 | 200 | 4 | 15 | 91 | 0.85 | 0.84 | 1 | 1.083 |
| 200 | 200 | 4 | 20 | 95.2 | 0.85 | 0.62 | 1 | 1.083 |
| 200 | 200 | 4 | 30 | 96.8 | 0.85 | 0.39 | 1 | 1.083 |
| 200 | 200 | 4 | 45 | 98.1 | 0.85 | 0.23 | 1 | 1.083 |
| 200 | 200 | 4 | 50 | 98.4 | 0.85 | 0.19 | 1 | 1.083 |
| 200 | 200 | 6 | 15 | 95.6 | 0.85 | 0.84 | 1.077 | 1.083 |
| 200 | 200 | 6 | 20 | 97.8 | 0.85 | 0.62 | 1.077 | 1.083 |
| 200 | 200 | 6 | 30 | 98.5 | 0.85 | 0.39 | 1.077 | 1.083 |
| 200 | 200 | 6 | 45 | 99.2 | 0.85 | 0.23 | 1.077 | 1.083 |
| 200 | 200 | 6 | 50 | 99.4 | 0.85 | 0.19 | 1.077 | 1.083 |
| 200 | 200 | 8 | 15 | 98.3 | 0.85 | 0.84 | 1.154 | 1.083 |
| 200 | 200 | 8 | 20 | 99.1 | 0.85 | 0.62 | 1.154 | 1.083 |
| 200 | 200 | 8 | 30 | 99.4 | 0.85 | 0.39 | 1.154 | 1.083 |
| 200 | 200 | 8 | 45 | 99.6 | 0.85 | 0.23 | 1.154 | 1.083 |
| 200 | 200 | 8 | 50 | 99.7 | 0.85 | 0.19 | 1.154 | 1.083 |

RESPONSE SURFACE GENERATION

In this effort, *method i* uses the Response Surface Method (RSM) to find optimal values of ERE , Q_w , Q_{inj} , W_{rel} and C_{rel} for acceptable values of ΔP_o , ΔP_f , L_{comb} and α . The approach of RSM is to perform a series of experiments, or numerical analyses, for a prescribed set of design points, and to construct a response surface of the measured quantity over the design space. In the present context, the five responses of interest are ERE , Q_w , Q_{inj} , W_{rel} and C_{rel} . The design space consists of the set of relevant design variables ΔP_o , ΔP_f , L_{comb} and α . The response surfaces are fit by standard least-squares regression with a quadratic polynomial using the JMP¹⁸ statistical analysis software. JMP is an interactive, spreadsheet-based program which provides a variety of statistical analysis functions. A backward elimination procedure based on t-statistics is used to discard terms and improve the prediction accuracy¹⁹.

INDIVIDUAL RESPONSE SURFACES

When the JMP software is used to analyze the 163 design points, five individual full response surfaces for the variables in the design space are approximated by quadratic polynomials that contain 15 terms each. Using the t-statistics approach noted above and detailed in Tucker et al⁷, unnecessary terms in each equation can be eliminated to give the reduced surfaces shown below in equations 3-7.

$$ERE = 0.0028L_{comb}\Delta P_o - 0.0043L_{comb}\Delta P_f - 0.2248L_{comb}^2 + 0.00024\Delta P_o\alpha - 0.00051\Delta P_f\alpha - 0.0445L_{comb}\alpha \quad (3)$$

$$-0.006\alpha^2 - 0.0311\Delta P_o + 0.0547\Delta P_f + 5.268L_{comb} + 0.814\alpha + 63.344$$

$$Q_w = 0.000017\Delta P_o^2 - 0.000021\Delta P_o\Delta P_f + 0.0000075\Delta P_f^2 - 0.0043\Delta P_o + 0.0029\Delta P_f + 0.959 \quad (4)$$

$$H_{impinge} = 0.00000345\Delta P_f^2 + 0.000028\Delta P_f\alpha + 0.00058\alpha^2 - 0.0027\Delta P_f - 0.061\alpha + 1.924 \quad (5)$$

$$W_{rel} = 0.0385L_{comb} + 0.846 \quad (6)$$

$$C_{rel} = -0.0000035\Delta P_o^2 + 0.0000065\Delta P_f^2 - 0.0043\Delta P_o - 0.00096\Delta P_f + 0.845 \quad (7)$$

A survey of the reduced response surfaces indicates that the equations reflect the functionality used to construct the models for the dependent variables.

JOINT RESPONSE SURFACES

In the current study, it is desirable to attempt to maximize ERE and while simultaneously minimizing Q_w , Q_{inj} , W_{rel} and C_{rel} . One method of optimizing multiple responses simultaneously is to build from the individual responses a composite response known as the desirability function. The method allows for a designer's own priorities for the response values to be built into the optimization procedure. The first step in the method is to develop a desirability, d , for each response. In the case where a response should be maximized, such as ERE , the desirability takes the form:

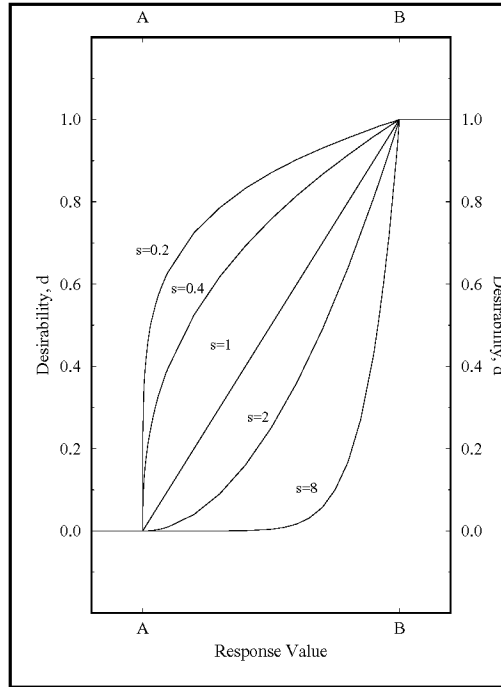
$$d_1 = \left(\frac{ERE - A}{B - A} \right)^s \quad (8)$$

where B is the target value and A is the lowest acceptable value such that $d = 1$ for any $ERE > B$ and $d = 0$ for $ERE < A$. The power value s is set according to one's subjective impression about the role of the response in the total desirability of the product. In the case where a response is to be minimized, such as Q_w , the desirability takes on the form:

$$d_2 = \left(\frac{Q - E}{C - E} \right)^t \quad (9)$$

where C is the target value and E is the highest acceptable value such that $d = 1$ for any $Q_w < C$ and $d = 0$ for $Q_w > E$. Choices for $A, B, C,$ and E are chosen according to the designer's priorities or, as in the present study, simply as the boundary values of the domain of ERE and Q_w .

Figure 2. Desirability Function for Various Weight Factors, s .



Choices for s and t are more difficult, but plots such as Figure 2 can be instructive. Figure 2 shows the appearance of the desirability function for the case of maximizing a response. Desirabilities with $s < 1$ imply that a product need not be close to the response target value, B , to be quite acceptable. But $s = 8$, say, implies that the product is nearly unacceptable unless the response is close to B . A single composite response is developed which is the geometric mean of the desirabilities of the individual responses. The composite response is defined as:

$$D = (d_1 \cdot d_2 \cdot d_3 \dots d_m)^m \tag{10}$$

The complete joint response surface for the present case is given by:

$$D = (d_{ERE} d_{Q_w} d_{Q_{in}} d_{W_{in}} d_{C_{in}})^5 \tag{11}$$

OPTIMIZATION RESULTS & DISCUSSION

Three set of results are presented below to demonstrate the capability of *method i* for the current injector design. These three examples illustrate the effect of each variable on the optimum design, the trade-offs between life and performance issues, and the effect on the design of extracting the last increment of performance.

EFFECT OF EACH VARIABLE ON THE DESIGN USING ORIGINAL CONSTRAINTS & EQUAL WEIGHTS

The results in this section were obtained by building the joint response surface with the addition of one dependent variable at a time. The results are shown in Table 3. Since current non-optimizer based design methods yield high-performing injector elements, simply maximizing the *ERE* is not a challenge. Accordingly, the initial results (Case 1) are obtained with a joint *ERE* and Q_w response surface. The results in Case 2 have the impingement height added, Case 3 adds the relative chamber weight and the relative cost is added in Case 4. All results are obtained using the original independent variable constraints and all dependent variables have equal weights of one. The results for Case 1 show that *ERE* is at its maximum and Q_w is very near its minimum desirability limit. Minimizing Q_w requires a small ΔP_f relative to ΔP_o as evidenced by the values of 100 psi and 183 psi, respectively. Maximum *ERE* values are found at the longest chamber length, $L_{comb}=8$ inches. Even with the relatively high value of 183 psi for ΔP_o and low value of ΔP_f of 100 psi, *ERE* is maximized to 99.9% with an impingement half-angle of 33.1°.

Table 3. Effect of Each Variable on the Design--Optimal Designs for Original Constraints & Equal Weights

| Independent Variable | Constraints | Results Case 1 | Results Case 2 | Results Case 3 | Results Case 4 |
|----------------------|---------------------|----------------|----------------------------|--|--|
| ΔP_o | 100-200 | 183 | 183 | 179 | 100 |
| ΔP_f | 100-200 | 100 | 132 | 149 | 100 |
| L_{comb} | 2-8 | 8.0 | 8.0 | 6.6 | 6.5 |
| α | 15-50 | 33.1 | 18.9 | 22.3 | 24.0 |
| Dependent Variable | Desirability Limits | ERE & Q_w | ERE, Q_w , $H_{impinge}$ | ERE, Q_w , $H_{impinge}$, W_{rel} | ERE, Q_w , $H_{impinge}$, W_{rel} , C_{rel} |
| ERE | 95.0-99.9 | 99.9 | 98.3 | 98.0 | 98.0 |
| Q_w | 0.7-1.3 | 0.74 | 0.76 | 0.79 | 0.86 |
| $H_{impinge}$ | 0.2-1.0 | — | 0.75 | 0.61 | 0.63 |
| W_{rel} | 0.9-1.2 | — | — | 1.1 | 1.1 |
| C_{rel} | 0.7-1.1 | — | — | — | 0.93 |

Addition of the impingement height to Case 2 to model the injector face heat flux, Q_{inj} , forces α lower to increase $H_{impinge}$ and decrease Q_{inj} . This decrease in the radial component of the fuel momentum has an adverse affect on *ERE*. This effect is mitigated to a degree by increasing the ΔP_f by 32 psi to 132 psi. *ERE* is still reduced by 1.6%. Also, the increase in ΔP_f causes increased penetration of the fuel jet which results in a slightly higher Q_w .

Case 3 adds the relative combustor weight to the list of dependent variables modeled. Since W_{rel} is only a function of L_{comb} , minimizing W_{rel} shortens the combustor length from 8 to 6.6 inches. The shorter L_{comb} tends to lower *ERE*. This effect is offset to a large degree by increases in ΔP_f and α , both of which increase the radial component of the fuel momentum. The increase in ΔP_f also causes a slight increase in Q_w . The increase in α causes a significant decrease in $H_{impinge}$ which increases the injector face heat flux.

Finally, the relative cost of the injector is added in Case 5. Since C_{rel} is only a function of propellant pressure drops, both ΔP_o and ΔP_f are driven to their respective minimum values. This and a slight increase in α allow *ERE* to be maintained at 98%, even with a slight decrease in L_{comb} . The largest effect of this fairly dramatic decrease in propellant pressure drops is on Q_w . Even though the values for ΔP_o and ΔP_f fell, ΔP_f increased relative to ΔP_o causing Q_w to increase by almost 9%. Impingement height and relative combustor weight are essentially unchanged.

Although several of the variables included in this exercise are qualitative, an important conclusion can still be drawn. The sequential addition of dependent variables to an existing design results in changes to both the independent and dependent variables in the existing design. The direction and magnitude of these changes depends on the sensitivity of the variables, but the changes may well be significant. The design in Case 4 is

quite different than the one in Case 1. Consideration of a larger design space results in a different design—the sooner the additional variables are considered, the more robust the final design will be.

EMPHASIS ON LIFE & PERFORMANCE ISSUES USING ORIGINAL CONSTRAINTS & UNEQUAL WEIGHTS

The purpose of this section is to illustrate the effect of emphasizing certain aspects of the design during the optimization process. *Method i* allows this emphasis via the weights applied to the desirability functions in the joint response surface. The set of results shown in Table 4 facilitate the illustration. The Case 1 (baseline) results are repeated from Case 4 in Table 3 where the entire design space is considered with the original constraints and equal weights for the dependent variables. The results in the Case 2 column are obtained by emphasizing the minimization of the wall and injector face heat fluxes. Desirability functions for both of these variables are given a weight of five. Since lower heat fluxes tend to increase component life, weighting these two variables is equivalent to emphasizing a life-type issue in the design. As expected, α is decreased to increase $H_{impinge}$, thus decreasing Q_{inj} . Since the fuel pressure drop is already at the minimum, the oxidizer pressure drop is increased by 58% to decrease Q_w . Both of these changes tend to decrease ERE . While ERE does decrease, the effect is somewhat mitigated by an increase in L_{comb} . The increases in L_{comb} and ΔP_o cause increases in W_{rel} and C_{rel} , respectively. The emphasis on life extracts the expected penalty on performance. Additionally, for the current model, there are also weight and cost penalties.

Table 4. Effect of Emphasizing & Life & Performance Issues—Optimal Designs for Original Constraints and Modified Weights

| Independent Variable | Constraints | Results Case 1 | Constraints | Results Case 2 | Constraints | Results Case 3 |
|----------------------|--------------------------|----------------|----------------------|----------------|-------------------------------|----------------|
| ΔP_o | 100-200 | 100 | 100-200 | 158 | 100-200 | 100 |
| ΔP_f | 100-200 | 100 | 100-200 | 100 | 100-200 | 137 |
| L_{comb} | 2-8 | 6.5 | 2-8 | 7.7 | 2-8 | 5.2 |
| α | 15-50 | 24.0 | 15-50 | 15.0 | 15-50 | 36.0 |
| Dependent Variable | Baseline Variable Weight | | Life Variable Weight | | Thrust/Weight Variable Weight | |
| ERE | 1 | 98.0 | 1 | 96.7 | 5 | 99.1 |
| Q_w | 1 | 0.86 | 5 | 0.75 | 1 | 0.95 |
| $H_{impinge}$ | 1 | 0.63 | 5 | 0.94 | 1 | 0.32 |
| W_{rel} | 1 | 1.10 | 1 | 1.14 | 5 | 1.05 |
| C_{rel} | 1 | 0.93 | 1 | 0.97 | 1 | 0.95 |

The results for Case 3 are obtained by emphasizing maximization of ERE and minimization of W_{rel} with desirability weightings of five. Increased weighting for these two variables is equivalent to emphasizing a thrust to weight goal for the injector/chamber. The relative chamber length is shortened to lower W_{rel} . ERE is maximized by increasing the radial momentum of the fuel jet. Both ΔP_f and α are increased to accomplish ERE maximization. As noted earlier, increasing ΔP_f and α lead to increased wall and injector heat fluxes, respectively. Reference to Table 4 indicates that to be the case here. For this case, emphasis on thrust and weight tend to have an adverse affect on both Q_w and Q_{inj} . Relative cost, for the current model, is not significantly affected.

EXTRACTION OF LAST PERFORMANCE & WEIGHT INCREMENTS (MODIFIED CONSTRAINTS & UNEQUAL WEIGHTS)

Here, the high marginal cost of realizing the last increment of thrust to weight is shown. This section illustrates the capability to modify the constraints on the independent variables and use unequal weights on the dependent variables at the same time. The results for Case 3 in Table 4 are carried over to Case 1 in Table 5 as the baseline for this example. Here the original constraints are used but increased weights have been applied to emphasize ERE and W_{rel} . Cases 2 and 3 modify the constraints on the propellant pressure drops, raising the minimum pressure drop from 100 psi to 150 psi. For Case 2, both ΔP_o and ΔP_f are now at the minimum level for the modified constraints. L_{comb} is increased slightly to maintain ERE . The decrease of ΔP_f relative to ΔP_o causes a decrease in Q_w . The slightly higher pressure drops also cause C_{rel} to increase somewhat. Other variables are not changed appreciably.

Table 5. Effects of Realizing the Last Increments of Performance & Weight—Optimum Designs for Modified Constraints and Unequal Weights

| Independent Variable | Original Constraints | Results Case 1 | Modified ΔP Constraints | Results Case 2 | Modified ΔP Constraints | Results Case 3 |
|----------------------|-----------------------|----------------|---------------------------------|----------------|---------------------------------|----------------|
| ΔP_o | 100-200 | 100 | 150-200 | 150 | 150-200 | 150 |
| ΔP_f | 100-200 | 137 | 150-200 | 150 | 150-200 | 200 |
| L_{comb} | 2-8 | 5.2 | 2-8 | 5.4 | 2-8 | 4.4 |
| α | 15-50 | 36.0 | 15-50 | 35.6 | 15-50 | 44.8 |
| Dependent Variable | Variable Weight (5:1) | | Variable Weight (5:1) | | Variable Weight (100:1) | |
| ERE | 5 | 99.1 | 5 | 99.0 | 10 | 99.1 |
| Q_w | 1 | 0.95 | 1 | 0.84 | 0.1 | 0.95 |
| $H_{impinge}$ | 1 | 0.32 | 1 | 0.31 | 0.1 | 0.21 |
| W_{rel} | 5 | 1.05 | 5 | 1.05 | 10 | 1.01 |
| C_{rel} | 1 | 0.95 | 1 | 1.00 | 0.1 | 1.07 |

For Case 3, ERE and W_{rel} are further emphasized by increasing their desirability weights to 10 while decreasing the other weights to 0.1. L_{comb} is shortened to respond to the increased emphasis on weight minimization. Maintaining the high level of ERE requires large increases in ΔP_f and α to increase the radial component of the fuel jet momentum. The increase in ΔP_f causes over-penetration of the fuel jet which results in an increase in wall heat flux. The large increase in α yields the expected decrease in $H_{impinge}$ which increases the injector face heat flux. The additional emphasis on ERE and C_{rel} yields essentially no increase in ERE in this range of ΔP 's, although a small weight savings is seen. These marginal improvements are offset by fairly large increases in C_{rel} and Q_{inj} .

SUMMARY

An unlike impinging GO_2/GH_2 injector element design has been employed to facilitate optimization studies. Starting with propellant pressure drops, combustor length, and impingement half-angle, an empirical design methodology was used to calculate the dependent variables for 163 design points. The dependent variables were energy release efficiency, chamber wall and injector face heat fluxes, relative chamber weight, and relative injector cost. The response surface methodology was used to fit the results with quadratic polynomials. Desirability functions were used to create joint response surfaces which were used in the optimization studies.

Three sets of results were generated to illustrate the capability of *method i* in the context of injector design and optimization. The first set of results started with a design optimized for ERE and Q_w , then added the other three dependent variables to the design one at a time. Each sequential optimal design was different than previous designs with the final design being quite different than the initial design. The result qualitatively showed the importance of including as many variables as possible early in the design. The optimization techniques embodied in *method i* facilitate this early inclusion by allowing efficient management of large amounts of data.

The second set of results focuses on the inherent design trade-offs between performance and component life issues. Different weights were applied to emphasize variables related to performance (ERE and W_{rel}). While the thrust to weight ratio was improved, the adverse affect on variables related to component life (Q_w and Q_{inj}) were clearly shown. Conversely, when Q_w and Q_{inj} were emphasized, the toll on the performance variables was clear. These techniques can be used to identify both qualitative trends and to examine the quantitative trade-offs present in this and other design processes.

Finally, a third set of results was used to illustrate the effect on the over all design of different degrees of emphasis on certain variables. Over a narrower range of some of the independent variables, ERE and W_{rel} were weighted over the other variables by a factor of 5 and then by a factor of 100 in the composite desirability function. As the emphasis on ERE and W_{rel} was increased, the resulting marginal improvements were shown to be offset by the fairly large adverse effects on the other variables. *Method i* allows the designer to objectively evaluate these adverse effects as he seeks to improve the design.

The flexibility and utility of *method i* have been demonstrated in this effort. Use of *method i* can allow an injector designer to confidently and efficiently manage large amounts of data to conduct a range of design optimization studies. Constraints on independent variables can be modified to allow optimum designs to be sought in specific portions of the parameter space. Also, individual or specific groups of dependent variables can be emphasized to reflect a designer's priorities in the design optimization process.

A similar study will be conducted for a GO_2/GH_2 swirl coaxial injector element. Then, the data and response surfaces generated for the shear coaxial, swirl coaxial, and impinging elements will be used to demonstrate the ability of *method i* to select an optimum element type based on a range of constraints and design priorities.

REFERENCES

1. Personal Communication with Garry Lyles.
2. Rupe, J. H., "An Experimental Correlation of the Nonreactive Properties of Injection Schemes and Combustion Effects in a Liquid Rocket Engine," NASA TR 32-255, 1965.
3. Pieper, J. L., "Oxygen/Hydrocarbon Injector Characterization," PL-TR 91-3029, October, 1991.
4. Nurick, J. H., "DROPMIX - A PC Based Program for Rocket Engine Injector Design," JANNAF Propulsion Conference, Cheyenne, Wyoming, 1990.
5. Dickerson, R., Tate, K., Nurick, W., "Correlation of Spray Injector Parameters with Rocket Engine Performance," AFRPL-TR-68-11, January, 1968.
6. Pavli, A. L., "Design and Evaluation of High Performance Rocket Engine Injectors for Use with Hydrocarbon Fuels," NASA TM 79319, 1979.
7. Tucker, P. K., Shyy, W, Sloan, J. G., "An Integrated Design/Optimization for Rocket Engine Injectors," 34th AIAA/ASME/SAE/ASEE Joint Propulsion Conference and Exhibit, July 13-15, 1998, AIAA 98-3513, Cleveland, OH.
8. Shyy, W, Tucker, P. K. and Vaidyanathan, R., "Response Surface and Neural Network Techniques for Rocket Engine Injector Optimization," 35th AIAA/ASME/SAE/ASEE Joint Propulsion Conference and Exhibit, June 20-23, 1999, AIAA 99-2455, Los Angeles, CA.
9. Calhoon, D., Ito, J. and Kors, D., "Investigation of Gaseous Propellant Combustion and Associated Injector-Chamber Design Guidelines," Aerojet Liquid Rocket Company, NASA CR-121234, Contract NAS3-13379, July 1973.
10. Calhoon, D., Ito, J. and Kors, D., "Handbook for Design of Gaseous Propellant Injectors and Combustion Chambers," NASA CR-121234, Contract NAS3-13379, July 1973

11. Foust, M. J., Pal S., and Santoro, R. J. "Gaseous Propellant Rocket Studies Using Raman Spectroscopy," AIAA 96-2766, 32nd AIAA/ASME/SAE/ASEE Joint Propulsion Conference, July 1-3, 1996, Lake Buena Vista, FL.
12. Moser, M. D. Pal, S. and Santoro R. J., "Laser Light Scattering Measurements in a GO₂/GH₂ Uni-Element Rocket Chamber," AIAA 95-0137, 33rd Aerospace Sciences Meeting and Exhibit, January 9-12, 1995, Reno NV.
13. Santoro, R. J., "An Experimental Study of Characteristic Combustion-Driven Flow for CFD Validation," Final Report for NASA Contract NAS8-38862, October, 1997.
14. Tucker, P. K., Klem, M. D., Smith, T. D., Farhangi, S., Fisher, S. C., and Santoro, R. J., "Design of Efficient GO₂/GH₂ Injectors: A NASA, Industry and University Effort," AIAA 97-3350, 33rd AIAA/ASME/SAE/ASEE Joint Propulsion Conference, July 6-9, 1997, Seattle, WA.
15. Schley, C. A., Hagemann, G., Tucker, P. K., Venkateswaran, S. and Merkle, C. L., "Comparison of Computational Codes for Modeling Hydrogen-Oxygen Injectors," AIAA 97-3302, 33rd AIAA/ASME/SAE/ASEE Joint Propulsion Conference, July 6-9, 1997, Seattle, WA.
16. Myers, R.H. and Montgomery, D. C., Response Surface Methodology-Process and Product Optimization Using Designed Experiments, John Wiley & Sons, 1995.
17. Gill, G. S., and Nurick, W. H., "Liquid Rocket Engine Injectors," NASA SP-8089, March, 1976.
18. SAS Institute Inc. (1995). JMP version 3. Cary, NC.
19. Microsoft Corporation. (1985-1996). Microsoft Excel 97

RAMAN SPECTROSCOPY FOR INSTANTANEOUS MULTIPOINT, MULTISPECIES GAS CONCENTRATION AND TEMPERATURE MEASUREMENTS IN ROCKET ENGINE PROPELLENT INJECTOR FLOWS

Joseph A. Wehrmeyer
Research Associate Professor
Mechanical Engineering Department
Vanderbilt University

Huu Phuoc Trinh
Combustion Devices Group
Subsystem and Component Development Department
Space Transportation Directorate

Abstract

Propellant injector development at MSFC includes experimental analysis using optical techniques, such as Raman, fluorescence, or Mie scattering. For the application of spontaneous Raman scattering to hydrocarbon-fueled flows a technique needs to be developed to remove the interfering polycyclic aromatic hydrocarbon fluorescence from the relatively weak Raman signals. A current application of such a technique is to the analysis of the mixing and combustion performance of multijet, impinging-jet candidate fuel injectors for the baseline Mars ascent engine, which will burn methane and liquid oxygen produced in-situ on Mars to reduce the propellant mass transported to Mars for future manned Mars missions. The present technique takes advantage of the strongly polarized nature of Raman scattering. It is shown to be discernable from unpolarized fluorescence interference by subtracting one polarized image from another. Both of these polarized images are obtained from a single laser pulse by using a polarization-separating calcite rhomb mounted in the imaging spectrograph. A demonstration in a propane-air flame is presented.

Introduction

Technology development associated with advanced space transportation propulsion systems includes design and analysis of new types of propellant injectors. An effort exists at NASA-Marshall to include experimentally-obtained reactant/product mixing/combustion information as part of the injector analysis. Hardware associated with this effort includes an optically-accessible high pressure combustion chamber sized for single-element fuel injectors (unielelement test article) and a newer, larger modular combustion test article (MCTA) that can accommodate multi-element fuel injector configurations and that is also optically-accessible. Optical accessibility allows laser-based methods, such as laser Mie scattering, fluorescence, and spontaneous Raman scattering, to be applied. Raman spectroscopy has been used to analyze an oxygen-rich gaseous hydrogen/liquid oxygen (GH_2/LOx) injector flow in the unielelement test article (1) and most recently is being considered for use in the MCTA to analyze the mixing and combustion performance of multijet, impinging-jet candidate fuel injectors for the baseline Mars ascent engine (2). This engine will burn methane (CH_4) and LOx produced in-situ on Mars to reduce the propellant mass transported to Mars for future manned Mars missions (3).

Application of Raman spectroscopy to hydrocarbon-fueled combustion brings the issue of interference of the weak Raman scattering light signals with strong laser-induced fluorescence. The fluorescence interference can be from polycyclic aromatic hydrocarbons (PAH's) which are excited and fluoresce across the ultraviolet and visible spectrum (4) and when using ultraviolet lasers can be due to the hydroxyl radical (OH) and to vibrationally-excited O₂, both of which are present in combustion reaction zones (5). By taking advantage of the polarization properties of Raman scattering, it is possible to discriminate the Raman signal from interfering fluorescence interference and hence apply Raman scattering to the analysis of hydrocarbon-fueled combustion. This can be done by obtaining two Raman images, one using a vertically polarized laser and one using a horizontally-polarized laser, and then subtracting the intensity of one image from another to obtain a net Raman signal (6). A second method that lends itself to single-pulse (and hence instantaneous) measurements is to obtain two simultaneous Raman images created from the same laser pulse. One of these images is the vertically-polarized signal and one is for the horizontally-polarized signal. The difference between these images provides the net Raman signal, free of fluorescence interference. This technique has been demonstrated for a time-averaged application (7) and this paper describes a single-pulse application of the technique.

Background

Raman scattering is a weak light scattering process that can be understood by realizing that molecular internal energy can be stored in several modes, including: electronic (quantum mechanical energy level described by the labels *X*, *A*, *B*, etc.), vibration ($v = 0, 1$, etc.), and rotation ($J = 0, 1$, etc.), and that light energy is quantized into photons and the energy of each photon is inversely proportional to wavelength. A Stokes Q-branch Raman scattering process involves an absorption of one laser photon at the laser wavelength λ_{LASER} and a subsequent emission of a photon with less energy at a longer wavelength. The Raman wavelength λ_{RAMAN} depends on the vibrational energy level spacing of the laser and hence is different for each molecule. The Raman scattering signals are linearly related to the density of each molecular species and are all relatively weak compared to other light scattering processes, such as Rayleigh scattering and fluorescence. To increase Raman signal strength a UV laser can be used because Raman signal strength for a given laser power increases with a decrease in laser wavelength (5). For the present work a pulsed UV laser, in particular a pulsed, narrowband, tunable KrF excimer laser is used which produces light in a 0.001 nm bandwidth that is tunable from 248 to 249 nm and is pulsed up to 50 Hz with a pulse energy of 400 mJ and a pulse length of 20 nsec. Using a pulsed laser allows rejection of continuous flame emission by gating the light detection system on only during the laser pulse. A narrowband, tunable laser is used to minimize the problem of laser-induced OH and O₂ fluorescence by tuning the laser bandwidth between fluorescence excitation lines (5), at least for atmospheric pressure flames, but for high pressure flames pressure broadening becomes so prevalent that some OH and O₂ is to be expected (1).

Figures 1a and 1b shows simulated Raman spectra, using RAMSES (8) for 300 K reactants in the baseline Mars ascent engine (CH₄ and O₂) for the baseline O/F ratio of 3. Figure 1b shows the expected Raman spectrum at adiabatic equilibrium and a chamber pressure of 250 psia. These spectra show how Raman scattering can reveal both the extent of mixing of propellents near the injector face (by the amount of simultaneous occurrence of CH₄ and O₂) and the extent of reaction (by the relative amounts of reactants and products detected). The signal strength of Raman scattering depends on two molecular invariants, the square of the mean polarizability $(\alpha')^2$ and the square of the anisotropic polarizability $(\gamma')^2$. These are used in an

equation for a constant Φ , that can be considered as the Raman scattering cross section for a single molecule. The value of Φ also depends on the polarization of the incident laser beam, the polarization of the detected Raman signal, and the angle of detected Raman signal with respect to incoming laser beam. For a 90° collection angle and for the Raman and laser beams both in a horizontal plane, the value of Φ for vertically polarized Raman signal is (9):

$$\Phi = (a')^2 + 1/45 (\gamma')^2$$

and for horizontally polarized Raman signal Φ is:

$$\Phi = 1/60 (\gamma')^2$$

Usually a'^2 and γ'^2 are similar in magnitude and thus the vertically polarized light is almost two orders of magnitude greater than the horizontally polarized light. Thus the Raman scattering signal essentially retains the polarization of the incoming laser beam. However a fluorescence light emission process does not retain the laser polarization because of the relatively long time the molecule exists in the excited state before fluorescing. During this time the molecule rotates, eliminating any correlation between the polarization of absorbed and emitted photons.

The difference in polarization properties between Raman and fluorescence is exploited in the experimental system shown schematically in Fig. 2. It represents a typical UV Raman system in that a pulsed, narrowband KrF UV laser is used as the light source and an imaging spectrograph coupled to a gated, intensified CCD camera is used as the detection device. The intensifier and laser are triggered simultaneously using a Princeton Instruments PG200 programmable pulser. The laser is focused to a beam waist of $250 \mu\text{m}$ using a 500 mm focal length lens. The unique feature of this system is the insertion of a calcite rhomb just behind the entrance slit of the spectrograph. This optical element displaces the horizontally polarized Raman image about 5 mm from the vertically polarized Raman image, which travels directly straight through the rhomb. The length of the entrance slit is limited to 4 mm to keep the two polarized images from overlapping. Figure 3 shows a typical single-pulse image obtained from the experimental system, and this image shows the relative strength of vertically polarized signal compared to horizontally polarized signal. The H_2O Raman signal (from air humidity) is almost completely polarized, while the N_2 signal is slightly depolarized and the O_2 signal is more depolarized than N_2 . This corresponds to others' experimental observations (6,10).

Spatially-integrated single-pulse Raman spectra are shown in Fig. 4, obtained from a slightly premixed C_3H_8 -air bunsen flame. One of these spectra is the vertically polarized Raman-fluorescence signal. The horizontally polarized signal shows essentially only the fluorescence signal, which has two contributions. A broadband component is caused by PAH fluorescence, extending from below 255 nm to above 275 nm . A second contribution to the fluorescence background is the OH fluorescence from about 265 to 270 nm , caused by tuning the laser slightly onto a strong OH transition. This is done to demonstrate the ability of the technique to simultaneously measure Raman spectra and OH fluorescence. Before subtracting the horizontally polarized signal from the vertical it is first multiplied by a factor of 2.22 to account for the ratio in transmission efficiency (for the spectrometer/calcite rhomb) between the vertically and horizontally polarized signals. The net signal shows a fluorescence-free Raman spectrum that shows the simultaneous occurrence of CO_2 and H_2O (products of combustion), CO

and H_2 (intermediate products), and unburned C_3H_8 . Information about the spatial structure of the flame can be revealed in the single-pulse image of Fig. 5. This image shows unburned C_3H_8 occurring near the 0 mm position. The cooler, denser unburned gas mixture also provides a stronger N_2 Raman signal near that location. At ~ 1.5 mm the C_3H_8 pyrolyzes into other hydrocarbons, including PAH's that cause a strip of broadband fluorescence to appear at this location. Farther into the flame chemical reactions involving oxidation take place, creating the OH intermediate. This shows up in Fig. 5 by the replacement of PAH fluorescence with OH fluorescence at flame positions greater than ~ 2.5 mm. By subtracting the scaled upper part of Fig. 5 (horizontally polarized fluorescence signal) from the bottom part (vertically polarized signal), and by summing the net Raman signal for each location (wavelength integration) a qualitative picture of the structure of the flame can be discerned, as in Fig. 6. This figure shows the drop in C_3H_8 signal and the concurrent increase in H_2O signal, showing the formation of that product occurring close to the fuel zone. In the same region the H_2 and CO signals are generally higher than in the fuel zone or in the OH reaction zone past 2.5 mm.

Summary and Conclusions

Taking advantage of the strongly polarized nature of Raman scattering, it can be discerned from unpolarized fluorescence interference by subtracting one polarized image from another. Both of these polarized images can be obtained from a single laser pulse by using a polarization-separating calcite rhomb mounted in the imaging spectrograph. This reduces the imaged laser beam length from 12.5 mm down to 4 mm but allows fluorescence-free Raman measurements in propane-air flames. In the pyrolysis zone of these flames considerable PAH fluorescence exists and in a separate flame zone there exists considerable OH fluorescence. However the polarization separation technique is robust enough to allow simultaneous Raman and OH fluorescence measurements to be obtained, which can provide even more information about flame chemical reaction zones.

References

1. Wehrmeyer, J. A., J. M. Cramer, R. H. Eskridge, and C. C. Dobson, "UV Raman Diagnostics for Rocket Engine Injector Development," AIAA Paper 97-2843, 1997.
2. Mueller, P. J., D. W. Plachta, T. Peters, J. C. Whitehead, "Subscale Precursor to a Human Mars Mission Using In-Situ Propellant Production," AIAA Paper 98-3301, 1998.
3. Kos, L., "The Human Mars Mission: Transportation Assessment," Space Technology and Applications International Forum Conference, Albuquerque, N.M., Conference Proceedings Part III, p. 1211, Jan. 1998.
4. Smyth, K., *Combustion and Flame*, 1999.
5. Wehrmeyer, J. A., T.-S. Cheng, and R. W. Pitz, "Raman Scattering Measurements in Flames Using a Tunable KrF Excimer Laser," *Applied Optics* 31: pp. 1495-1504, 1992.
6. Grünefeld, G., V. Beuhausen, and P. Andresen, "Interference-Free UV-Laser-Induced Raman and Rayleigh Measurements in Hydrocarbon Combustion Using Polarization Properties," *Applied Physics B* 61: pp. 473-478.
7. Hartfield, R., C. Dobson, R. Eskridge, and J. Wehrmeyer, "Development of a Technique for Separating Raman Scattering Signals from Background Emission with Single-Shot Measurement Potential," AIAA Paper 97-3357, 1997.
8. Hassel, E. P., "Ultraviolet Raman Scattering Measurements in Flames Using a Narrowband Excimer Laser," *Applied Optics* 32, 1993.
9. Long, D., "Raman Spectroscopy," McGraw-Hill, 1977.
10. Penney, C. M., L. M. Goldman, M. Lapp, "Raman Scattering Cross Sections," *Nature Physical Science* 235: pp. 110-112.

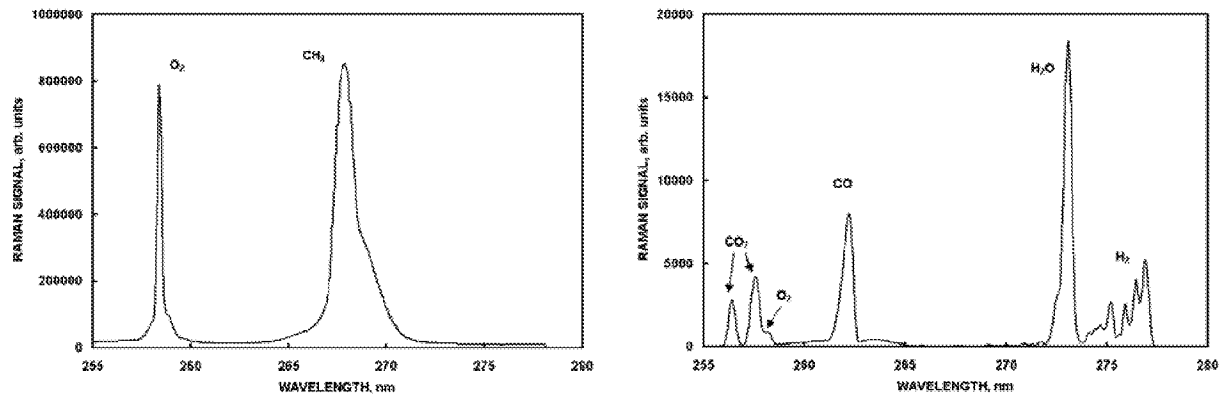


Fig. 1a,b. Simulated Raman spectra using RAMSES for Mars ascent engine baseline conditions: methane/oxygen mass ratio = 3, chamber pressure = 250 psia, adiabatic flame temperature = 3390 K. a (left) 300 K reactants. b(right) completely reacted products.

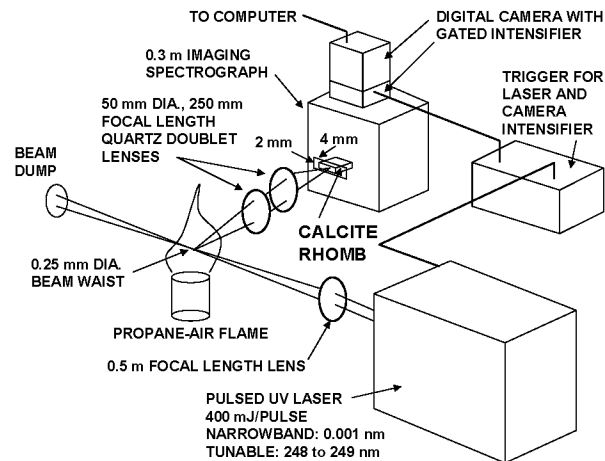


Fig. 2. Schematic of UV Raman system with calcite rhomb located inside imaging spectrograph.

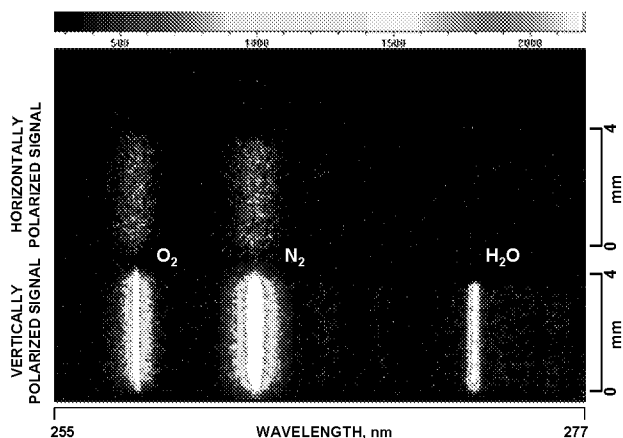


Fig. 3. Single-pulse, polarization-resolved Raman image in humid air.

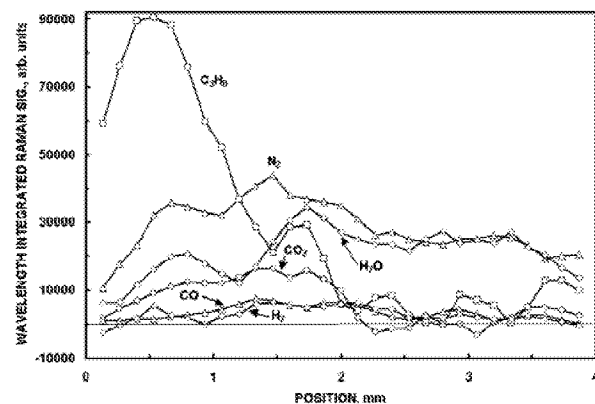


Fig. 6. Net wavelength-integrated Raman signal vs. position for image of Fig. 5.

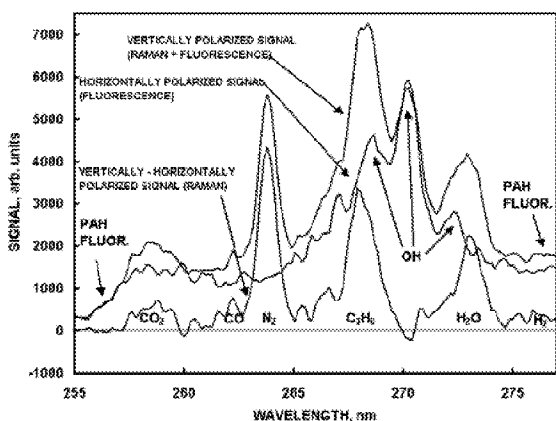


Fig. 4. Single-pulse, polarization-resolved Raman spectra in propane-air flame.

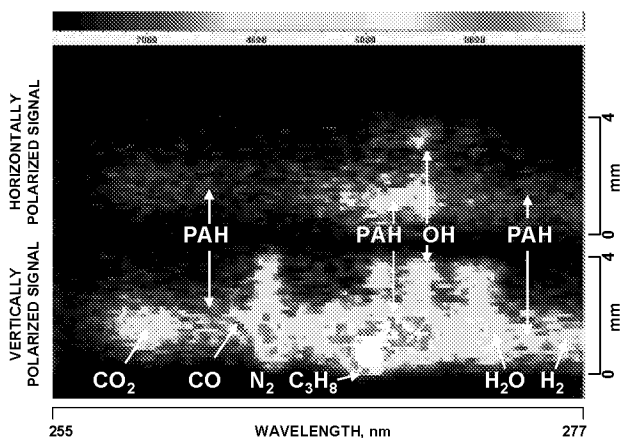


Fig. 5. Single-pulse, polarization-resolved Raman image in propane-air flame.



FASTRAC GAS GENERATOR TESTING

Tomas E. Nesman and Jay Dennis
Subsystem and Component Development Department
Space Transportation Directorate, NASA, MSFC

ABSTRACT

A rocket engine gas generator component development test was recently conducted at the Marshall Space Flight Center. This gas generator is intended to power a rocket engine turbopump by the combustion of Lox and RP-1. The testing demonstrated design requirements for start sequence, wall compatibility, performance, and stable combustion. During testing the gas generator injector was modified to improve distribution of outer wall coolant and the igniter boss was modified to investigate the use of a pyrotechnic igniter. Expected chamber pressure oscillations at longitudinal acoustic mode were measured for three different chamber lengths tested. High amplitude discrete oscillations resulted in the chamber-alone configurations when chamber acoustic modes coupled with feed-system acoustics modes. For the full gas generator configuration, which included a turbine inlet manifold, high amplitude oscillations occurred only at off-design very low power levels. This testing led to a successful gas generator design for the Fastrac 60,000 lb thrust engine.

NOMENCLATURE

| | |
|------|--------------------------------------|
| D | diameter |
| L | length |
| x | axial station downstream of injector |
| f | frequency |
| P | pressure |
| p' | fluctuating pressure |
| O/F | oxidizer to fuel mixture ratio |

SUBSCRIPTS

| | |
|-----|----------------------|
| g | turbulence generator |
| c | combustion chamber |

INTRODUCTION

A gas generator for a 60,000 pound thrust rocket engine was tested at the Marshall Space Flight Center (MSFC) test stand 116 (Figure 1) in 1997 and 1998. This was a Fastrac approach to design and development which required a robust design, success oriented schedule, and minimal testing. The gas generator is a small cylindrical chamber where Lox and RP-1 were injected and burned at a low oxidizer to fuel (O/F) mixture ratio. The gas generator chamber was tested alone and in combination with a turbine inlet manifold (TIM). In the engine configuration, the hot gas discharges from the gas generator into the turbine inlet manifold which is an annular volume where small nozzles direct the flow into the turbine blade rows to power the Fastrac turbopump. In the initial component test configuration, the hot gas discharges from the gas generator through a small nozzle into ambient atmosphere. In the final component test configuration, the hot gas discharges into a turbine inlet manifold before exiting to the atmosphere.

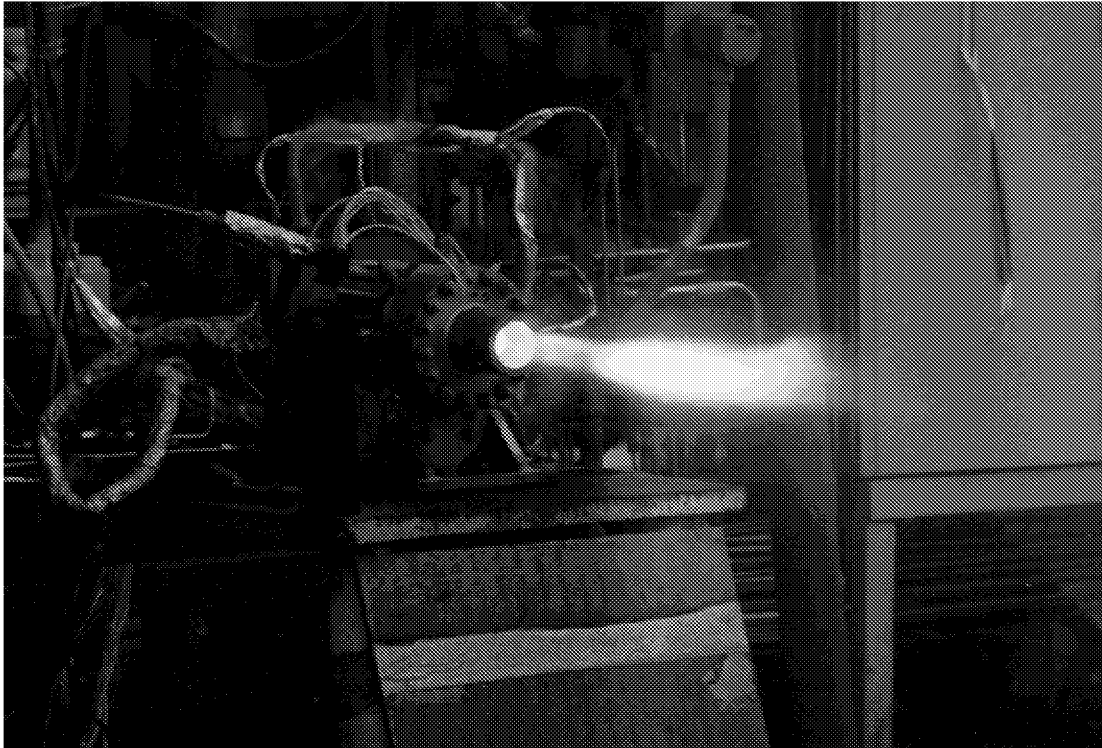


Figure 1. TS116 GG Component Hof fire

The objective of the gas generator testing was to develop a design that would operate on the Fastrac engine. This was to be accomplished by defining operational regimes, comparing some chamber and trip ring variations, and verifying wall compatibility. In the course of testing the issues that surfaced were: 1. Accurate properties of Lox/RP-1 combustion gas, 2. Injector pattern as it related to wall compatibility, 3. Ignition system design, and 4. Internal fluctuating pressure environment and potential effect on the turbine. These issues were all investigated using various configurations of the gas generator test article (Figure 2). The focus of this paper is on the last issue, i.e., the gas generator internal fluctuating pressure environments.

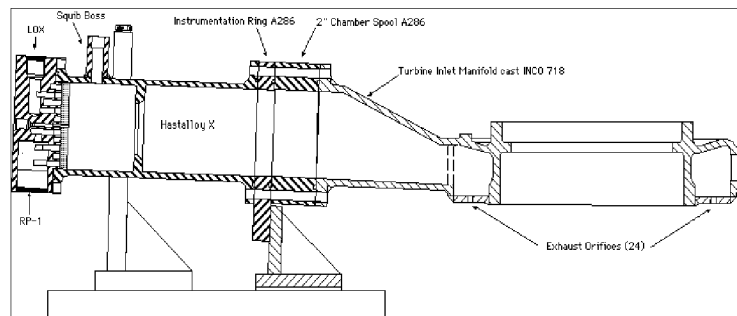


Figure 2. GG Test Article

TEST ARTICLE

The gas generator hardware consists of an injector, combustion chamber, turbulence ring, instrumentation ring, chamber spools, and turbine simulator. The gas generator component tests were conducted with several variations to the test article hardware. The combustion chamber diameter, D , remained constant and the turbulence generator diameter, D_g , at $0.6 D$ through all the testing. However the injector pattern, length of the chamber (L), position of the turbulence generator (x_g), and turbine simulator were all varied at some point in the testing.

The basic gas generator test article (Figure 3) is a cylindrical enclosure with an injector at the head end, a flow restrictive trip ring near the head end, and a concentric hole discharge. The injector elements were paired, self-impinging RP-1 orifices enshrouding a single oxidizer showerhead orifice (F-O-F triplet). An igniter boss is located near the injector face. The flow restrictive trip ring is a turbulence generator and was configured at either $x_g = 0.57 D$ or $x_g = 0.85 D$ downstream of the injector. This version of the test article differs from the engine configuration which has a gradually tapering discharge and an annular manifold. The test article chamber also had spools inserts to vary chamber length. An instrumentation ring was located at $x_g = 2.32 D$ down the chamber.

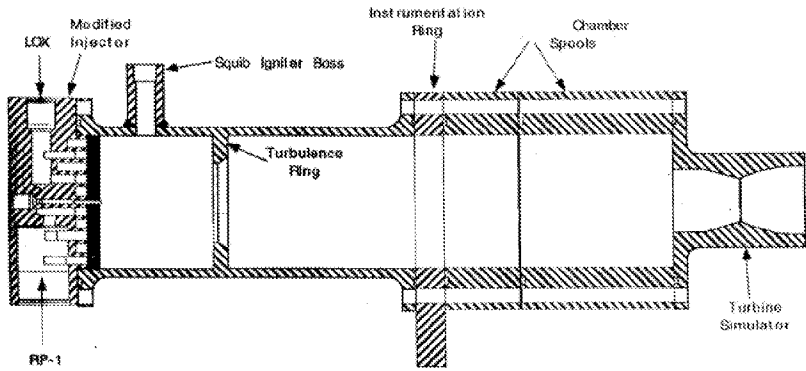


Figure 3. Cross-section of Basic GG Test Article

During testing the injector was modified to improve distribution of outer wall coolant and the igniter boss was also modified to investigate the use of a pyrotechnic igniter. After cooling, ignition, and combustion issues were resolved subsequent tests were conducted with a tapered gas generator discharge (Figure 4) and a turbine inlet manifold (Figure 5).

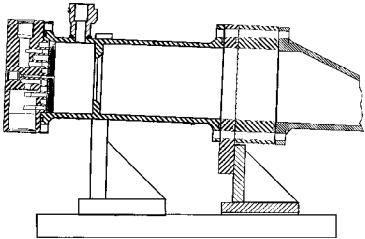


Figure 4. GG with Tapered Discharge

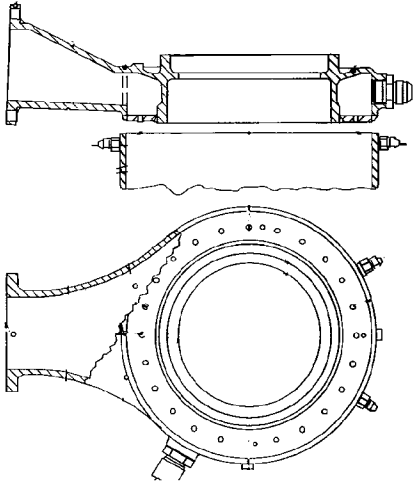


Figure 5. Tapered Discharge and Turbine Inlet Manifold

INSTRUMENTATION

The gas generator test article was designed with a ring that could be inserted into the chamber body with a full array of instrumentation. The instrumentation ring contained a high frequency pressure transducer and several thermocouples. Five thermocouples were inserted into the chamber through the instrumentation ring with varying depths of penetration.

Selected gas generator measurements were recorded on the test stand 116 high sample data system (Table 1). Typically from 11 to 14 of these measurements were recorded on any one test. The high sample test data were lowpass filtered at 10,000 Hz and then sampled at 40,000 samples per second. One dynamic pressure transducer was close-mounted to the chamber inner wall but the other pressure measurements were susceptible to senseline resonance with limited usefulness for evaluating fluctuating pressure amplitudes.

Table 1. High Sample Data Instrumentation

| MSID | NOMENCLATURE | UNITS |
|--------|----------------------------------|-------|
| P3001 | GG Pc dynamic pressure | PSI |
| P3004 | GG Pc pressure #1 | PSI |
| P3005 | GG Pc pressure #2 | PSI |
| P8307 | GG Pc upstream turb ring | PSI |
| A3001 | Axial accel injector | G PK |
| A3002 | Radial accel | G PK |
| A3003 | Injector inlet | G PK |
| P2305 | GG Lox injection | PSI |
| P4304 | GG TEA injection pressure | PSI |
| P7350 | Turbine inlet manifold simulator | PSI |
| P8306 | Fuel manifold pressure #1 | PSI |
| P8307 | Fuel manifold pressure #2 | PSI |
| P8308 | GG fuel inlet at RP1 filter | PSI |
| DP8309 | Fuel injection ΔP | PSI |
| T7301 | ¢ GG temp. at instr. ring | mV |
| TC7302 | ¼ dia. GG temp. at instr. ring | mV |

TEST RESULTS

Four series of gas generator hotfire tests were conducted at test stand 116. Thirty seven component hotfire tests in all were completed during the gas generator development. Series 1 consisted of tests 1 through 8 which were conducted in summer of 1997. These tests featured the modified triplet element injector with film coolant holes and the baseline gas generator combustion chamber. The eight tests were conducted with chamber pressures, at the injector end, ranging from 505 to 705 psia and oxidizer-to-fuel mixture ratios ranging from 0.25 to 0.36. The gas generator chamber was exhausted through a 1.1" diameter nozzle. Test duration varied from 64 seconds to 154 seconds (flight duration).

Series 2 consisted of tests 9 through 24 conducted in fall 1997. Tests 9 through 12 had the gas generator exhausting through outer nozzles, and tests 13 through 15 went back to the first nozzle configuration. Power spectral density analysis (PSD) showed an anomalous 1600 - 1870 Hz frequency in the chamber fluctuating pressure and accelerometers. This frequency appears to coincide with a broader acoustic mode frequency early on in test 13, the end of test 21, and throughout test 22. The oscillation showed up at a discrete 1660 Hz, with harmonics, on test 23 (Figure 6). The pressure oscillations produced vibrations of around 26 G rms (Figure 7).

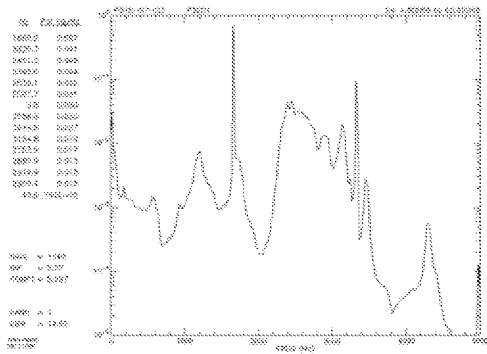
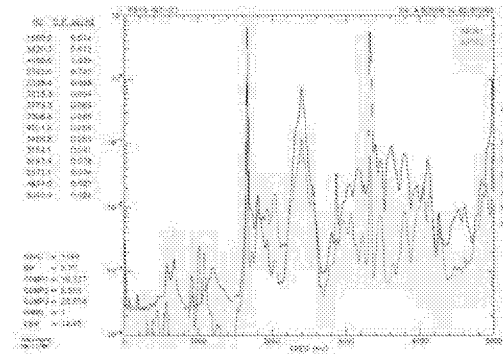


Figure 6. Chamber Pressure PSD



Series 4 consisted of tests 31 through 37 in fall of 1998. This series completed the planned gas generator component development test program. The primary objectives of this series of tests were to repeatedly demonstrate proper ignition of the gas generator using a new pyrotechnic igniter and operation at 40-50% power level. Additional objectives were to gather thermal environment data on the cast turbine inlet manifold and demonstrate good ignition with a helium atmosphere in the gas generator. All test objectives were met and the new igniters performed well. On these tests, however, the gas generator exhibits significant chamber pressure oscillations at chamber pressures below 260 psia (47% of nominal). An interesting example of this occurred on test 34 where a "jump" to higher oscillation levels (Figure 9) was coincident with a "shift" in chamber hot gas temperature (Figure 10) and some chamber oscillation frequencies changed from narrow band random peaks (Figure 11) to high amplitude discrete peaks (Figure 12).

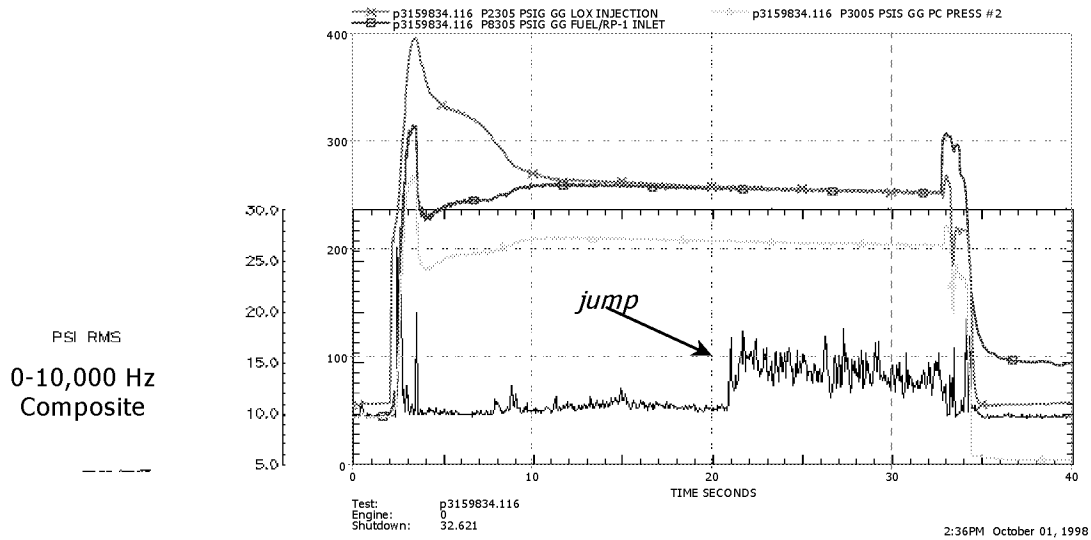


Figure 9. Low Pc Test "Jump" in Oscillation Amplitude

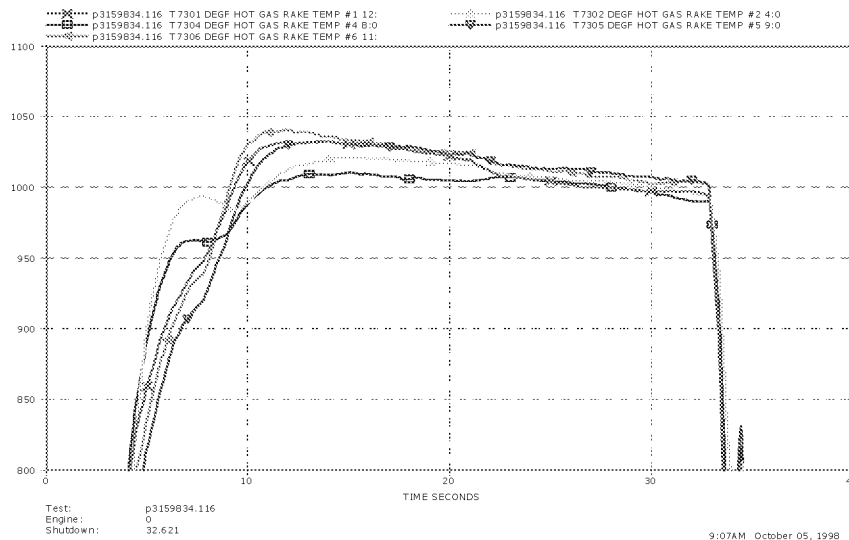


Figure 10. Low Pc Test "Shift" in Hot Gas Temperatures

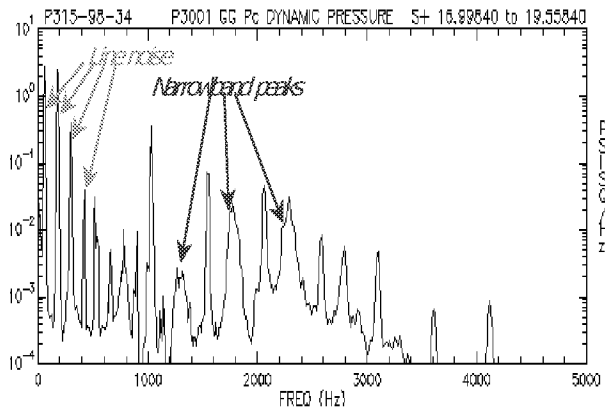


Figure 11. Low Pc Test "Before-Jump" PSD

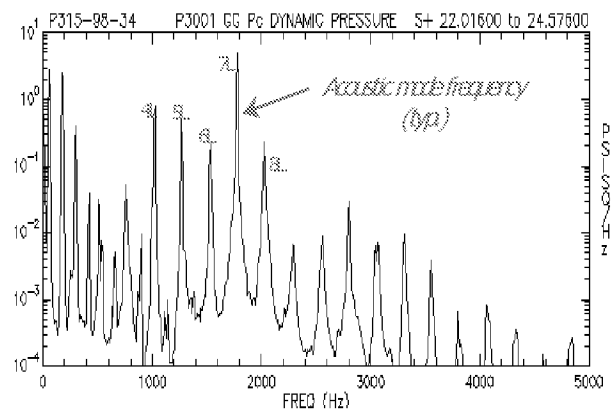


Figure 12. Low Pc Test "After-Jump" PSD

GENERAL RESULTS

Based on the general characteristics of gas generator chamber oscillations several oscillation mechanisms were postulated. Acoustic waveguides of the fluid systems were postulated as the resonators and fluid mechanisms as excitors. The acoustic modes of the gas generator were of prime importance. The chamber axial dimensions and oxidizer to fuel mixture ratio (O/F) were two of the key parameters affecting acoustics that were varied during Fastrac gas generator component testing. Three different gas generator chamber lengths, L , were tested. The range of test mixture ratios varied from a low O/F = 0.18 to a high O/F = 0.37. Table 2 shows the gas generator test numbers in a matrix of chamber length versus mixture ratio. The outlined test numbers in Table 2 indicate the use of turbulence ring at $x_g = 0.85 D$ downstream of the injector instead of $x_g = 0.57 D$.

Table 2. Test Matrix

| (O/F) | Test Numbers | | |
|---------------------------|--------------|------------------------|------------------------|
| | $L = 11''$ | $L = 15''$ | GG + TIM |
| Low MR (.18 - .26) | 10, 11, 12, | 13, 15, 16, 17, 18, | 28, 29 |
| Nominal MR (.27 - .32) | 3, 4, 5, | 6, 7, 8, 9, 19, 21, 23 | 26, 27, 30, 31, 34 |
| High MR (.33 - .37) | | 14, 20, 22, 24 | 25, 32, 33, 35, 36, 37 |

ACOUSTIC ANALYSIS

The properties of the Lox / RP-1 hot gas at mixture ratios of around 0.3 are difficult to determine. The best source of this information is a set of data and curve fits resulting from an Aerojet study.¹ Estimates of sound speed using equilibrium equations were higher than measured in the Aerojet study. An empirical analysis combining both sound speed estimations and measured hot gas temperature and pressure led to a nominal average chamber sound speed of 1441 ft/s. Furthermore, computational fluid dynamic analysis² showed sound speed varying from around 700 ft/s near the injector to 1000 ft/s at the turbulence generator and increasing towards the nozzle. The nominal fluid properties for the oxidizer and fuel are shown in Table 3 along with the hot gas properties at three different mixture ratios.

Table 3. Fluid Properties

| Component | Fluid | Flow rate (lb _m /s) | Temp (°R) | Press (psia) | Density (lb/ft ³) |
|----------------|----------|--------------------------------|-----------|--------------|-------------------------------|
| GG chamber | O/F=0.25 | 8.1 | 1,470 | 551 | 1.350 |
| | O/F=0.31 | 7.2 | 1,616 | 542 | 0.970 |
| | O/F=0.36 | 6.4 | 1,706 | 532 | 0.717 |
| Oxidizer Inlet | Lox | 1.7 | 211 | 686 | 63.03 |
| Fuel Inlet | RP-1 | 5.46 | 523 | 630 | 49.5 |

Since the gas generator is a long cylinder, standing acoustic waves were expected as in an organ pipe. Even with the turbine inlet manifold ring attached a variety of standing wave pressure patterns can be envisioned (Figure 13). For acoustic waves in the chamber, the injector will provide a near rigid termination as will the nozzle end for the gas generator alone configurations. The turbulence ring will serve to block some axial gas oscillation and will also generate downstream shear layer oscillations. The acoustic modal patterns can be checked for consistency with measured relative phase from available high frequency measurements.

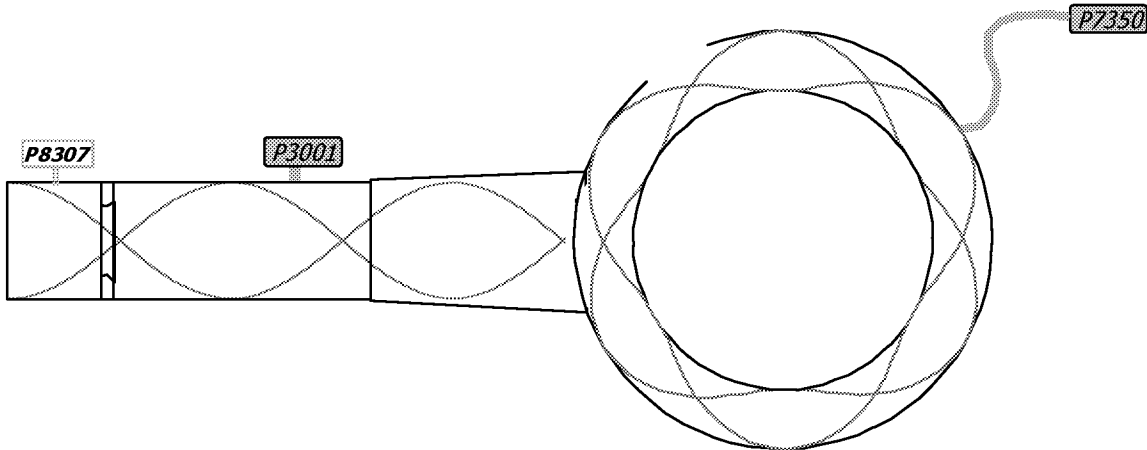


Figure 13. GG+TIM Acoustic Mode (typical)

Estimates were made of the gas generator test article acoustic mode frequencies where a constant sound speed of 1440 ft/s was assumed and the gas generator combustion chamber was modeled as a closed-closed pipe element. The GG + TIM frequencies were estimated determining the stem and top resonance frequencies of a T-tube pipe element.³ The physical system was approximated by assuming static (no flow) hot gas within a T-tube having all pipe radii equal. Various top and stem standing wave combinations were determined.

The major peaks from measured gas generator chamber dynamic pressure spectra were compiled for most tests. The spectral peaks occur in integer multiples as would be expected from longitudinal acoustic modes of the gas generator chamber. The measured peak frequency divided by integer multiple was plotted versus sound speed (Figure 14). This plot shows the data divides into three distinct linear trends based on the chamber length.

Table 4. Acoustic Mode Frequencies (Hz)

| Mode | GG 11 | GG 15 | GG + TIM |
|--------|-------|-------|----------|
| 1 T | 2,952 | 2,952 | 2,952 |
| 2 T | 4,897 | 4,897 | 4,897 |
| 1 R | 5970 | 5970 | 5970 |
| 1 L | 786 | 576 | 252 |
| 2 L | 1,572 | 1,153 | 511 |
| 3 L | 2,358 | 1,729 | 758 |
| 4 L | 3,144 | 2,306 | 1023 |
| TIM 1T | -- | -- | 765 |
| TIM 2T | -- | -- | 1275 |

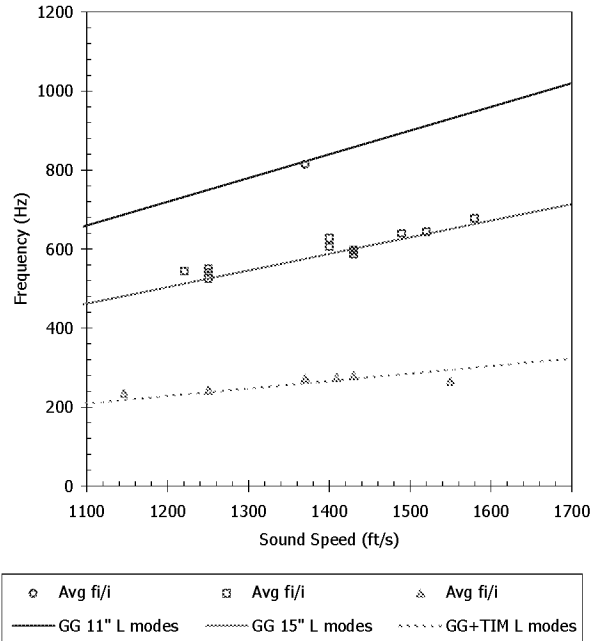


Figure 14. Measured GG Oscillation Frequencies

The instrumentation ring was well situated for measuring chamber pressure fluctuations, however, it would not be available on the gas generator used in turbopump and engine testing. For those tests the chamber pressure was measured at a boss located in the chamber wall between the injector and the turbulence ring. Some of the last gas generator component tests were conducted with dynamic pressure transducers located in the new location and in the instrumentation ring. The new transducer was able to detect most of the discrete spectral peaks from the chamber acoustic modes, however, the magnitudes were significantly lower than measured at the instrumentation ring (Figure 15).

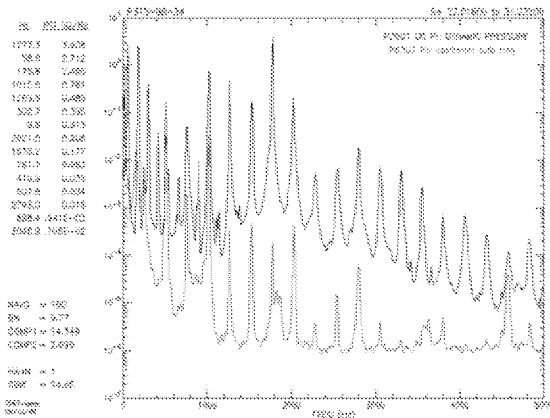


Figure 15. Measurement Location Change

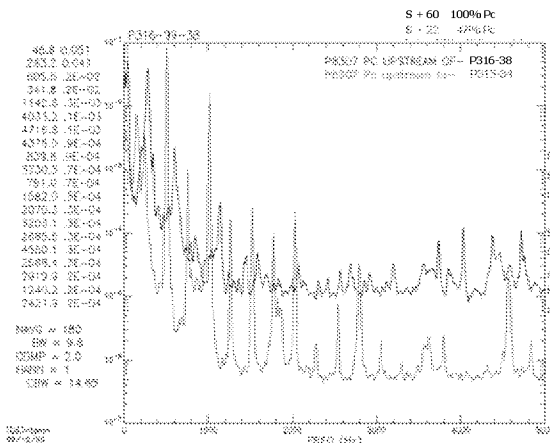


Figure 16. TPA and GG Pc Log PSD's

The turbopump assembly (TPA) was tested several times with a gas generator to power the turbine. On these tests the gas generator chamber fluctuations were measured at the boss between the injector and the turbulence generator. A comparison of the chamber fluctuations from the gas generator on the turbopump assembly to the gas generator component test (Figure 16) shows that in the former the acoustic modes are not excited.

Furthermore, the fluctuations that do occur have been identified as related to a 1.2 times synchronous frequency that is a rotating cavitation signature from the Lox pump. The pump related oscillations are of significantly lower amplitude than the acoustic resonance peaks from the gas generator test article as observed in the chamber pressure fluctuations (Figure 17) and injector accelerometers (Figure 18).

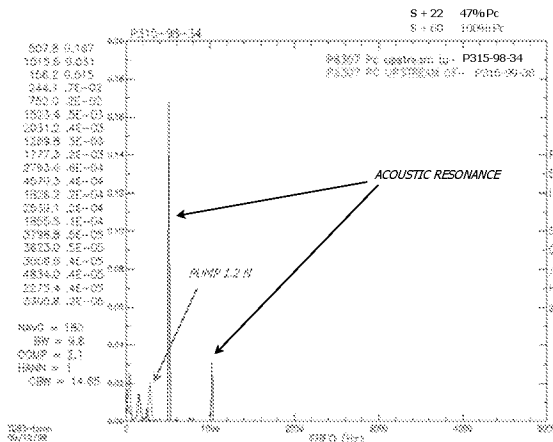


Figure 17. GG and TPA Pc Linear PSD's

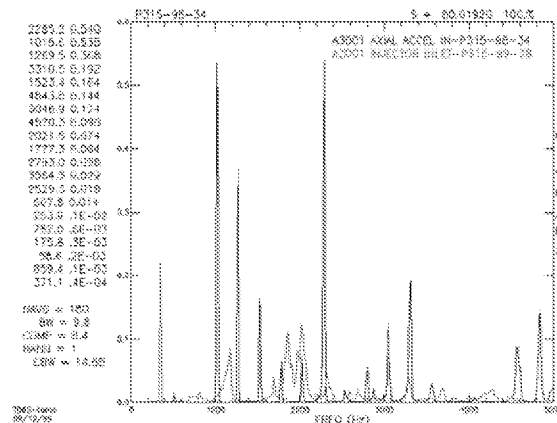


Figure 18. GG to TPA Accel Linear PSD's

EXCITATION ANALYSIS

High amplitude oscillations in the gas generator require excitation of the acoustic resonators. The potential flow exciters considered were broadband flow noise, discrete shear layer oscillation (self-excited), and vortex shedding. Another potential excitation considered was coincidence with feedsystem acoustics. The validity of each of these phenomena as the excitation mechanism for the high amplitude oscillation was assessed based on interpretation of the dynamic data.

The first flow excitation mechanism considered was broadband flow noise. The source of this noise would be the injector flow impingement, breakup, and mixing plus the secondary mixing from turbulence and diffusion. The response would be in the form of broad spectral peaks at the gas generator longitudinal acoustic mode frequencies. Since the high amplitude oscillation spectra display narrow (discrete) peaks, this mechanism was rejected.

The second flow excitation considered was a discrete shear layer oscillation. The source of this mechanism would be shearing flow at the turbulence generator ring. This would become a self-excited oscillation if the shearing flow impinges on the downstream nozzle with feedback to the flow separation point. The mechanism would be characterized by discrete spectral peaks, frequency variation with flow rate, and “lock-in” with acoustic modes. The measured oscillations fit this mechanism with nondimensional frequencies (Strouhal numbers) matching empirically estimated upper stage modes. High amplitude oscillations were observed with the GG+TIM configuration however, which did not have a downstream impingement point. For this reason this mechanism was rejected.

The third flow excitation mechanism is vortex shedding. The instrumentation ring thermocouple probes protruding into the hot gas flow were the only possible source of vortex shedding oscillations. The vortex shedding frequency would be expected to vary with flow rate. The estimated frequencies from this mechanism did not match the high amplitude oscillation frequencies, therefore this mechanism was rejected.

One final excitation considered was feedsystem coupling. In this type of oscillation, one of the feedlines would be in resonance with combustion chamber acoustics and the other feedline would be passive. Though flush mounted feedline pressure measurements were not available to identify feedline acoustic mode frequencies, some hint of these frequencies was detected in the existing pressure measurements despite the senseline effects.

In addition, frequency response functions showed some correlation between feedline measurements and chamber measurements during high amplitude oscillations. On test 34, for example, based on coherence (Figure 19) it appears that the lox feedline is a passive element in the high amplitude oscillation resonance. On this same test however, the fuel feedsystem (Figure 20) and the turbine inlet manifold (Figure 21) appear to participate in the acoustic resonance of the chamber.

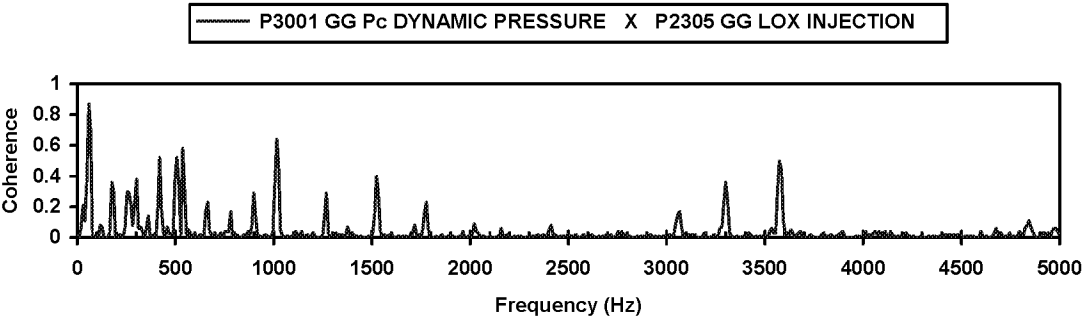


Figure 19. Lox Feedline to Chamber Coherence

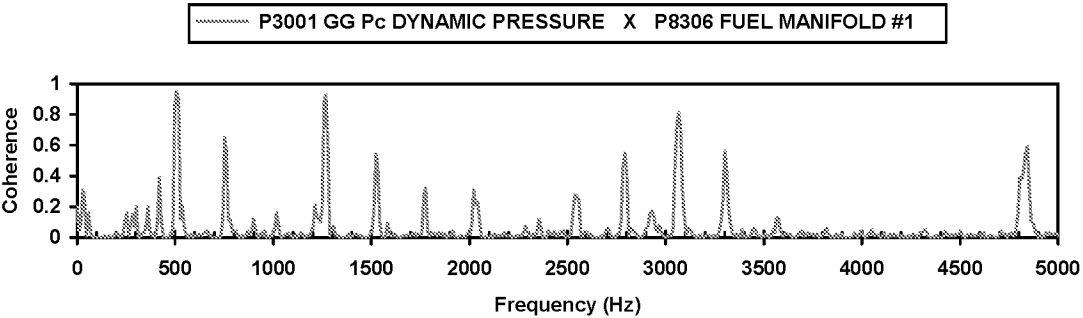


Figure 20. Fuel Feedline to Chamber Coherence

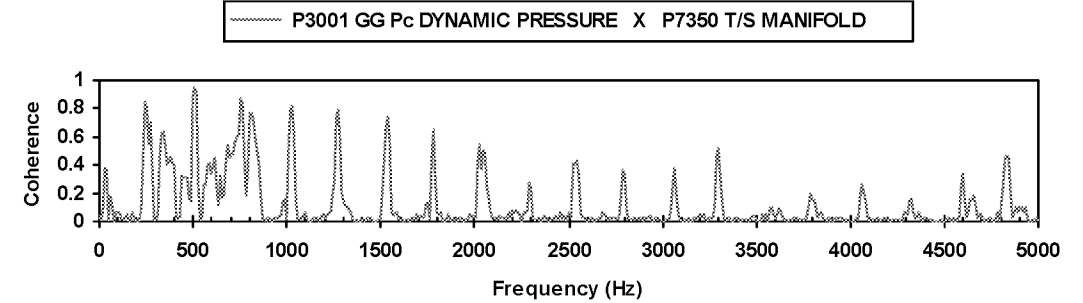


Figure 21. TIM to Chamber Coherence

CONCLUSIONS

Component testing was performed at MSFC to develop a gas generator design that would operate on the Fastrac engine. This was accomplished by performing 37 tests to address several design issues that surfaced. The gas generator internal fluctuating pressure environment was one of these issues. In early testing, it was observed that Fastrac gas generator chamber pressure oscillations occurred at or near longitudinal acoustic mode frequencies. The gas generator oscillations were shown to be dependent on gas generator length and hot gas sound speed, consistent with longitudinal acoustic modes of the gas generator. Three different Fastrac gas generator lengths were tested and with each configuration high amplitude chamber acoustic mode oscillations were observed under certain operating conditions. Elimination of the gas generator component test feedsystem, i.e., turbopump component testing, eliminated the high amplitude oscillations. Because of this last observation, and because of the high coherence between feedline and chamber pressures, the high amplitude oscillations observed in testing were attributed to acoustic modes of the gas generator in resonance with the acoustic modes of the feedsystem .

ACKNOWLEDGEMENTS

The design of the Fastrac gas generator was accomplished by the following team: Design Lead/ Jay Dennis; Structural and Loads Analysis/ Leigh Ann Perkins and Cynthia Stewart; Mechanical Design/ John Price and Andy Hissam; Thermal Analysis/ Hai Nguyen and Bruce Tiller; Pyrotechnic Igniter/ Eric Taylor; Combustion Physics/ Marvin Rucker, Huu Trinh, and John Hutt; Fluid Dynamics/ Francisco Canabal; Component Test/ Tim Sanders, Johnny Heflin, Cynthia Lee, and Matt Hammond; and Materials/ Tina Malone, Doug Wells, and Wayne Gamwell.

REFERENCES

1. Hernandez, R., Ito, J. I., and Niiya, K. Y., "Carbon Deposition Model For Oxygen-Hydrocarbon Combustion", Interim Final Report 2427-IFR for contract NAS8-34715, 1987
2. Canabal, F., *Fastrac 60K Engine CDR CFD Analysis: Gas Generator*, from Fastrac 60K Critical Design Review, NASA- Marshall Space Flight Center, March 1997
3. Merkli, P. "Acoustic Resonance Frequency for a T-tube," *J. Applied Math. & Physics (ZAMP)*, vol 29, 1978, pp 486-498



COMPUTATIONAL AEROACOUSTIC ANALYSIS SYSTEM DEVELOPMENT

A. Hadid, W. Lin, E. Ascoli, S. Barson, and M. Sindir

Rocketdyne Propulsion & Power

The Boeing Company

Canoga Park, CA 91309-7922

ABSTRACT

Many industrial and commercial products operate in a dynamic flow environment and the aerodynamically generated noise has become a very important factor in the design of these products. In light of the importance in characterizing this dynamic environment, Rocketdyne has initiated a multiyear effort to develop an advanced general-purpose Computational Aeroacoustic Analysis System (CAAS) to address these issues. This system will provide a high fidelity predictive capability for aeroacoustic design and analysis. The numerical platform is able to provide high temporal and spatial accuracy that is required for aeroacoustic calculations through the development of a high order spectral element numerical algorithm. The analysis system is integrated with well-established CAE tools, such as a graphical user interface (GUI) through PATRAN, to provide cost-effective access to all of the necessary tools. These include preprocessing (geometry import, grid generation and boundary condition specification), code set up (problem specification, user parameter definition, etc.), and postprocessing.

The purpose of the present paper is to assess the feasibility of such a system and to demonstrate the efficiency and accuracy of the numerical algorithm through numerical examples. Computations of vortex shedding noise were carried out in the context of a two-dimensional low Mach number turbulent flow past a square cylinder. The computational aeroacoustic approach that is used in CAAS relies on coupling a base flow solver to the acoustic solver throughout a computational cycle. The unsteady fluid motion, which is responsible for both the generation and propagation of acoustic waves, is calculated using a high order flow solver. The results of the flow field are then passed to the acoustic solver through an interpolator to map the field values into the acoustic grid. The acoustic field, which is governed by the linearized Euler equations, is then calculated using the flow results computed from the flow solver.

NOMENCLATURE

| | |
|-----|-----------------------|
| c | Speed of sound |
| f | forcing function |
| L | characteristic length |
| M | Mach number |
| m | number of equations |

| | |
|-----------------|---|
| p | pressure |
| Re | Reynolds number |
| t | non-dimensional time ($=L/c$) |
| \underline{u} | solution vector |
| u, v | velocities in x and y-directions respectively |
| x, y | Cartesian coordinates |
| ρ | density |
| δt | time step |

INTRODUCTION

Many aerospace and commercial products are operated in a dynamic flow environment. The structural integrity, performance and development costs of these products are affected by the unsteady flow fields they encounter. In a rocket propulsion system, dynamic loads are attributed as the cause of many life limiting and failure mechanisms. Unsteady flows can also be a very effective sound generating mechanism; George [1] states that the aerodynamically generated noise increases approximately as velocity to the 6th power. Sound may be generated whenever a relative motion exists between two fluids or between a fluid and a surface. Examples of flow-induced noise in an aerospace or automotive environment are numerous. Airplanes, helicopters, jet engines, turbomachinery and rockets all exhibit undesirable noise characteristics. In all these applications the common physical processes that are responsible for noise generation include turbulent fluid motion, structural vibration and unsteady aerodynamics. This coupled unsteady fluid dynamics and acoustic environment is poorly understood and engineering tools are required to analyze this phenomenon. In light of the importance in characterizing the dynamic fluid-acoustic environment, Rocketdyne has initiated a multi-year effort to develop a general-purpose computational fluid dynamics based analysis system for dynamic fluid-acoustic prediction. This is a fully integrated system that will provide high fidelity predictive capability through the development of a novel and accurate numerical algorithm. The numerical algorithm is a high order method based on the least squares spectral element method (LSSEM), which provides the required capability to accurately model complex geometries and rapidly varying flow and acoustic fields.

In what follows, we describe the coupled computational aeroacoustic system that is developed and the numerical method used with a demonstration of the accuracy and effectiveness of this method.

CAAS SYSTEM DEVELOPMENT

CAAS is an integrated general-purpose analysis tool for aeroacoustic engineering and design. It is intended to provide a detailed temporal description of an acoustic field in terms of signal intensity, frequency distribution, and propagation pattern. Numerical simulation of an acoustic field generally requires high temporal and spatial resolution. CAAS employs a highly accurate numerical algorithm based on the least-squares spectral element method. The code developed, Unstructured implicit Flow solver (UniFlo), is a high-order accurate numerical platform needed for acoustics calculations and is an expanded version of the original algorithm proposed by Chan [2]. It can accurately resolve the acoustic effects at the near and mid fields that are covered with a suitable mesh. The CAAS system consists of five basic components: a GUI, a preprocessor, an analysis code, a postprocessor, and a data base management system (DBMS). At the heart of the system is the analysis code that will actually carry out the aeroacoustic calculations. The other four components interface and work efficiently with the analysis code. The GUI provides the primary interface for users to interact with the system and perform the necessary code setup (boundary and initial conditions,

etc.). The pre- and postprocessors define the design geometry, construct the computational model to facilitate analysis, and graphically present the results of the calculations. The DBMS manages the various system databases and provides data access. The commercial software PATRAN from the MacNeal-Schwendler Corporation (MSC) is used as the platform for the GUI, pre-and postprocessing, and DBMS system modules. The numerical algorithm will be described in details in section 3. However, the other major system level features are described below.

GRAPHICAL USER INTERFACE (GUI)

The GUI is constructed to present the user with information needed to perform operations, during any step of the analysis cycle. The system will prompt the user for inputs to setup initial and boundary conditions for example. It incorporates a high degree of logic to prompt the user for inputs or it will fill relevant default values when none is selected. The system will also guide the user toward a faster setup and better code performance. There is also a set of tutorials for new users to get started through sample problems in a step by step fashion. A ‘help’ button is also available to provide the user with relevant information for the task at hand and access to online manuals.

PREPROCESSING

Preprocessing includes all steps needed to define the problem to be solved prior to executing the computational solver. This includes the ability to import or create the geometric description, generate a suitable computational mesh, and provide the required code inputs. The standard PATRAN capability has been enhanced to generate spectral elements of arbitrary order from finite elements (quads and hex) using special translator and grid generation tools. These tools support conversion from quadrilateral and hexahedral elements to a conforming spectral element grid of arbitrary order. Graphical display tools are provided to visualize both the geometry and the mesh generated together with the capability to manipulate and change the geometry and mesh for effective modeling of the design hardware. GUI panels also include code setup parameters such as fluid properties, control inputs and boundary conditions.

POSTPROCESSING

CAAS provides the user with the capability to extract and visualize results in different forms, from simple line plotting to 3D surface and vector plots. Transient flow visualization with animation schemes can also be employed. Graphics may be stored or exported in different forms, such as postscript, RGB, raster, gif or tif.

DATABASE MANAGEMENT SYSTEM (DBMS)

The CAAS database contains all of the preprocessing information (grid, setup parameters, boundary and initial conditions), solution files (stored at specified time intervals), and postprocessed information for both the flow and acoustic fields. The approach is to utilize existing PATRAN database which includes basic geometry information and other code setup together with a second database that is specific to aeroacoustic solutions. The spectral order computational grid will be stored in this database along with the solution variables at each specified time step. The two databases are linked and will appear as one to the user.

Other nongraphical system features are also available and are needed for effective use in a real design environment. These include “session file” that saves all meaningful keystrokes and mouse interactions

which will allow the user to quickly recover the work completed during a working session in case of an unplanned interruption (e.g. power failure) without repeating all of the commands. The system also allows the user to create a script including all desired operations and then run the script by executing a single command. Templates for a general class of problems can also be setup to avoid many redundant steps in the problem setup.

NUMERICAL METHOD

The numerical platform for both the flow and acoustic solvers is based on the least-squares spectral element method (LSSEM) operating exclusively in physical space in order to handle complex geometry and a variety of boundary conditions. The method has low dispersive and dissipative errors which renders it ideal for predicting signal propagation such as acoustic waves. The unsteady fluid motion which is governed by the incompressible Navier-Stokes equations are responsible for both the generation and propagation of acoustic waves which are governed by the linearized Euler equations derived from the perturbation expansion about Mach number in the subsonic regime. The LSSEM is an extension of the finite element method proposed by Jiang et al. [3] who cast the governing equations as a set of first order system as

$$L\vec{u} = \vec{f} \quad (1)$$

L is a first order partial differential operator given as;

$$L\vec{u} = \sum_{i=1}^{n_d} A_i \frac{\partial \vec{u}}{\partial x_i} + A_0 \vec{u} \quad (2)$$

$n_d = 2$ or 3 , depending on the spatial dimensions, x_i 's are the Cartesian coordinates, \vec{u} is an n -dimensional solution vector of the dependent variables, \vec{f} is the forcing function. A 's are $m \times n$ matrices, which describe the characteristics of the system of equations being solved. m is the number of equations in the system. The idea behind LSSEM is to minimize the residual function, \vec{R} such that $\vec{R} = L\vec{u} - \vec{f}$ and construct a least squares functional as

$$I(\vec{u}) = \frac{1}{2} \int_{\Omega} (L\vec{u} - \vec{f})^2 d\Omega \quad (3)$$

Isoparametric mapping is employed to transform the equations from the Cartesian (x,y) system to a generalized (ξ,η) coordinate system (in two-dimensions for example). The dependent variable \vec{u} is approximated as;

$$u(\xi_l, \eta_m) = \sum_i^M \sum_j^M \Psi_i(\xi_l) \Phi_j(\eta_m) \{a_{ij}\} \quad (4)$$

Where $\Psi_i(\xi_l)$ and $\Phi_j(\eta_m)$ are one-dimensional linearly independent shape functions. $\{a_{ij}\}$ are the unknown expansion coefficients for the dependent variables and M is the total number of basis functions (or degree of freedom) in each direction of an element. The basis functions used in the present study are the Lagrangian interpolant based on Legendre polynomials of the independent variables. Substituting Eq. (4) into Eq. (1), forming the residual and applying the method of least squares [4] with respect to the expansion

coefficients and using Gaussian quadrature for numerical integration leads to a set of algebraic equations. These equations are solved by the conjugate gradient method with Jacobi preconditioner.

For Euler equations, the working variables are density, velocities and pressure. For brevity, one can write the equations in the two-dimensional Cartesian coordinate system as;

$$\begin{bmatrix} \alpha_1 + \delta t M_\infty \frac{\partial}{\partial x} & \delta t \frac{\partial}{\partial x} & \delta t \frac{\partial}{\partial y} & 0 \\ 0 & \alpha_1 + \delta t M_\infty \frac{\partial}{\partial x} & 0 & \delta t \frac{\partial}{\partial x} \\ 0 & 0 & \alpha_1 + \delta t M_\infty \frac{\partial}{\partial x} & \delta t \frac{\partial}{\partial y} \\ 0 & \delta t \frac{\partial}{\partial x} & \delta t \frac{\partial}{\partial y} & \alpha_1 + \delta t M_\infty \frac{\partial}{\partial x} \end{bmatrix} \begin{bmatrix} \rho \\ u \\ v \\ p \end{bmatrix} = \begin{bmatrix} -\alpha_2 \rho^n - \alpha_3 \rho^{n-1} \\ -\alpha_2 u^n - \alpha_3 u^{n-1} \\ -\alpha_2 v^n - \alpha_3 v^{n-1} \\ -\alpha_2 p^n - \alpha_3 p^{n-1} \end{bmatrix}$$

In the above, the coefficients of the convective terms are treated as constant, though in practice, they are determined from the solution to the Navier-Stokes equations. The accuracy is second order in time with the application of a backward differencing scheme for which $\alpha_1 = 1.5$, $\alpha_2 = -2.0$, and $\alpha_3 = 0.5$. UniFlo employs isoparametric mapping to transform the above equation from the Cartesian coordinate system to a generalized coordinate system where the spatial discretization is performed. The spatial accuracy depends on the choice of basis functions and the type of elements used. In UniFlo, quadrilateral (in 2D) and hexahedral elements (in 3D) as well as Legendre polynomial based spectral element developed by Ronquist and Patera [5] are used.

NUMERICAL RESULTS

To evaluate the effectiveness of LSSEM, we apply it to three representative problems. The first two problems highlight the complex interaction of acoustic wave propagation and reflection, while the third problem shows the effects of vortices or wakes shedding from a square cylinder on the propagation of acoustic waves. Although the problems represented here are two-dimensional, CAAS in general has aeroacoustic predictive capability in 2D and 3D curvilinear problems as well.

ACOUSTIC PULSE IN A SEMI-INFINITE DOMAIN

This problem is one of the bench mark test cases suggested in the ICASE/LaRC workshop on computational aeroacoustics [6] to test the effectiveness of wall boundary conditions and the numerical schemes. Figure 1 shows a schematic of an acoustic pulse placed near a rigid wall in a semi-infinite domain. The computational domain used is $0 \leq x \leq 200$, $0 \leq y \leq 200$. The wall is at $y=0$. The linearized Euler equation in two-dimensions are

$$\frac{\partial}{\partial t} \begin{bmatrix} \rho \\ u \\ v \\ p \end{bmatrix} + \frac{\partial}{\partial x} \begin{bmatrix} M\rho + u \\ Mu + p \\ Mv \\ Mp + u \end{bmatrix} + \frac{\partial}{\partial y} \begin{bmatrix} v \\ 0 \\ p \\ v \end{bmatrix} = 0$$

M is the Mach number = 0.5. The initial condition is

$$\text{at time } t = 0, u = v = 0 \text{ and } p = \rho = \exp\left\{-\ln 2 \left[\frac{x_0^2 + (y_0 - 25)^2}{25}\right]\right\}$$

where $x_0=100, y_0=25$ are the coordinates of the initial pulse.

Figure 2 shows time history plots of an acoustic pulse reflected from a hard wall in a uniform flow at Mach 0.5 at times, $t = 15, 45, 60, 90, 100$ and 150 respectively. The lower boundary is a reflecting wall while the other boundaries are non-reflecting out-going wave boundaries. This problem was used to test the effectiveness of wall boundary condition and out-going wave conditions devised in the acoustic solver. Figure 3 shows a comparison of the computed acoustic pressure with the exact solution along the line $x=y$ at times $t=75, 90$ and 100 respectively. The computed results show good agreement with the exact solution.

As seen from figure 2, the acoustic pulse expands at the speed of sound and travels with the base flow at Mach 0.5. The downstream wave travels at Mach 1.5, three times faster than the upstream wave, and reaches the downstream boundary early and exits. The pulse reflects from the lower wall, as seen in the red spots, and expands as the original pulse does. Both original and reflected waves continue to expand and travel with the base flow, and then exit the right, left, and upper sides of the domain. The computed results show that both wall reflection and out-going wave conditions work very well, except at $t = 150$ there is a very tiny reflection of the reflected wave at the downstream boundary.

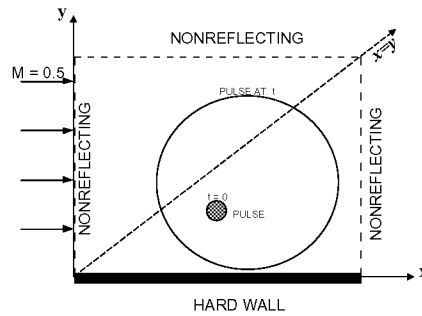


Figure 1. Problem Schematic for an Acoustic Pulse in a Semi-Infinite Domain

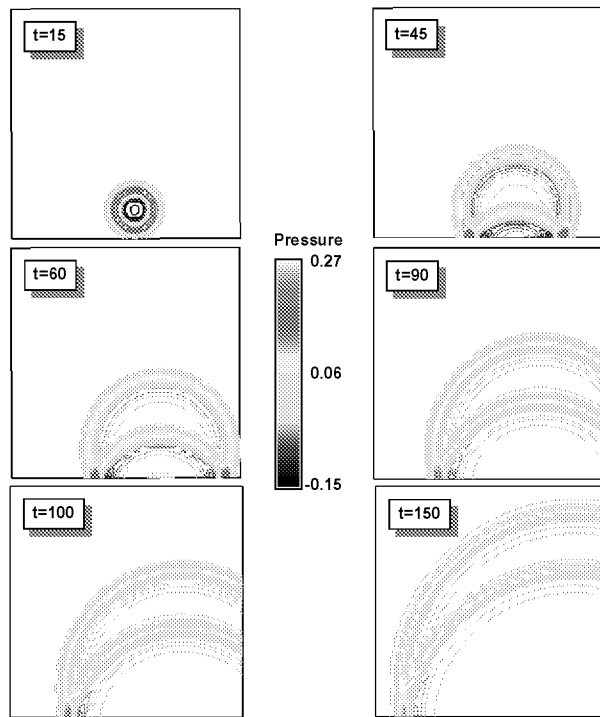


Figure 2. Acoustic pulse propagating in a semi-infinite domain with a uniform flow at Mach 0.5

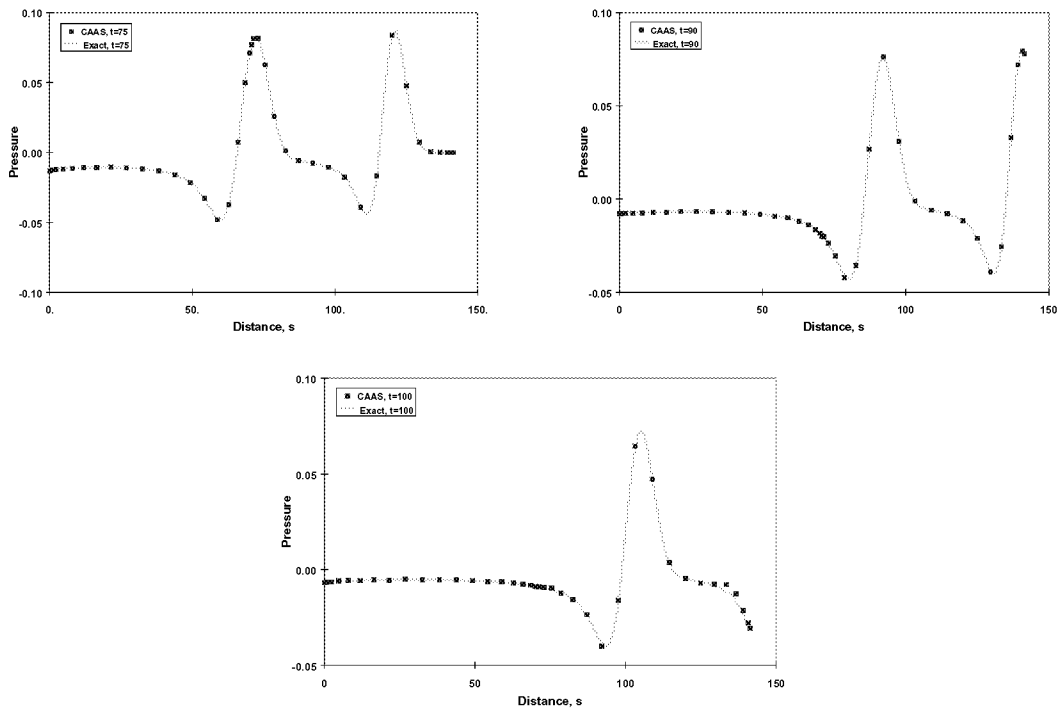


Figure 3. Acoustic pressure along the line $x = y$

Figure 4 shows a schematic of an acoustic pulse placed at the center of a duct. Figure 5 shows time history plots of the acoustic pulse traveling in a 2D duct with reflecting walls and a uniform flow at Mach 0.5. This example simulates the propagation of sound waves generated in the inlet and exhaust ducts of an internal combustion engine such as in an automobile. The problem is also used to test the effectiveness of hard wall conditions and nonreflecting (out-going wave) conditions. Initially the sound source is created by some mechanism in the center of the duct. It expands at the speed of sound, travels with the base flow at Mach 0.5, and forms waveguide patterns in the duct.

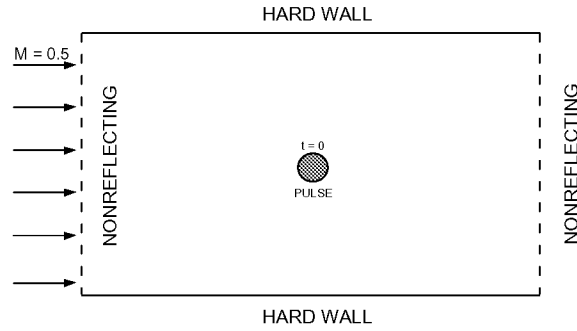


Figure 4. Problem schematic for acoustic pulse in a duct

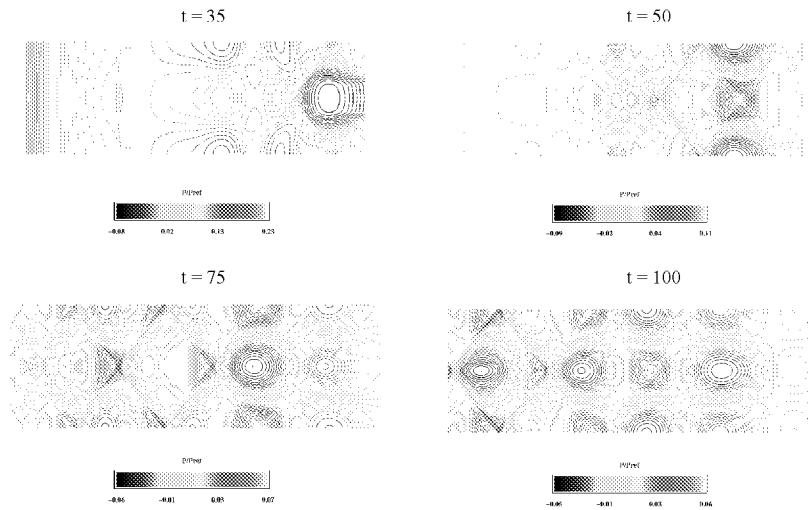


Figure 5. Acoustic pulse propagating in a duct

AEROACOUSTICS OF A 2D VORTEX SHEDDING FROM A RECTANGULAR CYLINDER

The sound generated by a viscous flow past a square cylinder at $Re=14,000$ is predicted using the linearized Euler equations approach. The time-dependent mean flow is calculated using a separate flow solver that is based on a second order accurate finite-volume method. Time accuracy of the flow solver is assured using the PISO methodology [7], which is essentially noniterative. The solution process is split into a series of steps whereby operations on pressure are decoupled from those on velocity at each time step. The avoidance of iterations substantially reduces the computational effort compared with that required by iterative methods such as in UniFlo.

Calculations are performed for the turbulent flow around a square obstacle of height H in a domain extending about $20H$ downstream and $2.5H$ upstream. The calculations using the two-equation $k-\epsilon$ turbulence model captured the vortex shedding phenomenon. The Reynolds number based on the inlet

velocity and the obstacle height is 14,000 with an assumed 6% turbulence intensity. The upper and lower boundaries were treated as free stream and a zero gradient outflow boundary condition was used at the exit. The computational domain is resolved by a fine grid of 250x80 cells with clustering at the obstacle walls. A time step of 0.1 msec was used in the calculations. Once an oscillatory periodic solution was obtained, the flow solver was coupled with the UniFlo acoustic solver to calculate the sound generated by the periodically shedding flow. Figure 6a, shows a marker particle trace, which illustrates the shedding pattern. Figure 6b, confirms the oscillating periodic nature of the flow with a single predominant frequency of about 4.7 Hz which is in agreement with the experimental results of Durão et al. [8]. Figure 7, shows contours of the sound pressure generated by the vortex shedding behind the square cylinder at three instants of time. The long-time behavior is to focus the acoustic pressure signal along the centerline of the flow axis. High sound pressure levels are generated close to the cylinder where the strength of vortices is highest.

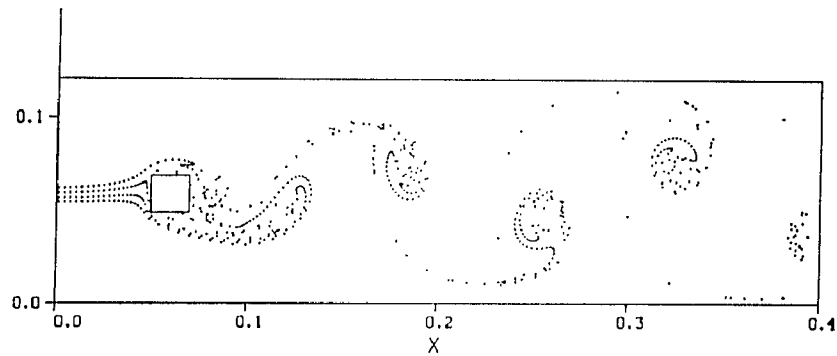


Figure 6a. Streak line plot

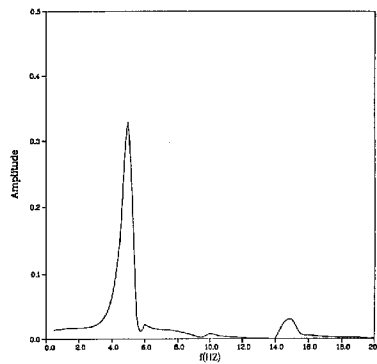


Figure 6b. Power spectrum of the vortex shedding

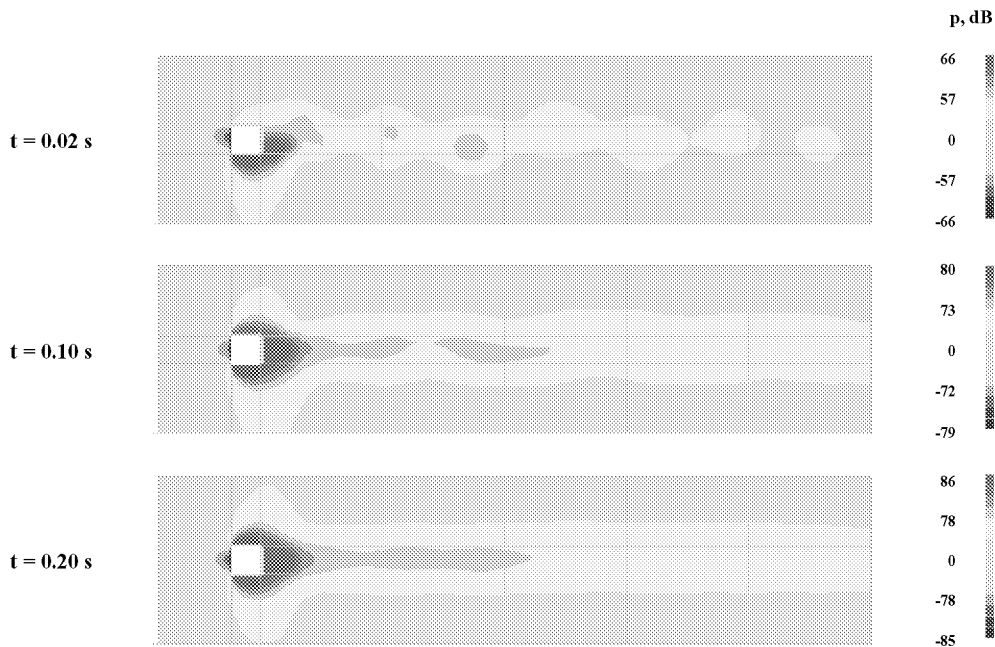


Figure 7. Sound pressure levels

CONCLUSIONS

A computational aeroacoustic analysis system (CAAS) has been developed. CAAS is a complete system that enables aeroacoustic analysis from a PATRAN-based graphical user interface (GUI). Significant customization of the PATRAN GUI was completed as was the development of several peripheral tools (e.g., spectral element grid generators, interpolators).

An acoustic module, based on the least squares spectral element method (LSSEM) has been developed and demonstrated on a variety of acoustic and aeroacoustic test cases, including the fully coupled solution of vortex shedding, sound generation, and sound propagation. Preliminary comparisons of flow and acoustic results show qualitatively good behavior, but further comparisons with benchmark test data are required to fully verify the current predictive capability.

ACKNOWLEDGMENTS

The authors would like to recognize a number of additional contributors. Funding for the CAAS program has been provided by NASA and three industry partners, Boeing/Rocketdyne, Ford Motor Company, and MacNeal-Schwendler (MSC). Further, a majority of the PATRAN GUI customization and database management was performed by MSC personnel.

REFERENCES

1. Albert R. George, "Automobile aerodynamic noise", SAE Transactions, 99(6): 434-457, 1990.
2. D. Chan, "A least squares spectral element method for incompressible flow simulation", Proceedings of the Fifteenth International Conference on Numerical Methods in Fluid Dynamics, 1996.

3. B. Jiang, T. Lin and L. Povinelli, "Large scale computation of incompressible viscous flow", *Comput. Meth. Appl. Mech. Eng.*, 114 : 213-231, 1994.
4. D. S. Burnett, "Finite element analysis: from concept to application", Addison-Wesley, 1987.
5. E. Ronquist and A. Patera, "A Legendre spectral element method for the Stefan problem", *Int. J. Num. Meth. Eng.*, 24 : 2273-2299, 1987.
6. ICASE/LaRC Workshop on Benchmark Problems in Computational Aeroacoustics (CAA), Editors, J. C. Hardin, J. R. Ristorcelli and C. K. W. Tam, 1995, NASA-CP 3300.
7. R. Issa, "Solution of the implicitly discretized fluid flow equations by operator-splitting", *J. Comput. Phys.*, 62 : 40- , 1986.
8. D. Durãõ, M. Heitor and J. Pereira, "Measurements of turbulent and periodic flows around a square cross-section cylinder", *Experiments in Fluids*, 6 : 298 - 304, 1988.

AN OVERVIEW OF COMPUTATIONAL AEROACOUSTIC MODELING AT NASA LANGLEY

DAVID P. LOCKARD

*Aerodynamics, Aerothermodynamics, and Acoustics Competency
NASA Langley Research Center
Hampton, VA 23681-2199, U.S.A*

ABSTRACT

The use of computational techniques in the area of acoustics is known as computational aeroacoustics and has shown great promise in recent years. Although an ultimate goal is to use computational simulations as a virtual wind tunnel, the problem is so complex that blind applications of traditional algorithms are typically unable to produce acceptable results. The phenomena of interest are inherently unsteady and cover a wide range of frequencies and amplitudes. Nonetheless, with appropriate simplifications and special care to resolve specific phenomena, currently available methods can be used to solve important acoustic problems. These simulations can be used to complement experiments, and often give much more detailed information than can be obtained in a wind tunnel. The use of acoustic analogy methods to inexpensively determine far-field acoustics from near-field unsteadiness has greatly reduced the computational requirements. A few examples of current applications of computational aeroacoustics at NASA Langley are given. There remains a large class of problems that require more accurate and efficient methods. Research to develop more advanced methods that are able to handle the geometric complexity of realistic problems using block-structured and unstructured grids are highlighted.

INTRODUCTION

Computational aeroacoustics is a very broad field that encompasses research that uses numerical simulations to better understand aerodynamic noise. There is a large computational effort at NASA Langley Research Center aimed at predicting and reducing aircraft noise, and this paper only attempts to give an overview of a representative fraction of that work. The problem is very difficult because the geometry and physics involved are often quite complex. It has taken 30 years to achieve significant noise reduction for jet engines. Although great strides have been made in the reduction of jet noise through the use of high-bypass ratio engines, there is a lack of understanding of the fundamental noise sources in subsonic jets. Today, tonal noise from large inlet fans is also important. There is a general theory for fan noise, but calculations are still somewhat limited. Extensive research is ongoing in the areas of duct and liner acoustics[1]. Furthermore, the engines are not the only noise source that must be considered. Reductions in jet noise have made the airframe a significant, and in some cases dominant source during landing. The flaps, slats, and landing gear are all important contributors to the sound field. To achieve significant noise reduction, these three major landing systems and the engines must all be quieted commensurately.

The physics behind the unsteadiness that generates noise is also very complicated. Fluctuations tend to grow in shear layers and vortical structures. Resolving these features in a mean flow calculation can be difficult. Trying to capture the unsteadiness growing in them is even more challenging. Separated regions, instabilities, and large and small scale turbulence structures can all contribute to the sound field. Furthermore, the energy that is radiated as noise is typically only a small fraction of the total energy near the source. This is part of the scale disparity between acoustic and hydrodynamic fluctuations. The human ear is able to distinguish between signals with vastly varying amplitudes, so it is typical to use a logarithmic scale to describe them. The sound pressure level (SPL) is given by

$$\text{SPL} = 20 \log\left(\frac{p'_{rms}}{p_{ref}}\right) \quad (1)$$

with units of decibels (dB). The reference pressure $p_{ref} = 20 \times 10^{-6}$ Pa is the threshold of human hearing, and *rms* means root mean square. The ratio of pressure amplitudes between a quiet conversation, 60 dB, and a rock concert, 120 dB, is 1000. In addition, atmospheric pressure is 3500 times greater than the pressure amplitude of a 120 dB signal. At 120 dB, one starts feeling discomfort and experiences a ringing in the ears. Although this level is very loud

to humans, it is so small that a typical computational fluid dynamics (CFD) simulation very easily loses the sound waves among the large hydrodynamic fluctuations. Simultaneously resolving the hydrodynamic fluctuations and the wide range of acoustic signals is very difficult.

Acousticians also have to deal with very disparate length and time scales. Mostly people can hear fairly well between frequencies of 100 Hz and 10 kHz. This corresponds to wavelengths of 0.11 ft (0.034 m) and 11 ft (3.4 m), respectively. Trying to have enough grid points in the domain to resolve the very short wavelength while having a domain large enough to encompass the long wavelength results in enormous grids. One is also faced with the challenge of trying to propagate the signal to observers located at great distances from the sources. A similar scale problem occurs temporally. The wavelength λ of an acoustic wave is related to the temporal period T by $\lambda = cT$ where c is the speed of sound. The periods for 100 Hz and 10 kHz are 0.0001 s and 0.01 s, respectively. Hence, one needs many time steps for the short period, and long run times to get a significant sample of the long period. This problem is usually exacerbated by initial transients in numerical solutions which must decay sufficiently before one can start sampling the acoustics. Even when using sampling techniques developed for experimental work, it is difficult to run codes long enough to get statistically significant samples of pseudo-random phenomena. Furthermore, the disparity between different acoustic waves is only part of the problem. One also has to compare the acoustic scales with those of other fluid phenomena and the geometry.

Faced with these challenges, one must inevitably make simplifying assumptions. However, computational methods are often able to relax those used in the past. The basic goal is to obtain an understanding of the underlying physics of the noise sources. One needs to know the strength, location, frequency, wavelength, and nature of the disturbances. With this information one can develop prediction methods that are general across different configurations that have similar source mechanisms generating the noise. Furthermore, one can begin attacking the sources in systematic ways that are more likely to lead to significant noise reduction. To get at the physics, we are using currently available tools and developing new ones to do bigger problems in the future. To reduce the complexity, most calculations concentrate on a small frequency range rather than trying to resolve all of the relevant frequencies at once. In addition, one can solve equations linearized about the mean flow[2, 3] to separate out the acoustic and hydrodynamic scales. Using these simplifications makes many problems tractable to modern methods. Furthermore, numerical applications of acoustic analogy methods have matured significantly, and they allow far-field acoustics to be calculated from unsteady fluctuations in the vicinity of the sources. This greatly reduces the computational effort and provides a means of finding the noise where the observers are actually located.

The remainder of the paper discusses some of the acoustic problems that have been solved using combinations of available methods. First, the CFD code CFL3D is described. It was used in many of the example computations. The acoustic analogy is explained in slightly more detail because it is key to most of the calculations and is less widely known. At the end of the paper, examples of several new technologies under development are discussed. These include high-order methods for block-structured and unstructured grids. Because of the great scale disparities in acoustics, one either needs high-accuracy methods that resolve waves with a minimal number of points-per-wavelength or standard methods with fine grids. Such comparisons[4, 5] have shown that high-order methods are more efficient at resolving acoustic phenomena than traditional methods with extremely fine grids. However, high-order methods often suffer from robustness problems for realistic configurations, and these new efforts are aimed at overcoming this difficulty.

COMPUTATIONAL TOOLS

THE COMPUTER CODE CFL3D

The computer code CFL3D [6, 7] is a robust, workhorse code used to compute both steady and unsteady flow fields. The CFL3D code was developed at NASA Langley Research Center to solve the three-dimensional, time-dependent, thin-layer (in each coordinate direction) Reynolds-averaged Navier-Stokes (RANS) equations using a finite-volume formulation. The code uses upwind-biased spatial differencing for the inviscid terms and flux limiting to obtain smooth solutions in the vicinity of shock waves. The viscous derivatives, when used, are computed by second order central differencing. Fluxes at the cell faces are calculated by flux-difference-splitting. An implicit three-factor approximate factorization method is used to advance the solution in time. Patched grid interfaces, overset grids, and slides zones are available for use at zone boundaries.

The time-dependent version of CFL3D uses subiterations to obtain second order temporal accuracy. In the $\tau - TS$ subiteration option [8], each of the subiterations is advanced with a pseudo-time step. This approach facilitates a

more rapid convergence to the result at each physical time step. The steady-state version of the code employs full multigrid acceleration.

ACOUSTIC ANALOGY

An acoustic analogy is a rearrangement of the governing equations of fluid motion such that the left-hand side consists of a wave operator in an undisturbed medium, and the right-hand side is comprised of acoustic source terms. The solution to the equation can be written as the convolution of the source terms with the Green function for the wave operator. Hence, if one can obtain the strengths of the source terms in the regions where they are significant, one can determine the acoustic signal at any point in the flow, including locations at long distances from the sources. Lighthill[9] was the first to propose this approach. Although this concept is relatively simple, extensive manipulations have been required to put the equations in the most useful forms for analytic and numerical applications.

The Ffowcs Williams and Hawkins [10] equation is the most general form of the Lighthill acoustic analogy and when provided with input of unsteady flow conditions, is appropriate for numerically computing the acoustic field. The equation is derived directly from the equations of conservation of mass and momentum. Following Brentner and Farassat [11], the FW-H equation may be written in differential form as

$$\square^2 c^2 \rho'(\mathbf{x}, t) = \frac{\partial^2}{\partial x_i \partial x_j} [T_{ij} H(f)] - \frac{\partial}{\partial x_i} [L_i \delta(f)] + \frac{\partial}{\partial t} [Q \delta(f)] \quad (2)$$

where: $\square^2 \equiv \frac{1}{c^2} \frac{\partial^2}{\partial t^2} - \nabla^2$ is the wave operator, c is the ambient speed of sound, t is observer time, ρ' is the perturbation density, ρ_0 is the ambient density, $f = 0$ describes the integration surface, $f < 0$ being inside the integration surface, $\delta(f)$ is the Dirac delta function, and $H(f)$ is the Heaviside function. The quantities Q , U_i and L_i are defined by

$$Q = (\rho_0 U_n), \quad U_i = (1 - \frac{\rho}{\rho_0}) v_i + \frac{\rho u_i}{\rho_0} \quad \text{and} \quad L_i = P_{ij} \hat{n}_j + \rho u_i (u_n - v_n). \quad (3)$$

In the above equations, ρ is the total density, ρu_i is the fluid momentum, v_i is the velocity of the integration surface $f = 0$, and P_{ij} is the compressive stress tensor. For an inviscid fluid, $P_{ij} = p' \delta_{ij}$ where p' is the perturbation pressure and δ_{ij} is the Kronecker delta. The Lighthill stress tensor is given by T_{ij} . The subscript n indicates the component of velocity in the direction normal to the surface.

An integral solution to the FW-H equation (2) can be written in terms of the acoustic pressure $p' = c^2 \rho'$ in the region $f > 0$. Utilizing formulation 1A of Farassat [12, 13], the integral representation has the form

$$p'(\mathbf{x}, t) = p'_T(\mathbf{x}, t) + p'_L(\mathbf{x}, t) + p'_Q(\mathbf{x}, t) \quad (4)$$

where

$$4\pi p'_Q(\mathbf{x}, t) = \int_{f=0} [P_Q(\mathbf{y}, \tau)]_{ret} dS, \quad 4\pi p'_L(\mathbf{x}, t) = \int_{f=0} [P_L(\mathbf{y}, \tau)]_{ret} dS \quad \text{and} \quad (5)$$

$$4\pi p'_T(\mathbf{x}, t) = \int_{f=0} [P_T(\mathbf{y}, \tau)]_{ret} dV. \quad (6)$$

The subscript *ret* means that the quantities must be evaluated at the appropriate retarded or emission time τ . The kernel functions P_T , P_L , P_Q are combinations of flow quantities and geometric parameters. For many numerical simulations it is desirable to let the integration surface be permeable and place it within the flow. However, when the surface coincides with a solid body, the terms take on simple meanings. The Q term is known as the thickness contribution and represents the noise generated by the unsteady displacement of fluid by the body. The L term involves the noise caused by the fluctuating loading on the body. The term p'_T accounts for all quadrupoles outside of the integration surface (i.e., $f > 0$). Quadrupole contributions include nonlinear effects and refraction. In most work, p'_T is small and can be neglected. This is important because the quadrupole term involves a volume integration, whereas p'_Q and p'_L only require an integration over the surface. All quadrupole contributions that are within the surface are accounted for by the surface integrations. Hence, the far-field pressure at any instance in time can usually be calculated by integrating the near-field flow quantities over a surface. This allows for very rapid calculations of noise a great distance away from the source region where the integration surface is typically placed.

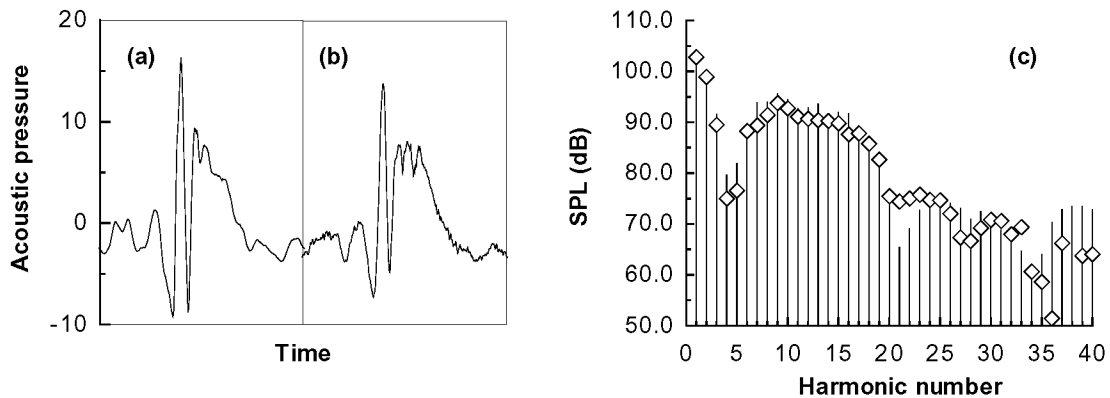


Figure 1. Comparison of measure and computed noise for a four-bladed Sikorsky model rotor. The microphone locations was nominally 25 deg. below the rotor plane on the advancing side, 1.5 rotor radii from the rotor hub. This is a descent condition. (a) Measure time history; (b) predicted time history; (c) spectral comparison (— measured; \diamond predicted)

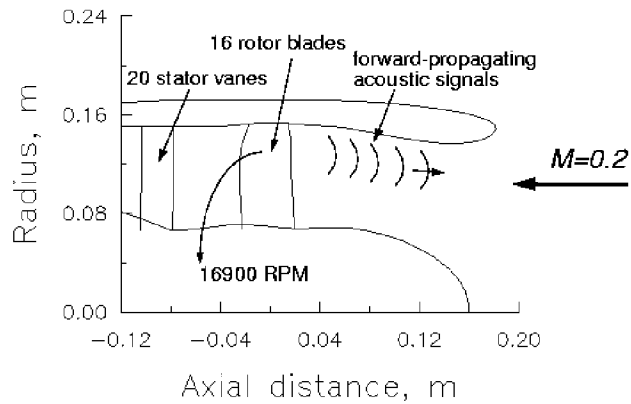
Rotorcraft acoustics is an area where the FW-H equation has been utilized with great success. The code WOPWOP[13] has been used extensively by industry and researchers to predict helicopter noise. Even for complex phenomena such as blade vortex interaction (BVI), WOPWOP correctly predicts the acoustic signature when it is given accurate pressure data as inputs. As an example, figure 1 compares the experimentally observed and computed acoustic signals[14] when experimentally measured surface pressures from a four bladed rotor were used as input to WOPWOP. The spectral comparison in figure 1 shows the agreement is good up to the 32nd harmonic. Similar comparisons using CFD data as input do not yield such good results. This underscores the importance of having accurate input data on the integration surface. The acoustic theory is mature enough for such complicated problems, but more accurate CFD is needed.

SAMPLE APPLICATIONS

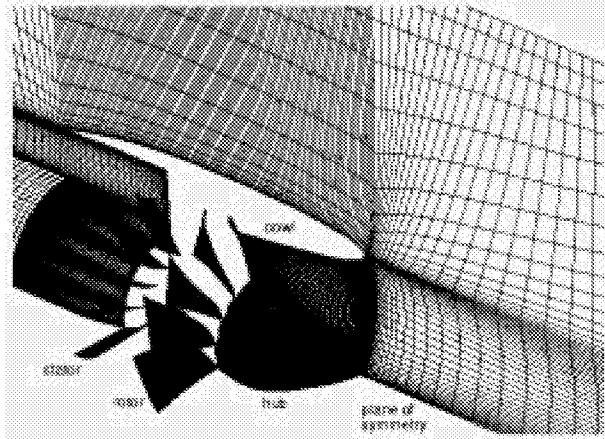
Although there are many problems that cannot be solved with conventional methods, appropriate assumptions can make many realistic problems tractable. This section provides several examples where current methods were successfully used to simulate important acoustic phenomena.

ROTOR NOISE

Rumsey *et al.*[15] used the Navier-Stokes code CFL3D to predict one of the ducted-fan engine acoustic modes that results from a rotor-wake/stator-blade interaction. A patched-sliding-zone interface was employed to pass information between the moving rotor-row and the stationary stator row. Figure 2 shows the geometry and 2.7 million point grid used in the calculation. The code produced averaged aerodynamic results downstream of the rotor that are in good agreement with a widely used average-passage code. The calculation was designed to capture a single acoustic mode, and the code successfully generated and propagated that mode upstream with minimal attenuation into a region of nearly uniform flow as shown in figure 3(a). Two acoustic codes were used to find the far-field noise. Propagation in the duct was computed by Eversmann's wave envelope code, which is based on a finite-element model. Propagation to the far field was accomplished by using the Kirchhoff formula for moving surfaces. The Kirchhoff method is used in a similar fashion to acoustic analogy methods, but is less general. Comparison of measured and computed far-field noise levels are in fair agreement in the range of directivity angles (20-40 deg.) where the peak radiation lobes are observed for the mode under investigation. Figure 3 compares the experimental and computed results. Although only a single acoustic mode was targeted in this study, it provided a proof of concept: Navier-Stokes codes can be used to both generate and propagate rotor-stator acoustic modes through and engine, where the results can be coupled to other far-field noise prediction codes.

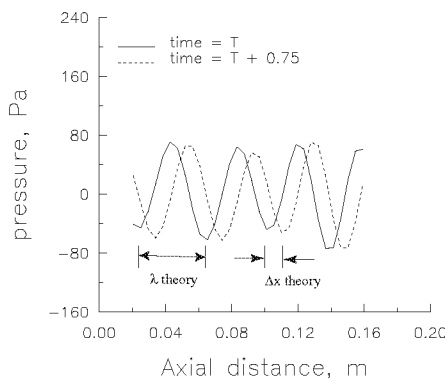


(a) Geometry.

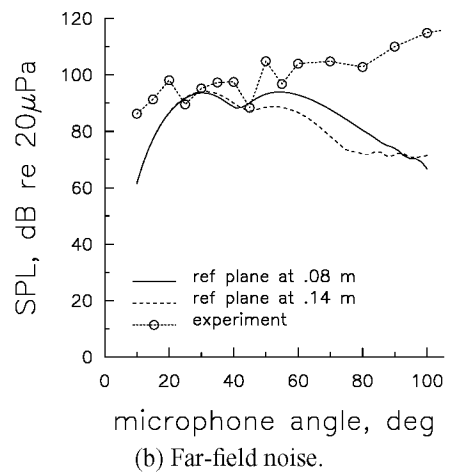


(b) 2.7 million point grid.

Figure 2. Geometry and grid for rotor-wake/stator-blade interaction problem.



(a) Near-field pressure.

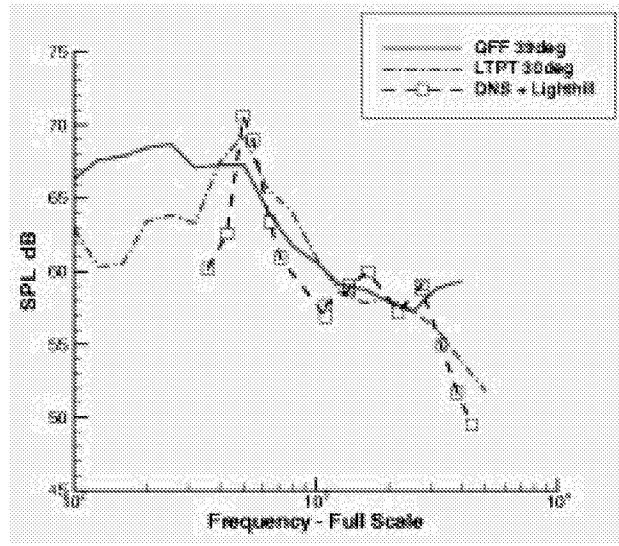


(b) Far-field noise.

Figure 3. Near-field pressure computed by CFL3D and far-field pressure computed by Eversmann's wave envelope code and a Kirchhoff technique.



(a) Vorticity Contours



(b) Spectra

Figure 4. (a) Vorticity contours from 2-D DNS of flap-edge flow (b) Comparison of computed and experimental spectra.

FLAP-EDGE NOISE

A different computational framework was developed to simulate the unsteadiness associated with the vortex system around the flap of a high-lift system. The vortex system is surprisingly complex, and a steady RANS calculation with sufficient resolution required 50 CRAY C-90 hours. Clearly, some approximations must be made to deal with the unsteady problem because a DNS would be intractable. Streett[16] simplified the problem by performing a 2-D, incompressible DNS linearized about the RANS mean flow. Because the vortex system varies relatively slowly in the streamwise direction, the DNS calculations were performed at several streamwise stations assuming locally parallel flow. Calculations were performed in a parameter space that included the frequency and a spanwise wavenumber. Figure 4(a) shows the vorticity contours for a case where the spanwise wavenumber was zero, and instabilities dominate in the shear layer formed on the under side of the flap. This instability was persistent from 5 to 30 kHz. For nonzero wavenumbers, an instability within the vortex on top of the flap grew rapidly. Although the DNS simulations show local unsteadiness, they do not reveal how much of that energy propagates to the far-field. The Lighthill acoustic analogy[9] was used for this purpose. This type of formulation allows the source strengths to be computed from incompressible flow because all of the acoustic propagation is taken into account by the analogy. However, the complex geometry in this problem required a numerical solution of the partial differential equation form of the acoustic analogy. The results of those calculations are compared with those from two experiments in figure 4(b). The comparison is quite good, and gives confidence that the instabilities identified by the DNS are indeed generating noise. With the detailed information about the frequencies, wavelengths, and locations of the instabilities from the DNS, techniques to reduce the noise at the source have been developed.

CYLINDER SHEDDING

To determine the sensitivity of the FW-H method to the integration surface location when it passes through a wake, Singer *et al.*[17] examined a circular cylinder in a cross flow. Equivalent calculations were also performed using a Kirchhoff technique. This was important because the shed vortices produce large, unsteady fluctuations as they pass through the surfaces. These fluctuations would be balanced by the quadrupole term in the FW-H if it were included, but it is much more desirable to avoid the volume integration. Furthermore, the Kirchhoff equation is derived from the acoustic wave equation and is strictly valid only in the region of the flow where the wave equation is the appropriate governing equation. This problem tested whether the Kirchhoff method can be used with near-field data that includes nonlinear, non-acoustic fluctuations.

Figure 5 renders an instantaneous vorticity field obtained from a CFL3D calculation with a superimposed grid

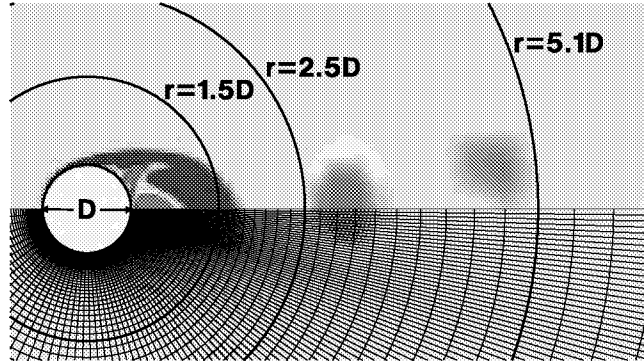


Figure 5. Vorticity field computed from CFD. FW-H integration surfaces are at $r = 0.5D$, $r = 1.5D$, $r = 2.5D$, and $r = 5.1D$

distribution on the lower portion of the figure. The positions of the FW-H integration surfaces are indicated in the upper portion of the figure. Figure 6(a) shows the computed pressure signals at the observer for the different integration surfaces using a Kirchhoff formulation, and figure 6(b) shows the results obtained with the FW-H formulation. The use of an integration surface that cuts through the cylinder wake does not appear to adversely affect the results obtained with the FW-H formulation. However, these variations are very small compared with the results of Figure 6(a), in which the pressure computed with a standard Kirchhoff formulation for the same problem with the same integration surfaces varies wildly. This result clearly demonstrates that the FW-H should be used instead of the Kirchhoff method. Furthermore, there is very little difference in the computational effort required for the two approaches.

TRAILING-EDGE SCATTERING

Calculation methods for acoustic fields that include trailing-edge noise currently are largely empirical [18]. Singer *et al.* [17], investigated the feasibility of directly computing the acoustic field generated by flow over a sharp trailing edge. A hybrid computational approach was taken wherein the CFL3D solver was used to accurately calculate the unsteady fluid dynamics over a relatively small region near the surface, and an acoustics code based on the Ffowcs Williams and Hawkins [10] (FW-H) equation computed the acoustic field generated by the previously calculated unsteady near flow field. To investigate edge scattering, an airfoil with vortices convecting past its trailing edge was simulated. A 2.6% thickness NACA 00 series airfoil was placed in a flow with a small, flat plate introduced perpendicular to the flow at 98% chord. In the presence of flow, vortices roll up just downstream of the flat plate, alternately near the plate's top and bottom edges.

Figure 7 shows vorticity magnitude contours in the vicinity of the trailing edge at a single time step. The circular concentrations of vorticity indicate the individual vortices that constitute the unsteady Karman vortex street downstream of the vortex-generator plate. Cases were run with Mach numbers ranging from 0.2 to 0.5 that produced regular Strouhal shedding at the plate. The frequency of the vortices convecting past the trailing edge is less distinct because the vortices shed from the vortex-generator plate often pair and interact with neighboring vortices, as shown in figure 7.

The FW-H code computed the acoustic field generated by the unsteady aerodynamic flow field. The far-field signals were obtained at several observer locations. Figure 8(a) shows spectra of the acoustic signals for several observer positions. The angular measurements are increasingly positive for counterclockwise rotations, with 0 degrees being directed downstream. The figure shows greatly reduced noise radiation directly upstream and directly downstream. Integration of each acoustic spectrum over the frequencies provides the mean square acoustic pressure. Variation of the mean square acoustic pressure as a function of Mach number is plotted in Figure 8(b). The symbols show the data, and the lines are linear least-squares fit to the logarithm of the data. For an observer at 30 degrees, the mean square pressure varies as the 5.2 power of Mach number. Accounting for the actual rms fluctuating velocity in the calculations, a theoretical scaling of $M^{5.36}$ is implied, which is in close agreement with the computationally observed scaling of $M^{5.2}$. These computations have helped to verify that the hybrid approach is valid and capable of accurately predicting fairly complicated, broadband, acoustic phenomena.

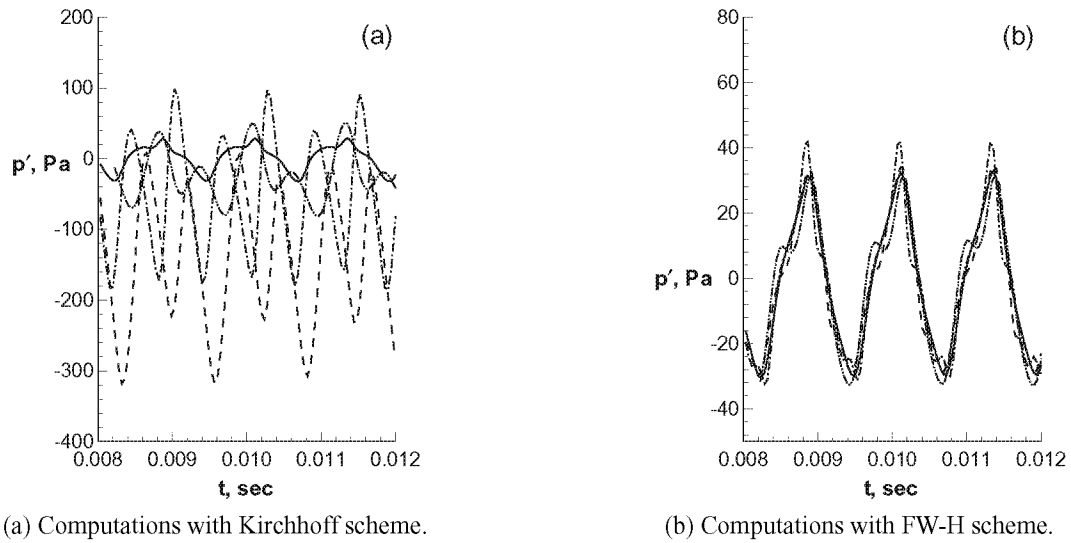


Figure 6. Acoustic signals computed for various integration surfaces that correspond to those indicated in Figure 5. Integration surfaces at ——— $r = 0.5D$, - - - - - $r = 1.5D$, - · - · - $r = 2.5D$, · · · · · $r = 5.1D$.

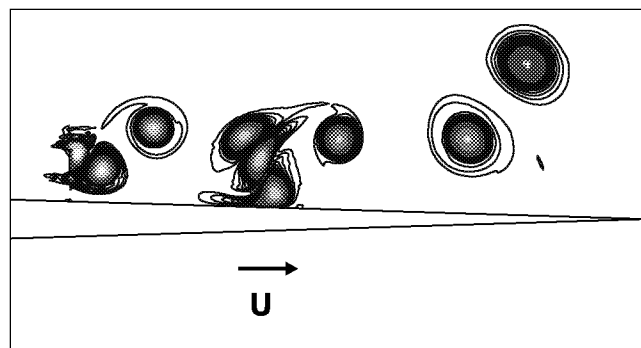


Figure 7. Instantaneous vorticity magnitude contours in vicinity of trailing edge for $M = 0.2$ case. Approximately 2% of aft portion of airfoil is shown.

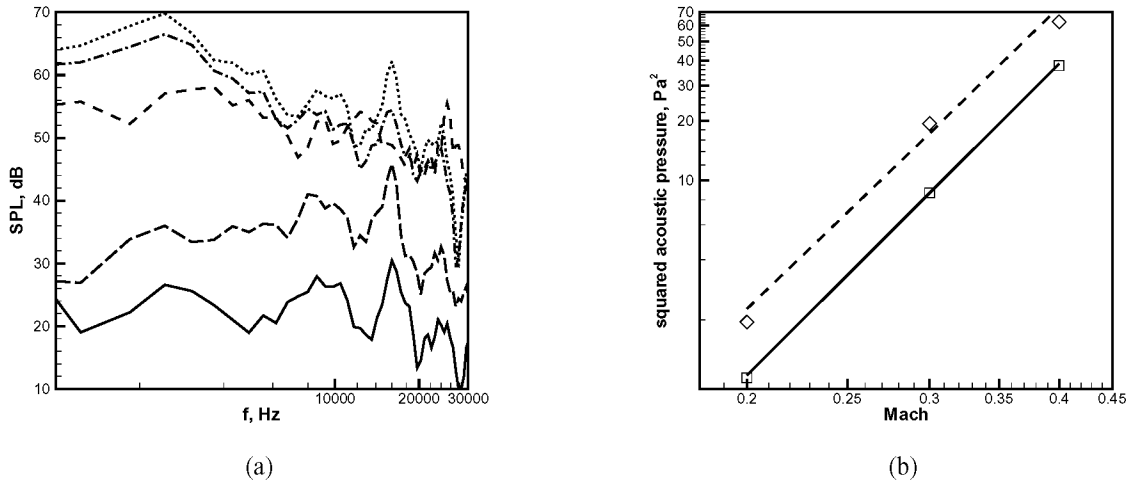


Figure 8. (a) Spectra of acoustic signals (referenced to $20\mu\text{Pa}$) for observers located $10C$ from trailing edge of airfoil; on-airfoil-body integration surface used, $M = 0.2$. Observers located at: ——— 0 deg., - - - - - 45 deg., - · - · - 90 deg., ····· 135 deg., - - - - - 180 deg. (b) Variation in mean square acoustic pressure versus Mach number; \square data for 30 deg., ——— least-squares fit for 30 deg., \diamond data for 45 deg., - - - - - least-squares fit for 45 deg.

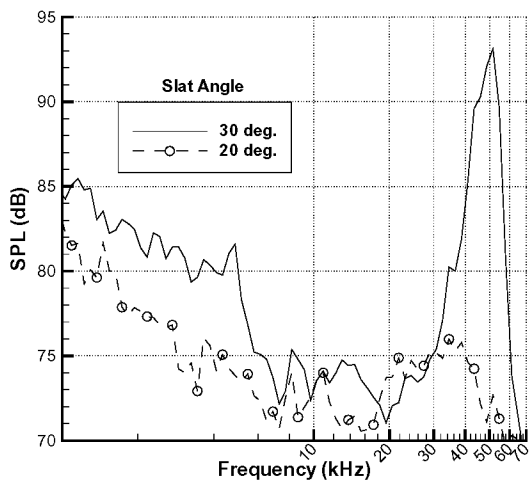
HIGH-LIFT CONFIGURATION

A cooperative test involving NASA's High-Lift Program Element and NASA's Airframe Noise Team was conducted in NASA Langley Research Center's Low-Turbulence Pressure Tunnel (LTPT). The model tested in the tunnel is known as the Energy Efficient Transport (EET) model. The EET model tested includes a full-span leading-edge slat and a part-span trailing flap. To obtain acoustic data, members of Boeing Commercial Airplane Company designed and built a microphone array that was installed in the wind tunnel. The microphone array and the subsequent data processing followed techniques developed earlier at Boeing [19].

Figure 9(a) illustrates one unexpected feature of the experimental data. For a slat deflection of $\delta_s = 30$ degrees, a very large amplitude peak was observed in the acoustic spectrum in the vicinity of 50 kHz. This peak rises almost 20 dB above the signal observed for the case in which the slat is deflected 20 degrees. During the course of the experiment, efforts to eliminate the high-frequency peak by altering the overhang of the slat were largely unsuccessful. Only for cases in which the overhang became unrealistically large was a significant change in the high-frequency acoustic peak observed. Increasing the configuration's angle-of-attack from 10 to 15 degrees, reduced the amplitude of the high-frequency peak by approximately 10 dB. For some time, no consistent explanation of the observed phenomena was available.

Khorrami et al [20] provides details of unsteady, two-dimensional (2D), Reynolds-averaged Navier-Stokes (RANS) calculations designed to mimic the experimental conditions. In particular, the RANS computation was specially designed to properly incorporate and resolve the small, but finite trailing-edge thickness of the slat. Extremely small grid cells were used in the vicinity of the slat trailing edge and the time step was chosen to ensure more than 120 time steps per period of a 50 kHz signal. Slat deflections of both 30 and 20 degrees were simulated. These calculations clearly show vortex shedding from the slat trailing edge for the case with a 30 degree slat deflection. Figure 9(b) shows a snapshot of the pressure fluctuations produced in the flow field. The vortex shedding virtually disappears for the case of a 20 degree slat deflection.

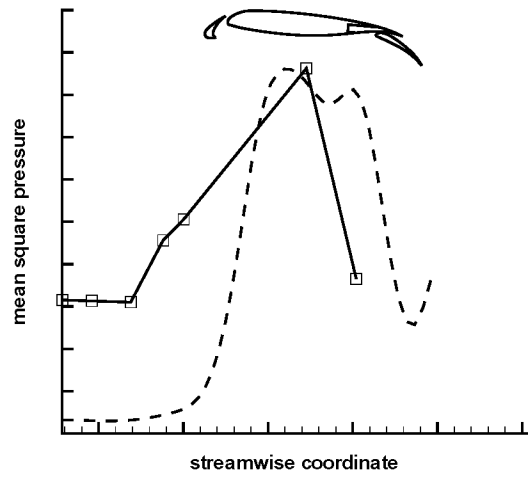
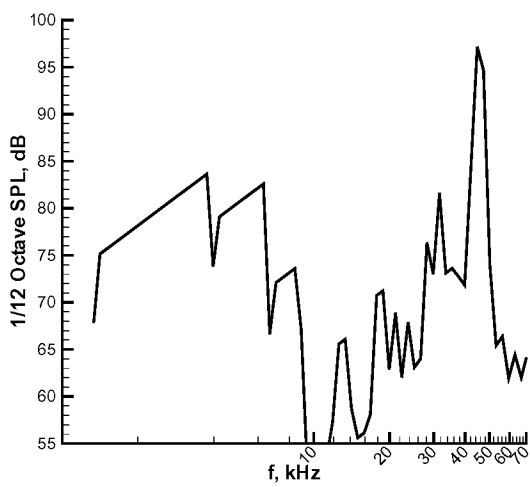
Singer *et al.*[21] discuss the aeroacoustic analysis of the unsteady data. As a first approximation, the code developed by Lockard[22] for computing the 2D acoustic field from 2D CFD data was used to predict the sound field. Figure 10(a) shows computed spectra based on $1/12^{\text{th}}$ octave bins for an observer located at 270 degrees. Clearly the computed noise also has a significant peak in the spectra in the same frequency range as the experiment. This confirmed that the fluctuations from the slat vortex shedding weren't just hydrodynamic fluctuations, but also



(a)

(b)

Figure 9. (a) Acoustic spectrum based upon 1/12th octave bins with array focussed on slat region. Configuration angle of attack is 10 deg., Reynolds number is 7.2 million, Mach number is 0.2. (b) Instantaneous fluctuation pressure, in vicinity of leading-edge slat, from CFD calculation. Slat deflection is 30 deg.



(a)

(b)

Figure 10. (a) Spectra for observer positioned at 270 deg. with 30 deg. slat deflection. (b) Comparison of squared acoustic pressure at individual microphones to that predicted computationally. Microphone positions and values are shown with squares; dashed line indicates computationally predicted values.

produced noise. Although the acoustic array used in the experiment was not intended to provide any directivity information, the high-frequency acoustic signal was so loud that it overwhelmed the intrinsic wind-tunnel noise and can be identified from the spectrum of some of the individual microphones used in the acoustic array. The relative amplitudes of the mean square fluctuating pressure in a frequency range around 50 kHz from a subset of microphones having approximately the same cross-stream location are compared with computed values in Fig. 10(b). The maximum amplitude of the microphone data is scaled with the maximum amplitude of the calculation. The non-zero microphone response far-upstream is associated with the wall-pressure fluctuations of the turbulent boundary layer along the wind-tunnel ceiling. These fluctuations are not included as part of the CFD calculations. Slightly upstream of the slat leading edge, the noise level rises. The maximum amplitude occurs in the mid-chord region followed by a sharp drop in amplitude. The qualitative features of the computations agree remarkably well with the microphone data, and the directivity results aided in the redesign of the acoustic array for a subsequent wind-tunnel test.

ADVANCED TOOLS

Although great strides have been made in simulating acoustic phenomena, the costs associated with some of the calculations are clearly limiting. The unsteady RANS calculation of the 2-D slat shedding required over 100 CRAY hours. The projection for a 3-D problem is enormous. It is unlikely that advances in computer power alone will make all of the needed calculations feasible. To help bridge the gap between available resources and needed simulations, some advanced methodologies are being developed that are much more efficient and accurate than traditional methods. Two main paths are being explored. Most grids used today are still block-structured, and the macro-element technique is being developed to provide more accurate interface conditions that can be retrofitted into current codes and used in new codes with high-order finite-difference spatial operators. The other technique being developed is the discontinuous Galerkin which provides high-order on unstructured grids.

DISCONTINUOUS GALERKIN

The process of generating a block-structured mesh with the smoothness required for high-accuracy schemes is a time-consuming process often measured in weeks or months. Unstructured grids about complex geometries are more easily generated, and for this reason, methods using unstructured grids have gained favor for aerodynamic analyses. However, they have not been utilized for acoustics problems because the methods are generally low-order and incapable of propagating waves without unacceptable levels of dissipation and dispersion. Attempts to extend finite-difference and finite-volume methods for unstructured grids to high-order by increasing the stencil size have introduced storage and robustness problems.

The discontinuous Galerkin method[23, 24] is a compact finite-element projection method that provides a practical framework for the development of a high-order method using unstructured grids. Higher-order accuracy is obtained by representing the solution as a high-degree polynomial whose time evolution is governed by a local Galerkin projection. This approach results in a compact and robust method whose accuracy is insensitive to mesh smoothness. The traditional implementation of the discontinuous Galerkin uses quadrature for the evaluation of the integral projections and is prohibitively expensive. Atkins and Shu[25] introduced the quadrature-free formulation in which the integrals are evaluated a-priori and exactly for a similarity element. The approach has been demonstrated to possess the accuracy required for acoustics even in cases where the grid is not smooth. Other issues such as boundary conditions and the treatment of non-linear fluxes have also been studied in earlier work[26, 27].

A major advantage of the discontinuous Galerkin method is that its compact form readily permits a non-heterogeneous treatment of a problem. That is, the shape of elements used, the degree of approximation, even the choice of governing equations, can be allowed to vary from element to element with no loss of rigor in the method. To take advantage of this flexibility, an object-oriented C++ computer program that implements the discontinuous Galerkin method has been developed and validated. However, many of the applications have involved benchmark problems for aeroacoustics[5] with relatively simple two-dimensional geometries and linearized equations with uniform mean flows. Recent work has been aimed at adding and validating additionally capability that is essential to the aeroacoustic analysis of large complex configurations.

Current applications of the method involve three-dimensional problems, the treatment of nonuniform mean flows, viscous flows, and the efficient use of parallel computing platforms. With these new capabilities, this tool will enable rapid aeroacoustic analyses of realistic aircraft configurations. When coupled with currently available grid generators and large parallel computers, the entire process of mesh generation, problem setup, and calculation can be performed

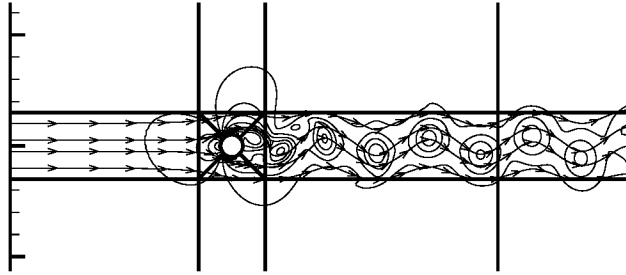


Figure 11. Density contours and streamlines for flow over a circular cylinder. The Mach number is 0.4 and the Reynolds number is 150. Dark lines represent macro-element boundaries.

rapidly.

MACRO-ELEMENT FINITE-DIFFERENCE

The most common approach used to handle complex geometries in CFD is the use of block-structured grids. There are many different varieties including one-to-one point matching, arbitrary patching, and overset zonal boundaries, but all require some sort of method to transfer information between the different blocks. Most codes rely on low-order interpolation formulas that can produce small but obvious artificial discontinuities in the flow variables across the boundaries. The problem is usually much more severe for unsteady problems when the grid is not sufficiently fine. Furthermore, interface conditions generally do not have suitable error properties and contribute to the nearly universal problem of codes not converging to design accuracy for realistic problems. Still, there has been a great deal of research into the proper methodologies for solving discrete equations efficiently on structured grids, and structured grids continue to be preferred for boundary layer flows.

In addition to the standard problems in CFD, most practitioners involved in unsteady computations, including aeroacoustics, prefer to use structured meshes. At several workshops[4, 5] on computational aeroacoustics, high-order, finite-difference methods have been shown to be much more efficient at minimizing dissipation and dispersion in propagating acoustic waves than traditional methods with many grid points. However, finite-difference methods perform best on smooth, structured grids which are often difficult to generate. Furthermore, high-order methods often suffer from robustness and stability problems stemming from non-smooth meshes and discontinuous flows. Blocking allows structured grids to be used around complex geometries, and makes it somewhat easier to make the grids smooth. However, standard patching techniques are wholly unsuited for high-order methods, especially for unsteady flows. Not only do they not provide adequate accuracy, they are often unstable. High-order methods would also benefit from interface conditions that could be used to break up larger domains so that subdomains could be run on different nodes of a parallel computer. With the continued advancements in parallel computers comprised of many scalar processors, this is becoming a very important issue.

In a coordinated effort, Carpenter *et al.*[28, 29] have developed high-order patching conditions with both order and stability proofs for high-order methods. The individual blocks are referred to as macro-elements. The only requirement for the grid is that the interface be point matched, or C_0 , but the derivatives may be discontinuous. Although not completely general, it does provide some significant flexibility in grid generation and is useful for splitting up a domain for a parallel computation. Conditions for fourth- and sixth-order explicit as well as fourth-order compact have been developed. Figure 11 shows density contours and streamlines around a circular cylinder with a grid partitioned into macro-elements. The Mach number is 0.4 and the Reynolds number is 150 which produces strong vortex shedding. Notice that there are nearly triangular shaped elements in the vicinity of the cylinder, yet there is no apparent distortion to the contours or streamlines. The macro-element conditions are general enough that they could even be used as interface conditions for an unstructured grid.

LOW-STORAGE RUNGE-KUTTA

Although most of the previous discussion has focused on the spatial operators, it is just as important to maintain temporal accuracy in unsteady problems. Explicit Runge-Kutta time-stepping provides a simple way to obtain high-accuracy in time, but most of the classical formulas have high memory requirements to store many previous solutions or residuals. Kennedy *et al.*[30] have developed fourth- and fifth-order explicit Runge-Kutta formulas that

only require $2N$ storage for N unknowns. This can be a substantial savings in memory, and can also be very beneficial in the run time on cache-based computers which are often limited by memory access. Furthermore, some of the new Runge-Kutta methods have embedded lower-order formulas that allow for automated time-stepping by using the solutions from the two orders to determine if there is too much error and the time step needs to be decreased.

A difficulty with explicit time stepping for unsteady problems is that the time step must be chosen to keep the smallest cell in the entire grid stable. In boundary layer flows with strong clustering towards walls, this can result in a time-step orders of magnitude smaller than what is needed for temporal accuracy. Research is ongoing into different implicit methods that can be used in regions where the grid spacing is extremely small.

SUMMARY

Despite the simplifications used in the examples, the cost of performing many of the acoustic calculations was still very high. Just obtaining a highly resolved mean flow for a high-lift flap system required 50 CRAY C-90 hours, and an unsteady RANS of a two-dimensional slat problem required over 100 hours. Nonetheless, some significant insight has been gained by applying currently available computational techniques to problems of interest. Typically, the calculations concentrated on resolving certain frequency ranges rather than trying to solve for all of the scales simultaneously. Because many important noise sources are narrow band, this approach is appropriate. The noise generated from vortex-shedding at a slat trailing edge is a good example in which this approach was taken, and a previously unknown noise source was identified. There remain many problems that cannot be solved today, and some of the efforts at NASA Langley to develop advanced tools that will enable the next generation of acoustic simulations have been highlighted.

ACKNOWLEDGMENTS

The author would like to thank the members of the Computational Modeling and Simulation Branch at NASA Langley Research Center for their significant contributions to this paper.

REFERENCES

1. W. R. WATSON, M. G. JONES, S. E. TANNER and T. L. PARROTT 1996 *AIAA Journal* **34**(3), 548–554. Validation of a numerical method for extracting liner impedance.
2. P. J. MORRIS, Q. WANG, L. N. LONG and D. P. LOCKARD 1997 *AIAA Paper No. 97-1598*. Numerical predictions of high-speed jet noise.
3. J. C. HARDIN and D. S. POPE 1994 *Theoretical and Computational Physics* **6**(5-6). An acoustic/viscous splitting technique for computational aeroacoustics.
4. J. C. Hardin and M. Y. Hussaini, editors 1993 *Computational Aeroacoustics*. Springer-Verlag. (Presentations at the Workshop on Computational Aeroacoustics sponsored by ICASE and the acoustics division of NASA LaRC on April 6-9.)
5. C. K. W. Tam and J. C. Hardin, editors 1997 *Second Computational Aeroacoustics (CAA) Workshop on Benchmark Problems*. NASA CP-3352. (Proceedings of a workshop sponsored by NASA and Florida State University in Tallahassee, Florida on Nov. 4-5, 1996.)
6. C. RUMSEY, R. BIEDRON and J. THOMAS 1997 *TM 112861*. NASA. (presented at the Godonov's Method for Gas Dynamics Symposium, Ann Arbor, MI.) CFL3D: Its history and some recent applications.
7. S. L. KRIST, R. T. BIEDRON and C. RUMSEY 1997. NASA Langley Research Center, Aerodynamic and Acoustic Methods Branch. *CFL3D User's Manual (Version 5)*.
8. C. L. RUMSEY, M. D. SANETRIK, R. T. BIEDRON, N. D. MELSON and E. B. PARLETTE 1996 *Computers and Fluids* **25**(2), 217–236. Efficiency and accuracy of time-accurate turbulent Navier-Stokes computations.
9. M. J. LIGHTHILL 1952 *Proceedings of the Royal Society* **A221**, 564–587. On sound generated aerodynamically, I: general theory.

10. J. E. FFWCS WILLIAMS and D. L. HAWKINGS 1969 *Philosophical Transactions of the Royal Society* **A264**(1151), 321–342. Sound generated by turbulence and surfaces in arbitrary motion.
11. K. S. BRENTNER and F. FARASSAT 1998 *AIAA Journal* **36**(8), 1379–1386. An analytical comparison of the acoustic analogy and kirchhoff formulation for moving surfaces.
12. F. FARASSAT and G. P. SUCCI 19883 *Vertica* **7**(4), 309–320. The prediction of helicopter discrete frequency noise.
13. K. S. BRENTNER 1986. NASA Langley Research Center. (NASA TM 87721.), *Prediction of Helicopter Discrete Frequency Rotor Noise – A Computer Program Incorporating Realistic Blade Motions and Advanced Formulation*
14. K. S. BRENTNER and F. FARASSAT 1994 *Journal of Sound and Vibration* **170**(1), 79–96. Helicopter noise prediction: The current status and future direction.
15. C. L. RUMSEY, R. BIEDRON, F. FARASSAT and P. L. SPENCE 1998 *Journal of Sound and Vibration* **213**(4), 643–664. Ducted-fan engine acoustic predictions using a Navier-Stokes code.
16. C. L. STRETT 1998 *AIAA Paper No.* 98-2226. Numerical simulation of a flap-edge flowfield.
17. B. A. SINGER, K. S. BRENTNER, D. L. LOCKARD and G. M. LILLEY 1999 *AIAA Paper No.* 99-0231. Simulation of acoustic scattering from a trailing edge.
18. S. WAGNER, R. BAREISS and G. GUIDATI 1996 *Wind Turbine Noise*. New York: Springer.
19. J. R. UNDERBRINK and R. P. DOUGHERTY 1996 *NOISECON 96*. Array design for non-intrusive measurements of noise sources.
20. M. R. KHORRAMI, M. E. BERKMAN, M. CHOUDHARI, B. A. SINGER, D. L. LOCKARD and K. S. BRENTNER 1999 *AIAA Paper No.* 99-1805. Unsteady flow computations of a slat with a blunt trailing edge.
21. B. A. SINGER, D. L. LOCKARD, K. S. BRENTNER, M. R. KHORRAMI, M. E. BERKMAN and M. CHOUDHARI 1999 *AIAA Paper No.* 99-1802. Computational acoustic analysis of slat trailing-edge flow.
22. D. P. LOCKARD. (to appear in *journal of sound and vibration*.) An efficient, two-dimensional implementation of the Ffowcs Williams and Hawkings equation.
23. C. JOHNSON and J. PITKARATA 1986 *Mathematics of Computation* **46**(176), 1–26. An analysis of the discontinuous Galerkin method for a scalar hyperbolic equation.
24. B. COCKBURN and C.-W. SHU 1998 *SIAM Journal of Numerical Analysis* **35**, 2440–2463. The local discontinuous Galerkin method for time-dependent convection-diffusion systems.
25. H. L. ATKINS and C. W. SHU 1997 *AIAA Journal* **36**(5), 775–782. Quadrature-free implementation of discontinuous Galerkin method for hyperbolic equations.
26. H. L. ATKINS 1997. AIAA Paper-97-1581. (Third Joint CEAS/AIAA Aeroacoustics Conference, May 12-14.) Continued development of the discontinuous Galerkin method for computational aeroacoustic applications.
27. H. L. ATKINS 1997. AIAA Paper 97-2032. (13th AIAA computational fluid dynamics conference, Snowmass Village, Colorado, June 29-July 2.) Local analysis of shock capturing using discontinuous Galerkin methodology.
28. M. H. CARPENTER, J. NORDSTROM and D. GOTTLIEB 1999 *Journal of Computational Physics* **148**, 341–365. A stable and conservative interface treatment of arbitrary spatial accuracy.
29. M. H. CARPENTER and J. NORDSTROM 1999 *Journal of Computational Physics* **148**, 621–645. Boundary and interface conditions for high-order finite-difference methods applied to the Euler and Navier-Stokes equations.
30. C. A. KENNEDY, M. H. CARPENTER and R. LEWIS. (to appear in *applied numerical mathematics*.) Low-storage explicit Runge-Kutta schemes for the compressible Navier-Stokes equations.



NUMERICAL MODELING OF HELIUM PRESSURIZATION SYSTEM OF PROPULSION TEST ARTICLE (PTA)

Todd Steadman and Alok Majumdar
Sverdrup Technology
Huntsville, AL

Kimberly Holt
Marshall Space Flight Center
Huntsville, AL

ABSTRACT

A transient model of the Propulsion Test Article (PTA) Helium Pressurization System was developed using the Generalized Fluid System Simulation Program (GFSSP). The model included feed lines from the facility interface to the engine purge interface and Liquid Oxygen (LOX) and Rocket Propellant 1 (RP-1) tanks, the propellant tanks themselves including ullage space and propellant feed lines to their respective pump interfaces. GFSSP's capability was extended to model a control valve to maintain ullage pressure within a specified limit and pressurization processes such as heat transfer between ullage gas, propellant and the tank wall. The purpose of the model is to predict the flow system characteristics in the entire pressurization system during 80 seconds of lower feed system priming, 420 seconds of fuel and LOX pump priming and 150 seconds of engine firing. Subsequent to the work presented here, the PTA model has been updated to include the LOX and RP-1 pumps, while the pressurization option itself has been modified to include the effects of mass transfer. This updated model will be compared with PTA test data as it becomes available.

INTRODUCTION

The Propulsion Test Article (PTA) provides a test bed environment to evaluate low cost solutions to booster technology. PTA consists of Liquid Oxygen (LOX) and Rocket Propellant 1 (RP-1) tanks with a total useable propellant load of 44000 lbs. The pressurization system is one of the major PTA subsystems. This system provides helium to the propellant tanks for pressurization, to valves for actuation, and to the engine for purges. A model was built to verify by analysis that the Main Propulsion System (MPS)/engine helium system requirements are met.

The pressurization system of PTA consists of a LOX tank and an RP-1 tank that are both pressurized by helium. A mathematical model was required to predict the ullage and propellant conditions for PTA during pressurization for lower feed system priming, pump priming, and engine firing. The model prediction will ensure that the helium system can provide adequate helium flow to both propellant tanks and the engine, the temperature levels inside the tanks remain within acceptable limits, and the propellant interface pressure satisfies the Net Positive Suction Pressure (NPSP) requirements of its respective pump. The pressurization of a propellant tank is a complex thermodynamic process with heat and mass transfer in a stratified environment. Ring[1] described the physical processes and heat transfer correlation in his monograph. Epstein and Anderson[2] developed an equation for the prediction of cryogenic pressurant requirements for axisymmetric propellant tanks. Recently, Van Dresar[3] improved the accuracy of Epstein and Anderson's correlation for liquid hydrogen tanks. A computer program[4] was also developed for Marshall Space Flight Center to simulate pressurization sequencing for the LOX and hydrogen tanks in the Technology Test Bed. This program employs a single node thermodynamic ullage model to calculate the ullage pressure based on ideal gas law, heat transfer and mixing. McRight[5] estimated the helium

requirement and sized the flow control orifices based on choked flow assumptions for the PTA Helium Pressurization System.

The objective of the present work is to develop an integrated mathematical model from the facility helium supply interface to the PTA/engine interfaces to model pressurization prior to and during engine operation. The model has four primary functions. They are:

- a. To verify by analysis that the MPS/engine requirements are met.
- b. To predict the flow rate and pressure distribution of the helium supply line feeding both the LOX and RP-1 tanks,
- c. To predict the ullage conditions considering heat and mass transfer between the ullage, propellant and the tank wall,
- d. To predict the propellant conditions leaving the tank.

The Generalized Fluid System Simulation Program (GFSSP) [6] has been used to develop this model. GFSSP is a general purpose fluid flow simulation program for modeling steady state and transient flow distribution in a fluid network. The transient capability of GFSSP has recently been extended[7] to model the pressurization process in a propellant tank. A simple 5-node model was developed to test the numerical stability and physical sensitivity of the formulation. The predicted pressurant requirement was also verified by comparing with Epstein and Anderson's[2] correlation.

This paper describes an integrated GFSSP model of the Helium Pressurization System of PTA. The model extends from facility interface to engine purge and pump interfaces. It includes all piping, fittings, orifices and valves. Both RP-1 and LOX tanks are included in the model. Each propellant tank has a diffuser and control system. Pressure and temperature are specified at the interfaces. The purpose of the model is to predict the pressure and flow rate distribution in the entire system. GFSSP predictions of helium requirements have also been compared with McRight's[5] analysis.

GFSSP MODEL

An integrated GFSSP model of the Helium Pressurization System of PTA is shown in Figure 1. The model consists of 61 nodes and 60 branches. The model contains six boundary nodes, which are listed along with the interface they represent in Table 1.

Table 1. PTA Boundary Node Locations

| Boundary Node | Interface |
|---------------|-------------------------------|
| 1 | Facility |
| 61 | Engine (Purge) |
| 53 | Ullage-propellant (LOX Tank) |
| 55 | LOX Pump |
| 30 | Ullage-propellant (RP-1 Tank) |
| 32 | RP-1 Pump |

It may be noted that the nodes representing the ullage-propellant interface (Node 53 and 30) are pseudo-boundary nodes. The code uses the calculated ullage pressure at the previous time step instead of pressures provided by the user through history files. Helium enters into the system from the facility interface through 1.5 inch outside diameter (OD) tubing. From this main line, helium is distributed into three parallel branches. The first branching takes place after 128 inches of tubing. This branch supplies helium to the engine for engine purges through 0.75 inch OD tubing. The second branching takes place 305 inches downstream of the first branch. This branch supplies helium to the LOX tank using 1.0-inch OD tubing. The remainder of the helium line is routed to pressurize the RP-1 tank using 0.75-inch OD tubing. All tubing sizes have a wall thickness of 0.109 inches. The lines leading to the LOX and RP-1 tanks each have two parallel legs, one of which remains closed during a given operation. The left leg of the circuit is used to pressurize the tank during lower feed system priming and pump priming operations while the right leg of the circuit is used to pressurize the tank just prior to and during engine firing. In the model discussed in

this paper, setting a high resistance in the appropriate branches eliminated the flow to the leg not being used for that particular run.

MODEL RESULTS

The GFSSP model shown in Figure 1 was broken into six separate runs that covered a period of 650 seconds, beginning at -500 seconds before engine start and continuing to +150 seconds after engine start using a time step of 0.1 second. The first three runs represent the lower feed system priming, the next two runs represent the pump priming and the final run represents the engine firing. The model was broken into multiple runs to accurately model the various propellant flow rates required at different stages of operation. These flow rates were achieved by altering the orifice sizes in branches 1054 and 1031 of Figure 1 until GFSSP predicted the calculated flow rate for that particular period of operation.

The first run is a steady state analysis, which is used exclusively to obtain an initial solution for use in the first transient run. Each run thereafter uses the previous run's final time step solution as its initial condition. The second run begins at -500 seconds and runs for one second to -499 seconds. During this time there is no flow leaving either the LOX or RP-1 tank. The ullages of each tank are initially at a pressure of 14.7 psia with their respective ullage pressure control set points set to a nominal pressure of 20 psia with a plus or minus 3 psi control band. The third run lasts for 79 seconds, beginning at -499 seconds and ending at -420 seconds. The ullage pressure control remains at a set point of 20 psia while there is now a 0.12 lbm/s propellant bleed flow from the LOX tank and a 0.1 lbm/s propellant bleed flow from the RP-1 tank. During a test, the RP-1 system is primed before the LOX system, but for simplicity, both propellant systems are primed at the same time during the analysis.

The fourth run covers a 60 second duration from -420 seconds to -360 seconds. At the beginning of this run the ullage pressure control set points increase to 67 psia for the LOX tank and 50 psia for the RP-1 tank with a plus or minus 3 psi control band. The propellant bleed flow rates see an increase to 1 lbm/s for the LOX tank and 0.25 lbm/s for the RP-1 tank. At the end of this run the RP-1 bleed is closed and the system is considered primed. The fifth run encompasses the remaining 360 seconds before engine start from -360 seconds to 0 seconds. The ullage pressure control set points remain the same for the first 240 seconds of this run. At -120 seconds prepress occurs and the set points for each tank rise by 5 psi, resulting in nominal set points of 72 psia for the LOX tank and 55 psia for the RP-1 tank with a plus or minus 3 psi control band. The propellant bleed flow rate for LOX remains at 1 lbm/s and there is no RP-1 propellant bleed flow during this time.

The sixth and final run covers the 150 second engine firing period from 0 seconds to +150 seconds. Initially, the ullage pressure control set points remain at their prepress values, but after 3 seconds they drop 5 psi to the run pressure of 67 psia for the LOX tank and 50 psia for the RP-1 tank with a plus or minus 3 psi control band. Propellant flow to the engine is 139 lbm/s for LOX and 64 lbm/s for RP-1.

PRESSURE

Figure 2 shows the predicted pressure history of the RP-1 ullage, RP-1 tank bottom, LOX ullage and LOX tank bottom pressures. The difference in pressure between the tank bottom and ullage is the gravitational head, which slowly reduces as propellant is drained from the tank. The saw tooth nature of the pressure profiles is due to the control valves that are set to close or open as the ullage pressures rise above or fall below the prescribed control band. This is especially evident in the LOX pressure predictions, where the propellant bleed flow and the ullage thermal characteristics cause enough pressure drop in the tank to cycle the control valve repeatedly. On the other hand the RP-1 propellant bleed flow is low enough that once the control valve closes there is not enough subsequent pressure drop in the tank to open the valve again until the next change in the ullage pressure control set point. Thus, the RP-1 pressure predictions appear as a series of straight lines prior to engine start.

Valve cycling is quite pronounced in both the LOX and RP-1 tank pressure predictions once the engine starts. The pressure predictions show that during engine firing the maximum tank bottom pressure in the RP-1 tank is 61.5 psia while the LOX tank bottom pressure achieves a maximum value of 83.5 psia. These maximum values are seen

during the first three seconds of engine firing when the ullage pressure control set points are still at their prepress levels. It is also observed that the frequency of pressure oscillation is larger in the LOX tank than the RP-1 tank. This observation is attributable to the higher volumetric flow rates and the ullage thermal collapse associated with the LOX tank as compared to those required for the RP-1 tank.

TEMPERATURE

Figure 3 shows the predicted ullage temperature history in the RP-1 tank. Initially wall and propellant temperatures were assumed equal at 70 °F. Heat transfer between the ullage gas and wall is not very significant in the RP-1 tank and as a result the tank wall temperature remains approximately constant over the 500 seconds before engine start and rises only two degrees during the 150 second engine firing. Ullage temperature, on the other hand, experiences two significant temperature spikes in the 500 seconds before engine start. These spikes are associated with increases in the ullage pressure set points (-493 sec, -416 sec) and the assumption that the helium enters at 120 °F. The second, and largest, spike peaks at 96 °F but ullage temperature drops down to 71 °F before engine start. During engine firing, ullage temperature increases by about 28 °F due to mixing and pressurization. Ullage temperature diminishes slightly during the period of valve closure. This is due to heat transfer from the ullage gas to the wall.

The predicted ullage temperature history in the LOX tank is shown in Figure 4. The LOX ullage temperature is assumed to be initially at -260 °F while the tank wall temperature is assumed to be initially at -300 °F. The tank wall temperature rise is more pronounced in the LOX tank than the RP-1 tank, rising 43 °F over the course of the 650-second run. Unlike RP-1, LOX ullage temperature fluctuates throughout the 500 seconds before engine start due to valve cycling. During this time, temperature spikes similar to those discussed with RP-1, which are associated with increase in the ullage pressure set points (-494 sec, -417 sec), are evident. The largest LOX ullage temperature spike peaks at a value of -88 °F but drops back to -255 °F at engine start. During engine firing, the temperature rise is 173 °F. The higher temperature rise in the LOX tank is primarily due to the fact that the LOX ullage is initially assumed to be at -260 °F and mixes with helium at 120 °F. On the other hand, the initial temperature difference between the RP-1 ullage and the helium pressurant is much smaller. The other contributing factor is the higher helium flow rate into the LOX tank.

MASS FLOW RATE

Figure 5 shows the helium flow rates. Helium flow rate varies over time due to the opening and closing of the control valves. The flow from the facility interface is distributed to three branches. A nearly constant flow rate (about 0.4 lbm/sec) is predicted to the engine purge interface for engine purges. The maximum flow rates to the LOX and RP-1 tanks are about 0.34 lbm/sec and 0.085 lbm/sec, respectively. Table 2 shows a comparison of GFSSP helium flow predictions with McRight's[3] pressurization analysis model.

Table 2. Comparison between GFSSP and McRight's[3] Helium Flow Rates

| GFSSP (lbm/sec) | | | | McRight (lbm/sec) | | | |
|--------------------|-------------|--------------|------------|----------------------|-------------|------------|-------------|
| Facility | LOX | RP-1 | Purge | Facility | LOX | RP-1 | Purge |
| 0.825 | 0.34 | 0.085 | 0.4 | 1.00 | 0.35 | 0.1 | 0.55 |

The comparison shown in Table 2 appears reasonable considering that McRight's analysis did not consider pressure loss in lines and fittings and choked flow rate through the orifice was calculated based on a facility pressure of 765 psia. GFSSP calculates pressure drop through the line, therefore the choked flow rate at lower pressure is evidently less than McRight's prediction.

The propellant flow rates from RP-1 and LOX tanks are shown in Figure 6. Figure 7 shows the RP-1 and LOX propellant flow rates in the period prior to engine start. All flow rates were achieved by altering the restrictions downstream of the LOX and RP-1 tanks to match the flow rates required at that point in time. This was done because of a lack of proper flow geometry information downstream of the propellant tanks. The observed

oscillation in flow rate is due to the ullage pressure control band. It should be noted that this model is based on prescribed pressures at inlet and outlet boundary. This oscillating flow prediction can be eliminated by extending the model further downstream to include the pumps and appropriate resistances the pumps must overcome in the system.

SUMMARY OF RESULTS

The GFSSP model of the PTA pressurization system predicts the following flow system characteristics during the 150-second engine operation period of the run except where noted.

Average LOX ullage pressure = 67.2 psia
Average LOX tank bottom pressure = 73.0 psia
LOX temperature = 160 R
Average LOX flow rate to the engine = 139.0 lbm/sec
Total LOX supply in the complete 650 second run = 324 ft³
LOX ullage temperature rise in the complete 650 second run = 173 R

Average RP-1 ullage pressure = 50.1 psia
Average RP-1 tank bottom pressure = 52.6 psia
RP-1 temperature = 530 R
Average RP-1 flow rate to the engine = 62.4 lbm/sec
Total RP-1 supply in the complete 650 second run = 198 ft³
RP-1 ullage temperature rise in the complete 650 second run = 29 R

Maximum Helium flow rate to LOX tank = 0.34 lbm/sec
Maximum Helium flow rate to RP-1 tank = 0.085 lbm/sec
Average Helium flow rate to Engine Interface = 0.4 lbm/sec
Maximum Helium flow rate from Facility Interface = 0.825 lbm/sec

CONCLUSIONS

A detailed numerical model of a pressurization system consisting of LOX and RP-1 tanks was developed using the Generalized Fluid System Simulation Program. GFSSP's pressurization capability was further extended by developing a numerical model for simulating a control system for maintaining ullage pressure within a specified limit. GFSSP's predicted pressure history shows the evidence of opening and closing of valves during the draining of propellant from the tank. The model also predicts the variation of valve cycling frequency due to changes in the flow rate, ullage volume and heat transfer. Future work will include adding the LOX and RP-1 pumps to the model for a more realistic prediction of system characteristics as well as modifying the pressurization option to account for the effects of mass transfer from propellant to the ullage. Model predictions will be compared with measured data from PTA tests.

ACKNOWLEDGEMENT

This work was performed under the Task Directive entitled "Propulsion System Analysis" for MSFC Science and Engineering Contract NAS 8-40836 with Dr. Charles Schafer of Marshall Space Flight Center as Task Initiator. The authors would like to acknowledge Mr. Tom Beasley of Sverdrup Technology for his suggestions and review.

REFERENCES

1. Ring, Elliot, "Rocket Propellant and Pressurization Systems", Prentice Hall, 1964.
2. Epstein, M., and Anderson, R.E., "An Equation for the Prediction of Cryogenic Pressurant Requirements for Axisymmetric Propellant Tanks," *Advances in Cryogenic Engineering*, Vol. 13, Plenum, New York, 1968, pp. 207-214.
3. Van Dresar, Neil T., "Prediction of Pressurant Mass Requirements for Axisymmetric Liquid Hydrogen Tanks", *Journal of Propulsion and Power*, Vol. 13, No. 6, 1997, pp. 796-799.
4. A Computer Program entitled "TTBSIM" for simulating Tank Pressurization for Technology Test Bed at Marshall Space Flight Center, June 1997.
5. McRight, P., "Pressurization Analysis- A Visual Basic Computer Program to calculate mass flow rate of compressible sonic flow", Marshall Space Flight Center, November 14, 1997
6. Majumdar, A, Bailey, J. W., Schallhorn, P., Steadman, T., "A Generalized Fluid System Simulation Program to Model Flow Distribution in Fluid Networks", Sverdrup Technology Report No. 331-201-97-005, Contract No. NAS8-40836, October 1997.
7. Majumdar, A and Steadman, T., "Numerical Modeling of Pressurization of a Propellant Tank", Paper No. AIAA 99-0879, 37th AIAA Aerospace Sciences Meeting Conference and Exhibit, January 11-14, 1999, Reno, Nevada.

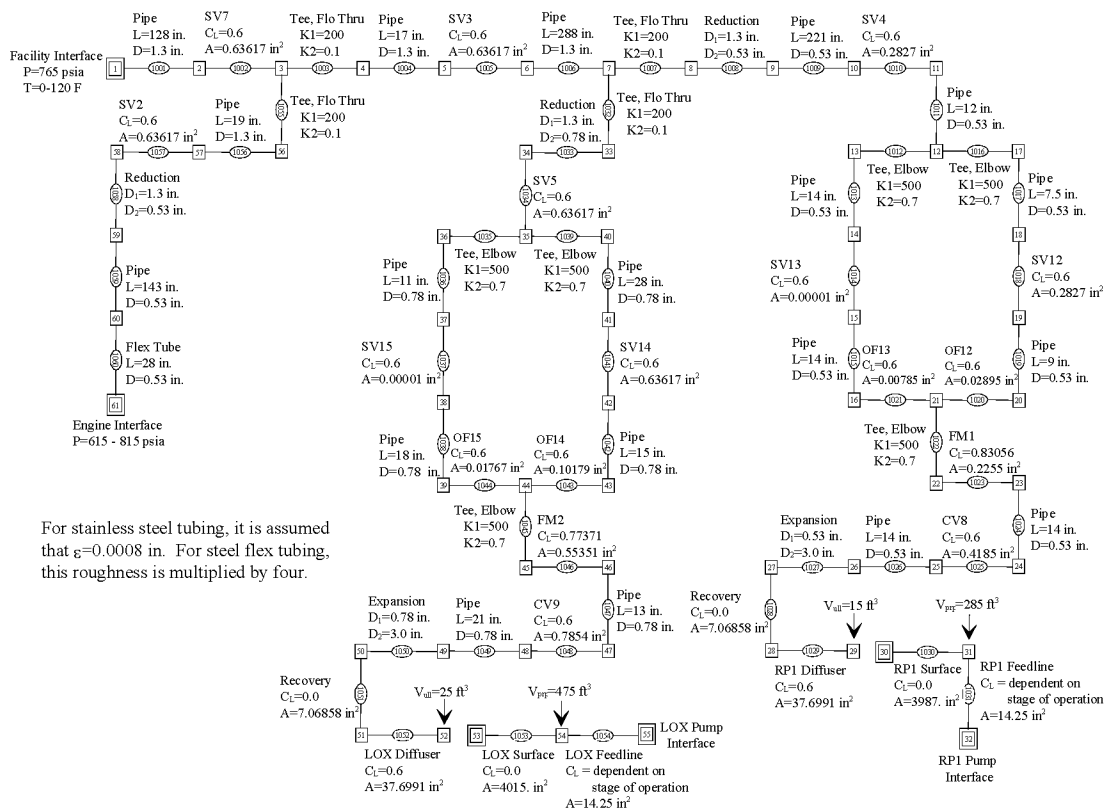


Figure 1. GFSSP Model of the PTA Pressurization System

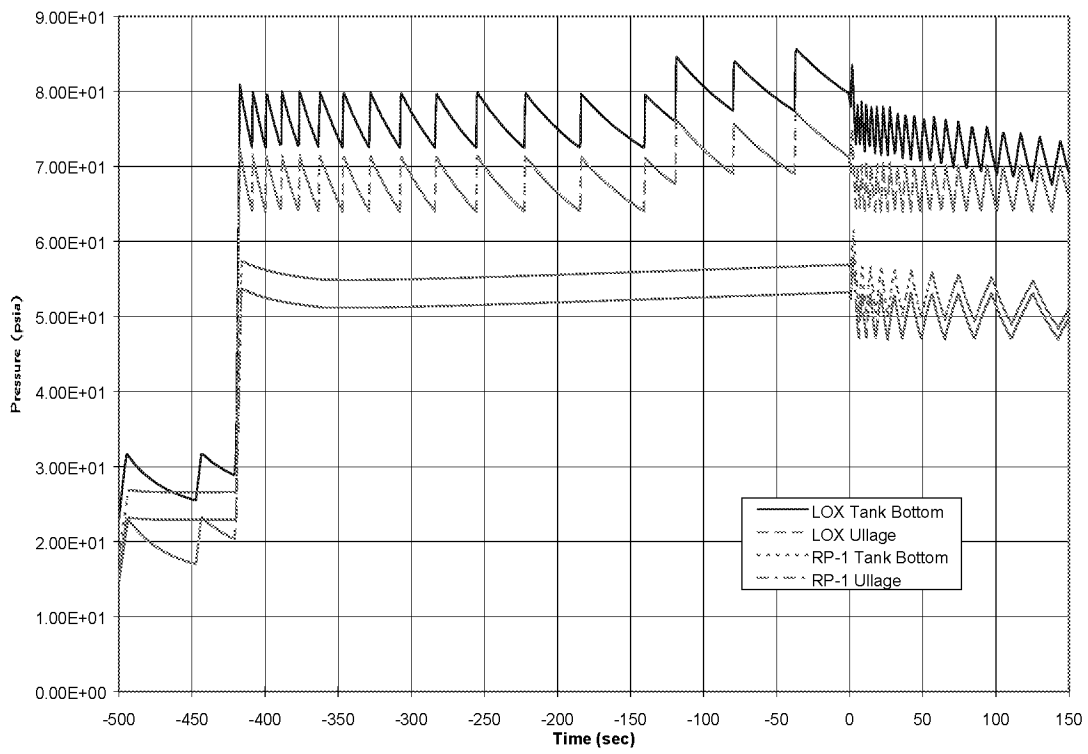


Figure 2. Propellant Tank Pressure History

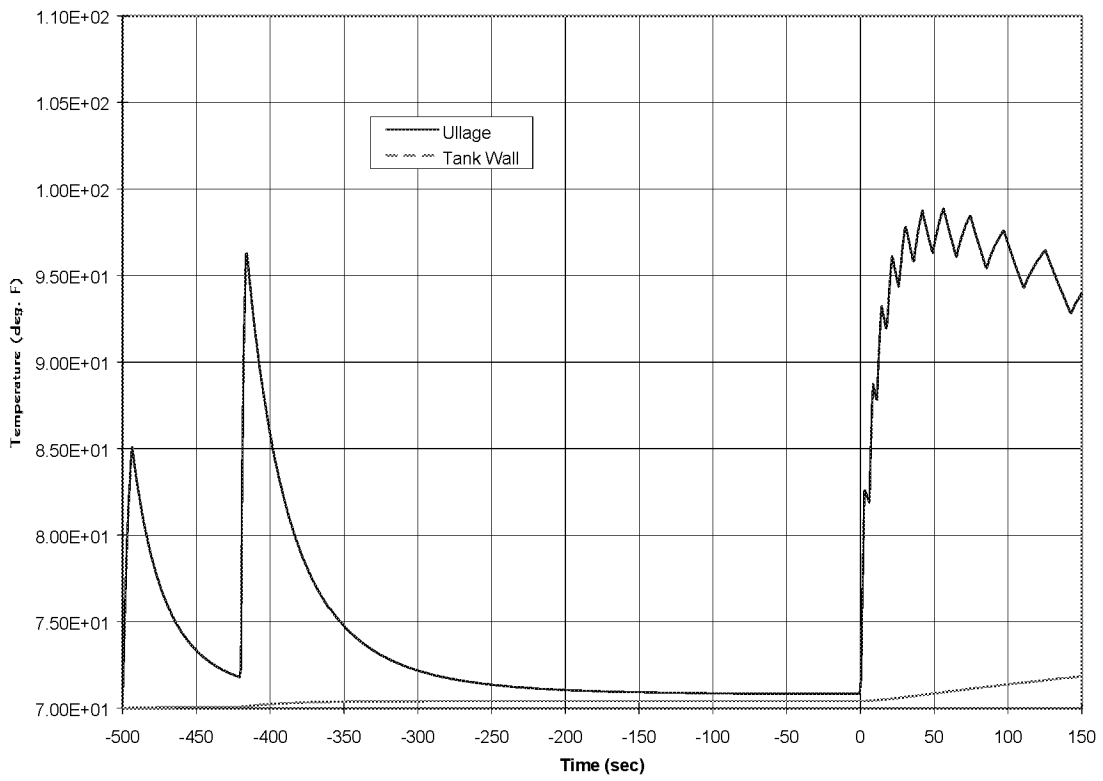


Figure 3. RP-1 Temperature History

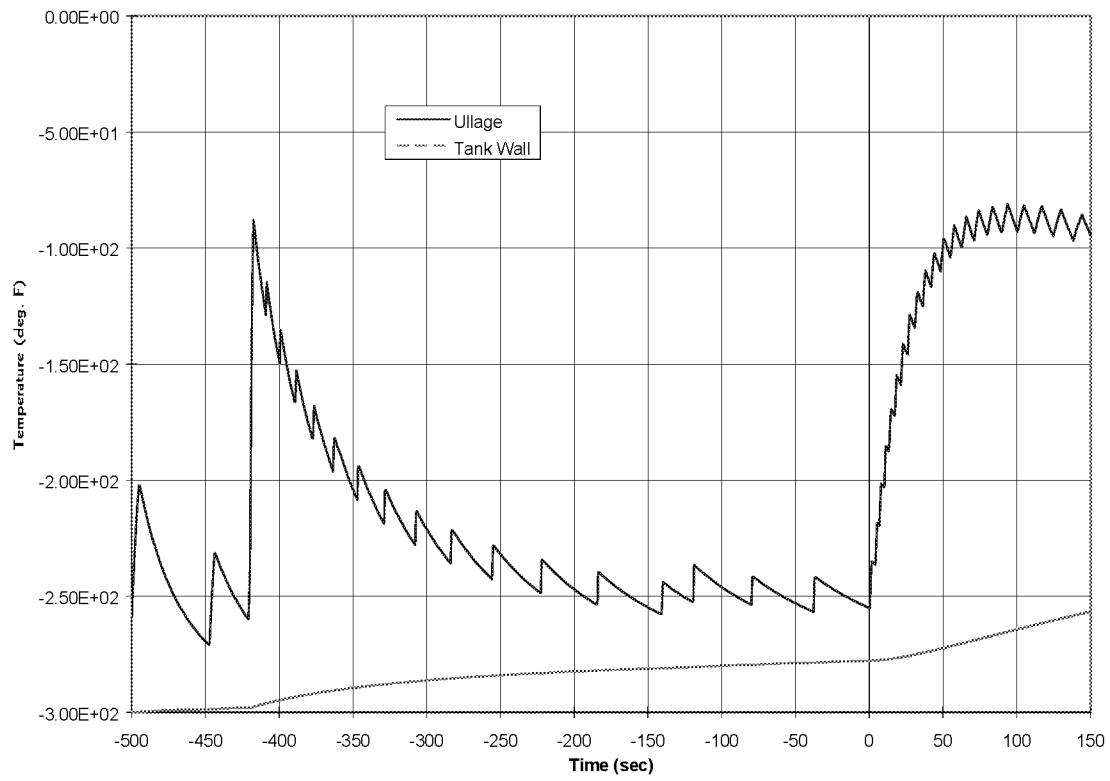


Figure 4. LOX Temperature History

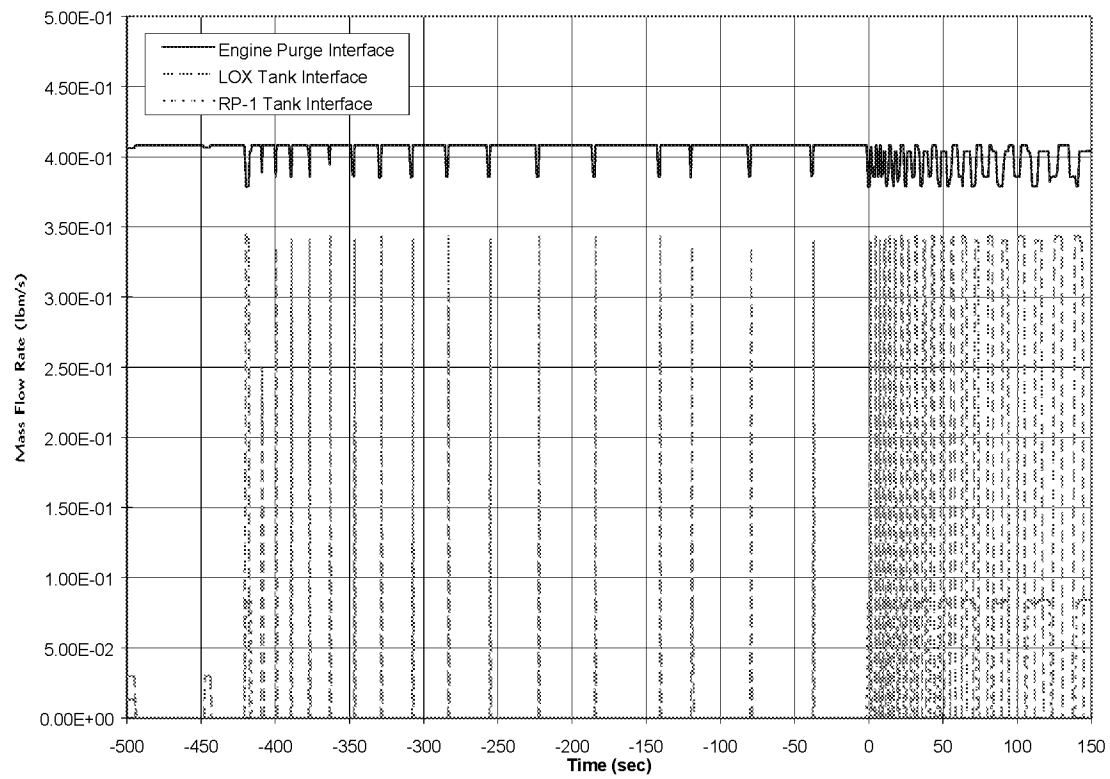


Figure 5. Helium Flow Rate History

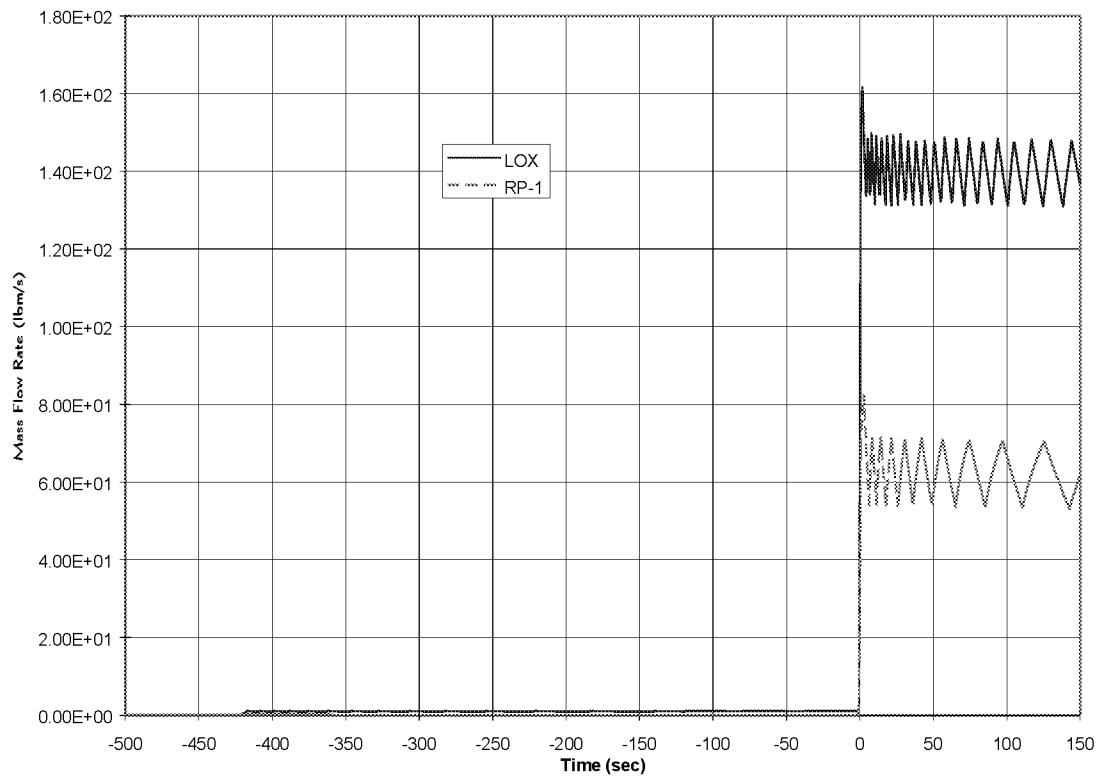


Figure 6. Propellant Flow Rate History

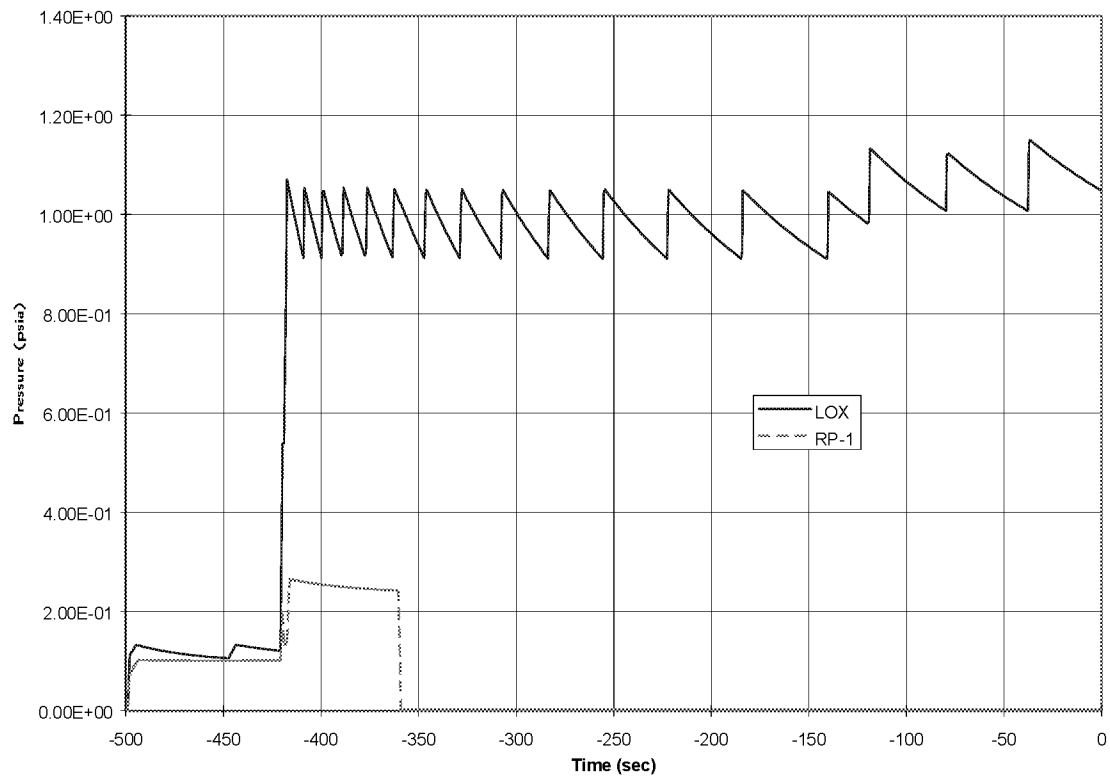


Figure 7. Propellant Bleed Flow Rate History Detail



ANALYTICAL ASSESSMENT OF A GROSS LEAKAGE EVENT WITHIN THE INTERNATIONAL SPACE STATION (ISS) NODE 2 INTERNAL ACTIVE THERMAL CONTROL SYSTEM (IATCS)

James M. Holt

National Aeronautics and Space Administration
Marshall Space Flight Center
MSFC, AL 35812

Stephen E. Clanton

Sverdrup Technology, Inc.
MSFC Group
Huntsville, AL 35806

ABSTRACT

Results of the International Space Station (ISS) Node 2 Internal Active Thermal Control System (IATCS) gross leakage analysis are presented for evaluating total leakage flow rates and volume discharge caused by a gross leakage event (i.e. open boundary condition). A Systems Improved Numerical Differencing Analyzer and Fluid Integrator (SINDA85/FLUINT) thermal hydraulic mathematical model (THMM) representing the Node 2 IATCS was developed to simulate system performance under steady-state nominal conditions as well as the transient flow effect resulting from an open line exposed to ambient. The objective of the analysis was to determine the adequacy of the leak detection software in limiting the quantity of fluid lost during a gross leakage event to within an acceptable level.

INTRODUCTION

Within the pressurized elements of the International Space Station (ISS), requirements exist to ensure a safe, habitable environment for the crew. Internal Active Thermal Control Systems (IATCS), typically pumped coolant loops utilizing a non-hazardous working fluid, have constraints on touch temperature, maximum design pressure and leakage. This paper addresses “gross” leakage, or leakage that is much greater than normal, specification leakage. Node 2 is required to limit the internal heat transport fluid leakage to no greater than one gallon per gross leakage event¹.

The quantity of fluid expelled during a gross leakage event is clearly defined, however the duration is only bounded in general terms by the “event.” Node 2 utilizes software to control IATCS functions, and thus, hardware and software response times must be taken into account to quantify the leakage “event.” The applicable software time constraints for gross leakage failure detection, isolation and recovery (FDIR) are as follows²:

| | |
|--|-------------|
| Time Averaged Accumulator Quantity Sensor Data | 1.7 seconds |
| Data Transfer Latency to INTSYS | 1.0 seconds |
| INTSYS Command to Node 2 Latency | 2.0 seconds |
| Pump Package Assembly (PPA) Response | 0.5 seconds |
| Total Time | 5.2 seconds |

Therefore, an “event” of 5.2 seconds must be analyzed to determine compliance of the Node 2 IATCS hardware and software (FDIR) designs with the gross leakage requirement. This paper presents an analysis of a gross leakage event for the Node 2 IATCS.

NODE 2 IATCS DESCRIPTION

The Node 2 IATCS consists of two separate single-phase, water coolant loops. The function of the IATCS is to provide heat rejection for subsystem avionics equipment, for the environmental control system and for subsystems and payloads within elements attached to Node 2. The two IATCS loops consist of a Low Temperature Loop (LTL), that provides coolant temperatures in the range of 38-43 °F, and a Moderate Temperature Loop (MTL), that provides coolant temperatures in the range of 61-65 °F. The Node 2 IATCS is schematically shown in Figure 1.

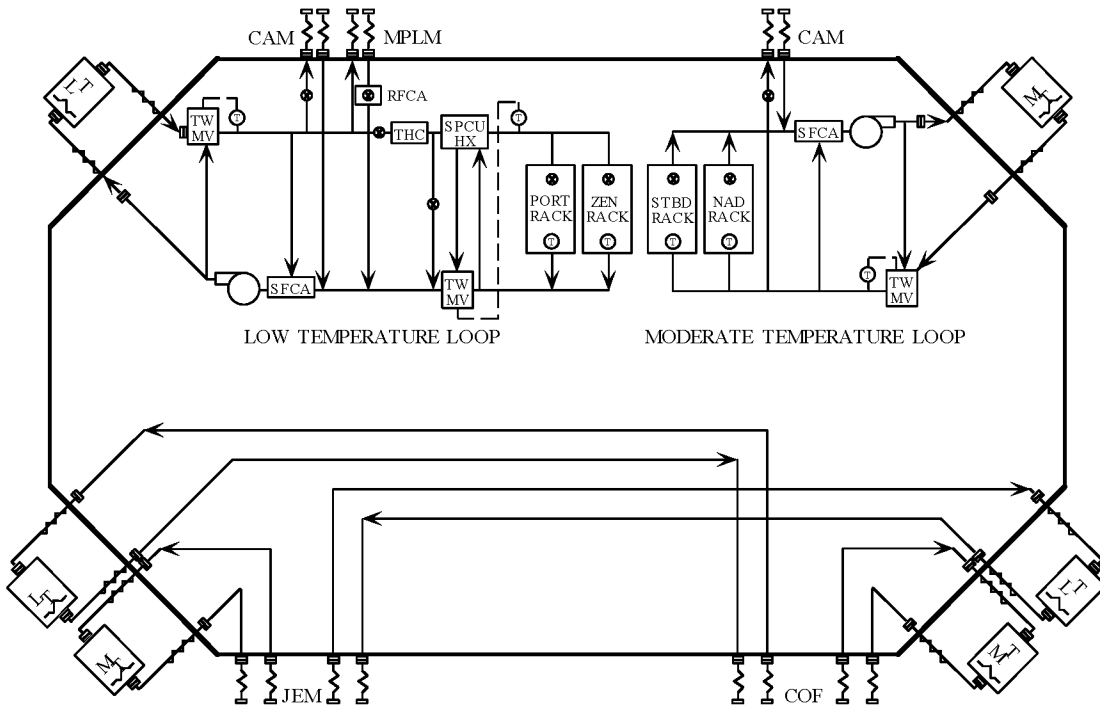


Figure 1. Node 2 IATCS

Each loop contains a Pump Package Assembly (PPA), capable of providing a mass flow rate of 3000 lbm/hr, and a System Flow Control Assembly (SFCA) that maintains a constant differential pressure across the system. Thermal control components include an ammonia/water heat exchanger, a Three-Way Mix Valve (TWMV), which controls the water supply temperature to subsystems and attached elements, and a regenerative heat exchanger (LTL only).

The PPA contains a centrifugal pump and an accumulator that maintains sufficient pressure at the pump inlet to avoid cavitation. The bellows within the accumulator is pressurized by gaseous nitrogen, actively controlled by a Nitrogen Interface Assembly (NIA). As will be presented, the accumulator plays a significant role, in addition to the pump, to the total fluid leakage during a gross leakage event. The accumulator has a gas side maximum design pressure of 35 psia, and a nominal operational pressure in the range of 18 to 30 psia. The accumulator has a fluid capacity of $680 \text{ in}^3 \pm 30 \text{ in}^3$ (2.8 gal. to 3.1 gal.)³. An accumulator

quantity sensor indicates the level of water within the accumulator, and at 59%, prompts the software to initiate the shutdown procedure⁴.

SINDA85/FLUINT THERMAL HYDRAULIC MATHEMATICAL MODEL

The gross leakage analysis is based on the Node 2 Design Review 1 (DR1) SINDA85/FLUINT IATCS Thermal Hydraulic Mathematical Model (THMM) developed by Alenia Aerospazio⁵. In order to analyze the transient, gross leakage event, a plenum at ambient pressure was added downstream of the leakage location, and inertia effects were added for all fluid lines. The most significant change to the model was logic added to simulate the transient pressure within the accumulator.

The mathematical model fluid network is constructed of "lumps" and "paths" and a set of governing equations are developed and solved within SINDA85/FLUINT. Three types of "lumps" exist within SINDA85/FLUINT: tank, junction and plenum. The Node 2 IATCS model primarily consists of tanks (finite volume) and junctions (zero volume), with a plenum (infinite volume) added to provide a "pressure" sink for the leakage location.

The algebraic forms of the mass and energy conservation equations for junctions are:

$$\sum \dot{m} = 0$$

$$\sum h \dot{m} + \dot{Q} = 0$$

where:

- \dot{m} mass flow rate
- h donor enthalpy
- \dot{Q} lump energy source or sink term.

Similarly, the governing equations for tanks are differential forms of the mass and energy conservation equations:

$$\sum \dot{m} = \frac{dM}{dt}$$

$$\sum h \dot{m} + \dot{Q} - P \left(\dot{V} + \frac{dP}{dt} VC \right) = \frac{dU}{dt}$$

where:

- M lump mass
- P lump pressure
- \dot{V} volumetric flow rate
- V lump volume
- C tank wall compliance factor
- U lump internal energy term.

The governing differential equation for tubes is a form of Newton's second law:

$$\frac{d\dot{m}}{dt} = \frac{A}{L} \left(\Delta P + HC + FC \dot{m} \left[\dot{m} \right]^{FPOW} + AC \dot{m}^2 - \frac{FK \dot{m}^2}{2\rho A^2} \right)$$

where:

| | |
|------------|--|
| ΔP | pressure difference |
| A | tube flow area |
| L | tube length |
| HC | head coefficient (pressure, body force) |
| AC | tube recoverable loss coefficient |
| FC | tube irrecoverable loss coefficient |
| FK | tube head loss coefficient |
| FPOW | flow rate exponent for FC; function of flow regime (ranges from 0, laminar, to 1, fully turbulent) |
| ρ | fluid density. |

Connectors can change flow rate instantaneously, and are governed by a linear algebraic constraint equation:

$$\dot{m}^{n+1} = \left(\frac{\partial \dot{m}}{\partial (\Delta P)} \right)^n (\Delta P_i - \Delta P_j)^{n+1} + \left(\dot{m}^{n+1} - \dot{m}^n \right)$$

where:

| | |
|--------|-------------------------------|
| i, j | upstream and downstream lumps |
| n | current time step |
| $n+1$ | next time step. |

The accumulator pressure can vary between 35 psia and 18 psia during operation. The accumulator pressure has a significant effect on the quantity of fluid expelled during a gross leakage event⁶, and must be modeled as a function of time to accurately predict the fluid expulsion. The accumulator is modeled as a reversible isothermal process, represented by the equation:

$$PV = \text{constant} = P_1V_1 = P_2V_2$$

where:

| | |
|------|---|
| P | nitrogen pressure |
| V | nitrogen volume |
| 1, 2 | nitrogen pressure and volume at t and t+ Δt . |

The nominal pre-charge accumulator volumes are 80% water and 20% nitrogen. Based on the variation of the volume specification ($680 \text{ in}^3 \pm 30 \text{ in}^3$), the resulting PV_{constant} differs and must be considered.

The volumetric increase of nitrogen, compensating for the volumetric water expulsion, is calculated by:

$$V_2 = V_1 + \dot{V} \Delta t$$

where:

- \dot{V} volumetric flow rate of water expelled from the system
- Δt computational time step.

The transient nitrogen pressure is then calculated by:

$$P_2 = PV_{\text{constant}}/V_2$$

ANALYSIS

Leakage scenarios were developed for both the MTL and LTL. These scenarios assume a critical Quick Disconnect (QD) seal failure at the Node 2 to attached element(s) IATCS interface. The scenarios analyzed were:

- Leakage at Node 2 to CAM MTL supply interface
- Leakage at CAM to Node 2 MTL return interface
- Leakage at Node 2 to MPLM LTL supply interface
- Leakage at MPLM to Node 2 LTL return interface
- Leakage at Node 2 to CAM LTL supply interface
- Leakage at CAM to Node 2 LTL return interface.

Steady state and transient simulations were performed for each leakage scenario. FASTIC and STDSTL solution routines were used to establish nominal, steady-state conditions prior to analyzing the gross leakage event. The FWDBCK solution routine was used for the transient analysis of the event. The computational time step was limited to no greater than 0.1 seconds⁷.

SINDA85/FLUINT analysis results for the aforementioned scenarios showed that the "leakage at Node 2 to CAM MTL return interface" provided the most severe leakage path in which to assess the IATCS system⁶. This scenario was considered for the purpose of this paper.

LEAKAGE AT CAM TO NODE 2 MTL RETURN INTERFACE

This scenario assumes that leakage occurs at the Quick Disconnect (QD) located on the Node 2 side of the CAM MTL return line. The QD on the CAM side of the return line is assumed to "seal" upon disconnection. Figure 2 depicts the IATCS MTL nodal network and leakage area. At the onset of the leakage event, nominal flow through the CAM from the supply line is "shut off" due to the sealed QD on the return line. The leakage area for the failed QD is calculated based on 100% exposure of the line cross-sectional area (0.3872 in²). The failed QD is exposed to an ambient pressure of 14.25 psia which coincides with the U. S. Laboratory (USL) module nitrogen introduction threshold.

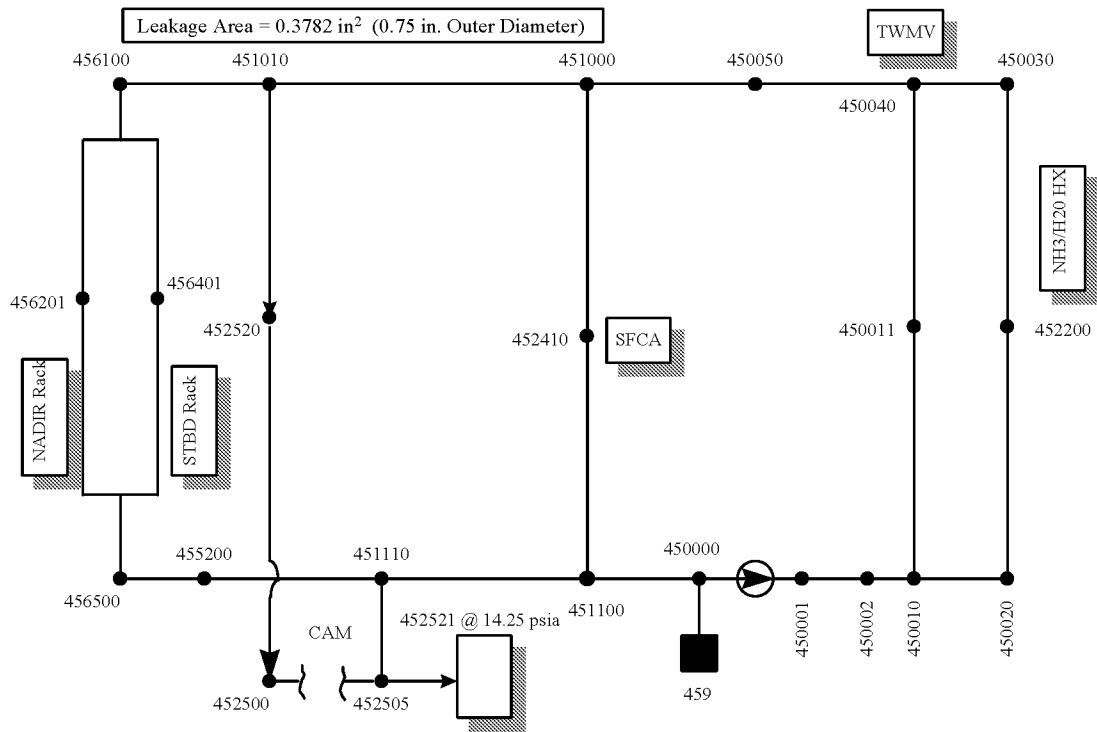


Figure 2. MTL Leakage at CAM to Node 2 Return Interface

Two cases were analyzed to assess the effects of accumulator volume on leakage quantity. The minimum and maximum accumulator volumes (650 in³ and 710 in³) were analyzed assuming a nitrogen pre-charge pressure of 35 psia.

Leakage detection is based on a 59% accumulator water level. PPA shutdown is complete at 5.2 seconds after detection. If the accumulator pressure drops below 18 psia and remains under 18 psia for 6 seconds prior to PPA shutdown, re-pressurization from the NIA will occur. However, for these analyses, re-pressurization was not considered.

RESULTS

Results for the two cases are summarized in Table 2 and shown in Figures 3 through 5 and Figures 6 through 8.

| Case Number | Total Accumulator Vol. (cu. in.) | Initial Gas Volume | Initial Gas Pressure (psia) | Time at Leak Detection (sec) | Volume Leaked at Pump Shutdown (gal) | Accumulator Pressure at Pump Shutdown (psia) | NIA Re-press Before Pump Shutdown |
|-------------|----------------------------------|--------------------|-----------------------------|------------------------------|--------------------------------------|--|-----------------------------------|
| 1 | 650 | 20% | 35 | 3.0 | 0.91 | 14.25 | No |
| 2 | 710 | 20% | 35 | 3.3 | > 1.0 | N/A | Yes |

Table 2. Results of Leakage at CAM to Node 2 MTL Return Interface Analysis

Figures 3 through 5 show the transient accumulator pressure, total leakage flow rate and total volumetric leakage for an accumulator volume of 650 in³. From Figure 4, the leakage contribution from the PPA is constant. However, the contribution from the accumulator (back-flow) decays rapidly after the initial spike as a result of the decreasing accumulator pressure. Figure 5 shows that the total quantity of fluid expelled during the event is approximately 0.91 gallons, which is in compliance with the requirement.

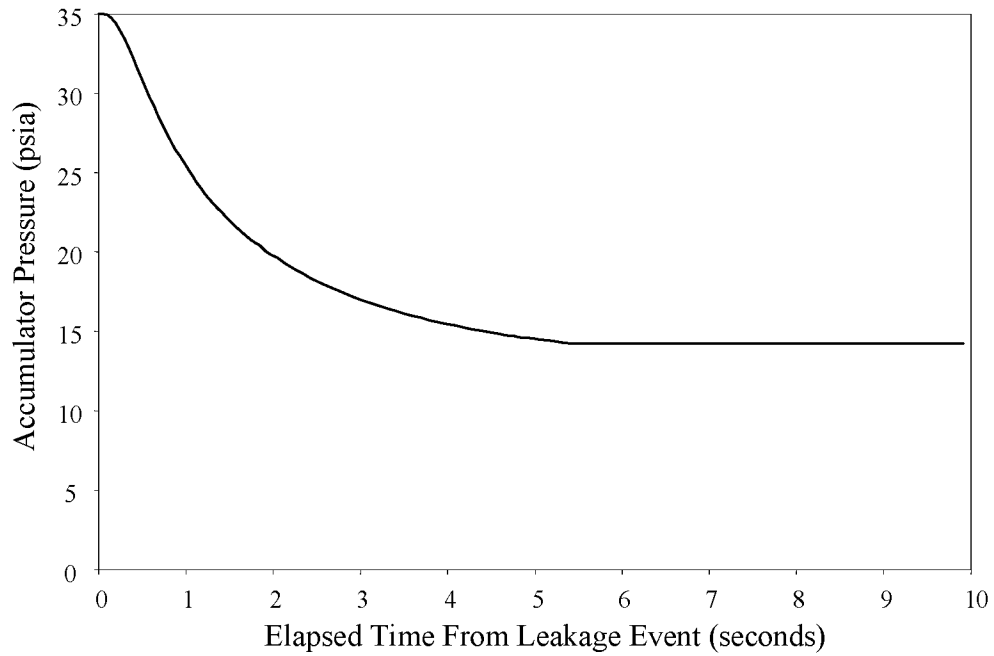


Figure 3. Transient Accumulator Pressure

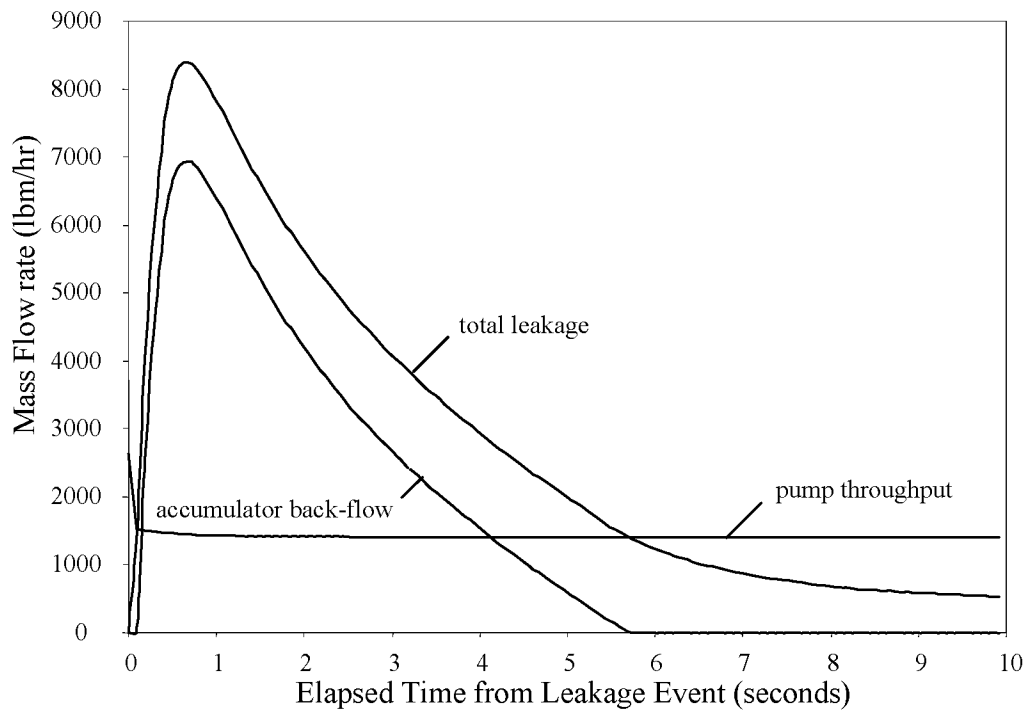


Figure 4. Total Leakage Flow Rate

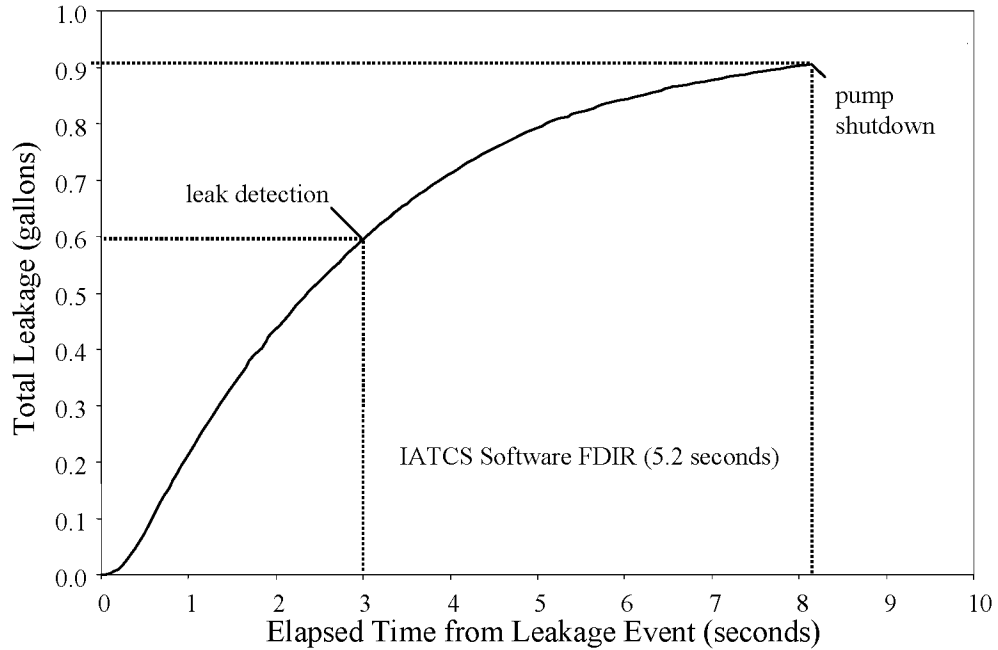


Figure 5. Total Volumetric Leakage

Figures 6 through 8 show the transient accumulator pressure, total leakage flow rate and total volumetric leakage for an accumulator volume of 710 in³. As from the previous results, the trends are identical. From Figure 6, the leakage contribution from the PPA is constant. Again, the contribution from the accumulator (back-flow) decays rapidly after the initial spike as a result of the decreasing accumulator pressure. Figure 8 shows that the total quantity of fluid expelled during the event is approximately 0.92 gal, which is in compliance with the requirement. However, from Figure 6, the accumulator pressure is below 18 psia for more than 6 seconds prior to PPA shutdown and re-pressurization of the accumulator must occur. If re-pressurization has been accounted for, the total quantity of fluid expelled would exceed 1.0 gal.

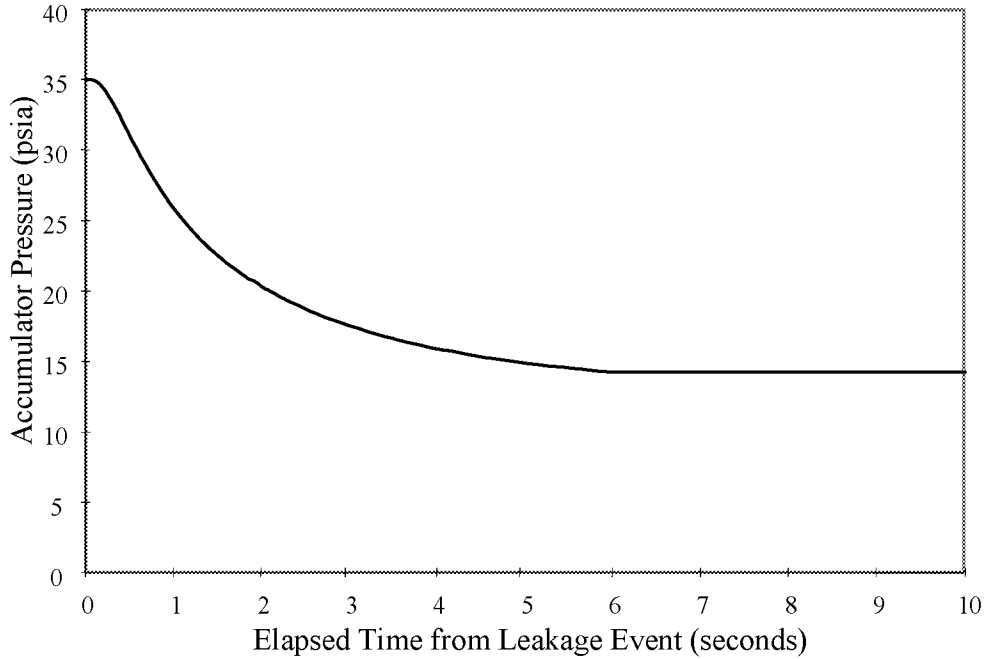


Figure 6. Transient Accumulator Pressure

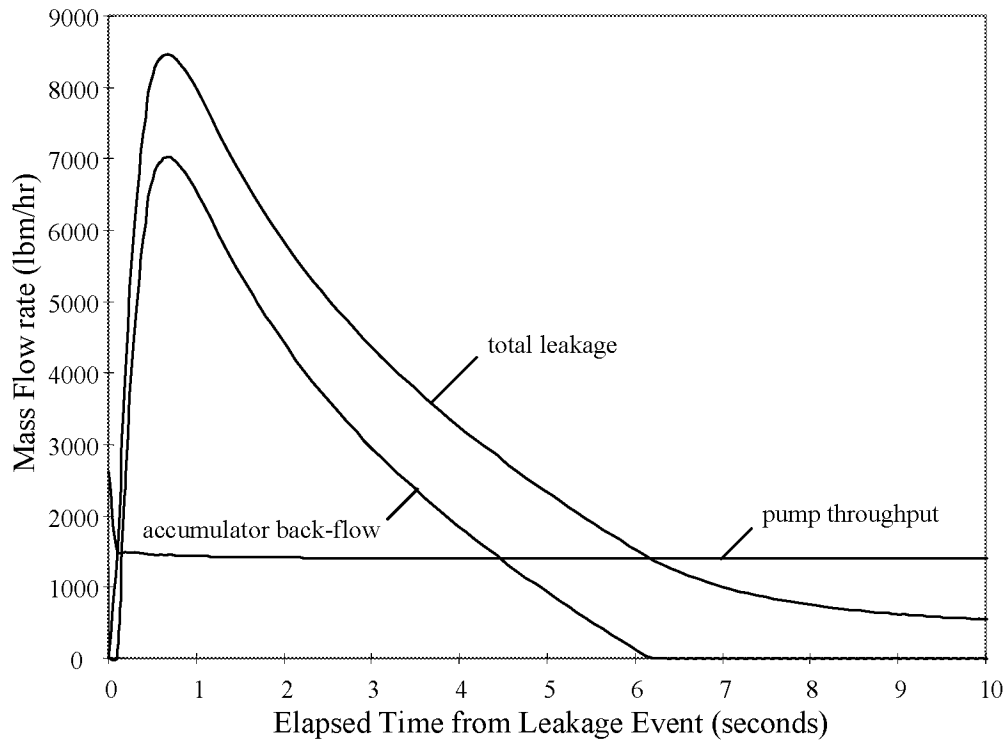


Figure 7. Total Leakage Flow Rate

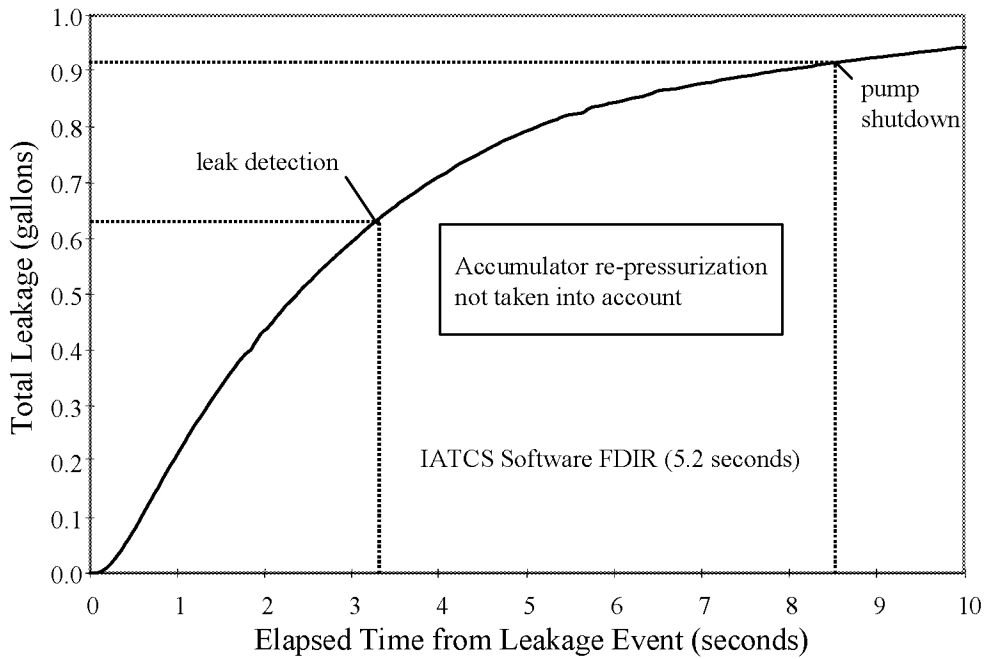


Figure 8. Total Volumetric Leakage

CONCLUSIONS

For an accumulator pre-charge ratio of 80% water and 20% nitrogen and a pressure of 35 psia, an accumulator of 650 in³ (minimum hardware specification) is in compliance with the gross leakage requirement with the current FDIR software. However, for the same pre-charge conditions, an accumulator of 710 in³ (maximum hardware specification) does not satisfy the requirement. Since the accumulator volume variation is a consequence of the manufacturing process, either the pre-charge water volume (80%) or the software leak detection threshold (59%) must be altered to insure that the requirement is not violated.

ACKNOWLEDGEMENTS

The authors wish to thank Giuseppe Valenzano and Silvia Lombardi of Alenia Aerospazio for development of the Node 2 IATCS THMM, and for their dedication not only to this problem, but to the many challenges of developing hardware and systems for the ISS. We also wish to thank Robert Hartung of Boeing-Huntsville, Darryl Gaines of NASA-MSFC and Deborah Kromis of Quality Research for their help with the software details of this problem.

REFERENCES

1. SSP 50290, Node 2 Prime Item Development Specification (PIDS)
2. Node 2 SSR/PDR
3. 2353866G, Prime Item Development Specification, Type B1, Pump Package Assembly, AlliedSignal Aerospace Company, Aerospace Equipment Systems.
4. Node 2 Software Requirements Specification
5. N2-TN-AI-0012, N2 IATCS Thermal-Hydraulic Analysis, Alenia Aerospazio, January 30, 1998.
6. 661-017-98-009, Node 2 IATCS Gross Leakage Analysis, Sverdrup Technology, September 23, 1998.
7. Systems Improved Numerical Differencing Analyzer and Fluid Integrator (SINDA85/FLUINT), Cullimore and Ring Technologies, Inc.

TIME-ACCURATE SOLUTIONS OF INCOMPRESSIBLE NAVIER-STOKES EQUATIONS FOR POTENTIAL TURBOPUMP APPLICATIONS

Cetin Kiris
MCAT, Inc.
Dochan Kwak
NASA Ames Research Center
Mail Stop T27B-1
Moffett Field, CA 94035

Abstract

Two numerical procedures, one based on artificial compressibility method and the other pressure projection method, are outlined for obtaining time-accurate solutions of the incompressible Navier-Stokes equations. The performance of the two methods are compared by obtaining unsteady solutions for the evolution of twin vortices behind a flat plate. Calculated results are compared with experimental and other numerical results. For an unsteady flow which requires small physical time step, pressure projection method was found to be computationally efficient since it does not require any subiterations procedure. It was observed that the artificial compressibility method requires a fast convergence scheme at each physical time step in order to satisfy incompressibility condition. This was obtained by using a GMRES-ILU(0) solver in our computations. When a line-relaxation scheme was used, the time accuracy was degraded and time-accurate computations became very expensive.

Introduction

The primary objective of this research is to support the design of liquid rocket systems for the Advanced Space Transportation System. Since the space launch systems in the near future are likely to rely on liquid rocket engines, increasing the efficiency and reliability of the engine components is an important task. One of the major problems in the liquid rocket engine is to understand fluid dynamics of fuel and oxidizer flows from the fuel tank to plume. Turbopumps in liquid rocket engines are one of the biggest source of vibrations. Understanding the flow through the entire turbopump geometry through numerical simulation will be of significant value toward design. This will help to improve safety of future space missions. One of the milestones of this effort is to develop, apply and demonstrate the capability and accuracy of 3D CFD methods as efficient design analysis tools on high performance computer platforms. In order to achieve flange-to-flange entire turbopump simulations, moving boundary capability and an efficient time-accurate integration method should be build in the numerical procedure. This paper, in particular, is concerned with the time integration procedure of incompressible Navier-Stokes equations.

The incompressible Navier-Stokes equations pose a special problem of satisfying the mass conservation equation because it is not coupled to the momentum equations. To satisfy incompressibility various procedures can be selected depending on the choice of formulations, variables, discretization and iterative schemes. In this paper, two formulations

are considered, the first one based on an artificial compressibility method and the second one on a pressure projection method. The artificial compressibility method¹ takes advantage of the advances made in conjunction with compressible flow computations. This approach relaxes the requirement of enforcing mass conservation equation rigorously at each time iteration, however, at the expense of introducing an artificial wave phenomenon. This approach can be viewed as a special case of a preconditioned compressible flow formulation. However, the computational efficiency is in general better than that of compressible flow solvers at the incompressible limit. This approach has been shown to be very robust in a wide range of applications²⁻⁴.

The first primitive variable method for incompressible flow was developed by Harlow and Welch⁵ using pressure projection. Numerous variants have been developed since. In this method, the pressure is used as a mapping parameter to satisfy the continuity equation. The usual computational procedure involves choosing the pressure field at the current time step such that continuity is satisfied at the next time step. The time step is advanced in multiple steps (fractional step) which is computationally convenient. However, governing equations are not coupled as in an artificial compressibility approach. This will affect the robustness and limit the maximum allowable time step size. Since this approach is time accurate, there are cases where the fractional step solver is computationally more efficient compared to the artificial compressibility method⁵⁻⁹.

Various numerical algorithms associated with these methods have been developed along with accompanying flow solvers. In the present paper, it is intended to outline the time integration procedures of the two methods discussed above. A new time integration scheme is also presented for pressure projection method. Numerical results from both formulations for the development of the twin vortices^{10,11} behind the flat plate are presented in computed results section.

Artificial Compressibility Formulation

The artificial compressibility algorithm introduces a time-derivative of the pressure term into the continuity equation; the elliptic-parabolic type partial differential equations are transformed into the hyperbolic-parabolic type. The artificial compressibility method by Chorin (1967) can be written as

$$\frac{1}{\beta} \frac{\partial p}{\partial t} + \frac{\partial u_i}{\partial x_i} = 0 \quad (1)$$

$$\frac{\partial u_i}{\partial t} = -\frac{\partial p}{\partial x_i} + h_i = -r_i \quad (2)$$

where t is time, x_i the Cartesian coordinates, u_i the corresponding velocity components, p the pressure, β artificial compressibility, and h_i contains both convective and viscous terms. At steady state the pressure term in continuity equation drops out and thus incompressibility is recovered. For time accurate computations, this has to be repeated at each time level to maintain incompressibility at each time step.

In the present study, the time derivatives in the momentum equations are differenced using a second-order, three-point, backward-difference formula.

$$\frac{3\mathbf{u}^{n+1} - 4\mathbf{u}^n + \mathbf{u}^{n-1}}{2\Delta t} = -\mathbf{r}^{n+1} \quad (3)$$

where \mathbf{u} and \mathbf{r} denote the dependent variable vector and the right hand side vector for the momentum equations, respectively. After the discretization in time, the pseudocompressibility term and pseudo-time level (m) are introduced to equations.

$$\begin{aligned} \frac{1}{\Delta\tau}(p^{n+1,m+1} - p^{n+1,m}) &= -\beta\nabla \cdot \mathbf{u}^{n+1,m+1} \\ \frac{1.5}{\Delta t}(\mathbf{u}^{n+1,m+1} - \mathbf{u}^{n+1,m}) &= -\mathbf{r}^{n+1,m+1} - \\ &\quad \frac{3\mathbf{u}^{n+1,m} - 4\mathbf{u}^n + \mathbf{u}^{n-1}}{2\Delta t} \end{aligned} \quad (4)$$

Here Δt , $\Delta\tau$, n , and m denote physical time step, pseudo-time step, physical time level, and subiteration time level, respectively. The equations are iterated to convergence in pseudo-time for each physical time step until the divergence of the velocity field has been reduced below a specified tolerance value. This typically requires 10 to 30 subiterations.

The matrix equation is solved iteratively by using a nonfactored Gauss-Seidel type line-relaxation scheme,¹² which maintains stability and allows a large pseudo-time step to be taken. Details of the numerical method can be found in Refs. 2-3. GMRES scheme has also been utilized for the solution of the resulting matrix equation¹³. Computer memory requirement for the corresponding flow solver (INS3D-UP code) with line-relaxation is 35 times number of grid points in words, and with GMRES-ILU(0) scheme is 220 times number of grid points in words. Extensive memory requirement for GMRES scheme makes the code unpractical for three-dimensional applications. Writing a matrix-free GMRES solver remains to be one of the items for future enhancements.

The original version of the INS3D code² with pseudocompressibility approach utilized the Beam-Warming¹⁴ approximate factorization algorithm and central differencing of the convective terms. Since the convective terms of the resulting equations are hyperbolic, upwind differencing can be applied to these terms. The current versions of the INS3D-UP code use flux-difference splitting based on the method of Roe.¹⁵ Chakravarthy¹⁶ outlines a class of high-accuracy flux-differencing schemes for the compressible flow equations. The third and fifth-order upwind differencing used here is an implementation of these schemes for the incompressible Navier-Stokes equations. The upwind differencing leads to a more diagonal dominant system than does central differencing and does not require a user-specified artificial dissipation. The viscous flux derivatives are computed by using central differencing.

Time-accurate artificial compressibility formulation has been used successfully for unsteady calculations. The only drawback of this formulation is the computational cost due to subiteration procedure.

Pressure Projection Method

The time integration scheme is based on operator splitting, which can be accomplished in several ways by combining the pressure, convective, and viscous terms in the momentum

equations. The fractional step method is based on the decomposition of vector field into a divergence free component and gradient of a scalar field. The common application of this method is done in two steps. The first step is to solve for an auxiliary velocity field using the momentum equations. In the second step, the velocity field is corrected by using the pressure which can map the auxiliary velocity onto a divergence free velocity field. The momentum equations are discretized in time using a second-order implicit Runge-Kutta method (RK2) which can also be viewed as a predictor-corrector method.

$$\frac{1}{\Delta t}(u_i^* - u_i^n) = -\frac{\partial p^n}{\partial x_i} + h(u_i^*) \quad (5)$$

and a corrector step

$$\frac{2}{\Delta t}(u_i^{n+1} - u_i^n) = -\frac{\partial p^{n+1}}{\partial x_i} + h(u_i^{n+1}) - \frac{\partial p^n}{\partial x_i} + h(u_i^*) \quad (6)$$

where u_i^* denotes the auxiliary velocity field. The h term in the momentum equations includes the convective and viscous terms. By using equation (5), equation (6) can be written as

$$\frac{2}{\Delta t}(u_i^{n+1} - u_i^*) = -\frac{\partial p^{n+1}}{\partial x_i} + h(u_i^{n+1}) - \frac{1}{\Delta t}(u_i^* - u_i^n) \quad (7)$$

By subtracting equation (5) from equation (7), we obtain

$$\frac{2}{\Delta t}(u_i^{n+1} - u_i^*) = -\nabla p' + h(u_i^{n+1}) - h(u_i^*) \quad (8)$$

where $p' = p^{n+1} - p^n$. At $n + 1$ time level, the velocity field has to satisfy the incompressibility condition which is the continuity equation.

$$\nabla \cdot \mathbf{u}^{n+1} = 0 \quad (9)$$

This incompressibility condition is enforced by using a Poisson equation for pressure.

$$\nabla^2 p' = \frac{2}{\Delta t} \nabla \cdot \mathbf{u}^* \quad (10)$$

The Poisson equation for pressure is obtained by taking the divergence of equation (8) and using equation (9). The only assumption is made in this procedure is that $h(u_i^{n+1}) - h(u_i^*)$ term in equation 8 is considered small. If the corrector step was explicit, this term would vanish.

In equations (5) and (7), both convective and viscous terms are treated implicitly. The residual term at the (*) and $(n + 1)$ level is linearized giving the following equations in delta form

$$\left[\frac{I}{\Delta t} + \left(\frac{\partial h}{\partial u_i} \right)^n \right] (u_i^* - u_i^n) = -\frac{\partial p^n}{\partial x_i} + h(u_i^n) \quad (11)$$

$$\left[\frac{2I}{\Delta t} + \left(\frac{\partial h}{\partial u_i} \right)^* \right] (u_i^{n+1} - u_i^*) = -\frac{\partial p^{n+1}}{\partial x_i} + h(u_i^*) - \frac{1}{\Delta t}(u_i^* - u_i^n) \quad (12)$$

where I is the identity matrix. Equation (12) can also be written in more familiar form of fractional-step method by substituting equation (5) in equation (12).

$$\left[\frac{2I}{\Delta t} + \left(\frac{\partial h}{\partial u_i} \right)^* \right] (u^{n+1} - u^*) = -\frac{\partial p'}{\partial x_i} \quad (13)$$

Equations (11), (10), and (12) give the proposed time integration procedure of the pressure projection method.

The algorithm for the pressure projection method is based on a finite-volume formulation and uses the pressure in the cell center and the mass fluxes across the faces of each cell as dependent variables. The discretization of the mass conservation equation in finite volume formulation gives

$$\begin{aligned} & (\mathbf{S}^\xi \cdot \mathbf{u})_{j+\frac{1}{2},k,l} - (\mathbf{S}^\xi \cdot \mathbf{u})_{j-\frac{1}{2},k,l} + \\ & (\mathbf{S}^\eta \cdot \mathbf{u})_{j,k+\frac{1}{2},l} - (\mathbf{S}^\eta \cdot \mathbf{u})_{j,k-\frac{1}{2},l} + \\ & (\mathbf{S}^\zeta \cdot \mathbf{u})_{j,k,l+\frac{1}{2}} - (\mathbf{S}^\zeta \cdot \mathbf{u})_{j,k,l-\frac{1}{2}} = 0 \end{aligned} \quad (14)$$

where \mathbf{S} is the surface area vector. The mass conservation equation is evaluated over the faces of a computational cell. Each term in equation (14) approximates the mass flux over the corresponding cell face. If the mass fluxes are chosen as unknowns, the continuity equation is satisfied automatically in generalized coordinate systems. The mass fluxes over the ξ , η , and ζ faces of the computational cell are

$$\begin{aligned} U^\xi &= \mathbf{S}^\xi \cdot \mathbf{u} \\ U^\eta &= \mathbf{S}^\eta \cdot \mathbf{u} \\ U^\zeta &= \mathbf{S}^\zeta \cdot \mathbf{u} \end{aligned} \quad (15)$$

The continuity equation with this choice of the dependent variables takes a form identical to the Cartesian case. Therefore, the mass fluxes are considered as the ‘natural’ dependent variables for projection methods in curvilinear coordinates. The mass conservation equation with new dependent variables in a generalized coordinate system becomes

$$\begin{aligned} & U_{j+\frac{1}{2},k,l}^\xi - U_{j-\frac{1}{2},k,l}^\xi + U_{j,k+\frac{1}{2},l}^\eta - U_{j,k-\frac{1}{2},l}^\eta + \\ & U_{j,k,l+\frac{1}{2}}^\zeta - U_{j,k,l-\frac{1}{2}}^\zeta = 0 \end{aligned} \quad (16)$$

Treating the mass fluxes as dependent variables in finite volume formulation is equivalent to using contravariant velocity components, scaled by the inverse of the transformation Jacobian, in a finite-difference formulation. This choice of mass fluxes as dependent variables complicates the discretization of the momentum equations. In order to replace \mathbf{u} by the new dependent variables U^l , the corresponding area vectors are dotted with the momentum equations. Then the integral momentum equation is evaluated on different computational cells for each unknown U^l . Each cell has the dimensions of $\Delta\xi \times \Delta\eta \times \Delta\zeta$, but the centers are located at $(j + \frac{1}{2}, k, l)$, $(j, k + \frac{1}{2}, l)$, and $(j, k, l + \frac{1}{2})$ for U^ξ , U^η , and

U^ζ momentum equations, respectively. The staggered grid orientation eliminates pressure checker-board-like oscillations in pressure and provides more compact stencils. The derivation of momentum equations and the solution procedure is outlined in reference 9. Since each equation is solved in a segregated fashion, memory requirements for GMRES solver in INS3D-FS is not as big as INS3D-UP code. Required memory for INS3D-FS is 70 times number of grid points in words.

Computed Results

In this section, numerical results for the time evolution of twin vortices behind a flat plate are presented in order to verify the time-dependent features of the two algorithms. In order to investigate different features of the algorithms, several cases are needed to run with various code related parameters. To speed up this process, a two dimensional test case is selected here. It should be noted that associated flow solvers, INS3D-UP for artificial compressibility method and INS3D-FS for pressure projection method, are written for three-dimensional applications. With this numerical experiment, it is intended to give some basis for selecting a method for large three-dimensional unsteady applications where computing resources become a critical issue.

Computed results from both methods are compared with the experimental data by Taneda and Honji¹⁰. The experiment has carried out in a water tank 40 cm wide. A thin test plate of size $H = 3cm$ immersed in the water was started from the rest impulsively at the velocity $U = 0.495cm/s$. Reynolds number for this case is 126 based on $U = 0.495cm/s$ velocity and the plate height H . Computational grid with size of 181x81x3 is presented in figure 1. Since INS3D-FS is written in finite volume staggered grid formulation, it requires one additional ghost cell in each direction. Figure 2 shows calculated velocity vectors obtained from INS3D-FS at various times. The flow separates the plate at each edge and forms a vortex pair. The twin vortices become longer in the flow direction with time.

The calculated time history of the stagnation point is compared with experimental results and other numerical results in figure 3. Symbols represent experimental measurements, solid line and dashed line represent results from INS3D-UP and INS3D-FS, respectively. Dotted line show the numerical results from finite element formulations of Yoshida and Nomura¹¹. The interval for time integration was 0.5 sec, which corresponds to nondimensional value of 0.0825, for all computations in figure 3. Eventhough the plate started impulsively in the experiment, the computations presented in figure 3 have a slow start procedure. Figure 4 shows prescribed velocity for an impulsive start (4a) and for a slow start (4b) used in INS3D-UP and INS3D-FS calculations. Reference 11 also used same slow start procedure in their calculations. When nondimensional time step of 0.0825 was used with an impulsive start, large discrepancies were observed between numerical results and the experimental measurements. This can be seen in figure 5a. When the time step is decreased, fairly good agreement was observed between numerical results and the measurements as seen in figure 5b. For the slow start case, the velocity profile shown in figure 4b is prescribed and the origin of time of calculation is appropriately shifted from the time of experiment. This unsteady computations with INS3D-FS ($\Delta t = 0.0825$) was completed in two hours of CPU time on single processor Cray-J90.

INS3D-UP computations with line-relaxation scheme is presented in figure 6. Various artificial compressibility parameters and number of subiterations were used. Figure 6 shows the effects of number of subiterations and the effects of using two different artificial compressibility parameters β . When the incompressibility conditions is not satisfied at each physical time step, numerical results can be erroneous in time-accurate computations. With line-relaxation scheme, INS3D-UP calculations required between 4 hours of CPU time (10 subiterations at each physical time step) and 14 hours (40 subiterations) on a single processor Cray-J90 computer. Our observation for the time-accurate computations from this numerical example is that the artificial compressibility method requires a fast convergence scheme at each physical time step in order to satisfy incompressibility condition. If this is not satisfied as seen in line-relaxation scheme, the time accuracy is degraded (see figure 6). In addition, artificial compressibility method with line relaxation scheme can be expensive for 3D time-accurate computations. In figure 7, INS3D-UP results with GMRES-ILU(0) solver are presented. These results were obtained less than 4 hours on a Cray-J90 computer. Fairly good agreement was obtained between the computed results and experimental data. With GMRES-ILU(0) solver, the mass flow ratio between inflow and exit was always satisfied. In addition, the discrepancies between numerical results are very small when two different values of artificial compressibility parameter were used. Figure 8 shows the results from artificial compressibility method with and without Poisson equation correction for the pressure. In artificial compressibility method, after the first sub-iteration, the Poisson equation is employed for the pressure correction. Chain-dashed line in figure 8 represents the results from this new procedure. With the Poisson equation correction, the line relaxation results compare well with experimental data and the GMRES results with 10 subiterations. With this new procedure, both computing time and memory requirement are substantially reduced (at least three times).

Concluding Remarks

Unsteady computations were performed using two different solution algorithms, which are artificial compressibility method and pressure projection method. When a fast converging scheme, such as GMRES-ILU(0) solver, was incorporated in artificial compressibility method, fairly good agreement was obtained between computed results and experimental data. Our numerical experiment showed that incompressibility condition was satisfied in 10 subiterations at each physical time step. Memory requirement of this scheme is the major drawback for three-dimensional large applications. However, memory requirement may not be an issue on the parallel platforms, such as SGI Origin 2000. The line-relaxation scheme in artificial compressibility method becomes very expensive and results in erroneous solution for time-accurate computations. For an unsteady flow which requires small physical time step, pressure projection method was found to be computationally efficient since it does not require any subiterations procedure. However, governing equations are not fully coupled as in the artificial compressibility approach. This may affect the robustness and limit the maximum allowable time step size. A new method is developed by combining pressure projection method with artificial compressibility method. With Poisson solver

correction, the number of subiteration was reduced to two iterations at each physical time step.

Acknowledgments

Computer time was provided by the Numerical Aerodynamic Simulation (NAS) Facility and the Central Computing Facility at NASA Ames Research Center.

References

1. Chorin, A., J., "A Numerical Method for Solving Incompressible Viscous Flow Problems," *Journal of Computational Physics*, Vol. 2, pp. 12-26, 1967.
2. Kwak, D., Chang, J. L. C., Shanks, S. P., and Chakravarthy, S., "A Three-Dimensional Incompressible Navier-Stokes Flow Solver Using Primitive Variables," *AIAA Journal*, Vol. 24, No. 3, pp. 390-396, 1977.
3. Rogers, S. E., Kwak, D. "Upwind Differencing for the Time-Accurate Incompressible Navier-Stokes Equations," *AIAA Journal*, Vol. 28, No. 2, pp. 253-262, 1990.
4. Rogers, S. E., Kwak, D. and Kiris, C., "Numerical Solution of the Incompressible Navier-Stokes Equations for Steady and Time-Dependent Problems," *AIAA Journal*, Vol. 29, No. 4, pp. 603-610, 1991.
5. Harlow, F. H., and Welch, J. E., "Numerical Calculation of Time-Dependent Viscous Incompressible Flow with Free Surface," *Phys. Fluids*, Vol. 8, No. 12, pp. 2182-2189, 1965.
6. Kim, J. and Moin, P., "Application of a Fractional-Step Method to Incompressible Navier-Stokes Equations," *J. Comp. Phys.*, Vol. 59, pp. 308-323, 1985.
7. Choi, H., and Moin, P., "Effects of the Computational Time Step on Numerical Solutions of Turbulent Flow," *J. Comp. Phys.*, Vol. 113, pp. 1-4, 1994.
8. Rosenfeld, M., Kwak, D., and Vinokur, M., "A Fractional-Step Method for the Unsteady Incompressible Navier-Stokes Equations in Generalized Coordinate Systems," AIAA Paper No. 88-0718, 1988.
J. Comp. Physics, Vol. 94, No. 1, pp. 102-137, 1991.
9. Kiris, C., and Kwak, D., "Numerical Solution of Incompressible Navier-Stokes Equations Using a Fractional-Step Approach," AIAA Paper No. 96-2089, 1996.
10. Taneda, S., and Honji, H., "Unsteady Flow Past a Flat Plate Normal to the Direction of Motion," *J. Phys. Soc. Japan*, Vol. 30, pp. 262-273, 1971.
11. Yoshida, Y., and Nomura, T., "A Transient Solution Method for the Finite Element Incompressible Navier-Stokes Equations," *Int. J. Num. Methods in Fluids*, Vol. 5, pp. 873-890, 1985.
12. MacCormack, R., W., "Current Status of Numerical Solutions of the Navier-Stokes Equations," AIAA Paper No. 85-0032, 1985.
13. Rogers, S. E., "A Comparison of Implicit Schemes for the Incompressible Navier-Stokes Equations and Artificial Compressibility," *AIAA Journal*, Vol. 33, No. 10, Oct. 1995
14. Beam, R. M., Warming, R. F., "An Implicit Factored Scheme for the Compressible Navier-Stokes Equations," *AIAA Journal*, Vol 16, pp. 393-401, 1978.

15 Roe, P.L., "Approximate Riemann Solvers, Parameter Vectors, and Difference Schemes," *Journal of Computational Physics*, Vol. 43, pp. 357-372 1981

16 Chakravarthy, S. R., Osher, S., "A New Class of High Accuracy TVD Schemes for Hyperbolic Conservation Laws," AIAA Paper No. 85-0363, 1985.

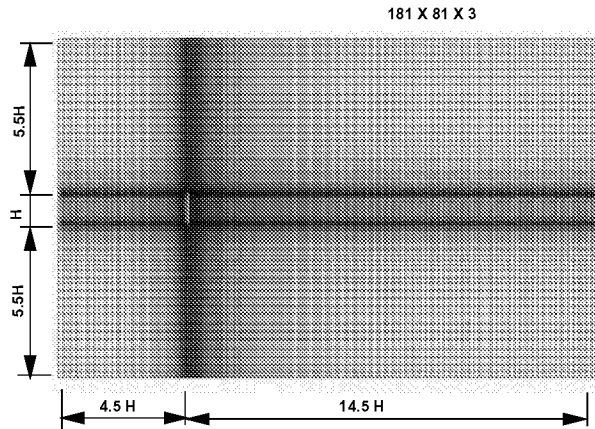


Figure 1 : Computational grid for the flow past a 90-degree flat plate. (plate tickness = $0.03H$)

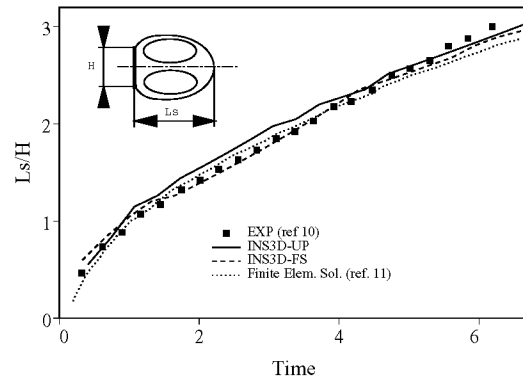


Figure 3 : Calculated time history of the stagnation point.

VELOCITY VECTORS AND MAGNITUDE CONTOURS (INS3D-FS)

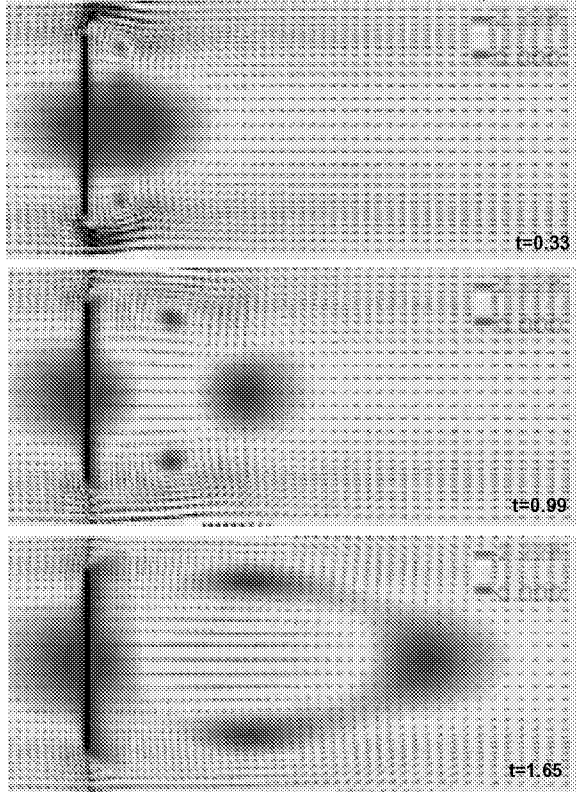


Figure 2a : Velocity vectors at various non-dimensional times (INS3D-FS).

VELOCITY VECTORS AND MAGNITUDE CONTOURS (INS3D-FS)

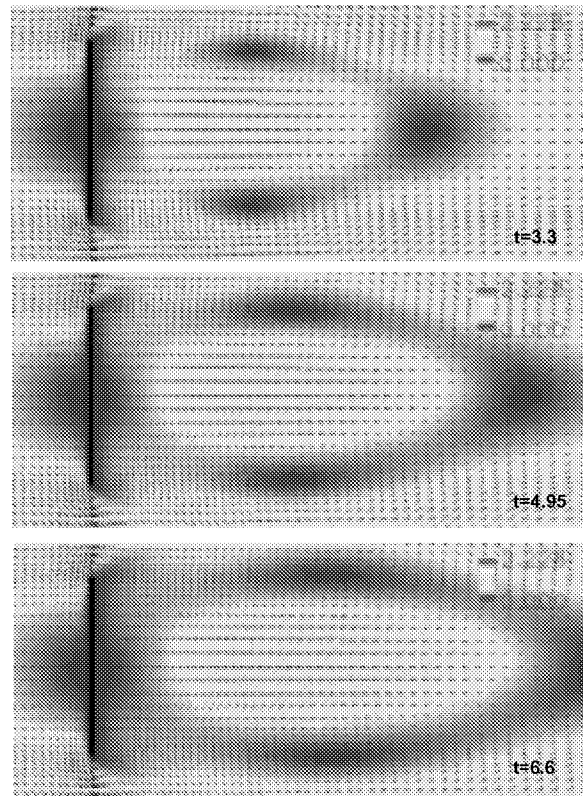


Figure 2b : Velocity vectors at various non-dimensional times (INS3D-FS).

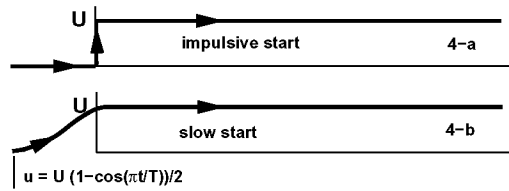


Figure 4 : Prescribed velocity for an impulsive start (a) and for a slow start(b).

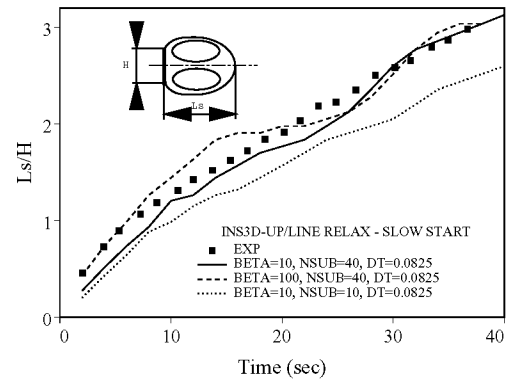


Figure 6 : Evaluation movement of stagnation point from INS3D-UP calculation with line-relaxation scheme.

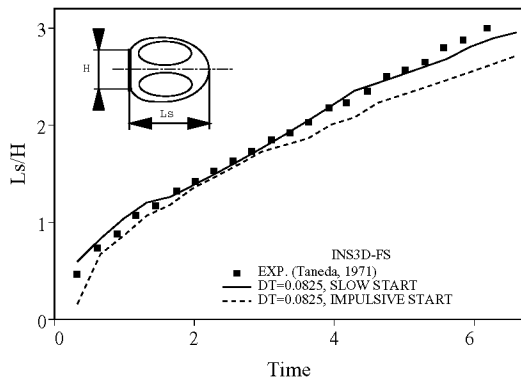


Figure 5a : Effects of starting procedure.

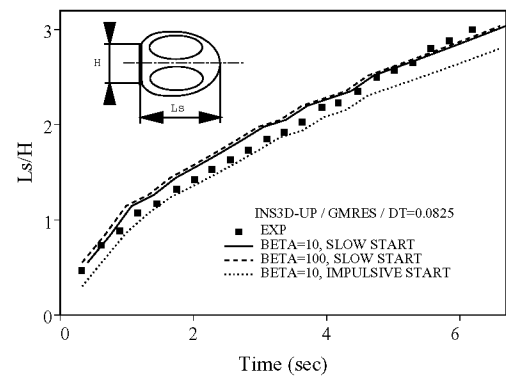


Figure 7 : Evaluation movement of stagnation point from INS3D-UP calculation with GMRES-ILU(0) scheme.

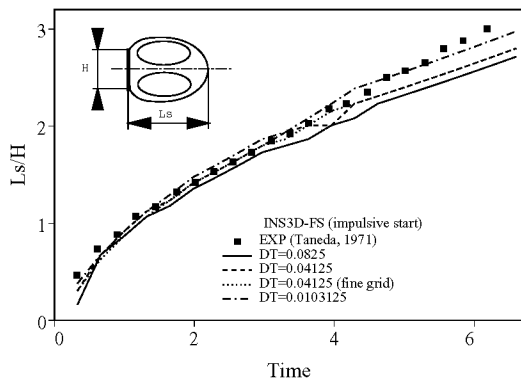


Figure 5b: Effects of time-step size for impulsive start.

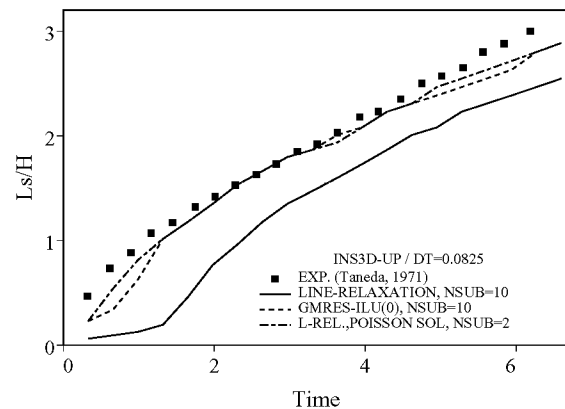


Figure 8 : Artificial compressibility results with and without Poisson equation correction.



UNSHROUDED CENTRIFUGAL TURBOPUMP IMPELLER DESIGN METHODOLOGY

George H. Prueger, Morgan Williams, Wei-chung Chen, John Paris
Boeing / Rocketdyne Propulsion and Power

Robert Williams, Eric Stewart
NASA – MSFC

ABSTRACT

Turbopump weight continues to be a dominant parameter in the trade space for reduction of engine weight. Space Shuttle Main Engine weight distribution indicates that the turbomachinery make up approximately 30% of the total engine weight. Weight reduction can be achieved through the reduction of envelope of the turbopump. Reduction in envelope relates to an increase in turbopump speed and an increase in impeller head coefficient. Speed can be increased until suction performance limits are achieved on the pump or due to alternate constraints the turbine or bearings limit speed. Once the speed of the turbopump is set the impeller tip speed sets the minimum head coefficient of the machine. To reduce impeller diameter the head coefficient must be increased. A significant limitation with increasing head coefficient is that the slope of the head-flow characteristic is affected and this can limit engine throttling range.

Unshrouded impellers offer a design option for increased turbopump speed without increasing the impeller head coefficient. However, there are several issues with regard to using an unshrouded impeller: there is a pump performance penalty due to the front open face recirculation flow, there is a potential pump axial thrust problem from the unbalanced front open face and the back shroud face, and since test data is very limited for this configuration, there is uncertainty in the magnitude and phase of the rotordynamic forces due to the front impeller passage. The purpose of the paper is to discuss the design of an unshrouded impeller and to examine the hydrodynamic performance, axial thrust, and rotordynamic performance. The design methodology will also be discussed. This work will help provide some guidelines for unshrouded impeller design.

INTRODUCTION

Unshrouded impellers are used commonly in compressors and some industrial turbopumps. In rocket engine applications unshrouded impellers are successfully employed on the Pratt & Whitney RL-10 upper stage engine. The current impetus to unshrouded impellers is the ability to increase impeller tip speed limits, which in some turbopump designs limit the operating speed of the machine. This would limit the speed at which the turbopump could operate and consequently set the lower bound for turbopump weight. The use of shrouded impellers in rocket turbopumps is based on the need to maintain performance levels at all required operating points in the design. The performance of an unshrouded impeller degrades as the tip clearance is increased, reference 1. This affects both the discharge pressure capability and the efficiency of the machine. High discharge pressure, cryogenic, turbopumps typically have substantial variation in impeller tip clearance from assembly, to chill, to operation. This is due to differences in materials between housing and rotor materials, as well as deflections in the housings due to pressure loads. The application of advanced computational fluid dynamic tools to design impellers which are less sensitive to tip clearance is one of the goals of the NRA8-21 Unshrouded High Performance Impeller Technology Project. Johannes Lauer, et. al, reference 2, conducted an experimental study on compressor impellers to ascertain what the design parameter drivers were for sensitivity to tip clearance. The study was not conclusive probably due to the variation in design parameters investigated, but lead to some insight into potential mechanisms for tip

clearance sensitivity. The tools will also be used to predict axial thrust and rotordynamic coefficients of an unshrouded impeller.

DESIGN METHODOLOGY

The design speed was previously set by a conceptual evaluation of the tip speed capability of an unshrouded titanium impeller. The selection of head coefficient of 0.53 was selected to success at achieving wide operating range. Thus, the diameter was calculated to be 15.75 inches. Table 1 lists the design parameters.

Table 1: Impeller Design Point Parameters

| Parameter | Value |
|------------------------------|--------|
| Pump Speed, RPM | 32 000 |
| Impeller Tip Diameter, Inch | 15.75 |
| Impeller Tip Speed, Feet/sec | 2200 |
| Impeller Head Coefficient | 0.53 |

Rocketdyne's LOSSISOLATION program was used to define the blade angles required to achieve the required head. Rocketdyne's centrifugal detail geometry through analysis tool, eTANGO, was used to develop the impeller contours, blade definition, initial pressure loading, and grids for subsequent

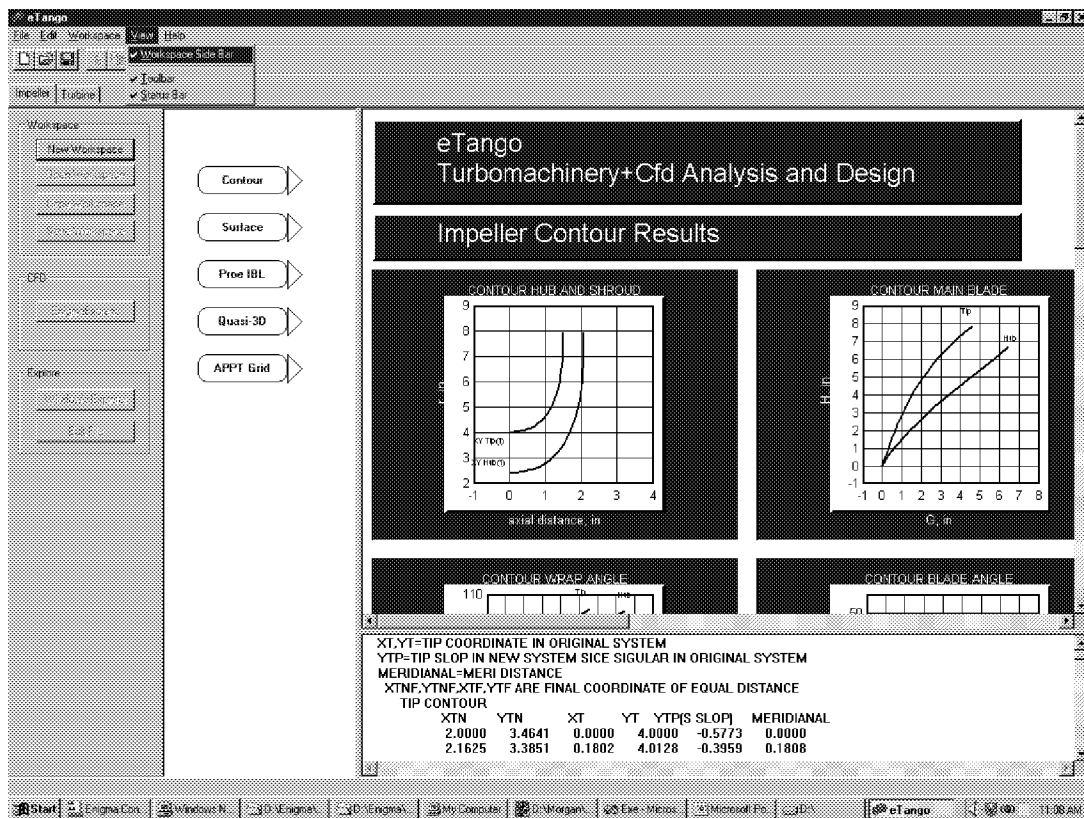


Figure 1: eTANGO Design / Analysis Interface

computational fluid dynamic (CFD) analysis of the geometry. Since Rocketdyne's typical impellers are shrouded, eTANGO was upgraded to incorporate tip clearance regions for the CFD analysis.

Figure 1 shows the eTANGO environment with the contours and blade description for a 6+6 impeller. The use of this design tool allowed the rapid generation of all the impeller designs required completing the ongoing trades study. The interface is intuitive and allows the design engineer to interactively make changes to the design variables and see the impact on the pressure loading. There is direct output from this tool to a Pro/ENGINEER generic model for rapid generation of the impeller solid model shown in figure 2, for a 6+6 impeller.

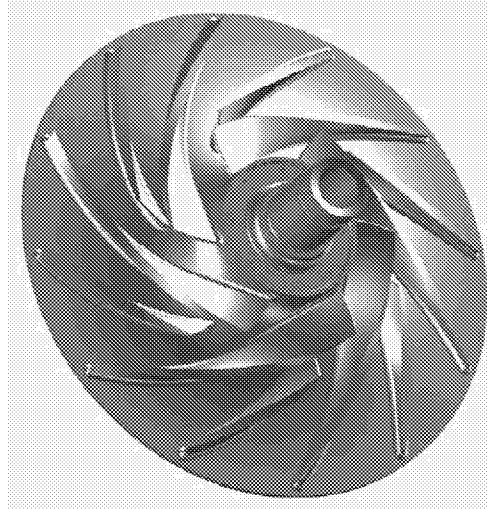


Figure 2: Generic Pro/ENGINEER Solid Model

DESIGN TRADES

Decreased performance sensitivity to tip clearance is a necessity to allow for incorporation of unshrouded impeller technology into rocket engine turbopumps. Based on literature review and tip clearance modeling assumptions, it was decided that the primary design parameters of interest are:

1. Blade solidity
2. Blade number
3. Blade wrap
4. Axial length
5. Diffusion factor
6. Cant angle
7. B_2 -width
8. Exit blade angle
9. Head coefficient

Further review of these parameters indicated that three were fixed due to engine balance constraints or need to minimize changes to the tester. These are:

1. Head coefficient
2. Axial length (shroud contour)
3. B_2 -width

With the above two parameters fixed, blade solidity, blade wrap, diffusion factor, and exit blade angle are all varied with change in blade number. This leaves blade number, and cant angle as the remaining parameters to study. Cant angle is most likely a second order affect on performance and was eliminated from the study. Although, cant could have a significant impact on structural design to meet increased tip speed.

The design parameter, which was held for further study, was the blade number. The following blade numbers were selected for further evaluation: 5+5, 6+6, and 8+8. Table 2 documents the final design parameters for each design.

Table 2 : Impeller Trade Study Design Parameters

| Parameter | Blade Number | | |
|---|--------------|-------|-------|
| | 5+5 | 6+6 | 8+8 |
| Head Coefficient | 0.53 | 0.53 | 0.53 |
| Exit Flow Coefficient | 0.128 | 0.118 | 0.117 |
| Diffusion Factor | 0.80 | 0.60 | 0.43 |
| Inlet Blade Angle, Degrees @ RMS | 22 | 22 | 22 |
| Inlet Blade Height, Inch | 1.6 | 1.6 | 1.6 |
| Tip Diameter, Inch | 15.8 | 15.8 | 15.8 |
| B ₂ -Width, Inch | 0.58 | 0.58 | 0.58 |
| Exit Blade Angle, Degrees | 74 | 49 | 38 |
| Total Blade Wrap, Degrees | 52 | 98 | 120 |
| Axial Length, Inch | 2.08 | 2.08 | 2.08 |
| W ₂ / W ₁ (Relative Velocity Ratio) | 0.88 | 0.90 | 0.90 |

The impeller grid distribution is shown in table 3, with a typical grid shown in the meridional and blade-to-blade planes in figure 3.

Table 3: Impeller Grid Distribution

| Zone ID | Nodes (Meridional x Radial x Blade-to-Blade) |
|---------|---|
| 1 | 7 x 11 x 33 |
| 2 | 11 x 11 x 29 |
| 3 | 17 x 11 x 13 |
| 4 | 17 x 11 x 13 |
| 5 | 5 x 29 x 33 |
| 6 | 23 x 11 x 33 |
| 7 | 33 x 5 x 33 |

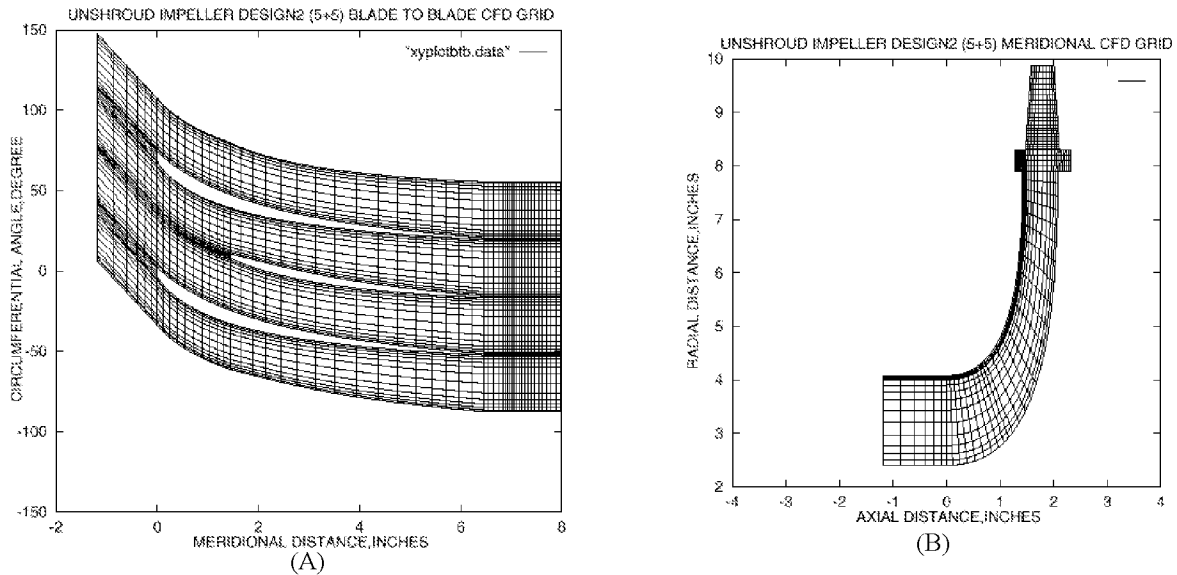


Figure 3: (A) Blade to blade plane, (B) Meridional Plane

PRELIMINARY RESULTS

The first impeller analyzed was a 7+7 configuration. Although this configuration is not part of the trade study space, the results are indicative of what to expect in terms of tip clearance impact. Table 4 lists the performance variables evaluated. Figure 4 shows the locations at which head and efficiency were calculated. These preliminary CFD results are consistent with the J-2 Oxidizer pump open face and shrouded impeller test results, reference 3. The test report shows the impeller efficiency drops about 10 points between shrouded impeller and open face with axial clearance of 10% impeller discharge vane height.

Table 4 : Results of Shrouded and Unshrouded 7+7 Impeller Designs

| | 7+7 Unshrouded Impeller | 7+7 Shrouded Impeller |
|---------------------------------|----------------------------|--------------------------|
| Model Flow Rate, GPM | 20,295 | 19,667 |
| Euler Head (A-B), ft | 128,486 | 141,379 |
| Actual Head (A-B), ft | 110,362 | 137,642 |
| Efficiency (A-B) | 0.86 | 0.974 |
| Static Pressure Rise (A-B), psi | 1975 | 2601 |
| Euler Head(C-D), ft | 141,014 | 153,169 |
| Actual Head(C-D), ft | 113,252 | 141,333 |
| Efficiency (C-D) | 0.8 | 0.92 |
| Static Pressure Rise (C-D), psi | 1976 | 2633 |
| Flow Split (suction / pressure) | 52% / 48% | 51% / 49% |
| Leakage Flow, % | 5.5% | N/A |

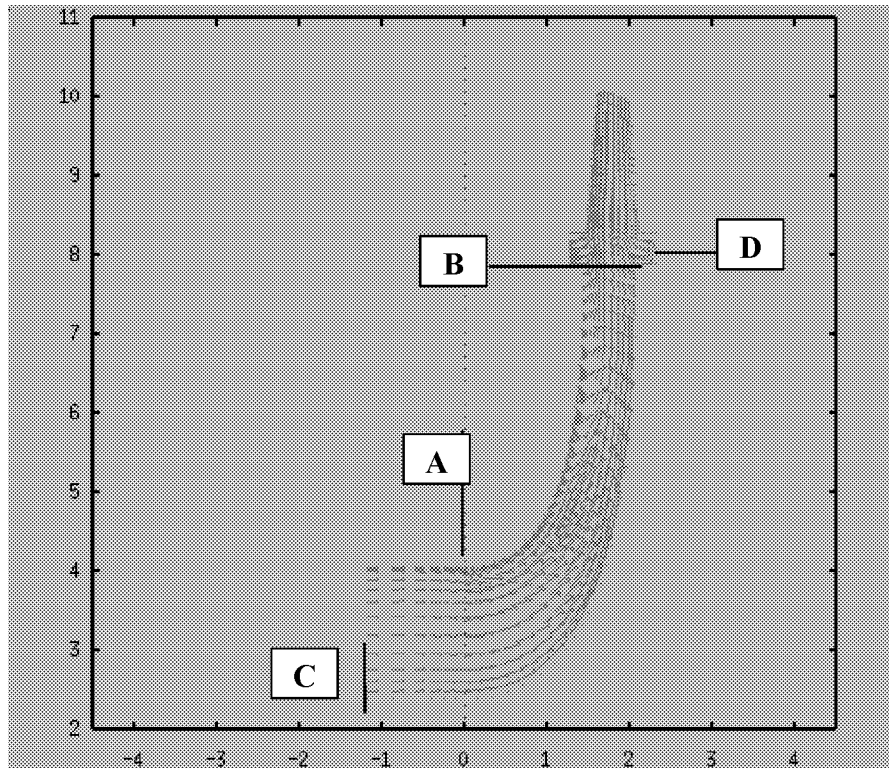


Figure 4 : Performance Calculation Planes

ROTORDYNAMIC ASSESSMENT

Stable turbomachinery operation depends on the damping of the rotor motion. Currently, rotordynamic stability parameters are estimated by using bulk flow theories and small perturbation (quasi-steady) assumptions. A well-established experience base with unshrouded impeller rotordynamic coefficients does not exist.

To help understand the unshrouded impeller's rotordynamic performance, Enigma's computational rotordynamic methodology was applied to the unshrouded impeller. This method directly simulates the rotor whirling motion (no quasi-steady assumptions) and can be, in principle, applied to large eccentricity whirl problems.

For Navier-Stokes based rotordynamic calculations, the impeller shaft/hub moves with an imposed whirling harmonic motion, figure 5, and the flow equations are integrated time-accurately until reaction force time periodicity is observed. The fluid reaction force vector time history is calculated; the force history can then be post-processed and decomposed into normal and tangential components. Because of the direct simulation of the moving hub, the flow model must consist of the complete three-dimensional geometry (full 360 degrees in circumference). A similar approach to access the rotordynamic fluid forces on seals has been fully described in reference 4.

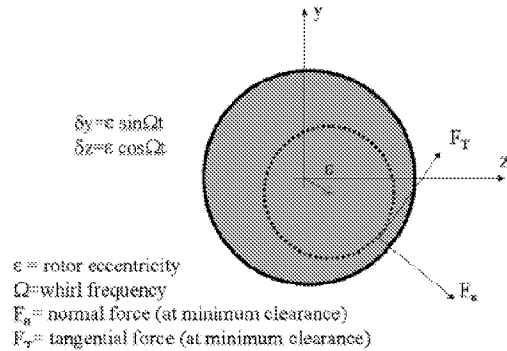


Figure 5: Whirling impeller rotor (hub)

Four whirl cases were computed: forward and backward synchronous, and forward and backward super synchronous. The effect of whirl ratio on the housing fluid forces are shown in figure 6. Using this calculation methodology rotordynamic coefficients can be supplied to the rotordynamics community to evaluate the impact on stability of the machine at all required operating points.

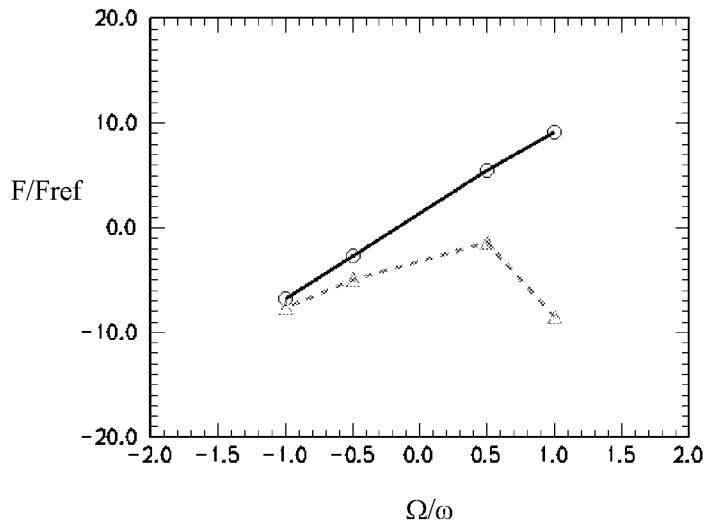


Figure 6: Computed normal and tangential forces

CONCLUSIONS

Performance degradation due to impeller tip clearance is well documented in literature. Two methods are available to combat this issue. Maintain tight tip clearances at all operating points or design an impeller with tip clearance insensitivity. The former is difficult to achieve in a high pressure turbopump due to housing deflections and material growth and shrink due operating speeds and cryogenic fluid temperatures. Literature review indicated that blade number variations could decrease tip clearance sensitivity. A trade study has been undertaken to evaluate blade number impact on performance with varying tip clearance. Rotordynamic assessment of turbopump stability is of great concern for rocket engine turbopumps. This is due to the inability to provide high levels of damping in the system at will. A method has been described for evaluating these forces with unshrouded impellers.

REFERENCE

1. Y. Senoo and M. Ishida, "Deterioration of Compressor Performance Due to Tip Clearance of Centrifugal Impellers," *Journal of Turbomachinery*, January 1987, Vol. 109, pp. 55-61
2. Johannes Lauer, et. al., "Tip Clearance Sensitivity of Centrifugal Pumps with Semi-Open Impeller," 1997 ASME Fluids Engineering Division Summer Meeting, FEDSM97-3366.
3. Hoshide, R. K. And C. E. Nielson, "Final Report, Study of Blade Clearance Effects on Centrifugal Pumps", NASA CR-12081, R-8806, November, 1972.
4. Williams, M. , W. Chen, L. Brozowski, A. Eastland, "Three-Dimensional Finite Difference Method for Rotordynamic Fluid Forces on Seals" *AIAA Journal*, Volume 35, Number 8, Pages 1417-1420, August 1997.

WATER FLOW PERFORMANCE OF A SUPERSCALE MODEL OF THE FASTRAC LIQUID OXYGEN PUMP

Stephen Skelley
and
Thomas Zoladz

Fluid Physics and Dynamics Group
Subsystem and Component Development Department
Space Transportation Directorate
Marshall Space Flight Center

ABSTRACT

As part of the National Aeronautics and Space Administration's ongoing effort to lower the cost of access to space, the Marshall Space Flight Center has developed a rocket engine with 60,000 pounds of thrust for use on the Reusable Launch Vehicle technology demonstrator slated for launch in 2000. This gas generator cycle engine, known as the Fastrac engine, uses liquid oxygen and RP-1 for propellants and includes single stage liquid oxygen and RP-1 pumps and a single stage supersonic turbine on a common shaft. The turbopump design effort included the first use and application of new suction capability prediction codes and three-dimensional blade generation codes in an attempt to reduce the turbomachinery design and certification costs typically associated with rocket engine development. To verify the pump's predicted cavitation performance, a water flow test of a superscale model of the Fastrac liquid oxygen pump was conducted to experimentally evaluate the liquid oxygen pump's performance at and around the design point.

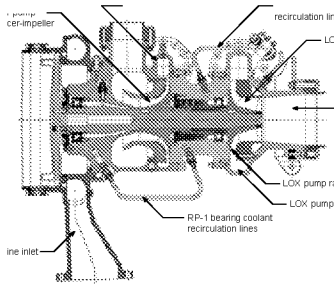
The water flow test article replicated the flow path of the Fastrac liquid oxygen pump in a 1.582x scale model, including scaled seal clearances for correct leakage flow at a model operating speed of 5000 revolutions per minute. Flow entered the 3-blade axial-flow inducer, transitioned to a shrouded, 6-blade radial impeller, and discharged into a vaneless radial diffuser and collection volute. The test article included approximately 50 total and static pressure measurement locations as well as flush-mounted, high frequency pressure transducers for complete mapping of the pressure environment. The primary objectives of the water flow test were to measure the steady-state and dynamic pressure environment of the liquid oxygen pump versus flow coefficient, suction specific speed, and back face leakage flow rate. Initial results showed acceptable correlation between the predicted and experimentally measured pump head rise at low suction specific speeds. Likewise, only small circumferential variations in steady-state

impeller exit and radial diffuser pressure distributions were observed from 80% to 120% of the design flow coefficient, matching the computational predictions and confirming that the integrated design approach has minimized any exit volute-induced distortions. The test article exhibited suction performance trends typically observed in inducer designs with virtually constant head rise with decreasing inlet pressure until complete pump head breakdown. Unfortunately, the net positive suction head at 3% head fall-off occurred far below that predicted at all tested flow coefficients, resulting in a negative net positive suction head margin at the design point in water. Additional testing to map the unsteady pressure environment was conducted and cavitation-induced flow disturbances at the inducer inlet were observed. Two distinct disturbances were identified, one rotating and one stationary relative to the fixed frame of reference, while the transition from one regime to the next produced significant effects on the steady state pump performance. The impact of the unsteady phenomena and the corresponding energy losses on the unexpectedly poor pump performance is also discussed.

INTRODUCTION

Marshall Space Flight Center (MSFC) has developed a 60,000 pound thrust rocket engine for use on the Reusable Launch Vehicle Technology Demonstrator vehicle (X-34). The gas generator cycle engine, also called the Fastrac engine, uses liquid oxygen and RP-1 for propellant. The turbopump integrates a single stage liquid oxygen pump, a single stage RP-1 pump, and single stage supersonic turbine into a compact assembly on a common shaft. A cross section of the turbopump appears in figure 1.

Figure 1. Fastrac Turbopump Cross Section



The engine was designed entirely by MSFC personnel and the turbopump design included the first use and application of new suction capability prediction methods and three-dimensional blade generation codes. In response to previous experiences with liquid oxygen pumps, a water flow test to evaluate the suction capability and head performance of the liquid oxygen pump was proposed. Using a superscale model of the pump, a test was conducted in MSFC's Inducer Test Loop during the first half of 1999 to evaluate the test article performance at scaled operating conditions in water. This document is intended to summarize the results from the experimental water flow test.

TEST FACILITY DESCRIPTION

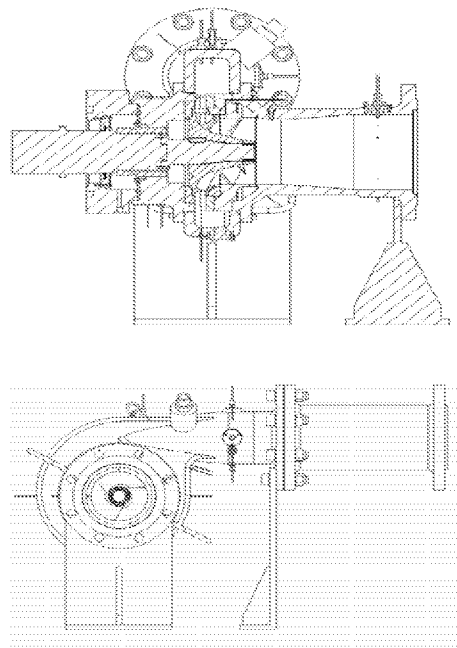
The Inducer Test Loop is a closed loop water flow test facility with manual set point control of flow rate, shaft speed, water temperature, and test article inlet pressure. In operation flow leaves the 300 gallon stainless steel reservoir through an 8 inch line, transitions to 6 inch line, passes through a flow straightener section, and enters the test article. High pressure discharge flow exits the test article, passes through a 6 inch turbine type flow meter, and returns to the reservoir. A 6 inch quiet valve provides remote back pressure control for flow rate adjustment. Test article inlet pressure is controlled by pressurizing or evacuating the small air volume at the top of the reservoir. This reservoir ullage pressure, coupled with the line losses between the reservoir and test article inlet and the height of the water in the reservoir itself, is used to set a wide range of inlet pressures - from 165 down to 3 pounds per square inch absolute. The test loop accommodates flow rates up to 4000 gallons per minute and is constructed primarily of schedule 40 and schedule 80 PVC. An auxiliary loop removes dissolved air from the test fluid and maintains water temperatures between 70 and 100 degrees Fahrenheit. The driveline consists of a 3-phase, 150 horsepower motor with a variable speed controller and belt driven bearing box. Design limit speed is approximately 6000 revolutions per minute, but higher speeds are

obtainable by changing the pulley ratio and belt material. Bearing temperatures, shaft speed, test article inlet pressure, flow rate, water temperature, and discharge pressure are monitored at the facility operator's control panel and an Orbiscope dissolved oxygen sensor is used to measure the water dissolved oxygen content. For all testing water dissolved oxygen content was maintained at or below 4 parts per million.

TEST ARTICLE DESCRIPTION

The test article was a superscale (1.582X) model of the Fastrac liquid oxygen pump and replicated the primary flow path including the front and rear leakage cavities. Bearing coolant flow, or back face leakage, was collected metered, and returned to the pump inlet through 2 external lines. A cross section and front view of the test article appears in figure 2.

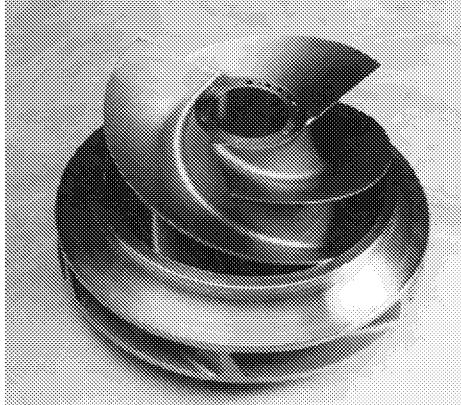
Figure 2. Test Article Cross Section and Front View



The stainless steel inducer-impeller shown in figure 3 was fabricated by Turbocam, Inc. and included 3 full length blades and 3 splitters, resulting in 6 shrouded flow passages at the impeller discharge. No back face pumping vanes were included on the test article inducer-impeller although the prototype includes this design feature. The stainless steel inducer-impeller was a replacement for the original aluminum inducer-impeller which was damaged after approximately 20 hours of testing. High cycle fatigue resulted in the loss of the tips of each of the 3 inducer blades. The

steel inducer-impeller suffered no fatigue or cavitation-induced damage during testing.

Figure 3. Inducer-Impeller Assembly



Impeller discharge flow was guided through a vaneless, constant width radial diffuser, rectangular cross section volute, and conical exit diffuser and directed away from the pump perpendicular to the axis of rotation. Table 1 summarizes the scaled and as-built geometric parameters for the test article. Table 2 summarizes the prototype and test article design point operating conditions.

Table 1. Test Article Geometric Parameters

| | |
|---|---------------|
| Number of Blades | 3 + 6 |
| Inlet Tip Diameter | 5.177 inch |
| Inlet Hub Diameter | 1.973 inch |
| Reference Blade Length (Hub to Tip) | 1.736 inch |
| Leading Edge Tip Thickness | 0.019 inch |
| Inlet Blade Angle at Tip | 10.5 degrees |
| Inducer Radial Clearance | 0.021 inch |
| Exit Tip Diameter | 7.056 inch |
| Exit Blade Height | 0.682 inch |
| Exit Blade Angle | 26.5 degrees |
| Radial Diffuser Inner Diameter | 7.147 inch |
| Radial Diffuser Outer Diameter | 9.487 inch |
| Radial Diffuser Passage Width | 0.684 inch |
| Volute Throat Area | 6.660 sq inch |
| Exit Diffuser Cone Angle | 6.00 degrees |
| Exit Diffuser Cone Length-to-Inlet Radius Ratio | 5.00 |
| Exit Diffuser Cone Exit Diameter | 4.182 inch |

Table 2. Prototype and Test Article Design Point

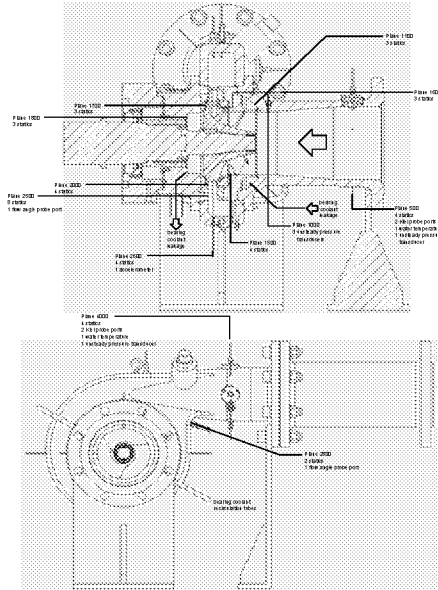
| Parameter | Prototype | Test Article |
|---------------------------------------|---------------|--------------|
| Fluid | Liquid Oxygen | Water |
| Fluid Temperature | 166 deg R | 90 deg F |
| Shaft Speed | 20,000 rpm | 5000 rpm |
| Inlet Flange Flow Rate | 880.4 gpm | 870 gpm |
| Impeller Flow Rate | 923.7 gpm | 913 gpm |
| Inlet Flange Total Pressure | 46.0 psia | 4.7 psia |
| Back Face Leakage Rate | 25.6 gpm | 25.3 gpm |
| Net Positive Suction Head | 59.2 ft | 9.2 ft |
| Inlet Tip Flow Coefficient | 0.135 | 0.135 |
| Suction Specific Speed (rpm, gpm, ft) | 27820 | 27820 |

All test article hardware except the inducer-impeller was fabricated of anodized 2219 aluminum by Dynamic Engineering, Inc. The test article design inlet pressure, shaft speed, and discharge pressure were 40 pounds per square inch absolute, 6000 revolutions per minute, and 165 pounds per square inch absolute, respectively.

INSTRUMENTATION

Steady-state measurements acquired during testing were used to confirm set point conditions, evaluate pump performance, and monitor test article health. Surface static pressure taps were distributed throughout the test article and grouped into 12 axial measurement planes. Total pressure probes at the inlet and discharge flanges were used to establish flange-to-flange pressure rise and a flow direction probe at the impeller discharge further defined pump performance. Flush-mounted high frequency response transducers were also located at 3 axial planes in the test article and at 4 locations in the facility piping for recording of system and pump pressure oscillations. Accelerometers on the test article were used to resolve motion of the stationary components. The approximate locations, types, and numbers of these measurements appear in figure 4.

Figure 4. Test Article Measurement Locations, Types, and Numbers



TEST PLAN

The objectives of the experimental water flow test were to

1. Measure the steady-state pump suction performance versus flow coefficient and back face leakage flow rate.
2. Measure the pump steady-state head performance versus flow coefficient and back face leakage flow rate.
3. Measure the pump dynamic pressure environment versus flow coefficient, suction specific speed, and back face leakage flow rate.
4. Measure pump intra-stage pressures for verification of design code predictions.

An implied objective was to provide a safe and inexpensive test article to support potential failure investigations or redesign efforts. The original test plan included pump operation as low as 50% of the design flow coefficient. Following the failure of the aluminum inducer-impeller, all testing and operation with the replacement steel inducer-impeller was confined to a range of 80% to 120% of the design flow coefficient. Likewise, the installed back face leakage routing lines included too much resistance, so operation with higher than the nominal scaled leakage flow rate was not possible. Test variables included flow coefficient, suction specific speed, and back face leakage flow rate. The test article set point variables were then water temperature, inlet flange flow rate, inlet flange total pressure, shaft speed, and back face leakage rate. The as-tested ranges of each

of the test variables appear in table 3 for a shaft speed of 5000 revolutions per minute.

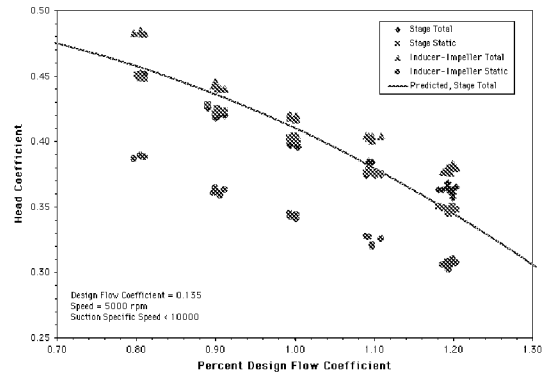
Table 3. Completed Test Matrix

| Back Face Leakage Rate | Percent Design Flow Coefficient | Suction Specific Speed |
|------------------------|---------------------------------|------------------------|
| Nominal | 80% | 6340 - 29010 |
| | 90% | 5670 - 28680 |
| | 100% | 5550 - 27580 |
| | 110% | 5780 - 26260 |
| | 120% | 5770 - 25170 |
| Half Nominal | 90% | 8030 - 24560 |
| | 100% | 5660 - 26000 |
| | 110% | 7530 - 24700 |
| Zero | 90% | 7820 - 28200 |
| | 100% | 7470 - 27830 |
| | 110% | 8030 - 26620 |

STEADY STATE PERFORMANCE

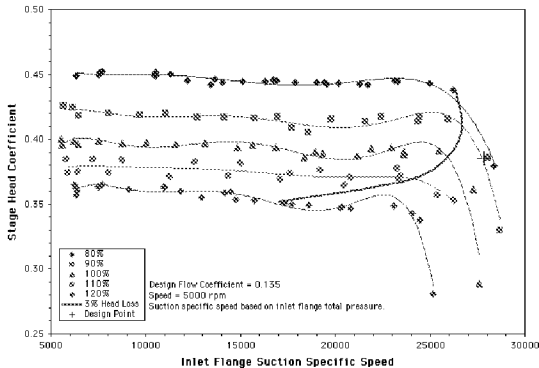
The overall stage total and static pressure rise as well as the total and static pressure rise of the inducer-impeller appear in figure 5 versus percent design flow coefficient. Pressure rise data in figure 5 are values corresponding to a suction specific speed at or below 10000 for the nominal back face leakage flow rate. Data has been non-dimensionalized by the impeller tip speed and the predicted performance curve included for reference. The trends are as expected with steadily decreasing pressure rise with increasing flow rate. The water flow test article appeared to underperform slightly at and below the design flow coefficient with head rise at the higher flow rates much closer to the predicted. Expressed in terms of degree of reaction, or the ratio of impeller static head rise to stage total head rise, the experimental value at the design flow coefficient was 0.83, indicating excellent conversion of available dynamic head to static pressure.

Figure 5. Stage and Inducer-Impeller Head Coefficient versus Percent Design Flow Coefficient



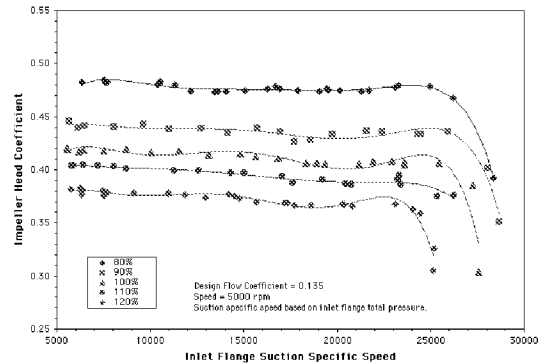
The experimental pump stage suction performance appears in figure 6 with stage head coefficient versus inlet flange suction specific speed. The individual curves correspond to flow coefficients from 80% to 120% of the design flow coefficient. The trends are as expected with inducer-impeller designs with virtually constant head coefficient with decreasing inlet pressure. The small reduction in steady state head rise at a suction specific speed of approximately 17000 to 21000 was attributed to the transition of a rotating, cavitation disturbance at the inlet to a synchronous, uniform cavity oscillation. Complete head breakdown soon follows. The approximate range of the inlet rotating disturbance was from a suction specific speed of 11500 to 17000 and further discussion of the observed unsteady phenomena appears in a later section. The pump design point and calculated 3% head loss curve are included for reference. As this curve illustrates, the test article failed to achieve the desired suction performance in water at the design flow coefficient with a calculated margin on net positive suction head of -9% between the demonstrated and required capability. The measured variation in head coefficient at the 110% design flow coefficient was attributed to electrical contamination of the stage pressure rise measurement during those set points. All other data included in this document remained unaffected.

Figure 6. Stage Head Coefficient versus Suction Specific Speed and Percent Design Flow Coefficient



For comparison the inducer-impeller head coefficient is plotted versus suction specific speed and percent design flow coefficient in figure 7. No variation is observed in the 110% design flow coefficient data.

Figure 7. Inducer-Impeller Head Coefficient versus Suction Specific Speed and Percent Design flow Coefficient



A primary design objective was to minimize the impeller discharge distortion and thereby minimize the fluid-induced pump sideloads. Figure 8 shows the measured static pressure distribution at the impeller discharge versus percent design flow coefficient. A view slightly further downstream appears in figure 9 with the static pressure distribution at the exit of the radial diffuser. Each location shows increasing influence of the volute cutwater – located at 24 degrees – with the least pressure variation at each location at the design flow coefficient. In each plot the static pressure coefficient is defined as the local pressure divided by the plane average static pressure and divided by the calculated dynamic pressure.

Figure 8. Static Pressure Distribution at the Impeller Discharge

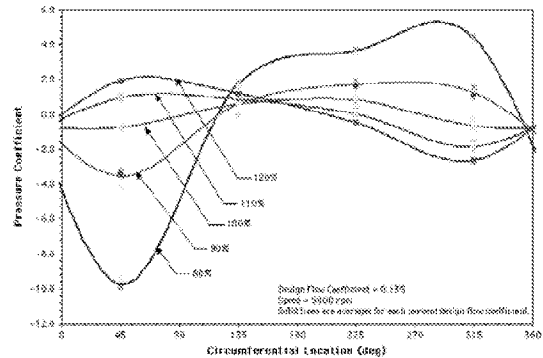
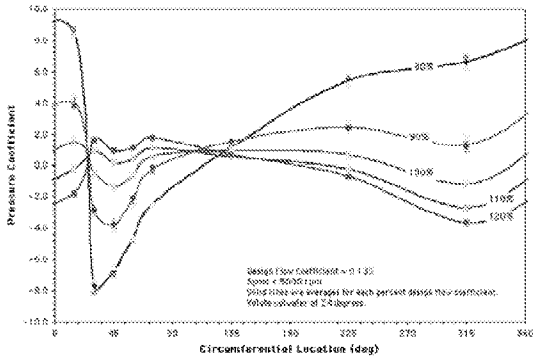
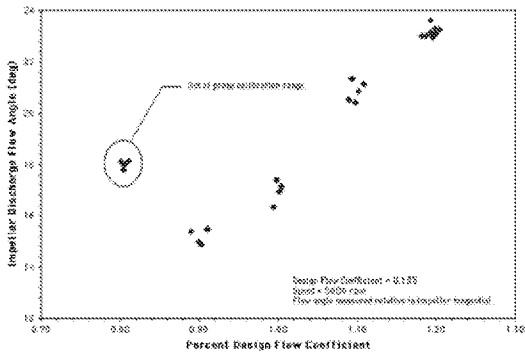


Figure 9. Static Pressure Distribution at the Radial Diffuser Discharge



The final check on inducer-impeller performance was via a single flow direction probe located slightly downstream of the impeller discharge in the center of the radial diffuser. Total pressure, static pressure, and probe-relative flow angle was then derived from the sensed pressures and the probe calibration results. The impeller discharge flow angle relative to impeller tangential versus percent design flow coefficient appears in figure 10. The predicted discharge flow angle at the design flow coefficient was 14 degrees relative to impeller tangential.

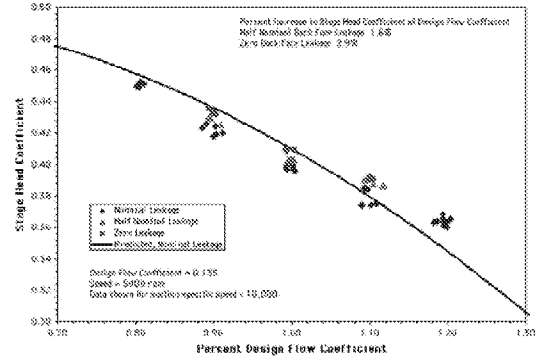
Figure 10. Impeller Discharge Flow Angle versus Percent Design Flow Coefficient



The majority of data was collected at a back face leakage rate corresponding to the nominal condition. However, limited performance data was collected at half the nominal leakage rate and with the external leakage metering lines closed. The effect of reducing the leakage rate on stage head rise appears in figure 11 for suction specific speeds at or less than 10000. As expected the stage head rise increases with decreasing leakage rate as work previously expended on the leakage flow is applied to the throughflow. The inducer actually operates at a slightly lower flow coefficient as the leakage flow is reduced at constant

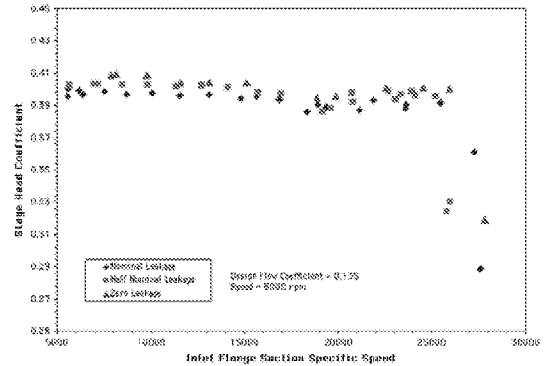
pump flow rate and thereby contributes a small amount to the increase in stage performance.

Figure 11. Stage Head Coefficient versus Percent Design Flow Coefficient and Leakage Rate



Although a small effect on suction performance appears in the leakage rate comparison in figure 12, the calculated differences are of the same order as the experimental uncertainty at these values of suction specific speed. No conclusion should then be drawn from these results. Figure 11 is then included to illustrate the repeatability of the small drop in stage performance, which appears for each configuration near a suction specific speed of 17000. This performance drop, as will be seen in the following section, corresponds to the highest amplitude of the synchronous cavity oscillation at the inducer inlet.

Figure 12. Stage Head Coefficient versus Suction Specific Speed and Leakage Rate at Design Flow Coefficient

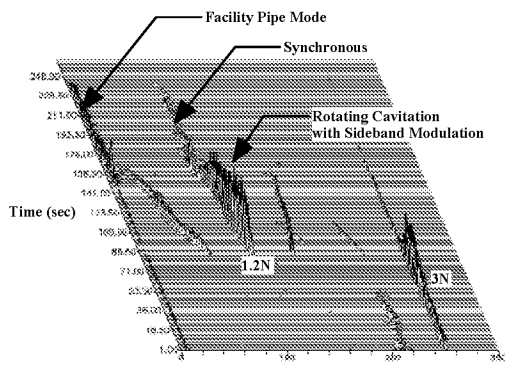


UNSTEADY PERFORMANCE

Figure 13 shows the progression of unsteady oscillations versus time as the pump inlet pressure was steadily reduced at a constant shaft speed of 5000 revolutions per minute (83.3 Hertz) at the design flow coefficient. At low suction specific speeds, the oscillation at 3 times shaft speed (3N)

was most prominent as was associated with the wakes from the 3 inducer blades. As suction specific speed approached 11000 at 88.5 seconds the 3N oscillation transitioned to a rotating disturbance moving at approximately 1.2 times the shaft speed (1.2N) as viewed from a stationary observer. This rotating disturbance was identified as a single cavitation cell moving opposite the direction of shaft rotation. Further reduction in inlet pressure causes the single-cell rotating disturbance to transition to a stationary oscillation with a frequency equal to the shaft speed. Simultaneously a higher amplitude oscillation appeared with a frequency very close to the fundamental frequency of the test facility piping – approximately 10 Hertz. These low frequency and synchronous oscillations persisted as inlet pressure was reduced and head breakdown was reached. The potential for dynamic coupling between the facility and pump was recognized and attempts were made to better isolate the pump from the facility. All were unsuccessful and the low frequency oscillation appeared to “lock-in” with the facility harmonic at all tested flow coefficients.

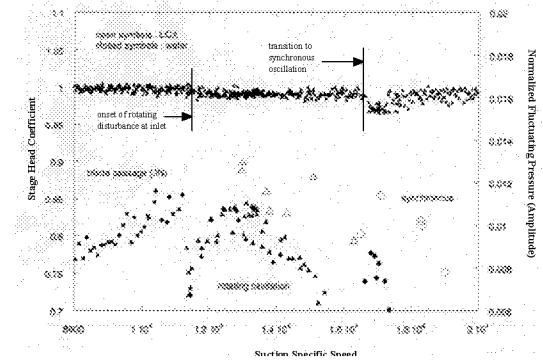
Figure 13. Oscillation Amplitudes versus Frequency and Time at Constant Speed and Design Flow Coefficient



The dynamic coupling between the test article and facility, combined with the presence of cavitation, suggested the occurrence of auto-oscillation, if only for a brief period. Brennen¹ noted severe steady state performance deficits due to the energy dissipation during auto-oscillation and the magnitude of the head loss at the design flow coefficient was approximately 3%. The nondimensional amplitudes of the oscillations noted in figure 13 and stage head coefficient appear in figure 14 versus suction specific speed. Oscillation amplitudes have been normalized by the dynamic pressure based on impeller tip speed while head coefficient has been normalized by the

non-cavitated value. For comparison the corresponding normalized amplitudes from recent component testing in liquid oxygen are included.

Figure 14. Oscillation Amplitudes versus Suction Specific Speed



Auto-oscillation is typically characterized by high amplitude, system-wide oscillations in pressure and flow rate. As seen in figure 13, pressure oscillations during auto-oscillation were highest at the onset of the phenomena. These oscillations appeared in conjunction with noticeable facility piping displacements and low frequency, shock-like vibrations. However, the period of these high intensity vibrations and pressure oscillations was brief and occupied only a very narrow band of suction specific speed values. The relationship between the synchronous oscillation and the appearance of auto-oscillation is still under review, but the transition of a rotating cavitation disturbance to a fixed number of cavitation cells oscillating in unison has been observed in other inducer performance investigations. Rosenmann² and others^{3,4} observed the transition of a rotating disturbance to a “unidirectional” or synchronous oscillations with frequency equal to the shaft speed just before head breakdown. The relationship between the uniform cavity or synchronous oscillation and the corresponding system dynamic response and the subsequent onset of auto-oscillation requires further investigation. Regardless, the pump and system dynamic interaction appears to have contributed to the inability of the test article to achieve the expected suction capability. Although beyond the scope of this document, the significance of the data in figure 14 for the prototype pump operating in liquid oxygen should be noted. Despite the difference in test facility configurations, the prototype exhibited similar unsteady performance characteristics with the appearance of a synchronous oscillation at high suction specific speeds. This may

suggest a sensitivity of the pump to dynamic system interactions.

UNCERTAINTY ANALYSIS

An uncertainty analysis incorporating the experimental precision and bias errors using the root-sum-square method was performed to quantify the worst case uncertainties associated with the measured and calculated quantities. A 95% confidence level was assumed. The estimated uncertainties for each of the parameters presented here are summarized in table 4. Since the estimated uncertainty associated with suction specific speed is dominated by the nonlinear function of pressure, the quoted uncertainty for suction specific speed in table 4 corresponds to a suction specific speed of 27000.

Table 4. Estimated Uncertainties

| Parameter | Uncertainty |
|---------------------------------|------------------|
| Stage Head Coefficient | ± 0.005 |
| Impeller Head Coefficient | ± 0.007 |
| Percent Design Flow Coefficient | ± 0.05 |
| Suction Specific Speed | ± 800 |
| Pressure Coefficient | ± 0.04 |
| Impeller Discharge Flow Angle | ± 1.2 degree |

CONCLUSIONS

Although this document is intended to merely summarize the experimental performance of the superscale water flow test, a few general conclusions regarding the Fastrac liquid oxygen pump performance can be made:

1. Steady state stage head rise was lower than predicted for 80% to 100% of the design flow coefficient. At 120% of the design flow coefficient, steady state stage head rise exceeded the predicted performance.
2. Suction performance in water failed to meet the desired capability with a margin on net positive suction head of -9%.
3. Three regimes of unsteady oscillations were observed, identified, and tracked versus pump operating parameters, including a brief period of auto-oscillation.
4. The appearance of auto-oscillation corresponded to drops in the steady state stage head rise of approximately 3% at the design flow coefficient.
5. The onset of auto-oscillation was unaffected by reduction in the pump back face leakage flow rate.

ACKNOWLEDGEMENTS

The authors gratefully acknowledge Jeff Moore and Teddy Stephens of the Experimental Fluid Dynamics Group for their operation of the experimental test

facility and assistance with test article and instrumentation installation. The measurement systems were designed, integrated, and maintained by Drew Smith and Herb Bush, also of the Experimental Fluid Dynamics Group. Richard Branick of Sverdrup was responsible for test article assembly. The authors would also like to recognize Stephen Fritz of Cortez III for his incredible electrical troubleshooting skills.

REFERENCES

- ¹ Brennen, C. E., Hydrodynamics of Pumps, Concepts ETI, Inc. and Oxford University Press, Norwich, 1994.
- ² Rosenmann, W., "Experimental Investigation of Hydrodynamically Induced Shaft Forces with a Three Bladed Inducer," Symposium on Cavitation in Fluid Machinery, ASME Winter Annual Meeting, Chicago, IL, Nov. 7-11, 1965.
- ³ Kamijo, K., Yoshida, M., and Tsujimoto, Y., "Hydraulic and Mechanical Performance of LE-7 LOX Pump Inducer," Journal of Propulsion and Power, vol. 9, no. 6, 819-826, 1993.
- ⁴ Kamijo, K., Shimura, T., and Watanabe, M., "A Visual Observation of Cavitating Inducer Instability," National Aerospace Lab (Japan) Report NAL TR-598T, 1980.



THE PERFORMANCE OF ANNULAR DIFFUSERS SUBJECT TO INLET FLOW FIELD VARIATIONS AND EXIT DISTORTION

Dr. David Japikse
Concepts ETI, Inc.
217 Billings Farm Road
White River Junction, Vermont 05001-9486

ABSTRACT

A series of studies has been conducted to evaluate the performance of annular diffusers subject to the influence of inlet swirl, boundary layer thickness, and distortion typical of turbine operation. Exit distortion, as imposed by an exit collector or hood has also been studied. Both a moderate length and a very short length annular diffuser have been included in this series of evaluations. Guidelines for design are presented as well as suggestions for CFD utilization in future designs.

NOMENCLATURE

| | |
|-------------------|---|
| AR | Area ratio |
| B | Aerodynamic Blockage |
| BL | Boundary Layer Method |
| $C1, B2$ | Specific diffuser names |
| $C_{p(0-2)}$ | Static pressure recovery from upstream to exit stations |
| $C_{p(1-2)}$ | Static pressure recovery from inlet to exit stations |
| $C_{p(1-p)}$ | Static pressure recovery from inlet to plenum stations |
| C_p | Static pressure recovery $(P_{exit} - P_{in})/(P_{0,in} - P_{in})$ |
| C_{pc} | Static pressure recovery along convex wall |
| E | Relative eccentricity, $\varepsilon/(r_3 - r_2)$ –see Figure 19 for symbols |
| L, ℓ | Length scales see Figure 16a or Figures 19 and 20. |
| $L/\Delta r$ | Diffuser non-dimensional length |
| M | Mach number |
| \bar{p}_2 | Average static pressure at diffuser exit |
| P_p | Average static pressure in exit plenum |
| R/B_1 | See Figure 11 |
| R, r | Radius, see Figures 16a, 19 and 20. |
| $r_{1t} - r_{1h}$ | Inlet span |
| SLC | Streamline curvature method |
| α | Swirl angle measured from meridional direction |
| ε | Eccentricity, see Figure 19 |
| ϕ_1, ϕ_2 | See Figure 19 |
| γ_2 | Passage exit mean angle with respect to a radial line |
| C_2 | Average diffuser exit velocity |

Subscripts:

0 – upstream station

1 – inlet station

2 – exit station

1. INTRODUCTION

The performance of annular diffusers is important to inter-stage and last-stage elements of many turbomachines. Recovering excessive kinetic energy in the form of a static pressure rise significantly improves stage efficiency. This conversion process, however, is influenced by diverse fluid dynamic phenomena as the flow adjacent to walls is decelerated and also by inlet and exit distortions. Designing and perfecting annular diffusers can be a complex process. Consequently, a series of consortia projects was organized and led by the author during a 1975 – 1981 period with specific project management and contributions by Japikse (1977, 1978, 1981), Goebel (1981), and Patel (1977). These results are now available by sponsors' consent and are gratefully acknowledged.

Prior contributions to the diffuser technical literature are numerous and are surveyed by Japikse (1984) and Japikse and Baines (1998). A short synopsis for turbine design is given by Japikse (1999). Several useful references are cited herein to provide data comparisons or trends. These include data from Sovran & Klomp (1967) giving the first annular diffuser map, Stevens & Williams (1980) showing an influence of inlet conditions, Takehira (1977) showing the influence of wall curvature, and Deych et.al. (1970) showing the influence of flow distortion from an exhaust hood.

Sovran and Klomp (1967), as shown in Figure 1 prepared early maps of diffuser performance. It should be understood that the Sovran and Klomp map is a composite of many different tests of their own and tests from other investigators. The details of those tests may be found in the appendix of the Sovran and Klomp reference. By way of illustration, several example points are taken from the appendix and overlaid in Figure 2. It may be observed that these particular overlays are in rough agreement with the general contours, but definitely not in precise agreement. This variance is to be expected when a generalized map is made as a composite of many individual or specific results from different investigators. Hence the map should be used for general guidance; for specific results, one should consider the specific test conditions of specific studies as referenced in the appendix to the Sovran and Klomp investigation.

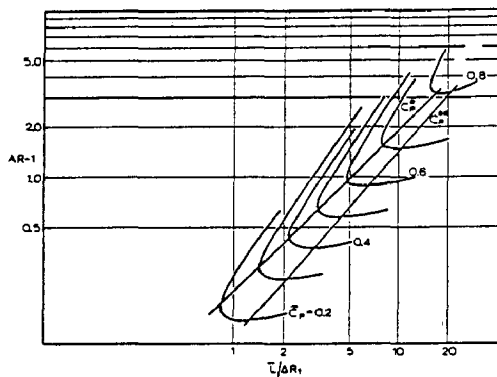


Figure 1: Annular diffuser performance chart, $B_1 = 0.02$ (Sovran and Klomp 1967).

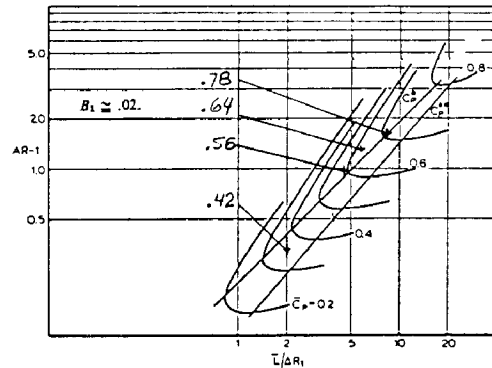


Figure 2: Sovran and Klomp map showing several original test points.

The investigation of this present study looked at all of the parameters discussed in the technical literature and evaluated annular diffusers under extreme conditions of geometric restriction as well as more generous design configurations. Figure 3 shows the geometric environment in which these diffusers were considered. Case 1 was the restricted length design frame which was a very tight configuration indeed (essentially permitting one to design a conveying passage as opposed to a diffuser passage). With extension plates, more radius could be employed and some additional diffusion might be achieved. The Case 2 design frame permitted a moderate length diffuser to be designed following more conventional norms of the diffuser literature and technology. Principle results for the Case 2 configuration are shown in Figure 4. It may be observed that good performance all the way up to a swirl angle of 40° has been achieved and that an exhaust hood (discussed later) has been utilized with no more than one point of pressure recovery penalty. Similar results for the B2 diffuser, which was optimized for the Case 1 restricted length design, are shown in Figure 5. For this B2 case, the compromise is quite severe, although 22% pressure

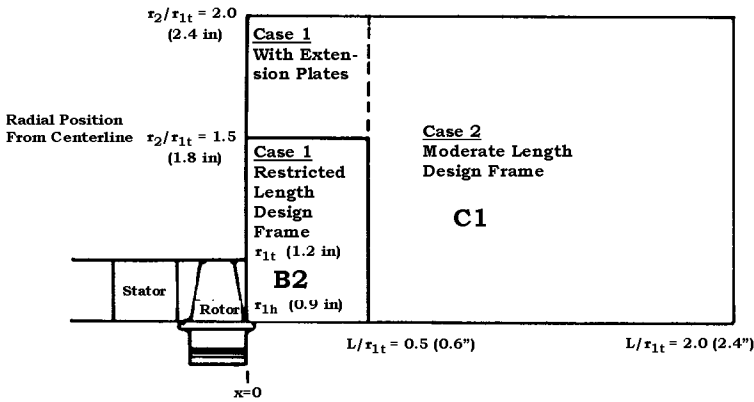


Figure 3a: Selected design frames.

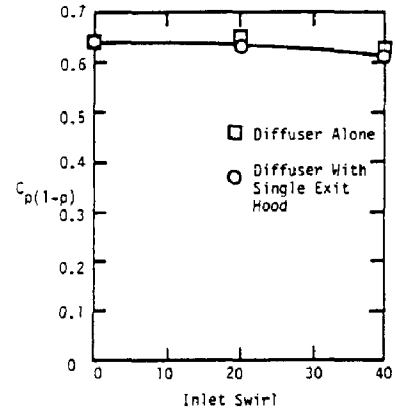


Figure 4: System pressure recovery coefficient as a function of inlet swirl for an optimally designed single exit hood and the C1 (moderate design frame) exhaust diffuser.

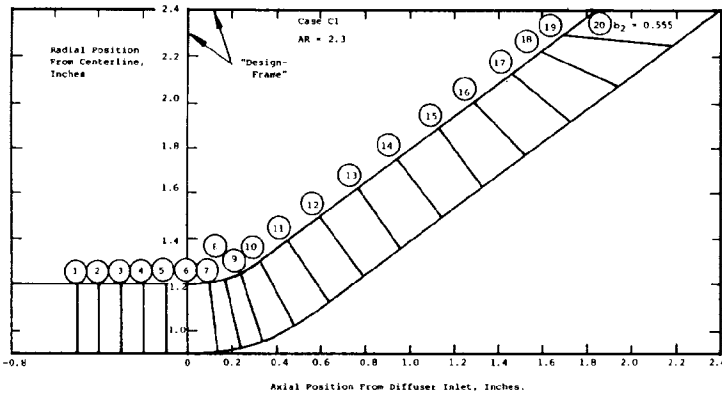


Figure 3b: C1 diffuser configuration showing quasi-orthogonal numbers for computation.

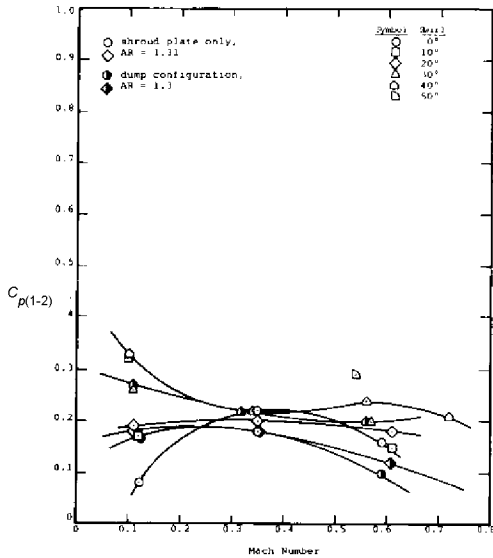


Figure 5a: $C_{p(0-2)}$ recovery for the B2 diffuser.

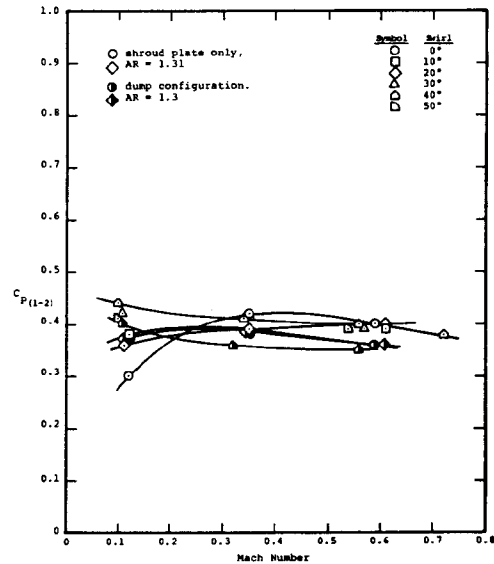


Figure 5b: $C_{p(1-2)}$ recovery for the B2 diffuser.

recovery has been achieved on the overall basis. Figure 6 shows a set of wall static pressure calculations and measurements for this design problem; it is evident that very large local pressure recoveries have been forced due to the strong bending of this flow field and the resultant pressure gradients (which follow the Euler-n equation).

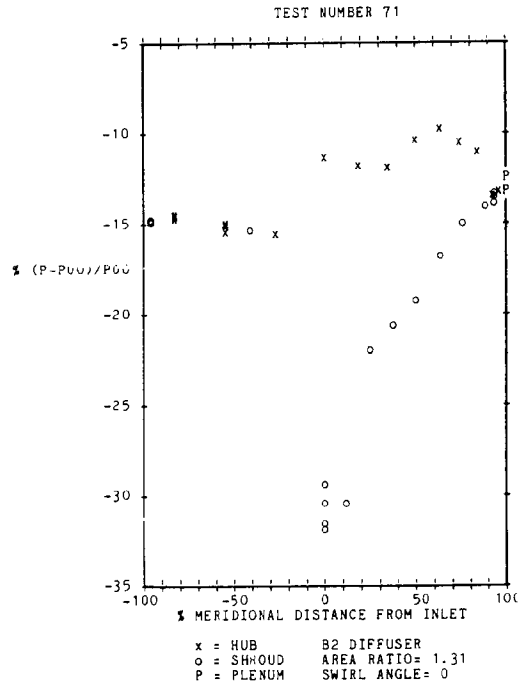


Figure 6: B2 wall pressure survey without shroud extension plate, $AR = 1.31$, $M = 0.59$, $\alpha = 0^\circ$.

2. INLET VARIATIONS (DISTORTION)

Test results for the C1 diffuser, as a function of the inlet aerodynamic blockage, are shown in Figure 7. It will be observed that the trend follows that of a simple boundary layer calculation to a reasonable first approximation. It is also clear that pressure recovery drops off substantially with inlet fluid dynamic blockage. One can safely conclude that fluid dynamic blockage is a first order aerodynamic parameter. This parameter, over a modest variance, can drop the pressure recovery coefficient by at least ten points.

Figure 8 shows an additional test of the C1 diffuser with the optimum hood (as described later) as tested behind an actual operating turbine. The inlet velocity profiles to the

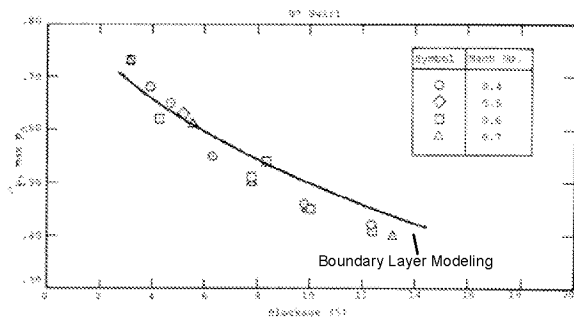


Figure 7: Measured and predicted annular diffuser recovery levels.

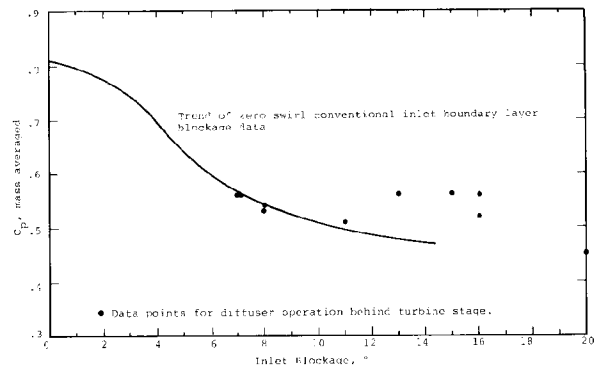


Figure 8: Comparison of diffuser recovery with conventional inlet boundary layer blockage and with operation behind an axial turbine.

annular diffuser were traversed during operation and fluid dynamic blockage was calculated. The measured pressure recovery during operation behind the rotor is displayed in Figure 8 versus blockage and the data trend from Figure 7 is also displayed. A sensible relationship between the performance on the engine and the performance deduced from the laboratory is shown.

The role of fluid dynamic blockage is an important one for diffusers in general. However, it is a little bit more difficult to discern the true trend, uniquely, for the annular diffusers due to the strong presence of swirl, curvature, inlet turbulence, and vorticity which always accompany a realistic production annular diffuser. Figures 9 and 10, which were prepared based on data from Stevens and Williams (1980) show some of the difficulty. Initially, the data shows a drop in performance with increasing blockage just as Figure 7 revealed. However, these investigators operated with a very long inlet duct, as one test option, so that nearly fully developed flow could be created. Consequently the data trend hooks back on itself and the pressure recovery again rises as blockage increases further. Part of this effect is surely due to increased turbulence and vorticity in the passage as fully developed flow sets in. This is partly supported by the use of outer wall turbulence generators as shown in Figure 9, which also raised the pressure recovery. Inlet turbulence grids also had a similar effect as the data with the circles in both Figures 9 and 10 illustrates. Hence the actual performance evaluation of an annular diffuser is extremely difficult. At the time of this writing, no computational method exists which can deal with all of the variances known to exist for an annular diffuser; likewise, no one has correlated all of these effects into simple database procedures at this time.

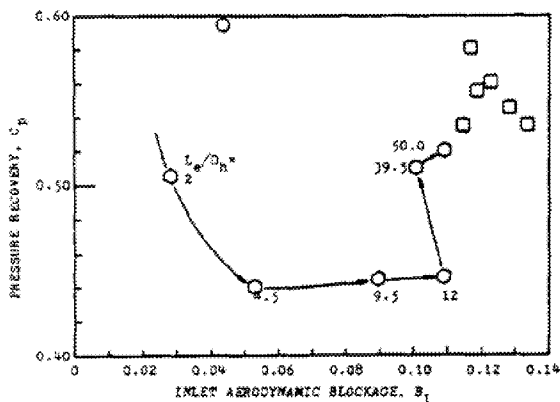


Figure 9: Pressure recovery for $AR = 2$, straight centerbody annular diffuser, $L/\Delta r = 5$. Hexagonal symbols denote low turbulence wall boundary layer blockage. Squares denote tests with outer wall turbulence generators. The circle denotes a test with an inlet turbulence grid.

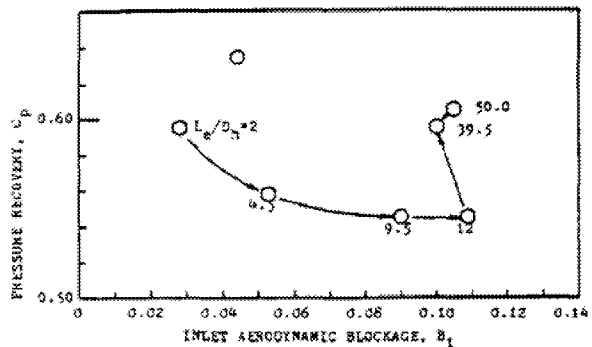


Figure 10: Pressure recovery for $AR = 2$, straight centerbody annular diffuser, $L/\Delta r = 7.5$. Symbols as per Figure 9.

An additional study of annular diffuser performance for turbines was reported by Takehira et al. (1977) based on work sponsored by Kawasaki. Their geometry is shown in Figure 11. This diffuser is in strong contrast to the figure shown in Figure 3b where all of the curvature was located at the inlet. The advantage of designing with inlet curvature, as opposed to exit curvature, is discussed by Japikse and Baines (1998, 1984), pages 1-10 through 1-13. The results of the Takehira study are shown in Figure 12 as the dark elliptical symbols. The first three symbols fall in the bottom range of the results obtained from the C1 diffuser study corresponding to the Case 2 moderate length design frame of Figure 3b. The value with a longer radius, $R/B_1 = 8.4$, where the effects of curvature are greatly reduced, fall in line with the C1 diffuser studies. The value shown at 100% recovery for their straight wall annular diffuser is clearly erroneous since this level of recovery cannot be achieved unless the fluid is inviscid and the length is infinite.

Computational techniques have been applied to the evaluation of annular diffuser performance. Calculations with simple boundary layer codes and two-dimensional core flow solvers are now illustrated. Good results have been achieved. An example of such calculations is shown in Figures 13 and 14. Good agreement with the C1 diffuser performance, Figure 13, and the more challenging geometry of B2, Figure 14, has been reported for higher Mach numbers as illustrated.

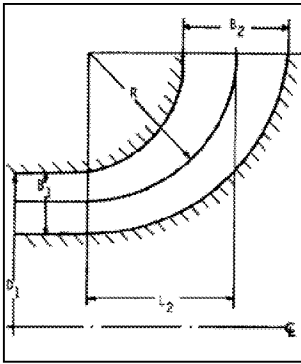


Figure 11: Geometrical characteristics of annular bent diffusers (Takehira et al. 1977).

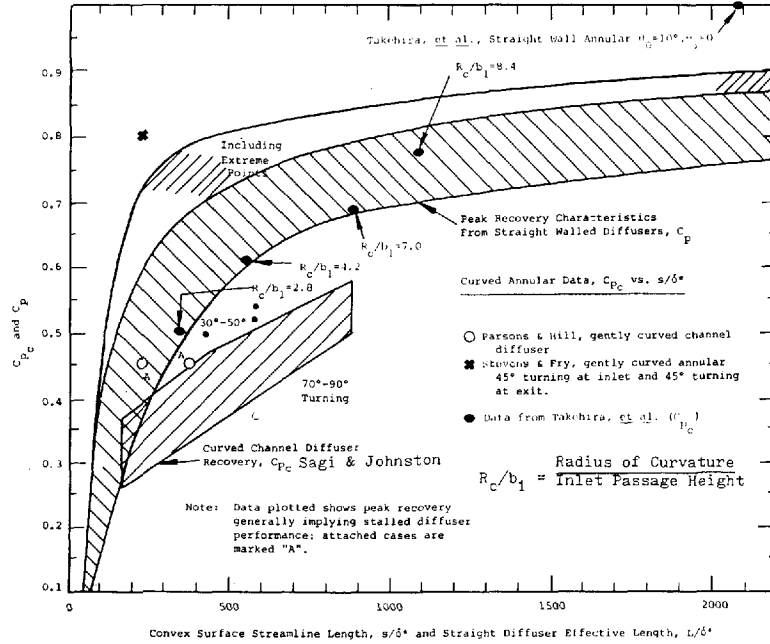


Figure 12: Comparison of Takehira's curved wall annular diffuser data with state-of-the-art reference bands. C_p = overall diffuser recovery, C_{pc} = local diffuser recovery along convex wall. The C1 diffuser data falls above the Takehira data in the reference band.

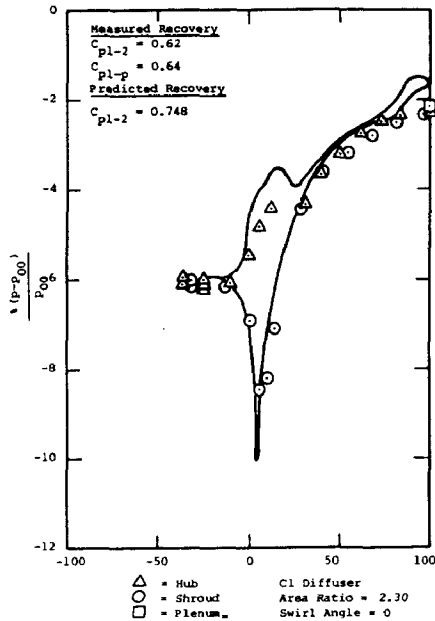


Figure 13a: Comparison of C1 diffuser pressures at $AR = 2.30$ and $\alpha = 0^\circ$, $M = 0.30$ with annular predicted pressures, Case 90.

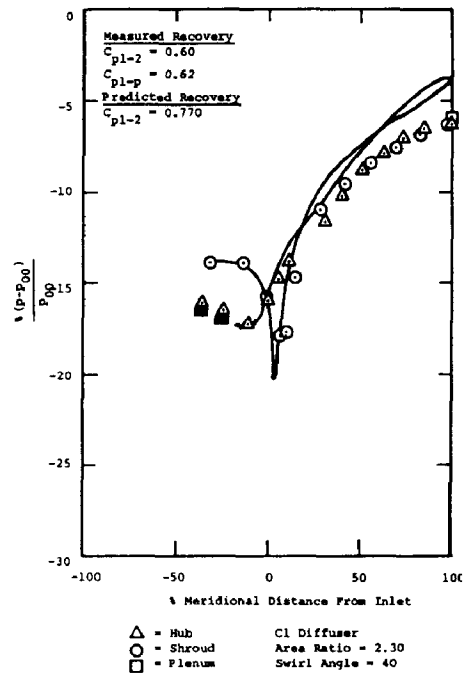


Figure 13b: Comparison of C1 diffuser pressures at $AR = 2.30$ and $\alpha = 40^\circ$, $M = 0.50$ with annular predicted pressures, Case 93.

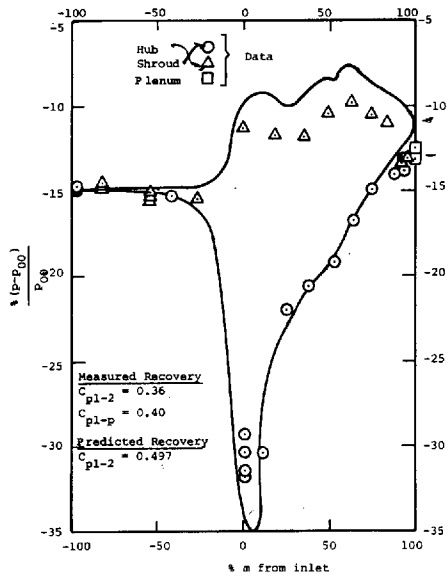


Figure 14a: Comparison of B2 diffuser pressures at $AR = 1.31$ and $\alpha = 0^\circ$, $M = 0.59$ with SLC + BL predicted pressures, Case 71.

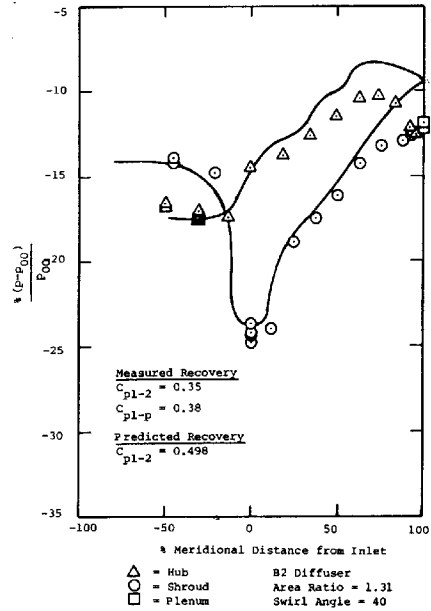


Figure 14b: Comparison of B2 diffuser pressures at $AR = 1.31$ and $\alpha = 40^\circ$, $M = 0.56$ with SLC + BL predicted pressures, Case 76.

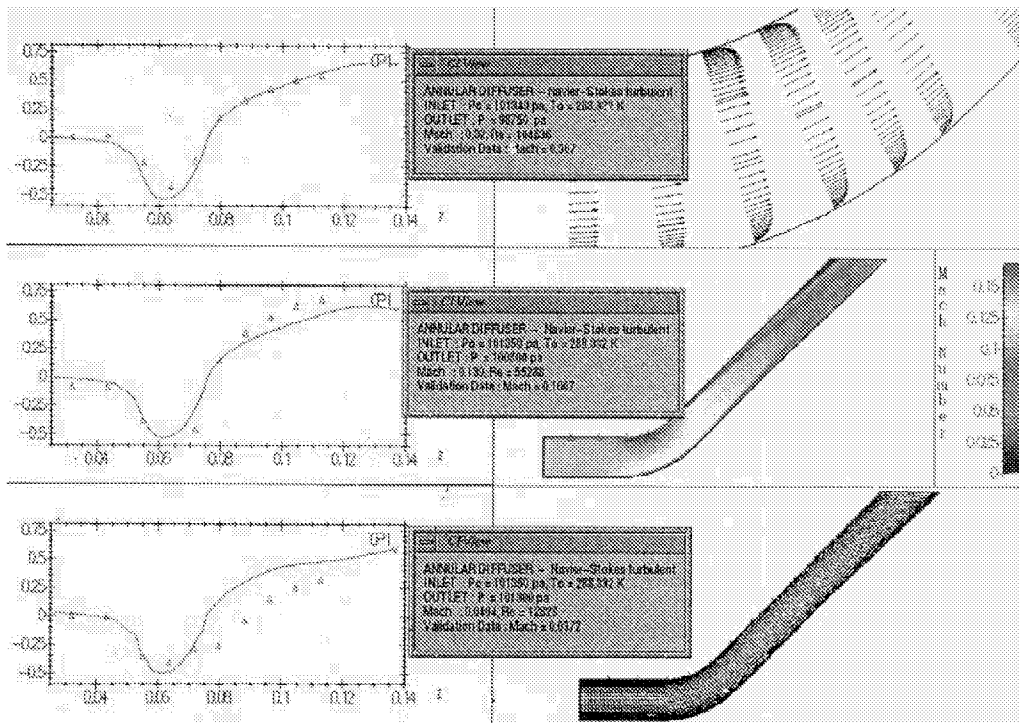


Figure 15: Measured and CFD coupled wall static pressures for the C1 annular diffuser. Case a is believed to be fully turbulent flow; cases b and c are believed to have transitory flow.

Obviously, modern designers prefer to use CFD codes; Figure 15 shows some CFD results with good agreement at high Mach number (top figure). However, as the Mach number is reduced, the agreement becomes less satisfactory. This problem is due to the transitional behavior of the flow and at lower Mach numbers lower Reynolds numbers also exist which correspond to transitional wall shear layers. CFD can be done only in fully turbulent flows, and can be used to study sensible system phenomena such as the effect of velocity profile and swirl distribution leaving a last turbine blade row and entering an annular diffuser. If desired, a complete exhaust hood can be modeled so that the complete coupling effects can be evaluated. System studies of this type are highly recommended for CFD examination at the present time. However, transitional boundary layers still elude the modern CFD modeling specialists.

3. HISTORICAL HOOD STUDIES

Frequently, it is necessary to collect the fluid exiting from an exhaust diffuser and turn it by approximately 90°. An extreme pressure distortion can therefore be expected under certain design conditions and with various turbine performance penalties associated. If an exhaust diffuser is employed, the performance of the diffuser can be

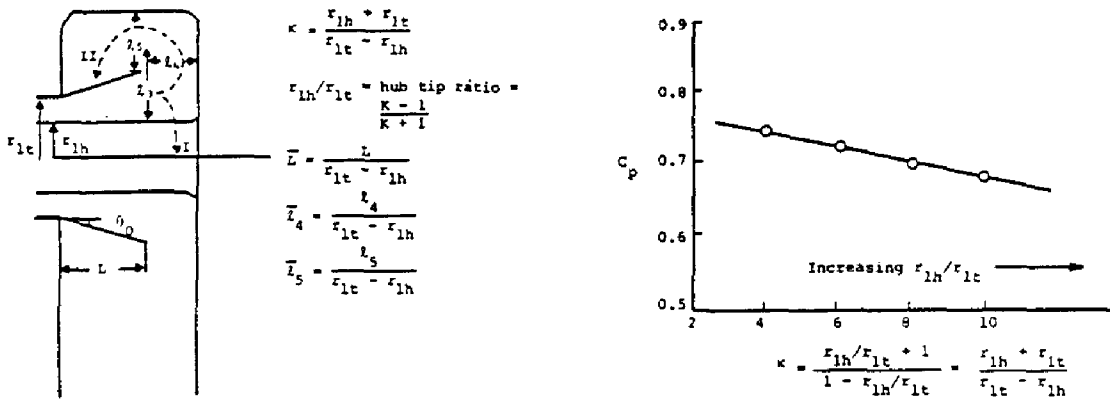


Figure 16b: C_p versus κ for straight annular diffuser (Deych et al. 1970.)

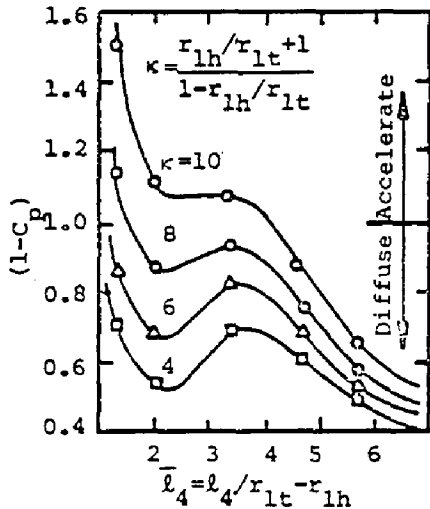


Figure 16c: Variation in the total loss factor $1-C_p$ depending on axial hood dimension l_4 and κ for annular diffusers with a hood. C_p includes the diffuser plus hood. (Deych et al. 1970)

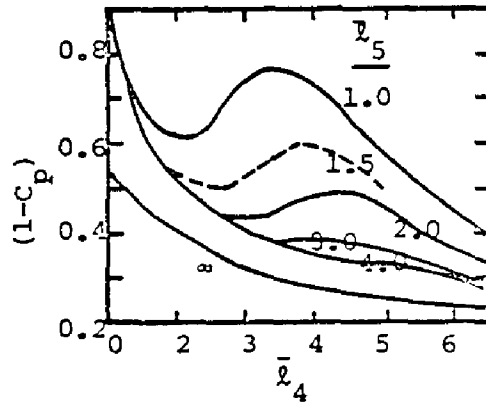


Figure 16d: Effect of radial hood dimension $L_5 = L_5/(r_{1t} - r_{1h})$ on the efficiency of exhaust ducts. (Deych et al. 1970)

adversely impacted by an inappropriate exit device. Figure 16 shows some of the key results from Deych et al. (1970) for straight-wall annular diffusers with exhaust hoods of various dimensions. Clearly, high levels of recovery can be achieved. Conversely, recovery can be readily destroyed if the flow states are not carefully evaluated.

Further examples of exhaust diffuser performance are evidenced in Figures 17 and 18 from the study by Japikse and Pampreen (1979). In that study, flow visualization was conducted to determine the basic flow patterns as shown in Figure 18. Corner vortices have developed which convect the fluid from the bottom of the collector along the sides and on to the collector discharge.

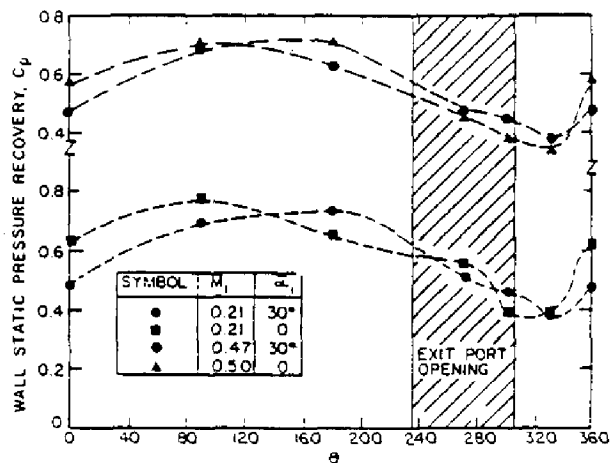


Figure 17: Angular distribution of shroud exit static pressure recovery based on mean-inlet conditions; exhaust diffuser with single exit collector. (Japikse and Pampreen, 1979)

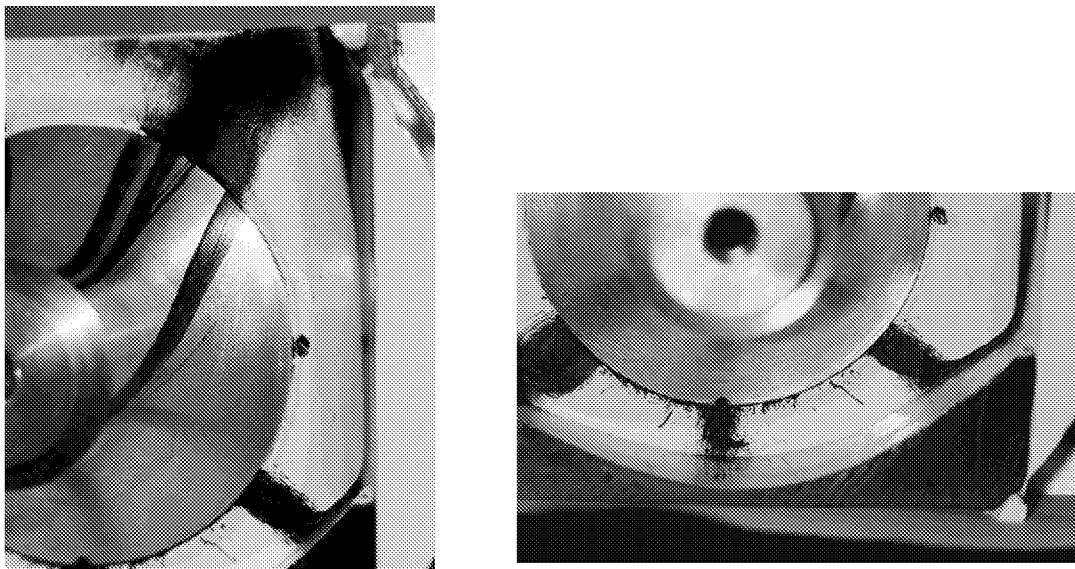


Figure 18: Flow patterns in the exhaust diffuser with a single-exit exhaust collector. The hub surface, left hand view, shows collector induced streamline distortion at the diffuser discharge and a complex vortex rising along the R.H.S.; the diffuser inlet is undistorted. The collector bottom region, right-hand view, reveals evidence of a three-dimensional vortex structure at the bottom and implies complex flow pathlines away from the surface.

4. EXIT HOODS AND DISTORTION

A further, and highly diverse, investigation of both single and double exit hoods, was planned by Japikse and Patel (circa 1976-1977) and conducted and reported by Patel (1978), with supporting notes by Japikse (1978). This investigation used the annular diffusers presented previously by Japikse (1977) was extended by and Goebel and Japikse (1981). The diffusers are different from those covered by Deych, above, in that they were designed to recover rotor exit swirl, and hence had substantial radial extent, as noted above. This study of hood performance, consequently, considered the effect of flow field swirl as well as other important fluid dynamic parameters.

The basic hood geometry is shown in Figure 19 (Figures 19-29 are from Patel, 1978) with various designations for important hood geometry, including eccentricity which is denoted by ϵ . The direction of flow field swirl ($+\alpha$), as utilized during the test program, is also shown in Figure 19. Geometry for the double exit discharge hood is shown in Figure 20 and this configuration has much less variance than the Figure 19 geometry. Principle experimental results for the single exit discharge are shown in Figures 21 and 22 for the concentric spacing of the single exit discharge, but with various values of L_4 and R_3 . The Figure 21 configuration corresponds to a centered discharge, from an axial perspective, whereas Figure 22 corresponds to the alignment of the diffuser hub wall with the back wall of the hood. Although it was noted in the investigation that the latter configuration gave the highest pressure recovery for the diffuser itself, the overall system pressure recovery is slightly impaired as a comparison of these two figures reveals. The important geometric variables covered in these two figures are the radius R_3 and the hood width L_4 . By achieving a hood width of at least 2.0, the effect of R_3 is no longer significant and once a value of L_4 of approximately 3 is achieved, one has obtained nearly the asymptotic limit corresponding to a full plenum discharge. The reference line of 0.64 shown in these figures corresponds to the prior tests of the diffuser alone with flow discharge into a simple plenum. These figures provide substantial guidance for the appropriate sizing of an exhaust hood and allow sensible economic tradeoff studies to be conducted.

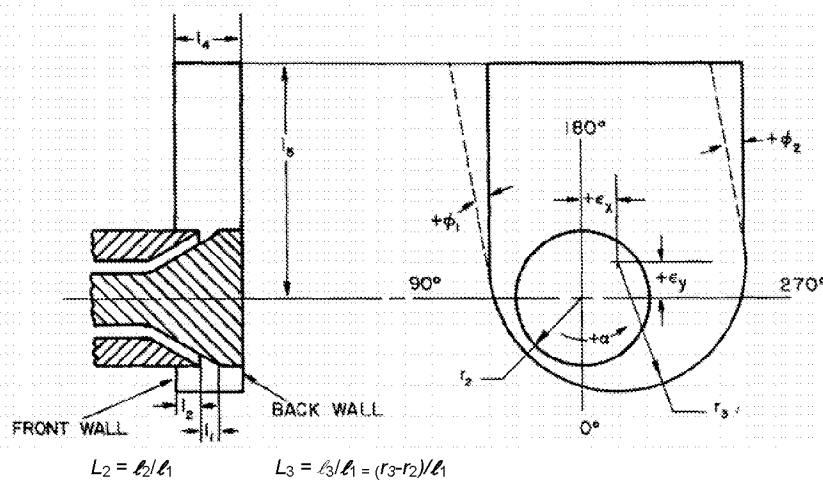


Figure 19: Nomenclature for the single exit hood.

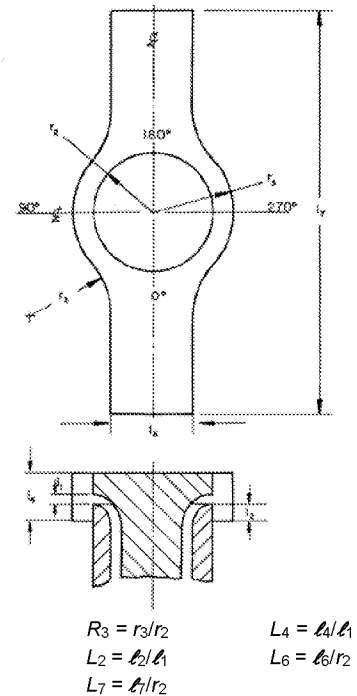


Figure 20: Nomenclature for the double exit hood.

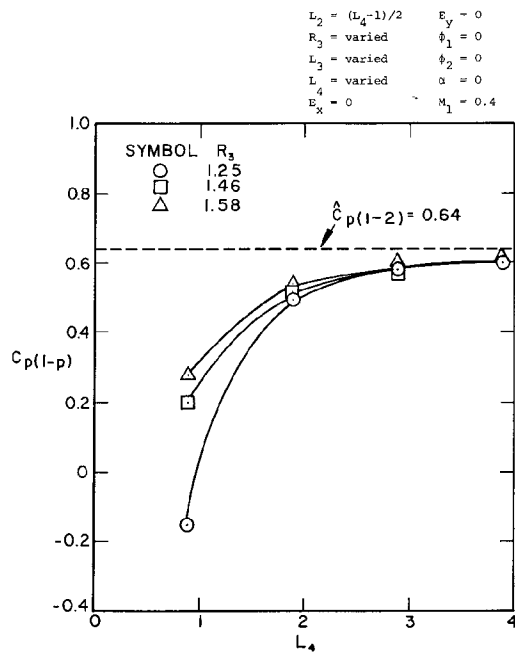


Figure 21: Variation of system pressure recovery coefficient $C_{p(1-p)}$ with hood size for $L_2 = (L_4 - 1)/2$.

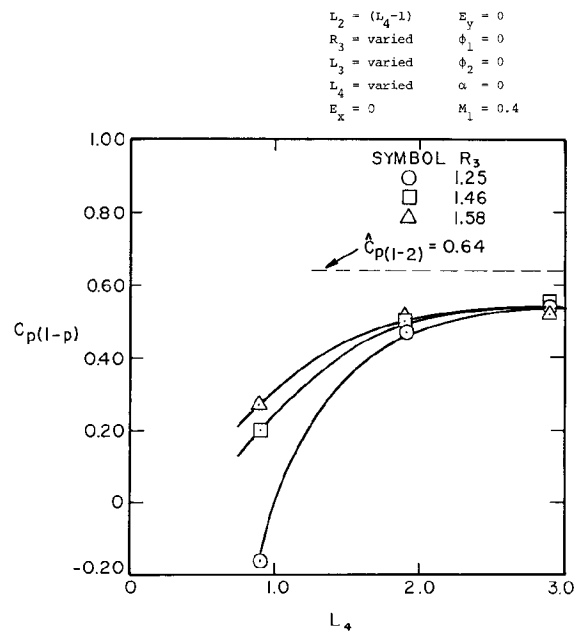


Figure 22: Variation of system pressure recovery coefficient $C_{p(1-p)}$ with hood size, for $L_2 = (L_4 - 1)$.

The influence of impeller exit swirl upon hood system performance is shown in Figure 23. For the cases displayed, performance only got better with swirl. Eccentricity is also a very important effect as shown in Figures 24 and 25 for the centered and backface aligned diffuser to plenum discharge configurations. The important case, Figure 24, shows that the performance improves by approximately six additional points when an eccentric

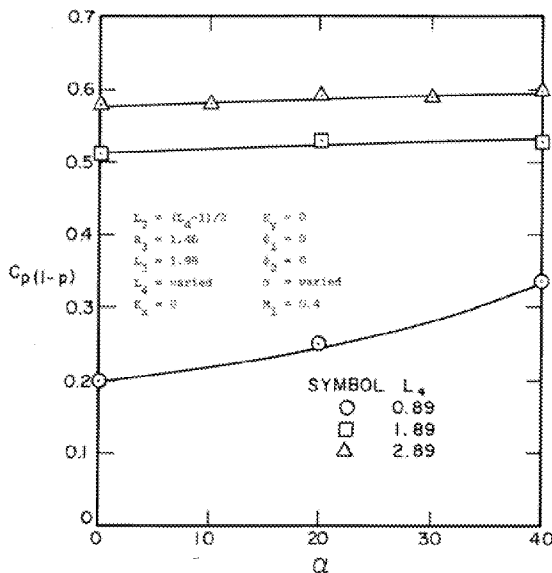


Figure 23: Variation of system pressure recovery coefficient $C_{p(1-p)}$ with inlet swirl α .

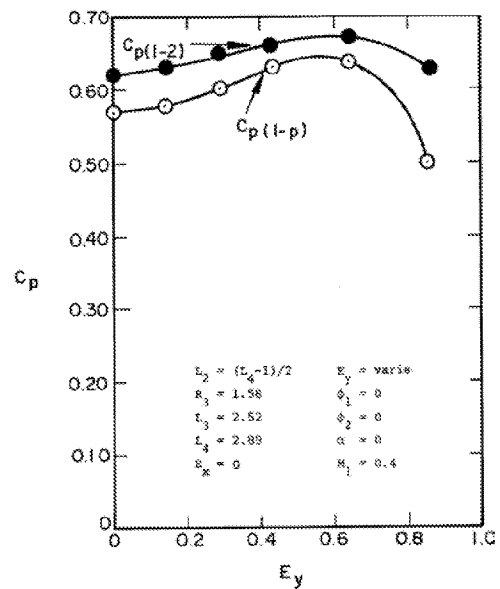


Figure 24: Variation of system and diffuser pressure recovery coefficients $C_{p(1-p)}$ and $C_{p(1-2)}$ with E_y .

configuration is utilized. Excessive eccentricity, of course, carries a strong penalty. This effect was an unexpected bonus for the investigation inasmuch as performance slightly above the base line data, as taken with a simple exit plenum, has been achieved. It is therefore clear that one can design a hood which is beneficial to overall system performance and can be superior to a pure plenum discharge. This is not directly the case for the backface aligned diffuser exit, as shown in Figure 25, but good effects are still achieved. Incidentally, the other geometric parameters shown in Figure 19, namely ϵ_x , ϕ_1 , and ϕ_2 were insignificant parameters concerning the performance of this system. Unfortunately, no tests were conducted with eccentricity and impeller exit swirl entering the diffuser. These tests would have been quite interesting, but it is probably safe to assume that the good effects for each phenomenon taken alone should be additive to give a good overall system performance under the influence of swirl. The study also extensively evaluated distortion at the exit of the hood and distortion effects upon the diffuser. In the region of good diffuser system performance, negligible distortion effects were fed back to the upstream rotor location.

As indicated above, two different sizes and styles of exhaust diffuser were considered in the entire diffuser and exhaust hood investigation series. The smaller diffuser, intended for extremely cramped configurations, was known as the "B2" diffuser and showed a modest level of recovery on an overall basis. This diffuser was also investigated in the hood configuration, with results as displayed in Figure 26. It will be observed that a definite penalty is now experienced due to the presence of the hood. Whereas 0.22 pressure recovery was achieved for a true plenum, the single exit hood now drops the peak level to approximately 0.05. Furthermore, an L_4 of close to 5 is necessary before asymptotic values can be reached. This diffuser, when evaluated with the largest size hood, also showed good response to diffuser inlet swirl and basically showed increasing trends with swirl angle. Eccentricity was again beneficial, and to about the same net level as illustrated above. This improvement brings the result of the diffuser and hood closer to the value achieved by the diffuser with a pure plenum, but there is still a noticeable deficit or penalty for the system.

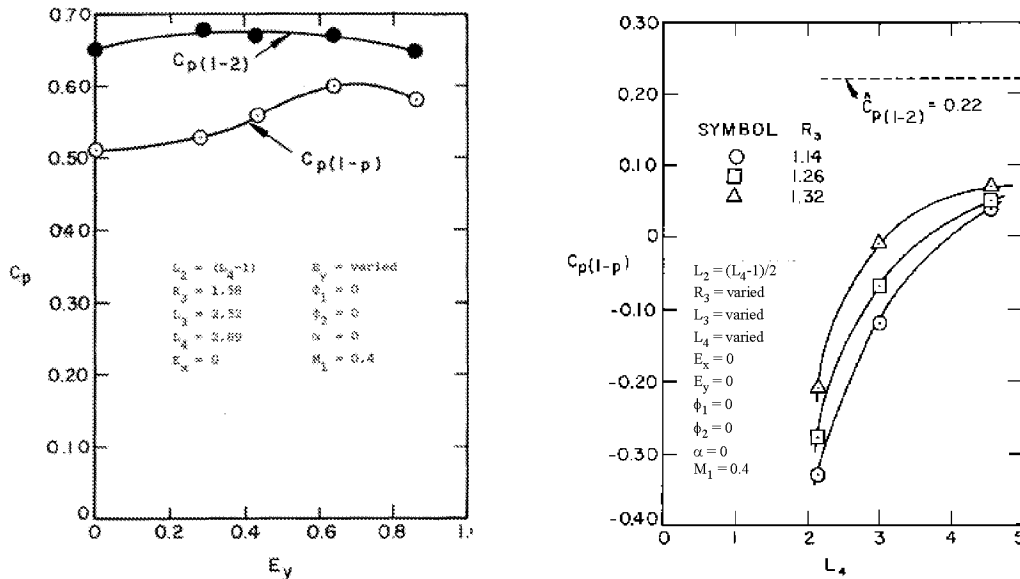


Figure 25: Variation of system and diffuser pressure recovery coefficients $C_{p(1-p)}$ and $C_{p(1-2)}$ with E_y for $L_2 = (L_4 - 1)$.

Further examination of the B2 diffuser was conducted using a double exit hood, to determine if this may provide some relief to the compromises forced by the single discharge hood. Figure 27 shows that significant improvement in the system performance and values above the diffuser alone (plus plenum) test configuration have been achieved. A summary of pertinent results for both diffusers, in terms of a hood-to-diffuser exit area ratio is shown in Figure 27. As this overall area ratio achieves a level in excess of 3.0, the large C1 diffuser shows results closely

approaching the plenum test value for that diffuser. Of course tests with an eccentric diffuser would exceed this reference level. In the same figure, the pertinent results for the B2 diffuser are displayed and it is clear that it is not possible, with a single exit hood, to match the levels of the B2 diffuser with a plenum discharge. However, when using two exit ports, levels of performance above that of the B2 diffuser with collector are displayed.

It is important to assure minimum area ratio, as Figure 27 suggests. The area ratio for these hoods and diffusers may be defined as follows:

$$AR_1 = \frac{\text{Hood exit area}}{\text{Diffuser exit area}} = \frac{2r_3l_4}{2\pi r_2l_1 \cos \gamma_2} = \frac{R_3 * L_4}{\pi \cos \gamma_2}$$

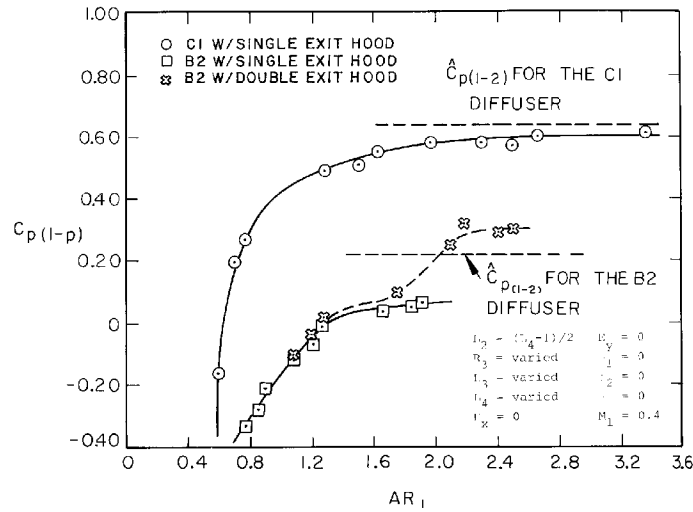


Figure 27: System pressure recovery coefficient $C_{p(1-p)}$ as a function of area ratio AR_1 .

For the particular diffusers utilized, γ_2 equals 54° for the C1 diffuser and 0° for the B2 diffuser. A further area ratio, which is of benefit to this analysis, can be defined by concentrating on the critical area in the hood, which would occur either at 90° or the 270° location for a single exit hood (see Figure 20). In the case of no eccentricity, this area is simply $(r_3 - r_2) l_4$. Forming an area ratio between the area at 90° and the sector of diffuser exit area from 0° to 90° , one obtains the following:

$$AR_2 = \frac{A_{90^\circ}}{\text{Area of the } 0^\circ \text{ to } 90^\circ \text{ sector at diffuser exit}}$$

which can also be rewritten as:

$$AR_2 = \frac{(r_3 - r_2) l_4}{1/4 \cdot 2\pi r_2 l_1 \cos \gamma_2} = \frac{2(r_3 - r_2) l_4}{\pi r_2 l_1 \cos \gamma_2}$$

This area ratio is a local area ratio in contrast to the AR_1 given above which is an overall hood area ratio. By plotting principle results in terms of this local area ratio, as shown in Figure 28, it is discovered that there is a minimum AR_2 of approximately 0.8 which is necessary to avoid serious penalties in the performance of the hood. In fact, a value

somewhat higher would be recommended whenever possible. Finally, a hood (static) pressure loss coefficient can be defined as follows:

$$L_{hood} = \frac{\bar{p}_2 - p_p}{\frac{1}{2}\rho\bar{C}_2^2}$$

The value of the diffuser exit velocity \bar{C}_2 must be estimated knowing the pressure recovery coefficient of the diffuser alone. When this is done, a hood loss coefficient as shown in Figure 29 is obtained. Interestingly, the data for each diffuser falls essentially on the same curve! It may be hypothesized that the effects of diffuser exit or hood inlet dynamic head have now been scaled out and that this parameter is controlled substantially by the area ratio. As with Figure 27, it appears that an area ratio on the order of two is preferable to obtain minimum system losses.

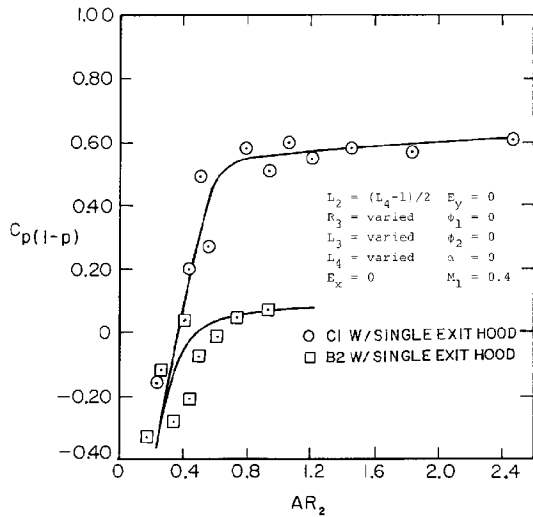


Figure 28: System pressure recovery coefficient $C_{p(1-p)}$ as a function of the area ratio AR_2 .

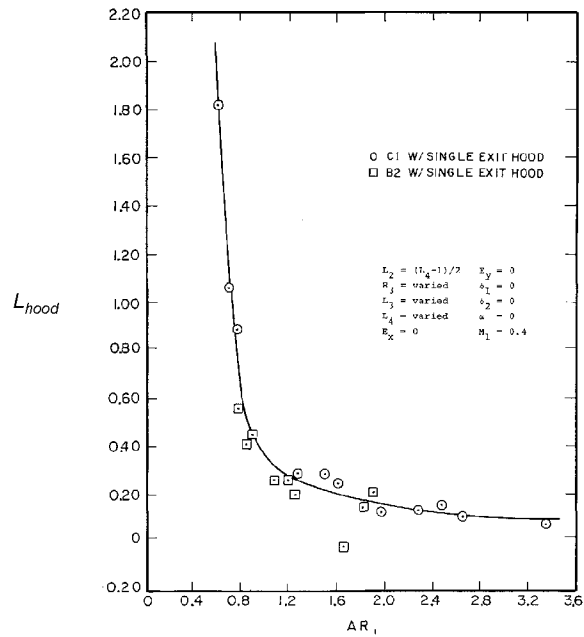


Figure 29: The hood loss coefficient L_{hood} as a function of the area ratio AR_1 .

Further tests were conducted by using a splitter plate as displayed in Figure 30 or a boat-tail strut as shown in Figure 31. Neither of these devices had any significant impact on the best performing configurations discussed previously. Occasionally, they had some positive effect on some of the lower performing geometric configurations. Hence, these are options for strengthening a hood structure.

These hood results, drawing largely on the reference work of Patel (1977) and the cited supporting work, greatly augment the database supplied by Deych (1970). It is clear that the designer must take great care in laying out an exhaust hood for a high-performance exhaust diffuser system, but it is equally clear that good data are available to guide an intelligent choice of these design parameters.

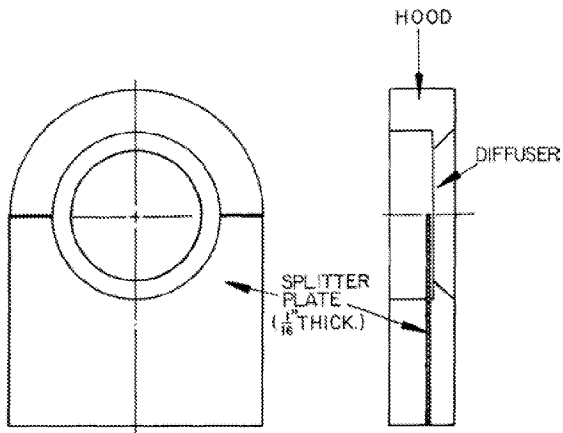


Figure 30: Schematic of the single exit hood with a hood splitter plate.

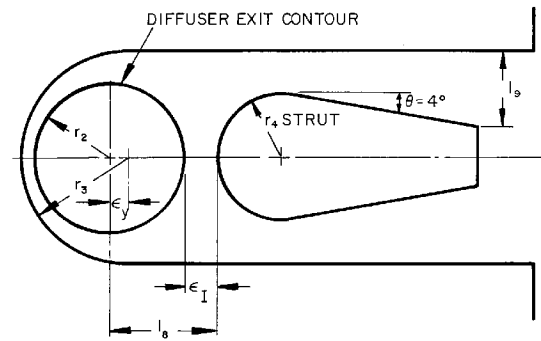


Figure 31: Schematic of the single exit hood with a "boat-tail" strut.

5. CONCLUSIONS

A series of annular diffusers has been designed subject to available technology and then tested according to influences of inlet boundary layer variations, passage curvature, inlet swirl and exit collector (hood) distortion effects. The following has been noted:

1. overall performance compares sensibly with the findings of Sovran & Klomp (1967);
2. performance changes dramatically with inlet boundary layer thickness, much as found for conical and channel diffusers, and strongly with means of artificial boundary layer thickening (trips, vortex generators, etc.) which cannot be predicted today;
3. curvature late in a passage is worse than curvature early in a passage;
4. swirl can help the performance of an annular diffuser if it is sensibly distributed and helps to unload the wall curvature effects;
5. the key to exhaust hood design is either very large collector size or a very special combination of design parameters, which should always be checked experimentally;
6. core flow and boundary layer calculations have successfully modeled bulk design effects such as gross blockage, passage shape, and inlet swirl; and,
7. fine scale CFD modeling has clarified some gross flow phenomena but cannot resolve many detailed observations.

6. ACKNOWLEDGEMENTS

The author wishes to acknowledge the important contributions of his co-workers, Messrs. Goebel and Patel. Mr. Jay Goebel served as project engineer for the studies with inlet blockage variations and Dr. Patel served as project director for the hood studies. Each made vital contributions to the totality of the work presented herein.

REFERENCES

1. Deych, M. Ye., and Zaryankin, A. Ye., "Dynamics of Diffusers and Exhaust Ducts of Turbomachines," NTIS AD 745 470, 1970.
2. Goebel, J. H., and Japikse, D., "The Performance of an Annular Diffuser Subject to Various Inlet Blockage and Rotor Discharge Effects," Creare TN-325 and Concepts ETI, Inc. TM-1, February 1981
3. Japikse, D., "The Design and Evaluation of Restricted Length Annular Exhaust Diffusers," Creare Inc. TN-257, May 1977.
4. Japikse, D., "The Use of Boat Tail Struts in Single Discharge Hoods," Appendix C, Creare Inc., TN-277, Hanover, NH, 1978.
5. Japikse, D., "Turbomachinery Diffuser Design Technology," Concepts ETI, Inc., Wilder, VT, 1984.
6. Japikse, D., "Exhaust Energy Recovery," Axial and Radial Turbine Technology Course, Concepts ETI, Inc., Wilder, VT, April 19-23, 1999.
7. Japikse, D., Baines, N., "Diffuser Design Technology," Concepts ETI, Inc., Wilder, VT, 1998.
8. Japikse, D., Pampreen, R., "Annular Diffuser Performance for an Automotive Gas Turbine," *Journ Eng for Power* 101: 358-372.
9. Patel, B., "Evaluation of the Performance of Single and Double Exit Hoods for Annular Exhaust Diffusers," Creare Inc., TN-277, Hanover, NH, 1978.
10. Sovran, G., Klomp, E. D., "Experimentally Determined Optimum Geometries for Rectilinear Diffusers with Rectangular, Conical or Annular Cross-Section," *Fluid Dynamics of Internal Flow*, Elsevier Publishing Co., Amsterdam, 1967.
11. Stevens, S. J., Williams, G. J., The influence of inlet conditions on the performance of annular diffusers. *Trans ASME Journ Fluids Eng* 102: 357-363. 1980
12. Takehira, A., et al., "An Experimental Study of the Annular Diffusers in Axial-Flow Compressors and Turbines," Paper No. 39, Tokyo Joint Gas Turbine Congress, 1977, also Paper No. 39, Japan Society of Mechanical Engineers, 1977.



ROTOR DESIGN FOR THE SSME FUEL FLOWMETER

Bogdan Marcu

Boeing

Rocketdyne Propulsion and Power

ABSTRACT

The present report describes the process of redesigning a new rotor for the SSME Fuel Flowmeter. The new design addresses the specific requirement of a lower rotor speed, which would allow the SSME operation at 115% rated power level and above. A series of calculations combining fleet flowmeters test data, airfoil fluid dynamics and CFD simulations of flow patterns behind the flowmeter's hexagonal straightener has led to a blade twist design $\alpha = \alpha(\text{radius})$ targeting a kf constant of 0.8256. The kf constant relates the fuel volume flow to the flowmeter rotor speed, for this particular value 17685 GPM at 3650 RPM. Based on this angle distribution, two actual blade designs were developed. A first design using the same blade airfoil as the original design targeted the new kf value only. A second design using a variable blade chord length and variable airfoil relative thickness targeted simultaneously the new kf value and an optimum blade design destined to provide smooth and stable operation and a significant increase in the blade natural frequency associated with the first bending mode, such that a comfortable margin could be obtained at 115% RPL. The second design is a result of a concurrent engineering process, during which several iterations were made in order to achieve a targeted blade natural frequency associated with the first bending mode of 1300 Hz. Water flow tests preliminary results indicate a kf value of 0.8179 for the first design, which is within 1% of the target value. The second design rotor shows a natural frequency associated with the first bending mode of 1308 Hz, and a water-flow calibration constant of $kf = 0.8169$.

NOMENCLATURE

| | |
|------------|---|
| U | blade tangential velocity |
| Ca | fluid axial velocity |
| W | fluid relative velocity |
| α | blade stagger angle |
| β | angle of relative fluid velocity |
| i | flow incidence angle on the blade |
| C_D, C_L | drag and lift coefficients |
| ρ | fluid density |
| b | blade chord length |
| K_f | flow meter calibration constant for engine operation |
| K_{fw} | flow meter calibration constant determined from water flow test |

1. INTRODUCTION

The Space Shuttle Main Engine uses a turbine type flow meter [3] to control the amount of fuel delivered to the engine and the mixture ratio between the fuel and oxidizer. The flow meter is located in a duct between the low pressure fuel pump discharge and the intake to the high pressure pump. The meter translates the volume flow of the liquid hydrogen based on its rotor speed and a calibration constant, denominated as K_f which relates the fuel volume flow rate to the rotor's rotational speed $K_f = 4 \cdot \text{RPM} / \text{GPM}$, where RPM is the rotor speed in rotations per minute and GPM the fuel volume flow rate in gallons per minute.

The original flow-meter design employed a flow straightener with a set of vanes forming channels with a square section, a configuration referred to as the "egg-crate" housing. This straightener was replaced by another design, with vanes forming a set of channels with hexagonal cross-section. In this new configuration, the flow meter rotor is mounted closer to hexagonal vanes, at approximately 1 inch distance (previously, in the egg-crate straightener housing it was mounted at approximately 2 inch distance). Over the years of SSME operation, a certain behavior was observed in the flow-meter operation [1]: at certain regimes, an apparent shift seems to occur in the K_f value, without a real change in the volume flow rate. The K_f shift phenomenon also appears to be associated with a fluctuation in the rotor's speed. Such fluctuation may be of high frequency, but since the rotation is only measured 4 times per one complete revolution, some aliasing phenomenon appears to occur in the measurements. Hence, the term of "aliasing" has been associated with the rotor speed fluctuations, occurring simultaneously with the K_f shifting.

Extensive work has been done to investigate these phenomena [2]. It was found that when the blade passes one of the wakes in the flow pattern generated behind the hex flow straightener, there is a momentary stall flow regime on the blade which slows down the rotor. The occurrence of successive stalls may produce the K_f shifting phenomenon, associated with a high frequency oscillation in the rotor speed referred to as "aliasing". The rotor wake interaction is stronger for the new hex housing due to the proximity of the rotor with respect to the straightener exit.

Another issue of concern generated by the new hex housing is a strong symmetry pattern in the flow field behind it, especially 12N and 18N symmetry patterns. Such symmetry patterns generate a blade excitation with frequencies approaching the flow meter rotor blade natural frequency associated with the first bending mode (~830 Hz) if the rotor speed is approaching 4000 RPM. For this reason, the fleet flow meters have a limitation in speed at 3800 RPM in order to maintain a safety frequency margin. In many cases, this limitation precludes the SSME reaching 115% Rated Power Level.

2. DESIGN REQUIREMENTS

The hexagonal housing is being modified by cutting the back face of the straightener vanes at a 21 degree angle. In this manner, the spacing between the vanes and the rotor is increased from 1.05 inches to 1.95 inches at the tip of the blade, while remaining 1.05 inch at the hub. Also, the flow meter rotor is re-designed in a manner destined to achieve a lower rotational speed. The requirement is to achieve a maximum rotational speed of 3650 RPM at 115% SSME rated power level, for which the nominal fuel volume flow rate is 17,685 GPM. For this regime, the flow calibration constant must have the value $K_f = 0.8256$. A slightly lower value is admissible.

This report addresses the rotor re-design effort.

3. BLADE GEOMETRY

3.1. ORIGINAL BLADE GEOMETRY.

A complete set of manufacturing design details of the original rotor has been made available for the redesign project. However, while such design details allow for a proper part fabrication, they yield insufficient information for the purpose of inferring the fluid dynamics criteria on which the design is based. Since these criteria were not available in the original design, they had to be reconstructed by processing the fabrication design data (blade sections defined at different radii) in combination with calibration data obtained from testing fleet rotors. Given the fact that a significant number of rotors were known to have small dimensional errors from manufacturing, data from a large number of rotors was necessary, with the hope that the statistics of the test results will generate mean values corresponding to a nominal design. Since the number of rotors with well documented test results was not large, data was selected for 10 rotors with good operational history (never recorded any anomaly in operation).

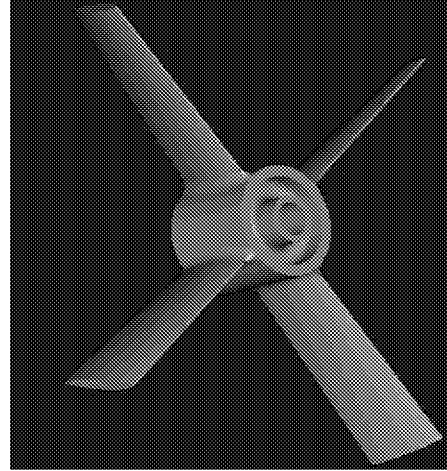


Figure 1. The flow meter rotor.

In order to organize a fluid dynamics design concept for the flowmeter rotor, one must understand a significant difference between a typical turbine destined to produce power, and the turbine flowmeter rotor at hand. A typical turbine rotor operates by organizing the working fluid flow within the channel formed between two adjacent blades in a way that maximizes loading, with a high degree of turning of the fluid, and with a strong interaction between the blades of the rotor. The flowmeter rotor on the other hand (shown in Figure 1), uses only 4 blades that operate practically independent of each other, as isolated rotating airfoils. If the rotor were to operate in a smooth, uniform incoming flow, its blades should operate at very small incidence angles at every radius. The situation is depicted in Figure 2. The incoming flow has a uniform axial velocity C_a and the rotor blade has the tangential velocity U as shown. Adding the two vector velocities results in the relative velocity with respect to the blade, W . The blade stagger angle α is not aligned with the relative velocity angle β , as the relative velocity impinges on the blade's leading edge at a small incidence angle i . Since the blade profile is symmetric the small incidence angle is necessary for the flow around the airfoil to produce some lift, besides drag. Only the tangential components of the forces acting on the rotor blade are of interest. The blade will adjust its tangential velocity in a way that will produce a very small incidence angle i for which the tangential component of drag and rotor bearings

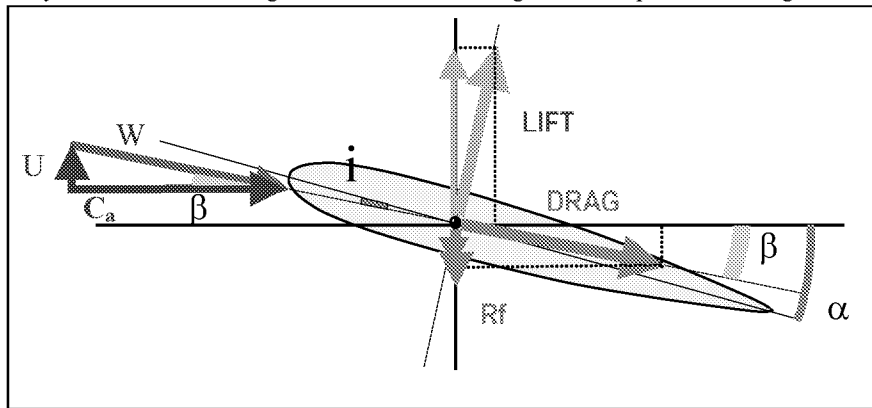


Figure 2. The blade load and force decomposition on the rotor blade.

friction resistance R_f will be compensated by the tangential component of lift. This model leads to a variable blade stagger angle which varies with the blade radius in a proportional manner if the small incidence angle is neglected, therefore we are seeking a relation of the form $\alpha = \alpha(R)$, where R is the blade radius. This relation depends on the required rotor speed at a given volume flow, and on the necessary incidence angle i at each blade radius. If we take under consideration the boundary layer development on the shroud and hub end walls, the incidence angle i then depends on the incoming flow axial velocity distribution with radius $C_a = C_a(R)$. Things are complicated more by considering the presence of the wakes in the incoming flow, which add a tangential dependency $C_a = C_a(R, \theta)$, where θ is a tangential angular coordinate. Such dependency further generates transient features that render the analysis too complex to obtain immediate useful results.

Therefore, let us consider an upstream flow that is characterized by a uniform axial velocity and no swirl. Based on this assumption, one could calculate a volume flow and a rotational speed of the original design rotor, at which the flow incidence i on the rotor blade is zero or close to zero at each radius. Is such a rotational speed is found for any given volume flow, the calculation verifies a free-vortex blade design. However, such calculation does not imply a stable rotation at the rotational speed calculated and no equilibrium of forces on the blade is assumed. This topic will be discussed in the next section.

By processing the original design blade profiles given at four radii, the blade stagger angles were obtained and used for the aforementioned calculation. The results show indeed a free vortex blade twist, with a theoretical flow calibration constant of $K_f = 0.8777$, and close to zero incidence angles, as indicated in the following table, third column.

Table 1.

| Blade Radius (% of blade height) | Blade angle α (degs) | Flow incidence angle i (for idealized, uniform upstream flow - degs) | Apparent flow incidence angle i (see Fig. 4) (calibration data - degs) |
|-------------------------------------|--------------------------------|--|--|
| 8.6 | 4.9 | -0.0049 | 0.04 |
| 38.3 | 9.06 | 0.0016 | 0.07 |
| 68.0 | 13.13 | -0.0011 | 0.10 |
| 97.7 | 17.06 | 0.0044 | 0.13 |

In operation, the upstream flow is not perfectly uniform, but distorted by wakes behind the hexagonal flow straightener, which together with the end-walls boundary layers generate an unsteady character of the incoming flow $C_a = C_a(R, \theta, t)$, in both tangential θ , and radial r directions. A good way to obtain an average flow calibration constant is to use all data points available from the calibration of the selected fleet rotors, and compute a calibration constant based on the mean square linear fit through the data. Figure 3 show this computation: the horizontal axis indicates the rotor speed measured in pips per second (a pip is a passage of one blade through a magnetic field of a sensor, hence 4 pips per rotation), while the vertical axis shows the liquid hydrogen volume flow through the meter, in gallons per minute. The dark line on the plot is a linear fit through the data points, yielding a flow calibration constant of $K_f = 0.8708$, while the light colored line corresponds to the idealized case of perfectly uniform flow upstream and zero flow incidence on the blade at all radii, for which the calibration constant value is $K_f = 0.8777$ as explained.

The difference between the two lines in figure 3 is very small, corresponding to calculated flow incidence angles shown in the fourth column of table 1. The largest flow incidence angle is calculated at 97.7% radius, a value of 0.13° . It is necessary to emphasize the fact that the flow incidence angles indicated in column 4 of Table 1 are not actual physical flow angles with respect to the blade, since the flow field at the blade leading edge is distorted by wakes and end-wall boundary layers as explained already. These incidence angles represent a model based on the forces and velocity diagram shown on Figure 2, a model intended to be used for redesign. The rationale behind these values is as follows: *A dimensional average of the selected fleet rotors is very close to the original rotor nominal design, as the possible small*

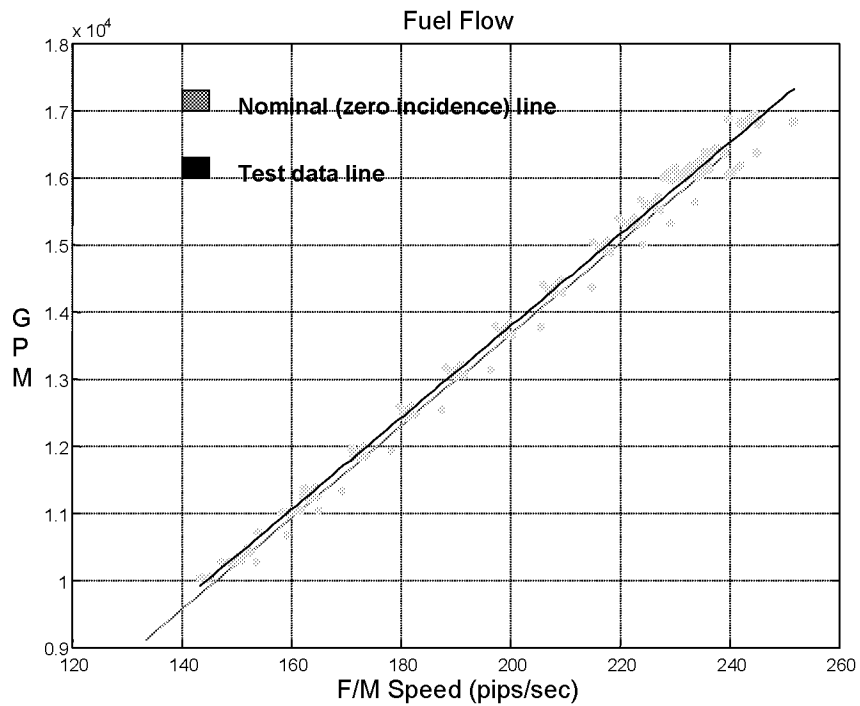


Figure 3. Calibration hot fire test data from fleet rotors, and linear fit of the data (dark line). The light colored line corresponds to the ideal case of uniform flow and zero flow incidence on the blade.

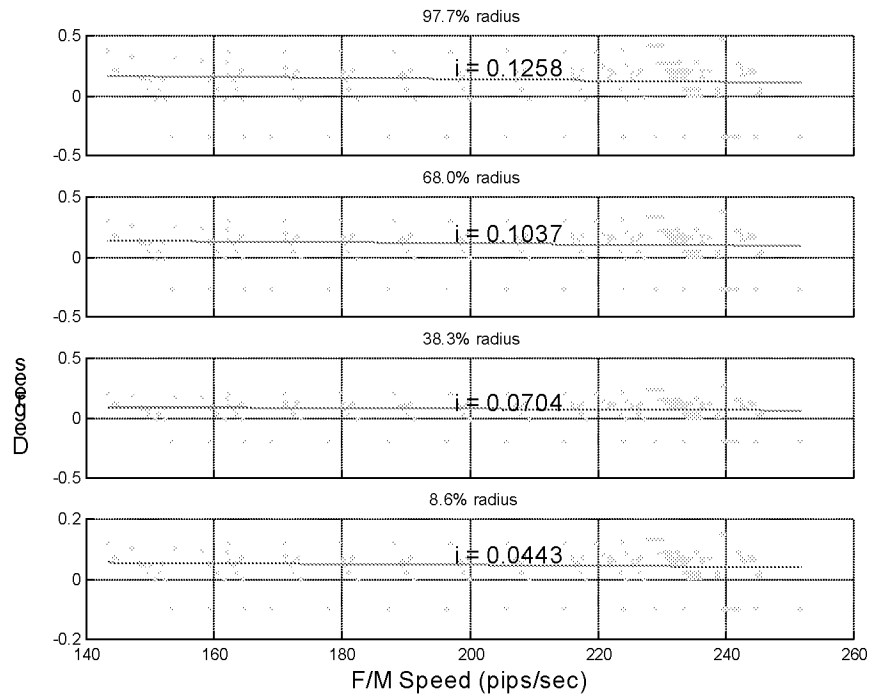


Figure 4. Apparent flow incidence angles at the radii where nominal blade design of the original rotor is specified. The line indicates a mean square linear fit through the data at each radius, while the numbers represent the average.

manufacturing errors statistically cancel out. The linearly fitted calibration data shows how fast does this virtually nominal rotor turn, for a given fluid volume flow. Assuming that this measured volume flow were perfectly uniform with no swirl, wakes or BL's present, and a rotor with nominal design were rotating with the measured speed (also from the linearly fitted calibration data), the flow incidence angles on the blade at the four specified radii would be those in column 4 of Table 1, denominated as apparent flow incidence angles.

The apparent flow incidence angle values listed in Table 1 are averaged over the entire pool of results shown in Figure 4. By knowing these values, a first approach to the design of a new rotor would be to simply retwist the blade at different stagger angles for the idealized case of zero flow incidences, then empirically add the apparent flow incidence angles to the blade stagger angles at each radius. However, data used for these calculations is obtained from the current flow meter configuration which uses the straight back hexagonal flow straightener. The wake flow structures behind the straightener has a significant influence on the measured flow calibration constants, and therefore a significant influence on the calculated apparent incidence angles. The new rotor design is destined to be mounted behind a cut-back hexagonal straightener, with a different wake flow pattern. For this reason, a more elaborate method is necessary for the new design, while using the apparent incidence angle presented in this section as a means of verification.

3.2. NEW BLADE GEOMETRY.

As specified in the previous section, by “blade geometry”, in this study, one means a blade profile stagger angle variation with radius, i.e. a relationship of the form $\alpha = \alpha(\mathbf{R})$, where \mathbf{R} is the blade radius and α is the blade angle (see Figure 2). The blade profile is symmetric at all radii, and the blades work independently from each other as rotating airfoils. The blade twist resulting from this relationship must provide a flow calibration constant of $\mathbf{K}_f = 0.8256$, as explained in section 1.

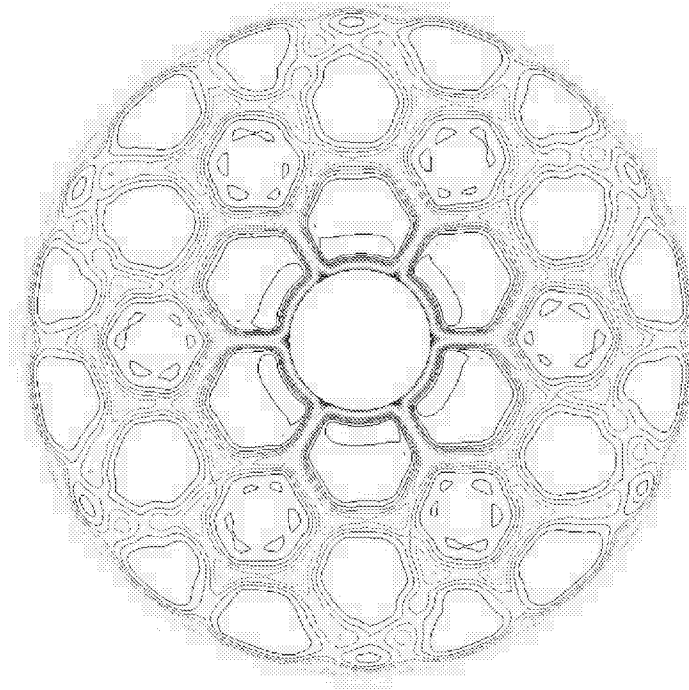


Figure 5. Axial fluid velocity field (CFD) behind the flow straightener, at a distance corresponding to the rotor blades leading edges locations.

The difficulty in choosing the new $\alpha = \alpha(\mathbf{R})$ design comes from the complex flow pattern generated behind the hexagonal flow straightener. Different studies [1,2] have shown that the proximity of the flow straightener to the rotor blade leading edges often generates anomalies in operations, such as shifts in the flow calibration constant associated with aliasing. Detailed CFD analysis [2] has shown the complexity of the upstream flow patterns and explained the \mathbf{K}_r shift as resulting from a periodical quasi-stall phenomenon induced by the strong interaction between the wakes at the exit of the hexagonal flow straightener and the rotor blades. Such interactions were shown to diminish significantly with the spacing between the straightener and the rotor. For these reasons, the design of a new rotor has been conceptualized in conjunction with a modification of the hexagonal straightener, whose exit plane is being cut back at a 21° angle, increasing the distance from its exit to the blade from 1.05 to 1.95 inches at the tip of the blade. At the rotor hub, the 1.05 inch distance is maintained. Therefore the new blade design must account for the flow pattern behind the new straightener configuration in order to obtain a proper blade twist and provide the reduced rotor speed required.

The calculations presented in section 3.1 have shown that the original rotor blade design is essentially a free-vortex design. However, in order to obtain a precise rotor speed at a given volume flow, the designer must allow for a small alteration of the free-vortex blade twist, in order to account for the effects generated by the flow non-uniformity. Such effects are quantified by the apparent flow incidence angles also presented in section 3.1. In order to obtain such quantification for the cut-back straightener configuration both water-flow rotor test data with a prototype hex housing and CFD computations are used.

Figure 5 shows a CFD generated flowfield behind the cut-back hex straightener in the form of axial fluid velocity distribution $C_a = C_a(\mathbf{R}, \theta)$, shown in the transversal plane containing the rotor blades' leading edges.

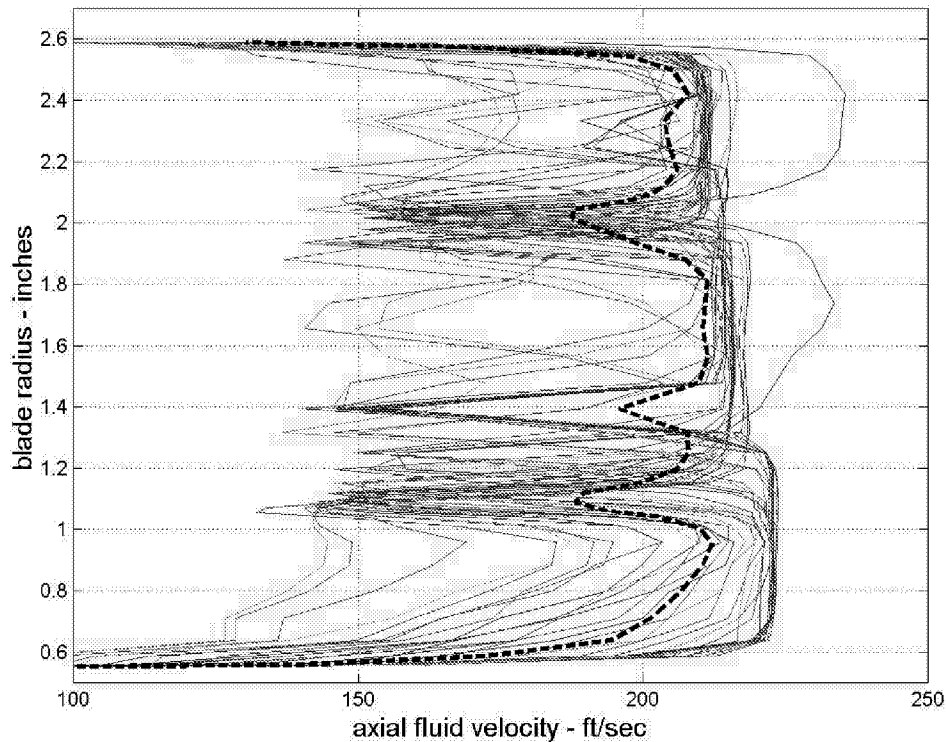


Figure 6. Radial distribution of the fluid axial velocity, plotted every 2.5 degrees for a 120 degrees sector. Data is extracted from the flow field shown in figure 5. The thick dotted line represents an average per one rotation in the tangential direction.

In this simulation, the rotor and its influence on the upstream flow is removed. Figure 6 shows, superimposed, several plots of the axial flow velocity distributions in the radial direction extracted every 2.5 degrees in the tangential direction from the flow field in figure 5. Basically these are the axial flow patterns that are “seen” successively by the rotor blade as it sweeps the flow field in its rotation. The average per one rotation in the tangential direction of the axial fluid velocity $\bar{C}_a = \bar{C}_a(R)$ is represented in Figure 6 by the thick dotted line. By examining this radial distribution of velocity one can understand that for a rotor blade twisted according to the free-vortex law, at any given instance, there are significant variations in fluid flow incidence angles \mathbf{i} along the tangential direction, and at all radii. The incidence angle \mathbf{i} can have positive as well as negative values within one complete rotation. Thus, at every moment, there are sections of the blade producing tangential forces in the direction of rotation, and other sections producing resistance. At each of these instances the flow around the entire blade is very complex, requiring significant resources to be resolved by real time CFD. The prohibitive cost of such resources in both equipment and man hours requires a different more practical approach.

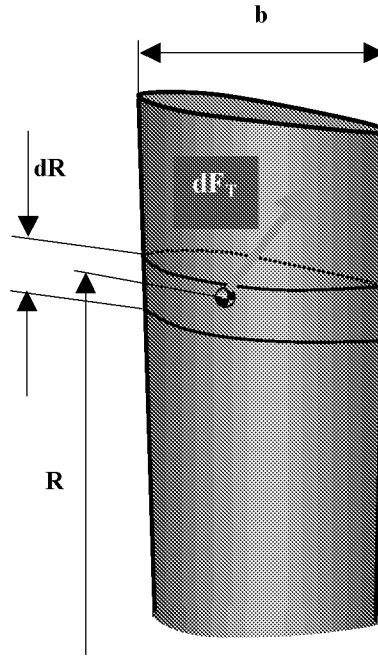


Figure 7. Force balance calculation on a rotor blade.

Figure 7 summarizes a calculation model that combines the aerodynamic principles expressed in Figure 2 with the available CFD data, and anchors them using test data. The rotor blade is divided in 32 horizontal bins as shown in the figure. Each bin produces, locally, either positive or resistive tangential force $d\mathbf{F}_T$, which, in turn, produces a positive or negative torque

$$d\mathbf{T} = d\mathbf{F}_T \mathbf{R} \quad (1)$$

The localized bin tangential force $d\mathbf{F}_T$, is a projection of the local drag and lift forces along the tangential direction (as shown in Figure 2) and a portion of the resistant bearings friction torque, which is small and can be neglected.

$$d\mathbf{F}_T = \frac{1}{2} \rho b d R W^2 \times [C_L(R) \cos(\beta(R)) - \zeta C_D(R) \sin(\beta(R))] \quad (2)$$

Here, \mathbf{b} is the blade's width, \mathbf{R} is the radius of the local bin, $d\mathbf{R}$ is the bin's radial width, $\beta(R)$ is the blade stagger angle, C_L and C_D are the local lift and drag coefficients — which depend on the local relative fluid velocity $\mathbf{W}(R)$ and local incidence angle $\mathbf{i}(R)$ — and ρ is the fluid density. For a given axial velocity distribution $\mathbf{C}_a = \mathbf{C}_a(R)$, a relative velocity distribution $\mathbf{W} = \mathbf{W}(R)$ results by vectorial addition with the tangential velocity $\mathbf{U}(R) = \mathbf{R} \times \boldsymbol{\omega}$, where $\boldsymbol{\omega}$ is the rotor's rotational speed which achieves a stable, constant value when equilibrium is achieved on the blade:

$$\int_{R_{\text{hub}}}^{R_{\text{tip}}} d\mathbf{T} = \mathbf{0} \quad (3)$$

The model is anchored for the $\mathbf{C}_a = \mathbf{C}_a(R)$ distribution indicated by the average velocity profile in Figure 6, and the rotation resulting from several water flow tests of a cut-back hex straightener using three separate rotors which indicate a \mathbf{K}_f value of **0.871**. The NACA 0016-64 airfoil C_L and C_D coefficient values are used in this calculations, since this NACA profile is closest to the original rotor blade profile from the available literature. It is important to note that in the model anchoring process one must account

empirically for several details associated with the physics of the problem at hand which are not accounted for in the model. Such details are: i) the nature of the working fluid is different from the fluid for which standard C_L and C_D are known, ii) the incident flow is characterized by intense fluctuations which alter the aerodynamic performance, iii) the three-dimensional character of the flow is neglected, locally, for each bin. The factor ζ in equation (2) is the anchoring factor. The choice of placing this factor in association with the drag force term is based on the consideration that, given the flow fluctuations, it is to be expected that the drag on the blade profile be actually larger than the literature indicates, while lift forces will be smaller. CFD analysis [2] of the K_f shifting phenomenon seems to be indicating the same trend. However, ζ values do not reflect a quantification of drag amplification, and must be regarded as purely empirical values destined to anchor a model and be used in the design process.

Using the average $\mathbf{Ca}=\mathbf{Ca}(\mathbf{R})$ velocity distribution in Figure 6, the measured $K_f = 0.871$ flow coefficient is matched by choosing $\zeta = 32.0$. Simulations show a very small sensitivity of the calculated K_f value with respect to ζ , and therefore a good tuning capability of this parameter. Using $\zeta = 32.0$, the new blade stagger angle $\alpha = \alpha(\mathbf{R})$ distribution is calculated based on a free-vortex blade twist altered by a small incidence angle distribution $\mathbf{i} = \mathbf{i}(\mathbf{R})$, found by repeated iterations. Figure 8 shows the new blade stagger angle design, plotted together with the original blade stagger angle design for comparison. The difference between the old and the new design is small: only 0.84 degrees at the blade tip.

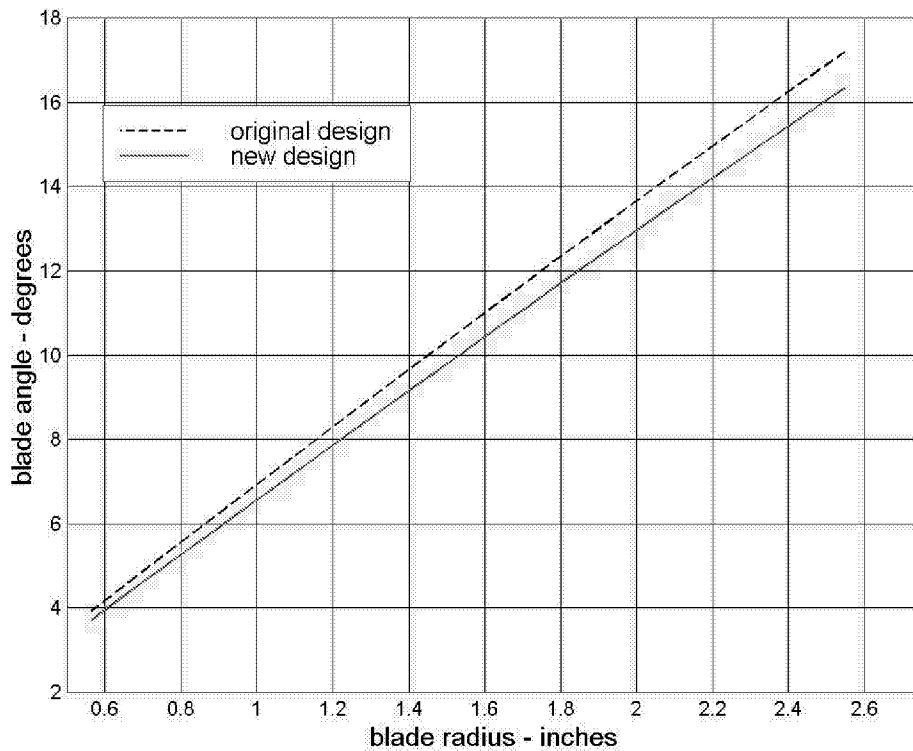


Figure 8. Blade stagger angle distribution

3.3. ROTOR DESIGN CONCEPT 1

Having determined the new blade radial twist, the first design concept uses the original blade profile in shaping up a new blade using the new stagger angle distribution shown in Figure 8. The original blade design is given in the specifications at four radial stations (expressed in percentages of blade height in Table 1 by coordinate points x, y). The data has been processed numerically and the profile has been mathematically reconstructed based on circle elements (0.016 inch radius and 0.005 inch radius for the leading and trailing edges respectively.) and sets of third order polynomials. Figure 9 shows the reconstructed profile, which has a chord length of 0.747 inches, and a maximum thickness of 16% (relative thickness expressed in percents of the chord length) at 40% of the chord length. For comparison, the NACA 0016-64 profile is plotted in the same figure.

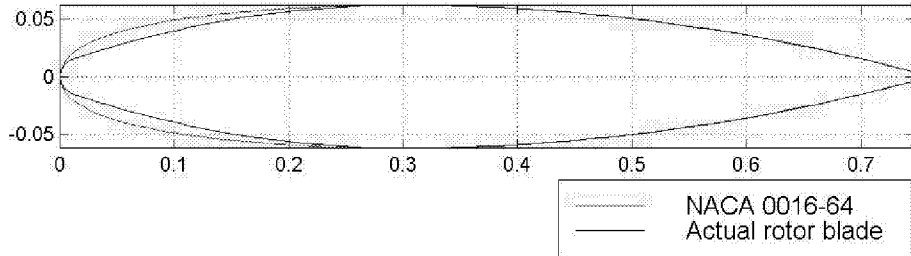


Figure 9. Rotor concept 1 and NACA 0016-64 airfoils. The rotor blade has been mathematically reconstructed from the x,y coordinates given in the original design documentation.

For the concept 1 rotor, the new blade natural frequency associated with the first bending mode is approximately 830 Hz. For a successful design, the rotor must not exceed 3650 RPM at a fuel volume flow of 17,685 GPM—which defines the regime at 115% SSME Rated Power Level—thus allowing for a 12% frequency margin with respect to the 12N symmetry excitation mode associated with the wake flow structures behind the hexagonal straightener. The 3650 RPM is a slow speed for such high volume flow, rendering the design calibration coefficient $K_f = 0.8256$ very sensitive to any alteration in the blade stagger angle. For 3650 RPM, at the blade mean diameter the relative flow velocity has an average angle of 9.6° , while the blade's stagger angle is 9.9° . Given the blade profile accepted tolerance field for the original design of ± 0.003 inches, a biased manufacturing within the 0.006 inch tolerance band as shown in Figure 10 can produce a stagger angle error of 0.46° , i.e. an error of 4.7%. This possible error places the rotor speed value in the 3475-3825 RPM range, which, for the right end of the range, not only reduces the frequency margin to 7.8%, but also exceeds the 3800 RPM limit. For these reasons, the flow of information from the design concept to the manufacturing of the hardware must be carefully controlled.

Such control is exerted by following the path of essential design information and ensure that minimum or no

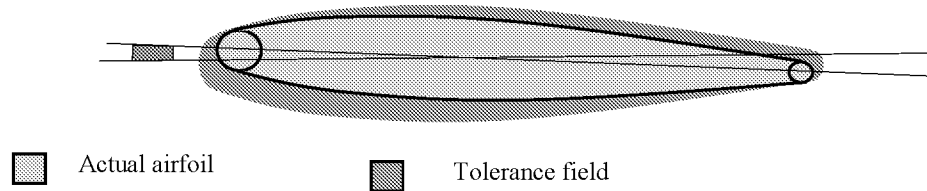


Figure 10. Stagger angle error due to biased manufacturing of the rotor airfoil, within the accepted tolerance band.

alteration of the original conceptual design geometry occurs. The blade geometry is imported into the solid modeling software via ASCII translation files. The airfoil geometry is therefore maintaining its original mathematical definition. Furthermore, airfoil tolerance band is decreased from ± 0.003 to ± 0.002 . The solid model of the rotor is further translated into an IGES ASCII translation file, and imported into the CNC software for manufacturing. Once in the manufacturing phase, information control of the geometry is weaker, and depends on the quality of the supplier's technology. For this reason, a feed-back loop into the information control is organized by extracting inspection-specific geometry data from the solid model, and inspect the final product. In this manner, the solid model becomes a process reference element to which the final product is compared. The details of this information loop will be the subject of a future report.

The rotor concept 1 has been manufactured and water-flow tested, in conjunction with three types of flow straighteners: i) the original egg-crate straightener, ii) the current design hex straightener and iii) the cut-back hex straightener. The water-flow calibration constants obtained are listed in Table 2.

Table 2. Rotor Concept 1 water-flow test results.

| Type of upstream straightener | Water-flow calibration coefficient |
|-------------------------------|------------------------------------|
| Egg-crate | $0.8180 \pm 0.94\%$ |
| Current design hex | $0.8456 \pm 0.7\%$ |
| Cut-back hex | $0.8179 \pm 0.18\%$ |

The water-flow calibration coefficient obtained for the cut-back hex straightener is $K_{fw} = 0.8179$, which is approximately 1% lower than the targeted value of 0.8256. Since the calculations were made for incompressible volume flows, this value should remain the same for engine operation. Nevertheless, in operation, the changes in Re number (a five fold increase) and nature of the fluid will slightly increase the value of the calibration constant, as the fleet testing experience shows. A quantification of this increase is difficult to predict.

3.3. ROTOR DESIGN CONCEPT 2.

The second design concept follows the same radial twist for the blade geometry, while targeting two additional objectives:

- ◆ An increase in the blade natural frequency associated with the first bending mode to 1300 Hz. For this frequency, at 115% RPL there is a 16% frequency margin above the excitation frequency associated with the 18N wake flow symmetry behind the hex straightener. Since 18N is the highest symmetry number, the blade natural frequency is above all excitation frequencies associated with the upstream flow in operation.
- ◆ An optimization of the flow around the blade in a manner that minimizes the effects of the strong wake structures at the hub—where there is only 1 inch separation between the rotor and the cut back hex straightener—and increases the role played by the flow around the upper half of the blade, located in a less perturbed flow field.

Both objectives are to be achieved by a tapered design of the blade geometry employing a variable blade chord length and a variable airfoil relative thickness from hub to tip. The design uses the modified NACA Four-digit series of airfoils whose relative thickness varies linearly from 24% at the hub to 13% at the tip. The chord length varies also linearly with radius, scaling the original design chord length by 109% at the hub and 100% at the tip. Figure 11 shows 8 radial sections of this design, by comparison to the original profile. The final design was obtained after 14 iterations, each iteration consisting of a mathematical model, translation and import into a solid modeling software, followed by export into a stress and natural frequency

analysis software. The manufactured rotor tested only 5 Hz difference from the predicted 1308 Hz natural blade frequency associated with the first bending mode.

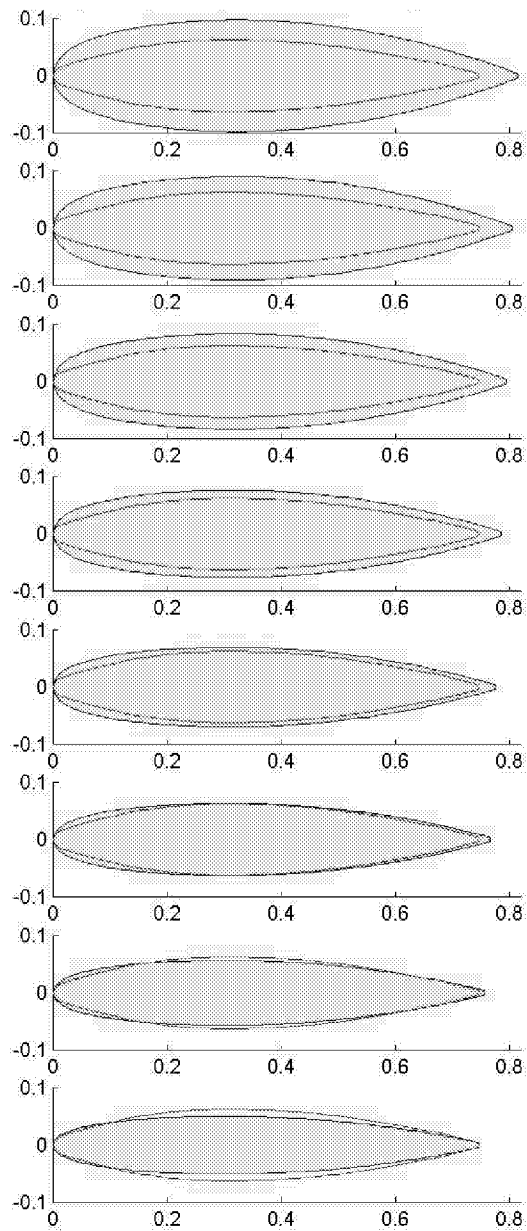


Figure 11. Rotor Concept 2 blade geometry shown at 8 equally spaced radial sections. The blade chord length varies linearly from 109% of the original chord length at the hub to 100% original chord length at the tip. Airfoil relative thickness varies linearly from 24% at the hub to 13% at the tip. Airfoils are modified NACA Four-digit series.

At the time of writing this report, only preliminary water flow tests of the second rotor design are available. The results are shown in Table 3.

Table 3. Rotor Concept 2 water-flow test results.

| Type of upstream straightener | Water-flow calibration coefficient |
|--------------------------------------|---|
| Egg-crate | 0.8154 ± 0.44% |
| Current design hex | 0.8436 ± 0.1% |
| Cut-back hex | 0.8169 ± 0.1% |

The numbers are very similar to the results obtained for rotor concept 1, slightly slower. The same observations made at the previous section regarding the change in flow regime for engine operation should be noted here as well. Preliminary real-time measurements from the magnetic detectors show a very smooth rotation for concept 2 rotor.

CONCLUSIONS

A new rotor design has been conceptualized for the SSME fuel flowmeter, in conjunction with a modification of the hexagonal flow straightener destined to increase the spacing between the straightener vanes and the rotor's blades at the rotor's blade tip. The design requirement, essentially a slower speed, will allow operation of the SSME at 115% rated power level and beyond. The new design is obtained by a retwist of the rotor blades, following a calculated radial distribution of the blade stagger angle $\alpha=\alpha(R)$. Based on the same stagger angle radial distribution, two design concepts have been finalized, prototyped and water-flow tested. The first concept follows the new blade twist using the same blade profile as the original design. The second concept uses a tapered blade design which increases the blade natural frequency associated with the first bending mode to 1308 Hz, while optimizing the flow around the blade, generating a smooth operation. The water flow tests indicate a flow calibration constant within 1% of the targeted value.

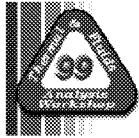
ACKNOWLEDGEMENTS

The author wishes to acknowledge the contributions of William Bowling-Jr for the innovative solid modeling of the rotor geometry. Mr. Bowling's feed back and contribution to the control of the design information is essential to this project. The formulation of design requirements, management of design iterations, stress and blade dynamics feed back to the author is due to John Ubowski. The team efficient management and coordination as well as scheduling of the intensive water flow tests is due to Henry Loureiro.

Special thanks to Dr. Edward D. Lynch for providing the CFD flow field data behind the hexagonal straightener, and for the interesting discussions regarding the flow regimes and instabilities past the meter rotor blades.

REFERENCES

1. Fox, T.H., "Possible Mechanism for Flometer Oscillations Seen on STS-8", Marshall Space Flight Center Letter, April 9, 1984
2. Ascoli, E. et. al. "Application of CFD to Explain Stall Behavior of the SSME Flowmeter", AIAA paper 99-2458, presented at the 35th AIAA/ASME/SAE/ASEE Joint Propulsion Conference and Exhibit.
3. J.T. France, "The Measurement of Fuel Flow", AGARD Flight Test Instrumentation Series, Volume 3, NATO publication, 1972.
4. Schlichting, H. "Boundary Layer Theory", McGraw Hill, 1979
5. Abbot, I.H. and von Doenhoff, A. E., "Theory of Wing Sections", Dover , 1949.



THE OFF-DESIGN PERFORMANCE OF A CAREFULLY INSTRUMENTED RADIAL INFLOW TURBINE

Dr. David Japikse

Concepts ETI, Inc.

217 Billings Farm Road

White River Junction, Vermont 05001-9486

ABSTRACT

The performance of a common radial inflow turbine, operating with a nozzle-less inflow volute and an exhaust diffuser, has been evaluated. Experimental techniques are discussed and test problems are reviewed. Internal data have been acquired for each sub-component. Fundamental questions about data interpretation are addressed. Suggested parameters for sub-component and overall data correlation are given. Important trends of basic loss and diffusion parameters are presented. Suggestions for additional studies are offered.

NOMENCLATURE

| | |
|----------|---|
| A | Area |
| b | Passage height (span) |
| C_0 | Isentropic expansion velocity based on enthalpy and Equation 13 or 16 |
| er | Expansion ratio, $p_{00} / \overline{p_4}$ or p_{00} / p_4 |
| f | Multiplicative loss adjustment factor |
| i_2 | Impeller incidence |
| L | Length |
| LC, K | Loss coefficient, see Figure 7 |
| m | Mass flow rate |
| N | Rotational Speed |
| p | Static pressure |
| p_0 | Total pressure |
| Q | Heat flux |
| r | Radius |
| T_0 | Total temperature |
| T_{ce} | Operating clearance |
| U | Wheel speed; usually U_2 by implication |

GREEK SYMBOLS

| | |
|-----------------------|---|
| α | Absolute swirl angle |
| $\overline{\alpha}$ | average of four core probes in Figures 9 and 10 |
| $\overline{\alpha}_4$ | Radial and circumferential average in Figures 14 and 15 |
| β | Blade angle; degrees from meridional surface |
| η | efficiency, also diffuser effectiveness ($C_p / C_{p,ideal}$) |
| θ | Blade angle, degrees from meridional |

STATIONS AND SUBSCRIPTS

| | |
|-----------|-----------------------------|
| 0 | Upstream stagnation, throat |
| 1 | Volute exit state |
| 2 | Impeller inlet state |
| 3 | Impeller exit state |
| 4 | Diffuser exit state |
| <i>D</i> | Diffuser exit state |
| <i>r</i> | referred state; also 'corr' |
| <i>ts</i> | total-to-static |

1. INTRODUCTION

The radial inflow turbine is an essential element of every low cost automotive turbocharger, produced in the level of three to five million copies per year around the globe. It is also used for small gas turbines and cryogenic expanders. It has received some extensive investigation over the past 50 years but receives very little research at the present time. Modeling of the radial inflow turbine is achieved with moderate accuracy, but as shown below, numerous questions concerning the fundamental performance of radial turbines still exist and have not been dealt with in the technical literature. This investigation establishes the base of current understanding for radial inflow turbines and presents extensive data from one thorough investigation of a radial inflow turbine including internal fluid dynamic and thermodynamic measurements as well as accurate overall measurements. This paper is presented with the permission of original consortium sponsors, which is appreciated.

2. PAST TECHNICAL CONTRIBUTIONS

A large number of technical contributions to the radial inflow turbine technology have been presented in various forms. These have been reviewed in detail by Japikse (1982) [1] and the literature survey has largely been incorporated in subsequent presentations by Baines (1999) [2] and others. Highlights of the original literature survey are summarized. The technical literature for radial flow turbines was found to fall almost exclusively into four categories, as follows:

1. Investigations by NASA
2. Investigations by American Industry:
3. Various English contributions, principally from Universities, and,
4. A useful variety of Japanese contributions.

The principal driving force for conducting these investigations was to study the radial inflow turbine for small gas turbine application (up to helicopter size engines), for turbochargers, and for space power applications. The strongest consistent industrial requirement, throughout the past decades and up to the present time, has clearly been the turbocharger application.

The reported survey of the technical literature revealed several significant observations:

1. Most of the reported measurements concerned overall power absorbed, and hence efficiency, plus referenced flow versus expansion ratio.
2. The most common internal measurement was a single impeller exit radial survey with a three-hole probe where total pressure and swirl angle were measured.
3. Other internal measurements were virtually non-existent in nearly all studies.
4. Most studies concentrated on simple design difference investigations such as changing operating clearance, changing blade number, changing axial length, or some other simple direct design variation.

The four preceding observations can be readily reconfirmed by the interested reader upon reviewing the literature surveys referenced above. Due to the absence of detailed internal data, all of the prediction models have failed to confirm their integrity by comparison to station-by-station velocity triangle, loss, and recovery measurements.

Instead, various adjustment factors within the ‘models’ have been manipulated at will to obtain good overall agreement on flow rate and efficiency with the hope that the adjustment in internal coefficients might have some basis in reality and might suggest a greater level of understanding. Nonetheless, lacking detailed internal data, there is no basis upon which the internal models can be rigorously confirmed or refuted. A particularly curious situation exists in the exit surveys which have been reported in the past studies. All the surveys showed significant variations in exit swirl angle. These variations were distinctly different from what might have been expected from flow codes which were available at the time of the investigations. In all cases, however, no effort was made to measure the static pressure distribution at the impeller exit and fundamental understanding of a swirling flow should lead an investigator to understand the need for measured static pressure variations to accompany the swirl angle variation.

3. RESEARCH OBJECTIVES

The objectives of the present investigation were to learn *how* to obtain good, reliable measurements inside a radial inflow turbine and to establish recommendations for future investigations. Additionally, it was desired to actually *obtain* a good set of measurements and interpret the measurements into fundamental modeling parameters for a single turbine stage.

To meet the objectives set forth, a radial inflow turbine was obtained and developed into a test facility. Figure 1 shows a contour outline of the radial inflow turbine showing the principal meanline dimensions. The impeller was comprised of radial elements and has a 0° inlet blade angle. Only the exhaust diffuser was modified slightly from the original configuration; specifically, the surface of the diffuser was machined to conform to exactly the dimensions shown in the figure, so that a proper machined surface would be available to facilitate repeatable measurements in the future (in other words, the rough cast surface was removed and replaced by a reliable, machined surface). Figure 2 displays the test facility created for the purpose of this investigation. Flow was delivered to the turbine test rig from a combustor in which kerosene was burned with compressed air. Inlet temperature could be controlled over a wide range of temperatures, as discussed below. The inlet state was found, by several casual traverses, to be quite uniform and well mixed-out. A set of three different inlet total pressure and three different inlet total temperature measurements were made as well as static pressure and flow rate. Rotational speed was measured as well. The entire turbine assembly was carefully insulated to minimize heat loss from the test

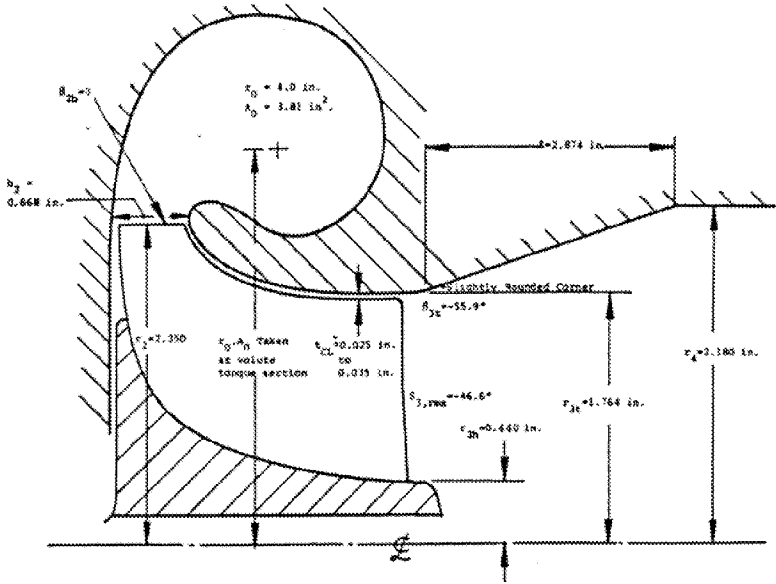


Figure 1. Principal one-dimensional geometry specification, not to scale.

rig. Several different options for exit flow field traversing were considered. Initial consideration was for traversing close to the impeller exit, but mechanical interference with the hub attachment (a common nut) ruled out this possibility and subsequently it was decided to traverse downstream of the exhaust diffuser. Four different circumferential positions were traversed giving a total of 8 different radii representing the exit flow field. Total pressure and absolute flow angle were initially measured (following the common technical literature of the day) and subsequently static pressure was also measured, as discussed below. In order to get a good exit total temperature, three elements of a Koch mixer were used as shown in the figure. This allowed a 99+% mixing completion to be achieved with a very uniform total temperature at the discharge. By using this total temperature (actually an average of six shielded probes), and the inlet total temperature, plus appropriate calibrations, a very accurate measurement of temperature drop could be achieved.

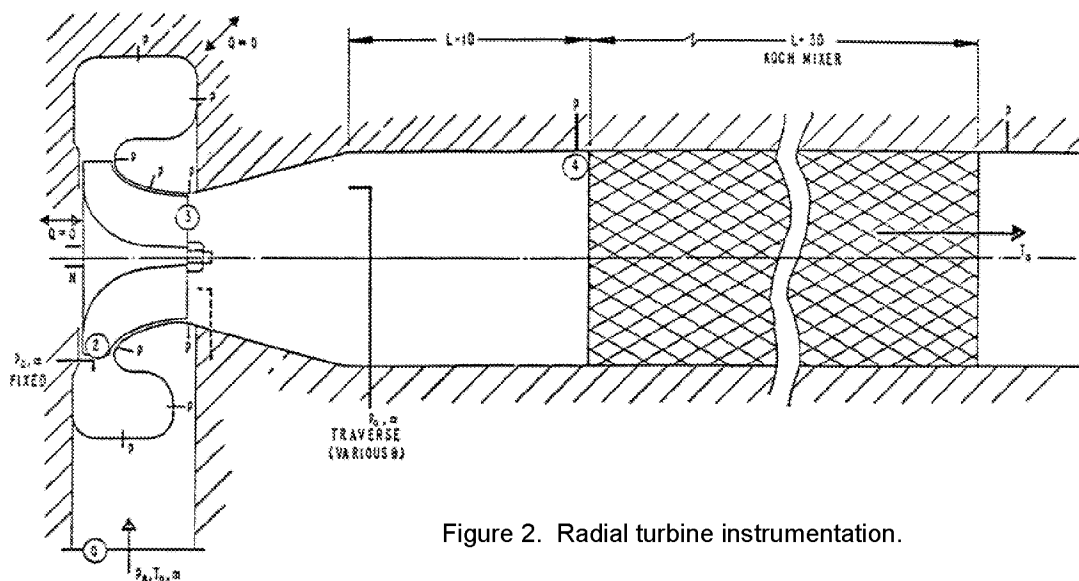


Figure 2. Radial turbine instrumentation.

In order to confirm the adequacy of the techniques utilized, a heat loss calibration was conducted. After removing the impeller and replacing it with a stationary hub flow deflector, the inlet and outlet temperatures were measured over a period of time. It was found that thermodynamic equilibrium could be achieved with all temperatures stabilized within approximately two hours. Additionally, a small drop in temperature from the inlet to the outlet was measured which was attributed principally to heat conduction down the shaft and through the bearing housing and also through the insulated walls. These tests were conducted while maintaining a steady flow of oil to the bearings (not rotating) at typical oil temperatures. The major results are shown in Figure 3. It should be mentioned that similar tests had been previously conducted on a different test rig (although principally to determine the flux of heat from the turbine into a compressor which was being tested). The results showed (not at all surprisingly) that a very linear relationship of the temperature difference, as suggested in Figure 3, would be achieved. For the present test, data was recorded at only two temperatures. The 800°R gas temperature corresponds to the lowest temperature which could be held with the combustor operating stably. The 580°R temperature corresponds to no combustor operation and simply the discharge temperature of the compressed gas leaving the supply compressors. Based on the prior data, a simple linear interpolation between these two conditions was used to estimate the amount of correction. Prior tests have also revealed that hot turbine operations should not be considered: the heat loss would be too great and the correction factor would amount to a significant percentage of the measured temperature drop through the turbine. By controlling operating temperatures in the lower range suggested by Figure 3, and carefully scheduling the tests, the maximum correction was usually held at less than 0.5° and the resultant uncertainty is probably no more than plus/minus one or two tenths of a degree Rankin. Consequently, the thermal adequacy of the test rig was reasonably demonstrated. It should also be mentioned that the temperature measuring probes were all half shielded thermocouples which have a known calibration characteristic for recovery factor and, consequently, good corrections for local Mach number were readily possible.

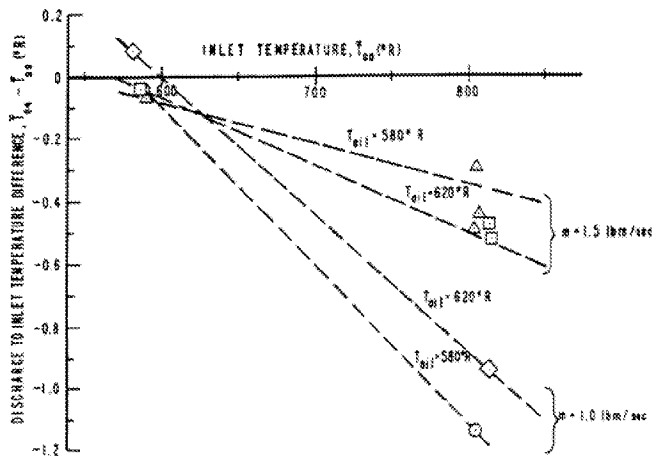


Figure 3. Turbine housing thermal calibration with impeller removed (zero on ordinate is no heat loss).

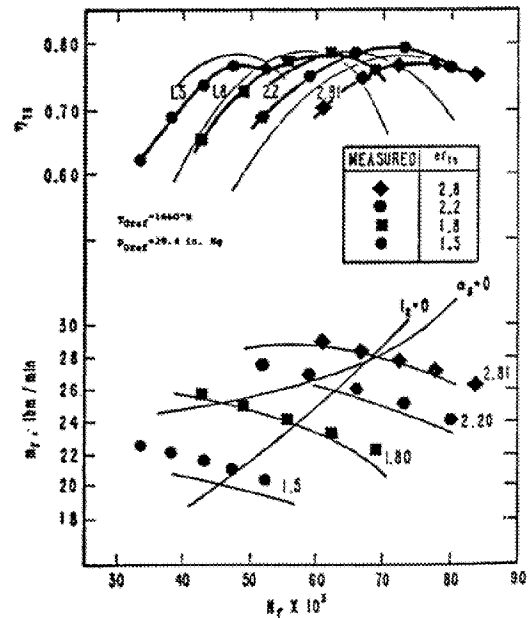


Figure 4. Turbine supplier's performance map and scoping calculations of this study.

Prior to conducting tests, careful sensitivity calculations were made in an attempt to discern which parameters might be of greater significance for detailed investigation. Figure 4 shows a set of measured results from the manufacture of the turbine with scoping calculations conducted by the author. The calculations used an early meanline performance code using common modeling techniques referred to later. The investigations clearly illustrated an unexpected sensitivity: small changes (not revealed in Figure 4) to the exit modeling conditions could significantly change the interpretation of the velocity triangle at the impeller inlet. In other words, by considering alternative models at the impeller exit, one could introduce a variety of different possible interpretations at the rotor inlet. This sensitivity had simply been overlooked in prior investigations since little attention had been given to station-by-station measurements and nearly exclusive attention was placed on the overall performance characteristics while taking great liberty to adjust any internal parameters desired (usually the rotor inlet conditions with indifference to the exit conditions).

Additional instrumentation included three-hole probes fixed at a location just upstream of the impeller inlet at mid-passage. These were located at four different circumferential positions corresponding to different sectors of the volute. It was originally desired to traverse the flow field at this location, but inadequate consortium sponsorship limited the degree to which measurements could be made at this location. Consequently, the four fixed probes were utilized in an effort to determine core, and possibly maximum, values of flow parameters at this location. This proved to be an exceedingly difficult measurement as noted below.

With these issues in focus, the test hardware was built and taken through a shakedown evaluation. The original shakedown evaluation of two hours produced data which reflected most of the expected trends and conditions for the planned test. However, strange signals from the fixed total pressure/yaw angle probes upstream of the impeller required careful examination. This examination revealed that the probes had simply been destroyed by particulate erosion in the two hours of testing with a small amount of damage to the impeller and volute. Consequently, significant efforts were expended to remove particulates from the test field. This required a startup period for the combustor with hot gas discharge bypassing the turbocharger for a startup transient of one or two hours and then the flow was brought into the impeller. Additionally, a particle separator was introduced upstream of the test rig. The resultant flow was much cleaner and a new rotor and volute housing showed only limited distress after many, many hours of operation. Additionally, the four fixed probes were replaced with Inconel probes (the original being

stainless steel) and these lasted throughout most of the resultant test program (although one or two probes did eventually fail near the end of the project). The shakedown tests with unexpected but essential modifications, did establish the means for obtaining accurate and reliable data which could be used for good model building.

Samples of key data are presented next. Figure 5 displays static pressure measurements conducted at key stations through and around the radial inflow turbine. The same data are measured at every single test point for the entire investigation; only one is presented here. The highest pressure is the inlet total pressure followed next by the inlet static pressure. Beneath this are two levels of static pressure, shown in a circumferential variation, which are taken around the volute (or scroll). The higher value is on the outer surface of the scroll, where the static pressure should be highest by the Euler-n equation, and the next one is on the sidewall of the volute. These values are not completely uniform showing that the volute does not have totally uniform static pressure in a circumferential sense, a task which would be extremely hard to effect in any volute design. At the impeller tip there is a very careful measurement of static pressure with taps at every 45°, and more closely spaced near the tongue of the volute. A definite variation of the static pressure at this location can be observed and this is a result of distortion from the volute. At the impeller exit, the static pressure is measured along the shroud surface and displayed with the x symbol. It is the lowest casing pressure recorded and falls below the downstream pressure (which has also been used to normalize all the pressures of this plot). It therefore appears that there is, in fact, a static pressure rise through the diffuser, at least along the shroud streamline as these taps would indicate.

One must be careful in interpreting the variation of static pressure in the volute particularly concerning the sudden drop in static pressure along the outer surface as suggested at the location of 90°. A careful examination of this particular tap was made and it was observed that the pressure tap fell into a pocket of casting porosity along the inside surface. This, of course, would introduce noticeable error, several percent of dynamic head at least, and therefore would give larger uncertainty in this measurement than in other measurements. The volute outer pressure measurements are subject to this uncertainty since there was no way to enter into the volute and smooth out the surface. However, the impeller tip and exit pressures were extremely accurate pressure taps drilled into a machined surface; hence these measurements can be considered to be of common accuracy ($\pm 0.05 - 0.08$ psia).

Figure 6 displays a sample of impeller cover static pressure data. In all cases, a smooth acceleration was noted with negligible circumferential variations in pressure.

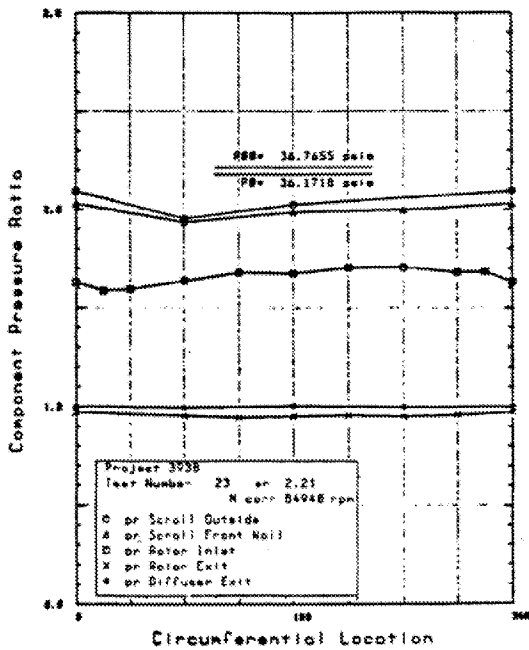


Figure 5. Circumferential pressure measurements at various key stations (divided by p_4).

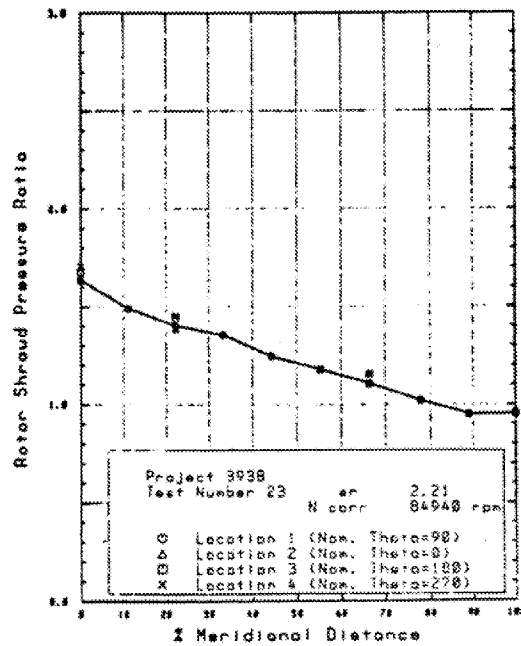


Figure 6. Impeller cover static pressure variation.

It was desired to learn as much about the flow angle at the volute discharge, that is the impeller inlet, as possible. Unfortunately, only core values could be measured but these are still very beneficial. The core loss coefficient was consequently calculated for the volute (while making no comments about the higher losses which must be found closer to the walls) as displayed in Figures 7 and 8. The second figure gives a nearly constant variation with respect to U/C_0 , but for reasons which are not immediately obvious from these plots, there is a maximum in loss at the expansion ratio of 2.2 with a drop-off at the higher expansion ratio of 2.8. It is clear that the core flow from the volute inlet flange up to the impeller inlet is not isentropic but that small losses on the order of 2% to 4% of the inlet stagnation pressure are evident. Losses near the walls would likely be much higher due to local boundary layer effects. Thus, even though this volute serves as a nozzle with continuously accelerating flow, the development of strong boundary layers (with skewed or secondary flow) along the sidewalls is substantial and reaches all the way across to the core region of the flow field giving losses in each of the four measured locations. None of the probes showed an isentropic core under any operating conditions.

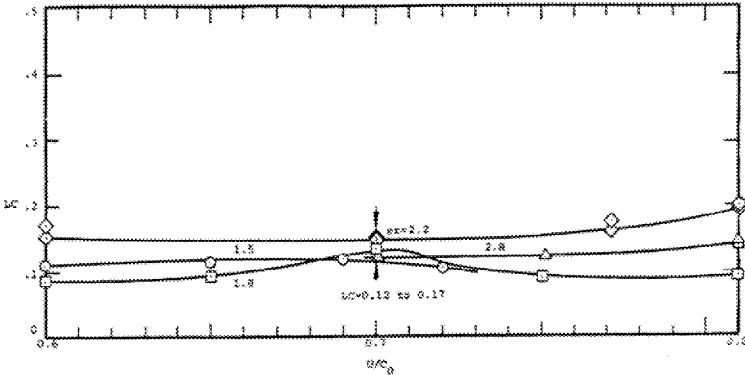


Figure 7. Volute core loss $\frac{P_1 - P_{02}}{P_{02} - P_2}$ versus U/C_0 .

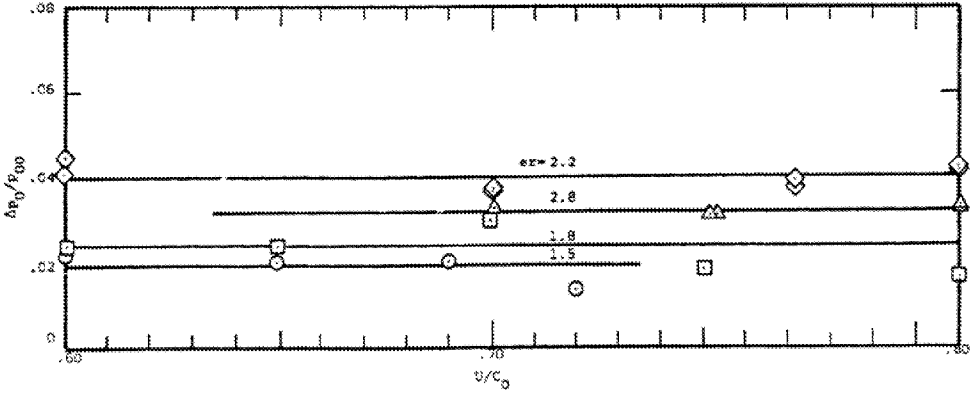


Figure 8. Volute core loss $(\Delta p_0/p_{00})$ versus U/C_0 .

Additionally, the measured (core region) swirl angles are displayed in Figures 9 and 10. The angle variation proceeds from approximately 69.5° at low expansion ratio up to approximately 73.5° at the highest expansion ratio with a tendency to increase in a nearly monotonic form. However, the measured data do show noticeable variation with U/C_0 . Figure 10 gives a reasonable first estimate of the general trends on an average basis. The strong variation at high values of expansion ratio would suggest further investigations.

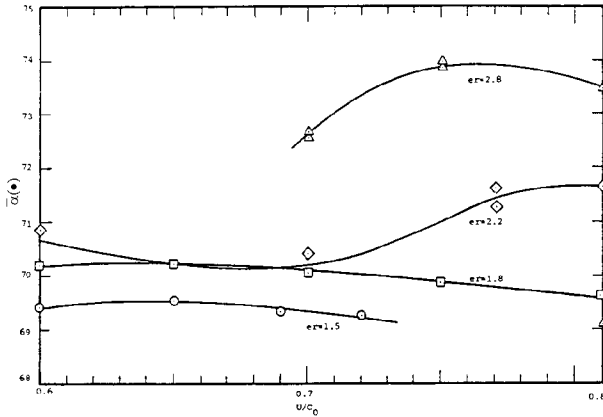


Figure 9. Volute exit swirl angle versus U/C_0 .

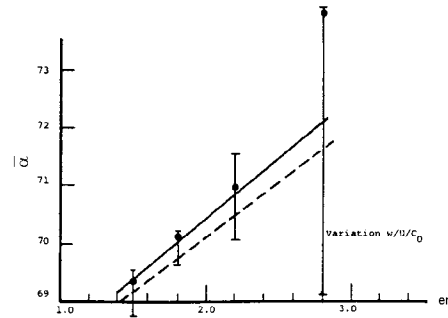


Figure 10. Volute exit core swirl angle versus stage expansion ratio.

Impeller exit flow field traverses were conducted for a set of six different operating points (discussed below) and required more than one week of continuous testing to log these data. Clearly, said data was not recorded for every single testing point, but only the select points due to economic limitations. It was felt that these data were important to anchor the results of the entire investigation. After the investigations were conducted, which unfortunately followed the current practice of the industry of recording swirl angle and total pressure, it became clear during data processing that an important link was missing: the static pressure must also be measured. Consequently, one test case was repeated as shown in Figures 11, 12 and 13 presenting the total pressure, the flow angle and the static pressure. These data clearly show that the static pressure is not constant but drops substantially toward the centerline of the test facility as a consequence of the strong swirl distribution. The static pressure variation is clearly important and must be at least recognized if proper data processing is to be achieved. To obtain this particular measurement, the three-hole probe was used in reverse and was calibrated for base pressure. Knowing this basic trend, corrections could be made for the comprehensive traverses conducted at the selected six operating points.

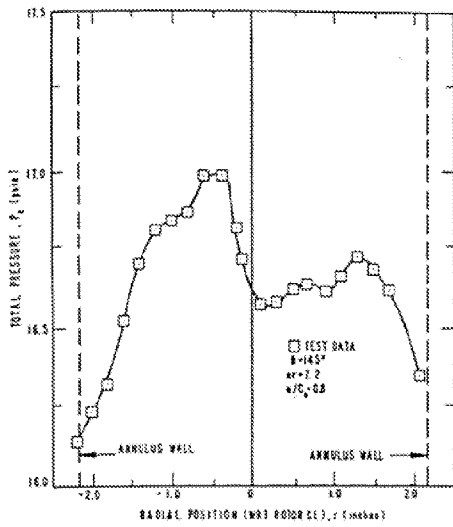


Figure 11. Radial turbine exhaust survey – total pressure.

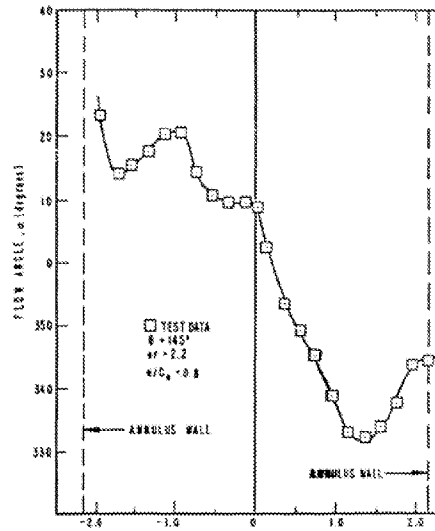


Figure 12. Radial turbine exhaust survey – flow angle.

Figure 13. Radial turbine exhaust survey – static pressure.

Figure 14 shows an exit static pressure correction factor that was developed for the diffuser exit as a function of exit swirl. This value was achieved by adjusting the level of static pressure used in the integration of the total pressure and swirl angle information from the traverses while satisfying the local measured mass flow rate. The investigation of the exit flow field via the traversing showed that the one oversight, in past investigations and initially in this investigation, was the lack of attention to the static pressure distribution in the exit pipe. When this parameter was sensibly adjusted, mass flow agreement was obtained and a rational correction to the static pressure was implied. This also resulted in improved values of exit swirl angle distribution since the weighting of the mass average parameters is consequently affected.

The Figure 14 correction factor was used with the six traverse points as indicated and, additionally, every other test point on the map had a single point recorded using the station 4 cobra (traverse) probe in a *fixed* radial position. The fixed position had been carefully selected to be a very representative point of the flow field which very nearly replicated the mass average value from the six traverses. Only the slightest correction was necessary since the location for the fixed probe was well chosen. As a consequence, all of the data for both the fixed probe and for the detailed traverses, giving a diffuser exit swirl angle, are displayed in Figure 15. It can be observed that the swirl distribution at the diffuser exit has been sensibly mapped. The six different traverse points indicated trends within $\pm 3^\circ$, an error which is quite modest on a trigonometric basis. Incidentally, it should be mentioned that the six traverse points were conducted at four different expansion ratio levels and, at the design expansion ratio of 2.2, also at three different values of U/C_0 varying from 0.65 to 0.72 to 0.81. Due to the particular style of load control in the test rig, it was possible to independently control U/C_0 while testing at a particular expansion ratio.

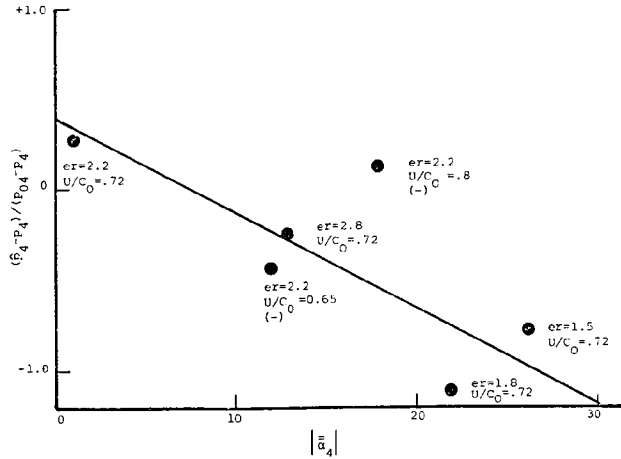


Figure 14. Possible diffuser exit static pressure correction factor as a function of $\bar{\alpha}$ and U/C_0 .

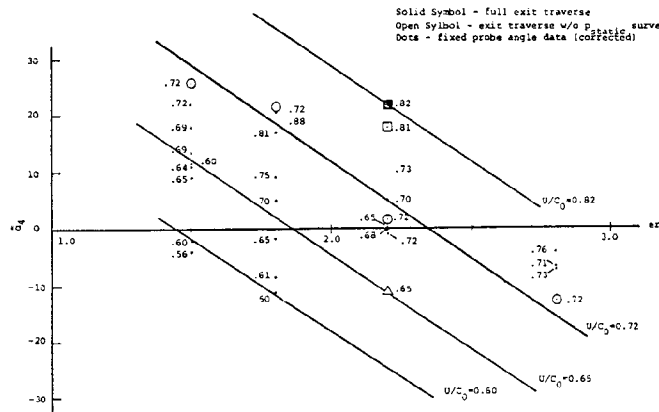


Figure 15. Deduced impeller exit flow angles as a function of U/C_0 and er .

4. DATA EVALUATION

Using the data obtained from this investigation, a series of loss calculations and flow state calculations were prepared. These, of course, required certain modeling equations as discussed now. Figure 16 shows a Mollier diagram that reveals the isentropic incremental basis for conducting loss calculations. This is one of the cleanest and most consistent methods of evaluating internal state changes for a radial flow turbomachinery stage. Table 1 shows the related equations. The denominator of incremental loss expressions is shown as equation 12 and the increments are based on the isentropic enthalpy or temperature at each intermediate state of the expansion process. Of particular note is the state 2m which corresponds to a mixed-out state at the impeller inlet. Equation 7 reveals part of the modeling picture: Mizumachi (1960) [3] suggested that a fraction of the kinetic energy associated with the velocity component normal to the blade would be lost irreversibly and would manifest itself as a total pressure loss and a static enthalpy gain. Other investigators assumed that 100% of this component was lost. At a later time, it was suggested that the component under consideration was not the component associated with the approach incidence but rather an effective incidence which would represent the difference between the gas angle and some special optimum flow angle. A reasonable deduction of the optimum flow angle might be the condition under which the blade tip is unloaded with the use of substantial approach (usually negative) incidence. The origin of this suggestion is no longer clear, but it may have started indirectly from an approach by Todd and Futral (1969) [4] or in a presentation by Japikse (1981 and 1986) [5,6]. Hence this model involves two parameters, the value β_{opt} and the 'f' coefficient from Mizumachi. Modeling Station 2 can also be effected substantially by understanding properly the value of p_{02} at the volute exit. Recognizing that a substantial velocity distribution exists at this location in the absolute frame, and that this distorted profile may not produce a full measure of useful work extraction in the relative frame, it is quite possible that a substantial mixing loss is implied by the character of the velocity profile at the volute exit. Thus, for purposes of evaluation, it can be hypothesized that a mixing calculation should be conducted at the volute exit to represent the degradation of the velocity profile at this location. Of course, the true profile has not been measured (or computed), but the core value has been modeled in a simple sudden expansion mixing calculation. Thus a classic Borda-Carnot mixing calculation can be made to obtain a value of $p_{02,m}$ which reflects profile mixing as well as the core loss. Other efficiency definitions are shown in Table 2.

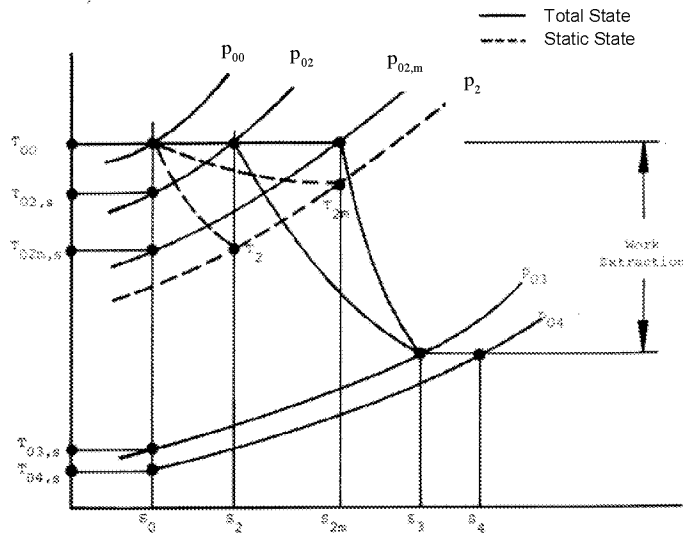


Figure 16. Basis for isentropic incremental loss calculations.

TABLE 1

STRATEGY 1 INCREMENTAL ISENTROPIC CHANGES

$$\begin{aligned}
 1) \quad \Delta \eta_{\text{scroll}} &= (T_{00} - T_{02,S})/X \\
 2) \quad \Delta \eta_{\text{rotor, tot}} &= (T_{02,S} - T_{03,S} - (T_{02} - T_{03}))/X \\
 3) \quad \Delta \eta_{\text{incidence}} &= (T_{02,S} - T_{02m,S})/X \\
 4) \quad \Delta \eta_{\text{rotor}} &= (T_{02m,S} - T_{03,S} - (T_{02} - T_{03}))/X \\
 5) \quad \Delta \eta_{\text{diffuser}} &= (T_{03,S} - T_{04,S})/X \\
 \text{where} \\
 6) \quad T_{02,S} &= T_{00} (p_{02}/p_{00})^{(k-1)/k} \\
 7) \quad T_{2m} &= T_2 + f W_2^2 \sin^2(i) \frac{k-1}{2kgR} \\
 &\quad (f=1.0, 0.75, 0.5) \\
 &\quad i = \beta - \beta_{\text{opt}} \\
 8) \quad p_{02m,S} &= p_2 / (T_{2m}/T_{00})^{k/(k-1)} \\
 9) \quad T_{02m,S} &= T_{00} (p_{02m,S}/p_{00})^{(k-1)/k} \\
 10) \quad T_{03,S} &= T_{00} (p_{03}/p_{00})^{(k-1)/k} \\
 11) \quad T_{04,S} &= T_{00} (p_{04}/p_{00})^{(k-1)/k} \\
 12) \quad X &= T_{00} - T_{04,S}
 \end{aligned}$$

TABLE 2

STRATEGY 2 ISENTROPIC EXPANSION BASIS

Scroll:

$$\begin{aligned}
 13) \quad \eta_{\text{scroll}} &= C_2^2 / C_{2S}^2 = C_2^2 / [(T_{00} - T_{2,S}) \frac{2kgR}{k-1}] \\
 T_{2,S} &= T_{00} (p_2/p_{00})^{(k-1)/k}
 \end{aligned}$$

Rotor:

$$\begin{aligned}
 14) \quad \eta_{\text{rotor}} &= W_3^2 / W_{3,S}^2 \\
 15) \quad W_{3,S}^2 &= \frac{2kgR}{k-1} (T_2 - T_{3,S}) + W_2^2 - U_2^2 + U_3^2 \\
 16) \quad T_{3,S} &= T_{00} (p_3/p_{02})^{(k-1)/k}
 \end{aligned}$$

An additional challenge is manifest in obtaining good values for Station 3. Although Station 4 has been reasonably well documented by full flow field traversing, it is necessary to back calculate from Station 4 to Station 3. This was initially done by assuming a fixed value of diffuser effectiveness and then was subsequently modified by using conservation of mass, conservation of angular momentum, conservation of energy and a simple density relationship. This allowed a simple back calculation from Station 4 to Station 3. Although a small amount of angular momentum is surely destroyed between Stations 3 and 4, testing of a wide variety of swirl producing and swirl controlling devices suggests that the angular momentum destruction over this short distance would be limited to simply 1% or 2% and might be neglected. (If desired, bracketing calculations could be conducted to reconsider this small variation.)

It is important to maintain a proper work balance across the impeller. The work balance must reflect the measured enthalpy drop on the one hand and the change in UC_θ on the other hand. The value of UC_θ at the impeller exit is distinctly smaller than the value at the impeller inlet, but not at all negligible. Fortunately, a good understanding of the C_θ values at Station 4 is available from the six traverses plus Figure 15 and reasonable estimates at Station 3 can consequently be rendered with only a small residual uncertainty. This allows closure on the value of $C_{\theta 2}$. It was quickly found that this value was noticeably different from the value of $C_{\theta 2}$ which might be estimated from the swirl angle measured at the central or core location at volute exit. This is not surprising since the core value might only be indicative of one extreme value of swirl angle at the volute exit and would not reasonably be expected to reflect a true average. Consequently, the value of $C_{\theta 2}$ was computed from the work input (measured to better than 1%) and the exit angular momentum. One of the most fundamental differences between this investigation and all prior radial inflow turbine studies is the careful attention given to issues involved at the rotor exit before an attempt was made to establish a value of $C_{\theta 2}$.

With the preceding concepts established, it is now possible to present a wide variety of measured results. Results are presented in plots against stage reaction and sometimes U/C_0 . Both reaction and U/C_0 were frequently used throughout this investigation, but better data trends were usually obtained with reaction rather than U/C_0 . It is recognized that the latter has been frequently employed in radial turbine literature and that reaction has only occasionally been used; nonetheless, the present study established a definite, although slight, preference for reaction as a plotting parameter.

Figure 17 shows a first comparison. Efficiency is shown plotted versus reaction and U/C_0 . In Case A the results are based on just a simple calculation from inlet flange to stage exit flange using the exit static pressure along the exit pipe wall. In other words, no attention was paid to detailed internal stage parameters. In Case B, however, all the aforementioned considerations were rendered and for this particular plot, the influence of exit static pressure correction is reflected in the data, meaning that a corrected core value of exit static pressure, based on the swirl profile, has been utilized. This changes both the value of calculated reaction (slightly) and the efficiency (modestly). In some cases, it lowered the efficiency slightly and in other cases it raised the efficiency slightly. Probably the most profound observation is the shift of the very high to much higher values of reaction. Indeed, the high expansion ratio data have always been a little unusual throughout this entire study and the one parameter which seems to shed some light on this set of data is reaction. This is the highest reaction data of the present investigation. Although many investigations of other radial inflow turbines present efficiency as one simple trend line as a function of U/C_0 , this was never found in the present study and always some variation with expansion ratio was found from one er line to the next. There is, of course, no fundamental reason why this cannot occur in a true compressible flow problem for a highly loaded turbine stage. Also shown in Figure 17b are the same results plotted versus U/C_0 and it may be noted that the high expansion ratio data falls in a strange location relative to the other trends.

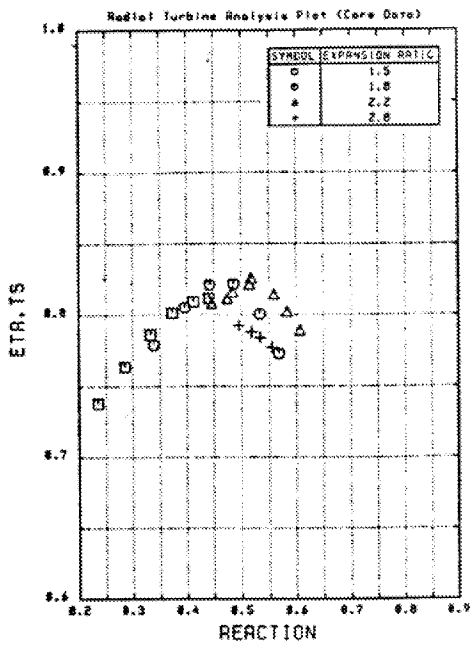


Figure 17a. Measured turbine efficiency, total-to-static versus reaction. Case A.

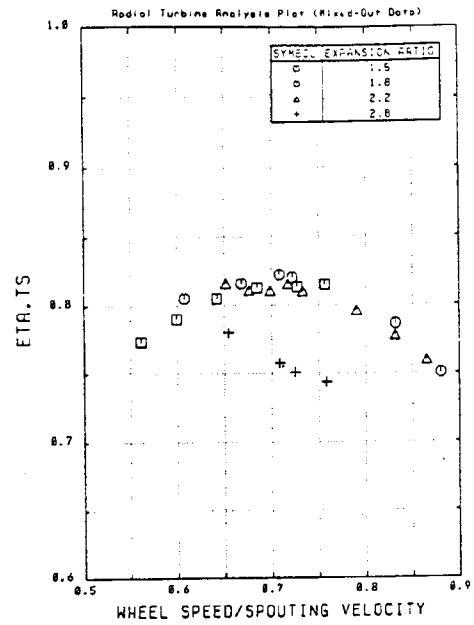


Figure 17b. Measured turbine efficiency, total-to-static versus U/C_0 . Case A.

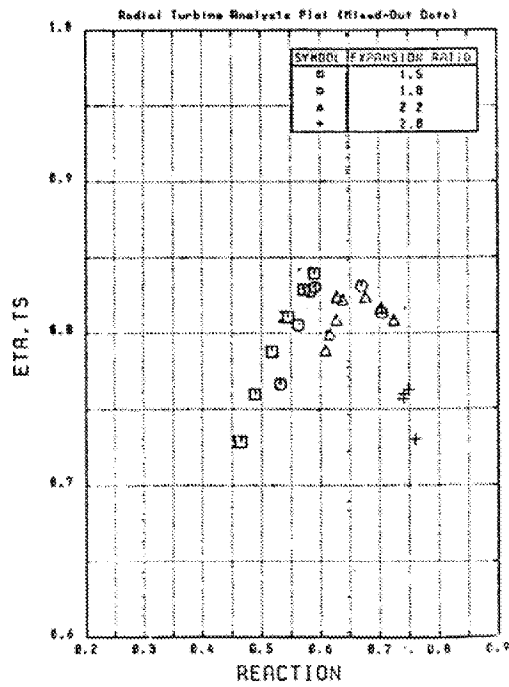


Figure 17c. Measured turbine efficiency, total-to-static, versus reaction. Case B.

Measured flow versus speed data at various levels of expansion ratio are plotted in Figure 18, following a form commonly used by the manufacturer of this particular turbine rotor. It is in sensible agreement with data taken by the manufacturer as well.

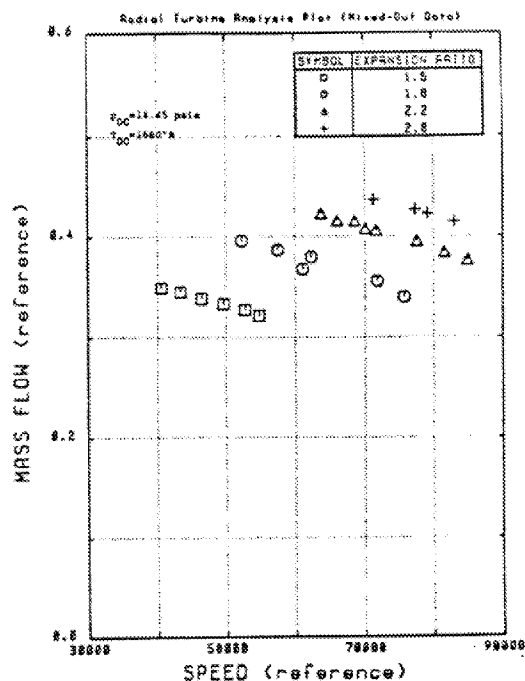


Figure 18. Measured turbine flow characteristic.

The isentropic incremental loss for the volute or scroll is shown in Figure 19. In the first case (Fig. 19a), only the simplest method of calculation was employed where the static pressure at the volute exit plus a velocity based on continuity and the core flow angle was used to close the set of calculations. By contrast, a much more careful calculation, where the core conditions at the volute exit were used to establish a blockage value with a subsequent Borda-Carnot sudden expansion mixing loss are used to establish the Case B total pressure loss for the volute. In this case, all four sets of data form a very sensible loss bucket with minimum values at a reaction level at a range of 0.65 to 0.7. Higher and lower levels of reaction show distinctly higher loss levels. The fundamental difference in the Case A and Case B presentation, of course, is a reflection of the detailed consideration given to the interpretation of data through sensible modeling. The second case is far more plausible. Figures 19b and 19c suggest that reaction is better than U/C_0 for correlating.

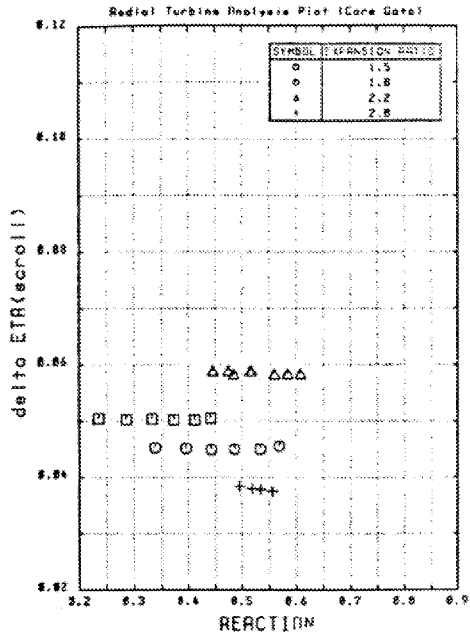


Figure 19a. Scroll efficiency decrement, Case A.

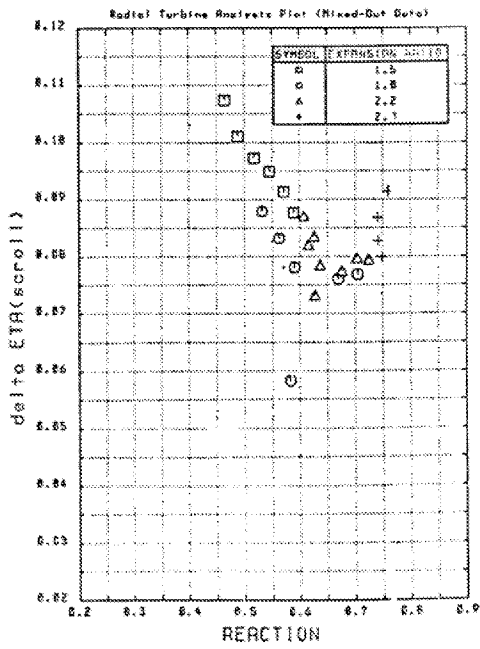


Figure 19b. Scroll efficiency decrement versus reaction, Case B.

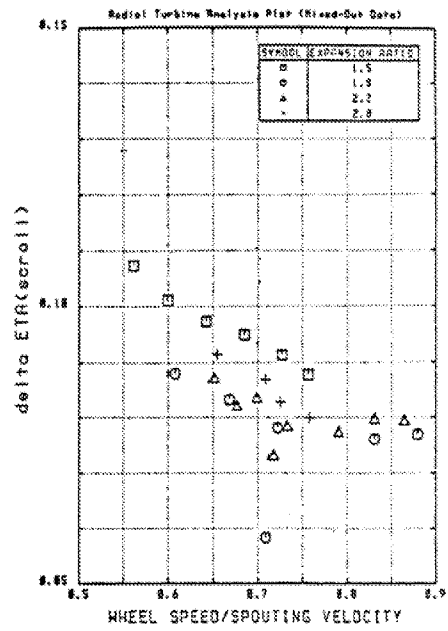


Figure 19c. Scroll efficiency decrement versus U/C_0 , Case B.

Likewise, interpretation of impeller losses can be made using the core values of Station 2 for Case A and including the diffuser with the impeller for the Case A calculation, as shown in Figure 20a. With the more detailed investigation, where Station 3 is carefully back calculated from Station 4 and Station 2 includes the mixing calculations, a more definitive rotor loss bucket is achieved as displayed for Case B (see Fig. 20b). This loss bucket is now quite tight and the two intermediate levels of expansion ratio define the bottom of the bucket whereas the highest and lowest expansion ratios define the wings of the bucket. The minimum occurs at a reaction of approximately 0.65. The same information can be presented in terms of approach incidence with the same modeling conditions as previously given; see Figure 21. Case B, of course, is preferred due to the careful attention given to splitting out detailed losses. It appears that the optimum performance falls at an approach incidence of approximately -40° , a condition where the blades may very well be substantially unloaded and rotor secondary flows may be minimal. However, the high expansion ratio data has not collapsed to the same low level as the other three cases.

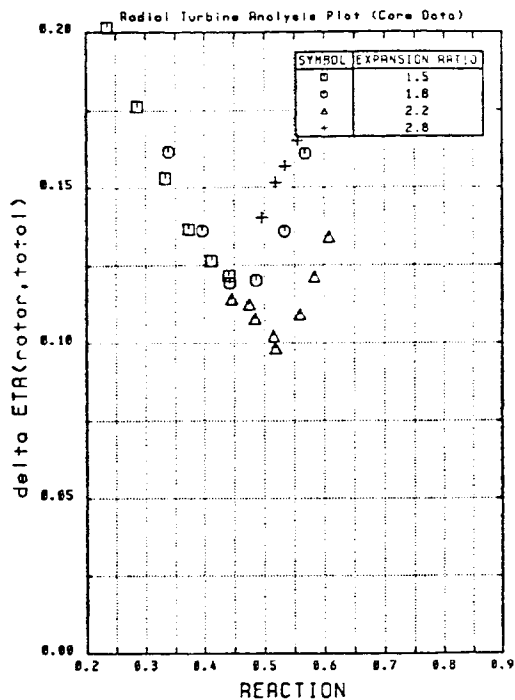


Figure 20a. Total efficiency decrement for the rotor versus reaction, Case A.

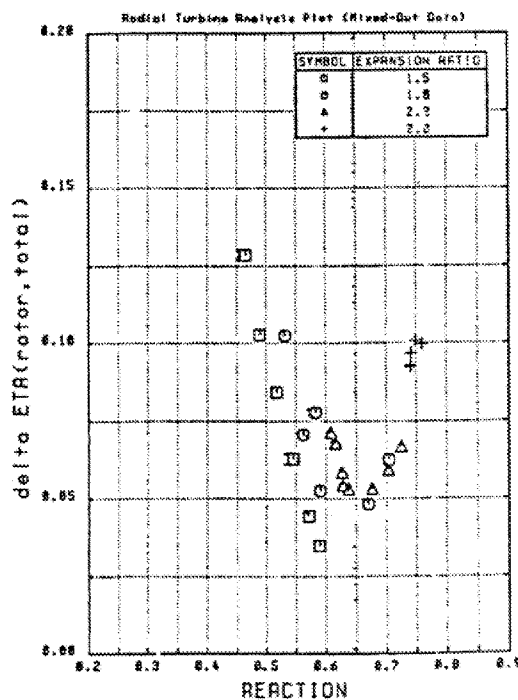


Figure 20b. Total efficiency decrement for the rotor versus reaction, Case B.

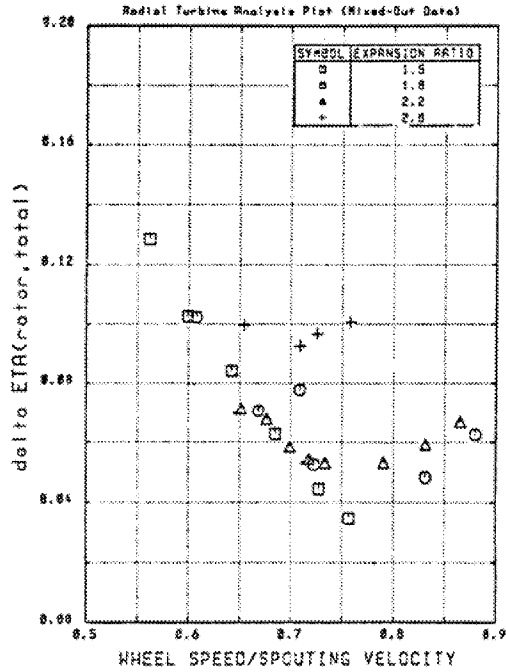


Figure 20c. Total efficiency decrement for the rotor versus U/C_0 , Case B.

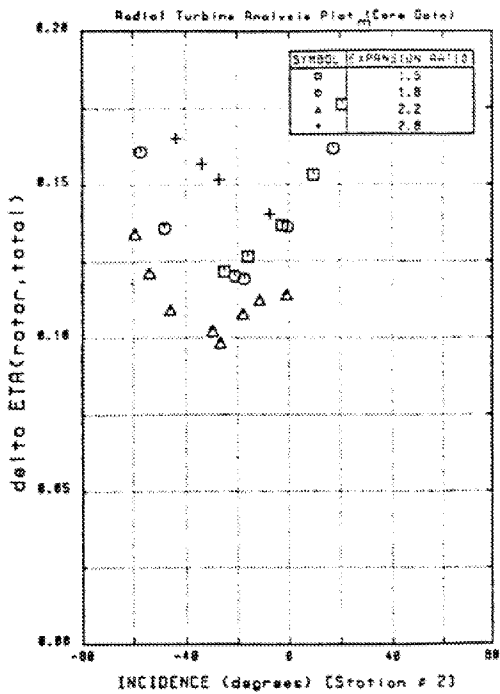


Figure 21a. Efficiency decrement for the rotor versus approach incidence, Case A.

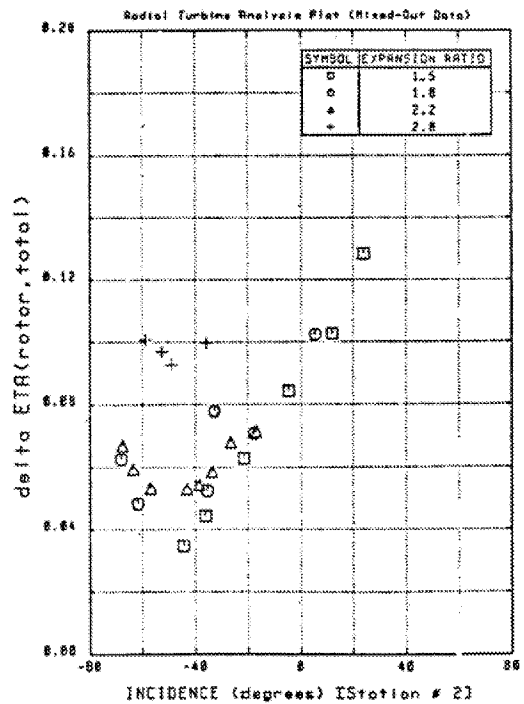


Figure 21b. Efficiency decrement for the rotor versus approach incidence, Case B.

A separate incidence loss can be computed based on the historical approach used by Benson, Mizumachi, NASA and others based on the perpendicular component of relative kinetic energy. For both Case A and Case B modeling these results are shown in Figures 22a and 22b. This is strictly an analytical estimate of what others have suggested could be an incidence loss, or perhaps an incidence effect on impeller internal secondary flow losses. If this full component (which is hypothetical) is removed from the rotor loss, than a revised rotor efficiency is achieved. The results are shown in Figures 22c and 22d as a resulting rotor loss coefficient. Clearly, there is a problem in this modeling. For Case B, the values go negative and the correction is overstated. Case A should not be considered a preferable condition since it is artificially high by ignoring the mixing losses in the volute and including the loss of the diffuser in with the impeller. The same results can be observed, as a function of approach incidence, in Figure 23a and 23b for Case A and Case B, respectively. The fact that the rotor loss has not been flattened out by removing the incidence for Case B is suggestive of the fact that not only is the correction overstated, but may be inappropriately applied. This issue is returned to later.

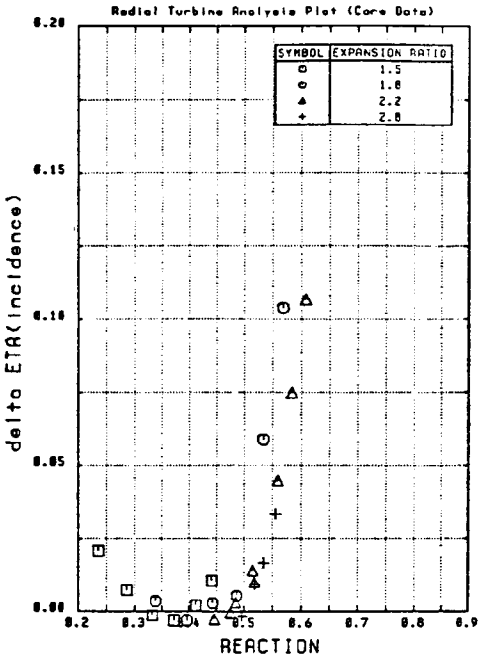


Figure 22a. Full $1/2W_n^2$ efficiency decrement (i.e., secondary flow portion) as a function of reaction, Case A.

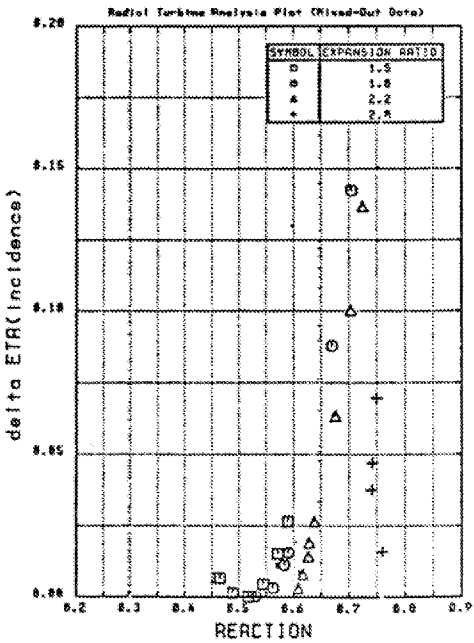


Figure 22b. Full $1/2W_n^2$ efficiency decrement (i.e., secondary flow portion) as a function of reaction, Case B.

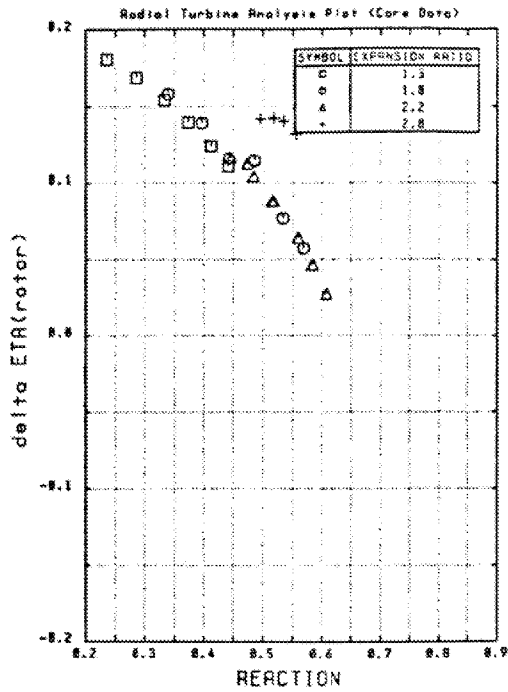


Figure 22c. Rotor (passage) efficiency decrement (i.e., with full $1/2W_n^2$ secondary flow component removed) as a function of reaction, Case A.

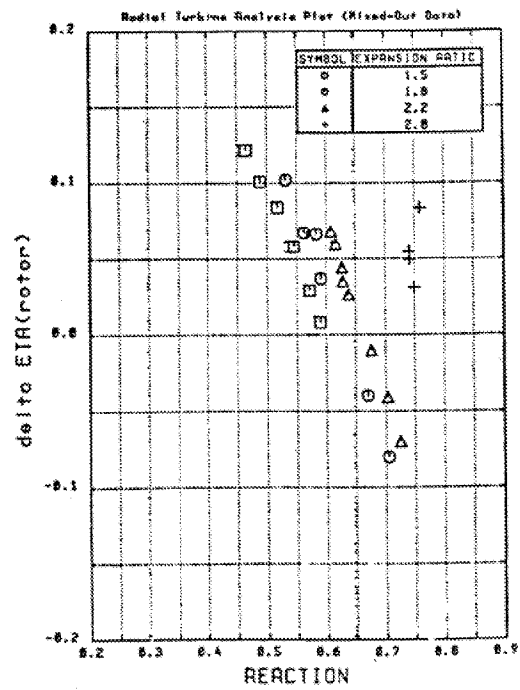


Figure 22d. Rotor (passage) efficiency decrement (i.e., with full $1/2W_n^2$ secondary flow component removed) as a function of reaction, Case B.

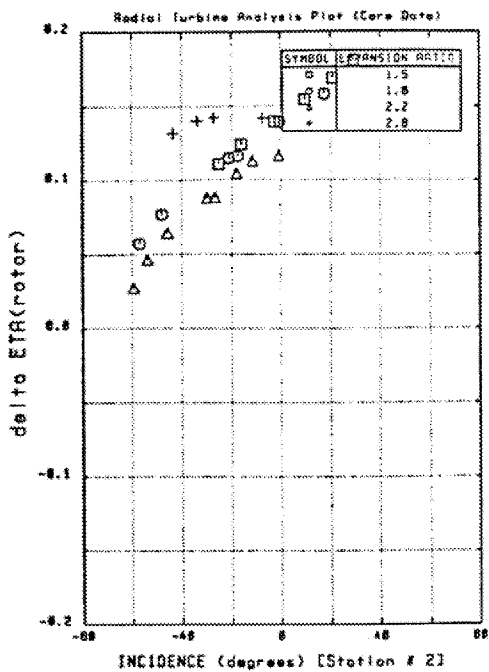


Figure 23a. Rotor (passage) efficiency decrement (i.e., with full $1/2W_n^2$ secondary flow component removed). Note the over correction at high-incidence, Case A.

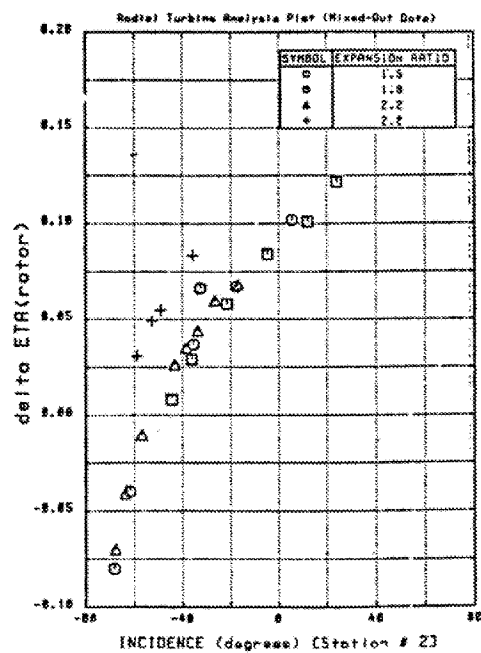


Figure 23b. Rotor (passage) efficiency decrement (i.e., with full $1/2W_n^2$ secondary flow component removed). Note the over correction at high-incidence, Case B.

The issue of rotor modeling can be extended by looking at the two variables in the historical incidence loss model of Equation 7. Observing that a β_{opt} of approximately -40° is sensible, a series of calculations were made with this value included. The resulting rotor efficiency (Equation 14) is shown in Figures 24a, 24b and 24c plotted versus reaction, U/C_0 and incidence, respectively. In this case, a very sensible rotor efficiency relationship is found with a peak at approximately 0.6 to 0.65 on reaction or approximately 0.72 – 0.75 for U/C_0 . These trends are encouraging as a fairly tight data variance is observed and the optimum corresponds with values expected from various turbine studies in the past. Plotting efficiency versus incidence, as shown in Figure 24c, shows a peak at approximately -40° which may well be the condition of the unloaded blade tip. Once the isentropic efficiency increment is computed and displayed versus incidence (see Figure 25), it may be observed that a tight variance is obtained, but not a truly flat characteristic. In order to flatten this trend, a different value of β_{opt} at each expansion ratio would be required. Further studies were conducted resulting in the data of Figure 26 where nearly constant trends are observed for two of the expansion ratios with the third one falling quite high. In this case, β_{opt} was varied at each expansion ratio line and an optimum value could not be found for $er = 1.5$, a value -55° was found for $er = 1.8$, a value -50° was found for $er = 2.2$ and a value for -45° was found for $er = 2.8$. Initial studies to change the coefficient of the term (labeled as f in Equation 7) did not yield meaningful results due to a lack of sensitivity in the data. This should be re-examined with additional data from other cases as this may be an important variable to bring all the trends together.

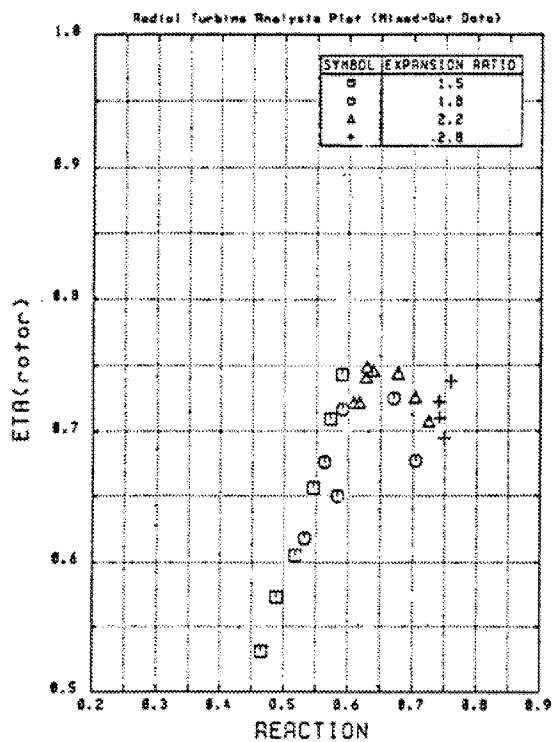


Figure 24a. Rotor efficiency versus reaction, Case B.

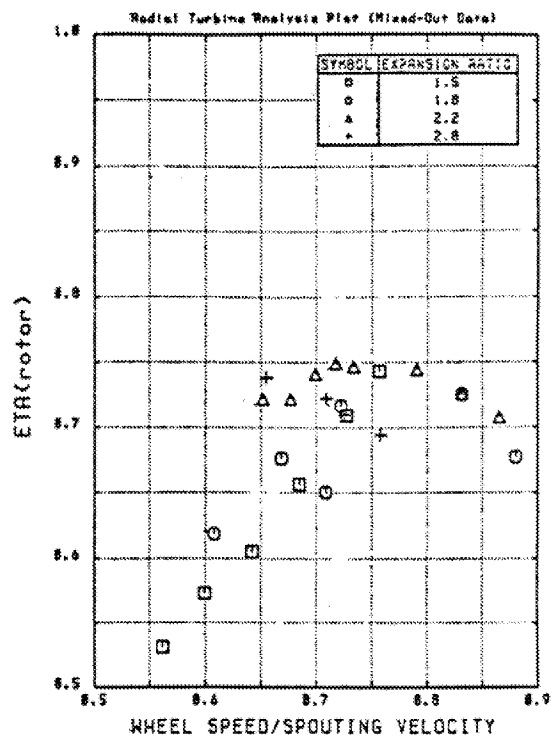


Figure 24b. Rotor efficiency versus U/C_0 , Case B.

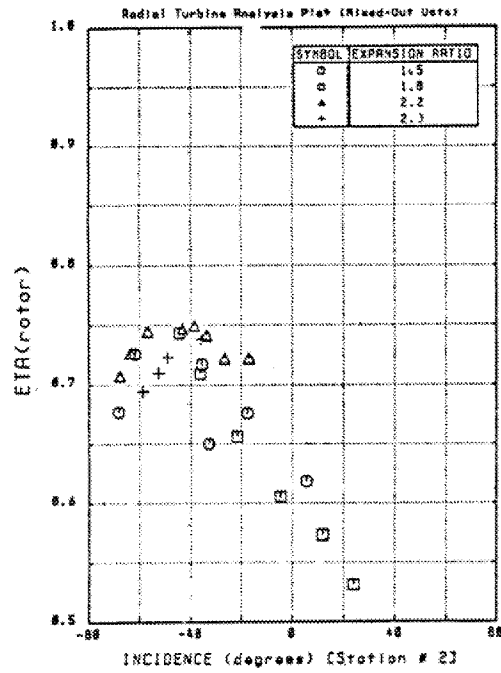


Figure 24c. Rotor efficiency versus incidence, Case B.

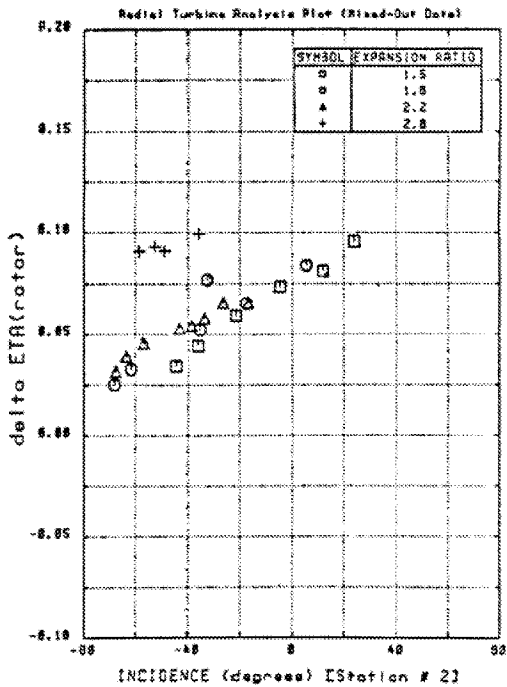


Figure 25. Rotor passage efficiency with $1/2W_n^2$ removed using $\beta_{optimum} = -40^\circ$. Note near constancy of $er=2.8$ data; for lower er 's, a different $\beta_{optimum}$ is needed, Case B.

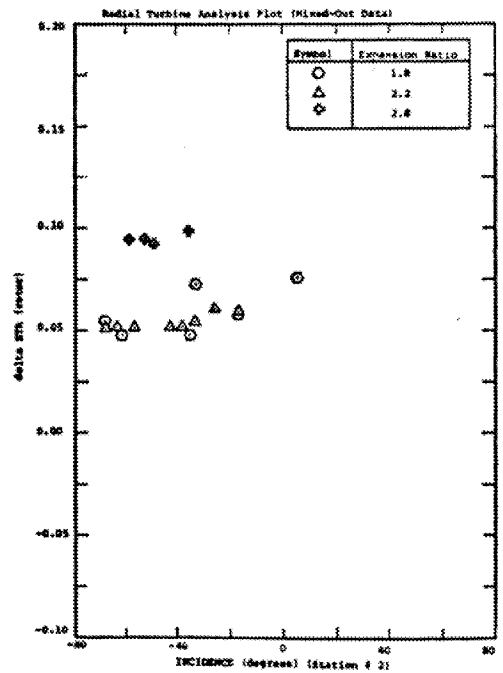


Figure 26. Rotor passage losses with variable β_{opt} per text, Case B.

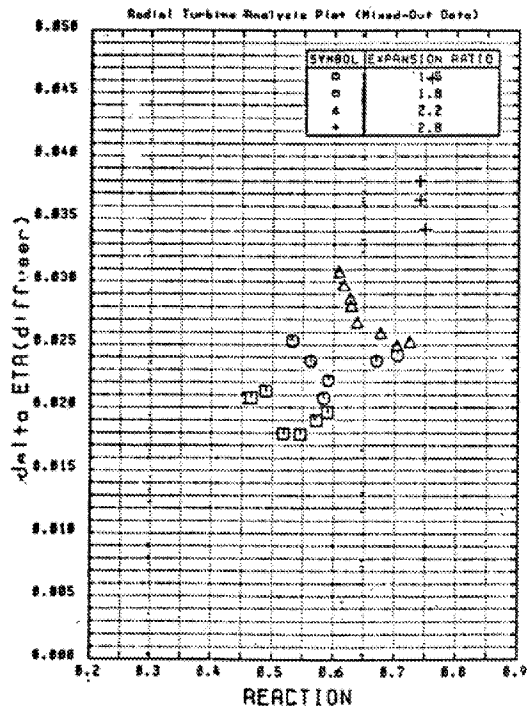


Figure 27. Computed exhaust diffuser efficiency decrement; Case B. Note that there is no Case A by definition.

In turn, the exhaust diffuser losses are computed and only the Case B results can be displayed (by definition Case A ignored the question). It will be observed that estimated losses through the exhaust diffuser are between approximately two and four points of stage efficiency. This is a modest loss and corresponds to a rather short diffuser. The leaving kinetic energy from the diffuser is displayed, in terms of stage efficiency, in Figure 28 for Case A and Case B. In this case, the results are understandably quite close together. Approximately two points of stage efficiency exist in kinetic energy at the diffuser exit. This does not mean that the diffuser performed well.

Additional studies were made to understand the performance of the exhaust diffuser. After correcting the static pressure distribution at Station 4 to a realistic level based on the existence of swirl, and back calculating to a sensible average value at Station 3, both static pressure recovery and total pressure loss for the diffuser could be computed. These are shown in Figures 29 and 30, respectively, plotted versus the swirl angle. A tight data variation is obtained and it is reasonably consistent with good diffuser performance as a function of inlet swirl (see Japikse (1999) [7]). Parameters can be plotted versus each other in a very important relationship where total pressure loss is related to static pressure recovery following the relationship of $K = C_{p_i} - C_p$ (see Japikse, 1984 [8]). These data are shown in Figure 31 for the present diffuser. Lines of constant diffuser effectiveness are shown as rays emanating from the virtual origin and three lines corresponding to 0.2, 0.33 and 0.5 for diffuser effectiveness are shown. It is clear that this diffuser has an effectiveness between approximately 0.2 and 0.4. Based on the carefully measured values of p_3 and p_4 with deduced corrections for the static pressure profile across the flow field, it appears that reasonable pressure levels have been established and sensible calculations of C_p have been achieved. It may be definitely concluded that the diffuser is recovering, even with the very erratic inlet total pressure distribution (see Fig. 11), static pressure, and swirl angle distribution. However, the very low diffuser effectiveness, 0.2 to 0.4, is surely amongst the lowest levels of diffuser recovery of any common industrial diffuser (note: a classic Borda-Carnot sudden expansion mixing has a peak diffuser effectiveness of 0.667).

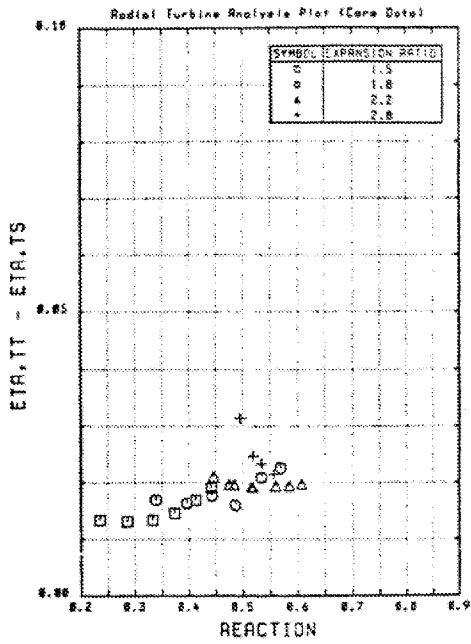


Figure 28a. Diffuser leaving loss (difference of stage total and static efficiencies), Case A.

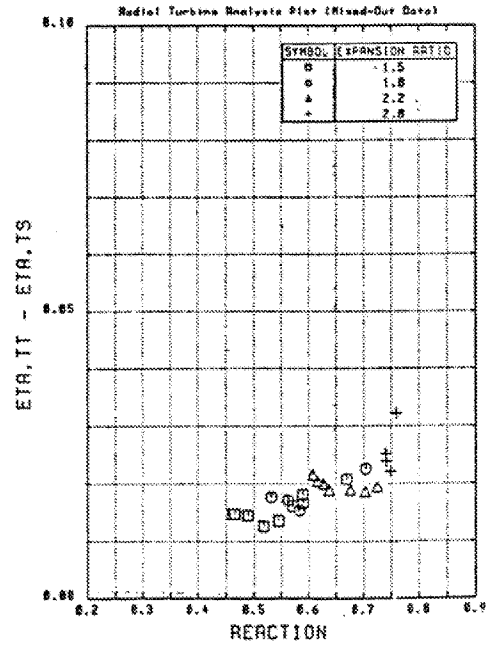


Figure 28b. Diffuser leaving loss (difference of stage total and static efficiencies), Case B.

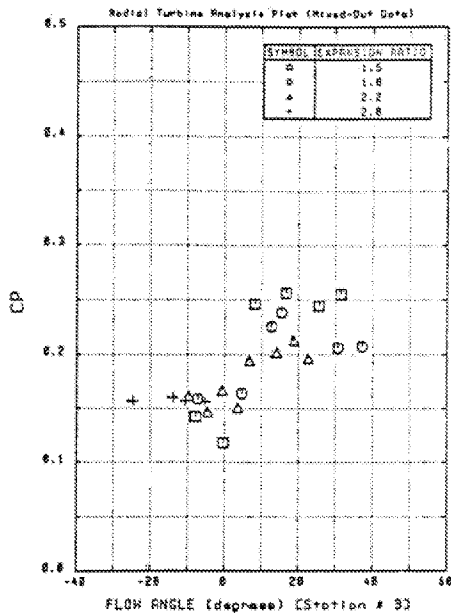


Figure 29. Diffuser pressure recovery versus α_3 , Case B.

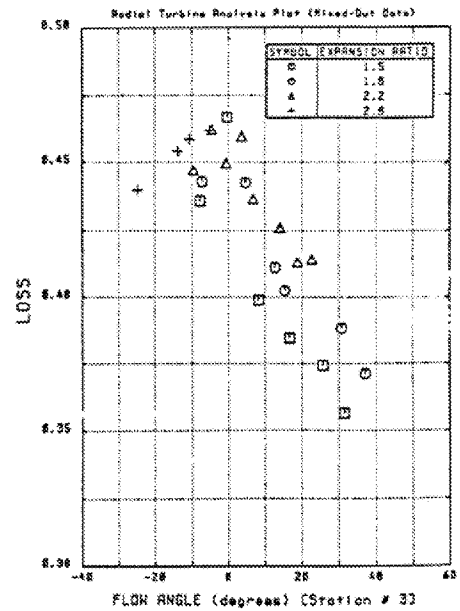


Figure 30. Diffuser loss coefficient versus α_3 , Case B.

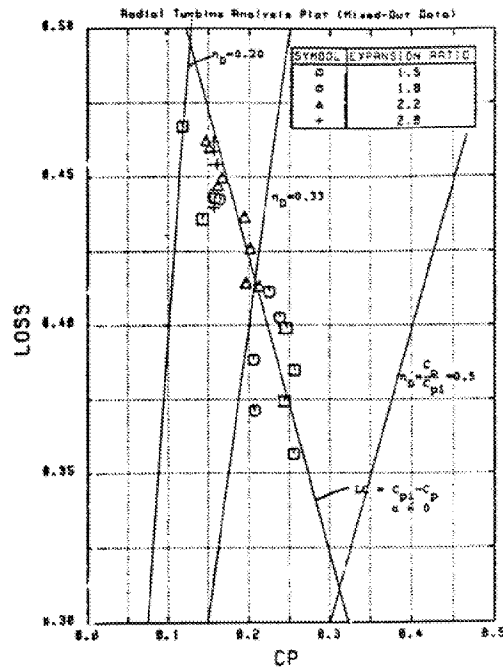


Figure 31. Exhaust diffuser loss versus recovery, Case B.

The determination of aerodynamic blockage at several key points in the stage was an important outcome of the present investigation. In order to calculate the sudden expansion Borda-Carnot mixing loss at Station 2, the local static pressure, total pressure, swirl angle (for the core flow) plus conservation of mass and total temperature were used to close the continuity equation and obtain a local blockage factor. This has been done for Case B as shown in Figures 32a and 32b. In Case A, only the blockage was calculated without any mixing calculation; in Case B the actual mixing calculation was conducted. It would be observed that the level of estimated blockage is definitely affected by the modeling approach employed and that the blockage is on the order of 50%, a result which is not too surprising when one considers the general character of this flow field. It is interesting, however, that there is a minimum at a reaction of approximately 0.65. The same results were also considered with blockage versus flow angle as shown in Figures 33a and 33b for Cases A and B, respectively. Although no definitive trend is shown, an examination of the Case B results suggest that perhaps there could be some parametric variation implied as a family of trend lines through the data sets. This has not been ascertained as yet, but would be an area for further investigation.

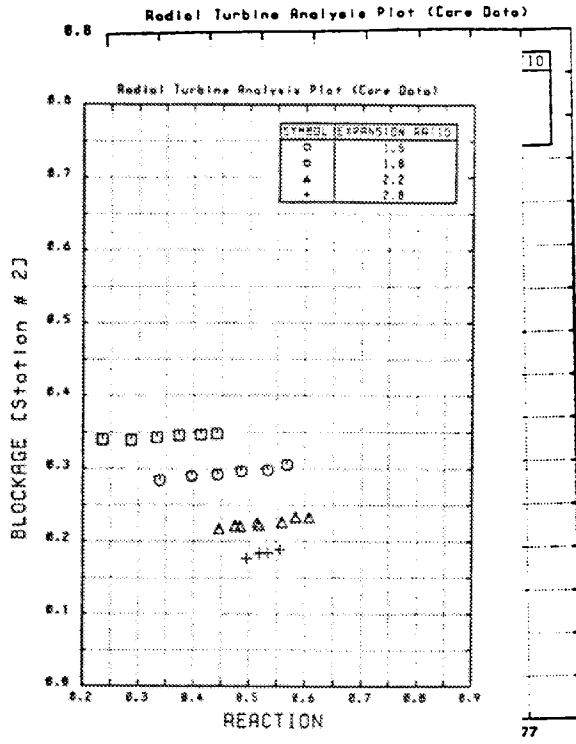


Figure 32a. Volute exit blockage, Case A.

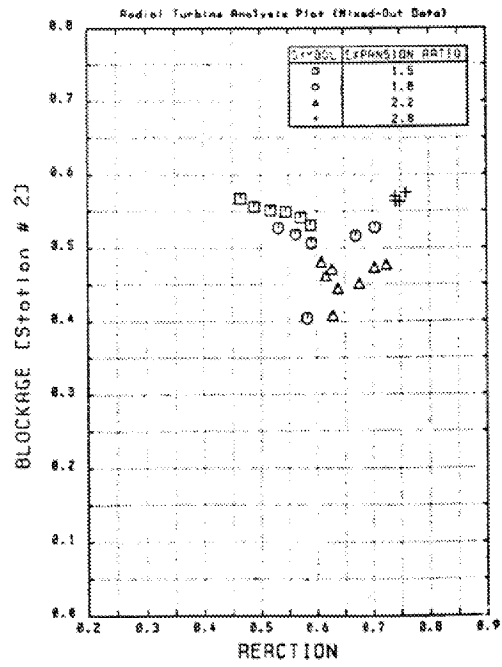


Figure 32b. Volute exit blockage, Case B.

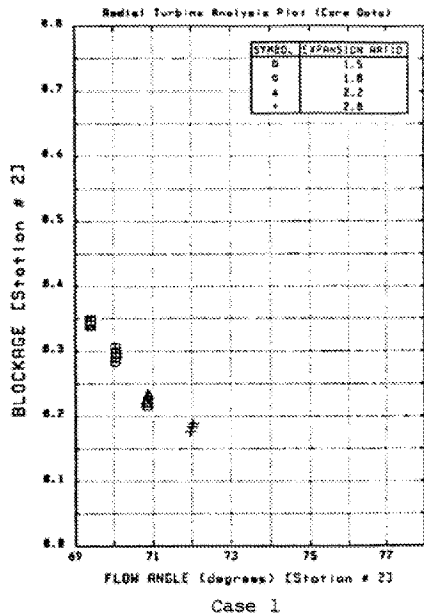


Figure 33a. Volute exit blockage as a function of volute exit swirl angle, Case A.

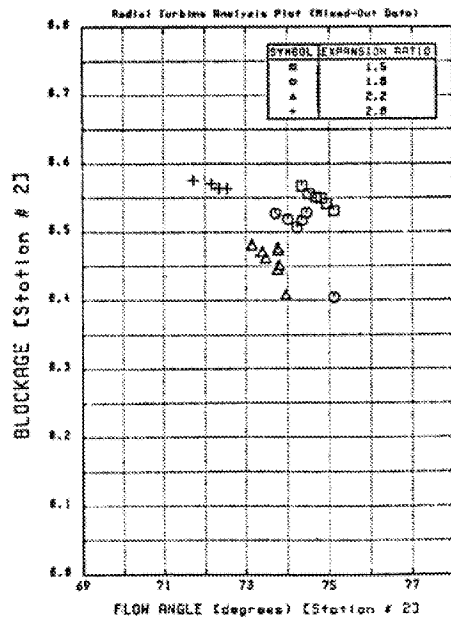


Figure 33b. Volute exit blockage as a function of volute exit swirl angle, Case B.

The efficiency of the volute alone can also be computed and is displayed in Figures 34a and 34b as a function of reaction and U/C_0 , respectively. As with other parameters, optimum values at approximately 0.6 and 0.72, respectively, have been observed. Again, reaction gives a better overall correlation of the variables. Likewise, a swirl coefficient can be defined for the volute as shown in Figures 35a and 35b when reaction and U/C_0 are used as plotting parameters. Once again, reaction has given a slightly superior modeling parameter.

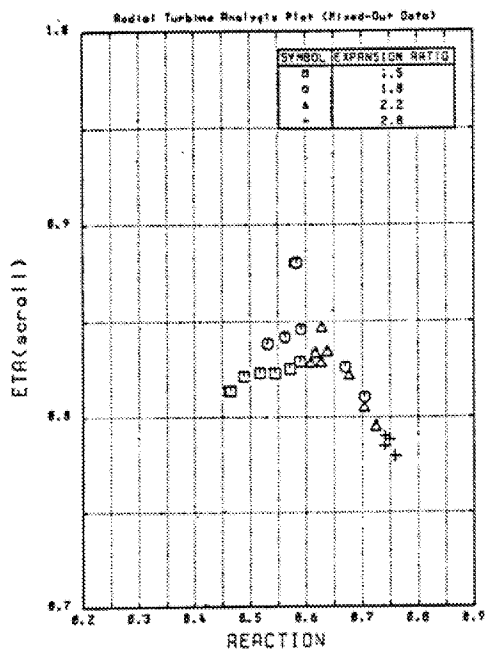


Figure 34a. Scroll efficiency versus reaction, Case B.

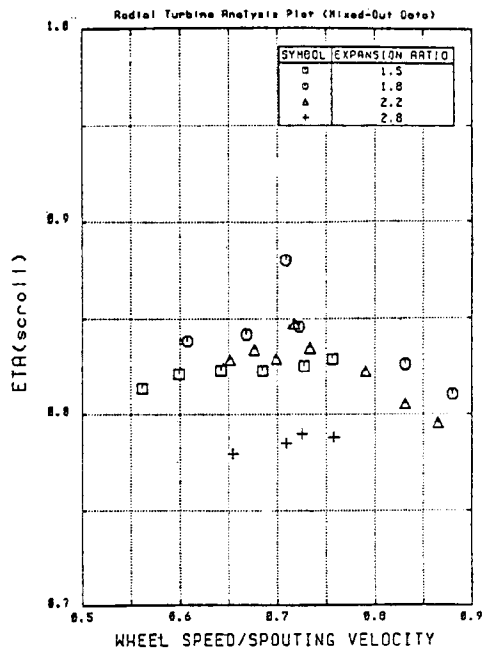


Figure 34b. Scroll efficiency versus U/C_0 , Case B.

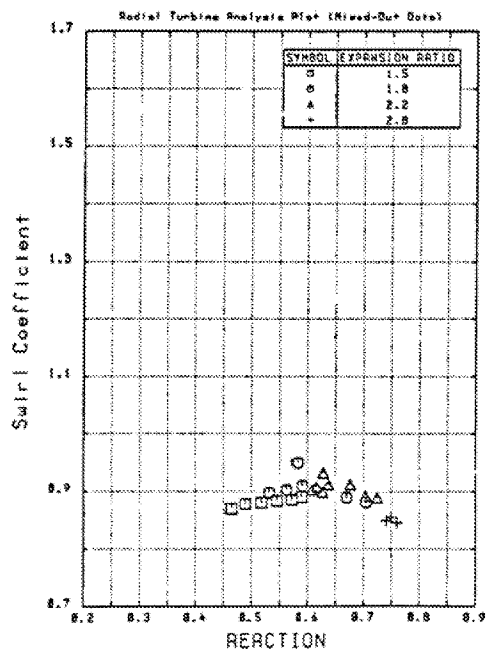


Figure 35a. Scroll swirl coefficient versus reaction, Case B.

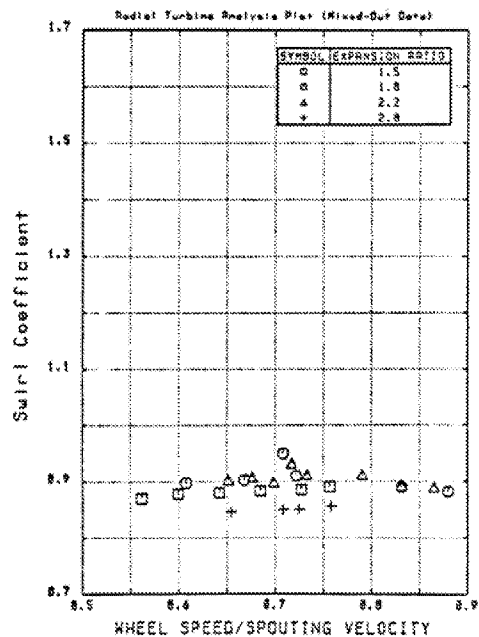


Figure 35b. Scroll swirl coefficient versus U/C_0 , Case B.

Finally, it is interesting to compare important modeling parameters from before the investigation with revised estimates after the investigation. Figure 4 showed the trial calculations that were made before tests were conducted in order to estimate important trends for future study. Table 3 displays a few of the important modeling parameters which were used both before and after the test series to model the stage. It may be seen that the original estimates of many test parameters were only nominally correct based on prior existing technical data. Indeed, having carefully measured internal parameters and then refining the levels of rotor efficiency, diffuser pressure recovery, swirl coefficient and other parameters forced us to realize the important trade-off between the different variables and the necessity of measuring internal flow states in order to define these with reasonable rigor.

| Parameter | Measured Value | Original "Estimate" (Before Testing) |
|-----------------------------|----------------------------|---|
| η_{scroll} | 0.825 ± 0.025 | N/A |
| SC | 0.90 ± 0.02 | 0.85 |
| B_1 | 0.06 ± 0.02 | 0.20 |
| $\beta_{2 \text{ optimum}}$ | -45° to -55° | -10° to -20° |
| η_{rotor} | 0.725 ± 0.025 | 0.82 to 0.98 |
| C_{pD} | 0.20 ± 0.05 | 0.30 |

5. CONCLUSIONS

Based on the work presented herein, a number of important conclusions have been reached for this study. They may be summarized as follows:

1. Accurate measurements of stage and component performance can be achieved by thorough instrumentation of a radial inflow turbine stage including flow field traverses at the impeller inlet, and the impeller or diffuser discharge, supplemented with static pressure taps at impeller tip, the impeller exit, and the diffuser exit, as well as the inlet station, augmented with inlet total pressure total temperatures upstream of the volute inlet and downstream total temperatures following a Koch mixer. By operating in sensible ranges of inlet temperatures, very accurate measurements of the work input can be achieved with a thermally calibrated rig.
2. Traversing the rotor exit requires measuring the static pressure distribution as well as the total pressure distribution and the yaw angle pressure distribution. At least six circumferential positions are recommended.
3. Reaction serves as an excellent correlating parameter for the various overall and internal parameters characterized in the performance of this radial inflow turbine stage. The alternative parameter, U/C_o , is also an excellent parameter that did not collapse data as well as reaction level.
4. Breaking the component losses into isentropic incremental efficiency decrements is a good way to examine sub-component performance.
5. The historical incidence loss model, which debits the impeller for a loss in proportion to the normal component of inlet relative velocity-based kinetic energy, offset by some optimum angle, appears to work sensibly for an important part of the impeller loss process. However, a preferred value of β_{optimum} has not been established and values for β_{opt} vary substantially, easily in the range of -40° to -60° for this study. Further investigations concerning the condition of unloading the impeller blade at inlet need to be conducted, both experimentally and analytically with CFD.

6. The volute can be well modeled with a nominal isentropic efficiency of 0.825 ± 0.025 with a modest variation with reaction or U/C_0 . It also has a swirl coefficient of approximately 0.9 ± 0.02 . These modeling parameters could likewise be deduced for a number of other stages if good data are taken and overall modeling parameters could consequently be correlated with additional geometric variations considered in the database. Inlet blockage for the volute is approximately $6 \pm 2\%$.
7. The exhaust diffuser definitely recovers and shows a pressure recovery coefficient of approximately 0.2 ± 0.05 . This diffuser performance corresponds to a very low effectiveness of 20% to 40%. The diffuser is operating with some useful effect even though the inlet profiles are highly distorted, even including reversed flow at inlet under certain operating conditions.

REFERENCES

1. Japikse, D., "The Comprehensive Performance Evaluation of a Radial Inflow Turbine," Creare R&D, Inc. TN-348, and Concepts ETI, Inc. TM 5, Nov. 1982.
2. Baines, N.C., "The Aerodynamic of Radial Turbines," Axial and Radial Turbines, Course Lecture Notes, Concepts ETI, Inc., Wilder, VT 1999.
3. Mizumachi, N., "A study of Radial Gas Turbines," Translation done at University of Michigan, Industry Program of the College of Engineering, IP-476, Nov. 1960.
4. Todd, C. A., Futral, S. M., "A Fortran IV Program to Estimate the Off-Design Performance of Radial-Inflow Turbines," NASA TN D-5059, March 1969.
5. Japikse, D., "Rotor Inlet Modeling For Radial Inflow Turbines," Design Data Sheet No. 3, *Turbomachinery Design Digest*, March 2, 1981.
6. Japikse, D., "Radial Turbine Design and Performance," Course Lecture Notes, Concepts ETI, Inc., Wilder, VT 1986.
7. Japikse, D. "Exhaust Energy Recovery," Axial and Radial Turbines, Lecture on Diffuser Performance, Course Lecture Notes, Concepts ETI, Inc., Wilder, VT 1999.
8. Japikse, D. (ed.), "A New Diffuser Mapping Technique – Studies in Component Performance: Part 1," ASME Paper No. 84-GT-237, Amsterdam, June 1984.

| REPORT DOCUMENTATION PAGE | | | Form Approved OMB No. 0704-0188 | |
|---|---|--|--|--|
| Public reporting burden for this collection of information is estimated to average 1 hour per response, including the time for reviewing instructions, searching existing data sources, gathering and maintaining the data needed, and completing and reviewing the collection of information. Send comments regarding this burden estimate or any other aspect of this collection of information, including suggestions for reducing this burden, to Washington Headquarters Services, Directorate for Information Operation and Reports, 1215 Jefferson Davis Highway, Suite 1204, Arlington, VA 22202-4302, and to the Office of Management and Budget, Paperwork Reduction Project (0704-0188), Washington, DC 20503 | | | | |
| 1. AGENCY USE ONLY (Leave Blank) | 2. REPORT DATE July 2001 | 3. REPORT TYPE AND DATES COVERED Conference Publication | | |
| 4. TITLE AND SUBTITLE The Tenth Thermal and Fluids Analysis Workshop | | | 5. FUNDING NUMBERS | |
| 6. AUTHORS Alok Majumdar, Compiler | | | | |
| 7. PERFORMING ORGANIZATION NAME(S) AND ADDRESS(ES) George C. Marshall Space Flight Center Marshall Space Flight Center, AL 35812 | | | 8. PERFORMING ORGANIZATION REPORT NUMBER M-1022 | |
| 9. SPONSORING/MONITORING AGENCY NAME(S) AND ADDRESS(ES) National Aeronautics and Space Administration Washington, DC 20546-0001 | | | 10. SPONSORING/MONITORING AGENCY REPORT NUMBER NASA/CP-2001-211141 | |
| 11. SUPPLEMENTARY NOTES Proceedings of a workshop held at NASA Marshall Space Flight Center, September 13-17, 1999. Workshop organizers: Jim Owen and Sheryl Kittredge of Marshall Space Flight Center. Prepared for Structures, Mechanics, and Thermal Department, Engineering Directorate | | | | |
| 12a. DISTRIBUTION/AVAILABILITY STATEMENT Unclassified-Unlimited Subject Category 34 Standard Distribution | | | 12b. DISTRIBUTION CODE | |
| 13. ABSTRACT (Maximum 200 words) The Tenth Thermal and Fluids Analysis Workshop (TFAWS 99) was held at the Bevill Center, University of Alabama in Huntsville, Huntsville, Alabama, September 13-17, 1999. The theme for the hands-on training workshop and conference was "Tools and Techniques Contributing to Engineering Excellence". Forty-seven technical papers were presented in four sessions. The sessions were: (1) Thermal Spacecraft/Payloads, (2) Thermal Propulsion/Vehicles, (3) Interdisciplinary Paper, and (4) Fluids Paper. Forty papers were published in these proceedings. The remaining seven papers were not available in electronic format at the time of publication. In addition to the technical papers, there were (a) nine hands-on classes on thermal and flow analyses softwares, (b) twelve short courses, (c) thirteen product overview lectures, and (d) three keynote lectures. The workshop resulted in participation of 171 persons representing NASA Centers, Government agencies, aerospace industries, academia, software providers, and private corporations. | | | | |
| 14. SUBJECT TERMS thermal analysis, computational fluid dynamics, numerical heat transfer, network flow analysis, thermal protection system, interdisciplinary analysis | | | 15. NUMBER OF PAGES 542 | |
| | | | 16. PRICE CODE | |
| 17. SECURITY CLASSIFICATION OF REPORT Unclassified | 18. SECURITY CLASSIFICATION OF THIS PAGE Unclassified | 19. SECURITY CLASSIFICATION OF ABSTRACT Unclassified | 20. LIMITATION OF ABSTRACT Unlimited | |